Basanta Raj Adhikari
Sreevalsa Kolathayar   *Editors*

Geohazard Mitigation

Select Proceedings of VCDRR 2021

Springer

Lecture Notes in Civil Engineering

Volume 192

Series Editors

Marco di Prisco, Politecnico di Milano, Milano, Italy

Sheng-Hong Chen, School of Water Resources and Hydropower Engineering, Wuhan University, Wuhan, China

Ioannis Vayas, Institute of Steel Structures, National Technical University of Athens, Athens, Greece

Sanjay Kumar Shukla, School of Engineering, Edith Cowan University, Joondalup, WA, Australia

Anuj Sharma, Iowa State University, Ames, IA, USA

Nagesh Kumar, Department of Civil Engineering, Indian Institute of Science Bangalore, Bengaluru, Karnataka, India

Chien Ming Wang, School of Civil Engineering, The University of Queensland, Brisbane, QLD, Australia

Lecture Notes in Civil Engineering (LNCE) publishes the latest developments in Civil Engineering—quickly, informally and in top quality. Though original research reported in proceedings and post-proceedings represents the core of LNCE, edited volumes of exceptionally high quality and interest may also be considered for publication. Volumes published in LNCE embrace all aspects and subfields of, as well as new challenges in, Civil Engineering. Topics in the series include:

- Construction and Structural Mechanics
- Building Materials
- Concrete, Steel and Timber Structures
- Geotechnical Engineering
- Earthquake Engineering
- Coastal Engineering
- Ocean and Offshore Engineering; Ships and Floating Structures
- Hydraulics, Hydrology and Water Resources Engineering
- Environmental Engineering and Sustainability
- Structural Health and Monitoring
- Surveying and Geographical Information Systems
- Indoor Environments
- Transportation and Traffic
- Risk Analysis
- Safety and Security

To submit a proposal or request further information, please contact the appropriate Springer Editor:

- Pierpaolo Riva at pierpaolo.riva@springer.com (Europe and Americas);
- Swati Meherishi at swati.meherishi@springer.com (Asia - except China, and Australia, New Zealand);
- Wayne Hu at wayne.hu@springer.com (China).

All books in the series now indexed by Scopus and EI Compendex database!

More information about this series at https://link.springer.com/bookseries/15087

Basanta Raj Adhikari · Sreevalsa Kolathayar
Editors

Geohazard Mitigation

Select Proceedings of VCDRR 2021

Springer

Editors
Basanta Raj Adhikari
Department of Civil Engineering
Institute of Engineering, Tribhuvan
University
Kathmandu, Nepal

Sreevalsa Kolathayar
Department of Civil Engineering
National Institute of Technology Karnataka
Mangalore, India

Preface and Acknowledgements

The active tectonics in the earth not only formed different kinds of geomorphic features but also created numerous geohazards in the world. Similarly, the combined effect of climate change and anthropogenic activities has also triggered many landslides, floods, storms, etc. Therefore, geohazard investigation and management is very important for the resilience infrastructure development and settlements. This book presents the select proceedings of the Virtual Conference on Disaster Risk Reduction (VCDRR 2021). All the papers in this volume are segregated into three clusters, e.g., multi-hazard assessment, landslide hazard assessment and mitigation and geotechnical engineering. The book is also a comprehensive volume on multi-hazards and their management for a sustainable built environment.

We thank all the staff of Springer for their full support and cooperation at all the stages of the publication of this book. We express our sincere thanks to the authors and reviewers for their contribution. We believe that these research papers provide new developments in the field of geohazard assessment and mitigation that will be useful for scientists, practitioners, engineers, policymakers and government officials for their activities related to geohazard investigation and management. The comments and suggestions from the readers are most welcome.

Kathmandu, Nepal   Basanta Raj Adhikari
Mangalore, India   Sreevalsa Kolathayar
September 2021

Contents

Geotechnical Engineering

About the Editors

Dr. Basanta Raj Adhikari is currently Asst. Professor, Department of Civil Engineering, Pulchowk Campus, Institute of Engineering, Tribhuvan University, Nepal. Dr. Adhikari has research interests in the tectonics of the Himalayas, climate change, hill-slope movement and human interaction, Himalayan sediment flux generation, and disaster risk reduction. He is the author of more than 40 scientific papers and book chapters and received various recognitions for his work in the field of earth science i.e. Young Scientist (Integrated Research on Disaster Risk), "young affiliates" (The World Academy of Sciences) and Sichuan 1000 Talents (Sichuan Province, China).

Dr. Sreevalsa Kolathayar pursued M.Tech. from IIT Kanpur, Ph.D. from Indian Institute of Science (IISc) and served as International Research Staff at UPC BarcelonaTech Spain. He is presently faculty in the Department of Civil Engineering, National Institute of Technology Karnataka, Surathkal, India. Dr. Sreevalsa has authored ten books and over 80 research papers. He is Associate Editor of two International Journals. His research interests include Geotechnical Earthquake Engineering, Seismic Hazard and Risk, Landslides, Disaster Risk Reduction, Reinforced earth and Water Geotechnics. In 2017, The New Indian Express honoured Dr. Sreevalsa with South India's Most Inspiring Young Teachers Award. He is the recipient of ISET DK Paul Research Award from Indian Society of Earthquake Technology in 2018. He is in the roster of two technical committees of ASCE Geo-Institute. He received "IEI Young Engineers Award" by The Institution of Engineers (India), in recognition of his contributions in the field of Civil Engineering. Recently Dr. Sreevalsa was featured by the American Society of Civil Engineers in their Geostrata Magazine.

Geohazard Investigation and Management: An Introduction

Basanta Raj Adhikari, **Varun Menon**,
and **Sreevalsa Kolathayar**

1 Introduction

Earth is a dynamic planet and experienced different kinds of tectonic activities. Different continents have moved to different directions due to different tectonic plate boundaries. The divergent plate boundaries play an important role to divert the tectonic plates whereas convergent plate boundaries formed different kinds of mountain chains, i.e., the Himalayas, Andes, rocky mountain, etc. These active tectonics not only formed different geomorphic features but also created numerous geohazards in the world. Similarly, the combined effect of climate change and anthropogenic activities have also triggered many landslides, floods, drought, and storms. Understanding of risk caused by geohazards and sharing information is very important in the present context. The use of recent investigation techniques to understand the dynamics and magnitude of geohazards gives us a better understanding of their extent and effects. The recent development of remote sensing techniques such as radio detection and ranging (RADAR) and interferometric synthetic aperture radar (InSAR) has provided opportunities for ground motion detection and monitoring. Similarly, the integration of laboratory-based physical modeling and numerical modeling has provided a new horizon of geohazard analysis for the prediction and establishment of early warning systems.

This book includes mainly three sections. The multi-hazard assessment section consists of different examples including liquefaction, landslide dam failure, reservoir sedimentation, forest fire, pyroclastic deposits, land cover changes, and landscape change due to deep excavation. The landslide hazard assessment section

B. R. Adhikari (✉)
Department of Civil Engineering, Pulchowk Campus, Institute of Engineering,
Tribhuvan University, Lalitpur, Nepal
e-mail: bradhikari@ioe.edu.np

V. Menon · S. Kolathayar
National Institute of Technology Karnataka, Surathkal, India

covers a wide range of assessment techniques including landslide–structure inter-action, landslide susceptibility analysis, co-seismic landslides, numerical investi-gation of soil–structure interaction, and prediction of landslides for the establishment of an early warning system. Similarly, the research papers in the geotechnical engineering technique section demonstrate different good investiga-tion techniques including site amplification using borehole and surface data, assessment of soil gas radon (Rn22) for the identification of precursors to impending earthquakes, dynamic analysis of soil reinforced with polypropylene geotextile, cushion effect in unconnected piled raft foundation, and direct shear strength of natural rock joints. We believe that these research papers provide new developments in the field of geohazard assessment and mitigation that will be useful for scientists, practitioners, engineers, policymakers, and government officials for their activities related to geohazard investigation and management.

2   Multi-hazard Assessment

There are varieties of natural and man-made disasters that are included in this section. Krishnan and Shukla have explained the use of colloidal silica at various percentages for improving the hydraulic conductivity of the sand used for the barrier materials that could give better chances for liquefaction mitigation in their paper titled *Rheological Characteristics of Sand Stabilized with Colloidal Silica for Barrier Material and Liquefaction Mitigation*. The study also revolves around the gel time and viscosity of the colloidal silica. Also, the use of colloidal silica has been backed up with previous studies conducted in the same field by other researchers [10, 26]. As per Sumanth and Govindaraju, in their paper titled *A Study on Liquefaction Susceptibility of Earthen Dams* explains how the liquefaction can affect such massive structures like earthen dams and the importance of ground improvement techniques that could give an edge against the failures that might occur in the filters and drains provided in the earthen dam structures. A typical earthquake data has been chosen for this current work with the help of a previously recorded earthquake of 6.9 magnitudes. And the model has been selected from a previously conducted study [28].

The paper titled *Evaluation of the Effectiveness of Flexible Debris Flow Barriers for Control of Huaycos Using Satellite Images and GIS, in the Basin of Rímac River, Perú* authored by Domínguez et al. discusses the debris flow barriers installed at the Quirio, Carossio, and Castilla creeks with use of satellite imagery and GIS software. It seems sometimes the data obtained through satellite imageries may be incomplete, and still, it is one of the methods that can be adopted when the field data collection is not possible [1]. The debris flow barriers provided safety to human life and being used now for further research. The dike breach in Tokke River in Saitama prefecture due to the after-effects of typhoon Hagibis in 2019 has been studied by Wickramasinghe and Tanaka in their paper titled *Investigation of Flow Structures Along the Embankment Generated Nearby Finite Riparian Vegetation.*

The study involves a series of flume experiments to simulate the effects in the flood embankment. There is a lot of supporting research on river hydrodynamics and wetland management to support the relation between riparian vegetations and fluvial systems that give the importance of this study [11, 12]. Dimri et al. in their paper titled *Sediment Yield Estimation and Reservoir Sedimentation Assessment Using Geospatial Tools: A Case Study of Tehri Dam Reservoir* discuss using software like ArcGIS with integrating Revised Universal Soil Loss Equation (RUSLE [24]) relation to investigating the sediment yield at Tehri Dam. The remote sensing and GIS techniques were successfully implemented for finding the sediment yield in this paper. In the paper titled *Stress and Deformation Analysis of Ground Subjected to Deep Excavation in Sandy Soil—A Man-Made Disaster* by Abhirami and Karthikeyan, the deep excavation techniques have been discussed, and the use of finite element software such as PLAXIS 3D has been elaborated in this paper. The soil parameters and material properties have been taken from previously conducted research [16]. This study promotes the use of strutted excavation rather than the use of retaining wall structures to reduce building damage [25]. Ahmed et al. have explained the various possible geohazards that might occur in the capital of Sudan in their paper titled *Khartoum Geo-hazard: An Assessment, and a Future Warning*. This paper deals with multi-hazards like flooding, earthquake, and liquefaction. Modern study methods like land use maps and satellite images were used to identify the climate change patterns and rainfall distributions in the area [8]. GIS has been one of the most used software for studying land-use patterns and hazard-prone areas in modern engineering practices. Zaheer et al. have investigated the soil erosion of the Sirajganj district in Bangladesh in the paper titled *Assessment of Land Use and Land Cover Changes on Soil Erosion in Sirajganj: A GIS and Remote Sensing-Based Approach*. Soil erosion can cause changes in the land-use pattern that could affect the ecosystem [23]. These methods seem to come helpful in times of pandemic when there will not be any possibilities for land surveys and soil tests. In the paper titled *A Study on Liquefaction Susceptibility of Road Infrastructure in Surat City* by Thakur et al., different locations were selected around the city of Surat to conduct various field assessments to determine the possibilities of liquefaction induced hazards. This study focuses on site-specific characteristics rather than laboratory experimentation as the former results seem to be dominant [15]. Froehlich studied the prediction of landslide dam outbursts with the 42 historical data on outburst floods in his paper titled *Predicting Landslide Dam Outburst Flood Peak Discharge*. The study focuses on a prediction equation based on the blockage types defined in earlier works [9]. In the paper titled *Subsidence Detection Using Persistent Scatterer Interferometry* authored by John and Sabu, the use of InSAR techniques [19] such as persistent scatterer interferometry (PSI) that can able to monitor the deformation of the ground is explained. Images are processed using SARproz software to study the area of Cochin international airport to identify the subsidence proneness of that area. Sinkholes are yet another natural hazard that may occur in the river banks that will attack the stability of the river bank due to the formation of the lateral flow [22]. Duong in his paper titled *Studying the Time-Dependent Reliability Index of the Riverbank Instability—*

A Case Study of the Vam Nao River Subjected to a Sinkhole, for predicting the time of riverbank instability for the Vam Nao River, the time-dependent reliability analysis is studied and identifies the severity of hazards of this location. In the paper titled *On the Features of Pyroclastic Deposits and Post-Eruption Natural Hazards*, Moscariello et al. compared the volcanic deposits derived from the eight volcanoes based on their physical properties. The paper deals with the post-eruption hazards that could occur like the slope stability problems due to the infiltration of rainfall and liquefaction in the area. The most recent natural hazards are also described and the physical and hydromechanical properties are also collected.

3 Landslide Hazard Assessment and Mitigation

Landslide is one of the major disasters of this century. One of its reason being the rainfall [5], Sumalatha recommends the use of software such as GEO5 to differentiate methods of slope stability improvement in her paper titled *Slope Stability Analysis Using In-Situ Ground Reinforcement Techniques for a Landslide Prone Area at Madikere, India*. The landslide-prone area located at Makkandur, Karnataka State, India, was studied to know the effect of in-situ ground reinforcement on the stability of existing slopes at this location in this study. A paper titled *Landslide Susceptibility Mapping Using GIS-Based Frequency Ratio Approach in Part of Kullu District, Himachal Pradesh, India* by Sujeewon and Sarkar uses GIS-based frequency ratio approach to study these regions and prepare a landslide susceptibility map based on factors such as slope, aspect, curvature, lithology, distance to roads, distance to faults/lineaments, distance to drainage, land use/land cover, and elevation. Manzoor et al. conducted a case study incorporating analysis software such as GEO5 to study the slopes on Sonmarg highway of J&K, India, in the paper titled *Evaluation and Remedial Measures for Unstable Slopes at Gagangir Sonmarg, J&K: A Case study.* This paper also includes the possible remedial measures for the unstable slopes of the selected site. The paper titled *Probabilistic Stability Analysis of Helical Soil Nailed Wall Using the Monte-Carlo Simulation* by Agarwal et al. used Monte-Carlo simulation, which is a prediction tool for estimating the risk and uncertainty in an event. The study is focused on developing an economical design for helical soil nailed walls. Many ground improvement techniques can be used for slope stabilization that will protect the slope against landslides. Gupta et al. emphasize the use of geogrids for slope protection in the paper titled *Effect of Geogrid on Landslide Prevention of Soil Slope Under Static Loading*. The geogrids can be used to increase the bearing capacity of soil and rock [21]. The paper focuses on the use of geogrids wraparounds to improve the bearing capacity of soil and the challenges posed by them. The use of digital elevation models (DEM) and lithological maps are a highlight of this study. The map prepared can be used by the authorities in the future to identify the most hazard-prone areas and focus their efforts to protect human life in these regions in case of any impending disaster. A similar study has been conducted by Jibran et al. in the paper

titled *Landslide Susceptibility of Madanpura (FatehpurSikri, Agra in Vindhyan hills, India) Using Arc GIS*. Here, the study area is selected as Madanpura, Agra, India. The best solution for an early evacuation to protect the life would be to get an early warning. Wanare et al. in their paper titled *Recent Advances in Early Warning Systems for Landslide Forecasting* focus on an extensive review of the current early warning systems in place to find out the probability of a landslide. Reshma et al. in their paper on *Numerical Modelling of Mechanically Stabilized Earth Walls for Slope Protection* communicate about the use of geosynthetics in the development of slope protection work. The researchers have used finite element analysis using software like PLAXIS 2D to conclude that the use of geosynthetics considerably affects the slope protection work. Mugesh and Pandit conducted a review on the landslides triggered by the earthquake in their paper on *Earthquake Induced Landslides in the Indian Himalayas and Glimpses of Code Provisions for Seismic Design of Slopes: A Review*. Especially in the region like the foothills of the mountains, landslide induced by the earthquake is a significant threat to human life [27]. The paper includes some case studies and the geological structure of the landslide materials. The paper titled *Numerical Investigation of Soil-Structure Interaction Behaviour of Landslide Prevention Piles* authored by Sreelakshmi and Asha uses a finite element software called ADONIS to study the soil–structure interaction. The use of anchored sheet pile walls is highly promoted in this study. The role of rainfall is very predominant in the case of a landslide [17]. The paper titled *Antecedent and Cumulative Rainfall as Thresholds in Detecting Possible Landslide Occurrence* authored by Khalid et al. deals with the importance of antecedent rainfall, and cumulative rainfall in case of triggering the landslide has been studied and recommended to use this as a threshold value for further research.

4 Geotechnical Engineering

This chapter mainly includes a versatile version of hazards around us in the geotechnical domain. In the paper titled *Assessment of Site Amplification Using Borehole and Surface Data: Variability of Site Effect Estimation from Different Phases of the Accelerogram* by Kumar et al., horizontal-to-vertical spectral ratio [20] has been used to find the site amplification and this can be helpful to identify the seismic hazard potential of the region. The paper titled *Effects of Complex Valley Topography on De-Amplification Scenerio for SH-Waves* by Kumar et al. studies the SH wave propagation along with different sub-valley models and how the de amplification and duration is affected by the complexity in the model. In another research, the radon emission from the soil has been studied to correlate it with the earthquake magnitude in the state of Gujarat, India. It seems to correlate with the earthquakes of medium magnitude with respect to the temporal evolution of the momentary energy of radon in the paper titled *Assessment of Soil Gas Radon (Rn222) emission in Kachchh, Gujarat, India: Influence of Meteorological Parameters and Identification of Precursors to Impending Earthquakes* by Sahoo

and Rao. This kind of research is going on all around the globe [2, 7, 13]. Tunneling is yet another very important aspect in the infrastructural development of a transportation system that comes in the geotechnical engineering domain. *Ground Responses due to the Effect of Tunnelling in Sandy Soil* by Ramasamy and Karthigeyan uses the finite element tool called PLAXIS 3D to analyze the significance of a tunnel system through the sandy soil. PLAXIS 2D is also a finite element tool with which Baburaj et al. have conducted a study titled *Dynamic Analysis of Soil Reinforced with Polypropylene Geotextile Using PLAXIS.* The use of geotextile materials is very popular in the geotechnical industry [14]. This study highlights the cost effectiveness of using geotextiles to machine foundations. PLAXIS 2D is a very vastly used geotechnical engineering finite element software by academicains, students, as well as industry in the modern era. *Numerical Analysis of Soil Nailed Vertical Wall Using PLAXIS* by Sreedevi et al. emphasize just that. The versatility of the software is that the user has the freedom to try the different combinations of ground improvement techniques to finally come up with the economical solution. Another one of the software that is very popular in the civil engineering industry is ANSYS [6]. Vinay et al. in their paper titled *Dynamic Soil-Structure Interaction Effects in Integrated Retaining Wall-Building System* use this software to create different models and analyze the retaining structure with different shear wave velocities to find out the better technique for the buildings with different levels. Software analysis is only one side of the research methodology, and the laboratory experimentation is also important where the parameters cannot be quantified to simulate in a software environment. *Laboratory Model Study on Erosion Control Using Coir Geotextile* by Muthukumar et al. shows the use of hydraulic flumes to simulate the real-world conditions while heavy rainfall inside a laboratory to study the importance of the use of natural fiber geotextiles such as coir to reduce soil erosion. Natural fiber is a very economical way to make geotextiles, and previous studies support the use of coir as geotextile [18]. The paper titled *Recent Innovations and Practices in Geotechnical Engineering for Sustainable Infrastructure Development* by Dalal et al. conducted a detailed review to highlight the recent innovations and practices in geotechnical engineering. Amalu and Jayalekshmi conducted a study on unconnected piled raft foundation systems to identify the controlling parameters in a cushion layer in the paper titled *Analysis of Cushion Effects in Unconnected Piled Raft Foundation.* The major implications of this work are for multi-storied building foundations. In the paper titled *Development of Innovative Soil Nails Using Recycled Plastic and C&D Waste in Nilgiris District for Slope Upgradation Works Using Slide program* by Perumal and Sreedevi, a software called SLIDE2 is used to compare the results obtained from the laboratory experimentations. Also, the recommended soil nails are made with recycled plastic waste, which will provide better durability and economy. Slope protection is recommended against the landslide in the Nilgiri district of Tamilnadu, India. The paper titled *Efficacy of Pervious Concrete Columns Vis-a-vis Stone Columns in Sandy Strata in Mitigating Liquefaction* by Rashma et al. focuses on the seismic performance of the pervious concrete columns in place of stone columns as a better means of liquefaction mitigation. *Direct Shear Strength of Natural Rock Joints* by

Bhardwaj and Rao shows the co-relation of the joint surface roughness of sandstone to the different joint shear criteria [3, 4] and assesses the joint roughness values on shear strength of natural rock joints.

5 Summary

The Sendai Framework of Disaster Risk Reduction (SFDRR) has spelled out its priority one to understand the risk. The other global agenda such as Sustainable Development Goals, Addis Ababa Action Agenda, Agenda for Humanity, New Urban Agenda, Paris Agreement, and 2030 agenda also stressed to understand the systemic risk. It is of utmost necessity to investigate geohazards and their management for sustainable development. This chapter summarizes the contents of the book titled geohazard investigation and management. All the chapters in this volume are segregated into three sections and hope to include the gist of this book for the readers. The geohazards can come in any form or shape, but the scientific and engineering community in our world is always ready to tackle any obstructions that come our way. The sharing of this knowledge will give them the wisdom to do so.

References

1. Alharbi, T., Sultan, M., Sefry, S., et al.: An assessment of landslide susceptibility in the Faifa area, Saudi Arabia, using remote sensing and GIS techniques. Nat. Hazards Earth Syst. Sci. **14**, 1553–1564 (2014). https://doi.org/10.5194/nhess-14-1553-2014
2. Arora, B.R., Kumar, A., Walia, V., et al.: Assesment of the response of the meteorological/hydrological parameters on the soil gas radon emission at Hsinchu, northern Taiwan: a prerequisite to identify earthquake precursors. J. Asian Earth Sci. **149**, 49–63 (2017). https://doi.org/10.1016/j.jseaes.2017.06.033
3. Barton, N.: Review of a new shear-strength criterion for rock joints. Eng. Geol. **7**, 287–332 (1973). https://doi.org/10.1016/0013-7952(73)90013-6
4. Barton, N., Choubey, V.: The shear strength of rock joints in theory and practice. Rock Mech Felsmechanik Mecanique des Roches **10**, 1–54 (1977). https://doi.org/10.1007/BF01261801
5. Bishop, A.W.: The influence of an undrained change in stress on the pore pressure in porous media of low compressibility. Géotechnique **23**, 435–442 (1973). https://doi.org/10.1680/geot.1973.23.3.435
6. Cakir, T.: Finite element based investigation of backfill effects on seismic behavior of a cantilever wall. Proc. Earth Planet Sci. **15**, 231–236 (2015). https://doi.org/10.1016/j.proeps.2015.08.056
7. Chambers, S.D., Hong, S.-B., Williams, A.G., et al.: Characterising terrestrial influences on Antarctic air masses using Radon-222 measurements at King George Island. Atmos. Chem. Phys. **14**, 9903–9916 (2014). https://doi.org/10.5194/acp-14-9903-2014
8. Davies, H.R.J., Walsh, R.P.D.: Historical changes in the flood hazard at Khartoum, Sudan: lessons and warnings for the future. Singap. J. Trop. Geogr. **18**, 123–140 (1997). https://doi.org/10.1111/1467-9493.00012

9. Fan, X., Dufresne, A., Siva Subramanian, S., et al.: The formation and impact of landslide dams—state of the art. Earth-Sci. Rev. **203**, 103116 (2020). https://doi.org/10.1016/j.earscirev.2020.103116

10. Gallagher, P.M., Koch, A.J.: Model testing of passive site stabilization: a new grouting technique. In: Grouting and Ground Treatment, pp. 1478–1489. American Society of Civil Engineers, Reston, VA (2003)

11. Gualtieri, C., Ianniruberto, M., Filizola, N., et al.: Hydraulic complexity at a large river confluence in the Amazon basin. Ecohydrology **10**, 1–12 (2017). https://doi.org/10.1002/eco.1863

12. Gurnell, A.: Plants as river system engineers. Earth Surf. Process Landforms **39**, 4–25 (2014). https://doi.org/10.1002/esp.3397

13. Hamada, H.: Estimation of groundwater flow rate using the decay of 222Rn in a well. J. Environ. Radioact. **47**, 1–13 (2000). https://doi.org/10.1016/S0265-931X(99)00012-0

14. Heerten, G.: Improving the bearing capacity of soils with geosynthetics, 37–55 (2007)

15. Hollander, R.D.D., Canada, G.H., Petroleum, D.: Liquefaction of sands, a collapse surface approach. Int J. Rock Mech. Min. Sci. Geomech. Abstr. **23**, 138 (1985). https://doi.org/10.1016/0148-9062(86)90748-5

16. Karthigeyan, S., Ramakrishna, V.V.G.S.T., Rajagopal, K.: Influence of vertical load on the lateral response of piles in sand. Comput. Geotech. **33**, 121–131 (2006). https://doi.org/10.1016/j.compgeo.2005.12.002

17. Kim, J., Jeong, S., Park, S., Sharma, J.: Influence of rainfall-induced wetting on the stability of slopes in weathered soils. Eng. Geol. **75**, 251–262 (2004). https://doi.org/10.1016/j.enggeo.2004.06.017

18. Lekha, K.R.: Field instrumentation and monitoring of soil erosion in coir geotextile stabilised slopes—a case study. Geotext Geomembranes **22**, 399–413 (2004). https://doi.org/10.1016/j.geotexmem.2003.12.003

19. Massonnet, D., Feigl, K.L.: Radar interferometry and its application to changes in the earth's surface. Rev. Geophys. **36**, 441–500 (1998). https://doi.org/10.1029/97RG03139

20. Nogoshi, M., Igarashi, T.: On the amplitude characteristics of microtremor (part 2). Zisin (J. Seismol. Soc. Japan 2nd Ser.) **24**, 26–40. https://doi.org/10.4294/zisin1948.24.1_26

21. Palmeira, E., Tatsuoka, F., Bathurst, R.J., et al.: Advances in geosynthetics materials and applications for soil reinforcement and environmental protection works. Electron. J. Geotech.

22. Papanicolaou, A.N., Elhakeem, M., Hilldale, R.: Secondary current effects on cohesive river bank erosion. Water Resour. Res. **43**, 1–14 (2007). https://doi.org/10.1029/2006WR005763

23. Park, S., Oh, C., Jeon, S., et al.: Soil erosion risk in Korean watersheds, assessed using the revised universal soil loss equation. J. Hydrol. **399**, 263–273 (2011). https://doi.org/10.1016/j.jhydrol.2011.01.004

24. Renard, K.G., Foster, G.R., Weesie, G.A. et al.: Predicting soil erosion by water: a guide to conservation planning with the revised universal soil loss equation (RUSLE) (1997)

25. Russo, G., Nicotera, M.V., Autuori, S.: Three-dimensional performance of a deep excavation in sand. J. Geotech. Geoenviron. Eng. **145**, 05019001 (2019). https://doi.org/10.1061/(asce)gt.1943-5606.0002037

26. Sharma, P., Krishnan, J., Shukla, S.: A feasibility study of colloidal silica as stabilizing material for passive site remediation. In: Sudheer, K.P., Kurian, B. (eds.) Singh RM, pp. 333–347. Springer, Singapore (2021)

27. Singh, K.K., Singh, A.: Detection of 2011 Sikkim earthquake-induced landslides using neuro-fuzzy classifier and digital elevation model. Nat. Hazards **83**, 1027–1044 (2016). https://doi.org/10.1007/s11069-016-2361-6

28. Sumanth, H.C., Govindaraju, L.: A comprehensive seismic slope stability assessment of earth dams. **3**, 1–14 (2021). https://doi.org/10.5281/zenodo.4447411

Multi-hazard Assessment

Rheological Characteristics of Sand Stabilized with Colloidal Silica for Barrier Material and Liquefaction Mitigation

Jiji Krishnan and Shruti Shukla

1 Introduction

Liquefaction is a phenomenon that produces excessive movements and extreme deformations due to vibrations or disturbances in saturated cohesionless sand. When the effective confining pressure of the saturated soil reaches the pore water pressure, then the process of liquefaction takes place [1–3]. The liquefaction happens when the soil is in a flowing state with sufficient loss of bearing capacity in the soil. The study on soil liquefaction by the empirical model and laboratory experiments were developed by many researchers to evaluate the liquefaction resistance after stabilizing the loose sand [4–8]. Liquefaction can be mainly divided into static liquefaction, dynamic liquefaction, and liquefaction due to blast. Static liquefaction occurs due to the excess weight of the structure and subsoil, whereas the other liquefactions are the combinations of excessive weights and vibrations in the structure and subsoil. The undrained triaxial test supports comprehending the static liquefaction behavior and helps to understand the liquefaction resistance as well [9–11]. The dynamic liquefaction can be evaluated with the help of centrifuge model studies and cyclic triaxial laboratory tests [12–15]. Many other laboratory tests such as shaking table tests, numerical simulations, bender element tests help to evaluate liquefaction in sand layers [16–21]. Soil stabilization or ground improvement methods help to mitigate the risk of seismic liquefaction.

Soil stabilization helps to improve the engineering and index properties of loose sands and weak clays. The traditional methods used for soil stabilization are vibro-compaction, cement grouting, micro piles, vibro-replacement, preloading of soil, and soil nailing [22–27]. It is challenging to improve the ground characteristics of already developed sites with the help of conventional soil stabilization techniques. Also, non-traditional soil stabilization helps to attain non-disruptive seismic lique-

Present Address:
J. Krishnan (✉) · S. Shukla
Sardar Vallabhbhai National Institute of Technology Surat, Surat, India

11

faction mitigation cost effectively as well as environmental friendly in large areas [28]. The traditional novel methods introduced by the researchers in the past decade are colloidal silica grouting, bentonite suspension grouting, bio-cementation, air injection, and induced partial saturation [29–32].

The studies on the ground improvement techniques by adding colloidal silica is growing gradually due to its mechanical strength/stability concerning other chemical grouts [29, 33–35]. The current study scientifically reports existing states of art and practices of colloidal silica sand stabilization methods. Also, the present paper is an effort to give a vast awareness about the rheological characteristics of colloidal silica stabilized sand for liquefaction mitigation and also the use of colloidal silica as a stabilizer in soil stabilization. The viscosity and gel time measurements of sand stabilized with colloidal silica at a 60% relative density are discussed in the current research.

2 Overview of Gel Time Measurements of Colloidal Silica

Gel time measurements for three different colloidal silica concentrations (5, 10, and 15%) were studied in the current study. In order to study the variations of gel time with the addition of salt, three different conditions were adopted. One: with no salt, second: with the addition of 0.2 N salt, and the third: with the addition of 0.5 N salt.

All the tests were conducted using reagent grade NaCl. A pH ranged from 4 to 9.5 was selected for all the laboratory experiments [36]. Variation of gel time by varying pH at three different concentrations is shown in Fig. 1. Adding the reagent grade salt in the colloidal silica solution reduces the gel time in all three concentrations of colloidal silica solutions. The longest gel time is observed when there is no addition of salt in colloidal silica solution. The lowest gel times occur by changing pH and ionic content by adding salts at a pH range from 4.5 to 6.5. The colloidal silica can be utilized in liquefaction susceptible areas due to its controllable and reproducible gel time. The pilot studies on the variation gel time by changing pH could be a proper evaluation to add the colloidal silica solution in untreated sand.

3 Overview of Viscosity Measurements of Colloidal Silica

Viscosity helps to govern the pumping fluid power and determine the frictional pressure drop for numerous fluid flow situations. Canon-Fenske reverse flow viscometer is used to measure the viscosity of various colloidal silica concentrations.

In situ injection method is designed with the help of viscosity versus time curve. Figure 2 shows the deviation in pH with the increase in viscosity over time. The viscosity versus time graph shape is typical in all relevant measurements as per the literature [37, 38]. Viscosity measurements were less than 10 cP (reasonably low) during the initial intervals and then increased rapidly after that and led to gelation. The pattern is similar to all the colloidal silica solutions with different weight

Fig. 1 Variation of gel time by varying pH at three different concentrations **a** 5% CS, **b** 10% CS **c** 15% CS
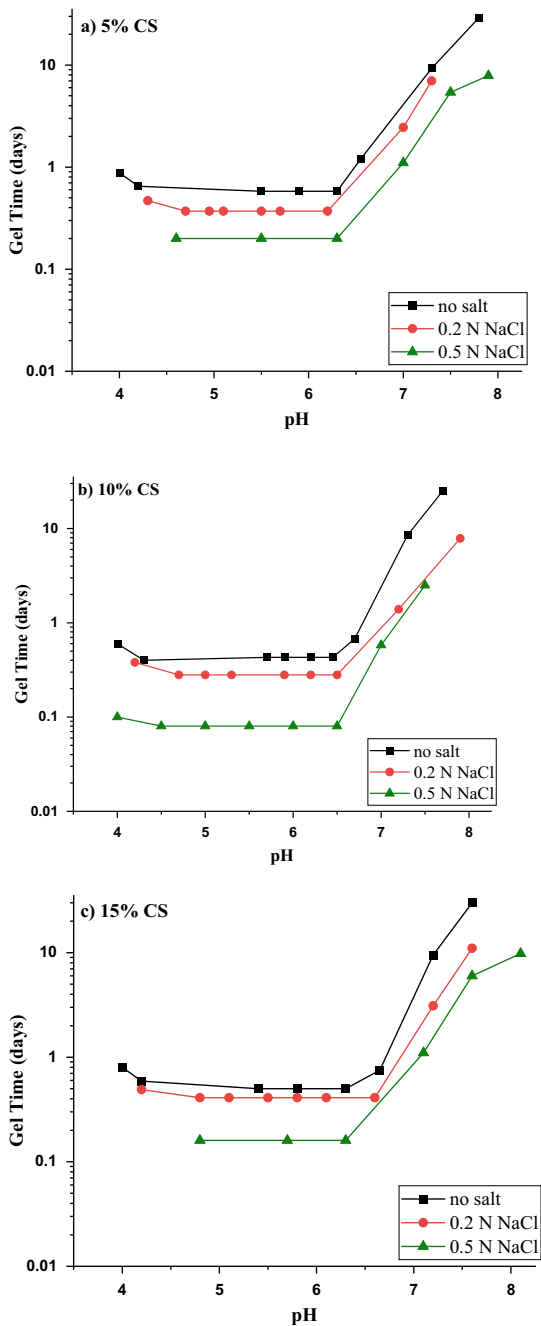
Fig. 2 Variation of viscosity with time at three different concentrations at pH between 5 and 6
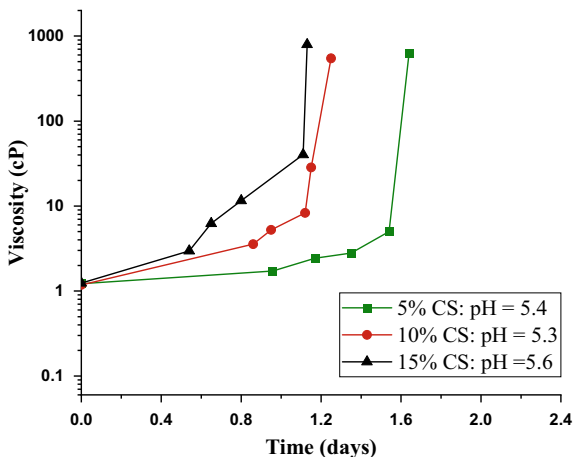
percentages. However, the viscosity reduces with an increase in colloidal silica weight percentages.

4   Overview of Hydraulic Conductivity Measurements of Colloidal Silica Stabilized Sand

Hydraulic conductivity was estimated with the help of an indirect method, and tests were conducted in the oedometer apparatus [39]. Hydraulic conductivity measurements of untreated and sand stabilized with colloidal silica at 60% relative density are shown in Fig. 3. The permeability of sand stabilized with colloidal silica was significantly reduced after a curing period of 7 days. Maximum permeability is

Fig. 3 Normal stress versus hydraulic conductivity plot of untreated and colloidal silica treated sand at 7 days curing
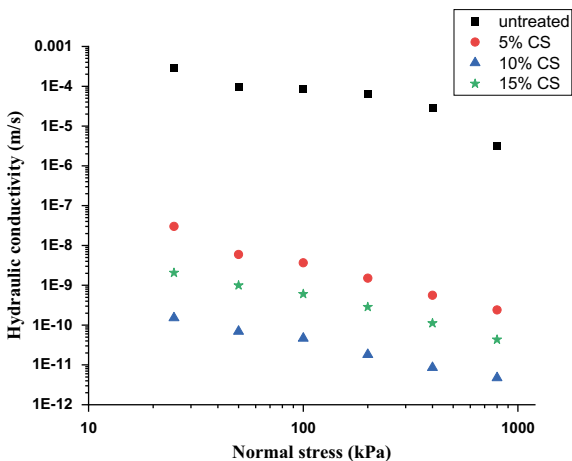
observed when the sand is treated with 10 wt% colloidal silica. The effect of applied loading pressures on hydraulic conductivity is less significant once it become more than 500 kPa in all the colloidal silica treated sand. Colloidal silica treated sand has a hydraulic conductivity range in the order of 10^{-8}–10^{-11} m/s, which in turn, is suitable for a barrier material [40]. The occurrence of liquefaction could be prevented by reducing the permeability by stabilizing the foundation soil with colloidal silica.

5 Conclusions

The conclusions achieved from the current study are as follows.

1. Gel time increased with an increment in the concentrations of reactants. The gel time of colloidal silica decreases from about 29 days to 4.8 h for different concentration of reagent grade NaCl reactants.
2. The viscosity of colloidal silica increases with the passage of time, and ultimately the solution alters into a rigid gel.
3. Colloidal silica treated sand has a hydraulic conductivity range in the order of 10^{-8} to 10^{-11} m/s, which is suitable for a barrier material.

References

1. Bommer, J.J., Marytínezpereira, A.: The effective duration of earthquake strong motion. J. Earthq. Eng. (1999). https://doi.org/10.1080/13632469909350343
2. Rayhani, M.H.T., El Naggar, M.H., Tabatabaei, S.H.: Nonlinear analysis of local site effects on seismic ground response in the bam earthquake. Geotech. Geol. Eng. (2008). https://doi.org/10.1007/s10706-007-9149-0
3. Ayoubi, P., Pak, A.: Liquefaction-induced settlement of shallow foundations on two-layered subsoil strata. Soil Dyn. Earthq. Eng. (2017). https://doi.org/10.1016/j.soildyn.2017.01.004
4. Ashour, M., Norris, G.: Liquefaction and undrained response evaluation of sands from drained formulation. J. Geotech. Geoenviron. Eng. (1999). https://doi.org/10.1061/(asce)1090-0241(1999)125:8(649)
5. Bartlett, S.F., Leslie Youd, T.: Empirical prediction of liquefaction-induced lateral spread. J. Geotech. Eng. (1995). https://doi.org/10.1061/(ASCE)0733-9410(1995)121:4(316)
6. Sonmez, B., Ulusay, R.: Liquefaction potential at Izmit bay: comparison of predicted and observed soil liquefaction during the Kocaeli earthquake. Bull. Eng. Geol. Environ. (2008). https://doi.org/10.1007/s10064-007-0105-2
7. Evans, M.D., Zhou, S.: Liquefaction behavior of sand-gravel composites. J. Geotech. Eng. (1995). https://doi.org/10.1061/(ASCE)0733-9410(1995)121:3(287)
8. Fear, C.E., McRoberts, E.C.: Reconsideration of initiation of liquefaction in sandy soils. J. Geotech. Eng. (1995). https://doi.org/10.1061/(ASCE)0733-9410(1995)121:3(249)
9. Yamamuro, J.A., Lade, P.V.: Static liquefaction of very loose sands. Can. Geotech. J. (1997). https://doi.org/10.1139/t97-057

10. Boukpeti, N., Mróz, Z., Drescher, A.: A model for static liquefaction in triaxial compression and extension. Can. Geotech. J. (2002). https://doi.org/10.1139/t02-066

11. Ibraim, E., Diambra, A., Muir Wood, D., Russell, A.R.: Static liquefaction of fibre reinforced sand under monotonic loading. Geotext. Geomembranes. (2010). https://doi.org/10.1016/j.geotexmem.2009.12.001

12. Byrne, P.M., Park, S.S., Beaty, M., Sharp, M., Gonzales, L., Abdoun, T.: Numerical modeling of liquefaction and comparison with centrifuge tests. Can. Geotech. J. (2004). https://doi.org/10.1139/t03-088

13. Zeghal, M., Goswami, N., Kutter, B.L., Manzari, M.T., Abdoun, T., Arduino, P., Armstrong, R., Beaty, M., Chen, Y.M., Ghofrani, A., Haigh, S., Hung, W.Y., Iai, S., Kokkali, P., Lee, C. J., Madabhushi, G., Tobita, T., Ueda, K., Zhou, Y.G., Ziotopoulou, K.: Stress-strain response of the LEAP-2015 centrifuge tests and numerical predictions. Soil Dyn. Earthq. Eng. (2018). https://doi.org/10.1016/j.soildyn.2017.10.014

14. Ishihara, K., Tatsuoka, F., Yasuda, S.: Undrained deformation and liquefaction of sand under cyclic streSSES. Soils Found. (1975). https://doi.org/10.3208/sandf1972.15.29

15. Bouferra, R., Benseddiq, N., Shahrour, I.: Saturation and preloading effects on the cyclic behavior of sand. Int. J. Geomech. (2007). https://doi.org/10.1061/(asce)1532-3641(2007)7:5 (396)

16. Jin, J., Song, C., Liang, B., Chen, Y., Su, M.: Dynamic characteristics of tailings reservoir under seismic load. Environ. Earth Sci. (2018). https://doi.org/10.1007/s12665-018-7836-1

17. Ye, B., Ye, G., Ye, W., Zhang, F.: A pneumatic shaking table and its application to a liquefaction test on saturated sand. Nat. Hazards. (2013). https://doi.org/10.1007/s11069-012-0489-6

18. Zhou, Y.G., Chen, Y.M., Ke, H.: Correlation of liquefaction resistance with shear wave velocity based on laboratory study using bender element. J. Zhejiang Univ. Sci. (2005). https://doi.org/10.1631/jzus.2005.A0805

19. Huang, B., Yin, J.H., Wu, S.M., Chen, Y.M.: Dynamic testing of silt using bender element. In: ISRM International Symposium 2000, IS 2000 (2018)

20. Lopez-Caballero, F., Modaressi Farahmand-Razavi, A.: Numerical simulation of liquefaction effects on seismic SSI. Soil Dyn. Earthq. Eng. (2008). https://doi.org/10.1016/j.soildyn.2007.05.006

21. Liyanathirana, D.S., Poulos, H.G.: Numerical simulation of soil liquefaction due to earthquake loading. Soil Dyn. Earthq. Eng. (2002). https://doi.org/10.1016/S0267-7261(02)00037-4

22. Esfahanizadeh, M., Atashband, S.: Vibro-probe technique evaluation in soil improvement against liquefaction. In: 15th World Conference on Earthquake Engineering (2012)

23. Fan, J., Wang, D., Qian, D.: Soil-cement mixture properties and design considerations for reinforced excavation. J. Rock Mech. Geotech. Eng. (2018). https://doi.org/10.1016/j.jrmge.2018.03.004

24. Sharma, B., Buragohain, P.: Behaviour of micropile groups under oblique pull out loads in sand. Indian Geotech. J. (2013). https://doi.org/10.1007/s40098-013-0091-1

25. Priebe, H.: The design of Vibro replacement. Gr. Eng. **28**(10), 1–16 (1995)

26. Sun, L.Q., Yan, S.W., Li, W., Wu, K.B.: Study of super-soft soil vacuum preloading model test. Yantu Lixue/Rock and Soil Mech. **32**(4), 984–990 (2011)

27. Ng, C.W.W., Lee, G.T.K.: A three-dimensional parametric study of the use of soil nails for stabilising tunnel faces. Comput. Geotech. (2002). https://doi.org/10.1016/S0266-352X(02)00012-5

28. Huang, Y., Wen, Z.: Recent developments of soil improvement methods for seismic liquefaction mitigation. Nat. Hazards **76**, 1927–1938 (2015). https://doi.org/10.1007/s11069-014-1558-9

29. Gallagher, P.M., Koch, A.J.: Model testing of passive site stabilisation: a new grouting technique. In: Geotechnical Special Publication (2003)

30. Mahawish, A., Bouazza, A., Gates, W.P.: Unconfined compressive strength and visualisation of the microstructure of coarse sand subjected to different biocementation levels. J. Geotech. Geoenvironmental Eng. (2019). https://doi.org/10.1061/(ASCE)GT.1943-5606.0002066

31. Yoon, J., Mohtar, C.E.: Dynamic rheological properties of sodium pyrophosphate-modified bentonite suspensions for liquefaction mitigation. Clays Clay Miner. (2013). https://doi.org/10.1346/CCMN.2013.0610411

32. Okamura, M., Takebayashi, M., Nishida, K., Fujii, N., Jinguji, M., Imasato, T., Yasuhara, H., Nakagawa, E.: In-situ desaturation test by air injection and its evaluation through field monitoring and multiphase flow simulation. J. Geotech. Geoenviron. Eng. (2011). https://doi.org/10.1061/(ASCE)GT.1943-5606.0000483

33. Sharma, P., Krishnan, J., Shruti, S.: A feasibility study of colloidal silica as stabilising material for passive site remediation. In: Singh, R.M., Sudheer, K.P., Kurian, B. (eds) Advances in Civil Engineering. Lecture Notes in Civil Engineering, vol. 83, pp. 333–347. Springer, Singapore. https://doi.org/10.1007/978-981-15-5644-9_24 (2020)

34. Krishnan, J., Shukla, S.: The behaviour of soil stabilised with nanoparticles: an extensive review of the present status and its applications. Arab. J. Geosci. 12, 436 (2019). https://doi.org/10.1007/s12517-019-4595-6

35. Gallagher, P.M., Conlee, C.T., Rollins, K.M.: Full-scale field testing of colloidal silica grouting for mitigation of liquefaction risk. J. Geotech. Geoenvironmental Eng. 133, 186–196 (2007). https://doi.org/10.1061/(ASCE)1090-0241(2007)133:2(186)

36. Gallagher, P.M., Mitchell, J.K.: Influence of colloidal silica grout on liquefaction potential and cyclic undrained behavior of loose sand. Soil Dyn. Earthq. Eng. 22, 1017–1026 (2002). https://doi.org/10.1016/s0267-7261(02)00126-4

37. Persoff, P., Apps, J., Moridis, G.J., Whang, J.M.: Effect of dilution and contaminants on sand grouted with colloidal silica. J. Geotech. Geoenviron. Eng. 125, 461–469 (2002). https://doi.org/10.1061/(ASCE)1090-0241(1999)125:6(461)

38. Gallagher, P.M., Lin, Y.: Colloidal silica transport through liquefiable porous media. J. Geotech. Geoenviron. Eng. 135, 1702–1712 (2009). https://doi.org/10.1061/(ASCE)GT.1943-5606.0000123

39. Olson, R., Daniel, D.: Measurement of the hydraulic conductivity of fine-grained soils. In: Permeability and Groundwater Contaminant Transport, pp. 18–18–47 (2009)

40. Benson, C.H., Daniel, D.E.: Minimum thickness of compacted soil liners: II. Analysis and case histories. J. Geotech. Eng. (1994). https://doi.org/10.1061/(ASCE)0733-9410(1994)120:1(153)

A Study on Liquefaction Susceptibility of Earthen Dams

H. C. Sumanth and **L. Govindaraju**

1 Introduction

Vibrations due to an event of earthquake can cause widespread damage to the habitat. Earthquake is shaking of the earth resulting from the sudden release of energy in earth's lithosphere that creates seismic waves. Earthquake is a hazard, and it becomes a disaster only when it hits the habitat. Earthquake does not kill people, damage to infrastructure causes death. For safety against earthquakes, earthquake resistant design is very much the need of the hour.

1.1 Earthquake Induced Liquefaction

Liquefaction is a phenomenon where strength and stiffness of a loose, saturated, and cohesionless soil is reduced due to cyclic or rapid loading. This effect can be attributed to effective stress reducing to zero, due to the generation of high pore water stresses when the ground is exposed to seismic vibrations. Liquefaction can produce differential settlements in the foundation of the structure and can also cause failure of important utility structures like dam, bridge, and highways. Underground facilities like pipelines, cables, and other services can also be affected.

Present Address:

H. C. Sumanth (✉) · L. Govindaraju

Department of Civil Engineering, University Visvesvaraya College of Engineering, Bangalore University, Bengaluru 560056, India

19

1.2   Earth Dams

In recent years, the need for services to the global community resulted in the construction of various types of infrastructure around the world, such as highways, bridges, and dams. A dam is a structure which acts as a barrier to stop or restrict the flow of water. For specific functions like water supply, irrigation, flood control, and hydroelectric power generation, dams are built. Most of large dams in the world were built during the middle of the twentieth century. There are two types of modern dams, they are embankment dams and concrete dams. Embankment dams are water impounding structures and are flexible to slightly deform to the deflection of the foundation. They are also called as dikes or banks. These dams are primarily made out of earth and rock fragments. Embankment dams can be classified into earth fill dams and rock fill dams. Embankment dams represent about 85% of dams all over the world. Largest structure ever built by man is an earth dam [1].

Several factors have to be considered in selecting an earth dam type such as topography, foundation conditions, environmental impacts, construction facilities, and socio-economic aspects. A feasible dam should be built from locally available materials and should be stable under all operating and loading conditions [2].

1.3   Objective of the Present Work

The objective of the present work is to determine the liquefaction susceptibility of filters, drains, and foundation of the earth dam (Fig. 1). The obtained results are verified by analytical procedure using Indian standard code for earth dam foundation (IS 1893:2016—Part 1) [3].
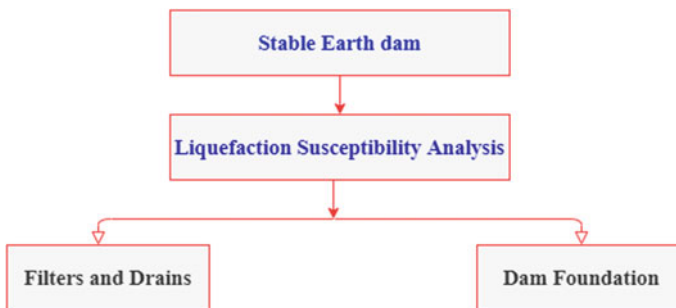
Fig. 1 Outline of the study

2 Outline of the Study

The most stable geometrical section (Fig. 2) obtained after a comprehensive static and seismic slope stability analysis from Sumanth et al. [4] is subjected to lique-faction susceptibility analysis. Cutoff, filters, and drains are incorporated into the dam geometry. The model has an upstream slope of 4H: 1V and downstream slope of 2.5H: 1V [4].

Table 1 shows the technical details of the dam. Depth of the foundation of an earth dam shall extend up to bed rock or through all soft, unstable, and permeable strata of overburden [1]. In the assessment of suitable and effective material for filters and drains section of the dam, earth dam is founded on hard soil of 20 m depth, which is equal to height of the dam. In liquefaction susceptibility analysis of dam foundation, hard rock is met at depth of 15 m in the foundation. Accordingly, foundation is extended up to 20 m by incorporating 5 m depth of hard rock in earth dam foundation. Table 2 shows the material properties for different sections of the earthen dam considered in this study.

Filter and drain sections are modeled with loose sand, medium dense sand, and dense sand. The potential of these materials against liquefaction is explored. Liquefaction susceptibility analysis of earth dam foundation is carried out numerically for three different cases. Liquefaction zones and cyclic stress ratio (CSR) values are obtained from numerical analysis. Results from numerical study are verified and validated using analytical procedure. Standard penetration resistance (N) values are obtained for different stratifications from literature, and correction factors are applied. The corrected N values are used to compute cyclic resistance ratio (CRR), and factor of safety (FOS) against liquefaction is determined. Based on FOS value obtained, the soil is regarded as liquefiable or non-liquefiable at that particular depth of consideration.

2.1 *Time Acceleration Record*

The acceleration time history considered in the present study is El Centro record (Imperial Valley earthquake), USA, 1940. The magnitude of the earthquake was 6.9
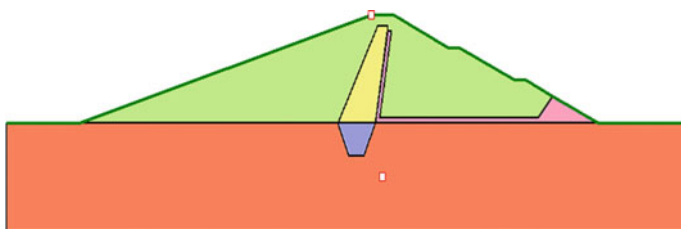
Fig. 2 Most stable geometrical section [4]

Table 1 Technical details of the dam

Height of the dam	20 m
Depth of foundation	20 m
Top width of the dam	6 m
Free board	2 m
MWL (maximum water level)	18 m
FSL (full supply level)	17 m
DSL (dead storage level)	5 m

Table 2 Material properties

Dam section	γ (kN/m^3)	E (MPa)	Damping ratio, ξ (%)	μ
Core	20	20	5	0.4
Shell	19	50	5	0.3
Foundation	19.8	60	5	0.3
Filter	19	50	5	0.3
Reference	Das [5]	Bowles [6]	Bowles [6]	Bowles [6]
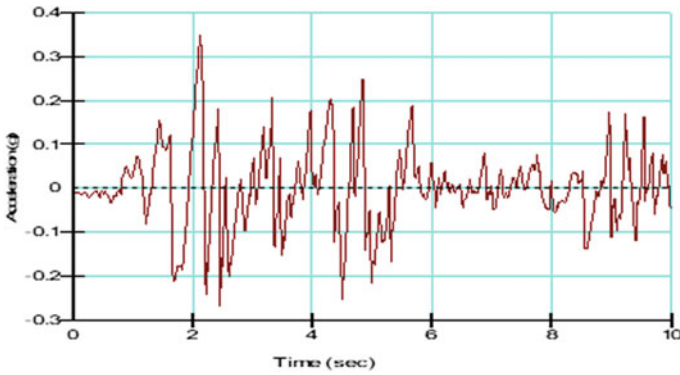
Fig. 3 El Centro Earthquake Record, USA (1940)

and peak ground acceleration of 0.35 g at 2.14 s. The total duration of the earthquake is 10 s. El Centro record, 1940 is represented in the form of a time acceleration plot as shown in Fig. 3.

3 Liquefaction Susceptibility of Filters and Drains

To dissipate the pore water seeping through the body and foundation of the dam, drainage facilities are employed. Filters are provided to ensure that, only the fluid reaches the drainage medium and carried away from the earth dam system.

Table 3 Material data for liquefaction analysis of filter and drain sections of the dam [6]

Type of Soil	γ (kN/m³)	Dr (%)	SPT (N)	μ	E (MPa)
Loose sand	17	<35	4–10	0.3	10–25
Medium dense sand	18.5	35–65	10–30	0.35	25–50
Dense sand	20	65–85	30–50	0.4	50–81

Post - earthquake sections

Loose sand   Medium dense sand

Dense sand
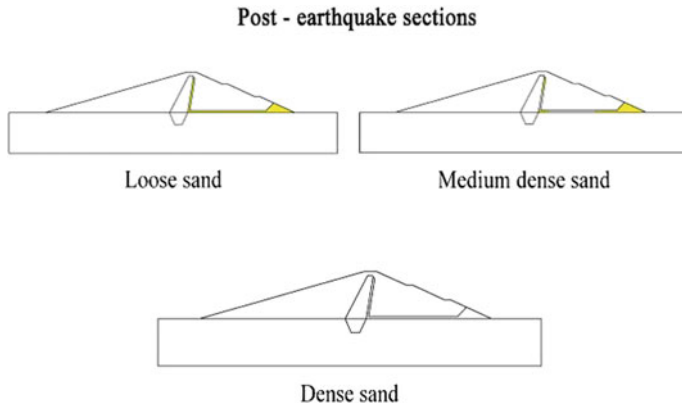
Fig. 4 Post-earthquake sections with liquefaction zones

Basically, filters and drains act to minimize seepage loss and its subsequent effects which may disrupt the functioning of the dam. For better drainage, granular material like sand or silty sand is used in the filter and drain sections of the dam. During an earthquake, high pore water pressure builds up in the granular soil material and reduces the effective stress. Soil behaves just like a viscous fluid and leads to high post-earthquake deformations.

In the present study, different types of sand are incorporated in the filter and drain sections of the earth dam and subjected to earthquake vibrations. The material properties are as shown in Table 3. The potential of these materials against liquefaction is assessed numerically, and results are as shown in Fig. 4.

Loose sand liquefies completely at 1.2 s, whereas medium dense sand liquefies incrementally when subjected to earthquake time history considered in this study. When density of the infill material for filters and drains is densified, soil has better potential against liquefaction. Improvement in soil density reduces the void space which in-turn minimizes the potential for excess pore water pressure generation. Hence, it increases the potential against liquefaction of the densified soil mass.

4   Liquefaction Susceptibility of Earth Dam Foundation

Evaluation of liquefaction susceptibility of earth dam foundation is one of the major aspect to be considered at project planning stage. Contributions from Seed and Idriss are considered as pioneer work in the area of liquefaction assessment. Basically, factor of safety against liquefaction is determined using relevant standards. Based on IS 1893:2016 [3] (Part-1), factor of safety is a ratio of cyclic resistance ratio (CRR) to cyclic stress ratio (CSR). In the present study, liquefaction potential is assessed based on standard penetration test (SPT). N values are normalized for standard hammer, energy, and other parameters, and CRR is found. CSR is obtained at different depths from numerical analysis. Liquefaction zones obtained from numerical analysis are verified with the analytical factor of safety values calculated from Indian standards.

Figure 5 shows the model considered in this study. In this model, hard rock overlays weathered rock overlays medium dense sand overlays fill. Material properties of different soil strata are as shown in Table 4.

Gmax values are defined as functions in the numerical analysis. Seepage analysis is carried out for reservoir full condition, and corresponding pore water stresses are incorporated to the coupled dynamic analysis. Liquefaction zones are obtained as a result of dynamic analysis as shown in Fig. 6. Top most soil strata comprising of fill liquefies after 1.2 s of earthquake, whereas medium dense sand liquefies progressively along the 10 s duration of shaking. Weathered rock and hard rock are non-liquefiable as liquefaction zones are absent in these layers. The numerical analysis results are verified analytically as shown in Table 5. Factor of safety is less than 1 up to 10 m depth, and corresponding soil strata are assessed to be liquefiable. Hence, numerical and analytical methods yield similar results.

Number of correction factors are applied to normalize the standard penetration resistance (N) to corrected value, $(N_1)_{60}$. It is corrected for standard hammer type (C_{HT}), hammer weight (C_{HW}), sampler with or without liners (C_{SS}), rod length (C_{RL}), borehole diameter (C_{BD}), and overburden pressure (C_N). As per IS 1893:2016 [3], (Part-1) various correction factors for SPT considered here are as shown in Table 6. CRR is determined for a 7.5 magnitude earthquake. But, later it is modified to match the current earthquake record by applying magnitude scaling factor (MSF). For El Centro earthquake record of magnitude 6.9, MSF is computed
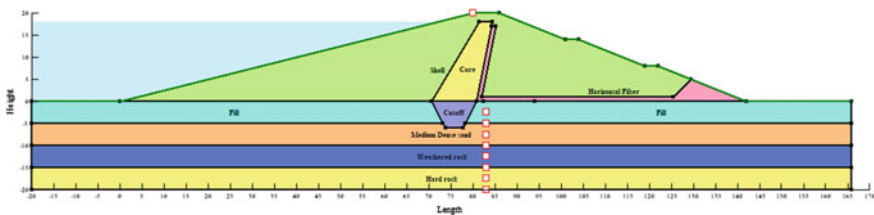
Fig. 5 Model for liquefaction analysis of dam foundation

Table 4 Material properties for liquefaction susceptibility analysis of earth dam foundation [6]

Type of Soil	γ (kN/m^3)	γ_{sat} (kN/m^3)	SPT (N)	μ
Fill	16	17	12	0.3
Medium dense sand	18.5	19.5	20	0.3
Weathered rock	22	23	50	0.3
Hard rock	25	26	80	0.3
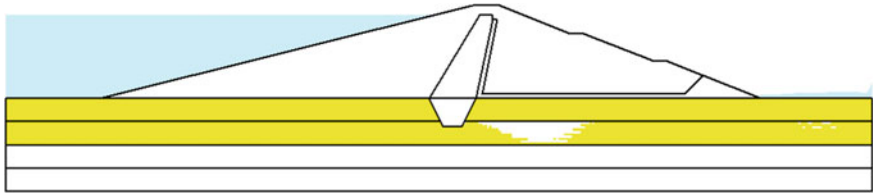
Fig. 6 Post-earthquake section for liquefaction analysis of dam foundation

and incorporated in the study. MSF converts the standard 7.5 magnitude to the current earthquake magnitude. Overburden correction factor ($K\sigma$) is applied for higher overburden stresses involving depths more than 15 m. Sloping ground correction factor (K_α) is assumed as unity as horizontal soil stratum is present in the ground model.

The SPT procedure to compute factor of safety against liquefaction involves various correction factors. Energy correction factor for energy transfer ratios other than 60% can be incorporated in the computations for reliable output. Cone penetration test (CPT), Becker penetrometer test (BPT), and multi-channel analysis of surface waves (MASW) can be effectively used to compute liquefaction susceptibility of a soil deposit.

When a certain stratum is qualified as liquefiable, design of suitable mitigation technique becomes a vital task. Mitigation technique can be an effective part in disaster risk reduction. Ground improvement solutions which use vibration technique to improve the soil mass are widely used in the area of disaster risk reduction. Vibro-compaction and vibro-replacement can be effectively employed to increase the density of the soil mass and mitigate liquefaction [7] Vibro-replacement can also be adopted in the form of stone columns which has better load bearing and settlement characteristics. Stone columns facilitate drainage and improve liquefaction potential of the soil mass. Passive site remediation techniques like colloidal silica or bentonite suspension grouting, bio-cementation, or induced partial saturation can also be employed based on the site conditions and complexity of the project [8].

Table 5 Analytical procedure as per IS 1893-2016 (Part-1) [3]

Depth, Z(m)	N	CSR	σ_τ kN/m²	Corrections for SPT						$(N_1)60$	$CRR_{7.5}$	MSF	K_α	$K\sigma$	CRR	FOS	Remarks
				C_{HT}	C_{HW}	C_{SS}	C_{RL}	C_{bd}	C_N								
2.5	10	0.485	19.2	1.33	0.98	0.9	0.75	1.05	1.7	16	0.28	1.24	1	1	0.35	0.72	Liquefiable
5	12	0452	38.45	1.33	0.98	0.9	0.85	1.05	1.61	20	0.32	1.24	1	1	0.40	0.88	Liquefiable
7.5	16	0.439	62.68	1.33	0.98	0.85	0.95	1.05	1.26	22	0.33	1.24	1	1	0.41	0.93	Liquefiable
10	20	0431	86.9	1.33	0.98	0.85	1.0	1.05	107	25	0.34	1.24	1	1	0.42	0.97	Liquefiable
12.5	35	0.221	119.9	1.33	0.98	0.8	1.0	1.05	091	35	0.5	1.24	1	1	0.62	2.8	Non-Liquefiable
15	50	0.201	152.9	1.33	0.98	0.8	1.0	1.05	0.8	44	0.5	1.24	1	1	0.62	3.08	Non-Liquefiable
17.5	64	0.192	193.3	1.33	0.98	0.8	1.0	1.05	0.72	50	0.5	1.24	1	0.80	0.50	2.6	Non-Liquefiable
20	80	0.182	233.8	1.33	0.98	0.9	1.0	1.05	0.65	57	0.5	1.24	1	0.74	0.46	2.52	Non-Liquefiable

Table 6 Corrections for SPT as per IS 1893:2016 (Part-1) [3]

Type of correction	Description	Value
C_{HT}	Correction for hammer type	1.33—donut hammer with trip/auto
C_{HW}	Correction for hammer weight	0.98—63.5 kg hammer with a free fall of 760 mm
C_{SS}	Correction for sampler with or without liners	With liners (value depends on stratification)
C_{RL}	Correction for rod length	Computed with respect to depth of drilling
C_{BD}	Correction for borehole diameter	1.05–150 mm borehole diameter
C_N	Correction for overburden pressure	Computed with respect to effective overburden pressure

5 Conclusions

- If loose and medium dense sands are used in the filters and drain sections of the dam, it would lead to liquefaction induced dam failure. By adopting the liquefaction mitigation technique like vibro-compaction, the filter and drain sections can be densified in order to improve the liquefaction resistance and enhance safety.
- Liquefaction failure may be triggered when dam foundation consists of cohesionless fill and medium dense sands. In such cases, a suitable mitigation technique is needed for dam safety.
- Soil softening in deeper soil stratum may also induce liquefaction in the strata lying above the liquefiable deposit.
- The presence of liquefaction susceptible soil does not mean that one has to abandon the site or install pile foundations. Ground improvement solutions can provide technically sound and cost effective solutions.

References

1. Sherard, J.L., Woodward, R.J., Gizienski, S.J., Clevenger, W.A.: Earth and Earth-Rock Dams. Wiley, New York (1963)
2. Novak, P.A., Moffat, I.B., Nalluri, C., Narayanan, R.: Hydraulic Structures. Unwin Hyman, London, UK (1990)
3. IS 1893-2016 (Part 1): Criteria for earthquake resistance design of structures. Bureau of Indian Standard, New Delhi, India
4. Sumanth, H.C., Govindaraju, L.: A Comprehensive seismic slope stability assessment of earth dams. J. Adv. Geotech. Eng. **3**(3), 1–14 (2021). https://doi.org/10.5281/zenodo.4447411
5. Das, B.M.: Advanced soil mechanics, 3rd edn. Taylor and Francis, London, New York (2008)
6. Bowles, J.E.: Foundation analysis and design. McGraw-Hill, New York (1988)

7. Annam, M.K., Raju, V.R.: Ground improvement solutions to mitigate liquefaction: case studies. Keller Asia, The Master Builder, Kn 6, vol. 1, pp. 33–39 (2015)
8. Yu, H., Wen, Z.: Recent developments of soil improvement methods for seismic liquefaction mitigation. Nat. Hazards **76**, 1927–1938 (2015)

Evaluation of the Effectiveness of Flexible Debris Flow Barriers for Control of Huaycos Using Satellite Images and GIS, in the Basin of Rímac River, Perú

Marco Antonio Pareja Dominguez⬤,
Henry Douglas Pascual Figueroa⬤,
and Marisa Rosana Silva Dávila⬤

1   Introduction

Debris flow is a very dangerous mass movement for urban environments in mountainous regions. A lot of work has been focused on mitigation, but there are still many aspects to be elucidated. One of the strategies is the use of an auscultation system implemented in the basins to record data on hydrological conditions and flow dynamics, and therefore, to better understand the conditions that trigger debris flows and how dynamic systems or barriers can be used as a mitigation element [1].

In Peru, debris flow, known as "huaycos," is recurrent in steeply sloping streams, mainly during the El Niño Southern Oscillation (ENSO) phenomenon, causing economic and human losses. The study area in Lima, the capital department of Peru, corresponds to Carossio, Castilla, and Quirio creeks (see Fig. 1).

Quirio and Carossio creeks are located on the right bank of the Rímac River, which flows to the Pacific Ocean, and Castilla is located on the left bank. The area belongs to Chosica city, in Lurigancho district, which is highly exposed to the occurrence of debris flows. Either due to natural causes, such as exceptional rains caused by ENSO phenomenon, morphology and/or relief, or anthropic. Their rapid growth occurred in formal and informal ways, mostly, with a lack of house planning, and the urban areas were multiplying and blocking the river's natural channel [2].

M. A. Pareja Dominguez · H. D. Pascual Figueroa (✉) · M. R. Silva Dávila
Peruvian University of Applied Sciences (UPC), Lima, Peru
e-mail: u201500072@upc.edu.pe

M. A. Pareja Dominguez
e-mail: u201501236@upc.edu.pe

M. R. Silva Dávila
e-mail: pccimasi@upc.edu.pe; marisi@uni.edu.pe
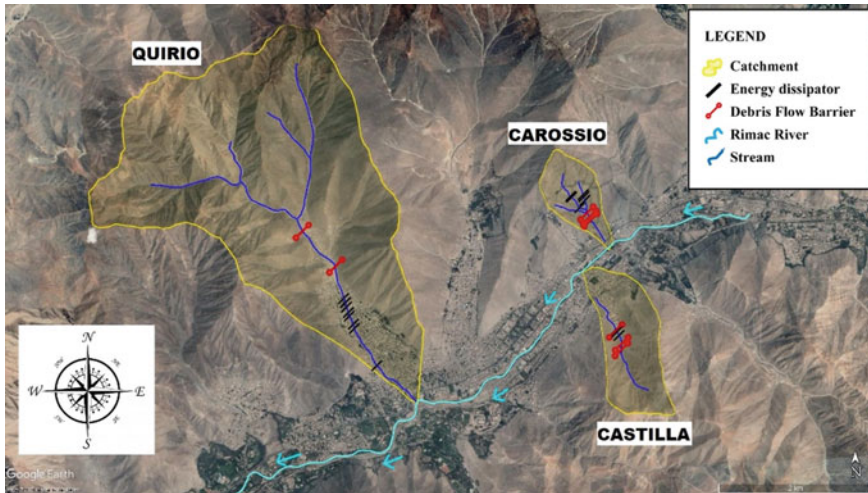
Fig. 1 Maps of the Quirio, Carossio, and Castilla creeks

There are many dangerous creeks around the city with historical records of debris flow occurrence which are already protected with debris flow barriers. The installation of the debris flow barriers made possible the reduction of damages caused by the debris flows because of the ENSO phenomenon occurrence in 2017.

To identify the types of debris flows, distribution, and control factors, susceptibility maps of the area must be generated. Alharbi et al. (2014) reported that using satellite images and GIS allows a spatial analysis of the data that cannot be collected in the field.

After processing, the in-risk levels of susceptibility zones are obtained with which comparisons, and predictions can be made about the direction of the flows. With this approach, a replicable model is created for other parts of the world where the study areas of difficult access are not an obstacle to the investigation of the problems with the debris flows [3].

2 Methodology

This research's main objective is to determine the effectiveness of debris flow barriers installed between November 2015 and February 2016 by analyzing satellite images with the Geographical Information System (GIS). For that, it is necessary to obtain the volumes of both soil erosion in the upper basin transported by the debris flow and the retained solids by the barriers.

Geological, geomorphological, and hydrological characteristics were evaluated, as well as the evolution of urbanization in the dejection cone. In the hydrological study, to determine the rainfall information of the areas under study, a series of

maximum precipitation data from the 1964 to 2009 period provided by SENAMHI [4] has been used. With the data obtained and the characterization of the streams under study, it was applied the hydrologic modeling system, HEC-HMS [5, 6], obtaining 100-year and 200-year peak discharges. It was selected because there are populations exposed to the danger and risk of loss of human life.

Topography and geomorphology of the study basins were digitally reconstructed with the cartographies available and satellite images using GIS. It was estimated the volume between a horizontal plane with an altitude equal to the top elevation of the highest barrier and the relief of the terrain for each TIN surface. Taking as reference planes the TIN surface corresponding to the year before the event against the TIN surface of the year after the event, the difference in volumes was calculated for estimating the volume of erosion soil in the period.

There are historical cartography maps on the scale of 1/100,000 prepared in 1960 by the National Geographic Institute of Peru, IGN [7], and maps on a scale of 1/25,000 prepared in 1976 by the Ministry of Agriculture [8].

To recreate the relief of the terrain, it is necessary to have optimal satellite images and/or corrected DEMs available and freely accessible. The satellite images were downloaded from the EARTHDATA [9] repository for dates before 1916. For later dates, the interface provided by the Google Earth Search Engine [10] and the Earth Engine Code [11] was used. It is a cloud-based platform that allows users to view and analyze satellite images of the entire planet.

It was selected and acquired the satellite images with elevation data, digital elevation model (DEM), having required resolution for the study and presenting cloudiness lower than 20%, and corresponding to the time prior and after the catastrophic debris flow events identified, as shown in Table 1.

Through the Google Earth Engine Code platform, the images from the years 2016, 2017, and 2018 were processed for the analysis of raster information. Through the Google Earth Engine Code platform, it was selected Sentinel 1 images, and then they were filtered by dates from January to April of years 2016, 2017, and 2018, and finally, the images were processed.

With the minimum and maximum elevation in the DEM, as well as the distance of travel, the slope in percentage was calculated.

3 Physical Characteristics

3.1 Hydrology and Geology

It was calculated the physiographic characteristics of the watershed, its pluviometry conditions, and the 100-year and 200-year peak discharges showed in Table 2. For the three basins, it was considered that the 100-year and 200-year representative maximum precipitation in 24 h are 46.3 mm and 50.5 mm, respectively.

Quirio basin presents a rocky outcrop, such as granodiorite—granite, in jointed, fractured, and weathered condition. As a result of weathering, blocks, and rocky

Table 1 Characteristics of the acquired satellite images

Radar	Product	Date	Resolution or size per pixel
ALOS PALSAR	AP_27249_FBS_F6940_RT1	2011	12.5 × 12.5 m
ASTER GDEM	ASTGTMV003_S12W077	2012	30 × 30 m
Sentinel 1	S1A_IW_SLC__1SDV_20160304T103909_20160304T103936_010218_00F16D_8AA2	2016/03/04	Best quality
Sentinel 1	S1B_IW_SLC__1SDV_20161223T103825_20161223T103852_003522_00605B_CE1D	2016/12/23	Best quality
Sentinel 1	S1B_IW_SLC__1SDV_20170317T103823_20170317T103850_004747_0084AE_8CA2	2017/03/17	Best quality
Sentinel 1	S1B_IW_SLC__1SDV_20170329T103823_20170329T103850_004922_0089AE_0B5B	2017/03/29	Best quality

Table 2 Physiographic parameters and peak discharges

Basin	Quirio	Carossio	Castilla
Main channel length (m)	2340	670	690
Maximum elevation (masl)	1800	1635	1750
Drainage area (km^2)	6.63	0.46	0.51
Average bed slope (%)	29	35	35
Q100 (m^3/s)	10.7	1.5	1.6
Q200 (m^3/s)	16	2.1	2.2

pebbles have been formed, with the presence of sands and gravels, also silts in a small proportion. All these materials constituted for the most part by colluvial quaternary deposits, many times they were unconsolidated, easily removed, mostly on the slopes of the creek, and a large part of the granulometry being heterogeneous [12].

The Carossio creek presents loose material in its channel, and it has three small gullies that merge downstream into one. It still maintains a steep slope leading the water to the Rímac River. The main channel has a length of 1360 m, with a maximum elevation of 1635 m above sea level, has a steep slope greater than 40%, part of its channel is made of the rocky basement, igneous rocks such as granodiorite in jointed, fractured and weathered condition, products from the weathering there are large blocks, rock fragments, gravels and sands, which have angular and/or subangular shape, and this material constituted for the most part by quaternary, colluvial deposits, with a large part of the heterogeneous granulometry [12].

The Mariscal Castilla creek is approximately 3.54 km long, its average slope for the upper part is 35%, and it has a steep slope, with a maximum elevation of 1620 m above sea level. In the lower part, the slope is approximately 25%. It presents rocky outcrop, igneous, and intrusive rocks such as granodiorite—tonalite, in cleated condition, fractured and weathered, forming blocks, angular to subangular rocky pebbles, with the presence of sand and gravel within the riverbed and, finally, in the dejection cone. These materials constituted for the most part by colluvial quaternary deposits [12].

In the three basins, when the creek is activated in the rainy season, the debris flows are produced, they drag rocks and blocks of different sizes from the upper part of the basin along with mud and gravel that carry out the material present on the slopes, causing serious damage to the populations settled in the deject cone. Their outlet point is obstructed by streets and houses, which magnifies the damage when the debris flow occurs [12].

3.2 Catastrophic Events

It was identified the most catastrophic debris flow events which had caused fatalities and damage properties occurred in 1972–1973, 1982–1983, 1997–1998, 2012, and 2017. All these, except the 2012 event are associated with the ENSO phenomenon.

The ENSO event that occurred from December 1997 to April 1998 was one of the most intense of the twentieth century, as it rained heavily on the coast and the flows in the main coastal rivers rose, producing exceptional floods that caused great devastation in the main economic sectors in Peru. In the year 1997, on March 9 between 4:00 pm and 7:30 pm, mudslides were produced in the torrential basins of the Lurigancho district, and these were caused by exceptional rainfall, causing damage to the population and infrastructure; the material damages were valued at 12.5 million dollars, more than 100 people lost their lives, the streams in which the landslides occurred were Quirio, Pedregal, and Corrales [2].

On April 5, 2012, an intense rain of more than 3 h was recorded, which caused numerous landslides, activating 11 streams between kilometers 27–42 of the Carretera Central, causing great destruction to infrastructures such as housing, water, and sewage networks. Roads were also blocked due to the impact of huge rocks and mud that flooded roads, streets, and avenues. The result of all this destruction caused a person to lose their life, and 371 homes were declared uninhabitable [13].

From January to March 2017, there were a series of extreme rainfall events on the coast of Peru, which caused serious floods with hundreds of human victims and billions of dollars in economic losses [14].

3.3 Debris Flow Barriers Installed

Debris flow barriers were installed between November 2015 and February 2016. The estimated retention capacity of each upper barrier in the function of its dimensions is in 4452 m^3 in Quirio, 2773 m^3 in Carossio, and 1584.25 m^3 in Castilla. Figures 2, 3 and 4 show debris flow barriers installed in each creek.

4 Geomorphological Changes

4.1 General Conditions

Although the debris flow barriers were installed after 2015, it was studied the geomorphological changes from 1960. The period 1960–1976 includes the occurrence of an ENSO phenomenon that occurred in 1972–1973.

There are no cartographies, and the available satellite images do not have enough both temporal and spatial resolution and present cloudiness greater than 20% since 2011. Due to this, it was not possible to estimate the eroded volumes for the 1982–1983 and 1997–1998 events.

For explaining the 2017 ENSO event, at the time of processing the information, the products obtained after processing the satellite images resulted in inconsistent

Fig. 2 Flexible debris flow barrier of the Quirio creek

Fig. 3 Flexible barrier of the Carossio creek

Fig. 4 Flexible barrier of the Castilla creek

information, and most cases, they were incomplete or presented NO DATA values, which generated a wrong topography and did not represent the study areas. For this reason, they did not obtain results, due to the flaws and errors present in their composition, there were no results.

For these reasons, it was not possible to calculate the efficiency of retention of the debris flow barriers.

4.2 Estimation of Volumes of Soil Erosion

It was estimated the potential volume of soil erosion in the entire basin. Also, it was calculated the volume of soil erosion for the sub-basin corresponding to the highest barrier installed in each creek; since at present, they are the first defense that retains the contribution of the debris flows. In both cases, the results were only erosion soil. Both the volumes of erosion soil in the entire basin and the volumes of erosion soil for the sub-basins delimited by the upper net were obtained are shown in Table 3.

4.3 Validation of Estimated Volumes of Soil Erosion

To validate the results, in 2019, a survey was carried out with the DJI Phantom Pro 4 drone. These devices currently allow obtaining highly precise cartographic information in a shorter period, especially in places that are difficult to access such as the studied creeks [15].

With the drone, it was not possible to cover the entire area because the flight height did not allow the advance of the drone and the speed of the wind made its flight difficult. The surveyed area is delimited with the red line in Fig. 5, and also the yellow dots show the approximate location of the debris flow barriers in each basin.

The range of levels of the surveyed area by the drone and the estimated volume for each year between terrain and a horizontal plane of reference is shown in Table 4. Note that these are reference volumes calculated for comparison purposes only.

Table 3 Volumes of erosion soil in the entire basin and sub-basin

Basin	1960–1976	2011–2012	Sub-basin	1960–1976	2011–2012
	Volume (m^3)			Volume (m^3)	
Quirio	238,655,259	142,452,701	Quirio	10,922	199
Carossio	11,073,925	2,276,743	Carossio	5051	760
Castilla	96,498,412	27,537,548	Castilla	7634	910
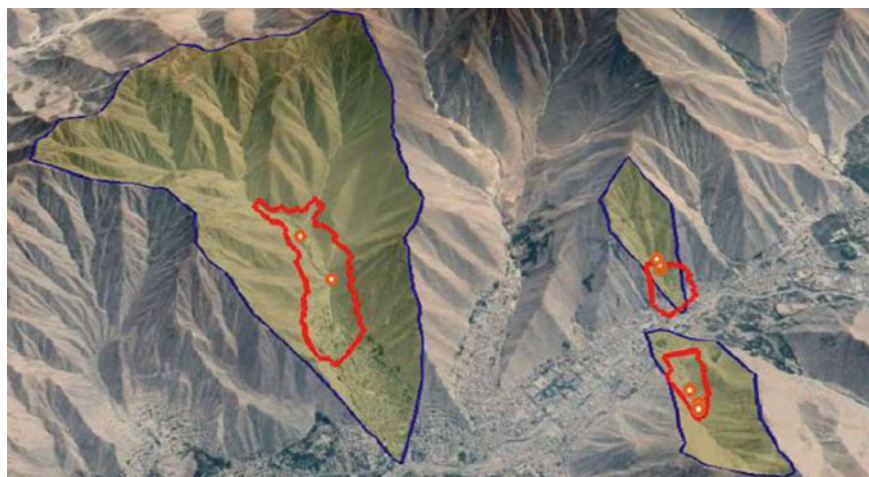
Fig. 5 Surveyed area by the drone

Table 4 Range of levels and referential volumes obtained with drone survey

Basin	Range of levels (m)	Referential volume (m^3)				
		1960	1976	2011	2013	2019
Quirio	1180–2000	3450	3501	3580	3625	3692
Carossio	1086–1700	2153	2196	2165	2176	2285
Castilla	1026–1650	1524	15331	1525	1536	1535

It can conclude that the estimated referential volumes were consistent, and the same conclusion could be applied to the estimated erosion soil volumes. The slope in the bed main channel in the surveyed area was also calculated, the values compared for each year and 2019, which correspond to the survey with the drone are shown in Table 5. For Quirio, there is a slight increase in the slope, and for Carossio and Castilla, there is a greater variation over time.

Also, longitudinal profiles in Carossio Creek in the surveyed area by drone are shown in Fig. 6.

Table 5 Bed slope

Creek	Bed slope (%)					
	1960	1976	2000	2011	2013	2019
Quirio	11	11	12	11	11	14
Carossio	18	43	34	31	35	29
Castilla	12	28	34	26	29	25
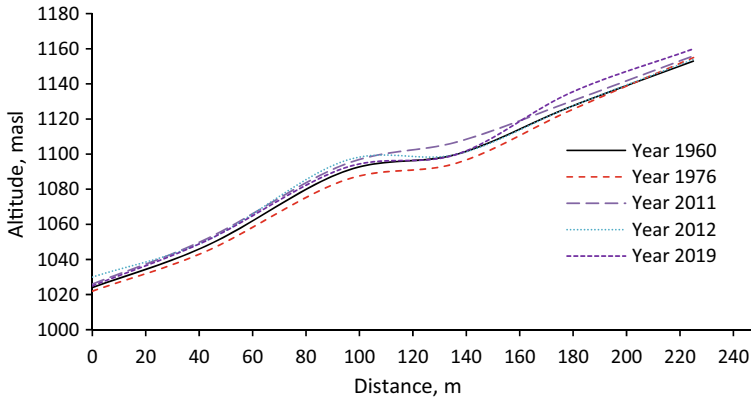
Fig. 6 Longitudinal profiles in Carossio Creek in the surveyed area by drone

5 The Volume of Solid Retained by Debris Flow Barriers

After the ENSO phenomenon event occurred between January and March 2017, maintenance work was made for installed debris flow barriers, in the basins with the occurrence of critical debris flows of the district of Lurigancho [16, 17].

It includes both an inspection to verify the operating conditions and to do cleaning works of the retained sediment by each barrier. It was observed that the retained debris flows solids are composed of gravel, sand, and silt made up of stone blocks from 30 to 60 cm [16, 17].

These debris flow barriers were effective for the control of debris flows, because they retained a large part of the coarse material, thus mitigating the destructive effects of the debris flows and avoiding loss of human life and material damage.

The results observed for the Castilla and Carossio streams are summarized below. Unfortunately, the information on the Quirio stream was not received.

On the other hand, in the field inspection carried out during this research in April 2018 in Quirio creek, it was verified that the debris flow barriers that are installed in the upper part of the riverbed had full retention volume.

5.1 Results in Carossio Basin

The report by Valle (2017) is presented below [16].

Between January and March of 2017, an inspection and verification of the operating conditions of the debris flow barriers that had been installed in the Carossio basin with the occurrence of critical debris flows were carried out, as a result. The retained volumes by each debris flow barrier installed in the upper part of the main channel were measured is shown in Table 6.

Table 6 Retained volumes by each debris flow barrier installed

Debris flow barrier	Retained volume (m^3)
1	43.51
1	11.09
3	876.22
4	2301.39

The installed barriers in the Carossio basin retained a large part of the contribution of debris flows, specifically the largest material such as rocks and/or stone blocks of 30, 60–90 cm; also, gravel and sand, giving time to evacuate the population exposed to danger.

5.2 Results in Castilla Basin

The report by Valle (2017) is presented below [17]. In the Castilla basin, a total of 3 debris flow barriers were installed, which have a height of 4 at 6 m and 25–30 m wide. From the field visit in April of 2017, it was verified that the three installed debris flow barriers had a 100% retention volume, as shown in Fig. 7.

However, it was observed that the bed of the stream presented loose material of large dimensions between 0.50 and 4.00 m in diameter, and this is due to the deposition by the action of gravity (colluvial deposits) and the weathering of the existing bedrock in the slopes of the creek. The volume retained in debris flow barrier N ° 7 was 36.29 m^3.

Fig. 7 Volume of solids retained in the Castilla debris flow barrier in 2017

6   Conclusions and Recommendation

Although satellite images and GIS allow the spatial analysis of the data that cannot be collected in the field, in this study in most cases, the results were incomplete or generated a wrong topography, mainly for ENSO 2017 event.

Because of that, it was not possible to compare the estimated volumes of erosion in the upper part of the basin with the volumes of the solids retained by the barriers during the occurrence of ENSO 2017, and the retention efficiency of the barrier was no calculated.

The field investigations after the ENSO 2017 occurrence made it possible to verify that the debris flow barriers allowed to mitigate the damages avoiding the loss of human life and material damage.

It is recommended to continue with this research because knowing and characterizing the geomorphological change using satellite information would allow a better understanding of the debris flow characteristics to analyze the convenience and technical requirements for the implementation of retention barriers in other dangerous streams that are difficult to access.

References

 1. Raimat, Q.: Dinámica y peligrosidad de las corrientes de derrubios: Aplicación en el Barranco de Erill, Pirineo Catalán. Tesis Doctoral Universitat Politècnica de Catalunya, Facultad de Ingeniería de Caminos. Cantalunya (2018)
 2. Abad, C.: Huaycos en 1987 en el distrito de Lurigancho – Chosica (Lima- Perú). Revista Bulletin de I´lnstitut francais d´études andines **38**(3), 475–486 (2009)
 3. Alharbi, T., Sultan, M., Sefry, S., ElKadiri, R., Ahmed, M., Chase, R., Chounaird, K.: An assessment of landslide susceptibility in the Faifa area, Saudi Arabia, using remote sensing and GIS techniques. Nat. Hazard. **14**(6), 1553 (2014)
 4. SENAMHI Homepage: Datos hidrometeorologicos https://www.senamhi.gob.pe/?&p=estaciones. Last accessed 14 Mar 2021
 5. USACE-HEC Hydrologic modeling system HEC-HMS technical reference manual. US Army Corps of Engineers, Hydrologic Engineering Centre (HEC), Davis, USA (2000)
 6. USACE-HEC Hydrologic modeling system HEC-HMS v3.2 user's manual. US Army Corps of Engineers, Hydrologic Engineering Center (HEC), Davis, USA (2008)
 7. Instituto geográfico del Peru, IGN Homepage: https://www.gob.pe/ign. Last accessed 14 Mar 2021
 8. Catastro Rural Ministerio de Agricultura Homepage: https://www.midagri.gob.pe/portal/664-catastro-rural. Last accessed 14 Mar 2021
 9. EARTHDATA Homepage: https://search.earthdata.nasa.gov/search. Last accessed 14 Mar 2021
10. Google Earth Search Engine Homepage: https://explorer.earthengine.google.com/#workspace. Last accessed 16 Jan 2020
11. Google Earth Engine Homepage: https://code.earthengine.google.com/. Last accessed 16 Jan 2020
12. Guadalupe G.E., Carrillo, H.N.: Caracterización y análisis de los huaycos del 5 de abril del 2012 Chosica- Lima. Revista Del Instituto De Investigación De La Facultad De Ingeniería Geológica, Minera, Metalúrgica Y Geográfica **15**(29), 69–82 (2013)

13. Instituto Nacional de Defensa Civil (INDECI) Homepage: Reporte de Situación N° 404 – 06/04/2012/COEN-INDECI/02:30 HORAS (REPORTE Nº 05). https://reliefweb.int/sites/reliefweb.int/files/resources/Full_Report_3748.pdf. Last accessed 10 July 2018
14. Son, R., Wang, S., Tseng, W., Barreto, C., Becker, E., Yoon, J.: Climate diagnostics of the extreme floods in Peru during early 2017. Clim. Dyn. **54**, 935–945 (2020)
15. Nex, F., Remondino, F.: UAV for 3D mapping applications: a review. Appl. Geomat. **6**, 1–15 (2014). https://doi.org/10.1007/s12518-013-0120-x
16. Valle, h.: Descolmatación y trabajos de rehabilitación y mantenimiento de las barreras dinámicas contra flujo de detritos, instaladas en la quebrada Carossio. GSH Genien SRL. Documento n.º ING-IG-IF-007_A. Lima (2017)
17. Valle, h.: Descolmatación y trabajos de rehabilitación y mantenimiento de las barreras dinámicas contra flujo de detritos, instaladas en la quebrada Mariscal Castilla. GSH Genien SRL. Documento n.º ING-IG-IF-005_A. Lima (2017)

Investigation of Flow Structures Along the Embankment Generated Nearby Finite Riparian Vegetation

Romitha Wickramasinghe and Norio Tanaka

1 Introduction

Vegetation growth in open-channel waterways has been a nuisance problem because it reduces the discharge capacity. On the other hand, driftwood and debris transported by floods can accumulate in riparian vegetation. They can block the flow and, consequently, backwater rise and, thus, overtop the near embankment. Therefore, river management authorities have removed the riparian vegetation regularly. However, nowadays, river and wetland management attitudes have been changing to recognize essential and complex interdependence between riparian vegetation and fluvial systems on river hydrodynamics, sediment transport, and morphology [5, 6]. Because of such importance, pioneering studies on vegetation hydrodynamics have been carried out over the last decades by combining experimental research in flumes and numerous field investigations.

Zong and Nepf [19] identified three distinct flow zones around a rectangular finite emergent vegetation patch placed at the edge of the flume channel, i.e., diverging flow at the leading edge of the patch, a fully developed area inside the patch, and high scouring shear layer region at the edge of the patch. Testing a rectangular emergent porous patch in the middle of a flume channel, Rominger and Nepf [15] discussed that two parallel edges in the streamwise generated Kelvin–Helmholtz (KH) vortex streets and communicated across the patch by penetrating. This leads to enhancing the strength of the generated vortex relative to vortices that form at a single interface. Meanwhile, Zeng and Li [18] observed a varied Reynolds stress profile and peak turbulence kinetic energy at the canopy downstream.

R. Wickramasinghe · N. Tanaka (✉)
Graduate School of Science and Engineering, Saitama University, Saitama, Japan
e-mail: tanaka01@mail.saitama-u.ac.jp

N. Tanaka
International Institute for Resilient Society, Graduate School of Science and Engineering, Saitama University, Saitama, Japan

Many authors have argued the role of patch density on developing flow zones around vegetation canopies. Rominger and Nepf [15] introduced a parameter called non-dimensional canopy flow blockage (C_Dab), which is a function of the cylinder drag coefficient (C_D), canopy solid volume fraction (a), and the canopy half-width (b). They classified canopies into two types as high flow blockage canopy ($C_Dab \geq 2$) and low flow blockage canopy ($C_Dab < 2$). Okamoto and Nezu [11] have reviewed that the streamlines in the development zone were accelerated for dense canopies compared to sparse canopies. This was also endorsed by the experiment of Zeng and Li [18]. They mentioned a shorter adjustment region with high turbulence observed inside the patch when density increases. Meantime, Kim et al. [8] disclosed that sediment deposition near the finite patch is influenced strongly by flow blockage, such that the deposition rate decreased as flow blockage increased. In addition, several authors have disclosed Von Karman (VK) vortex street forming behind the finite forest patches and its relation to the patch density. Takemura and Tanaka [17] revealed that gap spacing in the cross-stream direction of cylinders plays a vital role in the stability of Primitive Karman Vortex (PKV) street formed behind each cylinder. Besides, Chen et al. [2] discussed the VK vortex and spatial scale factor of adjustment length incorporated with wake structures behind an emergent porous forest model. They identified two types of turbulence regions within the patch, i.e., stem-scale turbulence within the patch and patch-scale turbulence (VK) at the edge of the patch. Behind the patch (in VK vortex street), high turbulence inhibits the deposition. The findings indicate that when C_DaD (here D is the patch diameter) increases, steam scale turbulence decreases, and patch-scale turbulence increases, and the position of the patch-scale turbulence shifts closer to the patch.

Despite that, historical information shows that debris jams also can control local channel hydraulics and lead to scouring and deposition around debris jam. Conversely, the natural formation of woody debris jams provides insights into habitat restoration and ecosystem-based watershed management [1, 3]. So far, authors have treated debris jams as single and tangible objects [4, 7, 16]. However, Gippel et al. [4] documented that, momentum approach is applicable only in individual items where they do not account for the wake interference effect of multiple debris. But in reality, debris is complex and porous accumulations of heterogeneous materials. This argument was supported by Manners et al. [10] by treating debris jams as complex and porous accumulations of heterogeneous materials, and they concluded that the assumption of debris' non-porosity could result in a 10–20% overestimation of drag force, which is not reflective of natural debris jams. The empirical equation for the drag force (F_d) is given by, $F_d = \frac{1}{2}\rho C_d A_{f(emp)} U_{AP}^2$ (where ρ: density of water, $A_{f(emp)}$ is measurable submerged frontal area of the obstruction and U_{AP} is approach velocity), and Manners et al. [10] acknowledged that the calculated back term $(C_d A_f)_{calc}$ has more useful for implementing the above drag equation because neither C_d nor A_f (emp) has precise physical meanings on their own. Meantime, an experimental study by Pagliara and Carnacina [12] characterized debris by roughness, shape, and porosity to imitate the

natural formation of debris. The interaction of two-dimensional flow and rough debris accumulations increases the shear stress and turbulence and, consequently, affects the scour evolution process. Yet different knowledge gathering on vegetation hydrodynamics and debris forming is excessive, hybrid studies concerning the entrapment of debris transported by floods by vegetation are lacking.

Meanwhile, a dike breach in the Toki River in Saitama Prefecture, Japan, occurred during the typhoon Hagibis in 2019 October. During the survey, it was found that finite vegetation Bamboo patches exist in the riparian zone with gaps to the embankment. Furthermore, we observed a large amount of debris has piled up at the edges of the vegetation patches. Considering Toki River dike breaching and previous assessments, the following questions were raised in this study.

1. Does the gap between the vegetation patch and open-channel embankment affect the flow hydrodynamics along the embankment?
2. Does the angle of the vegetation patch to streamline has an impact on flow hydrodynamics along the embankment?
3. What is the effect of debris trapping on in above 1 and 2?

2 Methodology

2.1 Preliminary Work

As the preliminary work, a field survey was conducted to collect data at the breached levee site in the Toki River. From there, following data were collected in the respective riparian Bamboo patch. To understand the debris trapping patterns, an UAV survey was conducted at the site. As per Fig. 1, the fringe faces of the forest patch had a high capacity for trapping debris. The trapped debris in the vegetation patch mainly consisted of grass, leaves, roots, and driftwood, where a high volume of grass could be observed.

2.2 Laboratory Experiment Methods

The flume experiments were conducted in a 5 m long, 0.7 m wide, and 0.5 m height glass-sided straight rectangular channel with a slope of 1/500 in Saitama University.

Considering the Froude number similarity, a subcritical flow condition was adopted to represent the hydraulic conditions in flood plains. A steady state was maintained throughout the experiment series to better understanding the phenomena. All the experiment cases were investigated for a constant flow rate of $0.014 \text{ m}^3 \text{ s}^{-1}$ (Fr ≈ 0.7).
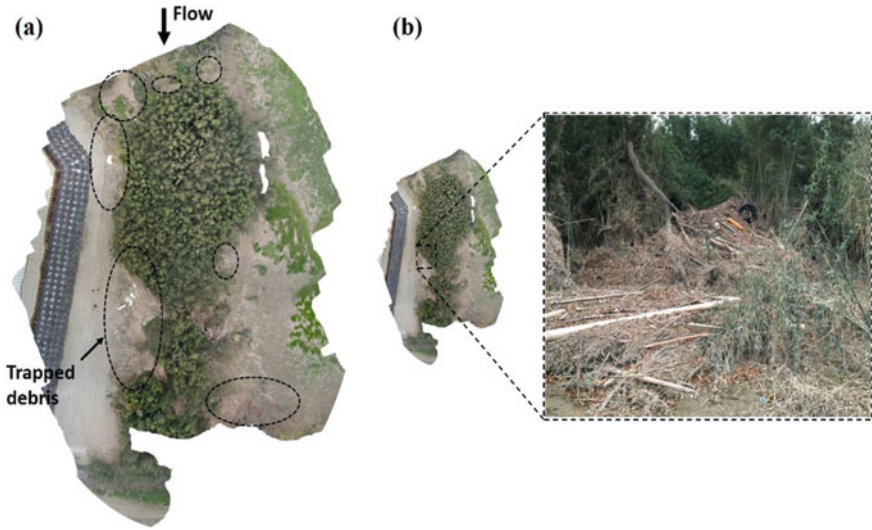
Fig. 1 Properties of debris trapping at the Toki River. **a** Debris was mostly trapped by the fringe faces of the vegetation patch. **b** Trapped debris mainly consisted of grass or woody type

Finite Vegetation Model (VM). The reduced scale ratio of the physical model to the prototype was approximated to be about 1:30. The reduced scale diameter of existing Bamboo trees (0.0012 m) was challenging to handle in the experiment. A matured Madake Bamboo tree has an average trunk diameter of approximately 0.15 m [9]. (Therefore, wooden cylinders of 0.005 m in diameter (D) were used to represent the vegetation. It is assumed that this model represents debris trapping by the trunk(s) only in the emergent condition, and the influence of the crown in VM was ignored. The vertical smooth wooden cylinders well represent the Bamboo trees in the riparian zone. The spacing between the wooden poles in the VM was based on the actual spacings found from the field survey (assuming all the trees have existed in an equiangular triangle array) and the scaled-down spacing (S) was 2 cm. The aspect ratio (width: length) of VM was selected as 1: 2.5, where the actual aspect ratio of the forest patch in the Toki River was found to be around 1: 2.4 (Google Earth). The VM width (W_v) and length (L_v) were generally selected as 12 cm × 30 cm respectively, to match the aspect ratio. Additionally, vegetation density can also be represented by G/D value [17], where G is the apparent spacing of cylinders in cross-stream direction. The corresponding G/D value is 1.5 and it is sparse (Fig. 2).

Debris Model Used (DM). The debris model used in the experiment was made from coconut fiber. This is to represent the actual nature of grass and roots trapped by the Bamboo patch. A rectangular shape coconut fiber mat was used as the DM. The debris mat's width was taken as 0.12 and 0.30 m to cover the fringe faces of VM, and the height was set to satisfy the emergent condition. The thickness of the DM to be around 0.025 m, and scaled up thickness is approximately 0.75 m.
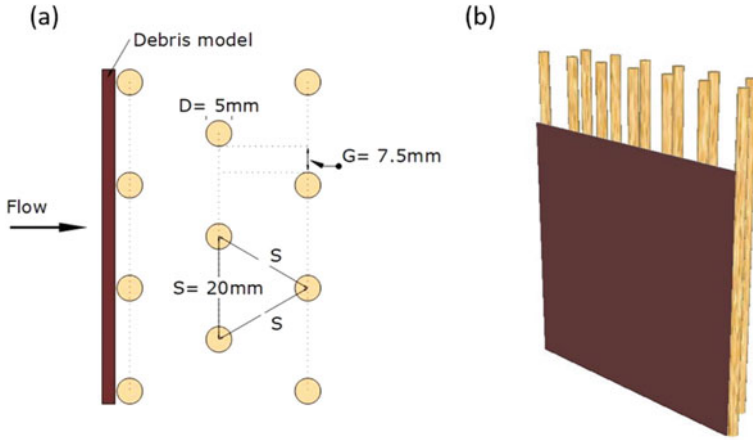
Fig. 2 Schematic view of the VM and DM. **a** Plan view. **b** Isometric view (not to the scale)

This value agrees well with the actual average trapped debris thickness found being about 0.64–1.03 m by a survey conducted in different areas of Saitama Prefecture, Japan, after the 2019 typhoon.

Experiment Cases. The gap between the flume wall and VM was defined as a non-dimensional parameter D_{nd} ($D_{nd} = d/W$, where d is the gap between the flume wall and VM, and W is the channel width). The angle (ϑ) between VM and streamline was set for six angles as 0, 30, 60, 90, 120, and 150° as in Fig. 3. Each configuration was tested for only VM and VM with DM to reproduce debris trapping as in Table 1.

During the experiment, the water depth along the right-hand side (rhs) wall was measured. To minimize the effect of the opposite left-hand side (lhs) wall, the D_{nd} was never larger than 0.375, or ≈50% of the total flume width. This kind of attention was also has done by [14, 15] in their studies. Moreover, during the test
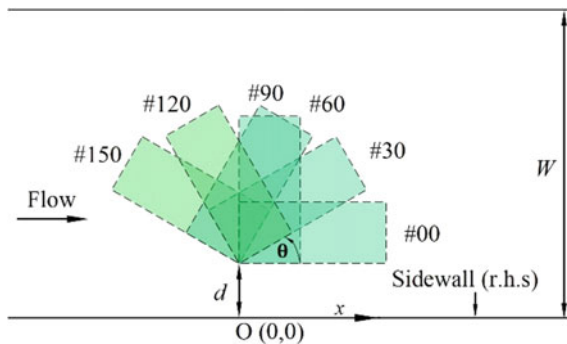
Fig. 3 Rotation of VM with respect to the reference point

Table 1 Experiment cases

Case ID	d (m)	(D_{nd})	DM	Θ (°)
A	0.00	0.00	Yes, No	0, 30, 60, 90, 120, 150
B	0.0875	0.125	Yes, no	0, 30, 60, 90, 120, 150
C	0.175	0.25	Yes, no	0, 30, 60, 90, 120, 150
D	0.2625	0.375	Yes, no	0, 30, 60, 90, 120, 150

run, it was verified no effect from the lhs streamlines on the concerned area. Thus, all experiment condition mimics the real flood plain embankment existence.

3   Results and Discussion

3.1   Water Depth Along the Sidewall

The water depths were presented as a non-dimensional parameter (h_{nd}) and defined as corresponding water depth with respect to nothing case water depth. An invariant maximum h_{nd} was observed along the sidewall upstream of the VM for each configuration as in Fig. 4. Therefore, the average h_{nd} in this upstream region was obtained to discuss the maximum afflux caused by the model.

h_{nd} for VM. According to Fig. 5, when D_{nd} increases, h_{nd} shows an overall decreasing trend for every angle. For, D_{nd} = 0–0.25, the h_{nd} is approximately the same, and beyond that (D_{nd} = 0.375), h_{nd} decreases for a given angle. Although 90° orientation has caused the highest afflux, the increment is not significant compared to other angles. This is because the porous vegetation model alters the flow direction and produces more diverse flows along the sidewall around the VM.

h_{nd} for DM. According to Fig. 6, debris trapping (DM) simulation cases, maximum h_{nd} shows a declining trend with increasing D_{nd} following a similar
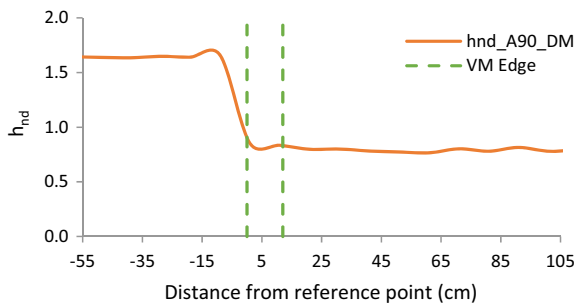
Fig. 4 h_{nd} along the sidewall of A90 debris trapping case. Maximum water depth was observed upstream of the VM
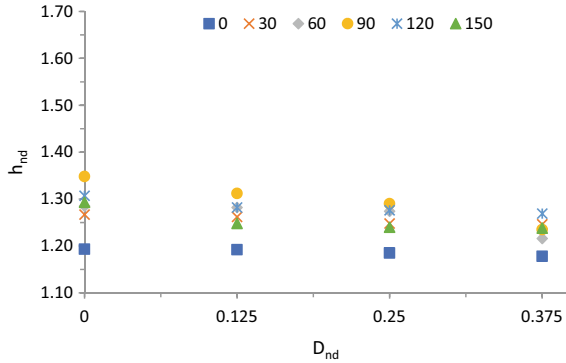
Fig. 5 Maximum h_{nd} along the side wall for VM. Here $D_{nd} = 0$, 0.125, 0.25, and 0.375 correspond to cases A, B, C, and D
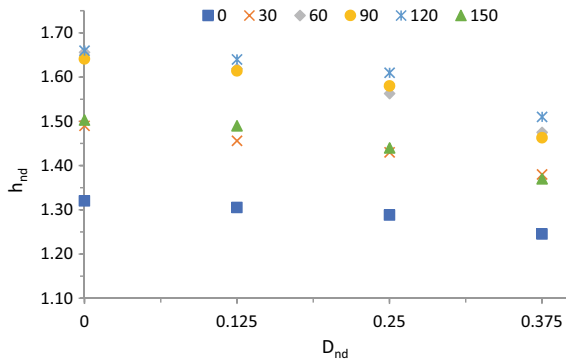
Fig. 6 Maximum h_{nd} along the side wall plotted for debris trapping cases. Here, $D_{nd} = 0$, 0.125, 0.25, and 0.375 correspond to cases A, B, C, and D

concept as in Fig. 5. Along the side wall, 60°, 90°, and 120° angles have recorded the highest h_{nd} without significant difference for all the D_{nd} values when simulating debris trapping. 60°, 90°, and 120° angles have reported maximum afflux of about 65% for $D_{nd} = 0$, compared to nothing cases. Additionally, the maximum h_{nd} recorded for 30° and 150° angles is nearly the same for all the D_{nd} values. They both have shown about 50% maximum afflux for $D_{nd} = 0$. In addition, the lowest afflux along the sidewall has been recorded by 0° angles despite the D_{nd}.

Canopy Blockage Ratio. The blockage ratio of the debris trapped models can be explained as below.

By assuming the non-porosity of DM, the projected length of the model normal to the flow can be calculated as per Fig. 7. The blockage length (l_d) is a function of the angle of VM. Thus, knowing l_d, we can calculate the blockage ratio (B). B is the ratio between l_d and flume width ($W = 70$ cm).
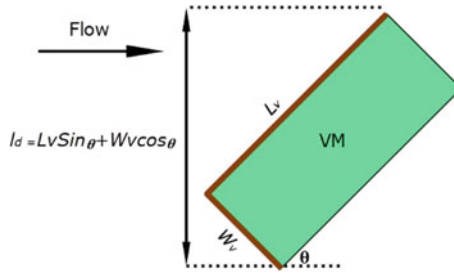
Fig. 7 Projected length of the model normal to the flow direction

Table 2 Blockage ratios of the canopy

$\theta°$	l_d (cm)	$B = l_d/W$
0	12.00	0.17
30	25.39	0.36
60	31.98	**0.46**
90	30.00	**0.43**
120	31.98	**0.46**
150	25.39	0.36

Table 2 shows 60°, 90° and 120° angles generate higher B due to inserting the debris mat. That is because compared to other angles, these three angles generate higher blocking length normal to the flow after trapping debris. 60°, 90° and 120° angles obstruct the flow area by 46%, 43% and 46% respectively, by debris trapping. These values are significant because Parola et al. [13] have argued that hydrodynamic forces can increase significantly as flow blockage (B) approaches about 30% of the total area. Therefore, in the current study, the flow obstruction contracts the flow around the sidewall, and consequently, the upstream flow velocity is reduced, and the water depth is increased.

3.2 Standing Wave Fields Generated Along the Sidewall

During the experiment, consecutive standing wave fields were observed along the sidewall. Figure 8 shows the phenomena of developing standing wave fields by interfering with secondary waves to primary waves along the flume sidewall for a DM case.

Standing wave fields along with the sidewall contain two peaks in its magnitude. The first peak (#1) is located at L_1 distance, and the second peak (#2) is formed at L_2 from the reference point O. The first peak is related to the resultant wave generated by reflection of approaching flow by the model. The resultant wave strikes the sidewall and produces the first peak. Because the debris mat has been
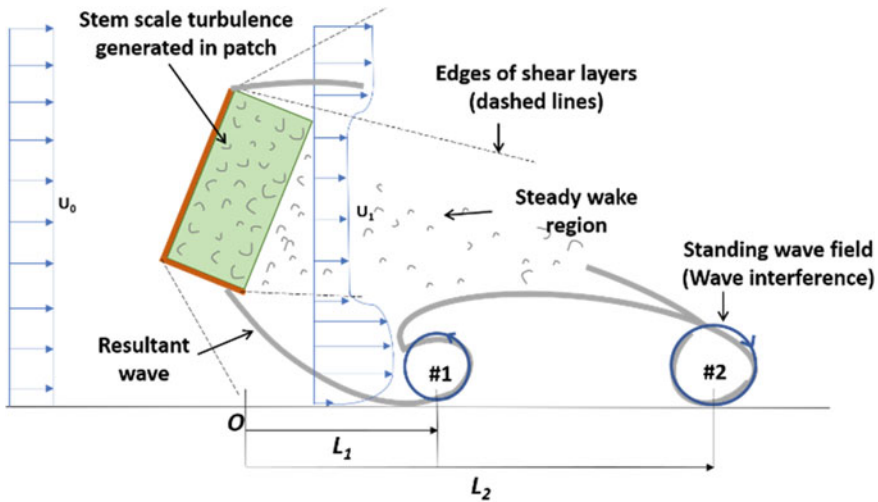
Fig. 8 Schematic view of generating standing wave fields along the sidewall

manufactured from coconut fiber and its porous quality, some flow could move through the patch while maintaining a low flow velocity behind the canopy. Previous authors have called this a 'steady wake region' [2]. A significant number of wake structures coming from steady wake region form a vortex street that propagates to the sidewall and interferes with the waves traveling through the constricted area to develop the second standing wave field along the sidewall.

As shown in Fig. 9, for case A, both L_1, and L_2 were not reported for VM and DM. Because streamlines are diverted away from the canopy when it is placed at the sidewall. For the DM configurations, L_1 has reported for case B and except 120° and 150° angles in case C. L_2 has reported for cases B, C, and D with high magnitude. By increasing the gap, L_1 diminishes because reflected resultant waves by the DM are unable to strike the sidewall due to the high gap between the canopy and sidewall. The same reason can be applied for L_1 of C120DM and C150DM, where the canopy orientation drives streamlines further downstream.

In contrast, VM alters the flow direction and produces flows that are more diverse along the sidewall near the model. Therefore, it could not distinguish the first peak standing wave field (L_1). However, in higher gaps, a significant wave field (L_2) was formed for cases C and D. When debris is trapped, intermediate gaps (B and C) generate two peak standing wave fields. Moreover, higher L_2 was reported for DM in C and D compared to the corresponding VM, showing that the standing wave field shifts further downstream when the debris mat is inserted. This is due to the acceleration of the wave paths by the debris model.
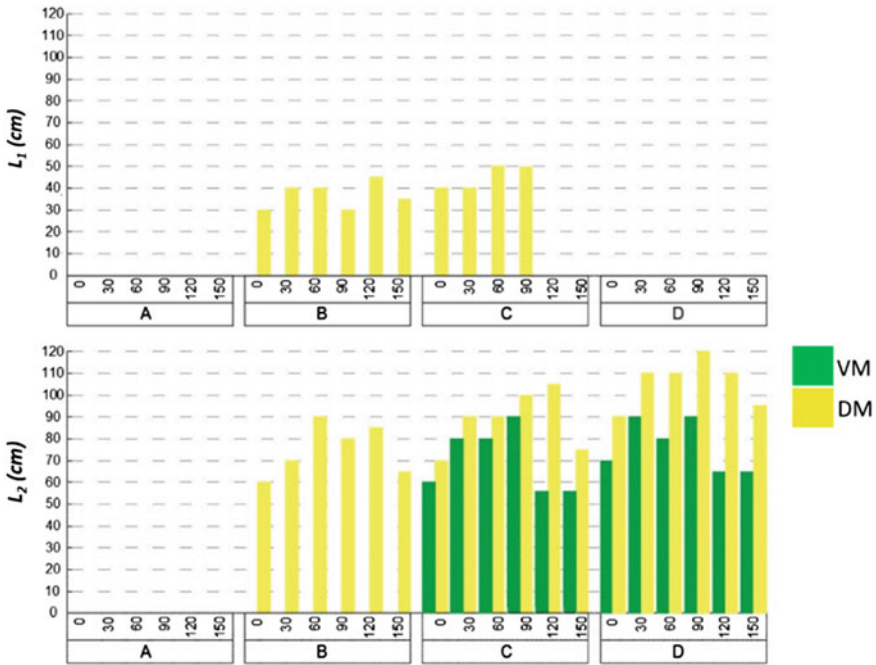
Fig. 9 Graphical representation of L_1 and L_2

4 Conclusion

A series of flume experiments simulating finite riparian vegetation showed that debris trapping in flood events could aggravate the flow structures along the flood embankment. Debris trapping increases the frontal density of forest canopies. Therefore, sparse forest canopies convert to a high flow blockage canopy. In that case, 60°, 90°, and 120° patch orientations can cause significant afflux along the open-channel wall.

Besides, the intensity of standing wave fields generated along the open-channel wall increased when introducing debris, particularly for intermediate gaps between vegetation canopy and open-channel wall. As a result, embankment erosion can be increased in the vicinity of a forest canopy by debris trapping. Therefore, considering the backwater rise along the embankment and erosion, it is recommended to avoid 60°, 90°, and 120° patch orientations and intermediate gaps between forest canopy and embankment.

References

1. Abbe, T.B., Montgomery, D.R.: Large woody debris jams, channel hydraulics and habitat formation in large rivers. Regul. Rivers: Res. Manage. **12**(2–3), 201–221 (1996)
2. Chen, Z., Ortiz, A., Zong, L., Nepf, H.: The wake structure behind a porous obstruction and its implications for deposition near a finite patch of emergent vegetation. Water Resour. Res. **48**(9), 1–12 (2012)
3. Fetherston, K.L., Naiman, R.J., Bilby, R.E.: Large woody debris, physical process, and riparian forest development in montane river networks of the Pacific Northwest. Geomorphology **13**(1–4), 133–144 (1995)
4. Gippel, C.J., O'Neill, I.C., Finlayson, B.L., Schnatz, I.: Hydraulic guidelines for the re-introduction and management of large woody debris in lowland rivers. Regul. Rivers: Res. Manage. **12**(2–3), 223–236 (1996)
5. Gualtieri, C., Ianniruberto, M., Filizola, N., Santos, R., Endreny, T.: Hydraulic complexity at a large river confluence in the Amazon basin. Ecohydrology **10**(7), 1–12 (2017)
6. Gurnell, A.: Plants as river system engineers. Earth Surf. Proc. Land. **39**(1), 4–25 (2014)
7. Hygelund, B., Manga, M.: Field measurements of drag coefficients for model large woody debris. Geomorphology **51**(1–3), 175–185 (2003)
8. Kim, H.S., Kimura, I., Shimizu, Y.: Bed morphological changes around a finite patch of vegetation. Earth Surf. Proc. Land. **40**(3), 375–388 (2015)
9. Ministry of Agriculture, Forestry and Fisheries: Main types of bamboo: https://www.rinya.maff.go.jp/j/tokuyou/take/syurui.html, last accessed 2021/03/03.
10. Manners, R.B., Doyle, M.W., Small, M.J.: Structure and hydraulics of natural woody debris jams. Water Resour. Res. **43**(6), 1–17 (2007)
11. Okamoto, T., Nezu, I.: Spatial evolution of coherent motions in finite-length vegetation patch flow. Environ. Fluid Mech. **13**(5), 417–434 (2013)
12. Pagliara, S., Carnacina, I.: Temporal scour evolution at bridge piers: effect of wood debris roughness and porosity. J. Hydraul. Res. **48**(1 EXTRA ISSUE), 3–13 (2010)
13. Parola, A.C., Apelt, C.J., Jempson, M.A.: NCHRP report 445: debris forces on highway bridges. Transportation Research Board (TRB), National Research Council, Washington DC (2000)
14. Pasha, G.A., Tanaka, N.: Effectiveness of finite length inland forest in trapping tsunami-borne wood debris. J. Earthq. Tsunami **10**(4), 1–26 (2016)
15. Rominger, J.T., Nepf, H.M.: Flow adjustment and interior flow associated with a rectangular porous obstruction. J. Fluid Mech. **680**, 636–659 (2011)
16. Shields, J.F.D., Gippel, C.J.: Prediction of effects of woody debris removal on flow resistance. J. Hydraul. Eng. **121**(4), 341–354 (1995)
17. Takemura, T., Tanaka, N.: Flow structures and drag characteristics of a colony-type emergent roughness model mounted on a flat plate in uniform flow. Fluid Dyn. Res. **39**(9–10), 694–710 (2007)
18. Zeng, C., Li, C.W.: Measurements and modeling of open-channel flows with finite semi-rigid vegetation patches. Environ. Fluid Mech. **14**(1), 113–134 (2014)
19. Zong, L., Nepf, H.: Flow and deposition in and around a finite patch of vegetation. Geomorphology **116**(3–4), 363–372 (2010)

Sediment Yield Estimation and Reservoir Sedimentation Assessment Using Geospatial Tools: A Case Study of Tehri Dam Reservoir

Tripti Dimri, Shamshad Ahmad, and Mohammad Sharif

1 Introduction

The soil, climate, terrain, ground cover, comprising the biophysical environment, and interactions between them modifies the soil erosion processes. The entire process of soil erosion is influenced by the terrain characteristics such as slope, length, aspect, and shape [1]. The increasing population of the country has led to growing demand of food and shelter which in turn has led to deforestation and removal of natural vegetation. The other direct and indirect human activities that have led to degradation of land are overgrazing, converting forests to farms, cultivating steep slopes, and over exploitation of the vegetation for domestic purpose. This over exploitation of vegetation cover in the form of removal or in situ burning of crop residues with no or least addition of organic manures and intensive cultivation has led to depletion of soil organic carbon.

This problem of erosion in a watershed poses a great threat when there is a dam or a reservoir at the downstream side of the watershed. The flow of water from the watershed upstream of the reservoir can erode the watershed area and can deposit eroded material either upstream of the reservoir or in the still water of the reservoir. Reservoir sedimentation is vital problem as every reservoir is bound to suffer a loss in their storage capacity potential because of silt load, for short or long period of time [2]. This accumulated sediment is deleterious to the reservoir because it decreases the storage of water by reducing the surface area. The soil erosion and reservoir sedimentation depend largely on the material in the watershed area, its slope, nature of ground cover, and drainage patterns. Heavy rainfall falling on erodible material on a steep slope with little ground cover resulting from

T. Dimri (✉) · S. Ahmad · M. Sharif
Department of Civil Engineering, Jamia Millia Islamia, New Delhi, India
e-mail: sahmad@jmi.ac.in

M. Sharif
e-mail: msharif@jmi.ac.in

55

overgrazing or wildfire can result in substantial sediment transport and significant reservoir sedimentation. This poses a bigger problem in case of reservoirs designed for hydropower production as their useful storage volume is lost thereby increasing the stream flows which may be insufficient during the low-flow periods. However, it is very rare that reservoirs may fill completely in areas of extremely high sediment yield. Large reservoirs efficiently trap sediment supplied by upstream source areas.

Reservoir sedimentation provides a reliable measure from which to compare estimates of basin sediment yield and/or flux rate derived from other approaches. Estimates of reservoir sedimentation therefore provide a robust measure of sediment yield. There are some physically based models are such as Water Erosion Prediction Project (WEPP) [3–5], Pan European Soil Erosion Risk Assessment (PESERA) [6, 7], and European Soil Erosion Model (EUROSEM) [8] which are used for estimating the sediment yield in a region. The main drawback of such physically based model is the requirement of huge amount of data, which is almost impossible to get on a large scale [8]. However, Universal Soil Loss Equation (USLE) is a widely applied empirical models for estimating the sediment yield which was developed by Wischmeier and Smith [9].

The Universal Soil Loss Equation (USLE) determines soil loss at an outlet in the watershed as a function of rainfall energy and intensity, soil erodibility, slope length, slope gradient, soil cover, and conservation practices prevailing in the watershed [9]. The Revised Universal Soil Loss Equation (RUSLE) has the same form as the USLE but has provision for slope length and slope gradient calculations with more elaborate calculations for soil cover and conservation practices [10]. However, RUSLE can estimate only annual average soil loss from rill and interill erosion caused by rainfall splash and overland flow, but not from gully and channel erosion [10]. Bhattarai and Dutta [11] were of the view that these models are the synthesis of individual components that affect the erosion process and have the capability of assessing both the spatial and temporal variability of erosion processes.

For water resources planning and land and water management system, computation of soil erosion, sediment conveyance and its deposition in reservoir, irrigation canal, hydropower systems should be taken as top priority. The capacity and useful life of reservoir should be known for harvesting the maximum quantity of water in the whole year for treatment plant, irrigation, hydroelectricity, flow balance, flood control, etc. Conventional techniques used for the evaluation of the reservoir capacity and the sedimentation in a reservoir, like inflow–outflow technique and hydrographic survey, integrated bathymetric survey, etc. are cumbersome, clumsy, time consuming and uneconomical, and even, they involve huge manpower. An alternative of traditional methods, GIS and remote sensing technique, is used in present work to compute the loss of storage capacity and sedimentation in a reservoir. Remote sensing provides an effective way to quantify this in mountainous region which is scarcely gauged. Using satellite data to study sedimentation in a reservoir requires a good understanding of the watershed contributing the reservoir [12–14].

2   Study Area

The study area is the Bhagirathi basin situated in the Himalayan range in the state of Uttarakhand. It lies between 31°25′35.8″ N–30°22′37.8″ N latitude and 78°08′24.6″ E–79°23′44.6″ E longitude (Fig. 1). It has two tributaries, namely Bhagirathi and Bhilangana rivers originating from Gangotri and Khatling glacier, respectively. The watershed experiences 40–60% of the rainfall during rainy season. The annual average precipitation varies from 1016 to 2630 mm. The Basin length is 141.35 km and catchment area 7294.51 km^2 and basin perimeter of 560.66 km. The outlet of the basin is Tehri Dam located at coordinates 30°22′40″ N and 78°28′50″ E. Tehri dam holds Tehri reservoir spread between 30°34′58″ N and 78°19′47.5″ E to 30°24′09.5″ N and 78°36′05.8″ E. Tehri dam is a earth and rock fill dam which is about
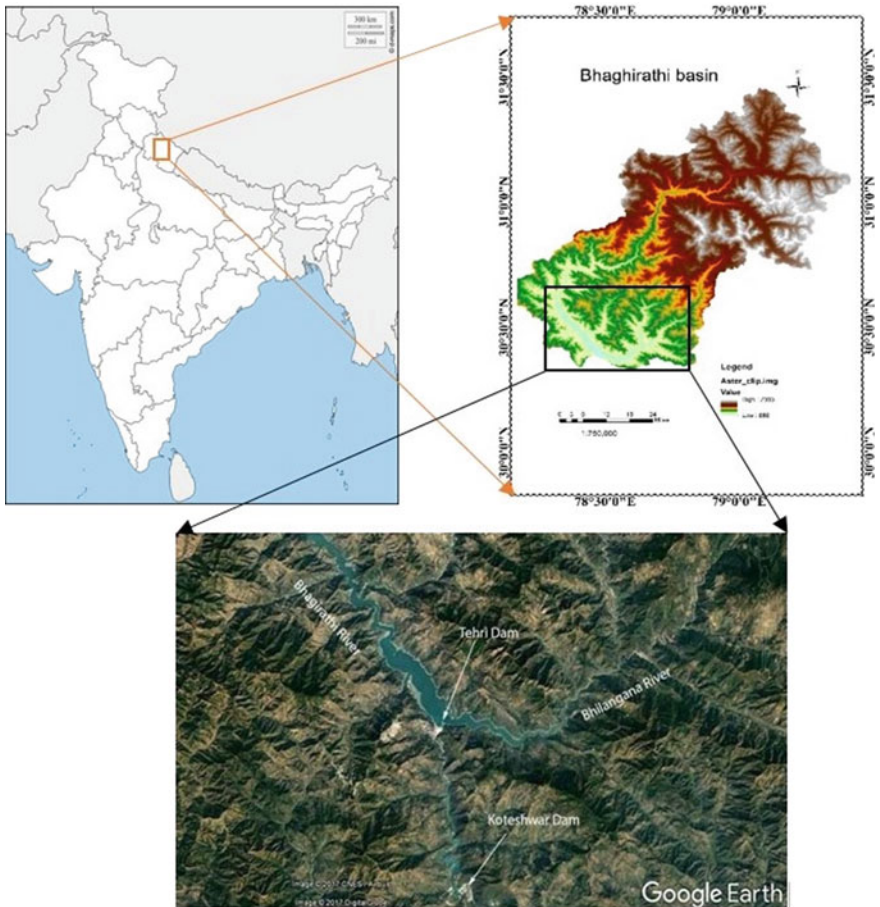
Fig. 1 Location of area of study

260.5 m high. It impounds 44 km along Bhagirathi River and 25 km along Bhilangana River, creating a dead storage of 925 mm^3 and live storage of 2615 mm^3. The total storage capacity of the reservoir is 3540 mm^3. Tehri dam operates between 835 masl (meters above sea level) maximum operating level (MFL) and 830 m (FRL) and 740 masl minimum operating level (dead storage level) [15, 16].

The geology and topographical features of the catchment along with the development activities in the watershed, such as deforestation and terrace cultivation, have increased the rate of erosion in the area. The river bed material consists of boulders, sand, and silt. The most significant sediment transport occurs during the rainy season. The specific annual sediment yield in the watershed is 907 t/km^2. The design sediment rate was estimated at 6.08 mm^3 per year. Currently, the total storage capacity is 3506 mm^3, and the live storage capacity is 2598 mm^3 [15, 16].

3 Data Used

For the RUSLE sediment yield study, Tropical Rainfall Measuring Mission (TRMM) rainfall data (https://giovanni.gsfc.nasa.gov/giovanni/) is used which is acquired through remote sensing. The soil type data is obtained from National Bureau of Soil Survey and Land Use Planning (NBSS and LUP) at 1:250,000 scale. ASTER DEM (https://lpdaac.usgs.gov/products/astgtmv003/) is used for delineating the watershed and preparation of base files.

For reservoir sedimentation study, multispectral images from Landsat-8 satellite having different bands have been taken from United States Geological Survey (USGS) Earth Explorer (https://earthexplorer.usgs.gov/). Landsat-8 carries operational land imager (OLI) and TIRS scanners covering Bands 1–9 in the visible and infrared range and band 10 and 11 in infrared range. The Band 2 (0.45–0.51 μm) of the OLI scanner is green and Band 5 (0.85–0.88 μm) is the NIR band. The data has been taken different years to facilitate the sedimentation study. Furthermore, field data form Tehri Hydro Development Corporation has also been taken. The Hydrographic survey has not been carried out till date, so the elevation capacity curve for year 2012 has been taken from previous studies.

4 Methodology

The Revised Universal Soil Loss Equation (RUSLE) is an empirical erosion model recognized as a standard method to calculate the average risk of erosion on arable land. It developed from the Universal Soil Loss Equation (USLE) developed in the US Department of Agriculture and has other similar variants such as the Modified USLE (MUSLE). The general methodology followed fir the study is summarized in Fig. 2.
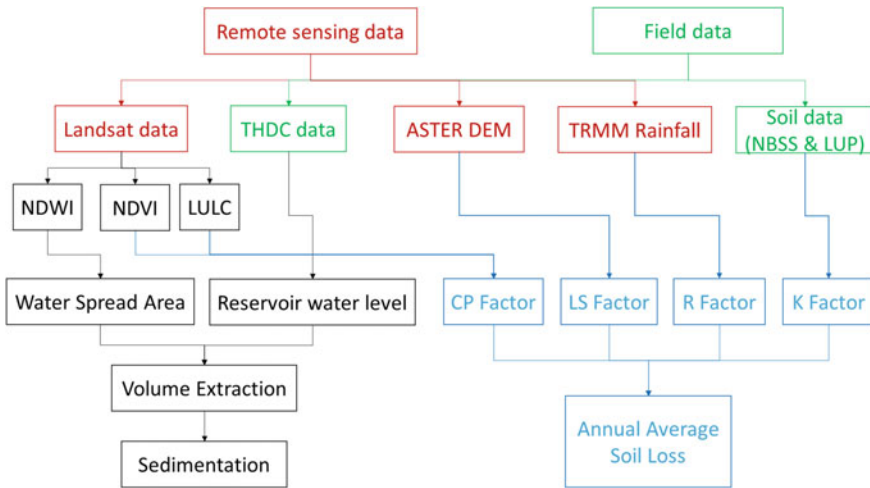
Fig. 2 General methodology followed

The governing equation for RUSLE is expressed in Eq. (1).

$$A = R * K * L * S * C * P \qquad (1)$$

where A = computed spatial average soil loss and temporal average soil loss per unit of area, expressed in the units selected for K and for the period selected for R, expressed in tons/hectare/year.

R = the erosivity factor of rainfall (R) (Fig. 3) is a function of the falling raindrop and the rainfall intensity and is the product of kinetic energy of the raindrop and the 30-min maximum rainfall intensity.

$$Ra = 79 + 0.363 * P \qquad (2)$$

where R = average erosion index and P = average rainfall (mm) obtained from TRMM data.

K = soil erodibility factor (Fig. 4) which indicates the soil loss rate per erosion index unit for a specified soil as measured on a standard plot, which is defined as a 72.6 ft (22.13 m) length of uniform 9% slope in continuous clean-tilled fallow. In RULSE, K is assumed to be constant throughout the year. Tables of K values are available in Soil Conservation Service Offices for most soils.

LS = The effect of topography on erosion in RUSLE is accounted for by the LS factor (Fig. 5). The slope length factor (LS) is calculated using following equation (iii) from ASTER DEM,
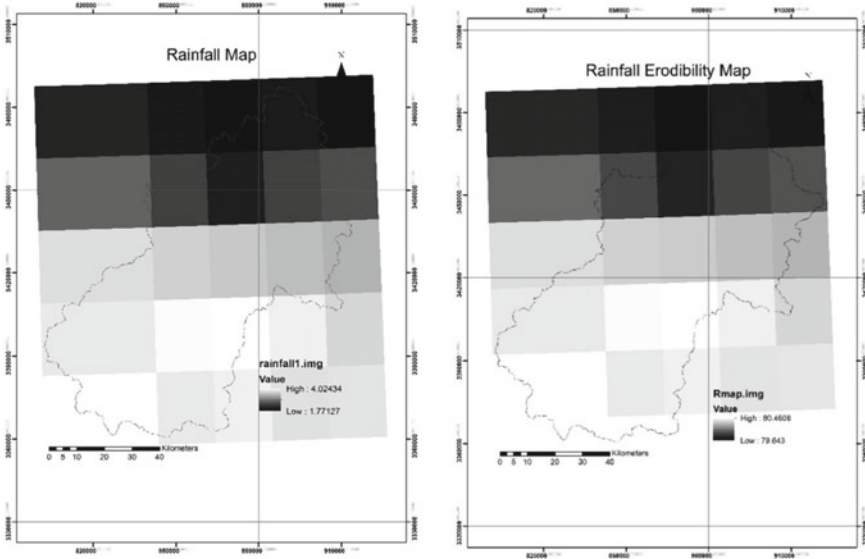
Fig. 3 Rainfall and rainfall erosivity (*R*) map
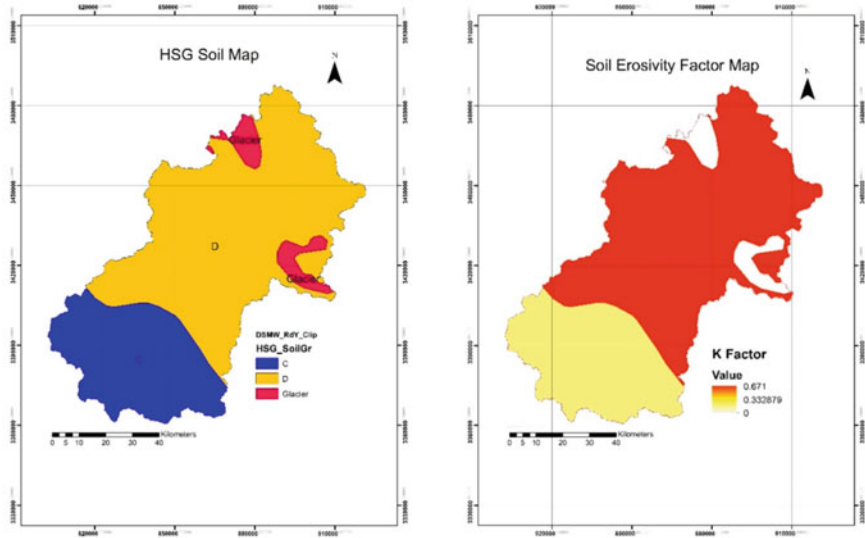
Fig. 4 Soil map and soil erodibility factor (*K*) map
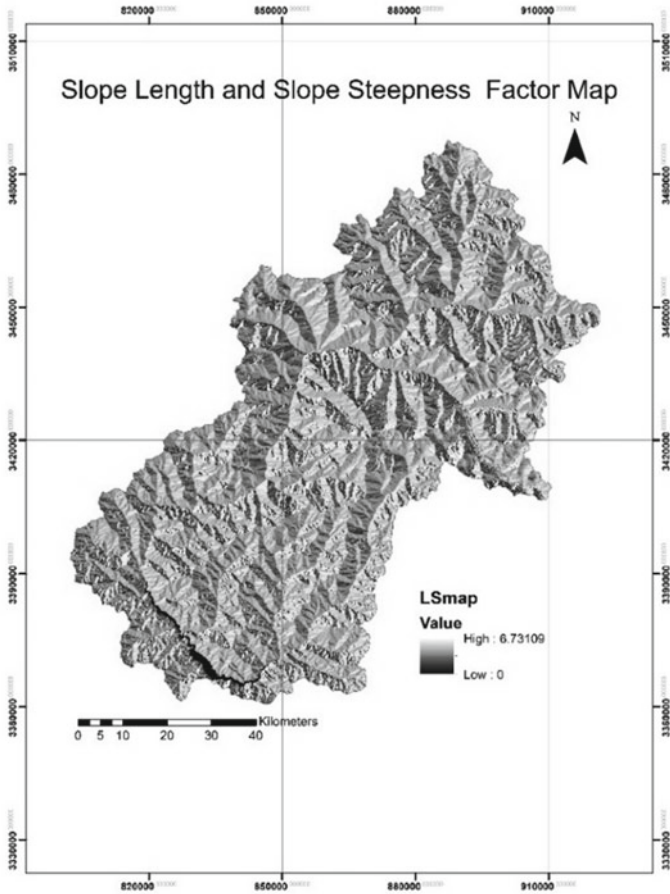
Fig. 5 Slope length factor (LS) map

$$LS = \left(\frac{\text{flow accumulation} * \text{cell size}}{22.13}\right)^{0.6} * \left(\frac{\sin(\text{slope}) * 0.01745}{0.09}\right)^{1.3} \quad (3)$$

CP = The cover-management factor (C) (Fig. 6) reflects the effect of cropping and other management practices on erosion rates. The risk of soil erosion is governed by the vegetation cover and the practices adopted for its conservation in the watershed. The vegetation cover is obtained from normalized difference vegetation index (NDVI) prepared using the Landsat-8 data. It helps in obtaining the C-factor values which range from 0 (indicating no erosion) to 1 (indicating heavy erosion).

The *P*-factor values indicate the rate of soil erosion as per the conservation practices in the study area. These conservation practices values are obtained from land use land cover of the watershed. For determination of the conservation practice
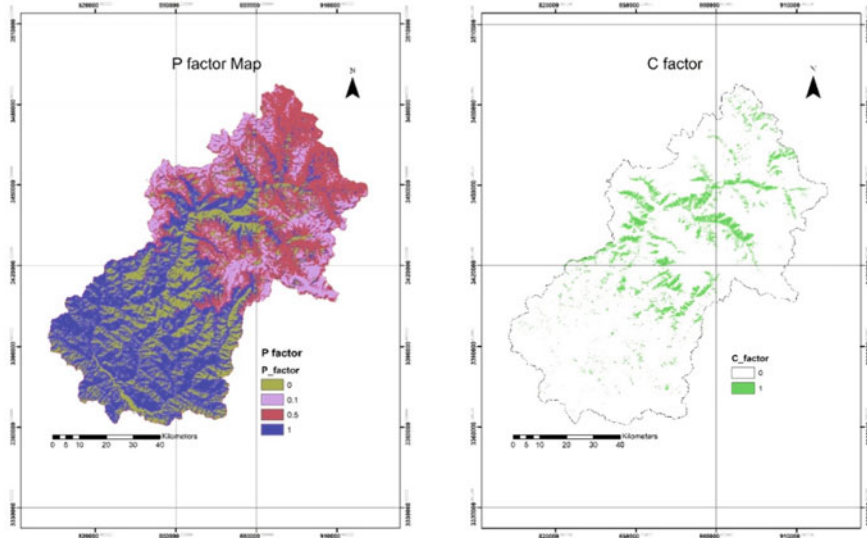
Fig. 6 Cover management (C) and conservation practices (P) factor map

of the study area, the LULC map is reclassified into four classes, namely dense evergreen forest, mixed forest, grass land and agriculture, barren land and waste land, and water bodies (Table 1).

Using the RUSLE relation (Eq. 1), these input data are integrated in ArcGIS environment to obtain estimated sediment yield in the study area. Once the sediment yield is quantified in the area, the sedimentation in the reservoir also needs to be quantified. For this reservoir, capacity is computed using prismoidal formula given by Eq. (4).

$$V = \frac{D}{3}[\text{first area} + \text{last area} + 4\Sigma\text{Even area} + 2\Sigma\text{odd areas}] \tag{4}$$

$$\text{Water spread Area} = \frac{\text{No. of Water Pixels} * \text{Pixel Area}}{1000000} \tag{5}$$

Table 1 Conservation practice factor

Reclass value	Conservation practice factor (P)
1	1
2	0.9
3	0.5
4	0

The area in the above Eq. (4) indicates the water spread area obtained by using Eq. (5). In order to identify the water pixels, Normalized Difference Water Index (NDWI) is used using green and NIR wavelength bands of Landsat-8.

$$NDWI = \frac{[Green - NIR]}{[Green + NIR]} \tag{6}$$

where green is a band that encompasses reflected green light and NIR represents near-infrared radiation.

5 Results and Discussion

A simple empirical soil erosion model of RUSLE is integrated with GIS and is applied to estimate soil erosion potential zones in Bhagirathi basin. The erosion severity map (Fig. 7) shows that the Bhagirathi basin is prioritized into three classes based on the severity condition. The basin is classified into three classes, viz., slight (<5), moderate (5–10), and high (>10). This erosion severity map revealed that about 46.67% of the area comes under high erosion category and about 26.66% each comes under moderate and slight erosion category. Suitable soil conservation practices need to be implemented in the area. The maximum value of erosion found in the Bhagirathi basin is 265.045 tons/hectare/year, and the average value of erosion found is 50.77 tons/hectare/year.

The data collected by Landsat-8 satellite from year 2013 to 2017 is used for calculating the revised capacity of the Tehri reservoir. The extraction of surface water bodies was done for the years 2013–2017 using the NDWI technique (Fig. 8), and a revised elevation capacity curve is prepared by plotting the storage capacities for different durations against the corresponding elevations. Original depth-elevation capacity curve of the year 2006 has been taken which is the year when the Tehri Dam was commissioned. The variation in the capacity depicts the loss of storage of the reservoir between the two-time intervals (from 2006 to 2017). NDWI method is used for extracting the extent of water spread and area is calculated for different elevations. The calculations are shown in Table 2. The variation of the calculated capacity of the reservoir with time is plotted against the original elevation curve (Fig. 9). In the curve, we can see the loss of storage capacity with time.

It is observed that the difference between the original elevation capacity curve and revised elevation capacity curve obtained from remote sensing technique shows the decrease in the storage capacity of the reservoir from 2006 to 2017. Since the base period (2006), the loss in live storage capacity, to 2017, is estimated to be 62.68 mm^3 (0.6268 Ha-m) which is 5.01% of the design storage capacity of the reservoir at 825 masl. Prismoidal formula is used to obtain the revised capacity between the maximum (824.75 masl) and minimum (748.4 masl) depths. The designed live capacity was 2150 mm^3, and revised capacity using remote sensing
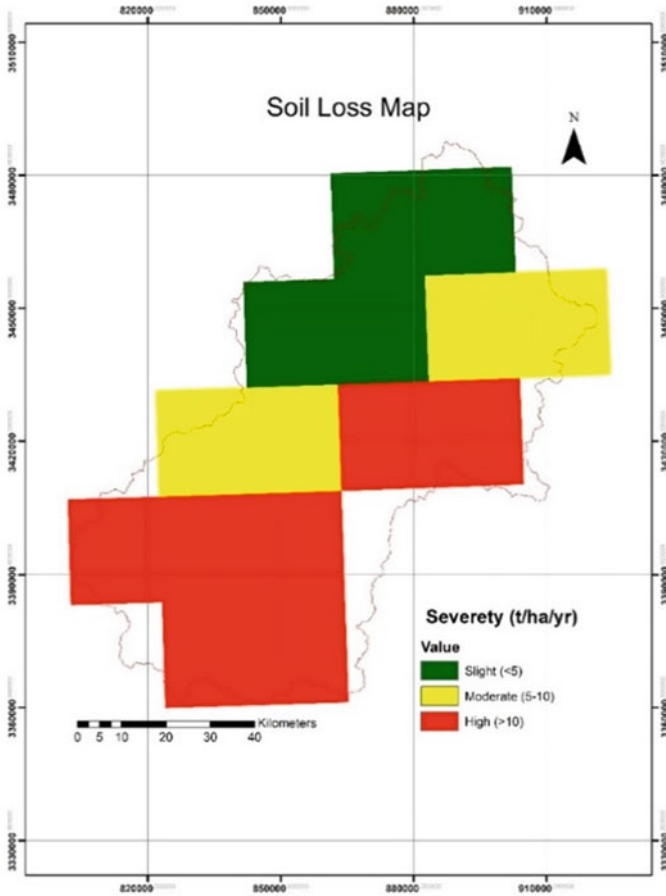
Fig. 7 Soil loss severity map

method was obtained as 2087 mm^3 in year 2017. The data for depth-area-capacity curve was taken form Tehri Hydro Development Corporation (THDC). The design capacity and the elevation from 2006 data were used to construct the depth-area-capacity curve which is used for calculating the variation of the current capacity of the reservoir from designed capacity (Fig. 9).

The sedimentation estimation is using remote sensing technique is highly sensitive for estimating the water spread area, water level information and original elevation-area-capacity curve. Its major drawback is that below the lowest observed level and above the highest observed level, sedimentation cannot be determined. This limitation of remote sensing technique does not hold importance as the zone of interest for sedimentation analysis is the live storage zone (from operation point of
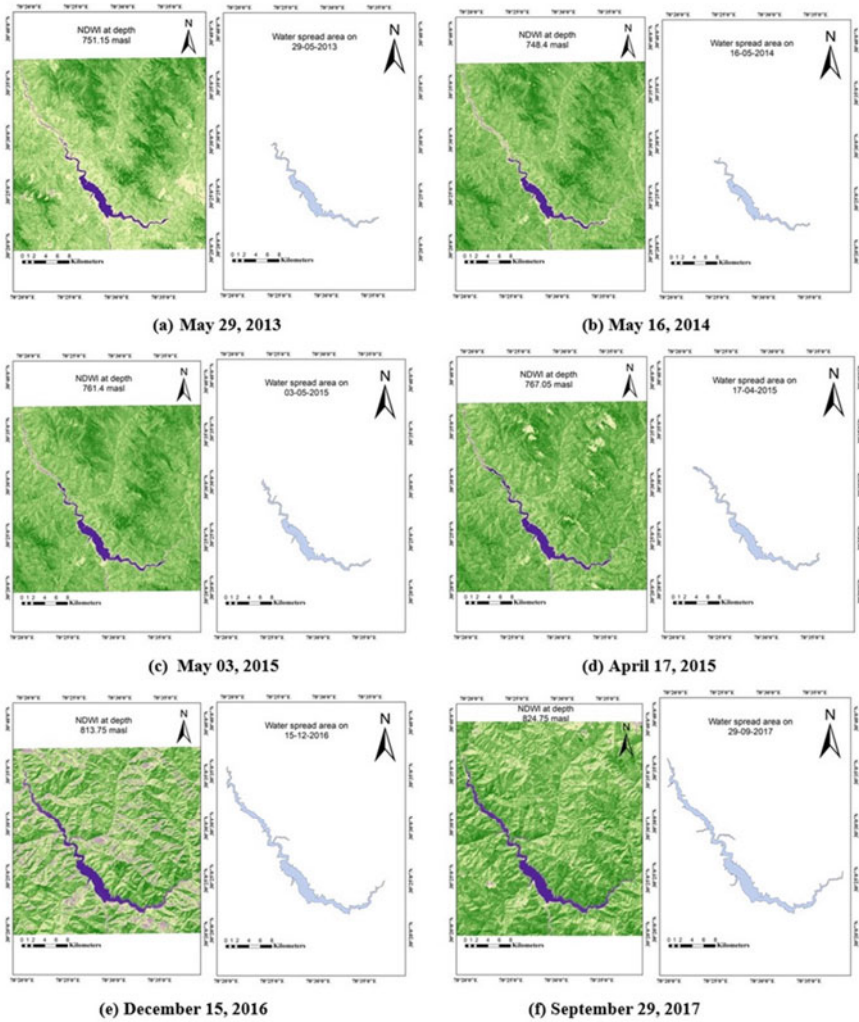
Fig. 8 NDWI and respective extracted area of reservoir at different dates

view). For sustainable use of the reservoir as a resource, the sediment accumulation in it should be controlled. In the past, several measures have been proposed and implemented against reservoir sedimentation. It is learnt that sediment management is not limited to reservoir only but it begins with upstream areas of watershed and extends to the downstream areas.

Table 2 Calculation of revised capacity of the reservoir

S. No	Date of satellite pass	Elevation (m)	Area (mm^2)	Elevation difference (H)	Capacity (mm^3)	Cumulative capacity (mm^3)
1	29/05/2013	748.4	16.81	–	–	0
2	16/05/2014	751.15	18.57	1.76	31.12	31.12
3	03/05/2015	761.4	20.27	10.25	198.99	230.11
4	17/04/2015	767.05	22.83	5.65	93.53	323.64
5	30/01/2016	788.8	28.75	21.75	559.69	883.33
6	15/12/2016	813.75	34.97	24.95	793.64	1676.97
7	29/09/2017	824.75	39.69	11	410.35	2087.32
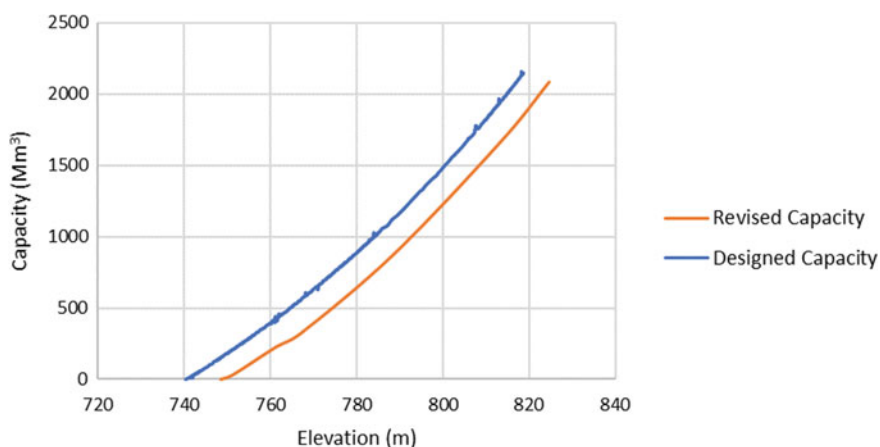
Fig. 9 Variation in the capacity of the reservoir and loss of storage

6 Conclusion

RUSLE method of soil loss estimation is used to quantify the sediment in Bhagirathi basin. Remote sensing and GIS techniques were successfully implemented to obtain the soil erosion severity map. The average soil loss rate was estimated as 50.77 tons/hectare/year and maximum value was found as 265.045 tons/hectare/year. The erosion is more severe in lower reaches of the basin compared to upper reaches. The results of the study help in making a decision about the type of practice to be adopted for soil conservation in the study area. These construction practices will be location specific depending on the severity of soil loss at that location.

The remote sensing technique used to carryout assessment of reservoir sedimentation for the years 2013–2017. The revised live storage capacity of the Tehri dam reservoir was found to be 2087.32 mm^3 in 2017 as against the live storage

capacity of 2150 mm^3 in 2006. Total 62.68 mm^3 reservoir capacity is estimated to be lost from 2006–2017. This accounts for about 5.01% loss in initial design capacity. These results indicate that there is an average annual loss of live storage from 2006 to 2017 which is quantified as 5.69 mm^3 per year (0.26%). The remote sensing approach is found to be a cost-effective method for estimating sedimentation yield in the watershed as well as for quantifying the sedimentation in a reservoir. The accuracy of this method can further be improved by integrating ground-based hydrographic surveys with remote sensing-based sedimentation surveys.

References

1. Ganasri, B., Ramesh, H.: Assessment of soil erosion by RUSLE model using remote sensing and GIS—A case study of Nethravathi Basin. Geosci. Front. **7**, 953–961 (2016)
2. Morris, G.L., Fan, J.: Reservoir sedimentation handbook: design and management of dams, reservoirs, and watersheds for sustainable use. McGraw-Hill, New York (1998)
3. Laften, J.M., Lane, L.J., Foster, G.R.: WEPP: a new generation of erosion prediction technology. J. Soil Water Conserv. **46**(1), 34–38 (1991)
4. Amore, E., Modica, C., Nearing, M.A., Santoro, V.C.: Scale effect in USLE and WEPP application for soil erosion computation from three Sicilian Basins. J. Hydrol. **293**(1–4), 100–114 (2004)
5. Baigorria, G.A., Romero, C.C.: Assessment of erosion hotspots in a watershed: Integrating the WEPP model and GIS in a case study in the Peruvian Andes. Environ. Model. Softw. **22**(8), 1175–1183 (2007)
6. Kirkby, M.J., Irvin, B.J., Jones, R.J.A., Gover, G.: PESERA team: The PESERA coarse scale erosion model for Europe I—Model rationale and implementation. Eur. J. Soil Sci. **59**(6), 1293–1306 (2008)
7. Licciardello, F., Govers, G., Cerdan, O., Kirkby, M.J., Vacca, A., Kwaad, F.J.P.M.: Evaluation of the PESERA model in two contrasting environments. Earth Surf. Proc. Land. **34** (5), 629–640 (2009)
8. Quinton, J.N., Krueger, T., Freer, J., Brazier, R.E., Bilotta, G.S.: A case study of uncertainty: Applying GLUE to EUROSEM. In: Morgan, R.P.C., Nearing, M.A. (eds.), Handbook of Erosion Modelling Chichester West Sussex. Wiley-Blackwell, pp. 80–97 (2011)
9. Wischmeier, W.H., Smith, D.D.: Predicting Rainfall-Erosion Loss, Agricultural Research Service Handbook No. 282, Washington DC USDA, p. 48 (1978)
10. Renard, K.G., Foster, G.R., Weesie, G.A., McCool, D.K., Yoder, D.C.: Predicting Soil Erosion by Water: a Guide to Conservation Planning with the Revised Universal Soil Loss Equation (RUSLE), Agriculture Handbook Number 703. US Department of Agriculture, Washington DC (1997)
11. Bhattarai, R., Dutta, D.: Estimation of soil erosion and sediment yield using GIS at catchment scale. Water Resour. Manag. **21**(10), 1635–1647 (2007)
12. Pandey, A., Chaube, U.C., Mishra, S.K., Kumar, D.: Assessment of reservoir sedimentation using remote sensing and recommendations for desilting Patratu Reservoir. India. Hydrol. Sci. J. **61**(4), 711–718 (2016)
13. Dadoria, D., Tiwari, H.L., Jaiswal, R.K.: Assessment of reservoir sedimentation in Chhattisgarh State using remote sensing and GIS. Int. J. Civil Eng. Technol. **8**(4), 526–534 (2017)

14. Foteh, R., Garg, V., Nikam, B.R., Khadatare, M.Y., Aggarwal, S.P., Kumar, A.S.: Reservoir sedimentation assessment through remote sensing and hydrological modelling. J. Indian Soc. Remote Sens. **46**(11), 1893–1905 (2018)
15. Khanduri, S., Sajwan, K.S., Rawat, A., Dhyani, C., Kapoor, S.: Disaster in Rudraprayag District of Uttarakhand Himalaya: A special emphasis on geomorphic changes and slope instability. J. Geogr. Nat. Disast. **8**, 218 (2018)
16. Kumar, R., Anbalagan, R.: Landslide susceptibility mapping of the Tehri reservoir rim area using the weights of evidence method. J. Earth Syst. Sci. **128**, 153 (2019)

Stress and Deformation Analysis of Ground Subjected to Deep Excavation in Sandy Soil—A Man-Made Disaster

B. Abhirami and S. Karthigeyan

1 Introduction

Buildings and their foundation systems are constructed in such a manner that it can withstand strong loads they are designed to carry. Due to limited space available in many cities, it is required to make use of the available space to construct new structures. In that case, during the excavation process, a large magnitude of ground movement takes place in all directions which tends to disturb and cause additional load to the surrounding structures which they are not designed to carry. Such ground movement can cause collateral damage.

The paper intends to analyze the ground movement numerically during the excavation process by simulating the same condition in the PLAXIS 3D software, thereby providing possible guidelines for reducing the magnitude of such deformation. Deep excavations are often equipped with different types of support systems such as sheet pile walls, diaphragm walls, struts and bracings, anchors, and nailing. Advanced methods of numerical analysis, based on the finite element method, are widely used for prediction of ground movements around deep excavations. Such analyses can simulate the construction process, modeling the various stages of excavation and support conditions.

The most common support systems include the combination of sheet pile walls with strut and bracings [1]. Many researches have analyzed the deformation behavior of the ground which took into consideration the various possible parameters which tend to affect the soil and support system. The influence of excavation in the form of indirect loading was analyzed based on the lateral response of single pile in sandy soil through numerical analysis by Karthigeyan and Samanta [2] in which the location of the pile from excavation and depth of excavation were the key parameters. Many studies were done on the behavior and performance of the retaining structure [3].

B. Abhirami (✉) · S. Karthigeyan
College of Engineering Guindy, Anna University, Chennai, India

Various parametric studies were explored based on excavation depth [3, 4], width of excavation, wall stiffness, and support systems. Hsiung and Dao [4] pointed out the drawbacks of using basic soil models like Mohr–Coulomb model which only adopts single Young's modulus and not distinguishing between loading and unloading stiffness for analyzing excavation related problems. Ramadan and Meguid [5] investigated the excavation behavior with the help of secant pile wall support system along with a wide range of other parameters and found that the key factors governing the behavior cantilever pile wall supporting system in sand are relative density of sand, excavation depth, wall flexural stiffness factor, and bonding between the piles in the wall. A design method allows to predict the vertical and horizontal ground movement adjacent to the excavation based on the key parameters.

The stability of the deep excavation was analyzed by Pratama et al. [6] with a combination of secant pile wall and number of ground anchors with different slope angles along with its application in a case study. It was also found that the application of a higher pre-stress load (not more than 200kN) on the anchor yielded better performance. A series of parameters were studied by Mohmed et al. [7] to evaluate the effect of strut stiffness and wall stiffness using the hardening soil model (HSM). The wall stiffness was found to be inversely proportional to the deformation of the ground but not in a linear fashion but only upto a certain extent. Gianpiero Russo et al. [8] did a settlement analysis around a 27 m deep excavation supported by diaphragm wall by adopting the top down construction method to reduce settlement to the adjacent historic monuments and structures in Italy. The maximum value of 25 mm settlement was observed in the building façade which is small compared to the horizontal settlement of 32 mm observed during the construction of the shaft but not a negligible one. Cheng et al. [9] proposed a simplified analytical solution which can be applied in practical situations to predict the ground deformations which claims to have a wider applicability than previous methods. They took into consideration the effect of Poisson's ratio of the soil and the supporting structure's deformation for linear elastic behavior of the soil.

From the literature survey, it can be noted that in most of the studies, the ground movement was analyzed only based on the response of the adjacent structures and supporting structure's performance. Also, the analysis and discussion of stress and study of its variation were very scarce. In this paper, it is intended to study the ground deformation during and after the excavation process along with the stress and strain analysis. The extent to which the soil could be strained due to excavations and location of plastic points shall be observed from the study. The stress analysis was done beyond the bottom of the excavation to investigate its effect on the soil.

2   Soil Model and Material Properties

The software PLAXIS 3D was used as the tool for analyzing the three-dimensional excavation condition in the study. The software contains constitutive soil models from simple linear elasticity to advanced elasto plastic cap soil models used for

simulating the behavior of different type of soil, both soft soils and stiff soils. The hardening soil model also accounts for stress dependency of stiffness module. This means that all stiffness increases with pressure. Hence, all input stiffness relates to a reference stress, being usually taken as 100 kPa (1 bar).

The material properties of the soil medium are given in Table 1 [10].

2.1 Geometry and Mesh Details

The finite element geometry was chosen such that the boundary limits are spacious enough to accommodate the response of the excavation analysis. Many trial dimensions were worked out before arriving at the chosen dimensions. The excavation has a width of 20 × 20 m on a 75 × 75 m mesh area. The four sides of the excavation weresupported by sheet pile walls. In the corners of excavations, the triangular lateral earth pressure distribution assumption might not be appropriate since the positive effect of corners due to the increased stiffness of the ground, arching effect, and inaccurate use of pressure distribution may lead to either over design or unsafe support systems [11]. Hence, it is required to study the 3D excavations than plain strain types. The accuracy of the finite element analysis depends on the meshing density of the model. Here, a finer mesh was adopted in the excavation area and coarser mesh was done for the remaining model. The work planes selected for extrusion of the geometry were incremented by 1 m till the 10 m excavation depth as shown in Fig. 1. The effect of water table was not assumed in the analysis.

Table 1 Soil parameters (hardening soil model)

Parameter	Soil type		Unit
	Loose sand	Dense sand	
γ (Bulk unit weight)	18	20	kN/m^3
γ_{sat} (Saturated unit weight)	20.9	22.392	kN/m^3
C (Cohesion)	0	0	kN/m^2
ϕ (Angle of internal friction)	30°	36	–
E_{50}^{ref} (Secant stiffness in standard drained triaxial test)	20×10^3	20×10^3	kN/m^2
E_{oed}^{ref} (Tangent stiffness for primary oedometer loading)	20×10^3	20×10^3	kN/m^2
E_{ur}^{ref} (Unloading/reloading stiffness (default $E_{ur}^{ref} = 3E_{50}^{ref}$))	60×10^3	60×10^3	kN/m^2
v_{ur} (Poisson's ratio for unloading–reloading (default $v_{ur} = 0.2$))	0.2	0.2	–
m	0.5	0.5	–
R_{inter}	0.667	0.667	–
Analysis type	Drained	Drained	–
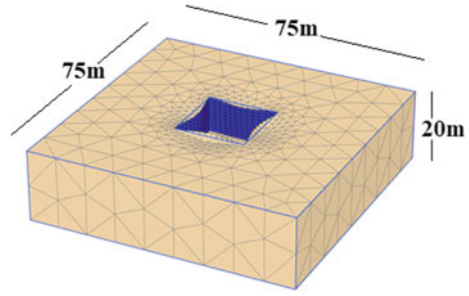
2.2 Support System Modeling

The support system for the excavation was sheet pile walls installed on the four
vertical sides of the excavation. The sheet pile walls were modeled using the plate
elements available in the PLAXIS 3D software. The crooked dimensions of the
sheet pile walls were made equivalent to the straight plate elements using the
formulas and equations adopted from Brinkgreve et al. [12] listed below.

$$d = h \tag{1}$$

$$\gamma = A\gamma_{\text{steel}}/d \tag{2}$$

$$E_1 = 12E_{\text{steel}}I/d^3 \tag{3}$$

The PLAXIS 3D software by default takes $E_1 = E_2$ and $G_1 = E_1/2$.

A linear elastic model was adopted to model the SPW. The properties of the pile
walls are given in Table 2.

The simulated model is shown in Fig. 1. The ground anchors were modeled with
the help of node to node anchors for the ungrouted portion and embedded beam
element for the grouted portion. Four ground anchors were provided with 8 m
distance in y-direction for the final comparative analysis (See Fig. 2).

The properties of the ground anchors are taken as $EA = 650 \times 10^3$ kN and that
of the grouted portion is as follows:

Table 2 Sheet pile wall properties

Thickness (t)	100	125	170	200	225	mm
Material	Steel	Steel	Steel	Steel	Steel	–
E_{steel}	78.5	78.5	78.5	78.5	78.5	kN/m^2
γ	4.804	4.797	4.48	5.25	5.338	kN/m^3
E_1	220.24	198.45	197.98	198.45	190.26	$\times 10^6$ kPa

$$E = 30 \times 10^6 \, \text{kN/m}^2$$
$$\gamma = 24 \, \text{kN/m}^2$$
$$A = 0.01539 \, \text{m}^2$$
$$\text{Diameter} = 0.14 \, \text{m}$$

3 Parametric Study

The effect of wall stiffness/thickness (t) and depth of embedment (Ed) of the sheet pile support system were considered and varied in the numerical analysis. The depth of embedment (Ed) of 2, 3, 4, 5, and 6 m was varied, and the thickness (t) of the sheet pile wall was varied by 100, 125, 170, 200, and 225 mm. All the experiments were done in the loose density condition. The intention of the study was to determine the cross section of the sheet pile wall which gave better performance with minimal ground deformation without additional support. The experiment also observed the effect of the minimum wall thickness and minimum depth of embedment for determining the maximum stress that can be induced into the soil during the excavation process. As a part of the study, one analysis was done to compare the effect of the same in dense sand condition.

4 Results and Discussions

The results and discussions for the parametric study are explained below. The minimum depth of embedment, 2 m for the 10 m deep excavation was observed for the maximum ground deformation it caused.

4.1 Effect of Wall Thickness

The effect of wall thickness (t) was analyzed by taking the minimum depth of embedment (Ed) and plotting the curve against the depth of excavation. The maximum possible deformation caused at the ground level during the process of excavation was noted by simultaneously observing the deformation after each layer of excavation of depth 1 m till 10 m. The horizontal and vertical ground deformations were plotted against the depth of excavation during loading as shown in Figs. 3 and 4.

It can been seen from figures that the maximum ground deformation takes place for the thin section 100 mm for both vertical and horizontal deformations alike. This section was taken as the critical one for the analysis.
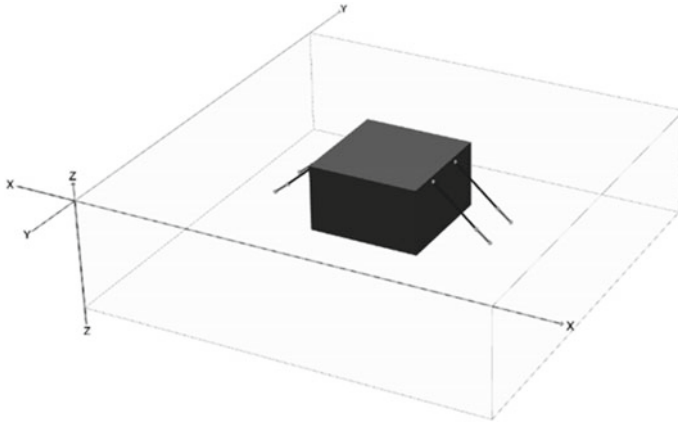
Fig. 2 Excavation model with sheet pile walls and ground anchors

Fig. 3 Horizontal ground deformation with respect to thickness of the sheet pile wall in loose sand
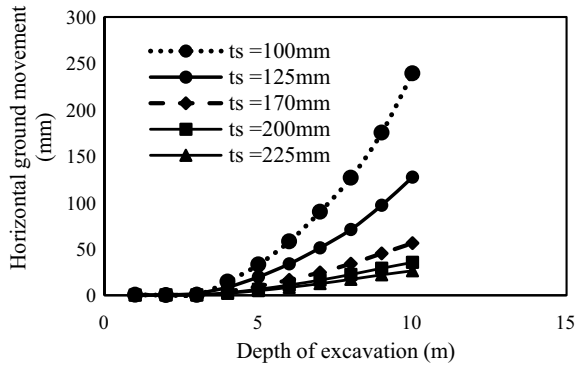
Horizontal movements are generally of similar magnitude and distribution to vertical movements [2]. The variation of horizontal and vertical ground deformations with respect to the distance from the excavation at three varying depths, approximately at the top, middle, and bottom of the excavation, is chosen and plotted as shown in Figs. 5 and 6.

4.2 Effect of Density of Sand

When the distance is increased from the excavation, the ground deformation seems to reduce as indicated in Figs. 7 and 8. The top layer of the excavation tends to deform more compared to the underlying layers. This predominant deformation near the ground level is plotted and compared with dense sand condition.

For the dense sand condition, the trend followed by the deformation curve seems similar to that of the loose sand condition except for the magnitude.

Fig. 4 Vertical ground deformation with respect to thickness of the sheet pile wall in loose sand
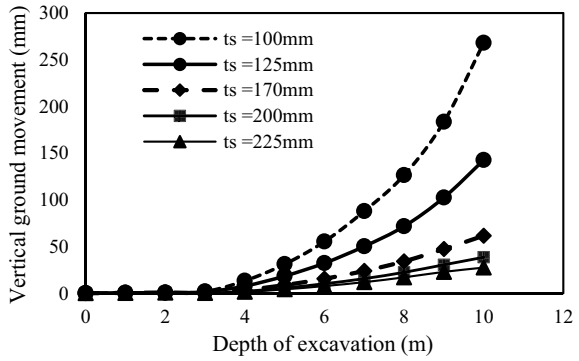
Fig. 5 Variation of the horizontal ground deformation with respect to distance from excavation in loose sand (Ed = 2 m, t = 100 mm)
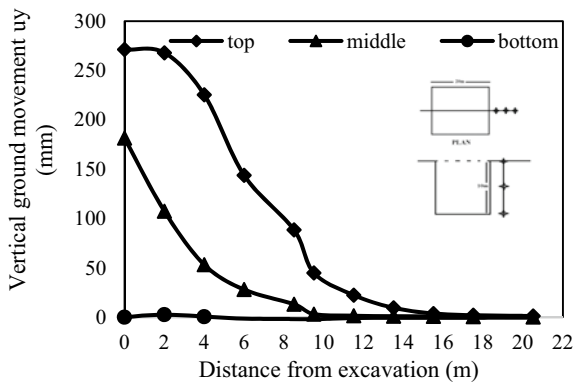
Fig. 6 Variation of the vertical ground deformation with respect to distance from excavation in loose sand (Ed = 2 m, t = 100 mm)
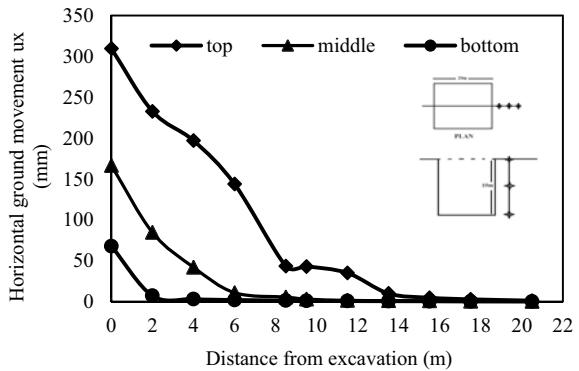
Fig. 7 Comparison of the variation of horizontal ground movement with respect to distance of excavation (Ed = 2 m, t = 100 mm)
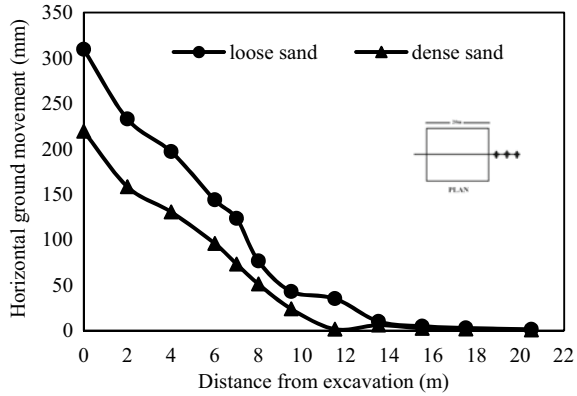
4.3 Effect of Embedment Depth

The critical section, i.e., the wall thickness (t) of 100 mm was chosen the analyzing the effect of embedment depth (Ed). The plot is taken such that the depth of embedment was varied keeping the wall thickness constant.

It can be clearly seen from the plot that the top layer of the soil adjacent to the excavation is subjected to maximum ground movement, both vertical and horizontal deformations alike compared to the bottom of excavation, validating the typical sandy soil behavior. Also, it is interesting to note from Figs. 9 and 10 that for the same section, when the depth of embedment of the sheet pile is varied, the deformation of the ground at the top of the excavation and at the bottom of the excavation is almost the same for embedment depths 4, 5 and 6 m although the path along the excavation layers varies in small magnitudes.

Fig. 8 Comparison of the variation of vertical ground movement with respect to distance of excavation (Ed = 2 m, t = 100 mm)
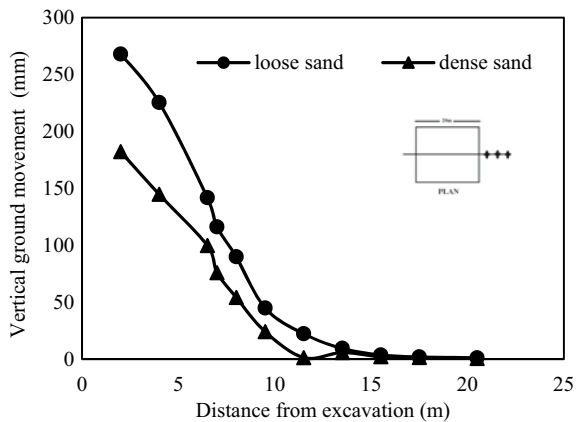
Fig. 9 Horizontal deformation of soil with respect to embedment depth for $t_s = 100$ mm in loose sand
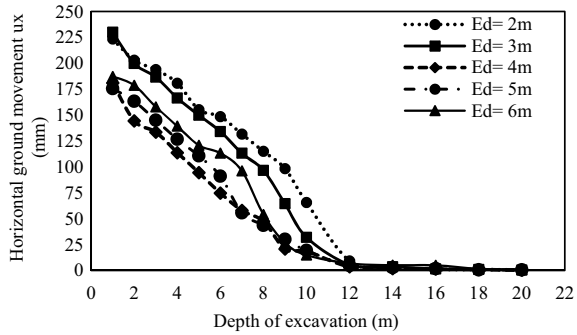
Therefore, it can be confirmed that for the 100 mm thickness of SPW considered, an embedment depth shall be chosen which need not go beyond 4 m as it would give the same performance but adding on the cost. Similarly from Fig. 10, it can be observed that the vertical movement of the ground is predominant only in the top layer of the soil near the excavation. The deformation trend seems to be the same for all the embedment depths.

The reduction of horizontal ground movement in the ground level when the embedment depth was increased from 2 to 6 m was 16%. The theoretical embedment depth for the installation of sheet pile wall was found to be 3 m. From the numerical analysis, it can be inferred that the 2 m embedment depth is sufficient to support the excavation without collapse but a considerable ground deformation.

4.4 Stress and Strain Analysis

The variation of stress along the depth of excavation and distance from excavation was observed separately. The results are presented in Fig. 11.

The effect of thickness of the sheet pile wall on the stress parameter was analyzed by taking the critical depth of embedment a constant value of 2 m. The thickness of sheet pile walls was varied from 100 to 225 mm. The thinnest section of the sheet pile wall $t_s = 100$ mm created the maximum magnitude of horizontal stress due to excavation as shown in Fig. 11. The trend followed by the vertical stress is also the same. Hence for further analysis, this section of SPW shall be taken to study the maximum strain value and its extent of disturbance caused from the excavation pit.

The stress analysis indicated that all the stress (horizontal and vertical stresses) increased till the bottom depth of excavation and then reduced till it becomes constant. When the stress was analyzed at the ground level during the course of excavation, the maximum magnitude of stress or the soil was stressed the most when the thickness was 100 mm without any soil collapse.
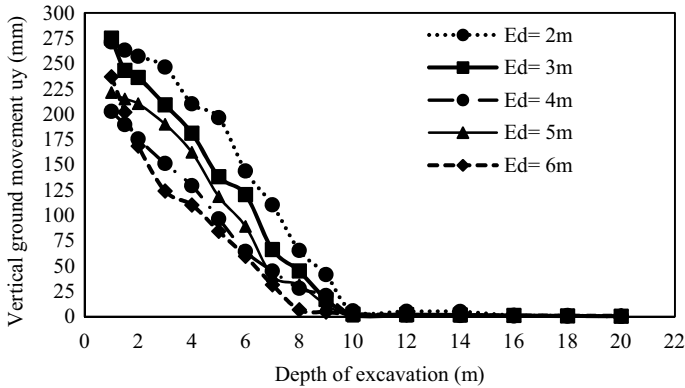
Fig. 10 Vertical deformation of soil with respect to embedment depth for t_s = 100 mm in loose sand

The embedment depth of 2 m with 100 mm SPW thickness combination was also observed for the maximum stress that can cause adjacent to the excavation for which a horizontal sectional analysis was done at the top layer, middle layer (at 5 m depth), and at the bottom of the excavation (at 10 m depth) (See Fig. 12).

It can see observed from Fig. 12 that the maximum stress variations are caused in the topmost layer (just below the ground level) adjacent to the excavation pit. The same observation was done to analyze the effect with dense sand condition. Hence, the top layer stress analysis and the maximum distance up to which the soil was stressed during the excavation process can be determined from the stress plots shown in Fig. 13 for both dense and loose conditions of the sandy soil.
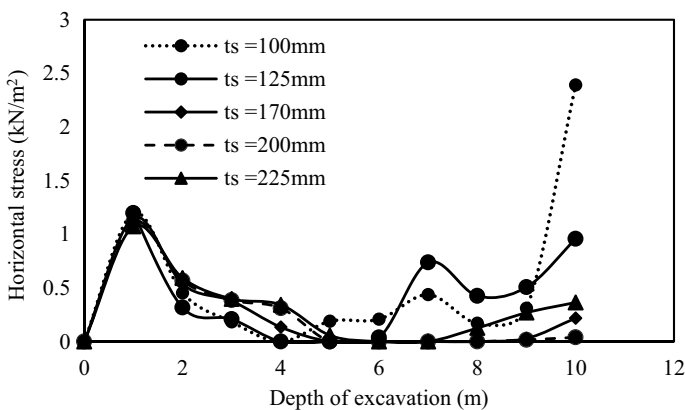
Fig. 11 Variation of horizontal stress at ground level during the excavation in loose sand
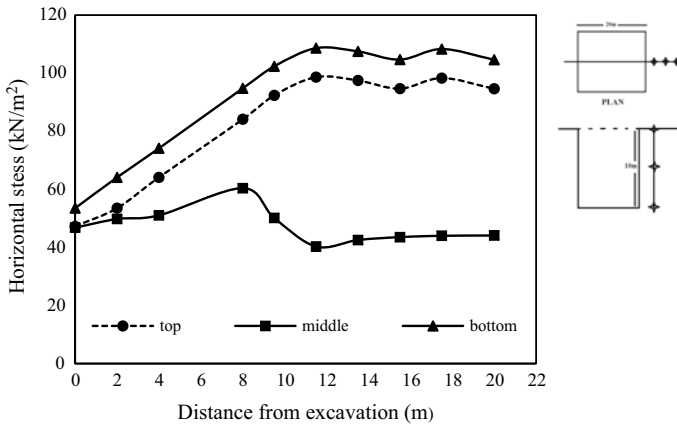
Fig. 12 Comparison of the variation of horizontal stress in the top, middle, and bottom layers of the soil after excavation (loose sand)

The horizontal and vertical stresses after the excavation process were observed as shown in Figs. 14 and 15. Both the stresses followed the same trend, the magnitude of stress increased subsequently from top to bottom showing the effect of loading at the bottom layers of the soil and stress released till the bottom of the excavation. Also, the variation of stress was more close and gradual till the bottom of the excavation after which it started to increase in considerable magnitudes.

The 100 mm section of SPW was observed to be sufficient for supporting an excavation in dense condition. This is because the difference in stress with the same thickness (100 mm) and embedment depth (2 m) was as high as 91.159 kN/m^2.

For observing the strain caused to the soil, the most critical section was chosen again. The observed value of the strain indicates the extent to which the soil adjacent to the excavation has been deformed (See Fig. 16). This plot is very much significant as it helps to determine the plastic points and elastic points adjacent to
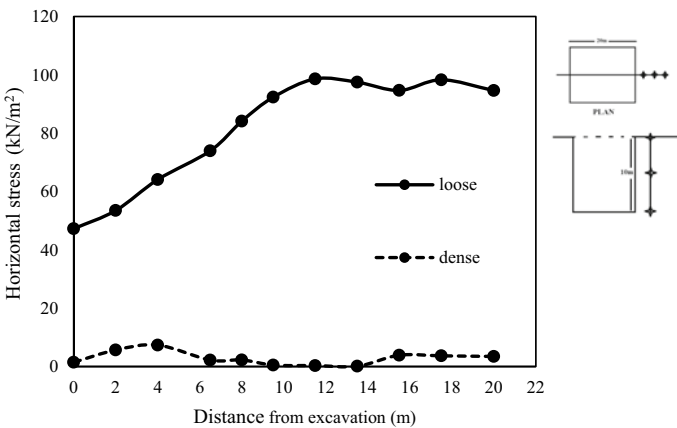
Fig. 13 Comparison of the horizontal stresses at the top layers in dense and loose sand

Fig. 14 Variation of horizontal stress with respect to depth
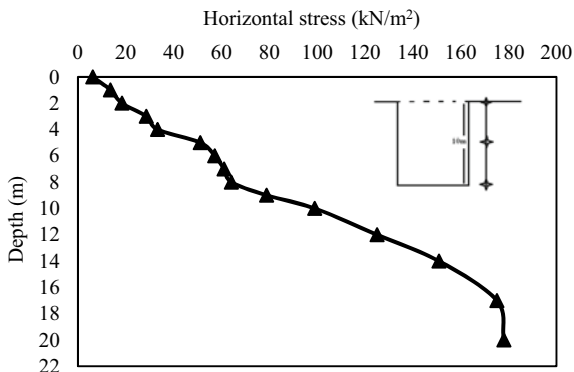
Fig. 15 Variation of vertical stress with respect to depth
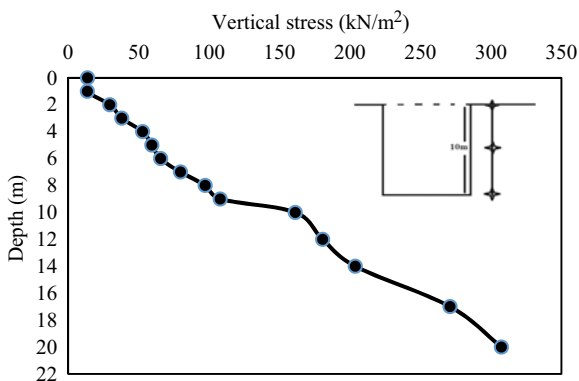
the excavation (See Fig. 17). This allows us to predict the problematic situations which tends to arise when any structure is built in these zones (Fig. 16).

From Fig. 15, it is clear that at the top layer of the soil adjacent to the excavation, up to a distance of 10 m, the soil is strained more after which it starts to reduce and become constant. The effect of excavation at the middle and bottom layers extends up to 8 m and 4 m, respectively.

4.5 Analysis with Ground Anchors

The critical section of 2 m embedment depth and sheet pile thickness of 100 mm was analyzed with the combined support system of sheet pile walls and ground anchors. The horizontal ground deformation, vertical ground deformation, stress and strain plots were plotted to compare the effectiveness of the additional support system.
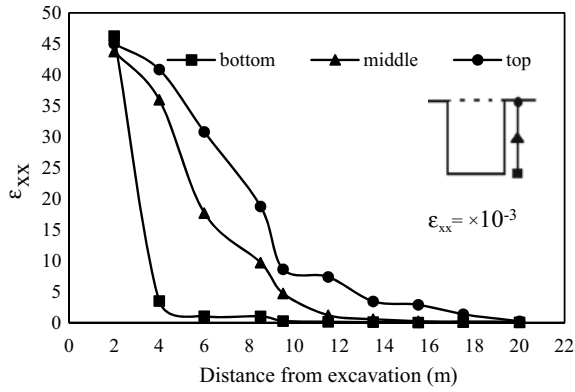
Fig. 16 Variation of strain as moved away from the excavation

Plastic points

■ Failure point   ◆ Cap + hardening point
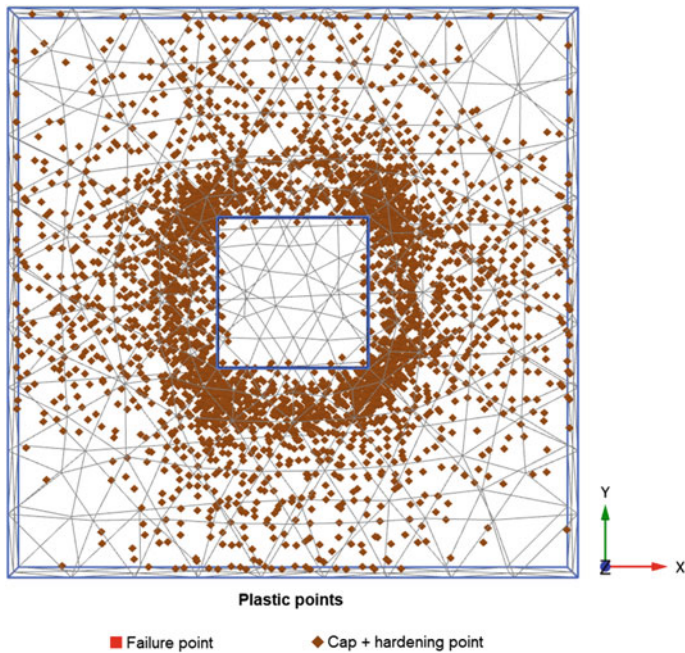
Fig. 17 Plastic points around the excavation pit

Four ground anchors were installed with a slope of 34°. The results are shown from Figs. 18, 19, 20 and 21.

The horizontal and vertical ground movements follow the same trend with a 20 mm variation in the magnitude of deformation. It can be observed from the charts that there is a considerable reduction in the ground movement after the installation of ground anchors.

Fig. 18 Comparison of horizontal ground movement with respect to distance from excavation with and without ground anchors
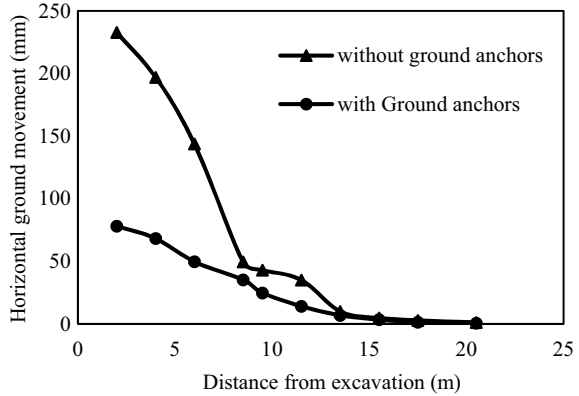
Fig. 19 Variation of vertical ground movement with respect to distance from excavation with ground anchors
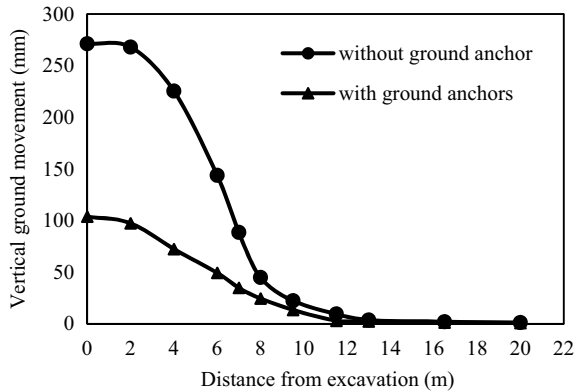
From Fig. 20, it is visible that the stress due to excavation extends up to 12 m after which it starts to take a constant path, whereas after the installation of ground anchors, the soil portion is stress only up to a maximum of 4 m and became constant. The magnitude of maximum stress observed at 2 m from the excavation. It was compared with the case when there was no additional support. The result shows that there was an 81.6% reduction in stress when the ground anchors were installed in addition to the existing sheet pile wall support.

The magnitude of strain at ground level was also plotted as shown in Fig. 20. It can be seen that the reduction in strain is uniform and tends to become constant after 13 m. It was found that there was a 46% reduction in strain after the installation of ground anchors.
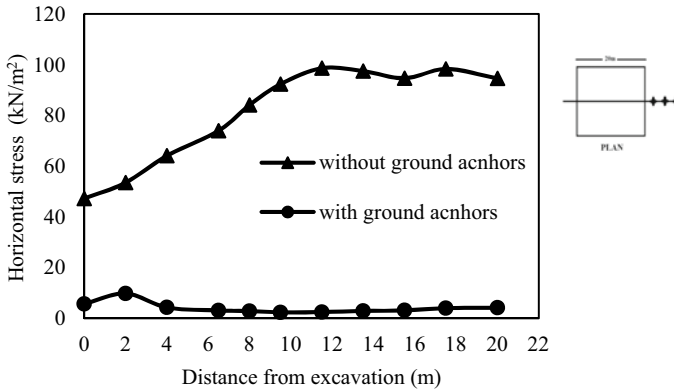
Fig. 20 Variation of horizontal stress with respect to distance from excavation with ground anchor support
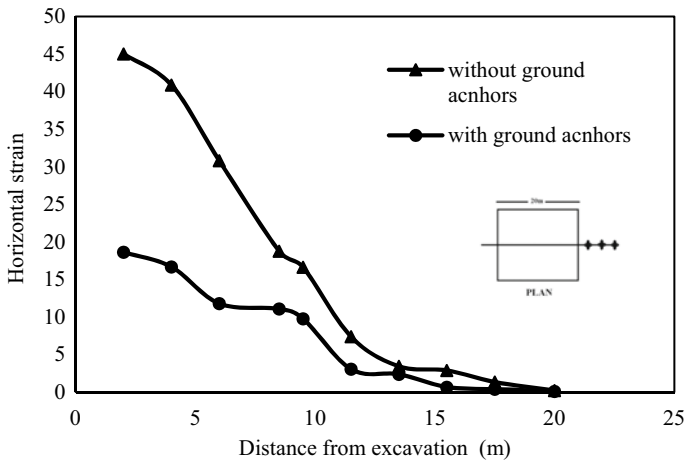
Fig. 21 Variation of strain when moved away from excavation (with ground anchors)

5 Conclusion

The effect of excavation and its associated ground movements were studied numerically with finite element analysis method in the software PLAXIS 3D. To study the ground deformations due to excavations, a 20 × 20 m pit was simulated using the software. The main parameters considered for the study were embedment depth and sheet pile wall thickness. The following conclusions can be drawn from the study.

1. The deformation analysis indicated that the effect of excavation process is maximum at the ground level for loose and dense sand. When the thickness of the wall was increased, the deformation seemed to reduce by 89%. Whereas for the embedment depth variation from 2 to 6 m, it was only a 9.31% reduction. From this, it is clear that the factor which affects the deformation of the ground is mainly the thickness of sheet pile wall.

2. There was a reduction in the stress of 60% when the thickness of sheet pile wall increased from 100 to 125 mm. A minimum of 125 mm shall be chosen for the sheet pile walls if the stress reduction and minimal disturbance to the adjacent structures of high priority. But 100 mm thickness is sufficient for supporting the excavation without collapse by compromising a considerable ground deformation.

3. When the analysis was compared with dense sand condition to loose, it was observed that there was a decrease in stress by 96%.

4. When the analysis was performed with respect to embedment depth, it was observed that both vertical and horizontal ground deformations are almost the same for 2, 4, and 6 m embedment depths at the top layer of soil and after 10 m depth from ground level. Moreover, the deeper embedded pile walls, i.e., 4–6 m also, the deformation plot followed the same trend from top to bottom.
   Hence, it is recommended to choose the minimum embedment depth of 2m and a maximum of 4m for supporting the excavation.

5. The horizontal strain analysis for t_s = 100 mm shows that the soil at the top layer has been strained the most till 10 m and extended till 20 m, i.e., two times the excavation depth. This analysis complements well with the stress and the deformation analysis. The horizontal stress and deformation become constant after 19 m and 18 m, respectively.
   Thus, it can be justified that the stress and deformation kept increasing till it reached approximately 20 m because the soil until this distance was strained due to the excavation process. The soil within this 20 m zone around the excavation is subjected to plastic deformation.

6. The analysis with additional support (Ground anchors) was compared with that with just sheet pile support. The result shows significant reduction in ground movement, stress, and strain which are 70.9%, 81.6%, and 46%, respectively. The soil which was found to be strained till 20 m from excavation was strained only till a maximum of 13 m after the installation of ground anchors.

The factors governing the stress and the soil deformation typically depend on the strength of the support system. In general, open excavations and those supported by cantilever retaining walls give rise to larger ground movements than strutted excavations and those constructed by top down methods. In urban situations, the latter are clearly to be preferred if building damage is to be minimized [8].

References

1. Hacheem, Z.: Simulation of Deep excavation in sand by finite element using Hardening soil model (HSM). Eng. Tech. J. **29**(15), 3079–3096 (2011)
2. Karthigeyan, S., Samanta, M.: Lateral response of pile under indirect loading due to adjacent excavations. In: Proceedings of Indian Geotechnical Conference, vol. 1, pp. 15–17, Kochi India (2011)
3. Chheng, C., Likitlersuang, S.: 3D Finite element modelling of sheet pile wall excavation: A Case Study in Bankok, Regional Conference in Civil Engineering (RCCE). In: The Third International Conference on Civil Engineering Research (ICCER), pp. 137–142, Indonesia (2017)
4. Hsiung, B.C.B., Dao, S.-D.: Evaluation of Constutive Soil Models for predicting movements caused by a deep excavation in sands. Electr. J. Geotech. Eng. 17325–17344 (2016)
5. Ramadan, M., Meguid, M.: Behaviour of cantilever secant pile wall supporting excavation in sandy soil considering pile to pile interaction. Arab. J. Geosci. **13**(1), 1–13 (2020)
6. Pratama, A.P., Hardyatmo, H.C., Faris, F.: Parametric study of the effect of Ground anchor on deep excavation stability. J. Civil Eng. Forum **6**, 19–26 (2020)
7. Mohamed, S., Zumrawi, M.M.E., Ahmed, A.: Numerical Analysis of deep excavation. Univ. Khartoum Eng. J. **9**, 47–51 (2019)
8. Russo, G., Nicotera, M.V., Autuori, S.: Three dimensional performance of a deep excavation in sand. J. Geotech. Geoenviron. Eng. **4**, 1–13 (2019) (American Society of Civil engineering)
9. Cheng, K., Riqing, X., Ying, H.-W.: Simplified method for calculating ground lateral displacement induced by foundation pit excavation. Eng. Comput. **37**(7) (2020)
10. Karthigeyan, S., Ramakrishna, V.V.G.S.T., Rajagopal, K.: Influence of vertical load on the lateral response of piles in sand. Comput. Geotech. **33**, 121–131 (2006)
11. Ahmadi, A., Ahmadi, M.: Three dimensional numerical analysis of corner effect of an excavation supported by ground anchors. Int. J. Geotech. Eng. 3–13 (2019)
12. Brinkgreve, R.B.J., Kumaraswamy, S., Swolfs, W.M., Waterman, D., Chearu, A., Bonnier, P. G., et al.: Plaxis 2015, PLAXIS by, The Netherlands (2015)

Khartoum Geohazard: An Assessment and a Future Warning

Mohammed Al-Ajamee , Mohamedelamin M. M. Mahmoud ,
and Awad M. Ali

1 Introduction

Geohazards are defined according to (ICG) as the geological conditions that can generate widespread damage or risk [1]. They can relatively be on a small scale, and they can also reach enormous amplitudes. Geohazards such as earthquakes, floods, and landslides have broad implications for human safety and regional economic stability, particularly in a semi-arid area such as Sudan, where significant climatic changes have occurred during the past years [2]. Sudan's capital—Khartoum—is located at the confluence of the Blue and White Niles, the main tributaries of the River Nile. The Nile is the longest river in the world with a length of 6650 km and runs across ten countries; then, the White Nile and the Blue Nile meet to create the Nile at Khartoum [3].

The Blue Nile flows from Lake Tana in the Ethiopian Highlands, which was formed by past volcanic activities, at an altitude of 2000–3000 m. It supplies about 60–69% of the main Nile discharge, even though it is shorter than the White Nile [4]. The rainfall system matches the seasonal solar heating above the Ethiopian Plateau, and the rainy season lasts roughly from June to September [5]. Rainfall has a major impact on the social and economic life of the region. A shortage of rainfall contributes to droughts, while extreme heavy rainfall will contribute to flooding. For example, during the drought of 1984 in Sudan, Khartoum received just 4.7 mm of rain between May and October [6]. This led to crop failure, and as a result,

M. Al-Ajamee (✉)
Department of Geotechnical Engineering, Building and Road Research Institute,
University of Khartoum, Khartoum, Sudan

M. M. M. Mahmoud
TEKNO Consultancy, Khartoum, Sudan

A. M. Ali
Water Research Center, University of Khartoum, Khartoum, Sudan

famine struck Sudan, leading to a large exodus of people in search of food and water [7]. Floods represent other extremes in precipitation variability. Several factors influence the severity of the flood, such as land slope, soil type, and the amount of water in the soil. On August 4, 1988, Central Khartoum received 210 mm of rainfall, in a duration of 24 h [8]. The previous highest daily rainfall recorded in Khartoum since records started in 1899 was 88 mm on 31 July 1920 [9]. This condition was catastrophic when the level of the Nile also rose around 7 m above average, leading to widespread property destruction. However, in 1988, it was predicted to have a rainfall of 200 mm at Khartoum with a return duration of around 500 years [8]. Several villages adjoin the banks of the Blue Nile and the Main Nile, and because of their proximity to the river banks, they are heavily impacted by years of over-average flooding, including the 2020 Khartoum floods.

These two extreme catastrophes were associated with the major abnormalities in the Pacific Sea Surface Temperature (SST): El Niño (1983) and La Niña (1988). El Niño/La Niña is a pattern in the Pacific Equatorial Ocean characterized by a positive/negative sea surface temperature (SST). The Southern Oscillation Index (SOI) is a calculation of the variation in air pressure between Tahiti in the east and Darwin, Australia, in the west relative to the previous peak of the same difference. Negative variations suggest El Niño conditions, as lower pressure in the eastern Pacific correlated with colder weather and stronger easterly trade winds. Positive SOI correlates to negative SST and La Niña indexes.

Here, we present an evaluation of the 1988 Khartoum flood, which was historically considered exceptional. Data obtained from the 2020 flood reconnaissance surveys in Khartoum has been used to develop land-use maps from flood-prone areas. In addition to the flood risks, earthquakes were also a trigger to hazards, as of August 1, 1993, with a Richter magnitude of 5.5, as well as November 15, 1993, with a Richter magnitude of 4.3, accompanied by several aftershocks. Relating to this, we evaluated the threat of earthquake-induced soil liquefaction in the central business district of the city (CBD). Drastic consequences of soil liquefaction are well recognized in many places worldwide, as liquefaction brings about a complete loss of soil shear strength, thereby affecting infrastructure.

2   Study Area

Khartoum is Sudan's capital city. It consists of three main cities: Khartoum, North Khartoum (Bahri), and Omdurman (see Fig. 1). The state lies in the north-eastern portion of the middle of the country at the confluence of the White and Blue Niles (the main tributaries of the great River Nile). It lies between a longitude of (31.5–34° E) east, and latitude of (15–16° N). The north is about 410 m above sea level. The total area of the state is estimated to be 22,736 km^2. The colonial rule left the country unplanned, except for the historic district of Khartoum. Later on, the Sudanese people came and resided in these areas, which eventually led to the concentration of development in specific places. The state became a center for
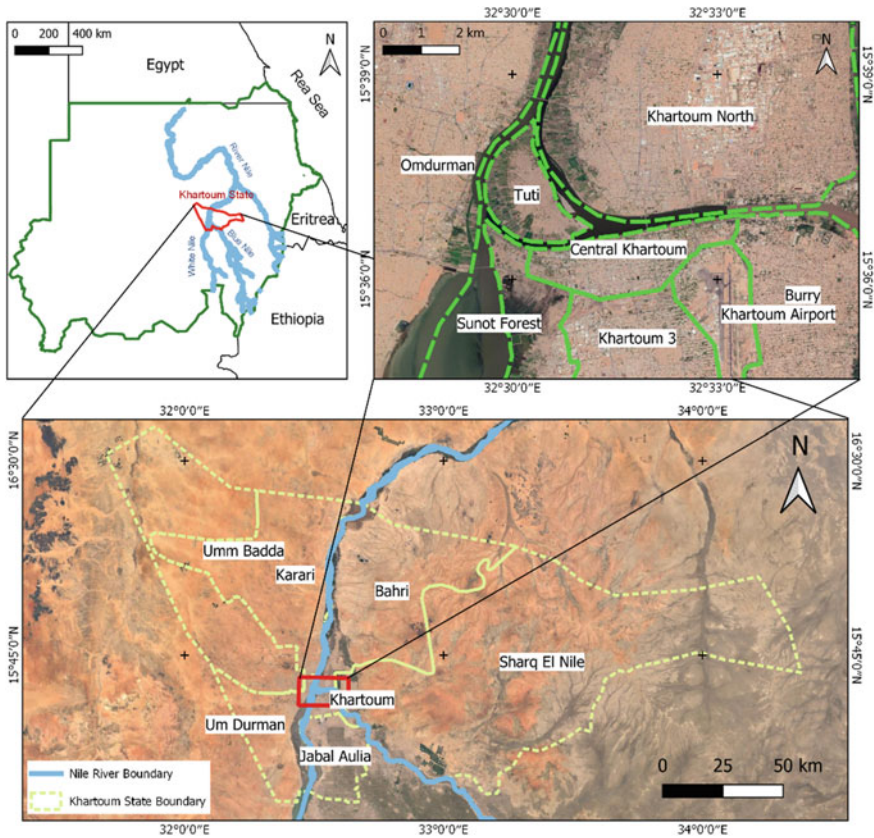
Fig. 1 Location of Khartoum State and Central Khartoum

urbanization, and the people kept flowing from various parts of the country, which led to a dramatic rise in the population that was estimated in 2018 to be around 8 million people [10], which represents more than 25% of the gross population of the whole country. This rapid urbanization, which is often synonymous with urban sprawl, results in exceptionally high population density, resulting in a steady reduction in urban infrastructure, including disaster risk management.

3 Flooding

3.1 Flooding in Khartoum

Extreme events associated with water, such as floods and droughts, have been an alarming problem. The Nile River, with its very unique nature, fed by rains on the

mountains of Equatorial Africa and the Ethiopian Highlands [11]. Two main kinds of floods in Khartoum are affecting the city currently, which are riverine flood and flash floods. Naturally, Nile flooding happens to some degree each year, when the Blue Nile experiences its peak flow between July and September. It is difficult to assess, prevent, or monitor local ephemeral watercourses, such that the free passage of their waters into the Nile can be blocked by high Nile levels. Owing to the rather low relief, the changing existence of their watercourses, and the infrequency of certain flooding, local run-off from urban areas is more diffuse and challenging to quantify, monitor, or assess. It is impossible to evaluate, prevent, or control the flood risks of these ephemeral watercourses. The sedimentary activity also disrupts drainage patterns between flood events.

However, destructive floods only occur during especially significant rainstorms, as in 1988 [12]. Figure 2 shows the damage of the 1988 Khartoum floods presented with slight modification [12]. Such rains can make desolation locally. While a fall of 200 mm might not have happened in Khartoum for a hundred years (although not showing here). Additionally, even though the Blue Nile rose drastically in 1988, there were four generally comparable floods before that century. Moreover, there has been an overall decrease in flood streams of the Blue Nile since the 1960s. Early warning framework would empower preliminary measures to be taken to adapt to a precisely anticipated Nile flood. Such floods as in 1988 are uncommon in Khartoum, which makes it daunting for a helpless nation like Sudan to warrant the presence of a complex and costly flood insurance components. The sprawling population density of the high city means that vegetated silt–clay soils compacted by traffic passage, pedestrians, and animals contributed to the overall worsening of the situation. If surface depression storages are surpassed, more frequent floods will occur.

3.2   Flooding and Climate Changes

The prehistoric settlement of the Sahara Desert was closely connected to climatic changes, as people migrated from one location to another seeking to adapt themselves to the climate. This close relationship has been shown by detailed radiocarbon evidence from archeological excavations in the now hyper-arid eastern Sahara [13]. It was indicated that the changes in climatology were related to changes in the orbital parameters of the Earth [14]. During the Middle Holocene, the latter was responsible for the greener Saharan Desert. Besides, the natural oscillation of the Pacific Ocean region also demonstrated that the eastern side of Africa has a major impact on the weather and climate [5, 15]. Along with El Niño-Southern Oscillation (ENSO) more prominent, Eltahir sought to prove that the annual flow of the Nile River correlates to the Pacific Ocean's sea surface temperature (SST) variations. Using the monthly distribution of Nile flow at Aswan, the flow closely follows a seasonal pattern, with one peak and extended recession. ENSO was linked with this natural variability in the annual flow of the Nile. He
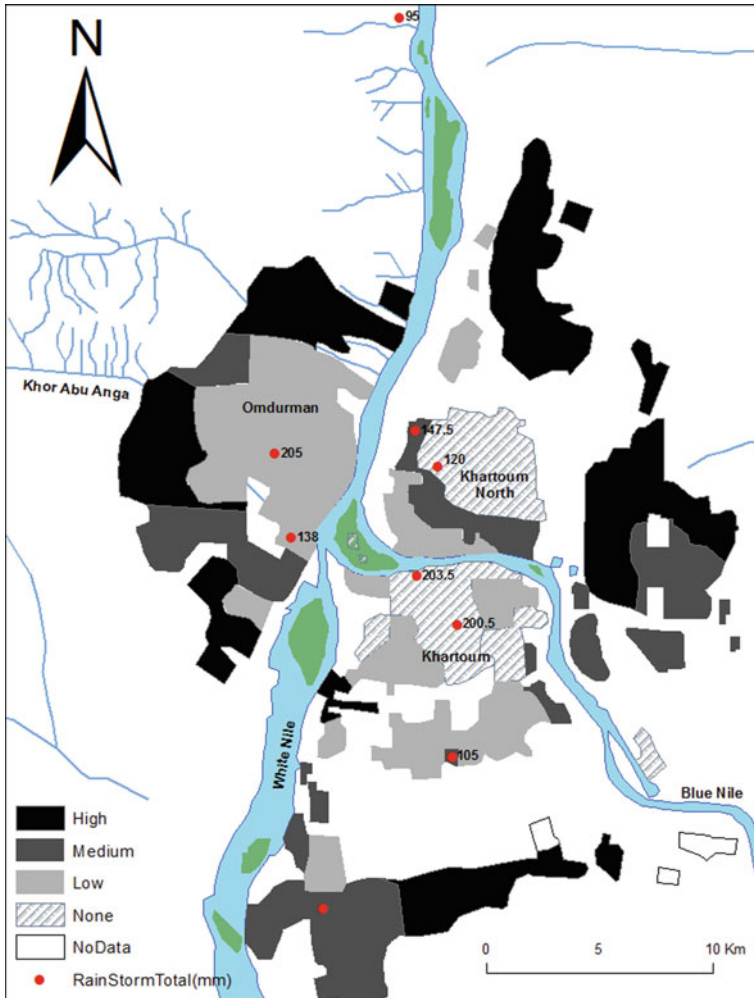
Fig. 2 Damage caused by the 1988 rainstorm after [12]

suggested this observed relation to increasing the predictability of the floods of the Nile [16]. Figure 3 shows variation of annual flow in Aswan, presented with some modification after [16]. Nile flood forecasts for medium to long ranges was carried out by Wang and Eltahir, who invoked the ENSO data and suggested an observational approach [17]. The interesting effect is that the signs of correlation and their phases relative to the seasonal cycle are quite viable (e.g., the negative association between ENSO and flooding in Blue Nile and seasonal Atbara Rivers is found by [15]. Abtew in 2009 indicated that high rainfall is likely to occur during La Niña years and low rainfall during El Niño years [18].
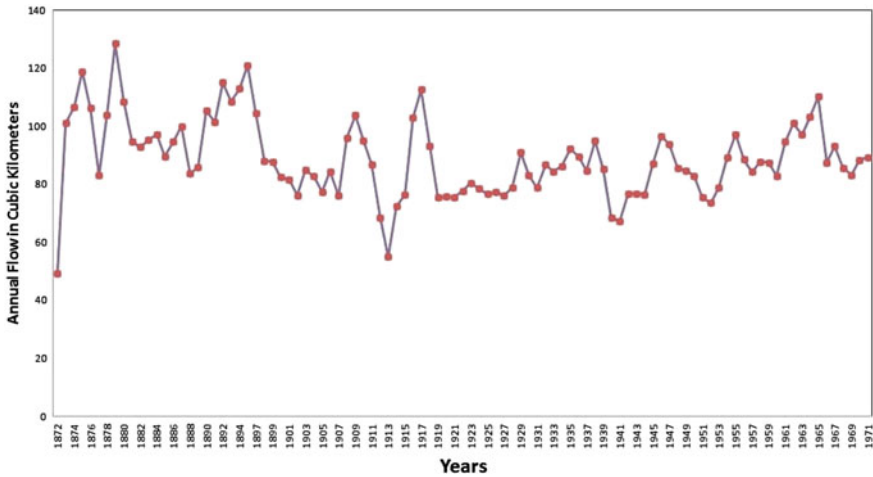
Fig. 3 Annual fluctuation of the Nile flow at Aswan Station [16]

Knowledge of the timing of El Niño and La Niña events to forecast flooding in the Nile River is useful. In 2014, Zaroug examined the significance of the observation of floods and droughts and the timing of El Niño and La Niña events in the upper catchment of the Blue Nile River using flow measurements from Eldiem station, located at the border between Sudan and Ethiopia; he found that droughts in the Blue Nile are susceptible to the timing of La Niña, with 67% of the cases in which El Niño has been observed by La Niña, and extreme floods have occurred in the Blue Nile [5].

4 Land-Use Mapping

Land-use maps for the region were developed using QGIS software. Initially, an annual 100 m spatial resolution of land-cover classification (LCC) from the water productivity through open access or remotely sensed devised data (WaPOR) portal was used. The data was then plotted against under-risk areas which were collected through field surveys and acquired from the Ministry of Infrastructure and Transportation of Khartoum State (MITKH). For information technological reasons, the whole study area was divided into a (2 * 2 km) grids as shown in Fig. 4. Only the adjacent under-risk grids were considered. Both total and under-risk areas for each land-cover type are shown in Table 1.

As illustrated in Figs. 2 and 4, the urbanization areas were the same as the 1988 floods plane, which should have never been occupied again, and an unexceptional rising in the Blue Nile discharge reaching 17.62 m head has not been recorded for a
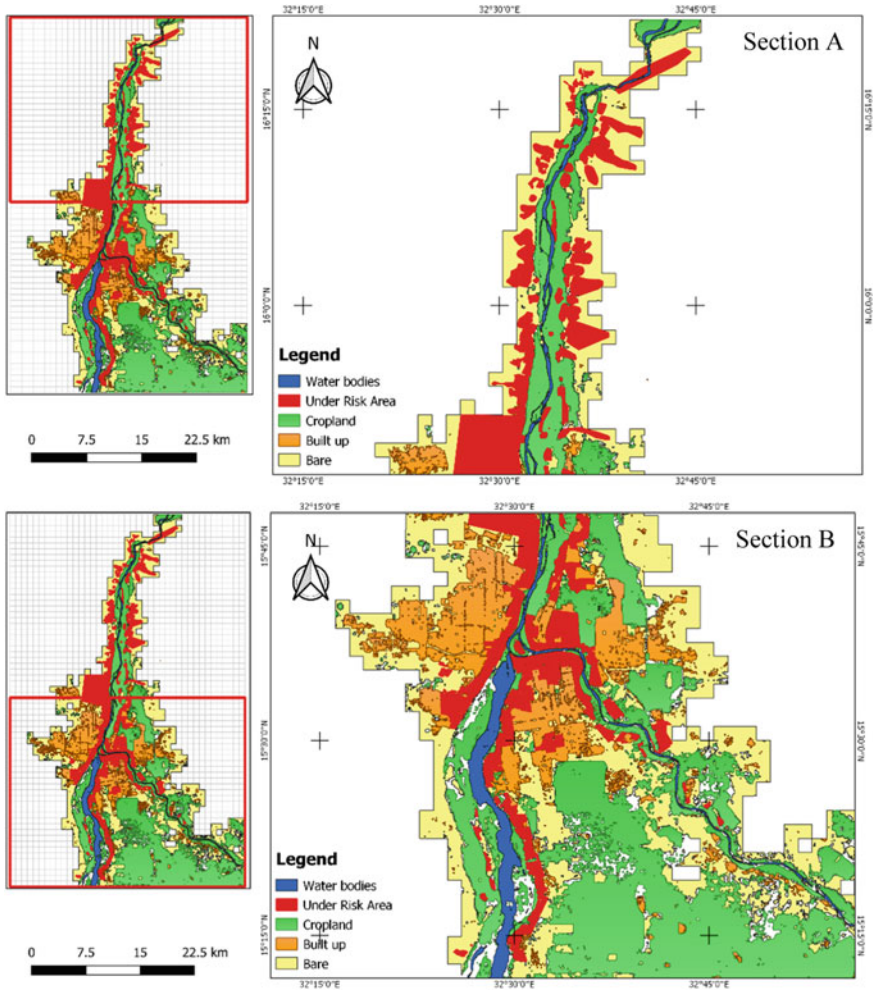
Fig. 4 Under-risk land-cover classification

Table 1 Total and under-risk areas for each land-cover classification for 2020 flooding

Land-cover	Total area		Under risk area	
	Area (km^2)	Percentage cover	Area (km^2)	Percentage cover
Water bodies	138.62	3.50	1.59	0.31
Croplands	1291.49	32.58	17.76	3.42
Built up	633.73	15.99	169.81	32.72
Bare	1594.52	40.22	302.06	58.20
Others	305.75	7.71	27.74	5.35
Total	3964.11	100	518.95	100

hundred year. According to the Ministry of Interior Affairs damage assessment, 141 reported fatalities, 81 injuries, and more than two million people were affected. One of the critical issues that has been demonstrated for simple comparison between 1988 and 2020 flooding is that the response mechanism between deferent agencies regarding to disasters and the structural interdependence among stakeholders is becoming complex and may pose a threat to the efficacy of the disaster response.

From Table 1, it is clear that most of the active areas affected by the 2020 flooding are the built-up areas. Fortunately, almost two-thirds of the inundated areas are bare. Therefore, an efficient flood risk management system should be implemented to diminish the extent of the susceptible regions.

5   Earthquake and Soil Liquefaction

In general, Sudan is regarded as a seismically stable region with infrequent earthquakes of low to moderate magnitude that can give rise to damaging intensities. However, parts of Southern Sudan are also prone to moderate to high seismic intensities (e.g., 1990 earthquake MS = 7.4 is one of the highest earthquakes in Africa [19–21]. In Central Khartoum, earthquakes were stimulated, among many sources, from the source of Abu Dulayq. The Abu Dulayq source is the one that essentially affects the central area of Khartoum [22]. 5.3 magnitude on the Richter scale was felt in Khartoum in November 2003; it lasted about 40 s and caused minor injuries, but no substantial damage was reported; it was also the source of another 3.5 of magnitude in July 2010.

This section provides a brief evaluation of the possibility of earthquake-induced soil liquefaction due to the presence of an alluvial deposit composed of loose to medium-dense saturated sands in the central business district of Khartoum (see Fig. 1). For this, we employed the simplified method outlined by Seed and Idriss [23–25].

Earthquake loading is expressed by cyclic stress ratio (CSR), whereas the cyclic resistance ratio (CRR) represents the resistance to liquefaction. The cyclic stress ratio (CSR) is expressed by:

$$CSR = 0.65 \frac{a_{max}}{g} \frac{\sigma_{v0}}{\sigma'_{v0}} \frac{r_d}{MSF * K_\sigma} \tag{1}$$

a_{max} the maximum ground acceleration
g   acceleration due to the gravity
σ_{v0} total overburden pressure
σ'_{v0} effective overburden pressure
MSF   magnitude scaling factor used to adjust the relation to different earthquakes.

K_σ overburden correction factor used to account for the effective confining pressure.

r_d depth reduction coefficient used to account for the flexibility for soil given by [25].

CRR can be evaluated from the field using in situ test parameters; here, we used the SPT-N value. The liquefaction occurs whenever CSR exceeds the CRR. Rearranging Eq. (1) leads to:

$$a_{\max} = \left(\frac{g}{0.65 r_d}\right)\left(\frac{\sigma'_{v0}}{\sigma_{v0}}\right) F(M,N,f) \qquad (2)$$

where the term $F(M,N,f)$ represents the earthquake magnitude (M), fine content (f), and SPT-N value (N) as a function of $a_{\max}$ [21–23]. Earthquake loading can be evaluated from probabilistic seismic hazard assessment procedure as in [22]. For Central Khartoum, the following relation was obtained:

$$\text{Log } (a) = 0.31M - 0.739 \qquad (3)$$

where:

a = ground acceleration in (cm/sec^2) and M = the earthquake magnitude.

Liquefaction occurs if $a_{\max}$ in Eq. (2) exceeds the acceleration from the earthquake in Eq. (3), assuming 15% fine content for a given earthquake magnitude, the function f can be written as:

$$F(M,N,f) = \Phi e^{N\varphi} \qquad (4)$$

where Φ and φ are constants determined from the regression, with Φ ranging from 0.145 to 0.978 and $\varphi = 0.74$. Then, using the rule of conditional probability and dividing the study into two zones, according to the subsoil conditions, the number of earthquakes that can cause liquefaction annually is obtained as:

$$N_L = \sum [L|M] * (P(M)) \qquad (5)$$

N_L = number of earthquakes that can cause liquefaction, $[L|M]$ is the conditional probability that for a given earthquake magnitude will cause liquefaction, and $P(M)$ represents the recurrence probability of a specific earthquake magnitude. Assuming the Poisson type of distribution for the (t) year exposure time, the probability of at least one event causing liquefaction $p[L]$ is expressed as:

Table 2 Free field probability of liquefaction

Time (year)	Value of N_L	
	0.00073	0.00073
	Zone (1)	Zone (2)
10	0.73	0.52
20	1.45	1.03
30	2.16	1.52
40	2.89	2.05
50	3.54	2.54
100	7.23	5.01
250	17.71	12.03

$$p[L] = 1 - e^{-N_L t} \qquad (6)$$

Table 2 shows the free field probability of liquefaction for zone (1 and 2). Although the probability of liquefaction is minimal, zone one is more susceptible to liquefaction, which may attribute to the soil condition, with looser to medium-dense sand in zone one.

6 Conclusion

This paper showcases two natural hazards affecting communities in Khartoum. With the aid of the 1988 Khartoum flooding and some recent earthquake activities, the following main conclusions have been drawn:

1) The impacts of global warming, the degradation of vegetation in catchments and the effects of a changed surface albedo are problematic. A huge rainstorm recurrence has been expanding and ongoing for a long time regardless of the drop in yearly precipitation.
2) The ever-expanding urban area will increase the dangers of rain flooding unless a greater attention is given to street drainage.
3) The natural variability of the flow of the Nile River is tied to the sea surface temperature (SST) in the Pacific Ocean.
4) It has been found that knowledge of the timing of El Niño and La Niña events to forecast flooding in the Nile is crucial; when El Niño has been observed by La Niña, extreme floods have occurred in the Blue Nile.
5) A high rainfall is likely to occur during La Niña years and a low rainfall during El Niño years.
6) The coordination system between different agencies in response to disasters and the structural interdependence among stakeholders is becoming complicated and

is posing a threat to the efficiency of the disaster response, which was clear in the case of the 2020 flood.

7) Relating to earthquakes; liquefiable saturated sand layers at different depths with respect to subsoil conditions were available in Central Khartoum. The likelihood of liquefaction in Central Khartoum varied between the two zones considered, showing a small chance of liquefaction.

References

1. International Centre for Geohazards (2005) [Internet] [cited 2021 Jan 20]. Available from: https://web.archive.org/web/20080430003548/http://www.geohazards.no/projects/offshoregeohazards.htm

2. O'rourke, T.D.: Geohazards and large, geographically distributed systems. Géotechnique **60**(7), 505–543 (2010)

3. Jury, M.R.: The coherent variability of African river flows: composite climate structure and the Atlantic circulation. Water Sa **29**(1), 1–10 (2004)

4. Dumont, H.J.: The Nile river system. In: The Ecology of River Systems, pp. 61–88. Springer, Dordrecht (1986)

5. Zaroug, M.A., Eltahir, E.A., Giorgi, F.: Droughts and floods over the upper catchment of the Blue Nile and their connections to the timing of El Niño and La Niña events. Hydrol. Earth Syst. Sci. **18**(3), 1239–1249 (2014)

6. Eltayeb, G.E.: UN-HABITAT Case Studies, London. Khartoum, Sudan (2003)

7. Teklu, T., Von Braun, J., Zaki, E.: Drought and famine relationships in Sudan: Policy implications. Food Nutr. Bull. **14**(2), 1–3 (1992)

8. Sutcliffe, J.V., Dugdale, G., Milford, J.R.: The Sudan floods of 1988. Hydrol. Sci. J. **34**(3), 355–364 (1989)

9. Hulme, M., Trilsbach, A.: The August 1988 storm over Khartoum: its climatology and impact. Weather **44**, 82–90 (1989)

10. Elnimeiri, M.K.M., Satti, S.S.M., Ibrahim, M.K.M.: Barriers of access and utilization of reproductive health services by adolescents-Khartoum state-Sudan-2020: study protocol. Reprod. Health [Internet] **17**(1), 121 (2020). Available from: https://doi.org/10.1186/s12978-020-00967-y

11. Sileet, E.T.: The past and the future of flood management in the Eastern Nile Basin

12. Davies, H.R., Walsh, R.P.: Historical changes in the flood hazard at Khartoum, Sudan: lessons and warnings for the future. Singap. J. Trop. Geogr. **18**(2), 123–140 (1997)

13. Kuper, R., Kröpelin, S.: Climate-controlled Holocene occupation in the Sahara: motor of Africa's evolution. Science (80) **313**(5788), 803–807 (2006)

14. Irizarry-Ortiz, M.M., Wang, G., Eltahir, E.A.: Role of the biosphere in the mid-Holocene climate of West Africa. J. Geophys. Res. Atmos. **108**(D2), ACL-5 (2003)

15. Amarasekera, K.N., Lee, R.F., Williams, E.R., Eltahir, E.A.: ENSO and the natural variability in the flow of tropical rivers. J. Hydrol. **200**(1–4), 24–39 (1997)

16. Eltahir, E.A.: El Niño and the natural variability in the flow of the Nile River. Water Resour. Res. **32**(1), 131–137 (1996)

17. Wang, G., Eltahir, E.A.: Use of ENSO information in medium-and long-range forecasting of the Nile floods. J. Clim. **12**(6), 1726–1737 (1999)

18. Abtew, W., Melesse, A.M., Dessalegne, T.: El Niño southern oscillation link to the Blue Nile River basin hydrology. Hydrol. Process. Int. J. **23**(26), 3653–3660 (2009)

19. Person, W.J., Jacobs, J.M.: Significant earthquakes of the world 1990

20. Abdalla, J.A., Mohamedzein, Y.E., Wahab, A.A.: Probabilistic seismic hazard assessment of Sudan and its vicinity. Earthq Spectra. **17**(3), 399–415 (2001)

21. Ambraseys, N.N., Adams, R.D.: Seismicity of the Sudan. Bull. Seism. Soc. Am. **76**, 483–493 (1986)
22. Al-Ajamee, M., Mahmoud, M.M.M., Ahmed, M.E.: Site-Specific Seismic ground response analysis for typical soil sites in Central Khartoum, Sudan. In: Sitharam, T.G., Jakka, R., Govindaraju, L. (eds.) Local Site Effects and Ground Failures: Select Proceedings of 7th ICRAGEE 2020 (2021)
23. Seed, H.B., Idriss, I.M.: Simplified procedure for evaluating soil liquefaction potential. J. Soil Mech. Found Div. (1971)
24. Seed, H.B., Idriss, I.M., Arango, I.: Evaluation of liquefaction potential using field performance data. J. Geotech. Eng. **109**(3), 458–482 (1983)
25. Bolton Seed, H., Tokimatsu, K., Harder, L.F., Chung, R.M.: Influence of SPT procedures in soil liquefaction resistance evaluations. J. Geotech. Eng. **111**(12), 1425–1445 (1985)

Assessment of Land-Use and Land-Cover Changes on Soil Erosion in Sirajganj: A GIS and Remote Sensing-Based Approach

Shabik Zaheer [ORCID]**, Ahmed Ashhab, Kh. Al sadikul Zarif, Md. Arshadul Islam, and Shad Hossain**

1 Introduction

1.1 Background

Transition in land-use and land-cover (LULC) pattern of the earth surface is the combined outcome of human activities and natural phenomena [1]. Among the most generic and critical environmental issues, soil or land erosion secures a significant spot. The quality of soil is adversely affected by soil erosion. Moreover, reduction in agricultural productivity, failure of effective water use, inundation, flow of debris, and devastation of habitats result from soil erosion [2].

The natural environment is significantly affected by natural vegetation, which is at risk at the expense of agricultural land expansion. Population in the developing countries due to rapid population up rise is causing LULC transition indiscriminately. Through unplanned urbanization and agricultural activities, natural resources are exhausted in an unsustainable manner to ease the economic pressure and earn a livelihood. A significant component of soil erosion that presents an increased danger to soil productivity is persistent agricultural land extension. The effect of climate change and instability takes time to detect. But, the impact of human land alteration is felt within a brief period due to soil erosion [3]. Because of such circumstances, it is essential to quantify the extent of soil erosion and resulting land depletion because soil degradation has adverse environmental impacts, which include inadequacy of organic substances and nutrients, the decline in farmland fertility, and the quality of water. Besides, soil erosion affects the water flow, river reservoir capacities, and freshwater ecosystem of both within and surrounding area with several disastrous environmental consequences. This initiates the deterioration of soil, decompression of the soil structure, and decline in the depths of agricul-

S. Zaheer (✉) · A. Ashhab · Kh. Al sadikul Zarif · Md. A. Islam · S. Hossain
Department of Urban and Regional Planning, Rajshahi University of Engineering and Technology (RUET), 6203 Rajshahi, Bangladesh

turally productive soil. Moreover, soil erosion decreases the fertility of organic and nutritious materials in agricultural fields. Sediment accumulation in riverbed decreases the water storage capacity of the river, enhancing risk of flood and sludge, which is the consequence of soil erosion in neighboring areas. Erosion of soil has an intimate connection with LULC change and percentage change in vegetation areas.

LULC change's impact on soil erosion can be estimated by retrieving satellite images of past years in order to study the potential of soil erosion in accordance with the land-cover changes of watershed or discharge of sediment at watershed openings [4]. Repeated surveillance of the study region with the help of remote sensing techniques and satellite imagery helps to trace the temporal disparity of the LULC. Assessment of LULC change dynamics will facilitate understanding of the present soil erosion and land risk scenario and will help in any future decision-making procedure. Failure to do so will result in taking inaccurate decision endangering the life and livelihoods of a huge population and causing a catastrophic situation.

Sirajganj is located in the North-Western region of Bangladesh and is the gateway to the Rajshahi division. Recently due to huge surge in population growth, rapid unplanned urbanization, and depletion of vegetation areas, Sirajganj has become prone to massive LULC transition, fueling soil erosion in the study region (Fig. 1). The core objective of this research is to assess the LULC change impact on soil erosion in the study region through geographic information systems (GIS) and remote sensing procedures and to aid in future decision-making procedures in the study region.
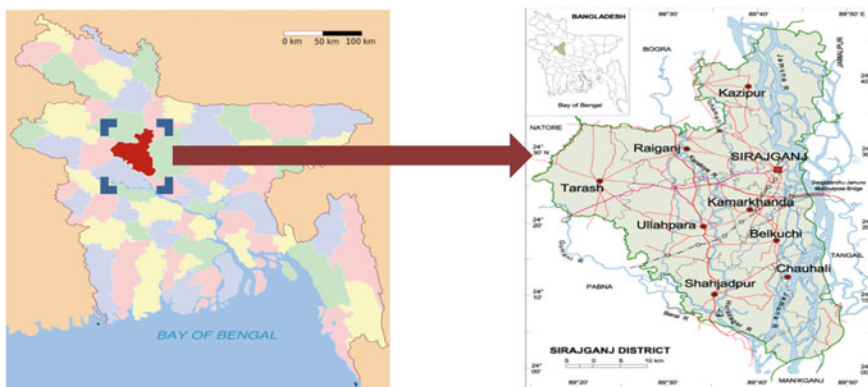
Fig. 1 Location map of Sirajganj

2 Methodology

2.1 Tools and Technologies

Landsat image, MS Excel, ArcMap 10.8.

2.2 Study Area and Data Source

Satellite images of past three decades were collected with an additional criterion of land cloud cover less than 10% for clear feature detection on ground. Each of these images contains several spectral bands. For year 2000, Landsat 7 image has been acquired that contains seven bands, for year 2010, Landsat 4–5 image has been acquired with nine spectral bands, and finally for year 2020, Landsat 8 image has been acquired containing 11 spectral bands in it. All these primary data have been provided from the United States Geo-Logical Survey (USGS).

2.3 Composite Image of Sirajganj Administrative Boundary

For further classification in LULC, all the spectral bands were needed to be brought under operation. All the bands were combined through image composition in ArcGIS environment. For each Landsat image of year 2000, 2010, and 2020, their identical number of bands were combined, and three composite band images were prepared. The administrative boundary of Sirajganj was extracted from the Landsat images with the help of national administrative boundary shape file of Sirajganj. Boundary line extraction produced an image containing features only inside Sirajganj boundary.

2.4 Feature Detection

The aim was to visualize the expansion and collapse between the main four features of the area that are urban area, vegetation, water body, and vegetated lands, which in later would relate to the reason of soil erosion. To identify these features, four types of training data were generated as different form of vector data. A total of 300 vector sample data was taken for each land use. Each of the sample data would act as reference for each feature on the soil. Maximum likelihood supervised classification will be processed after taking the samples. Training data will be acting a logic for the supervised classification algorithm of the ArcMap software.

2.5   Accuracy Measurement with Confusion Matrix

The whole operation is a software-based image analysis approach. The process has its own pros and cons. It is necessary to measure the accuracy of the classification itself. To calculate the accuracy, a specified range of points has been taken over the multispectral band image provided with the main Landsat file. These points will act as ground truth points for each feature. After that, raster value for the classified image will be generated through 'Extract Values to Points' tool. Raster value represents identical value of each raster of the image [5]. After calculating predicted value, a confusion matrix was prepared in the form of a pivot table. Following equations were used to calculate user's accuracy, producer's accuracy, overall accuracy, and kappa coefficient.

Overall Accuracy = sum of diagonal elements/total number of reference pixels

Producers Accuracy = sum of correctly classified pixels/number of training set pixels

Users Accuracy = sum of correctly classified pixels/total
number of pixels in that category (row total)

Kappa Coefficient,

$$K = \{(x * y) - z\}/(t - z)$$
$$x = \text{total}$$
$$y = \text{correct}$$
$$z = \text{sum all}$$
$$t = \text{total square } (x^2) \ [5]$$

3   Result and Discussion

3.1   Land Use and Land Cover

The year 2000 had the highest portion of vegetated land which is approximately 1050 km^2. This amount of vegetated area has not been seen in the past two decades. In 2010, vegetation decreased to 44% which is not very much noticeable. The lowest recorded vegetation land has been detected in 2020. The vegetated land kept disappearing until it drowns to 34%. This change is directly affected by expansion of urban area. A proportional change has been noticed between these two features over the years. In 2000, there was about 43% of urban land. It decreased by 1% in the next decade. In 2020, Sirajganj had the highest portions of urban land that have ever been built. The increase rate stood at 8% which was also highest of all time.

The present era supports the investigated result as every town and city is growing with modern urbanization concept. This also suggests that with time concrete built features will keep increasing in the future. This also urges the fact of consumption of vegetation land by concrete build (Table 1).

The disappearance of vegetation has a great impact on existing soil strength and its strength to sustain life, i.e., trees, microbes, etc. This relates directly to the statistics of barren land. In the year 2000, there was only 82 km^2 of barren lands which was 3% of total land use by then. This number surprisingly increased by 3% in next decade. In 2010, there was 85% of barren land. In 2020, it was the highest ever recorded with 9% increase than previous. Some previous barren land has been acquired by the urban area, but some new land emerged which can be a result of loss of soil strength. A very small change is seen among the water body. The year 2000 had the highest portion of water body. It kept decreasing by 1 and 3% consequently to the next three decades. In 2020, 138 km^2 of water body was recorded (Figs. 2, 3, 4).

The present trend of rapid expansion of urban culture and feature will keep acquiring vegetated lands unless the trend stops. This trend has been affecting the change in soil characteristics and loss in soil strength.

3.2 Accuracy Check of LULC

The following table illustrates feature-based accuracy which are user's and producer's accuracy. It also shows overall accuracy level and kappa coefficient. Over 80% of kappa coefficient indicates highest degree of agreement with the statistical data. It also indicates over 80% of data reliability [6] (Table 2).

All the accuracy are measured from the confusion matrix generated in the ArcMap environment. Achieved result is not 100% accurate but has almost perfect agreement on the scale of strength.

Table 1 Land-cover change detection

Year	Vegetation (%)	Barren land (%)	Water body (%)	Urban area (%)	Increase (+)/Decrease (−) (%)			
					Vegetation	Barren land	Water body	Buildable area
2000	45	3	9	43	–	–	–	–
2010	44	4	8	44	− 1	+ 1	− 1	+ 1
2020	34	9	6	51	− 11	+ 6	− 3	+ 8
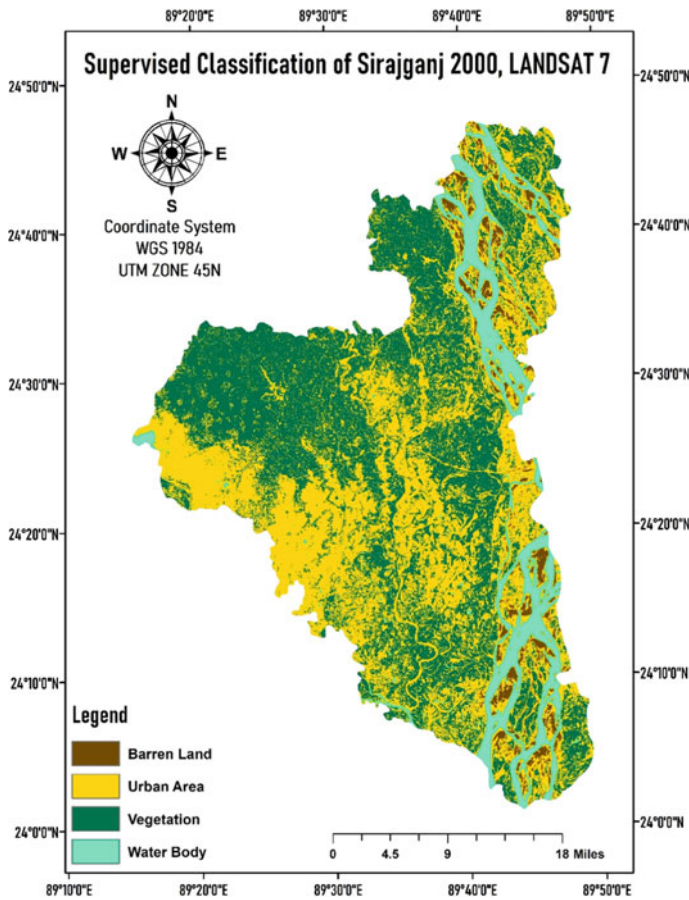
Fig. 2 LULC of Sirajganj, 2000

4 Conclusion

Rapid urbanization has brought us with enormous blessings. But unplanned urbanization brings us troubles unwanted and unknown. Soil erosion is one of the secret changes that cannot be seen but can be felt by investigation and consciousness. Unless the rapid construction of concrete feature is limited by authority, the process will continue itself bringing unwanted disaster. As a remote sensing
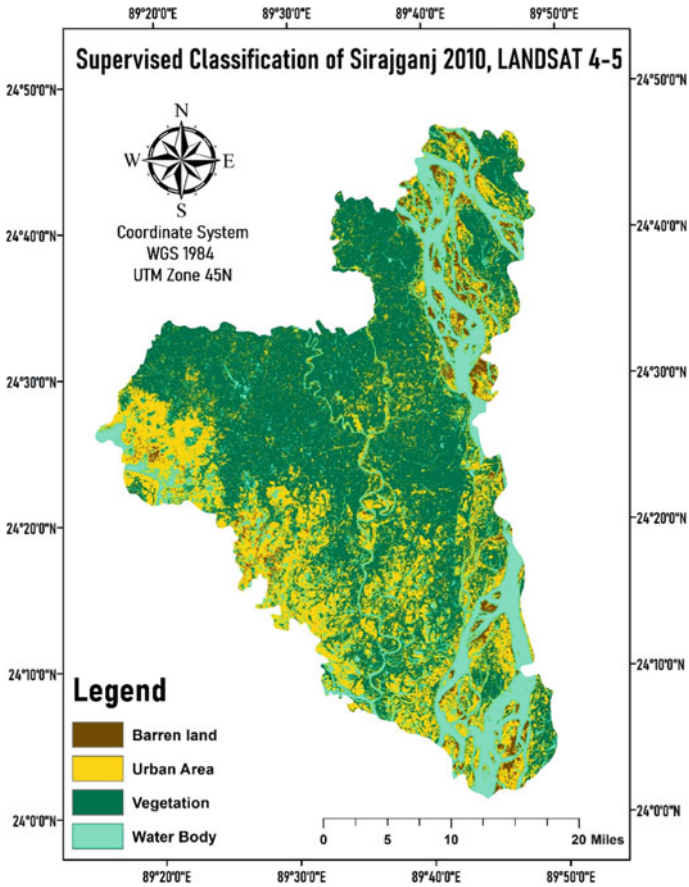
Fig. 3 LULC of Sirajganj, 2010

approach, this method cannot be 100% accurate by measure nor it may defeat practical surveys. But this approach can be considered as time-to-time surveillance of certain areas which are likely to face these problems. Also, these methods may come very helpful in the times of pandemic when there would not be a situation or budget for land surveys and soil test.
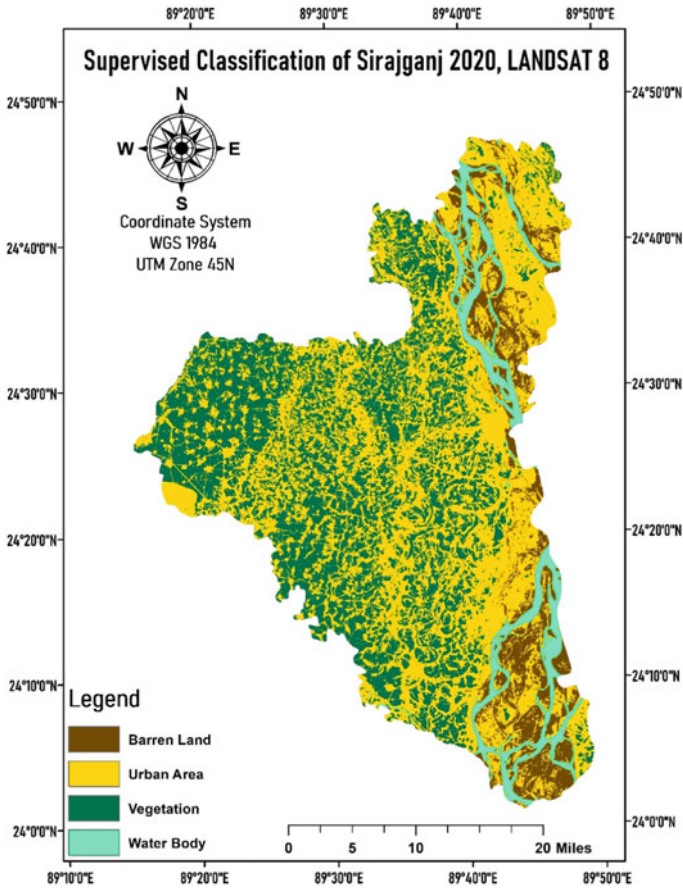
Fig. 4 LULC of Sirajganj, 2020

Table 2 Accuracy assessment

Year	Overall accuracy (%)	Producer's accuracy (%)				User's accuracy (%)				Kappa coefficient (K) (%)	Overall accuracy (Average) (%)
		Water body	Barren land	Vegetation	Urban area	Water body	Barren land	Vegetation	Urban area		
2000	88	98	96	95	98	99	100	99	88	96	89.67
2010	94	100	96	84	97	95	90	100	94	92	
2020	87	93	63	93	93	100	98	95	74	96	

References

1. Lambin, E.F., Geist, H.J. (eds.): Land-use and land-cover change: local processes and global impacts. Springer Science & Business Media (2008)
2. Park, S., Oh, C., Jeon, S., Jung, H., Choi, C.: Soil erosion risk in Korean watersheds, assessed using the revised universal soil loss equation. J. Hydrol. **399**(3–4), 263–273 (2011)
3. Tolessa, T., Senbeta, F., Kidane, M.: The impact of land use/land cover change on ecosystem services in the central highlands of Ethiopia. Ecosyst. Serv. **23**(Supplement C), 47–54 (2017)
4. Jordan, G., Van Rompaey, A., Szilassi, P., Csillag, G., Mannaerts, C., Woldai, T.: Historical land use changes and their impact on sediment fluxes in the Balaton basin (Hungary). Agric. Ecosyst Environ. **108**(2), 119–133 (2005)
5. Advanced Webinar: Accuracy Assessment of a Land Cover Classification Exercise 1: Accuracy Assessment Objectives. Accessed: 18 Mar, 2021 [Online]. Available: https://arset.gsfc.nasa.gov/land/webinars/advanced-land-classification
6. Sim, J., Wright, C.C.: The kappa statistic in reliability studies: use, interpretation, and sample size requirements. Phys. Ther. **85**(3), 257–268 (2005). https://doi.org/10.1093/ptj/85.3.257

A Study on Liquefaction Susceptibility of Road Infrastructure in Surat City

Shivam Thakur, Punit Bhanwar, and Trudeep Dave

1 Introduction

Liquefaction is the phenomenon when there is a loss of strength in saturated cohesion less soils because of increased pore water pressures and a reduction in effective stresses due to dynamic loading. Liquefaction commonly occurs in shallow, loose, and saturated cohesion less soils subjected to strong ground motions in earthquakes [1]. Often, pore water increase is associated with earthquakes; often, activity such as blasting can also cause it. Characteristics of the soil grains like distribution of shapes, sizes, shape, composition, etc., influence soil's susceptibility to liquefy. Also, stress history is a crucial parameter in determining the liquefaction resistances of soil as over consolidated soils are more resistant to particle rearrangement hence leading to a low possibility of liquefaction [2].

The liquefaction resistance of a soil deposit increases with depth as overburden pressure increases; therefore, soil deposits deeper than about 15 m are rarely found to have liquefied [3]. Further, rounded soil particles of uniform size are mostly susceptible to liquefaction [4], whereas well-graded soils, due to their stable interlocking configuration, are less prone to liquefaction. Researchers highlighted that non-plastic soil fines with dry surface texture do not create adhesion and do not provide appreciable resistance to particle rearrangement and liquefaction [5]. In addition, the permeability of soil also plays a significant role in liquefaction. When pore water movement within the soil is retarded by low permeability, pore water pressures are likely to generate during the cyclic loading [6].

Road embankments are usually made of granular materials and are prone to liquefaction if saturated and subjected to dynamic loading. The type of soil used in road embankment construction often depends on local conditions and geology. The road construction requirements typically limit the fines' size but are less stringent in

S. Thakur · P. Bhanwar · T. Dave (✉)
Institute of Infrastructure Technology Research and Management, Ahmedabad, India
e-mail: trudeepdave@iitram.ac.in

terms of the material's permeability values. Owing to this, the road embankments consisting of granular soils may suffer liquefaction when saturated and subjected to seismic shaking [7]. The liquefied granular soils of embankment may cause pavement damage such as ground settlement, embankment penetration, embankment spreading, lateral spread, ground oscillation, and flow failure [8].

1.1 Liquefaction Potential

Liquefaction potential is the indicator generally used to ascertain the susceptibility of soil to seismic liquefaction. Various laboratory methods like the cyclic tri-axial shear test, shake table test, etc., and field methods like cone penetration test and standard penetration test are used to determine liquefaction potential. However, in situ testing is the dominant approach in common engineering practice for quantitative assessment of liquefaction potential [9]. The evaluation of soils' liquefaction resistance requires calculating seismic demand on a soil layer, expressed in terms of the cyclic stress ratio (CSR). The soil's capacity to resist liquefaction is expressed in terms of the cyclic resistance ratio (CRR). If the cyclic stress ratio caused by the earthquake is greater than the cyclic resistance ratio of in situ soil, liquefaction could occur during an earthquake. The factor of safety against liquefaction is defined as the ratio of soil resistance to liquefaction (CRR) and stress caused by the earthquake load (CSR).

1.2 Seismicity of Surat Region

The Indian state Gujarat is one of the most seismic prone intercontinental regions globally, which has experienced two large earthquakes of magnitude 7.8 and 7.7 in 1819 and 2001, respectively, and seven earthquakes of magnitude 6.0 during the past two centuries. Surat city, which is at around 350 km from the seismically active sources of Kutch (Gujarat), received unexpectedly considerable damage from the Bhuj earthquake of 2001, which had a magnitude of 7.7. It is considered to be in an earthquake-prone area and is shaken by earthquake vibrations several times [10]. According to IS 1893: 2002 [11], Surat is placed in seismic zone III. Also, the Tapi river flows across the city increases the chances of soil liquefaction and failure vulnerability of road infrastructure in the future seismic event. Hence, it is essential to perform seismic hazard analysis for Surat city to avoid further expected losses. Such seismic analysis will be mainly focused on soil liquefaction potential studies and characterization of sites.

2 SPT Bore-Log Locations

The area of Surat city is about 326 km^2, and in the present study, SPT data from 30 boreholes were collected for analysis. Table 1 presents details of 30 locations with the respective bore-log number at which SPT test as per IS 2131: 1981 [12] was conducted. These bore-log numbers shall be repeatedly referenced for study and analysis.

Table 1 SPT bore-log number with respective test locations

Serial no	Name of the place	Bore-lognumber
1	Dinoli, SMC	1,011,034
2	Yogi Nagar	910,334
3	Dumas	910,295
4	Nandniketan	910,281
5	Hazira	910,279
6	Kribcho, Hazira	910,242
7	Housing Dept, SMC	910,187
8	Mora Tekara	910,147
9	Hanumar Tekti	809,006
10	Majura	809,009
11	Ichchhapore	809,011
12	Moje Sultanabad	809,017
13	Pal	607,106
14	Elum Park, Pal	607,101
15	Ultratech Cement Factory	607,102
16	Pumping Station, Pal	607,158
17	Jahangirpur	708,001
18	Vesu	809,035
19	Madhav Housing Society	809,050
20	Palanpur Ugat Road	809,109
21	Jakatnaka	809,108
22	Kosad, SMC	809,069
23	Sewage Plant, Kosad	910,017
24	Timaliawad	910,078
25	Velentine Cinema, Dumas	910,110
26	Kharvar Nagar	910,141
27	Bhatar	910,179
28	Sarathana Jakatnaka	910,261
29	Millenium market	910,288
30	Community Building Dumas	910,296

3 SPT-Based Procedure for Evaluating Liquefaction Potential

Evaluation of the liquefaction potential of soils in Surat near the river Tapi, which are most likely to be affected during earthquakes, was examined using semi-empirical procedures for use in practice [13]. The liquefaction potential analysis is done using the Standard Penetration Test (SPT) for differentiating between liquefiable and non-liquefiable regions in various parts of Surat city. The variables for differentiating between liquefiable and non-liquefiable conditions for all 30 locations via SPT bore-log data were referenced [13]. After which, CSR was evaluated using Eq. 1.

$$\text{CSR}_{M-7.5} = 0.65\{\sigma_{vo}|\sigma'_{vo}\}\{a_{\max}|g\}r_d/\text{MSF}.K_\sigma \tag{1}$$

where

$a_{\max}$ Maximum horizontal acceleration at the ground surface.
σ_{vo} Total vertical stress.
σ'_{vo} Effective vertical stress at depth 'z'.
r_d Stress reduction coefficient that accounts for the flexibility of the soil column.
MSF   Magnitude scaling factor.
K_σ Overburden correction factor.

This was followed by estimation of CRR value, where firstly SPT penetration resistance was adjusted by [8] to an equivalent clean sand value Eqs. (2) and (3).

$$(N_{1)})60cs = (N_1)_{60} + \Delta(N_1)_{60} \tag{2}$$

$$\Delta(N_1)_{60} = e^{1.63 + \frac{9.7}{FC} - \left(\frac{15.7}{FC}\right)^2} \tag{3}$$

The value of the CRR for a magnitude of earthquake = 7.5 and effective vertical stress of 1 Atm can be calculated on the basis of the value of $(N_1)_{60cs}$ using Eq. (4).

$$\text{CRR} = e^{\left(\frac{(N_1)60cs}{14.1}\right) + \left(\left(\frac{(N_1)60cs}{126}\right)^2\right) - \left(\left(\frac{(N_1)60cs}{23.6}\right)^3\right) + \left(\left(\frac{(N_1)60cs}{25.4}\right)^4\right) + (2.8)} \tag{4}$$

3.1 Results and Discussion

The calculated liquefaction potential from SPT-N-based simplified procedure, as suggested by Boulanger and Idriss [13] for all 30 locations is summarized in Table 2. As mentioned in Table 2, 6 sites out of 30 locations are susceptible to

Table 2 SPT bore-log number with respective test locations

S No.	Bore-log No	z(m)	$(N_1)60$	FC	$(N_1)60cs$	CSR	CRR	FS	Liquefaction susceptibility
1	1,011,034	3	10.444	85	15.973	0.115	0.164	1.43	No
2	910,334	3	11.343	82	16.881	0.114	0.172	1.50	No
3	910,295	9	12.379	88	17.899	0.184	0.182	0.98	Yes
4	910,281	4.5	10.555	85	16.084	0.178	0.165	0.92	Yes
5	910,279	4.5	9.859	85	15.388	0.172	0.159	0.92	Yes
6	910,242	3	11.107	18	15.195	0.117	0.157	1.34	No
7	910,187	4.5	15.285	14	18.187	0.226	0.185	0.82	Yes
8	910,147	3	16.620	70	22.195	0.114	0.236	2.06	No
9	809,006	3	30.073	14	32.975	0.110	0.755	6.81	No
10	809,009	3	13.413	89	18.930	0.114	0.193	1.69	No
11	809,011	3	19.205	25	24.276	0.112	0.273	2.44	No
12	809,017	4	5.655	95	11.155	0.133	0.126	0.94	Yes
13	607,106	3	18.519	24	23.503	0.113	0.258	2.27	No
14	607,101	3	24.641	88	30.161	0.111	0.495	4.45	No
15	607,102	3	7.328	84	12.860	0.116	0.138	1.19	No
16	607,158	4.5	21.544	74	27.107	0.116	0.350	2.99	No
17	708,001	4.5	11.276	81	16.817	0.134	0.172	1.27	No
18	809,035	3	5.140	93	10.646	0.206	0.122	0.59	Yes
19	809,050	3	10.238	87	15.761	0.115	0.162	1.40	No
20	809,109	3	12.499	91	18.011	0.114	0.183	1.60	No
21	809,108	2	8.827	88	14.347	0.112	0.150	1.33	No
22	809,069	3	12.326	97	17.821	0.114	0.181	1.58	No
23	910,017	3	14.163	95	19.663	0.114	0.201	1.76	No
24	910,078	3	11.280	44	16.882	0.115	0.172	1.50	No
25	910,110	3	20.271	64	25.863	0.112	0.311	2.76	No
26	910,141	2	24.513	59	30.118	0.105	0.492	4.65	No
27	910,179	3	11.639	16	15.212	0.116	0.157	1.36	No
28	910,261	3	14.551	57	20.159	0.113	0.207	1.83	No
29	910,288	3	10.474	75	16.034	0.114	0.165	1.43	No
30	910,296	3	16.039	76	21.596	0.113	0.227	1.99	No

liquefaction. Further, the deterministic analysis performed using LiqIT software was also carried out during the validation of results. In addition, the results obtained from both the methods viz. SPT-N-based simplified procedure and deterministic analyses are compared in terms of CSR-CRR. The results of variation in CSR-CRR with soil depth were compared and plotted. At various depths, the values of CSR-CRR were plotted against shear stress ratio via origin software as shown in Figs. 1, 2, 3 and 4. However, due to space constraints out of 30 site locations, 4 locations are discussed.

Fig. 1 Comparison between results from SPT-N Value method (**a**) and LiqIT analysis (**b**) for location no. 1011034
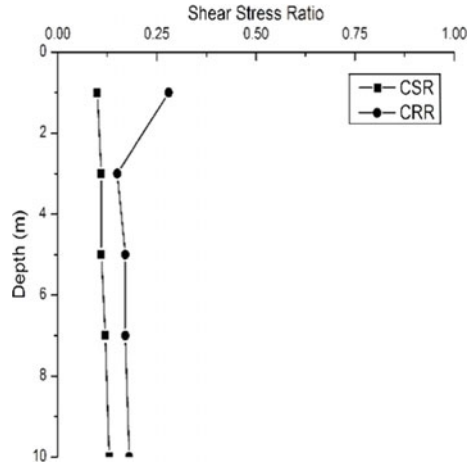
(a)
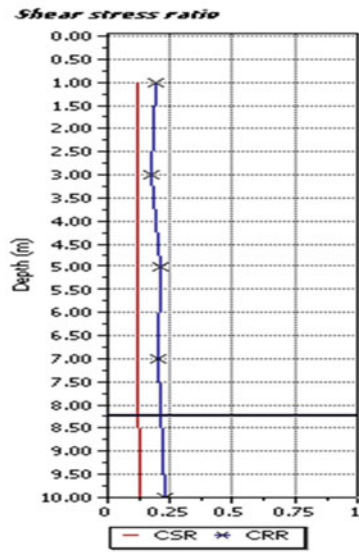
(b)

It can be concluded from Figs. 1, 2, 3 and 4 that results obtained from both the methods matched well with variation less than 5%. The factor of safety for places closer to the water bodies, i.e., the place with the high water table, was very low (less than 1), which hinted at these locations' liquefaction susceptibility. Hence, special measures must be taken for liquefaction mitigation to ensure that infrastructure constructed at such sites is less prone to liquefaction-induced losses. To ensure the road infrastructure's longevity and prevent infrastructure damage due to liquefaction, geotechnical site characterization, and ground response analysis

Fig. 2 Comparison between results from SPT-N Value method (**a**) and LiqIT analysis (**b**) for location no. 910281
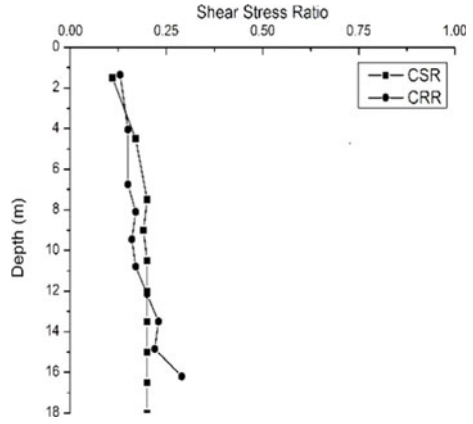
(a)
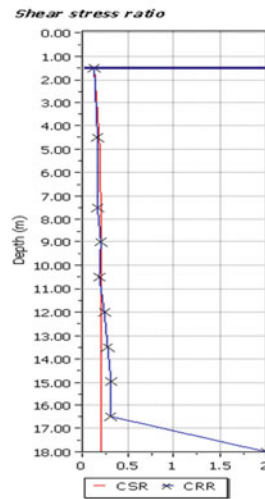
(b)

considering local site conditions are beneficial. This type of study provides information about liquefaction susceptibility and helps to decide on the requirement of active/passive remediation of sites prone to liquefaction.

4   Conclusion

The liquefaction susceptibility analysis was done for 30 locations across Surat city. The liquefaction potential was evaluated based on the SPT-N-based simplified procedure and compared with the deterministic analysis done by computational

Fig. 3 Comparison between results from SPT-N Value method (**a**) and LiqIT analysis (**b**) for location no. 910187

(a)

(b)
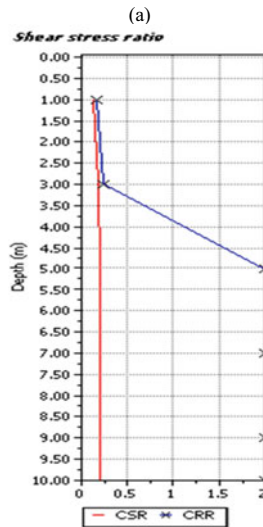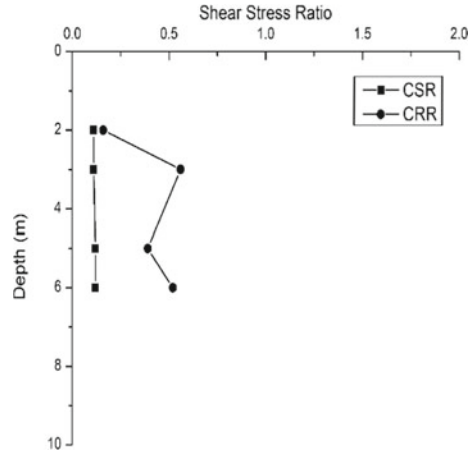
tool, i.e., LiqIT. Liquefaction susceptibility analysis was performed for 30 site locations. Regions like Dumas, Nandniketan, Hazira, Housing Department, Moje Sultanabad, and Vesu are found to be prone to liquefaction. Most of these places are situated near water bodies (the Arabian Sea beach or the river Tapi), which validates that liquefaction is more likely to happen at places with a higher water table. In other cases, i.e., some of the places (e.g., Dumas) with comparatively lower water table depth are also susceptible to liquefaction due to greater sand content in soil composition. Geotechnical site characterization and ground response analysis would benefit not only by increasing the road infrastructure's longevity, but also by deciding on implementing liquefaction mitigation measures at the site.

Fig. 4 Comparison between
results from SPT-N Value
method (**a**) and LiqIT analysis
(**b**) for location no. 910288
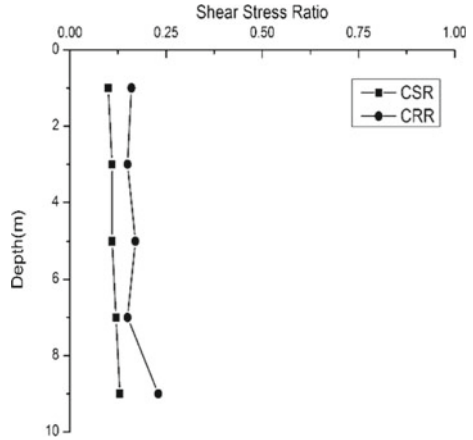
(a)
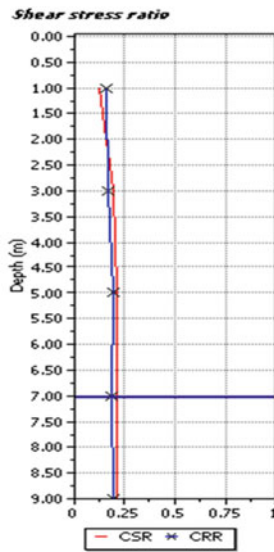
(b)

References

1. National Research Council's Committee on Earthquake Engineering (1985)
2. Seed, H.B.: Soil liquefaction and cyclic mobility evaluation for level ground during earthquake. J. Geotech. Eng. Div. ASCE **105**(GT2), 201–225 (1979)
3. Krinitzsky, E.L., Gould, J.P.: Fundamentals of earthquake resistant construction, ISBN: 0471839817 (1993)
4. Poulos, S.J., Castro, G., France, W.: Liquefaction evaluation procedure. J. Geotech. Eng. Div. ASCE **111**(6), 772–792 (1958)

5. Ishihara, K.: Liquefaction and flow failure during earthquakes. Rankine Lecture Geotechnique, ISSN 0016–8505, vol. 43, issue 3, pp. 351–451 (1993)
6. Koester, J.P.: The influence of fine type and content on cyclic strength. Ground failure under seismic conditions, pp. 17–33 (1994)
7. Querol, S.L., Blazquez, R.: Identification of failure mechanisms of road embankments due to liquefaction: optimal corrective measures at seismic sites. Can. Geotech. J. **43**, 889–902 (2006)
8. Boulanger, R.W., Idriss, I.M.: State normalization of penetration resistance and the effect of overburden stress on liquefaction resistance. In: Proceedings 11th Soil Dynamics and Earthquake Engineering and 3rd International Conference on Earthquake Geotechnical Engineering, Berkeley, CA (2004)
9. Sladen, J.A., Hollander, R.D., Krahn, J.: The liquefaction of sands, a collapse surface approach. Can. Geotech. J. **22**, 564–578 (1985)
10. Seismology Review 2017 edition, Institute of Seismological Research (Gujarat)
11. IS 1893 (Part 1): 2002. Criteria for Earthquake Resistant Design of Structures—General Provisions and Buildings, Bureau of Indian Standards (2002)
12. IS 2131:1981 (Reaffirmed 2002) Method for Standard Penetration Test for Soils, Bureau of Indian Standards
13. Boulanger, R.W., Idriss, I.M.: CPT and SPT based Liquefaction triggering procedures (2014)

Predicting Landslide Dam Outburst Flood Peak Discharge

David C. Froehlich

1 Introduction

The downward and outward movement of earth-slope materials, including rock, soil, artificial fill, or a combination of these, is known as a "landslide" [1]. The materials move by falling, toppling, sliding, spreading, or flowing owing to a wide variety of slope-destabilizing processes. A consequence of some large-scale slope failures, occasionally more disastrous than the collapse and rapid motion of the mass of rock and soil itself, is the blockage of a river resulting in upstream valley inundation and, possibly, a subsequent sudden release of a large quantity of impounded water known as an outburst flood.

Upstream inundation takes place as the created impoundment (known as a barrier lake) fills, usually slow enough so that people can evacuate in time. Although the danger to life may be minimal, property damage can be substantial. However, floods caused by a rapid breaching of the blockage can devastate communities and take many lives for hundreds of kilometers downstream. For example, the breaching of the 1786 earthquake-triggered rockslide that blocked the Dadu River in Sichuan, China, produced the most destructive outburst flood in recorded history [2]. Ten days after forming, the dam failed suddenly, releasing more than 50 Mm^3 of impounded water in a short time. The tremendous surge that was generated engulfed numerous downstream communities drowning more than 100,000 people.

A rapid method for estimating the peak discharge from a breached landslide dam is needed to provide sufficient warning to the downstream population if a failure is possible. Peak outflow rates from 42 outburst floods are analyzed in this study to create such a procedure. Systematic classification of the blockages based on their material composition, sedimentological features, and travel distances is first used to assess the erodibility of a dam, which controls the size (height and width) of a

D. C. Froehlich (✉)
Cary, NC, USA
e-mail: dcfroehlich@aol.com

breach and the speed at which it forms. Three categories or types of obstructions are defined. The blockage type, the dam's height, and the water volume impounded by the barrier inform a regression equation that gives the expected outburst flood peak discharge. Additionally, the prediction interval of peak discharge is calculated based on sound statistical reasoning, which provides a margin of error useful in assessing the potential downstream flood hazards.

2 Landslide Characteristics

2.1 Types of Landslides

A variety of mass-movement processes combined with the range of geologic, topographic, and climatic environments in which they occur complicate landslide classification. Generally, landslides are of two types: those in rock and those in fine-grained and coarse-textured unconsolidated sediments (soils). However, many landslides have an initial failure mechanism different from subsequent mass movement styles [3]. Examples include rockfalls that evolve into rock avalanches and rockslides that transform into large debris flows [4]. The only similarity to landslides is their generally accepted definition: the downslope movements of earth material under gravity's influence.

The landslide dams examined in this analysis were caused by mass wasting, which is the spontaneous downhill movement of soil, regolith, and rock and soil under the influence of gravity. The landslides analyzed range from rockslides or jumbled bedrock fragments to bedrock slumps, in which most of the bedrock remained intact as it moved. Many of the landslides were initiated by earthquakes, others by extended periods of intense rainfall.

2.2 Movements that Create Barrier Lakes

From a study of 184 landslide dams, Costa and Schuster [5] found that most mass movements that blocked streams and created barrier lakes were the product of avalanches, slumps and slides, and earth flows. Rockfalls and slope failures in sensitive clays produced comparatively few river blockages that have led to devasting floods. The number of dams caused by clay slides is small because such movements occur mostly in low relief areas and travel short distances. Rockfalls produce few large blockages because the volume of material in this type of mass movement is small.

As described by Hewitt [6], the tallest blockages generally form in steep-walled narrow valleys because there is only a small area for the landslide mass to spread out. Large-volume earth and rock slumps and slides, and rock and debris

avalanches, are particularly likely to form high dams because they occur on steep slopes and move rapidly, which produces an almost instant stream blockage. The sudden halting against the opposite valley wall creates a densely compacted mass, which forms a nearly impermeable blockage that can be hundreds of meters high. Debris lobes that spread far up and down the valley help resist erosion by over-topping flows and add strength to the dam. The new or undisturbed rock avalanche surface usually consists of large boulders. However, in the main body of material where erosion cuts through, a dense matrix of crushed and pulverized rock envelop the sizeable clasts.

3   Landslide Dam Classification

In this study, a systematic classification of landslide dams that have common characteristics based on the composition material and sedimentological features is used to assess the erodibility of a blockage, which controls the size (height and width) of a breach and the speed at which it forms. From the onsite investigations of more than 30 large landslide dams, Fan [7, pp. 37–38] and Fan et al. [8] organize them into the following three categories or types—the order of which is revised here to reflect the breach formation potential from most to least erodible:

- Type 1 Landslide Dams: These blockages are composed primarily of small-sized unconsolidated material usually formed by debris flows, avalanches, and slides with long runout (that is, the travel distance) and substantial entrainment along their traveling path. Landslides with long runouts are more likely to fragment and disintegrate during their movement, producing crushed debris topped by a thin boulder carapace [9]. These dams show low stability and are eroded comparatively easily by flows that overtop the blockage. Many landslide dams formed by post-earthquake debris flows belong to this type.
- Type 2 Landslide Dams: These dams are composed mostly of large boulders and blocks formed by rock avalanches or by rockfalls initiating from densely jointed rock slopes. Rock avalanche deposits could also have a dual structure with comminuted debris inside that is overlain by a blocky carapace [9].
- Type 3 Landslide Dams: These barriers have partly intact rock strata at their base and are topped by large boulders and blocks or soil with rock fragments, showing a two-layered or three-layered internal structure. Such dams are typi-cally formed by deep-seated rockslides or avalanches that fail as an intact mass followed by short runouts into narrow valleys. Because of the topographic constraints on the landslide movement, the sliding rock mass cannot disintegrate completely, which keeps the original geological structure that is highly resistant to erosion partly intact.

Fan et al. [8] found that Type 3 blockages are more consolidated than Types 1 and 2 and are less likely to be breached for their entire height. The almost intact

rock mass in the dam body can be impenetrable, although the fine sediment on the top or middle layer may be eroded by overtopping flows. They also found that dams formed from Type 2 blockages are composed of boulders and blocks that are more resistant to erosion than Type 1 dams containing unconsolidated or highly permeable debris.

The material types and the landslide runout distance also control the stability of blockages. Dams consisting of large wedges of carbonate rocks and sandstone are generally stable. In contrast, those composed of fine-grained materials, such as weathered mudstone, slate, or phyllite, erode more easily when overtopped by impounded flows. Runout distance also influences the ultimate composition, and thus the ability to resist erosion, of the blockages. Long runouts produce intense fracturing and disintegration of the slide clasts and textural segregation within the mass of material.

4 Assembled Data

Outburst flood peak discharges, and other pertinent data, for 42 rapidly breached landslide dams were assembled from various sources and are presented in Tables 1 and 2 grouped by the blockage type (1, 2, or 3). Data in Table 1 briefly identify the dam and include the landslide's common name, the blocked river's name, the country, and the dam's formation date. Table 2 data summarize measures of the blockage and the outburst flood as follows: H_d = the dam or blockage height (measured from the lowest point along the blockage crest down to the original streambed), W_d = the blockage width (the distance between the upstream and downstream blockage toes), V_{lake} = the total volume of impounded water at the time of breaching, H_b = the final breach height (measured from the lowest point along the crest down to the bottom of the eroded opening), V_w = the volume of impounded water above the final breach bottom at the start of failure, and Q_p = the peak discharge of the landslide dam outburst flood.

4.1 Blockage Type

The type of blockage (1, 2, or 3) that formed each dam was determined from the following information:

1. Written descriptions of the physical characteristics of the earth or rock formation; its composition, structure, texture, and hardness.
2. Maps, aerial photographs, and satellite images showing the slide origin and its runout distance.
3. Post-breach photographs that provided visual documentation of the blockage composition and written descriptions of the internal structure of the dam.

Table 1 Landslide dam location and formation date

	Landslide common name	Blocked river	Country	Formation date (yyyy.mm.dd)
Blockage type 1	Ambon Island	Way Ela	Indonesia	2012.07.15
	Donghekou	Qingzhu	China	2008.05.12
	El Chichón	Magdalena	Mexico	1982.04.03
	Elk Rock Lake	North Fork Toutle	United States	1980.05.18
	Hongshihe	Hongshi	China	2008.05.12
	Jackson Creek Lake	North Fork Toutle	United States	1980.05.18
	Lake Yashilkul	Tegermach	Kyrgyzstan	1835.00.00
	Mt. Iwakura	Shinano	Japan	1847.05.08
	Tobata	Azusa	Japan	1757.06.24
	Tonzang	Tui Lam Lui	Myanmar	2015.07.16
	Tsatichhu	Tsatichhu	Bhutan	2003.09.10
	Xiaolin	Qishan	Taiwan	2009.08.09
	Yigong	Yigong Zangbo	China	2000.04.09
Blockage type 2	Baige 2	Jinsha	China	2018.11.03
	Bairaman	Bairaman	Papua New Guinea	1985.05.11
	Baisari	Kali Gandaki	Nepal	2015.04.25
	Gyalha	Yarlung Tsangpo	China	2018.10.17
	Hattian Bala	Kali	Pakistan	2005.10.08
	Jishi Gorge	Yellow	China	∼1920 BCE
	Kali Gandaki	Kali Gandaki	Nepal	2015.05.24
	Lago Carri Lauquen	Barrancas	Argentina	1489.00.00
	Lower Aral	Kokomeren	Kyrgyzstan	∼5000 BCE
	Lower Gros Ventre	Gros Ventre	United States	1925.06.23
	Mount Adams	Poerua	New Zealand	1999.10.06
	Nonoo	Mimikawa	Japan	2005.09.01
	Peilong	Zangbu	China	1986.06.20
	Pisque	Pisque	Ecuador	1990.01.02
	Tanggudong	Yalong	China	1967.06.08
	Toro	Toro	Costa Rica	1992.06.13
	Tsao-Ling 2	Ching-Shui	Taiwan	1979.08.15
	Tunawaea	Tunawaea	New Zealand	1991.08.17
	Xiaogangjian	Mianyuan	China	2008.05.12
	Zepozhu	Dong	China	1965.10.27
Blockage type 3	Baige 1	Jinsha	China	2018.10.10
	Condor-Sencca	Mantaro	Peru	1945.08.16
	Gohna Lake	Bireh-Ganga	India	1893.09.22

(continued)

Table 1 (continued)

	Landslide common name	Blocked river	Country	Formation date (yyyy.mm.dd)
	La Josefina	Paute	Ecuador	1993.03.29
	Lichar Gah	Indus	Pakistan	1840.12.07
	Mayunmarca	Mantaro	Peru	1974.04.25
	Tangjiashan	Tongkou	China	2008.05.12
	Tsao-Ling 1	Ching-Shui	Taiwan	1942.08.10
	Xiaojiaqiao	Chaping	China	2008.05.12

Blockages created by debris flow (particularly those generated by earthquakes), and other slides consisting of weathered rock particles that resided above solid, unaltered rock (often triggered by intense rainfall of long direction), were consistently categorized Type 1 dams. Deep-seated rockslides or avalanches that failed as an intact mass followed by exceptionally short runouts into narrow valleys were always classed as Type 3 dams. If neither Type 1 nor Type 3 categorization was readily apparent, the blockage was considered a Type 2 dam.

4.2   Peak Discharge Measurement

All outburst flood peak discharges were determined by indirect means rather than direct measurement using current meters or other flow measurement devices. The several indirect methods used to calculate the peak flow rates are described as follows:

1. The technique used most often, and perhaps the most accurate if carried out by knowledgeable analysts, is the slope-area method [10]. The accuracy of the calculated peak discharge depends on the reliability of measured high-water marks, the correctness of estimated roughness coefficients, appropriateness of the one-dimensional flow supposition, and the distance of the measurement downstream from the breached dam.
2. Estimation based on barrier lake volume change during a short-time interval is the second most frequently used approach, which assumes a nearly level water surface upstream of the dam and, in most cases, zero inflow to the lake. Discharge accuracy is reduced by the latter assumption for overtopping failures caused by large floods. Length of the time interval used in the calculation and

Table 2 Landslide dam dimensions and outburst flood volume and peak discharge

	Landslide common name	Dam height H_d (m)	Dam width W_d (m)	Lake volume V_{lake} (Mm³)	Breach height H_b (m)	Water volume released V_w (Mm³)	Peak discharge Q_p (m³/s)
Blockage type 1	Ambon Island	70	1660	27.6	70	27.6	17,000
	Donghekou	20	750	10	10	4.0	1000
	El Chichón	30	2000	40	30	40	11,000
	Elk Rock Lake	16	1000	0.31	16	0.31	250
	Hongshihe	10	500	2.0	10	2.0	600
	Jackson Creek Lake	4.5	300	2.5	4.5	2.5	480
	Lake Yashilkul	120	580	6.6	90	6.5	4960
	Mt. Iwakura	70	1000	350	70	300	34,000
	Tobata	150	700	98	150	98.0	27,000
	Tonzang	50	1500	15.5	35	11.6	4000
	Tsatichhu	140	700	7.0	140	7.0	6900
	Xiaolin	52	1500	19.5	52	19.5	9300
	Yigong	58	2500	3000	54	2015	173,000
Blockage type 2	Baige 2	81	1000	494	51	442	33,900
	Bairaman	210	3000	50	70	40	7400
	Baisari	30	200	8.0	30	8.0	1700
	Gyalha	79	1900	510	56	490	32,000
	Hattian Bala	75	1300	70	40	36	5500
	Jishi Gorge	195	1300	14,400	120	13,700	400,000
	Kali Gandaki	40	200	8.0	30	8.0	1700
	Lago Carri Lauquen	100	3000	1550	95	1550	97,000
	Lower Aral	80	550	200	70	200	29,000
	Lower Gros Ventre	70	3000	105	40	74	8000
	Mount Adams	90	700	7.0	80	7.0	2500
	Nonoo	57	370	12	57	11	3000
	Peilong	29	1500	30	16	23	2100
	Pisque	58	300	3.6	30	1.56	700
	Tanggudong	175	3000	680	88	640	53,500
	Toro	85	600	0.55	50	0.47	400
	Tsao-Ling 2	90	700	40	70	35	7780
	Tunawaea	50	570	0.90	22	0.63	250
	Xiaogangjian	95	300	11.4	30	9.7	2850
	Zepozhu	51	1000	2.7	34	2.5	700

Table 2 (continued)

	Landslide common name	Dam height H_d (m)	Dam width W_d (m)	Lake volume V_{lake} (Mm³)	Breach height H_b (m)	Water volume released V_w (Mm³)	Peak discharge Q_p (m³/s)
Blockage type 3	Baige 1	61	1500	249	31	197	10,000
	Condor-Sencca	133	580	721	56	664	35,400
	Gohna Lake	275	3200	470	119	283	34,900
	La Josefina	102	1100	210	40	175	12,150
	Lichar Gah	300	3500	6500	230	6400	148,000
	Mayunmarca	107	3800	352	107	350	13,700
	Tangjiashan	82	1200	247	22	167	6500
	Tsao-Ling 1	140	4800	157	70	120	11,100
	Xiaojiaqiao	65	300	22	37	10	1000

the gauge used to record water levels also have unfavorable effects on the computed discharge accuracy.

3. Some peak discharges were calculated as twice the average outflow rate needed to empty the barrier lake within a specified time. Measurement accuracy depends mainly on the reported drainage-time reliability and inflows to the lake during the failure. This approach is probably the least accurate of all methods used to determine the peak outflow rate.

4. Unsteady flow numerical modeling of barrier lake outflows using the measured final breach dimensions and observed breach formation times is sometimes carried out to determine the outburst flood peak discharge. Combined with high-water marks at downstream locations and indirect measurements of peak discharge (by the slope-area method, from rating-curves at installed stream gages, and by calculations of flows through bridges and over dams), this approach can provide highly accurate estimates of the peak discharge from the breached dam.

5 Estimating Outburst Flood Peak Discharge

The expected value of an outburst flood peak discharge was evaluated by multivariate optimization that minimized the squared errors of predictions. Because downstream hazards from a potential outburst flood should be assessed using an adequate margin of error, peak discharge prediction intervals were also calculated.

5.1 *Expected Value*

A general mathematical model of the following form predicts the logarithm of the expected peak discharge well:

$$\ln \hat{Q}_p = \theta_1 + \theta_2 I_1 + \theta_3 I_2 + \theta_4 \ln\left(\frac{V_{\text{lake}}^{1/3}}{H_d}\right) + \theta_5 \ln\sqrt{gH_d^5} \tag{1}$$

where $\hat{Q}_p$ = the expected value of peak discharge and I_1 and I_2 are indicator variables denoting the type of blockage as follows:

$$I_1 = \begin{cases} 1, & \text{if the blockage is Type 2} \\ 0, & \text{otherwise} \end{cases} \quad \text{and } I_2 = \begin{cases} 1, & \text{if the blockage is Type 3} \\ 0, & \text{otherwise} \end{cases} \tag{2}$$

The blockage is Type 1 if both I_1 and I_2 are zero. Multivariate optimization gives the best-fit parameters $\theta_1 = -5.68$, $\theta_2 = -0.70$, $\theta_3 = -1.20$, $\theta_4 = 2$, and $\theta_5 = 1$, which have been rounded slightly. The coefficient of determination of Eq. (1) is $r_{\ln Q_p}^2 = 0.964$, and the standard-error-of-estimate is $s_{\ln Q_p} = 0.362$. Inserting parameter values in Eq. (1) gives

$$\hat{Q}_p = k_Q \times \left(\frac{V_{\text{lake}}^{1/3}}{H_d}\right)^2 \times \sqrt{gH_d^5} \tag{3}$$

after transformation, where the dam type factor

$$k_Q = \begin{cases} 0.0034, & \text{for Type 1 blockages} \\ 0.0017, & \text{for Type 2 blockages} \\ 0.0010, & \text{for Type 3 blockages} \end{cases}$$

Measured values of Q_p are plotted against values predicted by Eq. (1) in Fig. 1. The fit is of high quality, with the logarithmic errors uniformly distributed about the 1:1 line.

The ratio of blockage width to dam height, W_d/H_d, is an intuitively influential factor for predicting Q_p. As W_d increases with H_d constant, the overflow channel on the downstream slope of the blockage lengthens, making erosion more difficult and increasing the time needed for the breach to form, thereby lowering the peak outflow. Although W_d/H_d ranges from about 4 to nearly 67 within the dataset, the analysis reveals only a slight dependency on this factor. The number of samples is probably not large enough to adequately explain the effect. For this reason, the blockage width has not been included as an explanatory variable in Eq. (1).
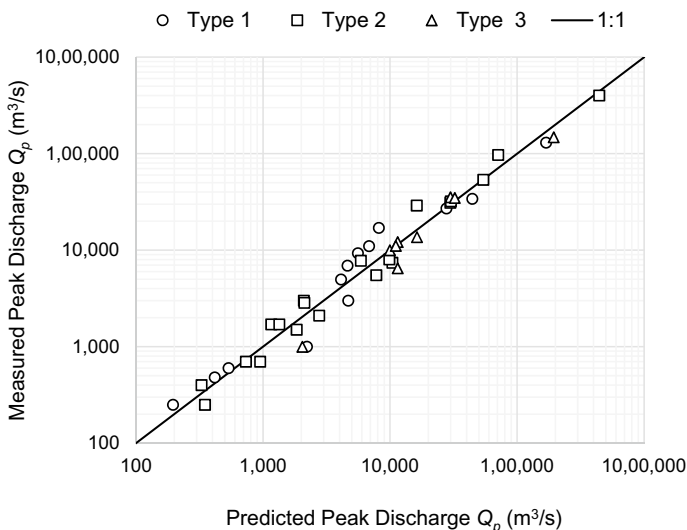
Fig. 1 Measured versus predicted (expected value) outburst flood peak discharge for the three categories of landslide dams

5.2 Prediction Interval

The delta method [11, p. 193] is used to obtain the $\ln Q_\mathrm{p}$ prediction interval around its expected value as

$$\ln Q_{\mathrm{p}\pm} = \ln \hat{Q}_\mathrm{p} \pm t_{2\alpha, n-p} \times \sqrt{s_{\ln Q_\mathrm{p}}^2 \times \left[1 + \mathbf{f}_0'(\mathbf{F}'\mathbf{F})_{\ln Q_\mathrm{p}}^{-1}\mathbf{f}_0\right]} \qquad (4)$$

where

$$\begin{aligned}
\mathbf{f}_0' &= \left(\frac{\partial f(\mathbf{x}_0; \boldsymbol{\theta})}{\partial \theta_1}, \frac{\partial f(\mathbf{x}_0; \boldsymbol{\theta})}{\partial \theta_2}, \frac{\partial f(\mathbf{x}_0; \boldsymbol{\theta})}{\partial \theta_3}, \frac{\partial f(\mathbf{x}_0; \boldsymbol{\theta})}{\partial \theta_4}, \frac{\partial f(\mathbf{x}_0; \boldsymbol{\theta})}{\partial \theta_5}\right) \\
&= \left(1, I_1, I_2, \ln\left(V_{\mathrm{lake}}^{1/3}\big/H_\mathrm{d}\right), \ln\sqrt{gH_\mathrm{d}^5}\right)
\end{aligned} \qquad (5)$$

$$\mathbf{x}_0' = \left(I_1, I_2, \ln\left(V_{\mathrm{lake}}^{1/3}\big/H_\mathrm{d}\right), \ln\sqrt{gH_\mathrm{d}^5}\right) \qquad (6)$$

$$\hat{\theta}' = (\theta_1, \theta_2, \theta_3, \theta_4, \theta_5) \qquad (7)$$

$f(\mathbf{x}_0; \boldsymbol{\theta}) = \ln Q_\mathrm{p}$ given by Eq. (1), α = the exceedance probability, t = the two-tailed Student's t-distribution (hence the need for an exceedance probability of 2α) with

$n - p$ degrees of freedom, $n = 42 =$ the number of measurements, $p = 5 =$ the number of parameters,

$$(\mathbf{F}'\mathbf{F})^{-1}_{\ln Q_p} = \begin{bmatrix} 0.0016 & -0.01863 & -0.03371 & -0.00070 & -0.00035 \\ -0.01863 & 0.43645 & 0.63543 & 0.01628 & 0.00162 \\ -0.03371 & 0.63543 & 1.19523 & 0.02325 & 0.00583 \\ -0.00070 & 0.01628 & 0.02325 & 0.03025 & -0.00192 \\ -0.00035 & 0.00162 & 0.00583 & -0.00192 & 0.00041 \end{bmatrix} \quad (8)$$

and

$$\mathbf{F} = \mathbf{F}(\boldsymbol{\theta}) = \left[\frac{\partial f(\mathbf{x}_i; \boldsymbol{\theta})}{\partial \theta_j}\right] \quad (9)$$

Measured peak discharges for each of the 42 samples are plotted against the upper prediction limit given by Eq. (4) for an exceedance probability $\alpha = 0.05$ in Fig. 2. All except one of the calculated 95% upper prediction limit flow peaks fall below the 1:1 line, which shows that the upper limit provides a flow rate not likely to be exceeded.
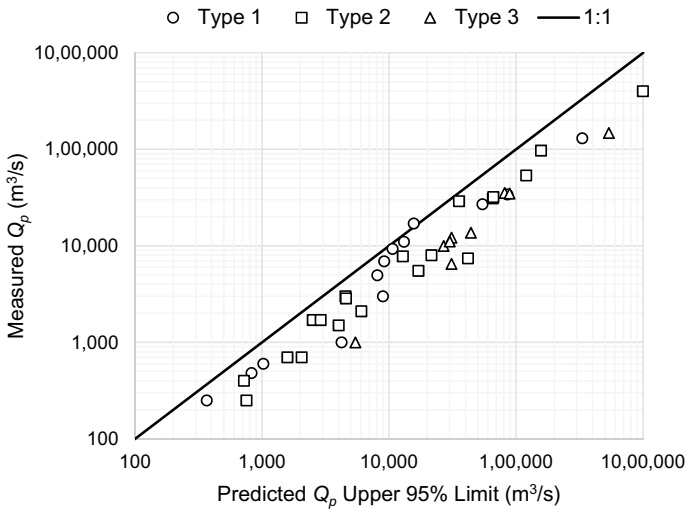

Fig. 2 Measured versus predicted (upper prediction limit) outburst flood peak discharge for the three categories of landslide dams

5.3   Example Application

A brief example shows how the prediction formulas evaluate the potential outburst flood peak discharge from a newly formed landslide dam. This Type 2 blockage ($I_1 = 1$, $I_2 = 0$) is 80 m high ($H_d = 80$ m) and can impound 220 Mm^3 of river inflows before overtopping and breaching ($V_{lake} = 220$ Mm^3). With $k_Q = 0.0017$, Eq. (3) gives

$$\hat{Q}_p = 0.0017 \times \left(\frac{(1,000,000 \times 220)^{1/3}}{80} \right)^2 \times \sqrt{9.806 \times 80^5} = 17,300 \, \text{m}^3/\text{s} \quad (10)$$

Of course, the uncertainty of this estimate of the peak discharge is substantial. It must be considered when assessing the downstream flood hazards. The estimated amount by which the peak discharge may exceed the expected value is given by the upper limit of the prediction interval obtained from Eq. (4). With $s_{\ln Q_p} = 0.362$, $n = 42$, $p = 5$, $\alpha = 0.05$, and

$$\mathbf{f}'_0 = \left(1, I_1, I_2, \ln \left(V_{lake}^{1/3} / H_d \right), \ln \sqrt{g H_d^5} \right)$$
$$= (1, 1, 0, 2.021, 24.193) \quad (11)$$

Equation (4) delivers

$$l \ln Q_{P+} = \ln \hat{Q}_p + t_{2\alpha, n-p} \times \sqrt{s_{\ln Q_p}^2 \times \left[1 + \mathbf{f}'_0 (\mathbf{F}'\mathbf{F})^{-1}_{\ln Q_p} \mathbf{f}_0 \right]}$$
$$= \ln(17,300) + 1.687 \times \sqrt{0.362^2 \times (1 + 0.652)} \quad (12)$$
$$= 10.544$$

where $(\mathbf{F}'\mathbf{F})^{-1}_{\ln Q_p}$ is given by Eq. (8). The upper 95% prediction limit (that is, the peak discharge that is exceeded with a probability of 0.05) is then $Q_{p\_upper} = \exp(10.544) = 37,950$ m^3/s, which is 2.2 times the expected peak flow rate. This discharge provides a margin of error that is not excessive and reasonable to use when assessing downstream flood hazards.

6   Summary and Conclusions

The mass movements that most often form landslide dams are rock and soil slumps and slides, mud, debris, earth flows, and rock and debris avalanches. The most common initiation mechanisms for dam-forming landslides are excessive rainfall

and snowmelt, and earthquakes. Blockage of rivers by landslides presents a significant hazard in most parts of the world, particularly in mountainous regions subject to massive earthquakes. Some of the jams attain heights and impound water volumes that exceed those of the largest constructed dams.

Landslide dams cause two types of floods: (1) upstream (backwater) flooding as the created barrier lake fills and (2) downstream flooding resulting from rapid breaching of the river blockage. Although less common than upstream inundation, downstream flooding is usually more severe and may be extremely destructive.

Most landslide dams do not fail catastrophically; instead, sediment slowly fills the formed barrier lakes. The blockage then erodes gradually by overtopping flows. Nonetheless, some landslide dams do breach rapidly, often soon after the blockage forms, generating a potentially disastrous flood. Evaluating the risk imposed on the downstream population and infrastructure by such an outburst requires a quick assessment of the maximum flow rate that would be produced. With this knowledge, outflow hydrographs can be estimated. Downstream flood routing, even by approximate methods, then provides a quick evaluation of the hazards.

A rapid method for estimating the peak discharge from a breached landslide dam is developed in this study from an analysis of 42 outburst floods. Because of the wide variety of mass movements that occur, a systematic classification of the river blockages based on their material composition and runout distance was used to assess their erodibility, which controls the size (height and width) of a breach and the speed at which it forms. Three categories or types of blockages are defined based on the work of Fan et al. [12]. The blockage type and measures of the dam height and the barrier lake volume inform a prediction equation for an outburst flood peak discharge. Prediction limits are also calculated, which provide a sound statistical assessment of the range of possible peak outflows. Knowing the potential consequence of an outburst flood, orderly evacuation of the downstream population when failure of a landslide blockage is approaching can then be carried out.

References

1. Cruden, D.M., Varnes, D.J.: Landslide types and processes. In: Landslides, Investigation and Mitigation: Special Report, pp. 36–75. Transportation Research Board, National Research Council, National Academy Press, Washington, D.C. (1996)
2. Dai, F.C., Lee, C.F., Deng, J.H., Tham, L.G.: The 1786 earthquake-triggered landslide dam and subsequent dam-break flood on the Dadu River, southwestern China. Geomorphology **65**(2), 205–221 (2005)
3. Varnes, D.J.: Slope movement types and processes. In: Landslides—Analysis and Control, pp. 11–33. National Academy of Sciences, Washington, D.C. (1978)
4. Hungr, O., Evans, S.: Entrainment of debris in rock avalanches: an analysis of a long run-out mechanism. Geol. Soc. Am. Bull. **116**(9–10), 1240–1252 (2004)
5. Costa, J.E., Schuster, R.L.: The formation and failure of natural dams. Geol. Soc. Am. Bull. **100**(7), 1054–1068 (1988)

6. Hewitt, K.: Gifts and perils of landslides: Catastrophic rockslides and related landscape developments are an integral part of human settlement along upper Indus streams. Am. Sci. **98** (5), 410–419 (2010)
7. Fan, X.: Understanding the causes and effects of earthquake-induced landslide dams. Unpublished Dissertation, University of Twente, Enschede, Netherlands (2013)
8. Fan, X., Xu, Q., van Westen, C.J., Huang, R., Tang, R.: Characteristics and classification of landslide dams associated with the 2008 Wenchuan earthquake. Geoenviron. Disasters **4**(12), 1–15 (2017)
9. Davies, T.R., McSaveney, M.: Dynamic simulation of the motion of fragmenting rock avalanches. Can. Geotech. J. **39**(4), 789–798 (2002)
10. Dalrymple, T., Benson, M.A.: Measurement of peak discharge by the slope-area method. In: Techniques of Water-Resources Investigations, Book 3, Chapter A2. U.S. Geological Survey, Washington, D.C. (1967)
11. Seber, G.A.F., Wild, C.J.: Nonlinear Regression. John Wiley and Sons, Hoboken, New Jersey (2003)
12. Fan, X., Dufresne, A., Subramanian, S.S., Strom, A., Hermanns, R., Stefanelli, C.T., Hewitt, K., Yunus, A.P., Dunning, S., Capra, L., Geertsema, M., Miller, B., Casagli, N., Jansen, J.D., Xu, Q.: The formation and impact of landslide dams—state of the art. Earth Sci. Rev. **203**, 1–28 (2020)

Subsidence Detection Using Persistent Scatterer Interferometry

Jeenu John and P. Sabu

1 Introduction

Subsidence of land is the gradual sinking of surface of earth, and this geological disaster is occurring across the world [1]. Natural as well as anthropogenic activities are responsible for the subsidence such as the movement of tectonic plates, compaction of sediment, groundwater extraction, water logging in the area as well as the over extraction of minerals and hydrocarbons [2]. Deformation of urban area triggers the subsidence of infrastructures leading hazards affecting human lives and economy [2–4]. In order to mitigate catastrophic incidence, deformation monitoring is necessary.

Conventional methods such as Global Navigation Satellite System, traditional leveling, and terrestrial laser scanner methods estimate subsidence. However, traditional methods require human power, and the process is time-consuming, and moreover, these methods estimate subsidence over point by point, limits the areal coverage [5–8].

Over the past few decades, Synthetic Aperture Radar Interferometry (InSAR) provides unique opportunity in estimating subtle measurements of surface deformation on a wide spatial scale with the generation of interferograms [9]. In the InSAR techniques, the differential InSAR approach (DInSAR), the phase difference of two temporal SAR images are analyzed along the line of satellite (LOS) for monitoring the deformation [10]. The interferogram pairs having small baseline and time line distance are less affected by temporal decorrelation. Numerous studies have undergone using DInSAR around the world such as caused by landslides [11], volcanism [12], land subsidence [13], and earthquakes [14, 15]. However,

J. John (✉)
University of Madras, Guindy, Chennai, India
e-mail: jeenujohn36@gmail.com

P. Sabu
College of Engineering Trivandrum, Thiruvananthapuram, India

geometrical distortion, temporal decorrelation, and distortion of signal due to the atmospheric influence the DInSAR measurement. Hence, an advancing technique known as persistent scatterer interferometry (PSI) estimates the subtle deformation at millimeter level accuracy through the analysis of stable backscattering characteristic of scatterer points by analyzing the phase information of multiple SAR images [15–17]. In the DInSAR techniques, the deformation is estimated through the analysis of two interferograms while in PSI multiple interferograms of the region are generated [18]. Since PSI techniques use stable backscattered points, it overcomes the temporal decorrelation in DInSAR and overcomes the geometrical decorrelation as size of scatterer points is small [19–22].

PSI approach is the first generation of the advanced interferometry technique. In non-urban areas, distributed scatterer points such as the exposed rocks, uncultivated field, soil, and the backscattered energy from these scatterer points are low and remain homogenous over the analysis are used for the second generation advanced interferometry technique [23].

Hence, interferometric methods are chosen based on the characteristics of the study area. In this study, PSI techniques along with GPS measurements are used to monitor subsidence of Nedumbassery airport and the surrounding areas. If the runway or the surrounding area is subsided, then it can cause accidents during the take-off and landing. InSAR techniques such as PSI are useful in determining the subsidence of the airport region with millimeter accuracy. Some studies focused on the subsidence of the airport region, lying over the reclaimed land or permafrost environment. In addition to the natural phenomenon, over exploitation of underground water and hydrocarbon extraction also induces subsidence. Therefore, it is necessary to monitor the subsidence of the airport regions for their sustainability, and the main objectives of the study are (i) to investigate the subsidence encountered by the airport region (ii) to validate the measurements using hand held GPS.

2   Study Area and Data Sets

Nedumbassery airport and its surrounding area, situated at the northeast region of Cochin, in the state of Kerala, India is the study area (Fig. 1). Nedumbassery airport is constructed on a low-lying agricultural land, lies on the flood plain of the river Periyar.

Chengal creek a distributary of the river Periyar collects excess water from the river and distributes to the lower streams and 3 irrigation canals which provide water to nearby paddy fields were realigned for the construction of 3.6 km runway. The drainage of the airport is finally led to the Chengal Thodu, which in turns is connected to the Periyar. Since the flood plain is reclaimed for the construction of the airport, the susceptibility of the region toward the flood is still the same.

In the present study, Sentinel 1A Interferometric Wide (IW) swath C-band data is used, delivered by the European Space agency at free of cost. Sentinel 1A

Fig. 1 Larger tile is showing the area covered by Sentinel 1 and smaller tile showing the study area

satellite is launched on April 3, 2014, which have a swath width of 250 km with 5 m $\times$ 20 m spatial resolution. Table 1 shows the Sentinel 1A data used for the period.

3 Methodology

Sentinel 1A images are processed using SARproz software especially used for the PSI technique in which a hybrid approach of Quasi-PS InSAR [24] and PS InSAR [25] is employed.

The image which have the least geometric distortion and having the least baseline distance to other slaves images was chosen as the master image (Fig. 3). Also to avoid compromising with the quality of interferogram, the image which is least affected by atmospheric disturbance is considered while selecting the master image (Fig. 2).

In order to compensate the distortions induced by the phase term, deramping is performed to the master image and the slave image. After the selection of the master image, all the slave images were co-registered to align the pixels of slave image

Table 1 Sentinel 1A data used for the period

Date of acquisition	Polarization
3rd June 2017	VV
15th June 2017	VV
27th June 2017	VV
21st July 2017	VV
14th August 2017	VV
26th August 2017	VV
07th September 2017	VV
1st October 2017	VV
25th October2017	VV
18th November 2017	VV
30th November 2017	VV
20th January 2018	VV
06th March 2018	VV
18th March 2018	VV
23th April 2018	VV
05th May 2018	VV
29th May 2018	VV
10th June 2018	VV
22th June 2018	VV
04th July 2018	VV
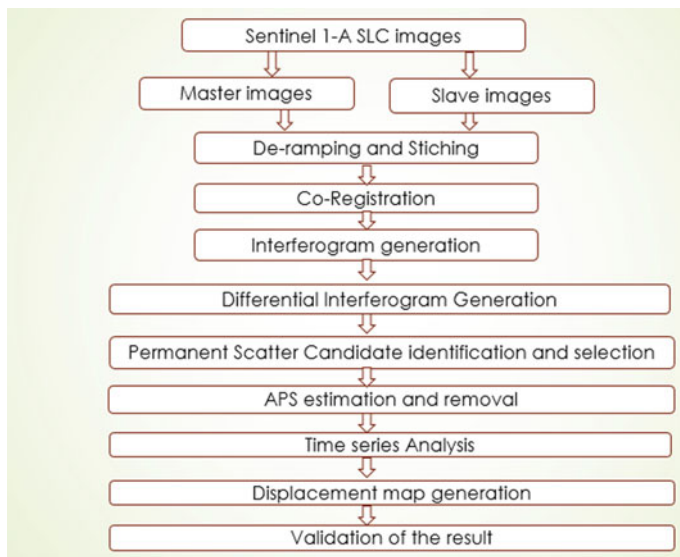
Fig. 2 Methodology for the PSI
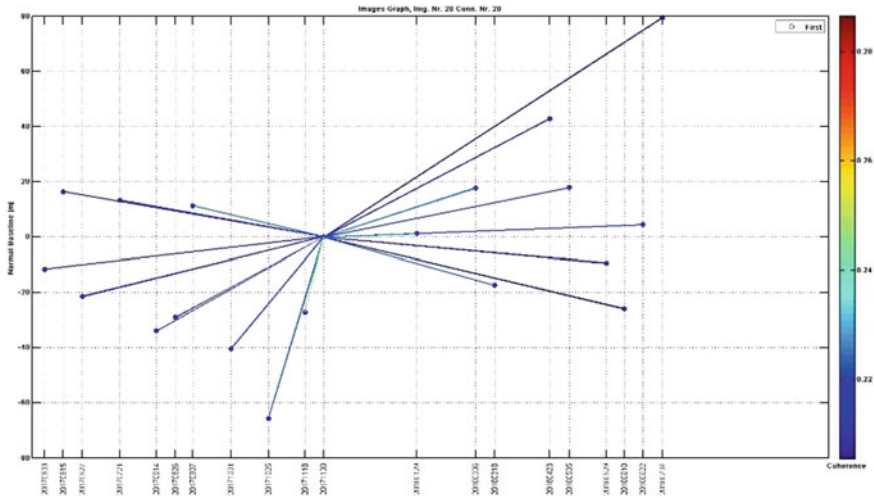
Fig. 3 Baseline distance from the master image to the slave image

with the master image (Fig. 2). The total phase variation in the generated interferograms is equal to the

$$\Delta\phi = \Delta\phi_{flat} + \Delta\phi_{elevation} + \Delta\phi_{displacement} + \Delta\phi_{atmosphere} + \Delta\phi_{noise}$$

where $\Delta\varphi_{flat}$ is the $\Delta\varphi_{elevation}$ $\Delta\varphi_{displacement}$ $\Delta\varphi_{atmosphere}$ φ_{noise}. Using the precise orbital data, the perpendicular baseline is obtained, and the phase variation due to topography can be deducted.

The perpendicular baseline is identified from precise orbital data, and the second phase term can be from the interferometric phase. Persistent scatterer (PS) candidates are selected using a threshold of 0.75 for the amplitude stability index.

It is a parameter which emphasis on the constant backscattered energy from the permanent candidates. The candidates which give a constant amplitude on the time-series analysis is taken into consideration. Vegetation is excluded from the PS criteria since it does not have a stable backscatter energy due to the temporal changes.

$$D_A = \frac{\sigma_A}{\mu_A} \tag{1}$$

where the ratio of standard deviation (σ) to mean (μ) of pixel gives the amplitude dispersion (D_A)

$$ASI = 1 - D_A \tag{2}$$

The time series ranges from the start date of acquisition to the end of the acquisition. 21 images from June 3, 2017 to July 4, 2018, are taken for the study.

The selected PS points are undergone Goldstein filtering to remove the atmospheric interferences (See Figs. 4 and 5). During the analysis, each scatter point shows the deformation occurred on the specific period. Hence, the time-series analysis determines the displacement and the velocity of movement of the scatterer. The displacement map is showing the rate of subsidence and velocity of the movement of the points occurred per year.
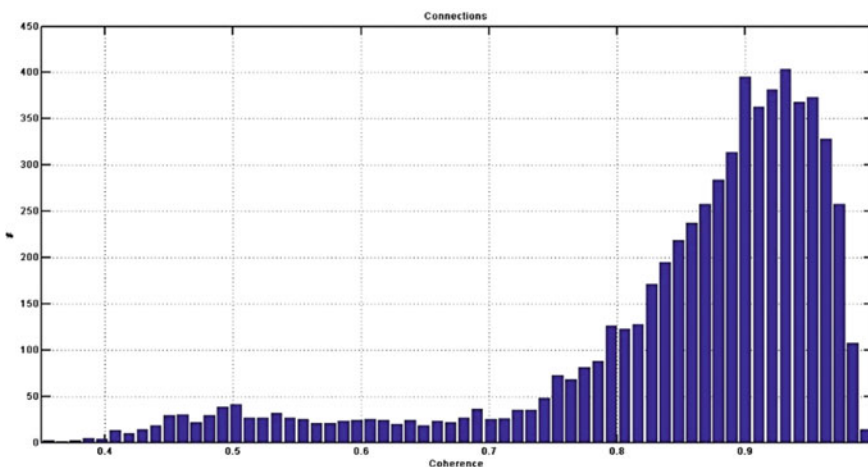
Fig. 4 PS points before applying filtering
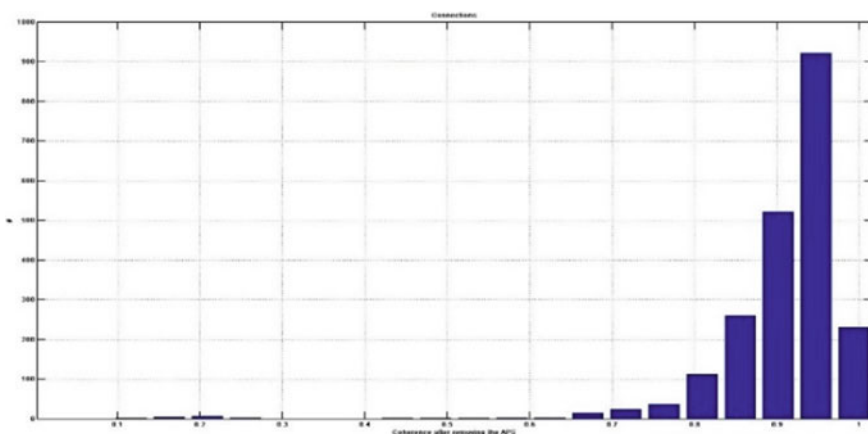
Fig. 5 PS points after applying filtering

4 Results and Discussion

The image November 30, 2017, is chosen as the master image since it have the least distance from the other slave images, and it suffers least atmospheric disturbances. There is a limit of normal baseline line distance from the master to a slave image, and the selected slave images lies within the limit (Fig. 3).

Based on the temporal coherence, the scatterers with point ID 486, 521, 551, 610, and 614 lie inside the airport region and the points with point ID 1139, 2539, 3087 and 2072 lie outside airport region were selected, since those point ID lies above the threshold 0.8 in comparison with the other ground point's available for observation.

Fig. 6 **a** Cumulative displacement of the PS points during the time period. **b** Cumulative velocity of the PS points during the time period

Table 2 Details of the PS points lying inside the region

ID	Displacement	Velocity	Coherence
486	−3.1	−2.8	0.97
521	−1.8	−1.6	0.98
551	−3.5	−1.8	0.93
610	1.2	1.1	0.90
614	−1.1	−1.3	0.92

Table 3 Details of PS points situated outside the airport region

ID	Displacement	Velocity	Coherence
1139	−10.5	−9.7	0.88
2539	0.9	0.84	0.92
3087	−29.1	−32.1	0.86
2072	28.5	30	0.95

A validation is applied to the deformation results obtained from PSI approach using ground observation with the help of Global Navigation Satellite System (GNSS). The cumulative displacement obtained through the time-series analysis of the points lying inside the airport region is 486, 521, 551, 610, and 614 in the order of −3.1, −1.8, −3.5, 1.2, and −1.1 mm, and also the cumu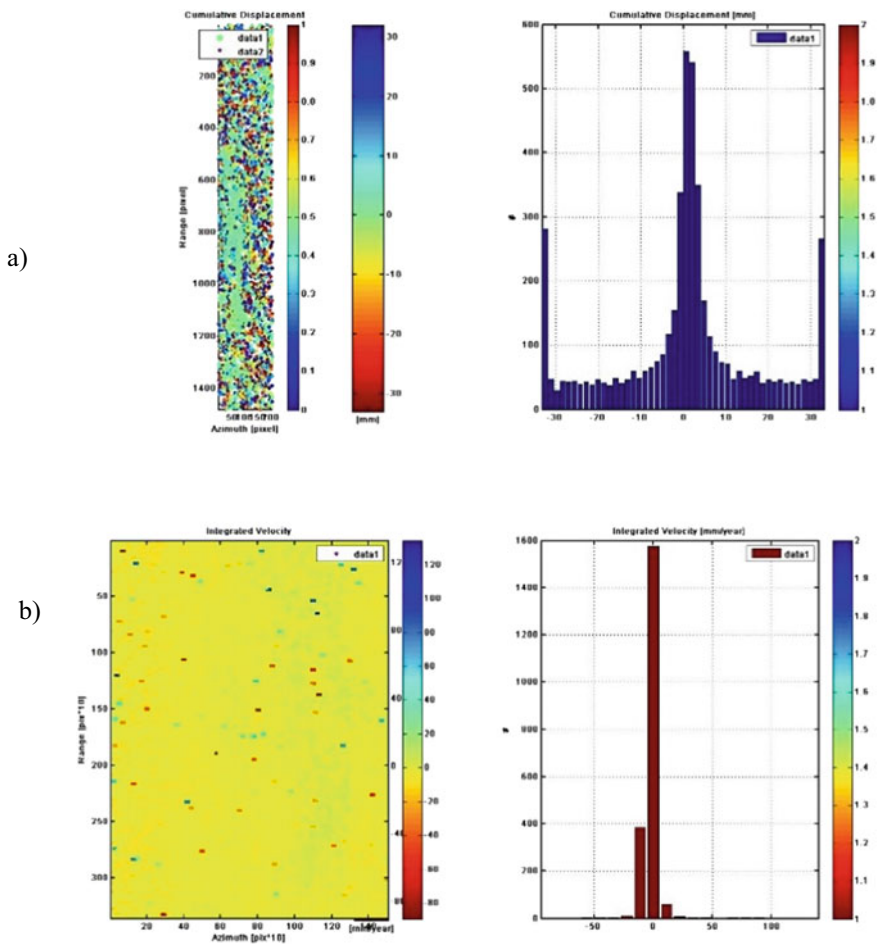lative displacement of point ID lying outside the airport region 1139, 2539, 3087, and 2072 was in the order of −10.5, −0.9, −29.1and 28.5 mm. The ground-based observations of the corresponding scatterer lying outside the airport region are found to have cumulative displacement of −11, −1.25, −28, and 27.56 mm. The cumulative displacement found to lie in the range of −30 to 30 mm with the cumulative velocity of −10 to 10 mm/year (Fig. 6; Tables 2 and 3).

5 Conclusion

In this study, PSI approach is used for the deformation study of Nedumbassery airport region which lies in the range of 30 mm/year (LOS) and −30 mm/year (subsiding), respectively. A small stack of Sentinel 1 images is used with a higher threshold in filtering which resulted in the less stable scatterer points on the study area; thus, the total available ground points are not used for the validation. Deformation of the ground surface is due to the clayey soil of the flood plain. Furthermore, the present study reveals the efficiency of the PSI technique in studying ground deformation with highest level of accuracy.

References

1. Raucoules, D., et al.: Ground deformation detection of the greater area of Thessaloniki (Northern Greece) using radar interferometry techniques. Nat. Hazards Earth Syst. Sci. (2008). https://doi.org/10.5194/nhess-8-779-2008
2. Ehlen, J., Haneberg, W.C., Larson, R.A., Holzer, T.L., Galloway, D.L.: Impacts of land subsidence caused by withdrawal of underground fluids in the United States. In: Humans as Geologic Agents (2007)
3. Cigna, F., et al.: Monitoring land subsidence and its induced geological hazard with synthetic aperture radar interferometry: a case study in Morelia, Mexico. Remote Sens. Environ. (2012). https://doi.org/10.1016/j.rse.2011.09.005
4. Herrera, G., Fernández, J.A., Tomás, R., Cooksley, G., Mulas, J.: Advanced interpretation of subsidence in Murcia (SE Spain) using A-DInSAR data—modelling and validation. Nat. Hazards Earth Syst. Sci. (2009). https://doi.org/10.5194/nhess-9-647-2009
5. Jung, H.C., Kim, S.W., Jung, H.S., Min, K.D., Won, J.S.: Satellite observation of coal mining subsidence by persistent scatterer analysis. Eng. Geol. (2007). https://doi.org/10.1016/j.enggeo.2007.02.007
6. Raspini, F., Cigna, F., Moretti, S.: Multi-temporal mapping of land subsidence at basin scale exploiting persistent scatterer interferometry: case study of Gioia Tauro plain (Italy). J. Maps **8**(4), 514–524 (2012). https://doi.org/10.1080/17445647.2012.743440
7. Yuan, W., Wang, Q., Fan, J., Li, H.: Mining land subsidence monitoring using sentinel-1 SAR data (2017). https://doi.org/10.5194/isprs-archives-XLII-2-W7-655-2017
8. Ferretti, A., et al.: Submillimeter accuracy of InSAR time series: experimental validation. IEEE Trans. Geosci. Remote Sens. (2007). https://doi.org/10.1109/TGRS.2007.894440
9. Rosen, P.A.: Synthetic aperture radar interferometry. Proc. IEEE (2000). https://doi.org/10.1109/5.838084
10. Massonnet, D., Feigl, K.L.: Radar interferometry and its application to changes in the earth's surface. Rev. Geophys. (1998). https://doi.org/10.1029/97RG03139
11. Zhao, C., Lu, Z., Zhang, Q., de la Fuente, J.: Large-area landslide detection and monitoring with ALOS/PALSAR imagery data over Northern California and Southern Oregon, USA. Remote Sens. Environ. (2012). https://doi.org/10.1016/j.rse.2012.05.025
12. González, P.J., et al.: The 2014–2015 eruption of Fogo volcano: geodetic modeling of Sentinel-1 TOPS interferometry. Geophys. Res. Lett. (2015). https://doi.org/10.1002/2015GL066003
13. Liu, G., et al.: Exploration of subsidence estimation by persistent scatterer InSAR on time series of high resolution TerraSAR-X images. IEEE J. Sel. Top. Appl. Earth Obs. Remote Sens. (2011). https://doi.org/10.1109/JSTARS.2010.2067446
14. Mora, O., Ordoqui, P., Iglesias, R., Blanco, P.: Earthquake rapid mapping using ascending and descending Sentinel-1 TOPSAR interferograms (2016). https://doi.org/10.1016/j.procs.2016.09.266
15. Ferretti, A., Prati, C., Rocca, F.: Nonlinear subsidence rate estimation using permanent scatterers in differential SAR interferometry. IEEE Trans. Geosci. Remote Sens. (2000). https://doi.org/10.1109/36.868878
16. Usai, S.: Use of man-made features for long time scale INSAR (1997). https://doi.org/10.1109/igarss.1997.608936
17. Ferretti, A., Prati, C., Rocca, F.: Permanent scatterers in SAR interferometry. IEEE Trans. Geosci. Remote Sens. (2001). https://doi.org/10.1109/36.898661
18. Tomás, R., et al.: Radar interferometry techniques for the study of ground subsidence phenomena: a review of practical issues through cases in Spain. Environ. Earth Sci. (2014). https://doi.org/10.1007/s12665-013-2422-z
19. Heleno, S.I.N., et al.: Persistent scatterers interferometry detects and measures ground subsidence in Lisbon. Remote Sens. Environ. (2011). https://doi.org/10.1016/j.rse.2011.04.021

20. Cafaro, F., Cotecchia, F., Lenti, V., Pagliarulo, R.: Interpretation and modelling of the subsidence at the archaeological site of Sybaris (Southern Italy) (2013). https://doi.org/10.1201/b14895-23
21. Huang, Q., Crosetto, M., Monserrat, O., Crippa, B.: Displacement monitoring and modelling of a high-speed railway bridge using C-band Sentinel-1 data. ISPRS J. Photogramm. Remote Sens. (2017). https://doi.org/10.1016/j.isprsjprs.2017.03.016
22. Zhang, Q., et al.: Research on recent characteristics of spatio-temporal evolution and mechanism of Xi'an land subsidence and ground fissure by using GPS and InSAR techniques. Acta Geophys. Sin. (2009). https://doi.org/10.3969/j.issn.0001-5733.2009.05.010
23. Zhao, C., Lu, Z., Zhang, Q.: Time-series deformation monitoring over mining regions with SAR intensity-based offset measurements. Remote Sens. Lett. (2013). https://doi.org/10.1080/2150704X.2012.746482
24. Perissin, D., Wang, T.: Repeat-pass SAR interferometry with partially coherent targets. IEEE Trans. Geosci. Remote Sens. (2012). https://doi.org/10.1109/TGRS.2011.2160644
25. Ferretti, A., Fumagalli, A., Novali, F., Prati, C., Rocca, F., Rucci, A.: A new algorithm for processing interferometric data-stacks: SqueeSAR (2011). https://doi.org/10.1109/TGRS.2011.2124465

Studying the Time-Dependent Reliability Index of the Riverbank Instability—A Case Study of the Vam Nao River Subjected to a Sinkhole

Tham Hong Duong

1 Introduction

Riverbank instability is a vast topic in which there are many modes of failure and causes. In some specific conditions, the hydrological regime is rather complicated with periodical possible changes in a day, weekly, or months, even the same time through years. And the safety factor of instability is not constant all the time. This leads to some sudden failure of the riverbank and causes damages to the civil properties without any warnings. The action of the flow regime is varied according to the water tidal regime. The uncertainties about the mechanical properties of soil, both in data collection and analyzing models permanently exist. And the most important thing resulting in the riverbank instability is the hydrological regime of the river which is strongly related to secondary flows attacking laterally the soil riverbank [1] and not the same throughout every cross-section to be studied. The hydrological regime of the river that changes rapidly from time-to-time results in an inappropriate solution for assessing the riverbank stability. As such, the model using a specified dataset of constant parameters, variables, and boundary conditions is not practicable.

The downstream section of Mekong River running through provinces of Viet Nam has two branches, namely called Tien Giang and Hau Giang. Unfortunately, there is a small river connecting these two branches, the Vam Nao river (Fig. 1). Due to this connection as a joint, the hydrological regime of the Vam Nao river is so astonishingly complicated that up to now, data of the flow of the river is not sufficiently collected [2]. Very giant and deep sinkholes of which the depth can compare to that of a six-story building appears, with severe turbulent flows. A serious riverbank failure occurs on April 24th, 2017, when a very long slide surface happened suddenly, more than 19 houses on the riverbank fell into the water

T. H. Duong (✉)

Ho Chi Minh City Open University, Ho Chi Minh City, Viet Nam

e-mail: tham.dh@ou.edu.vn
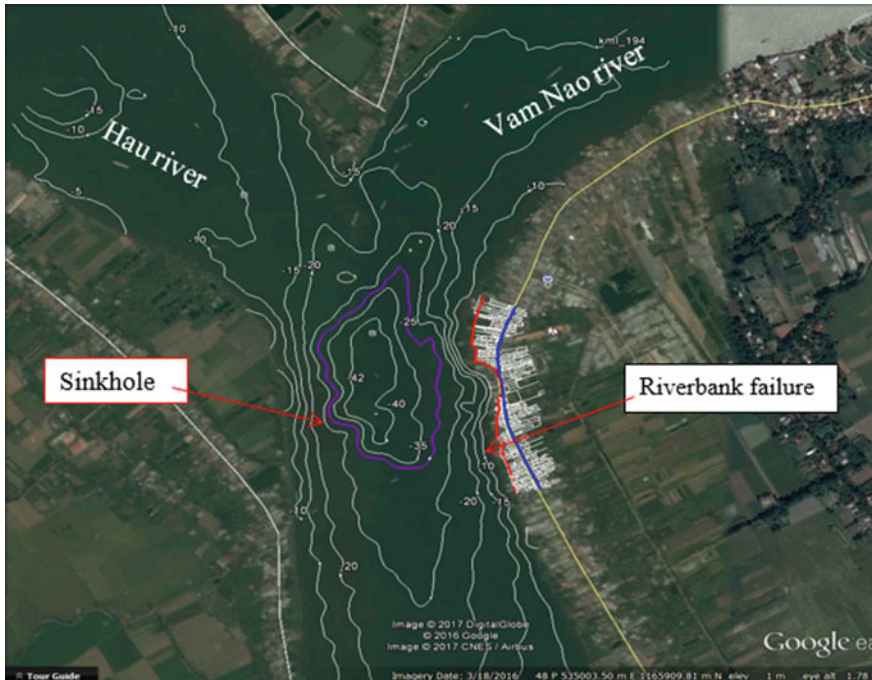
Fig. 1 Investigation site the Vam Nao River, an Giang Province [2]

just in not a minute [3]. The mechanism of sinkhole occurrence has not been thoroughly understood at the moment. The case of Vam Nao River failure still attracts a permanently controversial consideration.

This article will study the time-dependent reliability index of the Vam Nao riverbank instability in terms of varied geometrical configuration due to filtration flow in the local site, hydrological issues, and toe scour or sinkhole. Time-dependent data are tentatively taken into account. Method of Taylor's series was used to compute the index of reliability, and then trend prediction is established.

2 Methodology

2.1 Model of the Study

Data. This paper studies the left-hand branch of the scheme detailed in Fig. 2. Data involved in the problem are suitably processed by some conventional methods of statistics especially soil data and river flow. But for considering the time-dependent

Fig. 2 Uncertainties in the
analyzing model
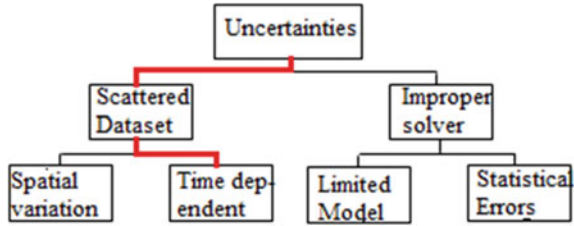
attribute of these data, daily values and periodical others are obtained and kept them
as detailed as possible.

Basically, the data for the problem taken the soil properties and their soil
homogeneity, the geomorphology and roughness the of the riverbed, the geomet-
rical configuration of the riverbank, fluid dynamics of the water flow and the water
surface, the direction of the secondary lateral flow together with its angle of attack,
etc. For ensuring the compatibility suitably relevant to real conditions, planar slide
mechanism for both kinds of cohesive and granular soil is studied [4], but sinkhole
could be supplemented in the toe of the soil slope of riverbank cliff. Sinkhole is a
consequence of the natural flow [2].

Procedure. Strategy plan for solving the problem of time-dependent reliability
index or probability of failure includes three steps, as described in Fig. 2. Step 1
with preparation of input. Random data and the law of distribution are prescribed.
To find out the most effective factors (i.e., variables and parameters) on the safety
factor of instability, analysis of sensitivity is conducted. Step 2 is the process of
building the performance function. The next step is to quantify the uncertainties,
concerning the time-dependent attributes of factors; in this step, the performance
function $G(X, t) = R(t) - S(t)$ is formulated in which X is the set of randomly varied
independent variables, t is the time to be studied, R is the load resistance or bearing
capacity, and S is the driving force. Failure occurs when $G(X, t) = R(t) - S$
(t) equals to zero (Fig. 3b). For calculating the reliability index and predicting the
time of failure, a relevant method of reliability is selected. The First Order
Reliability Method (FORM) is viable one, for requiring fewer number of variables,
providing the fast convergent speed and yielding rather stable results; Monte Carlo
simulation (MCS) or Taylor's series expansion with partial derivatives terms could
be applied alternatively [5, 6]. The reliability indexes with respect to the different
performance function are plotted in the same way of the performance functions.
And the trend analysis could be analyzed to predict the time of intersecting with a
target value of reliability index β_{target} (Fig. 3c).

Model of soil riverbank instability. This 2D model is suggested by Thorne
et al. [4] with planar sliding surface (Fig. 4). K is the depth of crack in cohesive
soil, K_H is the depth of the previous cracks left after riverbank retreat, H is the
height of the slope, and H' is the height of the slope before the sinkhole. FR and FD
are the resisting force and the driving force, respectively. Other geometrical
parameters are shown in Fig. 4.
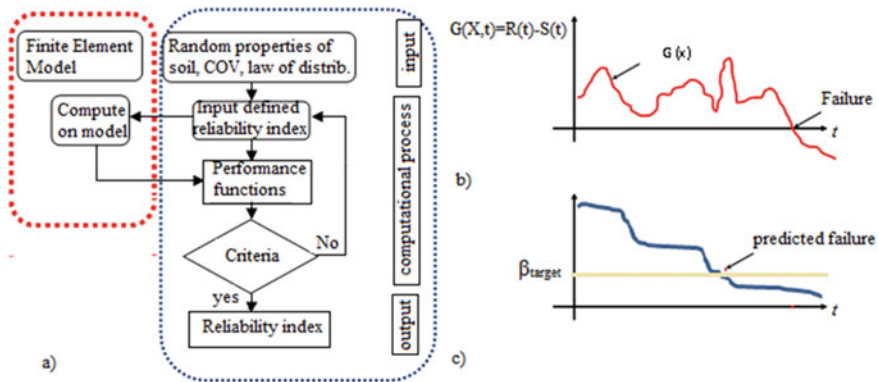
Fig. 3 a Steps for computing the time-dependent reliability index for the problem;
b time-dependent performance function
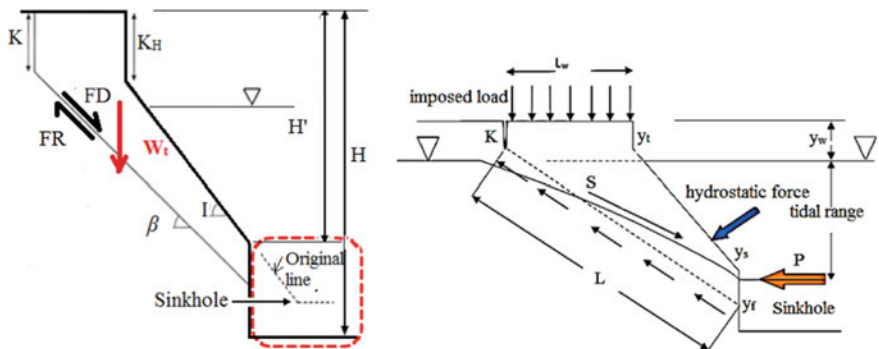
Fig. 4 Thorne's model of soil instability with modification of sinkhole

Imposed load is the facility building on the ground surface, normally 10–20 kPa.
S is the seepage load of which the intensity is computed by the hydraulic gradient of
the filtration; the F_{cp} or the hydrostatic force exerted perpendicular the slope is
calculated with respect to the location of the water surface, by the following
formulas:

The elevation of the water surface in a day may be one among cases as follows
[4]:

i. Case of the highest water level, or $y_w > y_t$;

$$F_{cp} = \sqrt{\left(\frac{\gamma_w}{2}(y_w - y_t)^2\right)^2 + \left[\frac{\gamma_w}{2}\cot I\left\{(y_w - y_s)^2 - (y_w - y_t)^2\right\}\right]^2} \quad (1)$$

ii. Case of the standing water level: On the middle distance of the inclined slope, or $y_s < y_w < y_t$;

$$F_{cp} = \sqrt{\left(\frac{\gamma_w}{2}(y_w - y_t)^2\right)^2 + \left[\frac{\gamma_w}{2}\cot I\left\{(y_w - y_s)^2\right\}\right]^2}$$ (2)

iii. Case of the lowest water level, or $y_w < y_s$

$$F_{cp} = \frac{\gamma_w}{2}(y_w - y_t)^2$$ (3)

With the different locations of the water surface, the values of hydrostatic force F_{sp} change remarkably. This definitely affects the safety factor of the soil instability, nevertheless only in a day.

Safety factor (SF) of the soil riverbank instability. By prescribing the sink-hole, supplementary force P that stands for the wave loading, S the seepage force due to filtration over the soil mass, and the planar sliding surface, the safety factor or the ratio of the resisting forces divided by the driving forces could be modified from Thorne [4] and Samadi et al. [7] to be as below:

$$SF = \frac{c'L + \left[\left\{\frac{\gamma}{2}\left(\frac{H^2 - K^2}{\tan \beta} - \frac{H'^2 - K_h^2}{\tan i}\right) - U_W\right\}\cos\beta + F_{cp}\cos\alpha\right]\tan\phi'}{\frac{\gamma}{2}\left(\frac{H^2 - K^2}{\tan\beta} - \frac{H'^2 - K_h^2}{\tan i}\right)\sin\beta - F_{cp}\sin\alpha - P\cos\beta + S + qL_W}$$ (4)

where P wave loading, which depends on the water depth, the width or distance of blowing wind flow over the water surface, etc., S is the seepage force that varies along to the phreatic surface and makes the sliding mass heavier in weight due to tidal water. In the planar model, the seepage approximately equals filtration pressure j multiplied by the volume of the sliding mass instead of taking analytical line integral [8]. For a partially merged-in-water slope, the saturation must take the suction S_w into account (Fredlund et al. [9]). The water suction at the interface of air–soil, under the surface tension, might increase because of a negative value of air pressure in pore water; b is the inclination of the sliding surface, and a is the inclination of the existing slope. The SF of the partially sunk slope is suggested by Fredlund et al. [9] as below:

$$SF = \frac{\sum_{i=1}^{I} c'L + S_i\tan\varphi_i^b + [W_i\cos\beta - U_i + P_i\cos(\alpha - \beta)]\tan\phi_i'}{\sum_{i=1}^{I}\frac{\gamma}{2}[W_i\sin\beta - P\sin(\alpha - \beta)]}$$ (5)

It is recognized that without taking S into account may be on the safe side for yielding the smaller value of the numerator to be checked. The SF calculated by the formula (4) using a spreadsheet (Appendix).

2.2   Sensitivity Analysis for Selecting the Key Factors

For checking the modified Thorne's model of analysis, some independent variables are considered:

- **Geometrical configuration of the slope**: The depth of cracks Y and Y_k, the depths H, H' and/or H_o, the inclination of the retreated slope, angles, etc. The total number of variables is assumed to be **Y, H, and inclination i**.
- **Geotechnical properties**: Cohesion and internal friction angle. As for the latter, although sensitivity analysis indicates that the friction angle is more sensitive than cohesion, although the coefficient of variation is smaller. As such, **cohesion** and φ are both selected in the calculation.
- **Hydrological factor**: This kind of variable relates to the tidal range daily, weekly, annually. These time-dependent variables are **water elevation y_w** (with datum is the ground surface) **and the lateral flow** (secondary flow).
- **Surcharges** on the ground level q. It may happen that at the early stage of the retreat, the surcharge locates far from the edge of the riverbank, but during many times of riverbank erosion, the edge gradually retreats backward. Other loads are the **Seepage** (due to filtration), **wave loading** P (due to wind over broad distance).

According to Samadi et al. [8], there are six sensitive variables:

- 3 strengthening variables relating to increase stability, i.e., E, friction angle φ and cohesion.
- 3 weakening variables decrease stability, i.e., sinkhole, crack K and y (or water level).

Sensitivity is calculated statistically from the equations below:

$$\alpha(X_i) = \frac{\sum_{i=1}^{n} \eta_{SS,i}}{\sum_{i=1}^{N} \sum \eta_{SS,i}}; \quad \eta_{SS} = \eta_{SR} \frac{\max x_R - \min x_R}{x} \tag{6}$$

For real soil data in local sites, the sensitivity analysis carried out over variables is shown as in Fig. 5 [6].
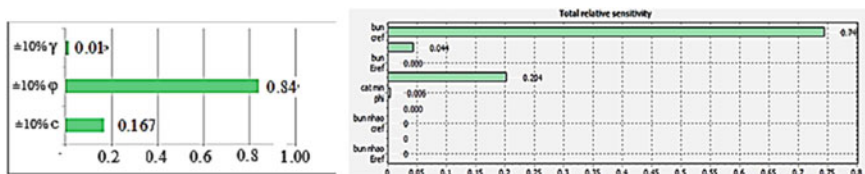

Fig. 5 Sensitivity of soil properties in the modified Thorne's model [6, 10]

2.3   Time-Dependent Variables in the Model

In the site around the Vam Nao River, the water elevation varied periodically, i.e., daily (twice a day), monthly, and yearly. Variation of the water level during months in a year is as follows (Fig. 6).

Data of water level during months in a year are listed in Table 1.

The average elevation and standard deviation for each condition of the water level variation are elevation +3.28 and 0.532 for the highest level of tidal range and elevation +1.45 and 0.172 for the lowest level. As such, the former has the coefficient of variation (COV) of 16% and the latter, 12%. In the local sites, the observed data (collected in 2017) indicates that in July, the water level varied with the coefficient of variation of 19%. These coefficients associated with the other months are less than 10% or can be viewed as the constant. In the different months from May to December, the time for the highest level and lowest is prescribed in Table 2.

The average level for data in Table 2 is +2.42, and the standard deviation is 0.089 for the highest water level and +1.62, and the standard deviation is 0.019 for the lowest water level (COV is 3.6% and 1.18%, respectively). As such, some main benchmarks are as follows:

- The highest water elevation H_{max}, being +4.03 (January and February).
- Standing water level: +3.25 (June, September).
- Average water level: +2.25 (October, November, December).
- The lowest water level H_{min}, +1.60 (January, February, March).
- Standing water level: +1.5 (April, June).
- The lowest water level: +1 to 1.25 (October, November, December).

July has the widest range of water tidal levels, the highest value of COV, 48%. The lowest water level will be in February, and the highest water level will be in
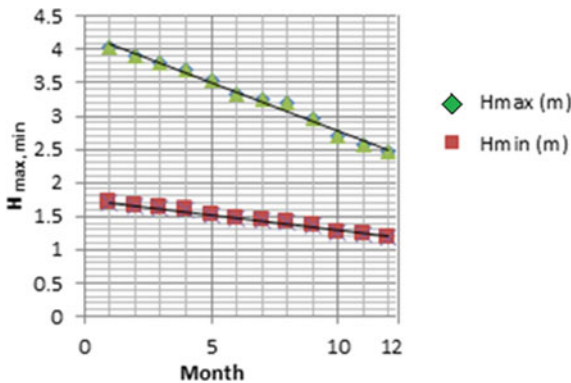

Fig. 6 The highest H_{max} and lowest H_{min} water level in months

Table 1 Water levels in various months in 2017 [10]

Average water level	1	2	3	4	5	6	7	8	9	10	11	12
H_{max}	4.03	3.9	3.81	3.7	3.53	3.32	**3.25**	3.19	2.96	2.69	2.56	2.46
H_{min}	1.7	1.65	1.62	1.59	1.53	1.47	**1.44**	1.42	1.35	1.26	1.22	1.19

Bold numbers indicates the average water levels, of month 1 and month 12 in a year

Table 2 Water levels in a day

Water level	Month							
	5	6	7	8	9	10	11	12
H_{max}	2.51	2.54	2.48	2.44	2.40	2.38	2.32	2.29
t	20:25	21:10	22:05	23:05	0:00	01:10	01:35	2:40
H_{min}	1.62	1.61	1.62	1.62	1.62	1.65	1.62	1.58
t	16:05	16:50	17:35	18:20	19:10	20:00	21:20	22:05

October. An acceptable coefficient of variation for the water level therefore could be 48%, 11% for the height of the riverbank, and 35% for the cracks. It is recognized that the strengthening variables (beneficial factors) which increase the stability have a greater variation in the normal distribution than those of the weakening variables (unfavorable factors) such as the water level, depth of cracks. This is explained by the specific data observed at the site under study.

The tidal water level was observed in a day, many days in a month, many months in a year, and the same periods through years. It is practicable that the highest water level occurs in October, the average elevation is +3.28 and +1.45 for the highest and the lowest level, respectively. The tidal range of the water level or the difference between the highest and the lowest level is 1.83 m, and the average elevation is +2.61 m instead of the mean between the highest and the lowest, +2.36.

2.4 Select the Time-Dependent Variables and Their Statistical Values

Some key data are summarized as below:

- The size of the samples is more than 30, so the statistics is required.
- There is no significant variation (i.e., COV < 10%) for months except the water level of July, COV = 19%.
- Sensitive strengthening variables that increase the stability have greater variation. Main sensitive factors have COV = 85.48% for the modulus of deformation, or E; COV = 75.03% for internal friction angle, and COV = 73.8% for the cohesion.

- Sensitive weakening variables that decrease the stability have the COV = 48% for the water level, COV = 11% for the height of slope, and COV = 35% for the depth of cracks.
- The time-dependent variables are the water level, COV = 48%, and the average elevation is +2.61.
- For taking the time into account, the safety factor for the highest and the lowest water level for 12 months will be determined, i.e., data in Table 1. The confined water hydrostatic load F_{cp} is calculated by Eqs. (1)–(3) for the highest level to the lowest level. For a more practical analysis, high-water months, i.e., between July and December in a year will be studied, and the most dangerous time is expected to be at the high and low water level during these time. As such, there are at least 6 factors of safety (FS) for calculating the time-dependent reliability index.

2.5 Strategy for Solution of the Time-Dependent Reliability Index

For time-dependent reliability analysis using the First Order Reliability Method (FORM) will be a statistical study on the mean of the safety factors and the coefficient of variation of the factor, COV, to the time [11]. By assuming that some soil properties and other factors did not change to the time, the procedure will be as follows:

Step 1: Calculate the safety factor of riverbank instability to the average values of the data, namely $\mu(X)$ at the individual time step.
Step 2: Do as step 1 with many different time steps. Plot the variation chart of the factors to the time steps.
Step 3: Determine the mean value of the safety factors,
Step 4: Calculate the COV to a specific time and do as steps from abovementioned steps 2 to 3, for the COV.
Step 5: based on results of safety factors and COV to time, calculate the FORM's reliability index in time steps using Eq. (7) as below [11]:

$$\beta(t) = \frac{E(\mathrm{FS}) - 1}{\sigma(\mathrm{FS})} \tag{7}$$

where $E(\mathrm{FS})$, $\sigma(\mathrm{FS})$ is the mean value and the standard deviation of the SF, respectively.
Step 6: By assigning a target reliability index, the predicted time of failure would be determined (Fig. 3c).

3 Results

3.1 Probability of Failure

The reliability index could be calculated by using Monte Carlo Simulation (MCS) with $N = 10^4$ trials. All the variables are of the normal distribution, so the simulated value would be generated by the formula as follows:

$$X = \mu_X + Z\sigma_X \qquad (8)$$

In which μ_X and σ_X are the mean and standard deviation values of random variable X, respectively, and Z is standard normal variate [12]. All the computation over all the variables is given as shown in Fig. 7:

3.2 Time-Dependent Reliability Index

By substituting the different mean and standard deviation values of the water levels, cracks K, tidal range, and depth of sinkhole in the worksheet (Fig. 7), with different soil data as strengthening variables (or beneficial variables), the probability of failure P_f is computed. Then the reliability index is converted by the formula (9):

$$\beta(t) = -\Phi^{-1}(P_f(t)) \qquad (9)$$

By dividing a year into three periods for simplifying the problem, results of the probability of failure are shown in Fig. 8 as below:

		weakening variable				strengthening variables			Pf=sum()/10000 (sum-up values = 1 in the last column)		
				Hmax - Hmin	Depth of sinkhole	modulus E	friction angle,	cohesion c (kPa)	FR = resisting forces, numerator	FD=driving forces, de-nominator	if X(g)
4	STT	crack K	height H								
5	2	0.541301	7.58857	5.184875	38.15342	2269.055	10.83335	16.47662	9	11	1
6	3	1.012306	7.459035	0.236471	9.49023	388.7259	5.137505	16.68879	29	9	0
7	4	1.279964	6.162539	1.953464	10.30567	2857.361	7.250713	14.2304	24	3	0
		. . . .	. . . .	. . . .	. . . . . .	. . . .	. . . .	. . . .	. .	. .	. .
9999	9997	0.746023	7.584528	0.102403	25.77291	-255.776	12.97397	15.78228	25	3	0
10000	9998	2.203817	7.506475	3.245358	25.18233	938.5695	12.84359	15.83945	30	11	0
10001	9999	1.011223	7.186153	3.209438	39.63570	300.5787	12.26627	13.44423	14	8	0
10002	10000	1.076994	5.503962	2.222176	22.82479	520.2565	19.29791	15.78063	4	8	1

Fig. 7 MCS with 10^4 trials for calculating the probability of failure P_f
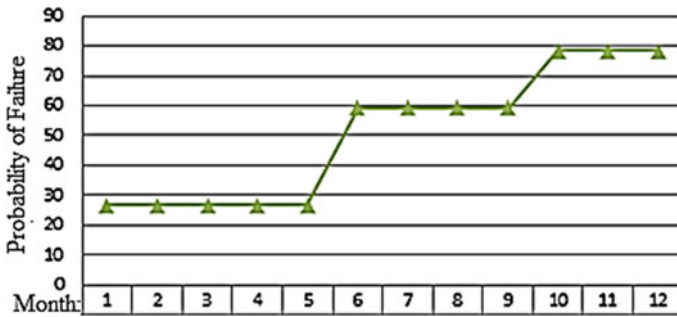
Fig. 8 Probability of failure during a year, by MCS for the Vam Nao Riverbank

For three specific cases of water level in a day, i.e., the lowest, standing, and the highest water levels, the safety factors are 0.422, 1.186, and 1.988, respectively (c.f Appendix). Then the mean value of the safety factor is $E(FS) = 1.198$ and the standard deviation $\sigma(FS) = 0.783$, then the time-dependent reliability index for an arbitrary day will be $\beta(t) = 0.25$, corresponding to $P_f = 1 - 0.401 = 59.9\%$. For seven sets of randomly varied data as in Fig. 6, the safety factor is the ratio between the values in the last two columns (i.e., FD/FR); then $E(FS) = 3.615$ and the standard deviation $\sigma(FS) = 3.003$, time-dependent reliability index will be $\beta(t) = 0.87$, resulting in a probability of failure $P_f = 1 - 0.192 = 0.808$ or 80.8%. This value of P_f is comparable to that of months from September to December (Fig. 8). For a satisfactory performance level, the target reliability index should be at least 2. This means the stability of the Vam Nao River is very low as compared to the expected value, both in safety factor and in reliability index. The probability of failure over 16% to the varied water level in a day, in months points out that the site Vam Nao is quite hazardous all in a year, always with sinkhole [11].

4   Conclusions

Vam Nao River is a small river connecting two big branches of the Mekong River, i.e., Tien River and Hau River. The hydrological regime of the Vam Nao River is very complicated. For predicting the time of riverbank instability for this site, the time-dependent reliability analysis is studied. There are three strengthening variables and three weakening variables which the latter are time-dependent ones. Data for analysis are obtained through different times a day, days in weeks or months, and the same periods between years. Riverbank instability could be occurred both at any time a day because of the twice-a-day tidal elevations in months between the high-level water of July to December. For soil data at the site of failure, Vam Nao River, a modified formula of the safety factor is studied, taking the seepage forces, the wave load, and the sinkhole into account. A deep sinkhole has been a complicated natural hazard of the Vam Nao River, and the approach to model it like a sudden cut in the depth of Fig. 4.

By developing some spreadsheet for calculating the safety factor concerning different levels of the water surface, a series of the factors are found to the time in a day, days in a month, and different months in a year. The probability of failure is calculated by applying a Monte Carlo Simulation with 10^4 trials. The result is P_f may vary from nearly 60–80%. Moreover, it is found that the safety factor will be less than 1 in cases of the lowest water levels in a day, during the time around 18:20 to 22:05 (July to December). And the reliability index for riverbank stability equals nearly 0.87 for a probability of failure of 80%. This value of the reliability index might vary at various times of the same periods through the years. The result indicates that the Vam Nao River's stability is so vulnerable reality that the failure may happen at a wide range of evening time in a day. This is actually a highly hazardous region.

Appendix: Spreadsheet for Calculating the Safety Factor of Riverbank Stability [6]

References

1. Papanicolaou, A.N., Elhakeem, M., Hilldale, R.: Secondary current effects on cohesive river bank erosion. J. Water Resour. Res. **43**, W12418, 1–14 (2007). https://doi.org/10.1029/2006WR005763

2. Department of Natural Resources and Environment, An Giang Province.: Statistical Data on Riverbank Erosion, Report No. 27/BC-STNMT, dated Feb, 1st (2018)

3. Directorate of Water Resource (Ministry of Agriculture and Rural Development.: Vam Nao riverbank erosion—Causes and measures for mitigation (in Vietnamese: Sạt lở bờ sông Vam Nao—Nguyên nhân và giải pháp khắc phục http://www.tongcucthuyloi.gov.vn/Tin-tuc-Su-kien/Tin-chi-dao-dieu-hanh/catid/13/item/3165/sat-lo-bo-song-vam-nao–an-giang—nguyen-nhan-va-giai-phap-khac-phuc; video clip: https://youtu.be/1tbqUGRutfY (2017)

4. Thorne, C.R., Abt, S.R.: Analysis of riverbanks instability due to toe scour and lateral erosion. Earth Surf. Proc. Land. **18**(9), 835–843 (1993)

5. Fishman, G.S.: Monte Carlo Concepts, Algorithms and Applications. Springer, New York (1995). ISBN 0-387-94527-x

6. Tu, T.M., Tham, D.H.: Safety factor of the riverbank soil stability, J. Constr. (2017). ISSN: 0866-8762

7. Amiri-Tokaldany, E., Samadi, A., Darby, S.E.: Sensitivity analysis of the effective parameters in the riverbank stability. In: Proceedings of the Kubaba Congress on River Flow, pp 1297–1304, Iran. Department and Travel Services (2008). ISBN 978-605-60136-2-1

8. Samadi, A., Amiri-Tokaldany, E., Darby, S.E.: Integrated effect of parameter uncertainty in riverbank stability modelling. In: Dittrich, Koll, Aberle, Geisenhainer. (eds.) Proceedings on River Flow 2010. © Bundesanstalt für Wasserbau (2010). ISBN 978-3-939230-00-7

9. Fredlund, M.D., Feng, T.Q., Fredlund, D.D., Van Zyl, D.: Reasonable variation between slope stability analysis methods. In: Proceedings of the 11th International Conference on Geomechanics, New Zealand (2012)

10. Geotechnical Report of the My Hoi Dong Elementary school, Cho Moi Ward, An Giang Province, South VietNam. Documentation & Contract 717008/2017/HĐTV by Thoai Ha Company, An Giang (2017)

11. Mousavi, S., Noorzad, A.: Dynamic reliability analysis of earth dam's slope stability. In: Bennett, T., Bibeau. (eds.) Proceedings of the International Conference on Sustainable and Safe Dams Around the World, Canadian Dam Association (2019). ISBN 978-0-367-33422-2

12. Nowak, A.S., Collins, K.R.: Reliability of Structures. McGraw Hill International Editions (2000)

On the Features of Pyroclastic Deposits and Post-eruption Natural Hazards

Mariagiovanna Moscariello, Sabatino Cuomo, Valérie Baumann, and Costanza Bonadonna

1   Introduction

Volcanic deposits can be massive or stratified; the latter with alternating coarse- and fine-grained layers with high spatial variation of physical properties [10].

The physical properties of volcanic deposits are typically highly variable in relation to the style and intensity of the eruption and magma composition. Volcanic deposits are usually classified based on their origin as: pyroclastic or epiclastic [25]. Pyroclastic deposits include tephra-fallout deposits and deposits associated with pyroclastic density currents (PDCs; mixture of gas and pyroclasts). Epiclastic deposits include all the forms of volcanoclastic remobilization on the landscape post-deposition and the deposits originated by debris avalanches, debris flow, and hyperconcentrated streamflow. Moreover, the epiclastic deposits include the deposits originated by alluvium on the flank of a volcano and volcanic loess (i.e. deposited by wind in more arid and high-altitude environments). The instability of the slopes mantled by the volcanic deposits, and more in general, the natural hazards which can affect them have been formerly investigated through experimental works [4, 15, 17, 21], field data and numerical observations [6, 8]. Hereafter, eight volcanic deposits are selected, seven in the pyroclastic class (5 tephra-fallout deposits and 2 PDC deposits) and one from the epiclastic class, to evaluate their common features.

M. Moscariello · S. Cuomo (✉)
Geotechnical Engineering Group (GEG), University of Salerno, Fisciano, Italy
e-mail: scuomo@unisa.it

V. Baumann
Institute of Earth Sciences, University of Lausanne, Lausanne, Switzerland

C. Bonadonna
Department of Earth Sciences, University of Geneva, Geneva, Switzerland

2 Origin and Examples of Pyroclastic Deposits

Pyroclastic material derives from the fallout of tephra (collective term for airborne volcanic ejecta irrespective of size, composition or shape) or PDCs. Explosive volcanic eruptions typically produce volcanic plumes that carry tephra to high altitudes where it is dispersed by winds up to thousands of kilometres from the source [33]. Tephra particles range from ash (<2 mm) to lapilli (2–64 mm) or blocks and bombs (>64 mm). Tephra-fallout deposits are unconsolidated, loose and highly erodible during rainstorms [28]. In contrast, PDCs flow down the slopes of volcanoes and the associated deposits fill the valleys. Tephra-fallout deposits typically decrease their grain size with distance from the vent and generate poorly sorted deposits and polymodal grain-size distribution [5, 18].

The mineralogy of pyroclastic deposits determines the mass density, since both light (G_s < 2.8–3.0) and heavy (G_s > 2.8–3.0) minerals are present. Common minerals in pyroclastic deposits are volcanic glass (G_s = 2.2–2.4), feldespars (G_s = 2.6–2.7), quartz (G_s = 2.6–2.65), hornblend (G_s = 3–3.4), hyperstène (G_s = 3.2–3.9), augite (G_s = 3.2–3.6), magnetite (G_s = 4.5–5), biotite (G_s = 2.9–3.4) and apatite (G_s = 3.1–3.2). These minerals do not have a fixed chemical composition, or a regular three-dimensional structural framework and their weathering denotes a diagenesis process (i.e. the dissolution of original minerals, the selective leakage and the re-precipitation of new minerals). The diagenesis process produces changes in particle size (from silt and sand size to clay-size), increases in void ratio and changes in mineralogy.

Pyroclastic deposits contain various proportion of silica-based glass, i.e. an amorphous solid, with a poorly ordered structure of silicate oxides and various proportions of aluminium and other elements [33]. Halloysite and gibbsite in the older volcanic soils indicate more advanced stages of weathering, as these minerals appear if non-crystalline minerals content decreases. The silica content indicates if a volcanic rock is resistant (high silica) or susceptible (low silica) to degradation to clays [24, 25].

Volcanic rocks can be classified by composition based on a plot of total alkalis (Na_2O + K_2O) against SiO_2 [14]. Considering the total silica content (SiO_2) from high silica to low silica, volcanic rocks are catalogued as rhyolite, dacite, andesite, basaltic-andesite and basalt. The rock type trachyte (La Fossa volcano, Table 1) is a felsic rock, with higher total alkalis than a dacite. The phonolite and phonolitic tephrite rock type (Vesuvius volcano, Table 1) is intermediate between felsic and mafic.

In this paper, we analyse the geotechnical properties of pyroclastic deposits less than 50 years old, originated from 7 recent volcanic eruptions and one volcanic sequence belonging to at least 5 eruptions between 8000 years BP to 1944 (Table 1).

The most recent eruption is the June 2011 eruption of Cordón Caulle, located near the border between Chile and Argentina. During the climactic phase of the eruption on 4–15 June 2011, high plumes dispersed most of the erupted tephra

Table 1 Main characteristics of the volcanoes studied in this work

Volcano	Country	Volcano types	Eruption style	Eruptions*	VEI	Main product	Composition
Unzen	Japan	Volcanic dome complex	DC	17/11/199–16/02/1995	2	9400 PDC	Andesitic to dacitic
Izu-Oshima	Japan	Stratovolcano, caldera, pyroclastic cones	EE	15/11/1986–23/11/1986	3	TF (scoria)	Basaltic
Pinatubo	Philippines	Stratovolcano, caldera, lava domes	Pl	02/04/1991–02/09/1991	6	TF and PDC	Dacite, basaltic-andesite
Vesuvio	Italy	Stratovolcano, caldera, lava domes	Str	5/07/1913–4/04/1944	3	TF and PDC	Phonolitic tephrite to tephrite
			sPl	AD 1631	4	TF and PDC	Phonolitic tephrite to tephritic phonolite
			sPl	AD 472 (Pollena)	4	TF and PDC	Phonolitic to phonolitic tephrite
			Pl	AD 79 (Pompeii Pumice)	5	TF and PDC	tephrite
			Pl	3800 b.p. (Avellino Pumice)	5	TF and PDC	
			Pl	8000 b.p. (Ottaviano Pumice)	5	TF and PDC	Phonolite
La Fossa (Vulcano)	Italy	Composite cone	Vul	1888–1890		TF	Latitic, traquitic and rhyolitic
Cordón Caulle	Chile	Volcanic complex	sPl	4/06/2011 until 1/04/2012	4	TF and PDC	Rhyolite
Irazú	Costa Rica	Old caldera structure with several crater	Str and Vul	03/1963 until 1965	3	TF (scoria) and PDC (dry and wet surges)	Basalts to andesites
Nevado del Ruiz	Colombia	Stratvolcano	Pl	13/11/1985	3	PDC	Dacite and andesite

*Eruptions analysed in this work; *VEI* Volcanic explosivity index; *PDC* Pyroclastic density currents; *TF* Tephra-Fallout; *DC* Dome collapse; *EE* Effusive and explosive activity; *Pl* Plinian; *sPl* Sub-plinian; *Str* Strombolian; *Vul* Vulcanian

eastward reaching Argentina and the Atlantic Ocean [22, 29]. The sequences in outcrops 25–50 km from the vent appears as a stratified fine lapilli deposit (unit I and II) [23], covered by multiple fine-ash layers, interbedded with coarse to fine-ash lapilli beds [28].

One of the largest volcanic eruption in the 20th Century is the climactic eruption of mount Pinatubo, along the western volcanic chain of Luzeon, Philippines. The flanks of Pinatubo were covered with PDCs in past 5000 years event, and the composition is mainly andesitic. The last eruption of Mount Pinatubo began with small explosions on April 1991, ash emission on June 3rd, and the first eruption occurred on June 9th. The largest explosion occurred on June 15st, forming a 20–40 km plume and ejecting a large amount of tephra (ash and pumice lapilli) that was dispersed over an area of about 850 × 400 km [29, 30]. About 5 km^3 of PDCs and 0.2 km^3 of tephra-fallout were emplaced during the climactic phase on the slopes of the volcano. The PDC deposits ranged from a few metres to 100–200 m at valley fills in the distal parts.

The deposits are predominantly made of ashes (silt or sands) and pumice (sands or gravels), and a small proportion with lithic rich facies is composed dominantly of gravel size dense lithic clasts.

The tephra-fallout deposits ranged from a few millimetres at about 50 km from the volcano to about 0.5 m near the crater [31, 35]. Post-eruption rainfall on erodible PDC deposits and lake outbreaks generated lahars (debris flow and hyperconcentrated flows), a serious hazard up to 50–60 km far away [28]. Orense et al. [26] analysed two samples: P01 in the distal area near the towns of Guagua and Bacolor, and P02 taken upstream about 18 km to the east of the volcano.

In the last 20,000 years, at least four high-magnitude Plinian eruptions of the Vesuvius occurred, and minor events over a large range of magnitude and intensity. After the Pompeii Pumice eruption (79 AD), the two largest sub-plinian eruptions occurred, in AD 472 (Pollena) and AD 1631. During the explosive eruptions, tephra-fallout deposits were dispersed from N–NE to S–SE up to 50 km far. We analyse two samples from the pyroclastic stratigraphic sequence located in Sarno, 20 km from the cone. In fact, the Pizzo d'Alvano upper slopes (Sarno) are mantled of multi-layered pyroclastic covers, with pumice lapilli layer and pedogenetisized ashy horizons from at least five different eruptions (Table 1) [14]. Between successive eruptions, the deposits were affected by pedogenesis, with the alteration of pumice levels and buried soils.

3   Special Features and Comparison of Pyroclastic Deposits

The products of eight volcanic complex are analysed, whose deposits are tephra-fallout (Vulcano, Irazù, Oshima, Cordon-Caulle and Vesuvio deposits), PDC (Uzen and Nevado del Ruiz) and epiclastic (Pinatubo), from ancient (Vesuvio) and

recent (Volcano, Cordón Caulle, Irazù, Oshima, Pinatubo, Unzen and Nevado del Ruiz) eruptions, i.e. at different weathering stage. Their special features are discussed, and the prediction bounds at various confidence levels are evaluated for some physical and hydro-mechanical properties.

The mechanical behaviour is strictly related to the grain particle size, as observed also for deposits associated with other geological processes. The main physical properties are detailed, and their confidence intervals estimated in a code written in MATLAB.

A first comparison is based on the shape and the spread of particle size distribution through two coefficients: Uniformity (U) and Curvature (C_c), defined as follows:

$$U = \frac{D_{60}}{D_{10}} \quad C_c = \frac{D_{30}^2}{D_{10} \cdot D_{60}} \tag{1}$$

D_{10}, D_{30} and D_{60} are the grain diameters at 10%, 30% and 60% passing, respectively.

In Fig. 1, the maximum, minimum and average values of U and C_c are shown for each deposit. The pyroclastic deposits originated from Vulcano, Unzen, Oshima and Pinatubo volcanoes are well graded. The coarser Vesuvian deposit (Vesuvio B) is a well-graded deposit with average coefficient of curvature ($C_{c,average}$) and average coefficient of uniformity ($U_{average}$) equal to 1.5 and 29.7, respectively. On the contrary, finer Vesuvian deposit (Vesuvio A) can be considered a gap graded deposit ($C_{c,average} = 0.7$ $U_{average} = 20.4$). The most interesting aspect of this graph is that most of the data lie within the 75% of the confidence level.

The grain size of small particles also governs the void size. Volcanic ash deposits usually have high void ratio (e); here the average is 1.38, but e varies
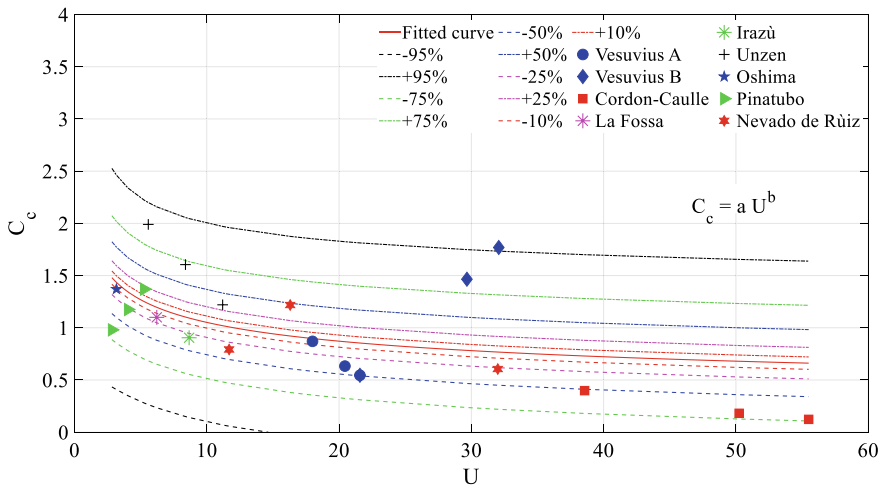
Fig. 1 Deposit gradation parameters, where $a = 1.96$ and $b = -0.27$ for the fitted curve

between 0.42 and 3.62. Void ratio has been here associated to the product $U * D_{50}$ (Fig. 2). For recent volcanic deposits (i.e. Cordón Caulle, Unzen, Oshima and Nevado del Ruiz), there is a small difference between the maximum and the minimum void ratio, as no significant consolidation has occurred yet. Low variability of void ratio is also observed for the Pinatubo samples derived from lahars deposits [27]; the opposite is for the Vesuvius soils. Some ancient volcanic deposits [21] and also mentioned hereafter. The volcanic soils from volcanoes in India (Dominica, West Indies) and Japan (Akaboku and Kuroboku volcanoes) are affected by diagenesis. The volcanic soils of Dominica site (allophanic non-cohesive soils) has void ratio from 1.9 to 4.1, while the soils from Japan volcanoes show two different void ratio ranges: 3.0–5.7 (organic cohesive soil, Kuroboku) and 1.0–6.1 (inorganic cohesive soil, Akaboku). Most of the data fall in the 75% confidence interval, with the maximum, median and minimum void ratio of Vesuvius B, Cordón Caulle, Vulcano, Irazù, Uzen, Oshima and Pinatubo included.

Due to the high percentage (70–95%) of light and non-crystalline minerals (see Sect. 2), these deposits have as distinctive feature a low specific gravity (G_s) varying between 2.30 and 2.80. Their specific gravity is related to the product $U * D_{50}$, and the trend is shown in Fig. 3. Most of the G_s values are included in the interval of confidence equals to 75%, and the Oshima deposit (basaltic composition) has higher G_s than the confidence level of 75%, while Vesuvius A and Cordón-Caulle have the minimum G_s lower than the bottom boundary of the confidence level 75%.

Volcanic tephra deposits exhibit a wide range of saturated permeability (k_{sat}) and tend to be more permeable than deposits/soils with the same median diameter or the
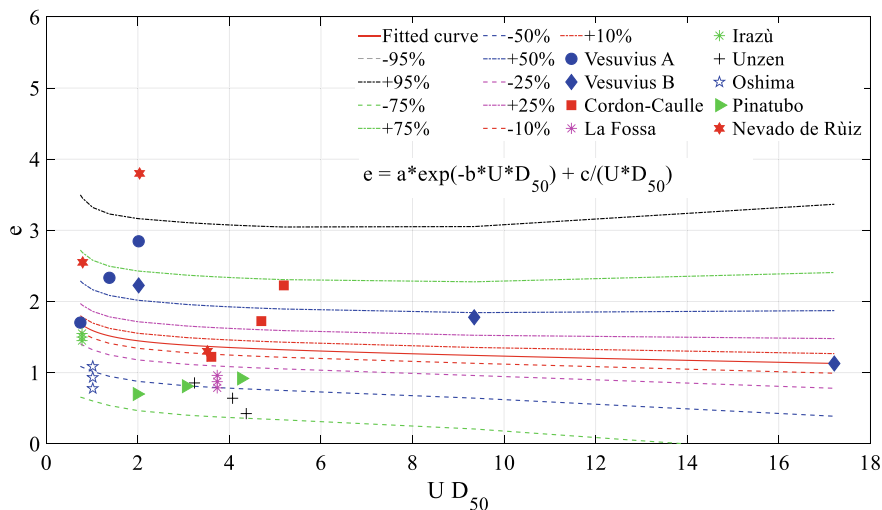
Fig. 2 Void ratio (e) versus the product UD_{50}, where $a = 1.34$ $b = 0.01$ and $c = 0.26$ for the fitted curve
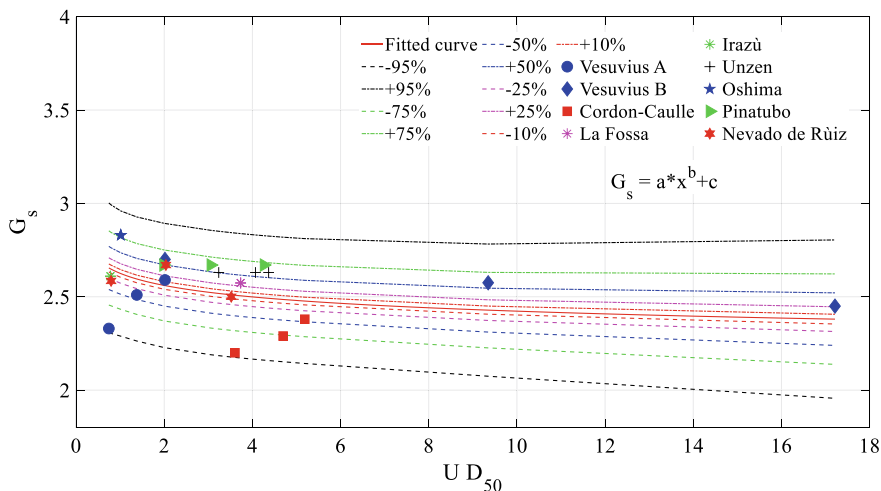
Fig. 3 Specific gravity (G_s) versus the product UD_{50}, $a = 1.23$ $b = 0.08$ and $c = 1.34$ for the fitted curve

same granulometric assortment [36, 37]. In literature, the permeability of volcanic deposits has been compared to some reference deposits as Toyura sand [21, 26], London Clay [37] or deposits originated by other geological processes [37].

This can be attributed to the grain's internal porosity, which increases the specific surface of each grain. The range of variability of k_{sat} is discussed also considering the presence of finer grains. The k_{sat} of the volcanic deposits studied is compared to the saturated permeability estimated through three literature models, which relate k_{sat} to some physical properties. The Hazen [20] equation (Eq. 2) well estimates the saturated permeability of uniformly graded sand but is also useful for fine sand to gravel range, with a domain of applicability for $U < 5$ and 0.1 mm $\leq D_{10} \leq 3$ mm. The Kozeny-Carman [13] equation (Eq. 3) well estimates the saturated permeability of silts, sands and gravelly sands, with $D_{10} \leq 3$ mm. Finally, the Beyer [2] equation (Eq. 4) has a large domain of applicability: $1 \leq U \leq 20$ and 0.06 mm $\leq D_{10} \leq 0.6$ mm.

$$k_{sat} = \frac{g}{v} \cdot 6 \cdot 10^{-4} \cdot [1 + 10 \cdot (n - 0.26)]D_{10}^2 \tag{2}$$

$$k_{sat} = \frac{\rho g}{\mu} \cdot \frac{1}{180} \cdot \left[\frac{n^3}{(1-n)^2}\right]D_{10}^2 \tag{3}$$

$$k_{sat} = \frac{g}{v} \cdot 6 \cdot 10^{-4} \cdot \log\left(\frac{500}{U}\right)D_{10}^2 \tag{4}$$

where D_{10}^2 and n are the mean grain diameters at 10% passing and the mean porosity, respectively, and U is the mean Uniformity coefficient.

The Hazen equation (Eq. 2) estimates a k_{sat} inside the variability range of the deposits derived from Nevado de Rùiz, Irazù, Oshima and Pinatubo; while for the others, volcanic deposits the results differ of some orders of magnitude (Fig. 4). The Kozeny-Carman equation (Eq. 3) estimates a k_{sat} into the variability range of deposits derived from Vesuvio (A and B), Irazù, Oshima and Pinatubo.

The Beyer equation (Eq. 4) estimates a k_{sat} into the variability range of the deposits derived from Oshima and Pinatubo. The saturated permeability of the deposits from Cordón Caulle, Unzen and Vulcano is not well estimated by none of the equations.

Particularly, all the equations (Eqs. 2–4) overestimate the saturated permeability of deposits of Uzen and Volcano, while the k_{sat} of the deposits of Cordón Caulle is underestimated by all the equations. Moreover, the Beyer equation (Eq. 4) provides lower values of k_{sat} than Hazen and Kozeny-Carman equations. The largest values are provided by Kozeny-Carman equation.

As the volcanic deposits are unsaturated for long time during the hydrological year, thus the description of the Soil Water Retention Curves (SWRCs) allows a deeper knowledge of the hydro-mechanical behaviour. The SWRCs of the deposits of Vesuvio and Irazù were obtained using controlled-suction pressure plate apparatus, volumetric extractor and oedometer [3, 19]. The SWRCs of the other pyroclastic deposits are estimated using the Kovacs model developed by Chapuis and Aubertin [13]. The model inputs are the grain-size data including the diameter corresponding to 10 and 60% passing on the grain-size curve (i.e., D_{10} and D_{60}) and the liquid limit (w_L). Every curve is described using van Genuchten model (1958):

$$\log(k_{sat}) = 2.34 \cdot 10^{-4} \cdot \log(D_{10}) + 1.82 \cdot 10^{-6}$$
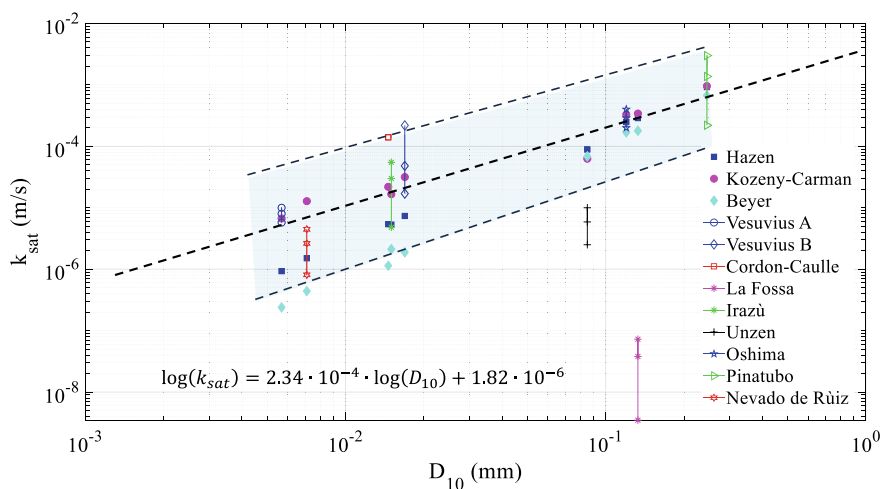
Fig. 4 Saturated permeability (k_{sat}) observed and the estimated through the Eqs. (2–4)

$$\theta = \theta_r + \frac{\theta_s - \theta_r}{[1 + (\alpha s)^n]^m} \tag{5}$$

where θ_s and θ_r are the volumetric water content saturated and residual, respectively, s is the matric suction (i.e. the difference between pore air pressure and pore water pressure), α is a model parameter whose reciprocal value can be assumed as the deposit's air entry value (a.e.v.) and n and $m = 1–1/n$ are fitting parameters for pore size.

Analysing the data of pyroclastic deposits derived from Vesuvio eruptive activity reported by Bilotta et al. [3], Sorbino and Foresta [34], it is found that the specimens in the class Vesuvio A have air entry values (a.e.v.) and volumetric water content higher than class Vesuvio B. The a.e.v of Vesuvio A soil is lower than 5 kPa for the tests performed at low net vertical stress, while it is >10 kPa for the same specimens at net vertical stress >100 kPa. The specimens of the class Vesuvio B do not have significant differences of a.e.v. at different net vertical stresses. The specimens from Irazù has an a.e.v. = 2 kPa at nil net vertical stress. Low air entry values (1.2/7.0 kPa) are also obtained from Kovacs model for the other volcanic deposits (Table 2).

The shear strength of volcanic deposits was formerly studied in saturated or unsaturated condition, with some different shear strength measured due to different failure mechanisms. In general, undisturbed specimens are cohesionless or with cohesion <5 kPa, while the remoulded specimens exhibit cohesion between 25 and 50 kPa.

Table 2 SWRCs obtained through experimental tests and numerical simulations

Volcano	θ_s	θ_r	α (kPa^{-1})	n	a.e.v. (kPa)
Vesuvio A	0.53–0.60–0.66	0.0	0.23–0.66–1.02	1.18–1.19–1.79	4.35–1.52–0.98
Vesuvio B	0.51–0.64–0.72	0–0.02–0.12	1.31–8.62–24.58	1.15–1.31–2.16	0.13–0.24–0.54
Cordón Caulle	0.62	0.02–0.03–0.03	0.14–0.32–0.50	1.83–1.98–2.12	6.98–3.10–1.99
La Fossa*	0.47	0.02–0.02–0.01	0.44–0.65–0.85	2.18–3.12–4.07	2.25–1.55–1.18
Unzen*	0.26–0.40–0.49	0.02–0.02–0.01	0.22–0.51–0.76	2.94–2.69–3.75	4.59–1.96–1.32
Oshima*	0.44–0.48–0.52	0.01	0.42–0.51–0.58	3.73–3.89–4.01	2.40–1.98–1.72
Pinatubo*	0.38–0.48–0.48	0.01	0.73–1.10–1.14	3.18–3.71–4.10	1.36–0.91–0.88
Irazù	0.6	0.018	0.91	2.19	1.10
Nevado de Ruiz	0.57–0.68–0.79	0.10–0.12–0.16	0.01–0.03–0.03	1.93–1.97–2.68	29.74–35.36–95.79

*Data obtained using Kovacs model

Particularly, direct shear tests, drained and undrained triaxial tests, and simple shear tests were performed on Vesuvian class A soil [15]. Cohesion was assumed equal to zero. The results of the direct shear (DS) and triaxial (TX) tests were univocally elaborated, and the results were close each other, both for friction angle (φ') and stress ratio at critical state (M), with an increasing trend related to the normalised displacement reached at critical state. Conversely, the interpretations of the SS results in the $q - p'$ or in the $\tau - \sigma'_v$ planes provided lower values than in the other equipments for both φ' and M. The deposits of Vulcano and Cordón Caulle were analysed through direct shear tests both at natural water content and in saturated condition [1, 29]. The strength and deformation properties of deposits originated from Oshima, Unzen and Pinatubo were investigated through monotonic drained tests using a hollow torsional apparatus [26, 27]. Shear strength parameters of deposits derived from Nevado de Ruiz were investigated through direct shear and triaxial tests [21]. Although investigated for different shearing mechanisms, the friction angle is higher for the recent volcanic deposits, probably due to diagenesis, as assumed by Herrera et al. [21] for the Colombian volcanic ash deposits. The friction angle evaluated in saturated volcanic deposit is >35° and can reach 42°, with an average of 38°.

The stress–strain behaviours of these pyroclastic deposits are detailed in literature [3, 4, 15, 17], and some similarities can be highlighted. A common feature concerns the variation of shear strength related to the magnitude of specimen disturbance. The suction also affects the shear strength, with significant increment of the shear strength of both undisturbed and remoulded deposits as the suction increases, more evident for remoulded specimens, probably due their different internal structure [4, 17, 21].

4   Post-eruption Natural Hazards

In areas around volcanoes, the slope stability of pyroclastic deposits is ensured by several factors, including cementation and suction. Along natural slopes, these deposits are usually steeper than sedimentary deposits, with steepness larger than friction angle. Hence, slope instability can easily occur, later evolving in complex landslides in the short term (as lahars) or long term (debris flow).

The slope instability mechanisms comprise rainfall infiltration and deposit shear failure, with various hydraulic boundary conditions acting as predisposing or triggering factors. However, runoff and superficial erosion is also a relevant mechanism, alternative or additional. Thus, multiple combined natural hazards may occur during a same rainstorm, including debris flows, flowslides, hyperconcentrated flows and debris floods. The associated hazard and risk scenarios are complex, and it is important to fully understand the mechanisms governing the stages of

such phenomena, namely triggering, eventual transition into a flow, propagation and final deposition.

Flow-like landslides are complex slope instability phenomena since they exhibit distinct stage with different kinematic characteristics [7, 9, 16]. The failure may relate to: (i) rainfall infiltration from the ground surface; (ii) water spring from the bedrock; (iii) ponding at the ground surface; (iv) combination of the previous factors. This implies the increase in pore water pressures, the consequent reduction of mean effective stress, and the formation of a continuous shear surface through the entire deposit mass or a diffuse failure [6, 11]. Wetting collapse or liquefaction can occur, for which void ratio and degree of saturation are indicators of the potential occurrence. Failure is ruled by saturation condition, permeability and shear strength. Thus, the identification of reliable intervals of variations in terms of SWRC and k_{sat} can improve the modelling of this stage using any of the several modelling approaches available: limit equilibrium method (LEM), finite element method (FEM), or Smooth Particle Hydrodynamics (SPH), among others. In the post-failure stage, the acceleration of failed mass possibly relates to: development of total or partial undrained conditions with high pore water pressures upon shearing; static liquefaction (Cascini et al. [6, 8]). The post-failure stage can be also nicely modelled using several approaches, with a consistent choice of the hydro-mechanical parameters.

Typical examples of flow-like landslides are those of the shallow unsaturated pyroclastic deposits originated by the explosive activity of the Somma-Vesuvius volcano [6, 8, 9]. In the literature, several contributions propose the numerical modelling of the failure and post-failure stages of shallow landslides. Frequent landslides also occur in the Coffee Zone (Colombia) in the pyroclastic deposits. The most common triggering mechanisms are: (i) heavy rainfall and earthquake, (ii) aggravated by loss of forest cover, (iii) non-planned land use and (iv) poor wastewater management. Debris flows are also frequent in "Pacific ring" Countries (as Philippines and Japan) [21].

The volcanic deposits can be also remobilized by lahars phenomena, which are mainly generated by the remobilization of tephra-fallout and PDC deposits; volcanic rocks from the collapse of destabilised sectors can also contribute to their triggering and volume. The occurrence of lahars is likewise influenced by the hydro-mechanical behaviour of the deposits. A right choice of the parameters related to saturated permeability, SWRC and shear strength allows improving the simulation of the phenomena.

Many lahars and related flood events occurred at Argentina-Chile border and the town of Villa la Angostura (48 km from the vent) and engaged the deposits originated by eruptive activity of Cordón Caulle vulcano. The spatial distribution of the potential lahar sources during long-lasting eruptions of Cordón Caulle vulcano using two slope stability models (SHALSTAB and TRIGRS) were reported in Baumann et al. [1].

5   Conclusions

The volcanic deposits derived from the eruptive activity of eight volcanoes were compared based on their physical properties. A variation trend for each variable was estimated as a function of the product $U * D_{50}$, which accounts for both the uniformity of grain-size distribution and the mean size of the grains. Five confidence levels were identified to propose a framework where to include later a wider database. The deposits derived from recent eruption exhibit an overall mean void ratio of 1.29 and specific gravity 2.54, while those derived from ancient eruption have higher mean void ratio (2.00) and a slightly low mean G_s (2.53). The hydro-mechanical properties were also discussed. The SWRC parameters are obtained through experimental tests or estimated using Kovac's model. Specially, the a.e.v values are compared, being <10 kPa for most of the volcanic deposits considered. The highest a.e.v. values are found for the deposits of Nevado de Ruiz. The mean saturated permeability of the recent deposits is one order of magnitude lower (3.02E−4 m/s) than the ancient ones (5.13E−5 m/s).

The shear strength properties, though evaluated through different devices share a common feature, i.e. the suction induces an increase of shear strength. Recent volcanic deposits have higher friction angle than old. The remolded specimens show higher shear strength than undisturbed, due to the rearrangement of internal structure.

The most frequent natural hazards are also described, and the physical and the more useful hydro-mechanical parameters to simulate the events are briefly recalled.

References

1. Baumann, V., Bonadonna, C., Cuomo, S., Moscariello, M., Manzella, I.: Slope stability models for rainfall-induced lahars during long-lasting eruptions. J. Volcanol. Geoth. Res. **359**, 78–94 (2018)
2. Beyer, W.: Zur Bestimmung der. Wasserdurchlässigkeit von Kiesen und (1964)
3. Bilotta, E., Cascini, L., Foresta, V., Sorbino, G.: Geotechnical characterisation of pyroclastic soils involved in huge flowslides. Geotech. Geol. Eng. **23**(4), 365–402 (2005)
4. Bilotta, E., Foresta, V., Migliaro, G.: The influence of suction on stiffness, viscosity and collapse of some volcanic ashy soils. In: 1st E-UNSAT 1, pp. 349–354 (2008)
5. Brown, R.J., Bonadonna, C., Durant, A.J.: A review of volcanic ash aggregation. Phys. Chem. Earth, Parts A/B/C **45**, 65–78 (2012)
6. Cascini, L., Cuomo, S., Pastor, M., Sacco, C.: Modelling the post-failure stage of rainfall-induced landslides of the flow-type. Can. Geotech. J. **50**(9), 924–934 (2013)
7. Cascini, L., Cuomo, S., Pastor, M., Sorbino, G., Piciullo, L.: SPH run-out modelling of channelized landslides of the flow type. Geomorphology **214**, 502–513 (2014)
8. Cascini, L., Cuomo, S., Pastor, M.: Inception of debris avalanches: remarks on geomechanical modelling. Landslides **10**(6), 701–711 (2013)

9. Cascini, L., Sorbino, G., Cuomo, S., Ferlisi, S.: Seasonal effects of rainfall on the shallow pyroclastic deposits of the Campania region (southern Italy). Landslides **11**(5), 779–792 (2014)
10. Cascini, L., Cuomo, S., Della Sala, M.: Spatial and temporal occurrence of rainfall-induced shallow landslides of flow type: a case of Sarno-Quindici, Italy. Geomorphology **126**(1–2), 148–158 (2011)
11. Cascini, L., Cuomo, S., Pastor, M., Sorbino, G.: Modelling of rainfall-induced shallow landslides of the flow-type. ASCE's J. Geotech. Geoenviron. Eng. **1**, 85–98 (2010)
12. Chadwick, O.A., Gavenda, R.T., Kelly, E.F., Ziegler, K., Olson, C.G., Elliott, W.C., Hendricks, D.M.: The impact of climate on the biogeochemical functioning of volcanic soils. Chem. Geol. **202**(3–4), 195–223 (2003)
13. Chapuis, R.P., Aubertin, M.: On the use of the Kozeny Carman equation to predict the hydraulic conductivity of soils. Can. Geotech. J. **40**(3), 616–628 (2003)
14. Crosta, G.B., Dal Negro, P.: Observations and modelling of soil slip-debris flow initiation processes in pyroclastic deposits: the Sarno 1998 event (2003)
15. Cuomo, S., Moscariello, M., Foresta, V.: Shear strength of a Vesuvian pyroclastic soil measured in different testing devices. In: Proceedings of Workshop on Volcanic Rocks and Soils, Ischia (Italy), pp. 231–236 (2015)
16. Cuomo, S., Pastor, M., Cascini, L., Castorino, G.C.: Interplay of rheology and entrainment in debris avalanches: a numerical study. Can. Geotech. J., 1–15 (2014)
17. Cuomo, S., Moscariello, M., Foresta, V.: Wetting tests of partially saturated soils under simple shear conditions. Géotech. Lett. **7**(2), 197–203 (2017)
18. Durant, A.J.: Research focus: toward a realistic formulation of fine-ash lifetime in volcanic clouds. Geology **43**(3), 271–272 (2015)
19. Eichenberger, J., Ferrari, A., Laloui, L.: Early warning thresholds for partially saturated slopes in volcanic ashes. Comput. Geotech. **49**, 79–89 (2013)
20. Hazen, A.: Some physical properties of sands and gravels with special reference to their use in filtration. In: The 24th Annual Report of the State Board of Health of Massachusetts.34, 553 (1892)
21. Herrera, M.C., Lizcano, A., Santamarina, J.C.: Colombian volcanic ash soils. In: Characterization and Engineering Properties of Natural Soils, pp. 2385–2409 (2007)
22. Lara, L.E., Moreno, H., Naranjo, J.A., Matthews, S., de Arce, C.P.: Magmatic evolution of the Puyehue-Cordón Caulle Volcanic Complex (40 S), Southern Andean Volcanic Zone: from shield to unusual rhyolitic fissure volcanism. J. Volcanol. Geoth. Res. **157**(4), 343–366 (2006)
23. Lara, L.E., Naranjo, J.A., Moreno, H.: Rhyodacitic fissure eruption in Southern Andes (Cordón Caulle; 40.5 S) after the 1960 (Mw: 9.5) Chilean earthquake: a structural interpretation. J. Volcanol. Geotherm. Res. **138**(1–2), 127–138 (2004)
24. Le Bas, M.J., Streckeisen, A.L.: The IUGS systematics of igneous rocks. J. Geol. Soc. **148**(5), 825–833 (1991)
25. Neall, V.E: Volcanic soils. In: Land Use, Land Cover and Soil Sciences, vol. 7, pp. 23–45 (2009)
26. Orense, R.P., Zapanta, A., Hata, A., Towhata, I.: Geotechnical characteristics of volcanic soils taken from recent eruptions. Geotech. Geol. Eng. **24**(1), 129–161 (2006)
27. O'Rourke, T.D., Crespo, E.: Geotechnical properties of cemented volcanic soil. J. Geotech. Eng. **114**(10), 1126–1147 (1988)
28. Pierson, T.C., Major, J.J.: Hydrogeomorphic effects of explosive volcanic eruptions on drainage basins. Annu. Rev. Earth Planet. Sci. **42**, 469–507 (2014)
29. Pistolesi, M., Cioni, R., Bonadonna, C., Elissondo, M., Baumann, V., Bertagnini, A., Chiari, L., Gonzales, R., Rosi, M., Francalanci, L.: Complex dynamics of small-moderate volcanic events: the example of the 2011 rhyolitic Cordón Caulle eruption, Chile. Bull. Volcanol. **77**(1), 3 (2015)
30. Rosi, M., Paladio-Melosantos, M., Di Muro, A., Leoni, R., Bacolcol, T.: Fall versus flow activity during the 1991 climactic eruption of Pinatubo Volcano (Philippines). Bull. Volcanol. **62**(8), 549–566 (2001)

31. Scott, W.E., Hoblitt, R.P., Torres, R.C., Self, S., Martinez, M.M.L., Nillos, T.: Pyroclastic flows of the June 15, 1991, climactic eruption of Mount Pinatubo. In: Fire and mud: Eruptions and lahars of Mount Pinatubo, Philippines, pp. 545–570 (1996)
32. Shoji, S., Dahlgren, R., Nanzyo, M.: Genesis of volcanic ash soils. In: Developments in Soil Science, vol. 21, pp. 37–71 (1993)
33. Sigurdsson, H., Houghton, B., McNutt, S., Rymer, H., Stix, J.: The Encyclopedia of Volcanoes. Elsevier (2015)
34. Sorbino, G., Foresta, V.: Unsaturated hydraulic characteristics of pyroclastic soils. In: Proceedings of the 3rd International Conference on Unsaturated Soils, vol. 1, pp. 405–410 (2002)
35. Tayag, J.C.: Pinatubo Volcano Wakes from 4 Century Slumber. Philippine Institute of Volcanology and Seismology Press, Quezon City (1991)
36. Wesley, L.D.: Geotechnical properties of two volcanic soils. In: Geotechnics on the Volcanic Edge: Tauranga, New Zealand, Geotechnical Society Symposium (2003)
37. Wesley, L.D.: Shear strength properties of halloysite and allophane clays in Java, Indonesia. IGeotechnique **27**(2), 125–136 (1977)

Landslide Hazard Assessment and Mitigation

Slope Stability Analysis Using In Situ Ground Reinforcement Techniques for a Landslide Prone Area at Madikere, India

J. Sumalatha

1   Introduction

The landslides due to seepage of water associated with extreme rainfall on soil slopes cause devastating natural disasters and destruction of a large range of resources [1–11]. The investigations conducted on landslides by various researchers revealed that the failures occur when the slope angle exceeds the critical angle of the slope or when the pore water pressure increases due to high levels of rainfall which causes reduction in the shear strength of soil [12–21]. From the correlation among the landslide occurrence and pore water pressure, it is noticeable that the presence of an undrained layer of soil multiplies the probability of landslides during excessive rainfall [22]. In the case of fine-grained soil slope, decrease in shear strength sourced by the loss of matric suction in the soil plays major role in slope failure [23]. Some research studies proved that shallow failures occur due to increase in positive pore water pressure and deep-seated failures mainly occurs due to a reduction in matric suction [24, 25].

The slope failure is progressive and become tough to control once it is started at one part of the slope [26]. Various kinds of losses occur due to a natural hazard, but much focus will be given to the losses related to buildings, roads, rail tracks, and other infrastructure [27–30]. But when rural areas are measured, the major losses are associated with agricultural fields which cause threat to the economic development of a country. During the risk analysis for any site subjected to natural hazard, the future damage will be considered as it provides the essential basis for strategies related to risk reduction and planning [31, 32]. In this regard, an attempt is made to identify the suitable ground improvement technique to avoid future landslides in this area. Four types of ground improvement techniques, i.e., anchors, nails, reinforcement, and anti-slide piles were studied to analyze their suitability

J. Sumalatha (✉)
Department of Civil Engineering, Ramaiah Institute of Technology, Bangalore, India

with respect to the soil properties. The analyses were carried out using the GEO5 software tool.

In certain conditions of construction, the anchored systems provide more advantages when compared with conventional systems both in economic and technical aspects. The anchor bond length should be chosen in such a way that it should intersect any potentially critical failure surfaces [33]. While designing the soil nail system for stabilizing slopes, the pullout resistance is more important than the shear resistance of the soil nail [7, 8]. The soil nail made of steel with a steel thickness of 2 mm should be coated with a layer of galvanized zinc to avoid rusting. In aggressive ground conditions, sometimes a high-density thermoplastic material is used as corrugated sheathing [34, 35]. Another feasible type of soil nails to stabilize slopes or excavation is the pipes made of glass fiber-reinforced polymer (GFRP). The various advantages with GFRP materials are corrosion resistance, low thermal stress, and more strength-to-weight ratio. However, it is to be noted that the GFRP soil nails suffer with the reduction in stiffness and fatigue potential [36].

The slope stability can be improved by installing piles along the slope, and as predictable, the factor of safety of the slope increases as the length of the pile increases, and it remains constant when the length of the pile reaches the critical length. Also, with decreasing pile spacing, the critical length increases, and the integrity of reinforced slopes increases with reduced pile spacing [37]. Reinforcement in the form of anti-sliding piles is a commonly applied measure for landslides those failed to meet the stability requirement [38]. The aim of this paper is to study the optimum sizes and spacings of materials required to implement the selected types of in situ ground reinforcement techniques. The slope stability analyses were carried out using five different methods, i.e., Bishop, Fellenius, Spencer, Janbu, and Morgenstern-Price, and the factors of safety (FoS) of the slopes were estimated.

2 Materials and Methods

2.1 Study Area

The study area is located at Makkandur, Kodagu district located in the Western Ghats of India. In 2018, high rainfall was recorded (2718 mm as per Karnatak State Natural Disaster Monitoring Center (KSNDM)). This caused severe landslides, flooding and large-scale displacement of soil. More than a thousand houses were destroyed, about five thousand people were displaced and at least 16 killed. To examine the in situ properties of the soil at the study area, the soil samples were collected from the site (Fig. 1) and tested in the laboratory. The slope angle and height of the slope were also measured. The slope angles are varying from 45° to 55°, and the heights of the slopes were ranging between 10 and 15.2 m. The analyses were carried out on slopes corresponding to 10 m height.

Fig. 1 Collection of soil samples at landslide affected area

Table 1 Properties of soil with and without additives

S. No.	Soil parameter	Value
1	Specific gravity	2.70
2	Plastic limit (%)	24.4
3	Liquid limit (%)	39.8
4	Plasticity index (%)	15.4
5	Shrinkage limit (%)	9.2
6	Maximum dry unit weight (kN/m^3)	18.89
7	OMC (%)	16.98
8	Unconfined compressive strength (q_u) (kN/m^2)	70.6
9	Undrained cohesion (Cu = q_u/2) (kN/m^2)	35.3
10	Shear strength parameters from triaxial test (UU test)	C^1 = 28 kN/m^2 $\emptyset^1$ = 22°

2.2 Properties of Soil

The index and engineering properties of soil samples were determined as per IS 2720. The in situ density and moisture content of the soil determined by core cutter method are 18.64 kN/m^3 and 25%, respectively. The in situ dry unit weight at the site is estimated as 14.91 kN/m^3. The soil composition is 0.75% gravel, 40.25% sand, and 59% fines. As per Indian Standard classification, it is classified as clay of intermediate plasticity (CI). The physical properties of soil are specified in Table 1.

2.3 Stability Analysis of Slopes

The soil slope was prepared using the interface option in GEO5 software tool (Fig. 2). The trial slip surface was drawn graphically, and critical slip surface was found using the 'optimization' option in the software. The analyses were carried out
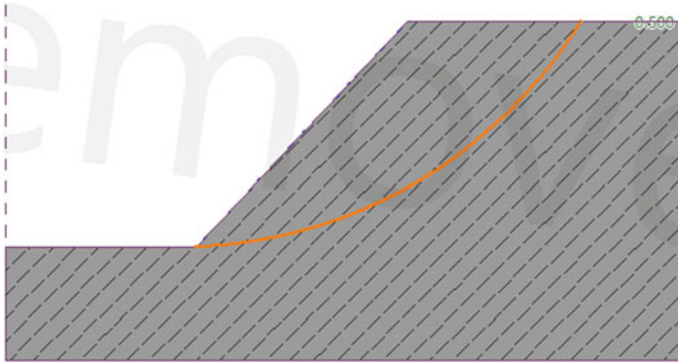
Fig. 2 Cross section of the slope with the slip surface

using five methods, i.e., Bishop, Fellenius, Spencer, Janbu, and Morgenstern-Price methods. The results showed that the slope is stable with respect to all the methods analyzed when the pore pressure effect is not taken. To introduce the effect of heavy rainfall in the study area, the pore pressure ratio (Ru) was taken as 0.5 and estimated the factors of safety. The estimated factors of safety of the slope with the pore pressure introduction were less than 1.5 for all the methods which indicates the instability of the slope. The results of stability analysis of the slope with and without the pore pressure consideration are shown in Figs. 3 and 4.
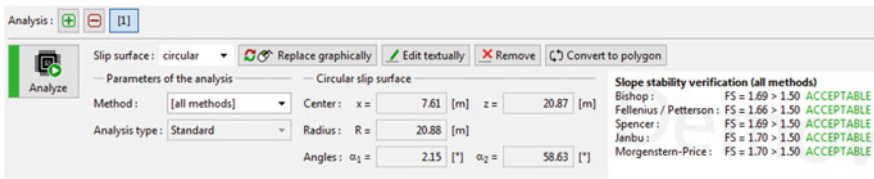
Fig. 3 Stability analysis without considering the pore pressure
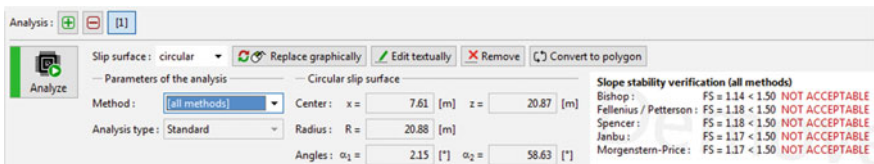
Fig. 4 Stability analysis by considering the pore pressure

3   Results and Discussion

3.1   Anchors as Ground Improvement Technique

The ground anchors were selected as the ground improvement technique, and the stability analysis with respect to the selected methods was carried out. The cross section of the slope and anchor details is given in Figs. 5 and 6. The results of stability analysis are shown in Fig. 7.

From Fig. 7, it can be observed that the stability analysis could not be performed with Spencer method, and hence, the method was analyzed separately by using optimization technique for the critical slip surface. Figures 8 and 9 show the critical slip surface obtained by optimization and the result of stability analysis. Hence, it can be concluded that the slope is stable with the selected arrangement of ground anchors.
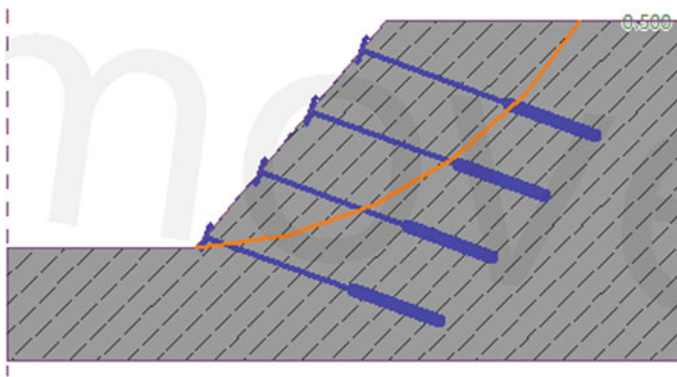
Fig. 5   Cross section of the slope with ground anchors

No. ▲	Origin		Free length	Root length	Slope	Anchor spacing	Force
	x [m]	z [m]	l [m]	l_k [m]	α [°]	b [m]	F [kN]
1	15.73	8.75	7.00	4.00	20.00	2.00	200.00
2	13.46	6.04	7.00	4.00	20.00	2.00	200.00
3	11.19	3.34	7.00	4.00	20.00	2.00	200.00
4	8.78	0.47	7.00	4.00	20.00	2.00	200.00

Fig. 6   Details of the ground anchors used for the study
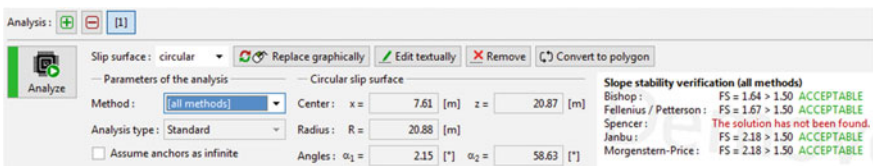
Fig. 7   Stability analysis of slope with the ground anchors
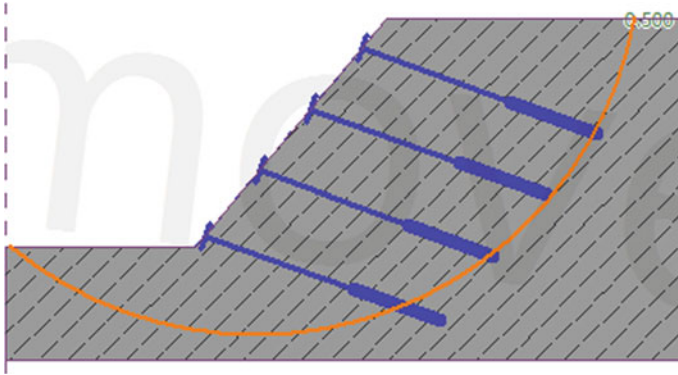
Fig. 8 Critical slip surface obtained by optimization option in Spencer method
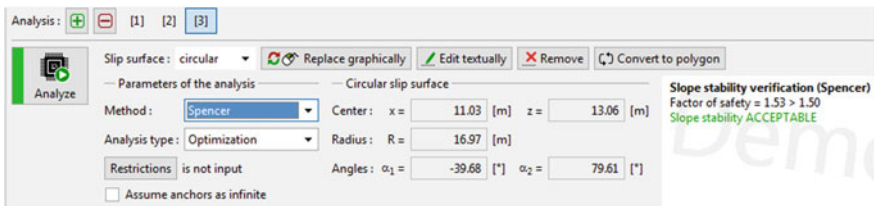
Fig. 9 Stability analysis of slope with ground anchors using Spencer's method

3.2 Nails as Ground Improvement Technique

The soil nails to improve the slope stability was evaluated for the site conditions. The cross section of the slope with soil nails is shown in Fig. 10. The results of stability analyses are shown in Fig. 11 where the slope is stable with the soil nails provided. The length and spacing of soil nails provided are 10 and 1 m, respectively, with an inclination of 150. The tensile strength, pull out resistance, and nail head strength of the nails were assumed as 100 kN, 50 kN, and 15 kN, respectively.

3.3 Reinforcement with Metal Bars as Ground Improvement Technique

The stability of the slope with soil reinforcement using metal bars was studied. The arrangement and details of the reinforcement are shown in Figs. 12 and 13. The output of the analyses is shown in Fig. 14.
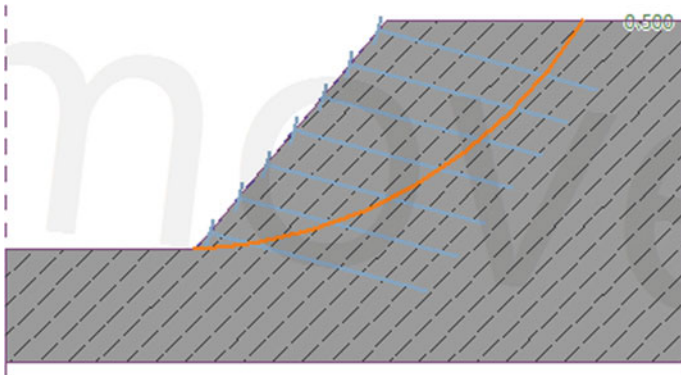
Fig. 10 Cross section of the slope with soil nails
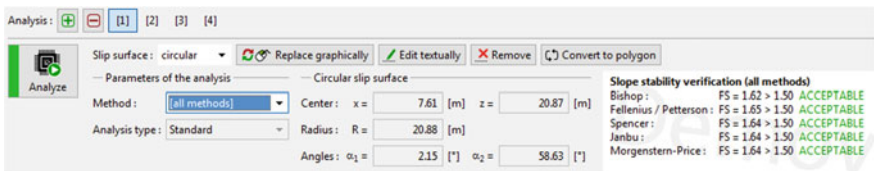
Fig. 11 Stability analysis of slope with soil nails
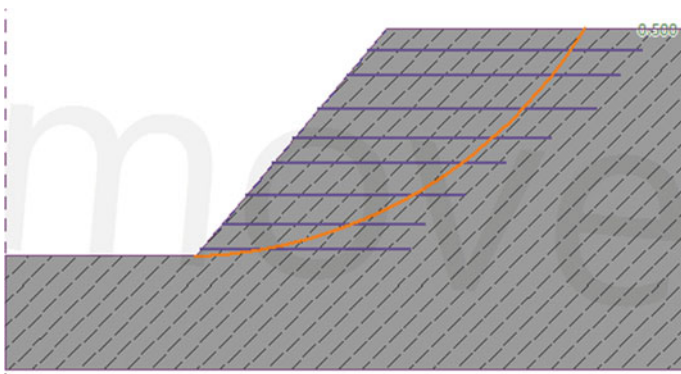
Fig. 12 Cross section of the slope reinforced with metal bars

3.4 Anti-slide Piles as Ground Improvement Technique

The piles of assumed diameter and spacing were analyzed using the 'pile verification' option given in the software tool, and thus, the load bearing capacity was estimated. The stability analysis was then carried by giving the estimated bearing

No. ▲	Point to the left		Point to the right		Length	Tensile strength	Pull out resistance	End of
	x [m]	z [m]	x [m]	z [m]	L [m]	R_t [kN/m]		reinf.
1	15.98	9.05	28.00	9.05	12.02	40.00	C = 0.70	Fixed
2	15.06	7.95	27.00	7.95	11.94	40.00	C = 0.70	Fixed
3	13.82	6.47	26.00	6.47	12.18	40.00	C = 0.70	Fixed
4	12.74	5.18	24.00	5.18	11.26	35.00	C = 0.70	Fixed
5	11.82	4.09	22.00	4.09	10.18	35.00	C = 0.70	Fixed
6	10.63	2.67	20.18	2.67	9.55	35.00	C = 0.70	Fixed
7	9.62	1.38	18.44	1.38	8.82	35.00	C = 0.70	Fixed
8	8.63	0.29	17.80	0.29	9.17	35.00	C = 0.70	Fixed

Fig. 13 Details of the reinforcement used for the study
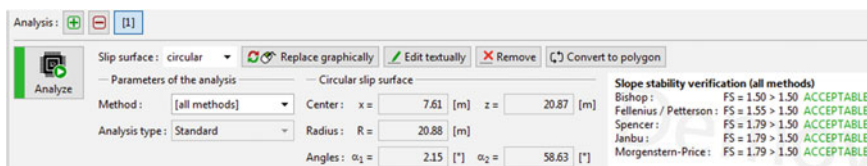
Fig. 14 Stability analysis of slope with reinforcement
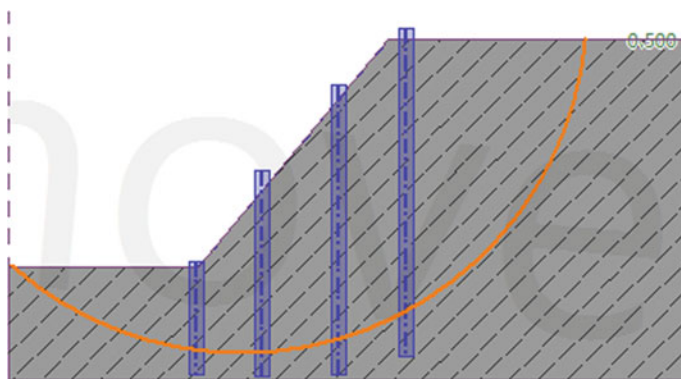
Fig. 15 Cross section of the slope with anti-slide piles

capacity of the piles as an input parameter. The diameter and spacing of the piles are 800 mm and 900 mm, respectively. The estimated bearing capacity of these piles is 137 kN. The pile lengths are in the range of 5–15 m and are extended beyond the critical slip surface. The cross section of the slope with anti-slide piles and the results of stability analyses, respectively, are shown in Figs. 15 and 16.

The estimated factors of safety using various methods gave the optimum sizes and spacings of the in situ reinforcement. Hence, it is evident that the selected methods of in situ ground reinforcement are effective in improving the stability of
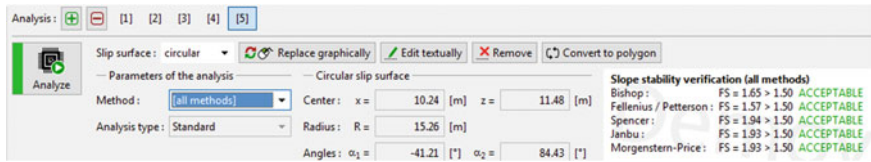
Fig. 16 Stability analysis of slope with anti-slide piles

soil slopes in the study area. As these methods are expensive, they can be used for limited areas such as residential areas. For agricultural fields, it is better to use terrace farming technique to avoid the effects of landslides.

4   Conclusions

The landslide prone area located at Makkandur, Karnataka State, India was studied to know the effect of in situ ground reinforcement on the stability of existing slopes at this location. The stability methods used for this study are Bishop, Fellenius, Spencer, Janbu, and Morgenstern-Price. The in situ ground improvement techniques adopted for this study are ground anchors, soil nails, reinforcement with metal bars, and anti-slide piles. The factors of safety were estimated for 10 m height slope using GEO5 software tool. The in situ soil properties were given as input to the software along with the trial values of reinforcement systems. The factors of safety were estimated with different trial values, and thus, the optimum sizes of the reinforcement were estimated. The optimum spacings of ground anchors obtained for 10 m height slope are 2 m. The soil nails with pullout resistance of 50 kPa and 1 m spacing gave optimal results. The reinforcement with 40 kN/m tensile strength and 1 m spacing shown satisfactory results. The optimal results with anti-slide piles were obtained with 650 mm diameter piles spaced 0.9 at 0.9 m center to center. The stability analyses carried out are useful to select the suitable reinforcement technique and their arrangement at the site to improve the slope stability. Thus, this research work is helpful to design the in situ ground reinforcement techniques at the area studied to avoid landslides in the future.

References

1. Sassa K.: Analysis on slope stability: II. Mainly on the basis of the indoor experiments using the standard sand produced in Toyoura, Japan. J. Jpn. Soc. Erosion Control Eng. **26**(3), 8–19 (1974)
2. Sassa K.: The mechanism starting liquefied landslides and debris flows. In: Proceedings of 4th International Symposium on Landslides, Toronto, Canada, vol. 2, pp. 349–354 (1984)
3. Zêzere, J.L., Garcia, R.A.C., Oliveira, S.C., Reis, E.: Probabilistic landslide risk analysis considering direct costs in the area north of Lisbon (Portugal). Geomorphology **94**, 467–495 (2008)

4. Chang, K., Chiang, S.: An integrated model for predicting rainfall-induced landslides. Geomorphology **105**, 366–373 (2009)
5. Petley, D.: Global patterns of loss of life from landslides. Geology **40**, 927–930 (2012)
6. Shokouhi, A., Gratchev, I., Kim, D.: Rock slope stability problems in Gold Coast area, Australia. Int J Geomate **4**(1), 501–504 (2013)
7. Kim, H.D., Gratchev, I., Balasubramaniam, A.: Determination of joint roughness coefficient (JRC) for slope stability analysis; a case study from the Gold Coast area, Australia. Landslides **10**(5), 657–664 (2013)
8. Kim, Y., Lee, S., Jeong, S., Kim, J.: The effect of pressure-grouted soil nails on the stability of weathered soil slopes. Comput. Geotech. **49**, 253–263 (2013)
9. Promper, C., Glade, T.: Multilayer-exposure maps as a basis for a regional vulnerability assessment for landslides: applied in Waidhofen/Ybbs. Austria. Nat. Hazards **82**, 111–127 (2016)
10. Peruccacci, S., Brunetti, M., Gariano, S., Melillo, M., Rossi, M., Guzzetti, F.: Rainfall thresholds for possible landslides occurrence in Italy. Geomorphology **290**, 39–57 (2017)
11. Salvati, P., Petrucci, O., Rossi, M., Bianchi, C., Pasqua, A.A., Guzzetti, F.: Gender, age and circumstances analysis of flood and landslide fatalities in Italy. Sci. Total Environ. **610–611**, 867–879 (2018)
12. Bishop, A.W.: The influence of an undrained change in stress on the pore pressure in porous media of low compressibility. Géotechnique **23**(3), 435–442 (1973)
13. Brand, E.W., Premchitt, J., Phillipson, H.B.: Relationship between rainfall and landslides in Hong Kong. In: Proceedings of 4th International Symposium on Landslides, Downsview, Ontario, Canada, pp. 377–384 (1984)
14. Craig, R.F.: Craig's Soil Mechanics. New Fetter Lane, London (2004)
15. Chien-Yuan, C., Tien-Chien, C., Fan-Chieh, Y., Wen-Hui, Y., Chun-Chieh, T.: Rainfall duration and debris-flow initiated studies for real-time monitoring. Environ. Geol. **47**(5), 715–724 (2005)
16. Dahal, R., Hasegawa, S.: Representative rainfall thresholds for landslides in the Nepal Himalaya. Geomorphology **100**, 429–443 (2008)
17. Gui, M., Han, K.: A case study on rainfall infiltration effect on the stability of two slopes. In: Landslides and Engineering Slopes, pp. 1737–1743 (2008)
18. Larsen, M., Simon, A.: A rainfall intensity–duration threshold for landslides in a humid-tropical environment. Puerto Rico. Geografiska Annaler. Ser. A. Phys. Geogr. **75**, 13–23 (1993)
19. Niroumand, H., Kassim, K.A., Ghafooripour, A., Nazir, R., Far, S.Y.Z.: Investigation of slope failures in soil mechanics. Electron J Geotech Eng **17**, 2703–2718 (2012)
20. Tay, J.E., Selaman, O.S.: A study on the rainfall and landslide along Sarawak Road using antecedent rainfall analysis (2019)
21. Tsaparas, I., Rahardjo, H., Toll, D., Leong, E.: Controlling parameters for rainfall-induced landslides. Comput. Geotech. **29**, 1–27 (2002)
22. Cogan, J., Gratchev, I: A study on the effect of rainfall and slope characteristics on landslide initiation by means of flume tests. Landslides **16**(12), 2369–2379 (2019)
23. Acharya, K.P., Bhandary, N.P., Dahal, R.K., Yatabe, R.: Seepage and slope stability modelling of rainfall-induced slope failures in topographic hollows. Geomat. Nat. Haz. Risk **7**(2), 721–746 (2016)
24. Corominas, J.: Landslides and climate. In: Keynote Lectures from the 8th International Symposium on Landslides, vol. 4, pp. 1–33 (2000)
25. Guzzetti, F., Cardinali, M., Reichenbach, P., Cipolla, F., Sebastiani, C., Galli, M., Salvati, P.: Landslides triggered by the 23 November 2000 rainfall event in the Imperia Province, Western Liguria, Italy. Eng. Geol. **73**(3–4), 229–245 (2004)
26. Wang, G., Sassa, K.: Pore-pressure generation and movement of rainfall-induced landslides: effects of grain size and fine-particle content. Eng. Geol. **69**(1), 109–125 (2003)

27. Del Soldato, M., Bianchini, S., Calcaterra, D., De Vita, P., Di Martire, D., Tomás, R.: A new approach for landslide-induced damage assessment. Geomat. Nat. Hazards Risk **8**, 1524–1537 (2017)
28. Calò, F., Calcaterra, D., Iodice, A., Parise, M., Ramondini, M.: Assessing the activity of a large landslide in southern Italy by ground-monitoring and SAR interferometric techniques. Int. J. Remote Sens. **33**, 3512–3530 (2012)
29. Calcaterra, D., Ramondini, M., Calò, F., Longobardi, V., Parise, M., Galzerano, C.M.: DInSAR techniques for monitoring slow-moving landslides. In: Cheng, Z., Zhang, J., Li, Z., Wu, F., Ho (Xi'an), K. (Eds.) Landslides and Engineered Slopes, Proceedings of the 10th International Symposium on Landslides, pp. 1095–1101 (2008)
30. Iovine, G., Parise, M.: Schema classificativo per il rilievo dei danni da frana in aree urbane. Mem. Soc. Geol. Ital. **57**, 595–603 (2002)
31. Van Westen, C.J., Asch, T.W.J., Soeters, R.: Landslide hazard and risk zonation—why is it still so difficult? Bull. Eng. Geol. Environ. **65**, 167–184 (2006)
32. Vranken, L., Van Turnhout, P., Van Den Eeckhaut, M., Vandekerckhove, L., Poesen, J.: Economic valuation of landslide damage in hilly regions: a case study from Flanders, Belgium. Sci. Total Environ. **447**, 323–336 (2013)
33. Sabatini, P.J., Pass, D.G., Bachus, R.C.: Ground anchors and anchored systems (No. FHWA-IF-99–015). United States. Federal Highway Administration. Office of Bridge Technology (1999)
34. Geotechnical Engineering Office (GEO).: Good practice in design of steel soil nails for soil cut slopes. GEO Technical Guidance Note No. 23, Civil Engineering and Development Dept., Government of Hong Kong Special Administrative Region, Hong Kong (2005)
35. Geotechnical Engineering Office (GEO).: Guide to soil nail design and construction. Geoguide 7, Civil Engineering and Development Dept., Government of Hong Kong Special Administrative Region, Hong Kong (2008)
36. Zhu, H.H., Yin, J.H., Yeung, A.T., Jin, W.: Field pullout testing and performance evaluation of GFRP soil nails. J. Geotech. Geoenviron. Eng. **137**(7), 633–642 (2011)
37. Yang, S., Ren, X., Zhang, J.: Study on embedded length of piles for slope reinforced with one row of piles. J. Rock Mech. Geotech. Eng. **3**(2), 167–178 (2011)
38. Nie, Z., Zhang, Z., Zheng, H.: Slope stability analysis using convergent strength reduction method. Eng. Anal. Boundary Elem. **108**, 402–410 (2019)

Landslide Susceptibility Mapping Using GIS-Based Frequency Ratio Approach in Part of Kullu District, Himachal Pradesh, India

Baboo Chooreshwarsingh Sujeewon and Raju Sarkar

1 Introduction

Landslide, a type of mass wasting, is defined as the downslope movement of slope forming materials by gravitational force.

Landslide occurrences in Himachal Pradesh have increased due to extreme climatic conditions coupled with rise in man-made activities which can be attributed to the high surge in tourism, hydropower generation, industrialization and road construction in the area ([3]). These catastrophic events entail severe socio-economic impact [9] through disruption of local businesses in terms of road blockage, destruction to infrastructure and loss of human life. Landslide susceptibility analysis is one important pre-hazard management tools used to delineate an area according to its degree of susceptibility to landslide incidence [6].

The most common susceptibility mapping approaches adopted by researchers are broadly classified as heuristic, statistic, deterministic and hybrid.

Heuristic approach (also known as knowledge-driven or qualitative) can be direct or indirect in nature, relying on knowledge of experts for geomorphological mapping or weight assignment of landslide causative factors thereby introducing a degree of subjectivity, whereas statistical (also known as data-driven or quantitative) approach can be grouped as bi-variate [4] and multi-variate methods, both based on the assumption that the combination of past and present landslides contributing factors aid in predicting future slides under the same condition [2].

Bi-variate approaches such as frequency ratio, information value, weight of evidence, etc., rely on the association of each parameter class to past landslide

B. C. Sujeewon (✉) · R. Sarkar
Delhi Technological University, New Delhi, India
e-mail: sujeewon_mt2k19@dtu.ac.in

R. Sarkar
e-mail: rajusarkar@dce.ac.in

occurrence instead of relative weight determination between factors [11] compared to multi-variate methods.

This paper is an attempt to delineate regions in the study area based on their proneness to landslides through a frequency ratio (FR) based landslide suscepti-bility mapping using geographical information system (GIS) environment and to understand the spatial link between the nine considered landslide-inducing factors with the updated landslide inventory. This inter-relationship can reveal patterns unique to the geographical area for better evaluation of landslide occurrences.

2 Study Area

The district of Kullu, one of the twelve districts of the state of Himachal Pradesh is bounded between 31° 20′ to 32° 26′ East and 76° 56′ to 77° 52′ North and located in the north-western Himalayan region of India as shown in Fig. 1. Bordering the district concerned are the districts of Lahaul and Spiti (North and North-east), Kangra (North-west), Kinnaur (South-east), Shimla (South and South-east) and Mandi (South-west to West). It includes four tehsils (Manali, Kullu, Banjar and Nirmand) and two sub-tehsils (Sainj and Anni) with an average annual rainfall of 1405.7 mm.
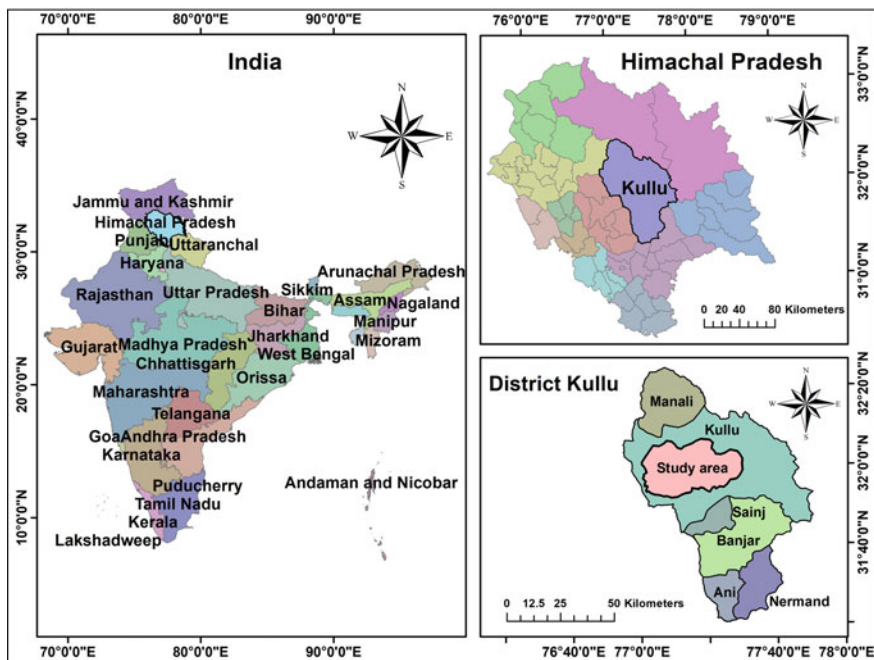
Fig. 1 Locator map of study area
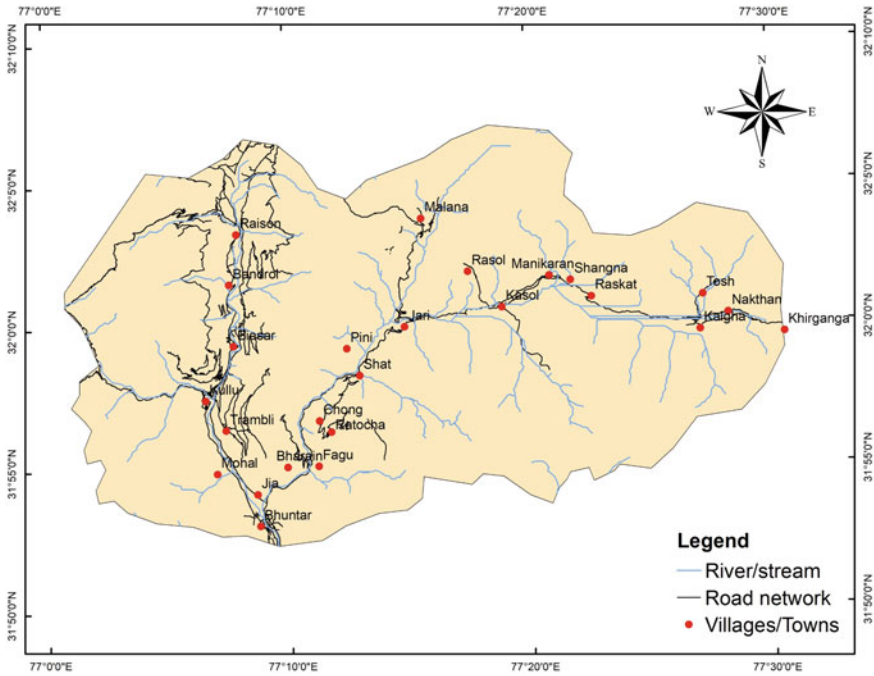
Fig. 2 Study area

The research area (part of the Kullu tehsil) as depicted in Fig. 2, covers an area of around 1000 km^2 with elevation ranging from 1050 to 4900 m. It is accessible by flight through the nearest airport at Bhuntar or by land through the major road networks in the area which are the national highway NH-3 and the major district roads of Kullu-Nagar-Manali and Jia-Manikaran.

Kullu and Kasol-Manikaran valleys run along the Beas and Parvati River attracting a considerable number of tourists with important and famous places like Kullu, Bhuntar, Malana, Kasol, Tosh, Khirganga.

3 Methodology

The adopted methodology in this study constitutes: (a) preparation of a compiled landslide incidence map; (b) selection of landslide-inducing factors and thematic maps generation; (c) frequency ratio calculation for each factor class; (d) landslide susceptibility index evaluation for each factor; (e) creation and classification of the final landslide susceptibility map; (f) model validation through the Area Under Curve (AUC) and Landslide Density Index (LDI) methods.

4 Data Preparation

Factors such as slope, aspect, curvature and drainage network were extracted using different tools from CartoSAT-1 DEM (spatial resolution of about 30 m) obtained from the web-based platform of Bhuvan, Indian Space Research Organization (ISRO), National Remote Sensing Centre (NRSC), Hyderabad.

Digital shape files for faults, lineaments, past landslides and lithology were obtained from Bhukosh, Geological Survey of India (GSI) and shape file for road network in the area was retrieved from Open Street Map website.

Landsat-8 images were obtained from the Earth Explorer, U.S. Geological Survey (USGS) for land use and land cover classification.

4.1 Landslide Inventory

Past landslide inventory for the study area was obtained from past literatures and Bhukosh web-platform of the Geological Survey of India (GSI) as shown in Fig. 3a. Clustering of most historical data near the Kullu-Bhuntar led to the creation of a new landslide inventory near the Parvati valley area through visual interpretation of high-resolution satellite imagery from Google Earth for the year 2002–2019. Change in vegetation and the presence of debris material were amongst the main criteria used for landslide mapping using Google Earth historical images [5].

Landslide scars can be rapidly lost or obscured with time due to excess vegetation, remediation works, etc. The use of scarp identification and contour connection method (SICCM) toolbox was made for semi-automatic scarp delineation of some obscured landslide features [2].

The compiled landslide incidence shape file consisting of 211 total mapped landslide polygons was resampled in cell resolution of 30×30 m for further processing. Random splitting of samples into training ($70\% \approx 147$ no.) and validating ($30\% \approx 64$ no.) datasets were done using a geostatistical analyst tool as shown in Fig. 3(b). Ground truthing for the newly mapped landslide locations was not carried out due to remoteness and travel limitation.

4.2 Thematic Maps Preparation

Nine causative factors were selected based on past literatures in the area and data availability. Nine thematic layers were then prepared in a GIS environment as in Figs. 4 and 5 for correlation analysis with landslide occurrence using the frequency ratio-based statistical method.
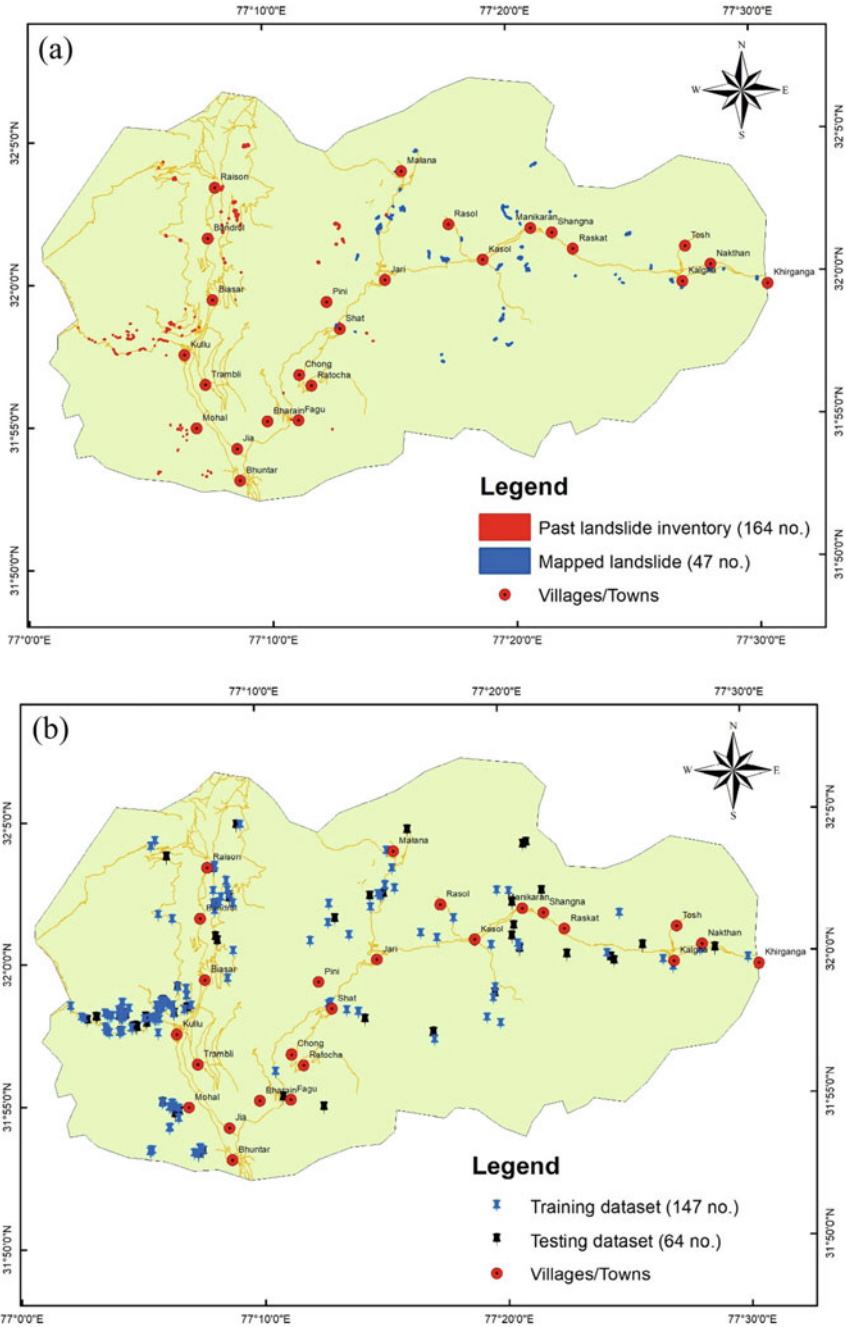
Fig. 3 Landslide inventory: **a** Past and updated inventory. **b** Training and testing datasets
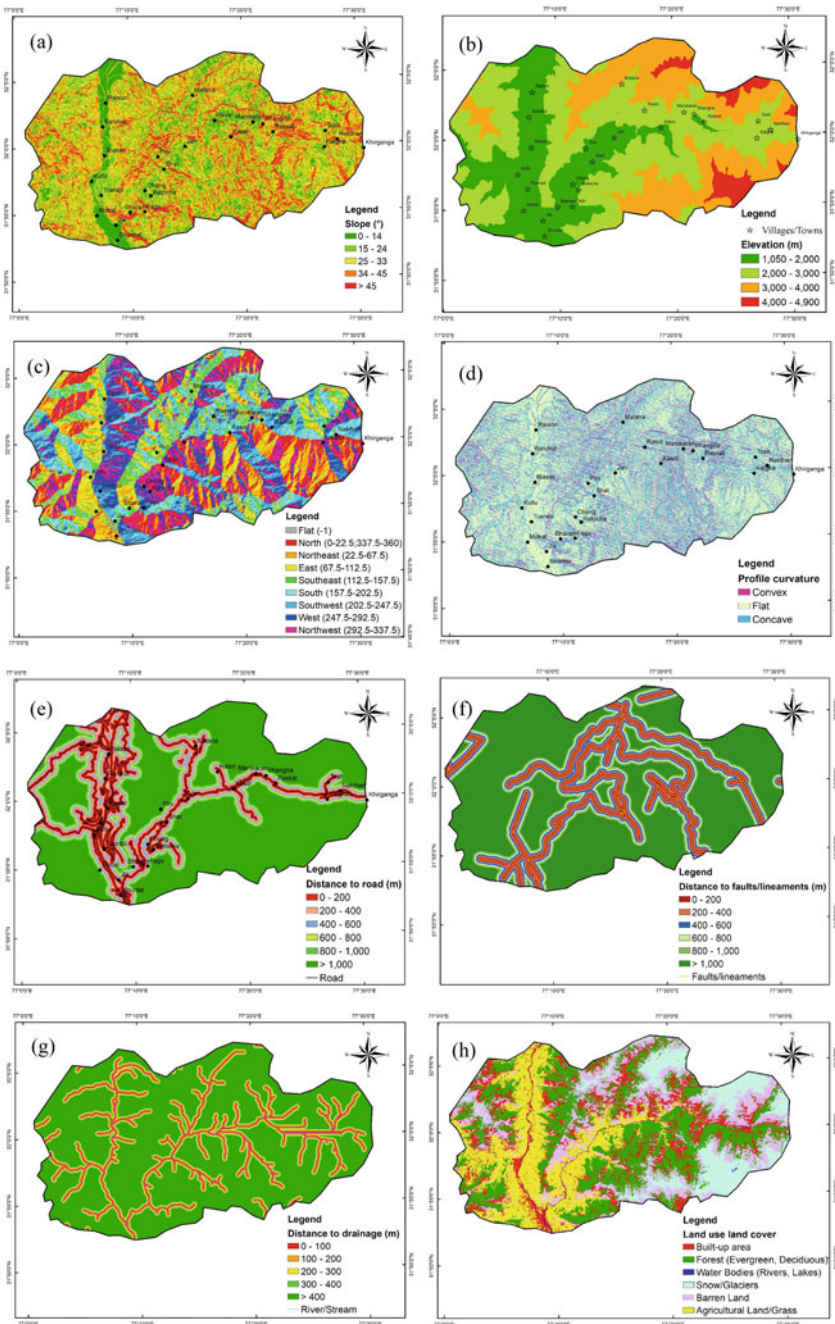
Fig. 4 **a** Slope map. **b** Elevation map. **c** Aspect map. **d** Profile curvature map. **e** Distance to road map. **f** Distance to faults/lineaments map. **g** Distance to drainage map. **h** Land use land cover map

Slope.

Slope map depicts the angle of slope of a particular area and is directly related to slope instability [2].

The slope map is derived from the CartoSAT-1 Digital Elevation Model (DEM) using surface (spatial analyst) tools in GIS platform. The resulting map is reclassified into five distinct classes namely 0°–14°, 15°–24°, 25°–33°, 34°–45°, >45° as in Fig. 4a.

Aspect.

The aspect map (Fig. 4c) indicates the facing direction of slopes. The direction faced by the slope is measured and classified from the DEM clockwise starting North at 0° back to North at 360° using the aspect tool in GIS platform. Flat areas (no slope and aspect) are denoted by grey cells with value –1.

Different slope orientations are exposed to different amount of direct sunlight and wind exposure along with other factors affecting vegetation type, vegetation density, soil moisture index, etc.

Curvature.

The profile curvature map derived from the DEM using curvature (spatial analyst) tool, indicates the degree of convexity/concavity of surfaces and also influences the acceleration/deceleration rate of surficial flows.

The resulting map has three classes with negative values (<–0.05) for convex surfaces, positive values (>0.05) for concave surfaces and near zero values (–0.05 to 0.05) for linear surfaces as in Fig. 4d.

Distance to drainage.

The distance to drainage map was created using the hydrology tools for stream order generation from the DEM and then the Euclidean distance tool was used for buffer at intervals of 100 m from stream network. The resulting map was divided into five distinct classes namely 0–100 m, 100–200 m, 200–300 m, 300–400 m and >400 m as in Fig. 4g.

Changes in the surface water levels along rivers affects slope saturation along the banks, pore water pressure and internal strength of slope forming material due to infiltration. High-rainfall intensity is followed by high-river discharge capacity causing bank erosion.

Elevation.

Elevation indirectly affects landslide occurrences since it influences other important factors such as vegetation type, rainfall intensity, temperature, wind exposure, etc.

Triangulated irregular networks (TIN) were generated from contour lines of the area before being converted and classified into the final elevation raster with four groups; 1050–2000 m, 2000–3000 m, 3000–4000 m and 4000–4900 m as in Fig. 4b. Human intervention is scarce at higher elevations (>4000 m) with lesser extent of land available and the presence of snow/glaciers all year round.
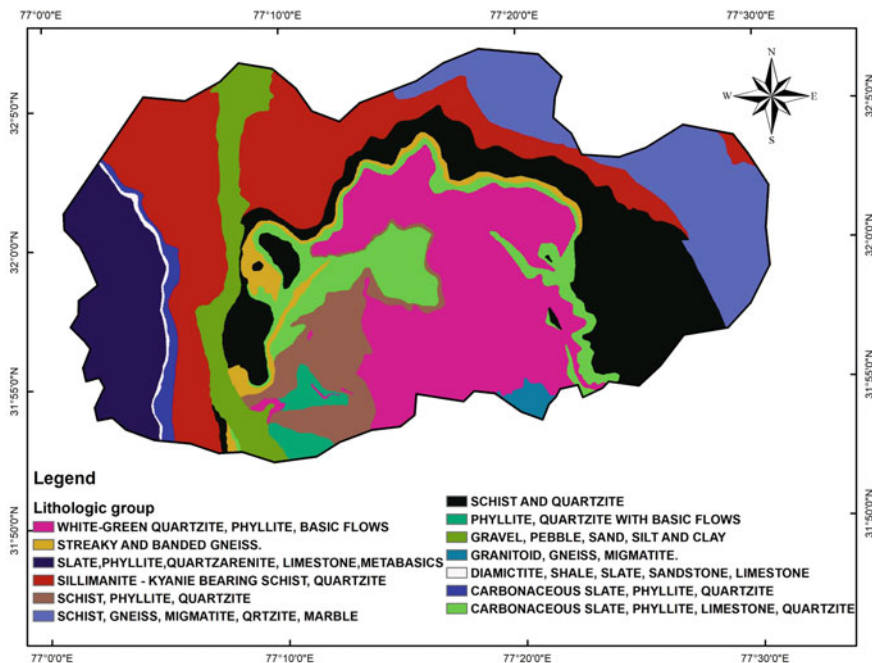
Fig. 5 Lithology map

Lithology.

The structure, strength, composition and plasticity potential for each unit are different [7], hence their individual influence on landslide incidence need to be evaluated.

The lithology digital shape file was rasterized and resampled to cell resolution of 30×30 m with a total of thirteen lithological units in the area as shown in Fig. 5.

Land use/land cover.

The Land use land cover (LULC) map was derived from Landsat-8 OLI/TRS images (courtesy of the United States Geological Survey (USGS) Earth Explorer) taken in October 2017 with cloud cover less than 10%. A supervised classification was performed using the Interactive supervised classification tool after selecting and merging training samples from the study area for each class. The five resulting classes are built-up area, agricultural land, barren land, forest (evergreen, deciduous), snow/glaciers and water bodies.

LULC map (Fig. 4h) can be associated to landslide occurrences since it illustrates the extent of human activity, agricultural land use, degree of deforestation amongst others.

Distance from faults/lineaments.

Landslides are more likely to occur in faulted and fractured regions which leads to inhomogeneity thereby reducing their stability and strength.

Buffer zones at interval of 200 m were created from the merged faults/lineaments shape file. The resulting map (Fig. 4f) was rasterized with 30 m cell resolution and reclassified into six categories namely 0–200 m, 200–400 m, 400–600 m, 600–800 m, 800–1000 m and >1000 m.

Distance to roads.

Road widening and construction in hilly areas often lead to vegetation removal, change in drainage pattern and alteration to slope profiles through slope-cutting process, all contributing to slope instability [12]. The road networks considered for analysis in the area consists of national highway, major district roads and local roads to better assess the spatial relationship between road network and landslide occurrence.

The resulting map was rasterized with 30 m cell resolution and reclassified into six categories with 200 m buffering intervals namely 0–200 m, 200–400 m, 400–600 m, 600–800 m, 800–1000 m and >1000 m.

5 Frequency Ratio Statistical Method

Frequency ratio, a data-driven statistical approach adopted in this study, has been used and validated by many researchers [1, 6, 8]. A table was created for all the nine landslide causative factors considered along with each of their classes.

The tabulate area tool was used to find out the pixel-wise contribution of every factor class to the training dataset of the updated landslide inventory for the calculation of frequency ratios (FR) as per Eq. (1).

$$\text{FR} = \frac{P_L / \sum_{i=1}^{n} P_L}{P_C / \sum_{i=1}^{n} P_C} \tag{1}$$

where

P_L = Landslide pixels in a particular class.

$\sum_{i=1}^{n} P_L$ = Sum of all landslide pixels covering the area.

P_C = Pixels of a particular class.

$\sum_{i=1}^{n} P_C$ = Sum of all pixels covering the area.

Values above unity signify high correlation, whereas values less than unity demonstrate low correlation. The results are summarized in Table 1.

The FR values were then used for the reclassification of each of the nine causative thematic maps in the GIS platform for the final susceptibility map preparation using the Landslide Susceptibility Index (LSI) values [11] computed as per Eq. (2).

$$LSI = \left(FR_{Slo} + FR_{Asp} + FR_{Curv} + FR_{Lulc} + FR_{Lith} + FR_{Ele} + FR_{D_R} + FR_{D_D} + FR_{D_{F/L}} \right)$$
(2)

where

FR_{Slo}, FR_{Asp},… = Sum of frequency ratios of each factor.

The final landslide susceptibility map was created using the Raster Calculator tool and reclassified into five categories using Natural Jenks break method namely very low, low, moderate, high and very high as in Fig. 6.

6 Results and Discussions

The Landslide Density Index (LDI) was computed as per Eq. (3) for each susceptibility class to evaluate the quality of produced landslide susceptibility map [13]. The increasing order of LDI (Table 2) imply that the frequency of landslide occurrence increases with increasing (very low to very high) susceptibility class.

$$LDI = \frac{\% \text{ landslide pixels in susceptibility class}}{\% \text{ class pixels in susceptibility class}}$$
(3)

Receiver operator characteristics (ROC) method was then used to assess the fitness and prediction accuracy of the model through the Area Under Curve (AUC) of the success rate curve and the prediction rate curve [10, 11] using the sampled training (70%) and validation (30%) datasets, respectively.

The computed AUC of the success rate curve (Fig. 7) and the prediction rate curve (Fig. 8) were 0.873 and 0.803, respectively, as shown in Fig. 5. This indicates that the model had 87.3% training accuracy and 80.3% prediction accuracy.

The fitness and prediction accuracy of this frequency ratio-based model were considered reasonable.

The frequency ratios computed as in Table 1 gives an insight about the landslide distribution in each factor class.

Table 1 Frequency ratio results for the nine factors considered

Land use land cover	Class pixels	% Class pixels	Landslide pixels	% Landslide pixels	FR
Built up	146,846	0.14516	23,400	0.17687	1.21842
Forest	308,834	0.3053	9900	0.07483	0.24511
Water Body	4629	0.00458	900	0.0068	1.48662
Snow/Glaciers	123,809	0.12239	1800	0.01361	0.11116
Barren Land	203,861	0.20153	15,300	0.11565	0.57385
Agricultural Land/Grass	223,609	0.22105	81,000	0.61224	2.76974
Slope (°)	Class pixels	% Class pixels	Landslide pixels	% Landslide pixels	FR
0–14	137,223	0.12973	5400	0.04082	0.31462
15–24	261,701	0.24741	18,900	0.14286	0.57741
25–33	321,808	0.30424	44,100	0.33333	1.09564
34–45	241,211	0.22804	49,500	0.37415	1.64071
>45	95,810	0.09058	14,400	0.10884	1.20164
Aspect	Class pixels	% Class pixels	Landslide pixels	% Landslide pixels	FR
Flat	87	0.00008	0	0	0
North	64,632	0.06111	8100	0.06122	1.00184
Northeast	125,781	0.11893	17,100	0.12925	1.08678
East	132,831	0.1256	20,700	0.15646	1.24576
Southeast	121,512	0.11489	19,800	0.14966	1.30259
South	121,435	0.1153	29,700	0.22449	1.94696
Southwest	156,412	0.11482	14,400	0.10884	0.94794
West	156,412	0.14789	14,400	0.10884	0.73596
Northwest	146,739	0.13875	4500	0.03401	0.24515
North	66,228	0.06262	3600	0.02721	0.43453
Profile curvature	Class pixels	% Class pixels	Landslide pixels	% Landslide pixels	FR
Convex	113,351	0.10555	16,200	0.12245	1.16009
Flat	669,252	0.6232	72,900	0.55102	0.88418
Concave	291,289	0.27125	43,200	0.32653	1.20382
Distance to road (m)	Class pixels	% Class pixels	Landslide pixels	% Landslide pixels	FR
0–200	138,618	0.13702	67,500	0.5102	3.72347
200–400	87,959	0.08695	6300	0.04762	0.54768
400–600	71,444	0.07062	3600	0.02721	0.3853

(continued)

Table 1 (continued)

Distance to road (m)	Class pixels	% Class pixels	Landslide pixels	% Landslide pixels	FR
600–800	59,745	0.05906	5400	0.04082	0.69112
800–1000	54,078	0.05346	11,700	0.08844	1.65435
>1000	599,789	0.59289	37,800	0.28571	0.4819
Distance to faults/ lineaments (m)	Class pixels	% Class pixels	Landslide pixels	% Landslide pixels	FR
0–200	95,610	0.09451	8100	0.06122	0.64781
200–400	87,818	0.08681	12,600	0.09524	1.09711
400–600	82,262	0.08132	9900	0.07483	0.92024
600–800	72,002	0.07117	4500	0.03401	0.47789
800–1,000	68,400	0.06761	11,700	0.08844	1.30796
>1000	605,541	0.59858	85,500	0.64626	1.07966
Distance to drainage (m)	Class pixels	% Class pixels	Landslide pixels	% Landslide pixels	FR
0–100	82,554	0.0861	15,300	0.11565	1.41715
100–200	69,486	0.06869	18,900	0.14286	2.07983
200–300	74,861	0.074	7200	0.05442	0.73543
300–400	61,776	0.06107	8100	0.06122	1.0026
>400	722,956	0.71464	82,800	0.62585	0.87575
Elevation (m)	Class pixels	% Class pixels	Landslide pixels	% Landslide pixels	FR
1050–2000	264,717	0.2603	101,700	0.76871	0.83979
2000–3000	430,533	0.42335	28,800	0.21769	0.14622
3000–4000	281,431	0.27674	1800	0.01361	0.05916
4000–4900	40,277	0.03961	0	0	0
Lithology	Class pixels	% Class pixels	Landslide pixels	% Landslide pixels	FR
Schist and quartzite	159,066	0.15724	8100	0.06122	0.38938
Carbonaceous slate, phyllite, limestone, quartzite	74,580	0.07372	1800	0.01361	0.18455
Carbonaceous slate, phyllite, quartzite	13,122	0.01297	0	0	0
Diamictite, shale, slate, sandstone, limestone	4463	0.00441	0	0	0
Sillimanite—kyanie bearing schist, quartzite	204,013	0.20167	60,300	0.45578	2.26007
White-green quartzite, phyllite, basic flows	197,575	0.1953	18,900	0.14286	0.73146

(continued)

Table 1 (continued)

Lithology	Class pixels	% Class pixels	Landslide pixels	% Landslide pixels	FR
Streaky and banded gneiss	23,534	0.02326	3600	0.02721	1.16969
Phyllite, quartzite with basic flows	13,721	0.01356	0	0	0
Schist, gneiss, migmatite, quartzite, marble	116,964	0.11562	2700	0.02041	0.17651
Schist, phyllite, quartzite	57,587	0.05692	4500	0.03401	0.59752
Slate, phyllite, quartzarenite, limestone, metabasics	87,693	0.08668	28,800	0.21769	2.51125
Granitoid, gneiss, migmatite	5695	0.00563	0	0	0
Gravel, pebble, sand, silt and clay	53,620	0.053	3600	0.02721	0.51338
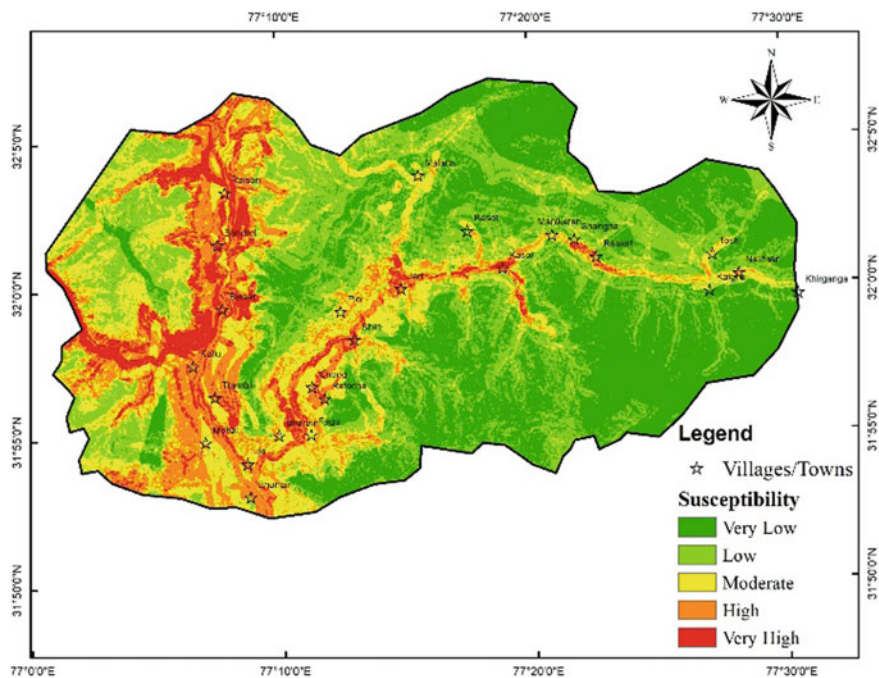
Fig. 6 Final landslide susceptibility map

Table 2 Landslide density index (LDI) calculation results

Susceptibility	Class pixels	% Class pixels	Landslide pixels	% Landslide pixels	LDI
Very low	335,136	0.33192	4500	0.07813	0.2354
Low	300,859	0.29797	9000	0.15625	0.5244
Moderate	183,862	0.18210	6300	0.10938	0.6006
High	136,632	0.13532	16,200	0.28125	2.0784
Very high	53,205	0.05269	21,600	0.37500	7.1166
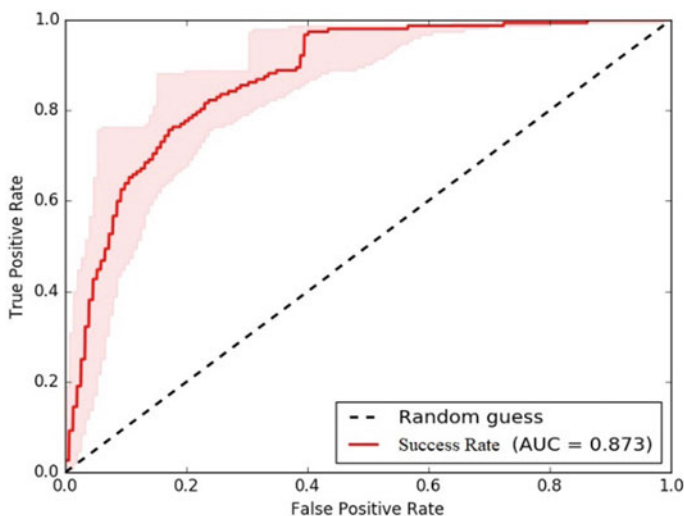
Fig. 7 Success rate curve

The LULC map showed highest landslide occurrences around the built-up area, agricultural land area and near water bodies, whilst the lowest being in the forest and snow/glaciers areas.

There was an increasing trend in landslide incidence as slope increased with highest value recorded for slope between 33° and 44°.

The south, south-east and east aspect were found more prone to landslides in the area whereas slope with no aspect had zero frequency ratio.

Convex and concave surfaces had highest values of frequency ratio compared to linear surfaces showing implication of convexity and concavity in landslide happening.

Increase in slope instability due to road construction in the area can be justified by the highest FR values (3.72347) obtained in the 0–100 m range of the buffered road network.
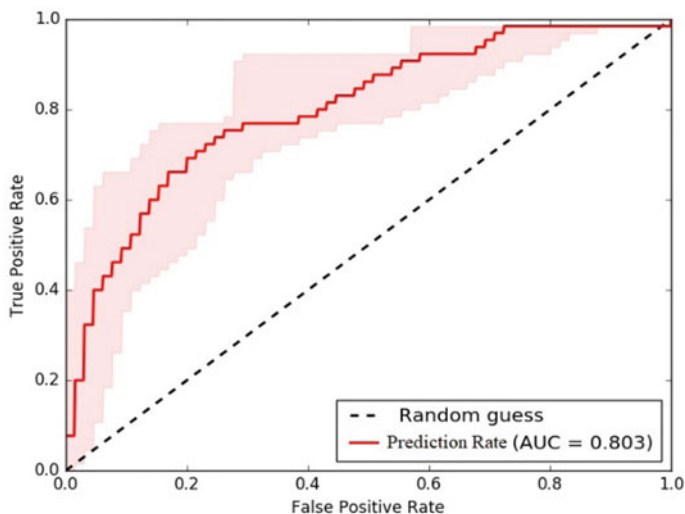
Fig. 8 Prediction rate curve

The highest frequency ratio values 1.41715 and 2.07983 for the drainage buffered zones of 0–100 m and 100–200 m, respectively, from the stream networks signify strong association to slope instability.

The lower two elevation zones (1050–2000 m and 2000–3000 m) have highest FR values (0.83979 and 0.14622) and also have more man-made activities compared to higher elevations in the area often covered with snow coupled with scarce human intervention and lesser extent of land.

For the lithologic contribution to landslides, the two groups namely slate, phyllite, quartzarenite, limestone, metabasics and sillimanite-kyanie bearing schist, quartzite have the highest FR values of 2.51125 and 2.26007, respectively, and out of thirteen, four groups had zero FR values, hence no contribution was observed.

7 Conclusion

The validation results showed reasonable prediction accuracy of the data-driven model adopted for mapping landslide susceptibility in this region using the nine selected factors. This model can be used for the generation of better landslide susceptibility maps for future planning and mitigation measures, but not as a replacement for detailed, localized studies performed by experts.

References

1. Avinash, K.G., Ashamanjari, K.G.: A GIS and frequency ratio-based landslide susceptibility mapping: Aghnashini river catchment, Uttara Kannada, India. Int. J. Geomat. Geosci. **1**(3), 343–354 (2010)
2. Bunn, M., Leshchinsky, B., Olsen, M., Booth, A.: A simplified, object-based framework for efficient landslide inventorying using LIDAR digital elevation model derivatives. Remote Sens. **11**(3)
3. Chandel, V.B.S., Brar, K.K., Chauhan, Y.: RS & GIS based landslide hazard zonation of mountainous terrains: a study from middle Himalayan Kullu District, Himachal Pradesh, India. Int. J. Geomat. Geosci. **2**(1), 121–132 (2011)
4. Chung, C.J.F., Fabbri, A.G.: Probabilistic prediction models for landslide hazard mapping. Photogramm. Eng. Remote. Sens. **65**(12), 1389–1399 (1999)
5. Dikau, R.: The recognition of landslides. In: Casale, R., Margottini, C. (Eds.) Floods and Landslides: Integrated Risk Assessment; Environmental Science. Springer, Science and Business Media: Berlin/Heidelberg, Germany (1999)
6. Fayez, L., Pazhman, D., Pham, B.T., Dholakia, M.B., Solanki, H.A., Khalid, M., Prakash, I.: Application of frequency ratio model for the development of landslide susceptibility mapping at part of Uttarakhand State, India. Int. J. Appl. Eng. Res. **13**(9), 6846–6854 (2018)
7. Kumar, A., Sharma, R., Bansal, V.: GIS-based landslide hazard mapping along NH-3 in mountainous terrain of Himachal Pradesh, India Using Weighted Overlay Analysis: IC_SWMD 2018 (2019)
8. Lee, S., Pradhan, B.: Landslide hazard mapping at Selangor, Malaysia using frequency ratio and logistic regression models. Landslides **4**(1), 33–41 (2007)
9. Mandal, S., Maiti, R.: Application of analytical hierarchy process (AHP) and frequency ratio (FR) model in assessing landslide susceptibility and risk. In: Semi-quantitative Approaches for Landslide Assessment and Prediction. Springer Natural Hazards. Springer, Singapore (2015)
10. Nohani, E., Moharrami, M., Sharafi, S., Khosravi, K., Pradhan, B., Pham, B.T., Lee, S., Melesse, A.M.: Landslide susceptibility mapping using different GIS-based bivariate models. Water **11**(7) (2019)
11. Pradhan, B.: Landslide susceptibility mapping of a catchment area using frequency ratio, fuzzy logic and multivariate logistic regression approaches. J. Indian Soc. Remote Sens. **38**(2), 301–320 (2010)
12. Ramani, S., Rajamanickam, G.V., Pichaimani, K.: Landslide susceptibility analysis using Probabilistic Certainty Factor Approach: a case study on Tevankarai stream watershed, India. J. Earth Syst. Sci. **121**(5)
13. Sarkar, S., Kanungo, D.P.: An integrated approach for landslide susceptibility mapping using remote sensing and GIS. Photogramm. Eng. Remote. Sens. **70**, 617–625 (2004)

Evaluation and Remedial Measures for Unstable Slopes at Gagangir Sonmarg, J&K: A Case Study

Shahzada Omer Manzoor(ID)**, Aadil Yousuf**(ID)**,
and Anil Kumar Sharma**(ID)

1 Introduction

Uncertainties in geotechnical Engineering are inevitable, often we see considerable variability in soil properties within a short-range thereby complicating analysis and design of structures like dams, buildings, etc. [1]. Slopes are an important part of geotechnical studies owing to their relation to human life and property. There are many methods available for analysis of failure susceptible slopes; however, the precision of analysis, mechanism of failure, and slip surface profile typically depend on the selection of the method for slope stability evaluation [2]. The factor of safety is used as a principal index for determining the failure vulnerability of a slope. Limit equilibrium methods and finite element methods are most popular methods for analysis each having advantages and disadvantages [3].

Limit equilibrium (LE) methods use Mohr–Coulomb failure criterion for evaluation of shear strength along a sliding surface and under this criterion failure does not occur due to normal stress or shear stress alone but due to a combination of both [3]. In limit equilibrium method, after working out slope geometry and soil properties, a comparison is made between forces resisting failure and forces causing failure to calculate Factor of Safety (FOS) or in other words, the FOS is calculated as the ratio of shear strength of the soil and mobilized shear strength of soil [3–5]. In LE method, slip surfaces (Circular or Non-circular) are divided into vertical slices, and then static equilibrium conditions (Force and Moment equilibrium) are used to calculate stresses and FOS on each slice [6, 7]. As of now, we have many LE methods available and these include Fellinius, Bishop, Sarma, Janbu, Morgenstern-Price method, etc., with each one having a distinct set of properties.

S. O. Manzoor (✉)
National Institute of Technology, Srinagar, India

A. Yousuf · A. K. Sharma
National Institute of Technology, Patna, India

In this study, advanced Bishop's method has been used through GEO-5 software for slope stability analysis.

The principal factors on which the instability of terrain depend are geologic, geomorphologic, drainage, usage of the land, anthropogenic activity, and climatic conditions, some of these factors like drainage, slope geometry, etc., can be determined rather easily, however, greater uncertainty is associated with factors like rainfall and earthquake anticipation [8, 9]. The above-mentioned factors don't act in isolation rather a combination of some factors cause failure [10]. Instability of natural and built-in slopes has been a serious geotechnical challenge, particularly in the Sonmarg area of the mountainous Kashmir region, where a large number of landslides and slip surface failures are experienced every year. The area exhibits undulating and rugged topography with highly mountainous terrain having little vegetation, the mountains are composed of sedimentary and igneous rocks that are being subjected to severe cold weathering and the altitude varies between 2500 and 3800 m above MSL [11]. Hill faces are made up of high-rocky escarpments, steep slopes, and moderate–Gentle slopes made up of slid debris. A good comprehension of analytical methods, tools of investigation, and that of stabilization techniques are important for solving slope instability issues [3]. A quantitative, as well as qualitative assessment of the safety factor, is important when decisions are made. It can be said that the primary aim of slope stability analysis is to work out the safe and economic design of excavations, embankments, and earth dams.

2   Scope and Site Location

Like other mountainous regions, Jammu & Kashmir has large variations in its topography. The high Himalayas on the periphery, the gentle to steep mountains in the middle, and the flat land on the interior have provided both opportunities and challenges [11]. Kashmir valley is connected to the Ladakh region through national Highway-1 through Srinagar-Sonmarg-Gumri road and this road remains closed for traffic for around 6-months per year owing to frequent blockades due to landslides. Alam et al. [12] prepared a landslide susceptibility zonation map of this area and from that it can be inferred that this particular road stretch is susceptible to moderate to high landslides. To ensure all-weather connectivity of the Ladakh region with Kashmir valley, the government started a project couple of years back which includes the construction of several tunnels and new roads through this mountainous terrain. One such under-construction road connects Z-Morh tunnel with the existing national highway and this road for the tunnel portal takes off from chainage km 69 + 00 of NH-1D Srinagar-Leh road to the western portal and makes a total length of 3.75 km. During my first site visit, cutting of slopes was completed for the initial kilometre and final kilometre of the proposed 3.75 km approach road of the Z-Morh tunnel. Soil samples were collected from two sites located at chainage 600, i.e., 600 m from the start point (Fig. 1) and chainage 700 (Fig. 2), i.e., 700 m from the start point of the road as these two points seemed very much susceptible to failure.

Fig. 1 Slope profile at Chainage-600

The scope of this study involves understanding the influence of factors impacting slope stability and how they govern the design of various stabilization methods. It also helps us in understanding the economic perspective and practical feasibility of different slope stabilization measures. This project started with a field visit to the site, i.e., Gagangir, Sonmarg for the collection of soil samples both disturbed as well as undisturbed and also for the collection of relevant data like the height of slope, slope angle, water table, geologic, and hydrologic data about the location. The research methodology adopted for this project was multi-phased, and in the initial phase laboratory, tests were conducted as per the Indian-Standard Codes for the evaluation of basic soil properties especially cohesion, angle of internal friction, unit weight, etc. Then, the next phase involved the usage of these properties as basic input parameters in the GEO-5 software for analysis of slopes. It's imperative to mention here that GEO-5 uses limit equilibrium for analysis and is easy to use the software. In the final stage, various slope models were analysed by using different

Fig. 2 Slope profile at Chainage-700

stabilization techniques for these unstable slopes and the factor of safety for all these configurations was evaluated. After considering the feasibility, practicality, and economy of all these measures, suggestions regarding the stabilization measures were made to the executing agency in the final report.

3   Laboratory Investigations

After collecting disturbed and undisturbed samples from the site, exhaustive laboratory testing was done for the evaluation of basic soil properties following the procedures mentioned in Indian standard Codes [16]. All the collected samples were oven-dried for 24 h at 105–110 °C temperature. Then Particle Size distribution [IS-2720-4(1985)] as shown in Fig. 3, Specific Gravity (IS-2720-3-1), Plastic & Liquid limit (IS-2720-5), Direct Shear test (IS-2720-13), and Triaxial test (IS-2720-11) were conducted to determine specific gravity, unit weight, moisture content, cohesion, and angle of internal friction, all of which are important for slope stability analysis. All these parameters are the basic input factors for the GEO-5 software to complete the analysis. These parameters have been tabulated in Table 1.

It is noteworthy to mention that Direct Shear tests on the remolded soil samples were initially performed to work out the cohesion and angle of internal friction as in

Table 1 Soil properties at two locations

Soil properties		Soil 1 (Chainage-600)	Soil 2 (Chainage-700)
Specific gravity		2.71	2.67
Moisture content (%)		19.4	16.2
Unit weight (kN/m^2)		19.00	18.3
Liquid limit (%)		36.5	33.1
Plastic limit (%)		24.7	23.8
Cohesion (kPa)	DST (Direct shear test)	27	23.5
	Triaxial	20	17
Angle of friction	DST (Direct shear test)	36.3	41.2
	Triaxial	28.4	33.5
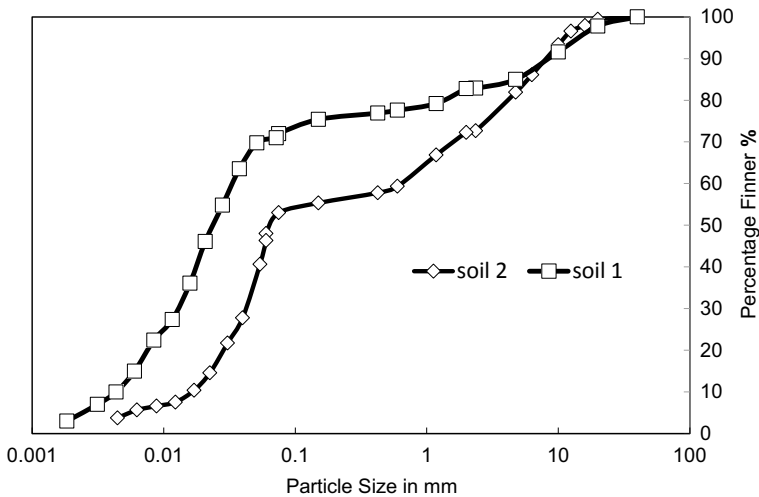
Fig. 3 Grain size distribution of soil samples

Fig. 4; however, the values of these two parameters were on the higher side quite contrary to the stability of the slopes, therefore, Triaxial tests were carried out under consolidated-undrained conditions to get more precise values of cohesion and angle of friction as shown in Fig. 5, and later these values were used for the slope stability analysis purposes. Also, Fig. 6 shows the specimen shape after shearing in the Triaxial test. The graphs corresponding to the above-mentioned investigations and the resulting parameters have been provided below.
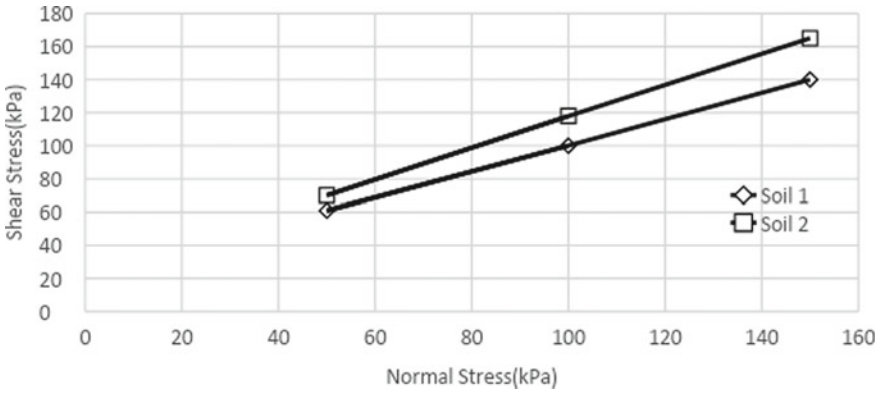
Fig. 4 Plot for direct shear test of soil samples
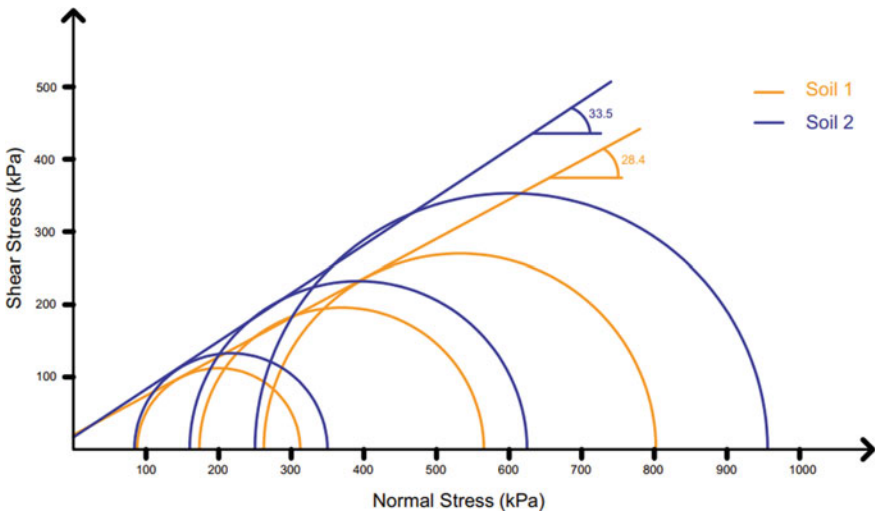
Fig. 5 Mohr circles of soil samples (Triaxial test)
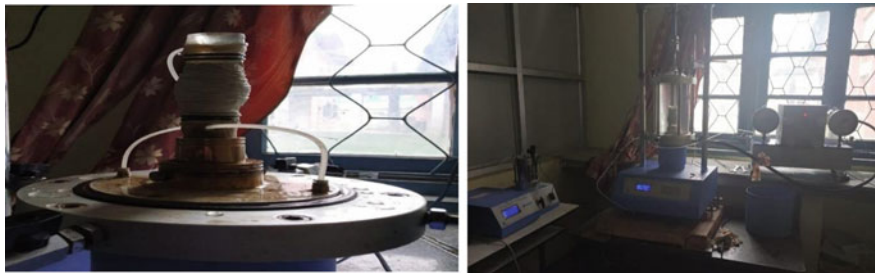
Fig. 6 Specimen shape after shearing in the Triaxial test

4   Analysis and Discussions

Analysis of slopes has traditionally been carried out by limit equilibrium-based Bishop's method which in principle depends on the static equilibrium of forces and moments [17]. After evaluating the basic properties of soil at a chosen location GEO-5 software was used for analysis purposes and also for the design of slope stabilization techniques [13]. The factor of safety was evaluated for multiple stages. The factor of safety (FOS) was evaluated for the existing condition as shown in figure, then the slope was varied by changing the cutting angle from 90° to 50° and subsequently, FOS was checked for each variation using GEO5, and also the cutting volume was calculated in AUTOCAD. Finally, either retaining wall/soil nailing or both were used as stabilizing measures, and the consequent increase in FOS was evaluated. Results of all these stages for two locations have been provided as follows.

4.1   Evaluation of Slope at Chainage 600 (Soil-1)

The existing slope profile at this location as shown in Fig. 7 has been created in AutoCAD wherein the height, width, slope angle, and other details are visible. The soil properties used as input parameters for GEO-5 analysis have been mentioned in the laboratory investigations section preceding this part.

4.1.1   Variation of FOS Due to Change of Cutting Angle

After varying the angle of cutting from 90° to 50° and calculating the cutting volume, it was found that FOS increases from 0.80 to 1.17. Considering the economic and safety perspective, it was found that a cutting angle of 60° will be
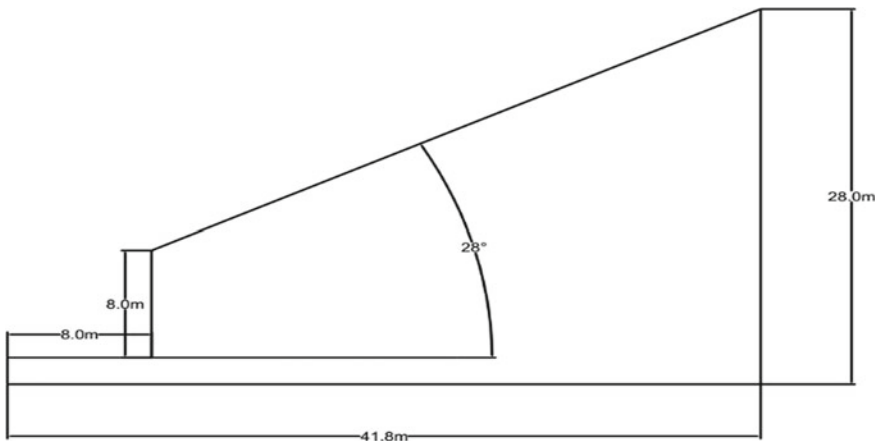
Fig. 7 Existing slope profile
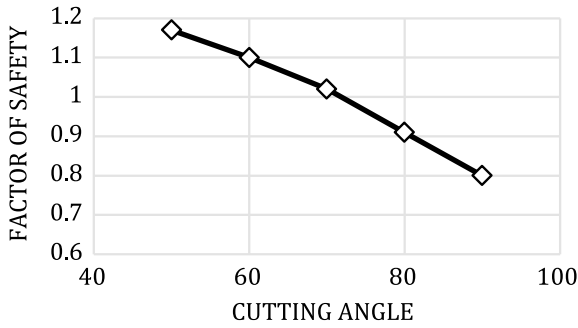
Fig. 8 FOS versus cutting angle
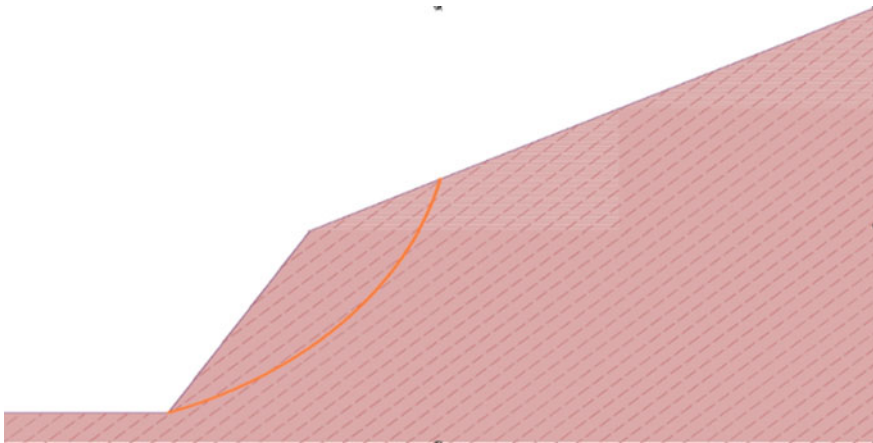
Fig. 9 GEO-5 profile of slip surface at 60° angle

adopted to have significant FOS (**1.10**) and lesser cutting volume. The following graphical plots show the AutoCAD layout (Fig. 10) of the slope, a variation of FOS with cutting angle (Fig. 8), and GEO-5 critical slip surface profile (Fig. 9).

4.1.2 Variation of FOS Due to the Placement of a Retaining Wall

After fixing the angle at 60°, the concrete retaining wall with a unit weight of 24 kN/m^3 was provided at the base and the same was modeled in GEO 5. During the modeling in GEO-5, the height and unit weight of retaining wall (RW) was varied [14], and a corresponding change in FOS was noted accordingly. Figure 11 shows the AutoCAD layout of a slope with RW, a variation of FOS with Height of retaining Wall (Fig. 12), and GEO-5 critical slip surface profile (Fig. 13).
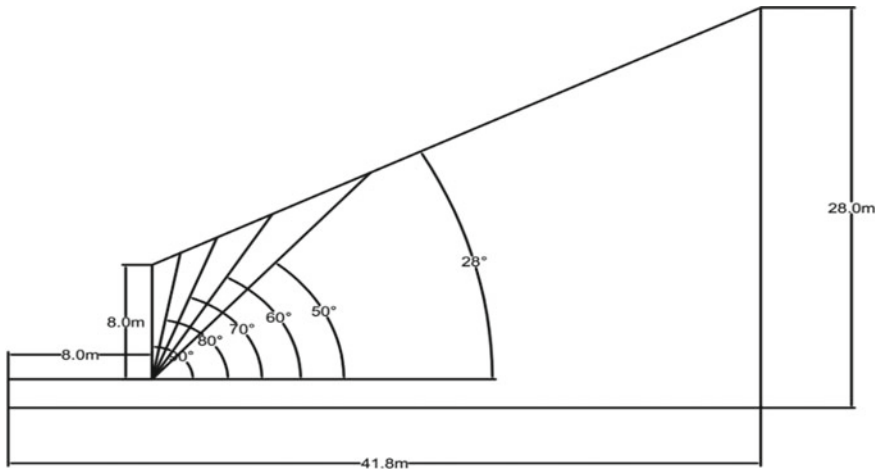
Fig. 10 Proposed geometric profile of slope at Ch-600
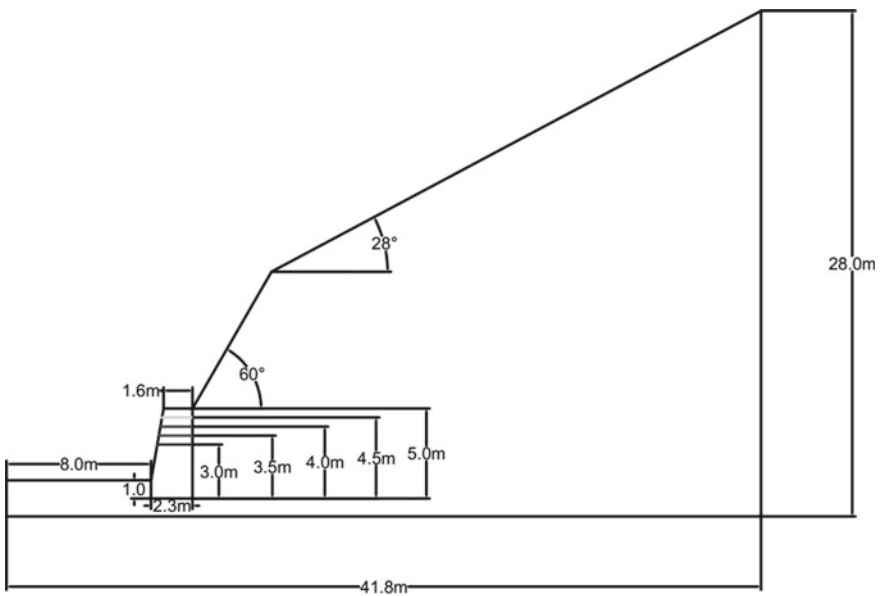
Fig. 11 Slope profile with retaining wall at 60° angle

4.1.3 Increase in Slope Stability Due to Soil Nailing

As is evident from the above results that the increase in factor of safety due to construction of retaining wall is 1.36 which is less than 1.50 and is insufficient considering the stability of the slope, thereby necessitating additional stabilization
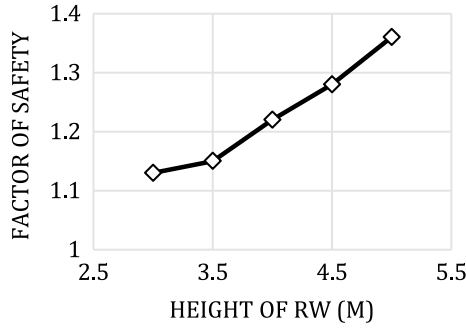
Fig. 12 FOS versus Height of RW
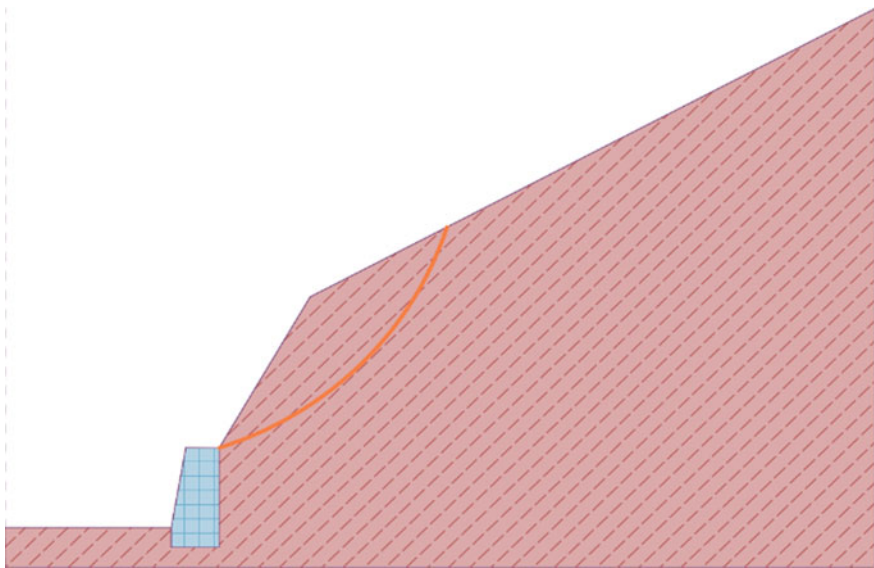
Fig. 13 GEO-5 profile of slip surface with RW

measures like soil nailing, anchoring, etc. However, after evaluating multiple measures based on economy, suitability, stability, ease of construction, etc., at the site, it was found that soil nailing is the only realistic option available which covers all these parameters, i.e., soil nailing apart from being economical also provides for increased safety and ease of construction. The design of soil nailing herein includes optimization of length, strength, inclination, and diameter of soil nails following the codal provisions [15]. Figure 14 shows the AutoCAD layout of a stabilized slope profile and GEO-5 slope profile (Fig. 15). The FOS increased to 1.60 well greater than 1.50 after soil nailing, soil nails with following specifications have been provided after optimization:
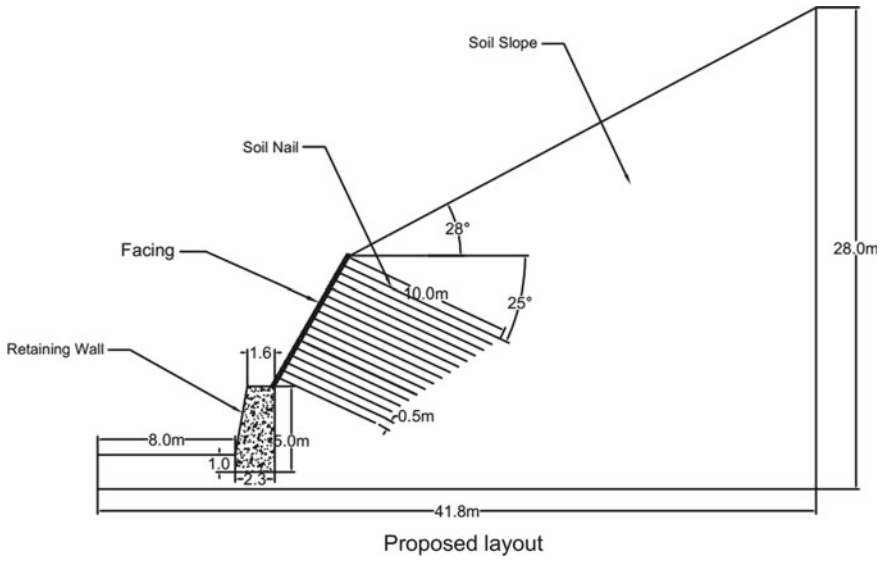
Fig. 14 Final proposed profile of stabilized soil slope at Ch-600
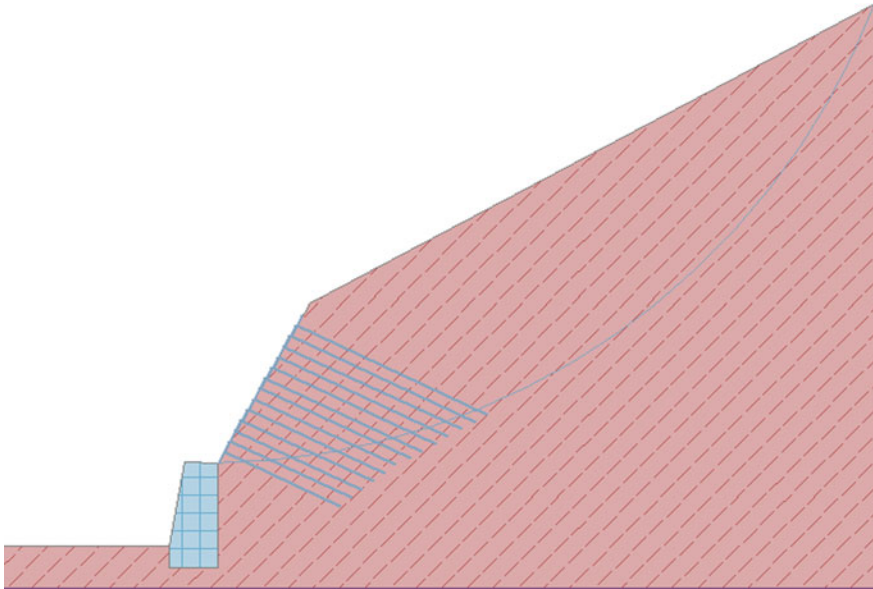
Fig. 15 GEO-5 profile of slip surface of slope with RW and soil nailing

Diameter = 20 mm, Angle of Inclination = 15°, Type of Steel = Fe-415 bars, Spacing = 0.5 m, Length varies from 10 m at top to 6.10 m at bottom, Total bars in 2-D plane = 13.

After analysing the FOS values for different cutting angles, a cutting angle of 60° was provided which led to an increase in overall FOS up to 1.10, however, any further cutting would have been uneconomical. Therefore, a retaining wall of 5-m height was provided which increased FOS to 1.36, still below a safe value of 1.5. Finally, soil nailing was done on the above the retaining wall for further stabilization of slope, and after optimization, soil nailing increased FOS to 1.60 well above the safe value of 1.5.

4.1.4 Impact of Earthquake on Slope Stability

For all the above-mentioned stages of slope stabilization, the pseudo-static analysis was done to check for the impact of the earthquake on stability because the site is located in an earthquake-prone area and comes under zone 4 of classification. The coefficients of acceleration in the horizontal direction are taken as 0.11 and that in vertical direction 0.08, respectively. The results from the analysis are given below, it can be inferred that slope cut at 60° has FOS less than 1.00 hence is unstable in case an earthquake strikes, whereas for slopes with retaining wall and soil nails FOS is well above 1.00 making these slopes quite stable, and the variation of FOS of slope under different earthquake conditions has been given in Table 2.

4.2 Evaluation of Slope at Chainage 700 (Soil-2)

The existing slope profile at this location as shown in Fig. 16 has been created in AutoCAD wherein the height, width, slope angle, and other details are visible. The soil properties used as input parameters for GEO-5 analysis have been mentioned in the laboratory investigations section preceding this part.

4.2.1 Variation of FOS Due to Change of Cutting Angle

After varying the angle of cutting from 90° to 50° and calculating the cutting volume, it was found that FOS increases from 0.86 to 1.25. Considering economic and safety perspective, it was found that a cutting angle of 65° will be adopted to

Table 2 FOS variation of slope systems during earthquake at Ch-600

No	Condition of slope	Factor of safety	Safety
1	Slope cut at 60° angle	0.95	Unsafe
2	Slope cut at 60° with a retaining wall	1.17	Safe
3	Slope cut at 60° with retaining wall and soil nails	1.38	Safe
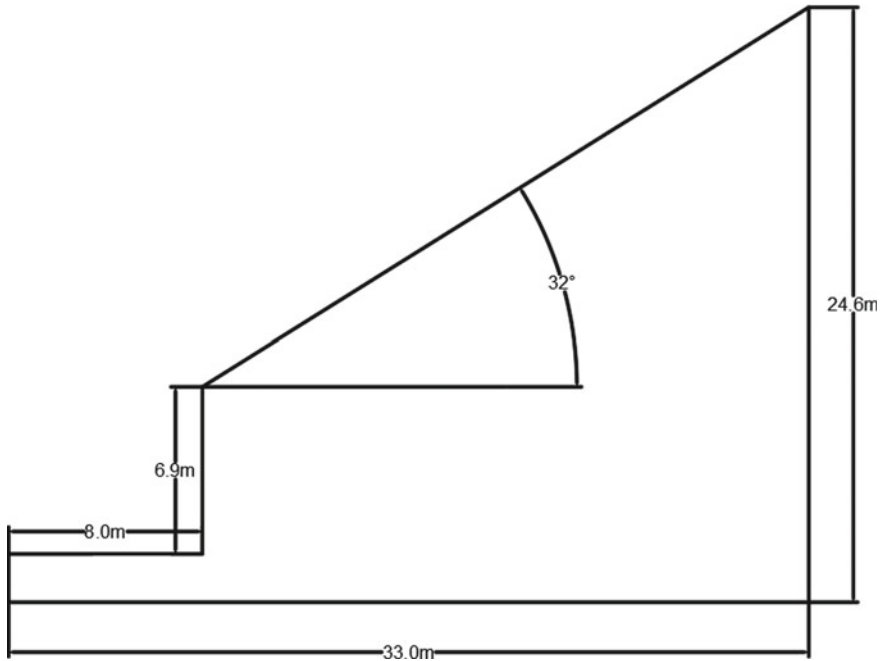
Fig. 16 Existing slope profile

have significant FOS (1.15) and lesser cutting volume. Following graphical plot in Fig. 17 shows AutoCAD layout of a slope, a variation of FOS with cutting angle (Fig. 18) and GEO-5 critical slip surface (Fig. 19).

4.2.2 Variation of FOS Due to the Placement of a Retaining Wall

After fixing the angle at 65°, a concrete retaining wall (RW) with a unit weight of 24 kN/m^3 was provided at the base and the same was modeled in GEO 5. During the modelling in GEO-5, the height and unit weight of retaining wall were varied and the corresponding change in FOS was noted accordingly. Figure 20 shows the variation of FOS with the height of RW, and, whereas GEO-5 profile of critical slip surface with RW is shown in Fig. 21. The AutoCAD layout of the slope is shown in Fig. 22.

After analysing the FOS values for different cutting angles, a cutting angle of 65° was provided which led to an increase in overall FOS up to 1.15, however, any further cutting would have been uneconomical. Therefore, a retaining wall of 4.5-m height above ground was provided which increased FOS to 1.53, well above the safe value of 1.5. Figure 23 shows the final proposed final AutoCAD layout of the slope.
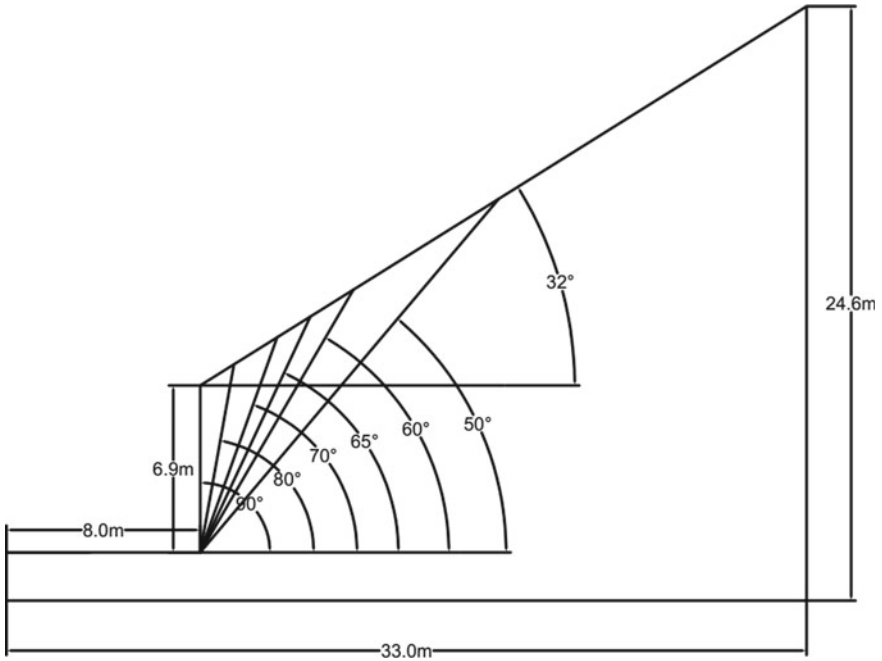
Fig. 17 Proposed geometric profile of slope at Ch-700

Fig. 18 FOS versus cutting angle
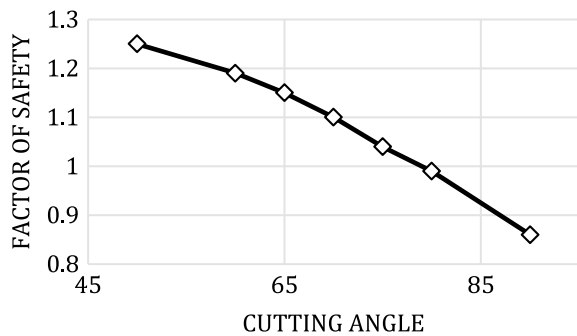
4.2.3 Impact of Earthquake on Slope Stability

The pseudo-static analysis was done for evaluating the impact of an earthquake on FOS of a slope. The coefficients of acceleration in the horizontal direction are taken as 0.11 and that in vertical direction 0.08, respectively. From the results, it can be inferred that slope cut at 65° has FOS greater than 1.00 hence is stable in case an earthquake strikes and also for the slope with retaining wall FOS is well above 1.00 making the slope quite stable, and the variation of FOS of slope under different earthquake conditions has been given in Table 3.
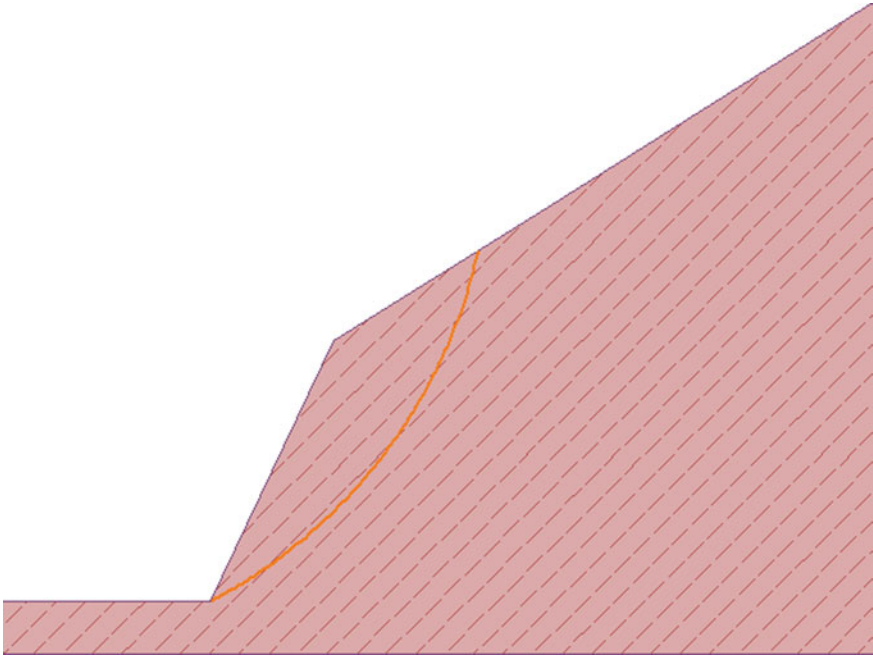
Fig. 19 GEO-5 profile of slip surface at 65° angle
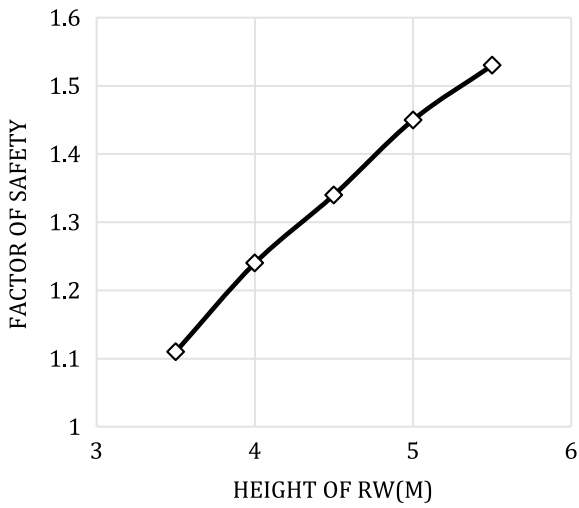
Fig. 20 FOS versus Height of RW
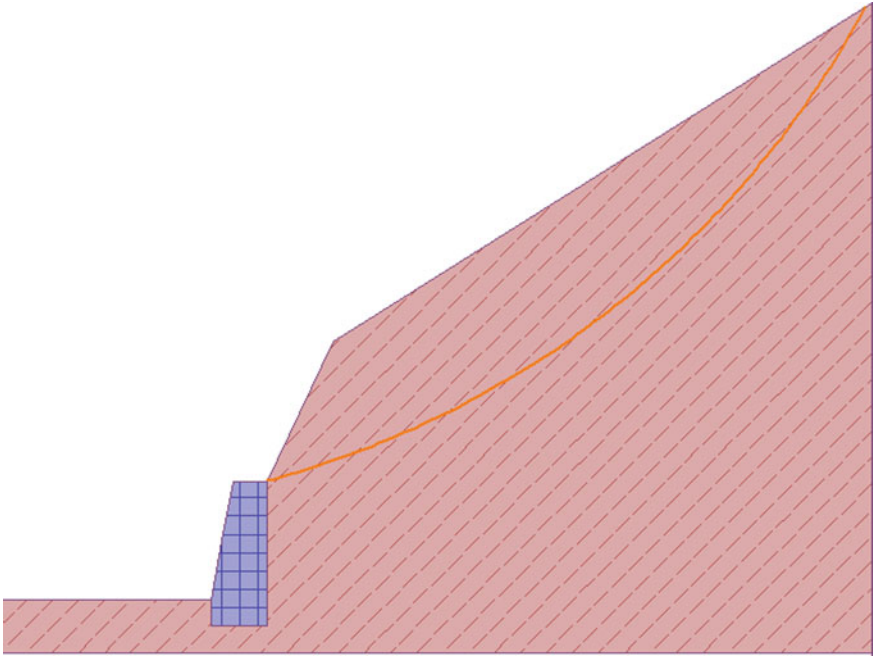
Fig. 21 GEO-5 profile of slip surface with RW
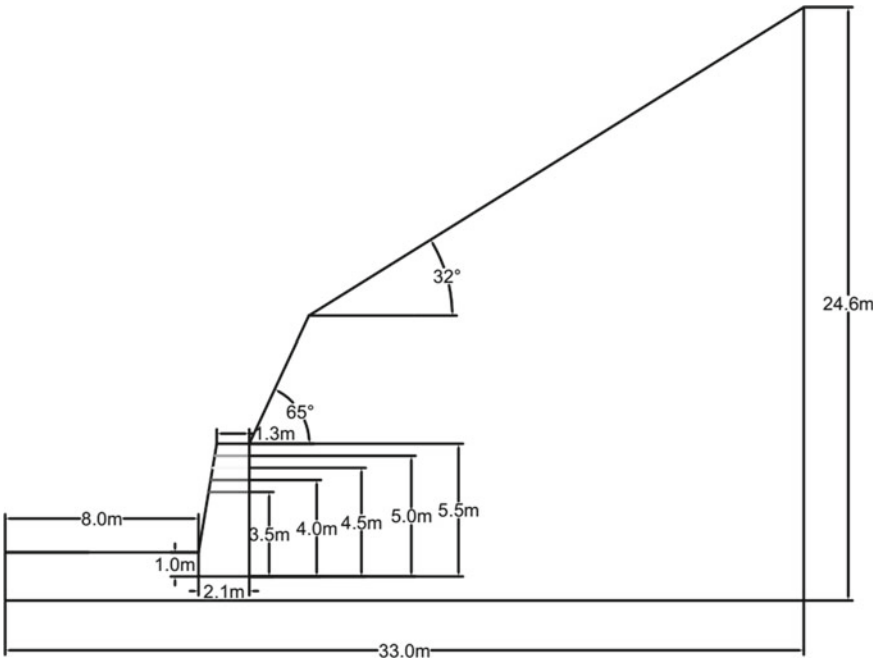
Fig. 22 Slope profile with retaining wall at Ch-700
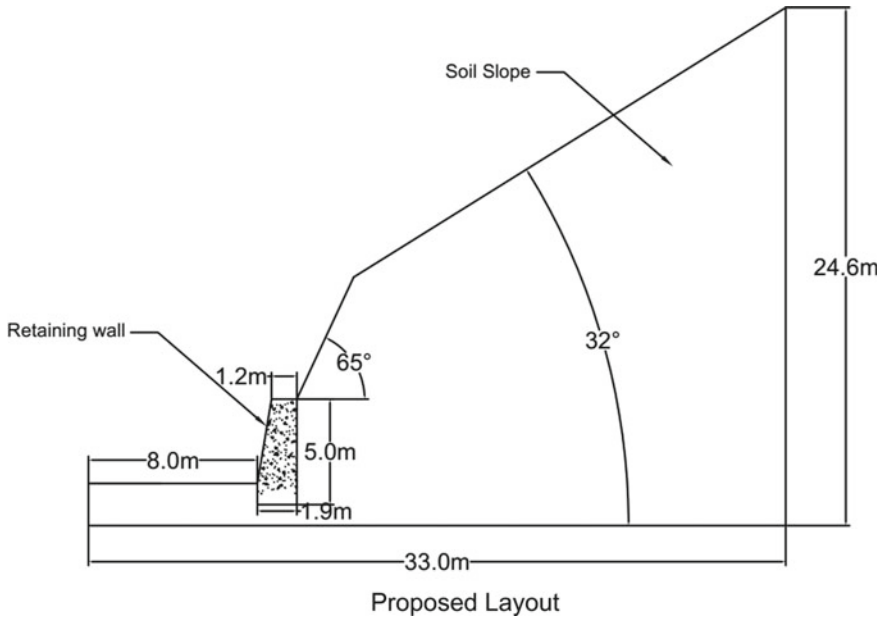
Fig. 23 Final proposed layout for slope at chainage 700

Table 3 FOS variation of slope systems during earthquake at Ch-700

No	Condition of slope	Factor of safety	Safety
1	Slope cut at 65° angle	1.05	Safe
2	Slope cut at 65° with a retaining wall	1.29	Safe

5 Conclusions

The research described in this thesis has achieved the objectives which can be summarized as follows:

- Gained a better understanding of factors that cause slope instability and their importance in the geotechnical analysis.
- Influence of shear strength parameters and other soil properties on slope stability.
- Evaluation of the stability of slopes at Gagangir Sonmarg along approach road of Z-Morh tunnel.
- Suggestions regarding stabilization measures for unstable slopes.
- Assessing the accuracy of locating the most critical slip surface and the associated factor of safety considering the type of searching technique.

In this study, two slopes along approach road of Z-Morh were analyzed for stability with the help of GEO-5 software which is a limit equilibrium-based software, and measures were suggested for increasing stability and for prevention of failure. For location-1 (Chainage-600), the slope was found to be unstable under natural conditions with FOS less than unity; therefore, remedial measures like construction of retaining wall and soil nails were suggested after evaluation and optimization with the help of GEO-5 software which consequently increased the FOS value up to 1.60, well above the safe value of 1.50. Similarly, for slope at location-2 (Chainage-700), the slope was unstable under natural conditions and had FOS value below the safe FOS value of 1.50, the construction of retaining wall increased FOS to 1.53, thereby making slope safe. Some of the inferences that can be made out of this study are as follows:

- The precision of analysis, mechanism of failure, and slip surface profile typically depend on the selection of the method of slope stability evaluation.
- GEO-5 has a very user-friendly interface, is easy to learn and is more precise as compared to other software available in market
- Optimization of slip surfaces is an important function of GEO-5 because it helps in identifying critical slip surface having maximum chances of failure
- Cohesion, angle of friction, the height of slope, slope angle, and unit weight of soil are the factors that govern the stability of the slope.

References

1. Ranjan, G., Rao, A.S.R.: Basic and Applied soil Mechanics, 3rd edn. New Age International (2016)
2. Bowles, L.E.: Foundation Analysis and Design, 5th edn. McGraw-Hill (1995)
3. Aryal, K.P.: Slope stability evaluations by limit equilibrium and finite element methods. PhD Thesis submitted to Norwegian University of Science and Technology (2006)
4. Nash, D.: Comprehensive Review of limit equilibrium methods of stability analysis. In: Andersen, M.G., Richards, K.S. (eds.) Slope Stability, Chapter 2, pp. 11–75. Wiley, New York (1987)
5. Sharma, S.: Slope stability and stabilization methods. In: Abramson, L.W., Lee, T.S., Sharma, S., Boyce, G.M. (eds.) Slope Stability Concepts, pp. 329–461. Wiley, New York (2002)
6. Bishop, A.W.: The use of the slip circle in the stability analysis of slopes. Geotechnique **5**(1), 7–17 (1955). https://doi.org/10.1680/geot.1955.5.1.7
7. Chen, W.F., Liu, X.L.: Limit Analysis in Soil Mechanics, 1st edn. Elsevier Science, Netherlands (1990)
8. Chingkhei, R.K., Shiroyleima, A., Singh, L.R., Kumar, A.: Landslide hazard zonation in NH-1A in Kashmir Himalaya, India. Int. J. Geosci. **4**(10), 1501–1508 (2013). https://doi.org/10.4236/ijg.2013.410147
9. Varnes, D.G.: Landslide Hazard Zonation: A Review of Principles and Practice. Unesco, Paris (1984)
10. Duncan, J.M., Wright, S.G., Brandon, T.L.: Soil Strength and Slope Stability, 2nd edn. Wiley, USA (2014)

11. Bhat, M.S.: Geomorphological field guide book on Kashmir Himalaya. In: Koul, M.N. (ed) 9th International Conference on Geomorphology of the International Association of Geomorphologists (IAG), pp. 1–27. Indian Institute of Geomorphologists (IGI), Allahabad (2017). https://doi.org/10.13140/rg.2.2.15736.55040
12. Alam, A., Bhat, M.S., Ahmad, B., Ahmad, S.: Landslide Susceptibility Zonation (LSZ) of Sonamarg—Gumri Road Section in Jammu and Kashmir, India. In: International Geographical Union (IGU), pp. 1–3. Jammu and Kashmir (2014)
13. GEO-5.: Stability Analysis. Users Guide Version 5 (2019). www.finesoftware.eu
14. Bureau of Indian standard-14458 (Part 1): 1998 for Retaining wall for hill area
15. BS 8081: 1989: International code of design for Soil-nailing
16. Bureau of Indian standard-2720-Part-III. (1980). Methods of test for soils, Part 3: Determination of specific gravity, Section 2: Fine, medium and coarse-grained soils [CED 43: Soil and Foundation Engineering]. Retrieved from https://law.resource.org/pub/in/bis/S03/is.2720.3.2.1980.pdf
17. Bureau of Indian standard -7894 code for Slope Stability Analysis

Probabilistic Stability Analysis of Helical Soil Nailed Wall Using the Monte-Carlo Simulation

Ekansh Agarwal⬤, Mahesh Sharma⬤, and Anindya Pain⬤

1 Introduction

Soil nailing is an effective technique which is broadly used for the stabilization of various geotechnical structures such as slopes, retaining walls and excavations [1–3]. Field engineers consider soil nailing to be a viable alternative in place of other available methods owing to its innumerable advantages such as ease of application and less environmental impact, to name a few. Moreover, soil nailed structures perform very well under seismic conditions even for ground accelerations as high as 0.7 g [4]. Few researchers [5, 6] had conducted centrifuge experiments using soil nails for stabilization and reported similar findings as stated by analytical studies.

Soil nailing technique is an in-situ earth-reinforcement technique. Therefore, its ability to stabilize the geotechnical structures depend upon the composite relationship between nail and soil. Numerous researchers have proposed the limit equilibrium approaches to analyze the conventional soil nailed walls and slopes [7, 8]. However, the pseudo-static approach of analytical analysis is mostly used in all the above stated literature. The pseudo-static approach does not consider the time dependent nature of the seismic forces and the amplification of acceleration. Due to these limitations, the pseudo-dynamic method was developed and used by many researchers for the stability analysis of reinforced retaining structures. However, this method too had some limitations including not satisfying the no stress boundary condition at the free surface. Therefore, Bellezza [9] has proposed a new

E. Agarwal (✉) · A. Pain
Academy of Scientific and Innovative Research (AcSIR), Ghaziabad 201002, India
e-mail: pain_anindya@cbri.res.in

E. Agarwal · A. Pain
Geotechnical Engineering Group, CSIR—Central Building Research Institute,
Roorkee 247667, India

M. Sharma
University of California, Davis 95616, USA

pseudo-dynamic method of analysis to account of all the limitations of its counterparts. This new modified pseudo-dynamic method (MPD) had been used by various researchers for the stability analysis of retaining structures [10–14]. However, there is a paucity of literature on the stability analysis of helical soil nailed wall using the modified pseudo-dynamic approach. Sharma et al. [15] had analyzed the seismic stability of helical soil-nailed wall using the modified pseudo-dynamic approach. The addition of helices to the soil nail improves its efficiency in comparison with the conventional soil nail. A helical soil nail mobilizes more pullout strength in comparison with its counterparts due to the presence of extra helices. Moreover, it accounts for the minimal site disturbances. Few researchers had studied the pullout behavior of helical soil nails through experiments and numerical analysis [16–18].

The deterministic approach of analyzing any geotechnical structure is unreliable, uneconomic, and inaccurate because it calculates a single value of factor of safety without considering the uncertainty of the input parameters. As a result, probabilistic analysis is performed to predict the true probability of failure of the reinforced retaining structure.

The literature review on the use of soil nailing for stabilization reveals the fact that there is a scarcity of literature on the probabilistic analysis of soil nailed structures. Many aspects are needed to be understood to apply the concepts of reliability on the soil–nail system, such as, the influence of variability of various soil parameters on the stability, role of different modes of failure, etc. Few researchers have attempted to explore the effect of uncertainty of soil input parameters on the stability analysis of soil nailed structures [19–22]. However, no study considering the helical soiled nailed walls in a probabilistic framework, using the MPD approach, has been conducted till date, which forms the basis of the present study. The current study employs the MPD method of analysis to calculate the factor of safety of the helical soil nailed wall (wall inclination angle (β) with the horizontal = 90°). The random variables considered in the study include soil internal friction angle (ϕ), unit weight (γ), and shear wave velocity (V_s) and the influence of uncertainty of these random variables on the stability analysis of helical soil nailed wall is studied in detail. The pullout mode of failure of helical soil nail is considered for the analysis, it being the critical and controlling design parameter in the stability analysis of a soil nailed wall. The probability of failure (P_f) and the reliability index (β_{min}) of helical soil nailed wall is estimated using the Monte-Carlo simulation (MCS). The P_f of wall reinforced using the conventional soil nails is compared with the helical soil nailed wall to provide a better understanding to the readers.

2 Deterministic Model

To analyze the soil nailed walls deterministically, the MPD method of analysis (Fig. 1) is used. The following assumptions are considered in the present study:

- Soil is dry and homogenous in nature.
- The effect of pore water pressure is neglected.
- The backfill of the wall is chosen to be cohesion less.
- The failure surface is considered as planar.

The pullout capacity of the helical soil nail is calculated using the following equation [15]:

$$P_o^i = \pi \sigma_i d L_{ei} \tan \delta + \sum_{i=1}^{n} A_i \sigma_i K_o N_q \tag{1}$$

where σ_i is the overburden pressure on the interface of the soil–nail; d is the nail shaft diameter; L_{ei} is the effective soil–nail length; δ is the peak interface friction angle; A_i is the bearing surface area of the circular disc given by $\pi (D_h - d)^2/4$; D_h is the helix diameter; K_o is the earth pressure coefficient at rest; N_q is the bearing capacity factor (calculated using the Mayerhof [23] equation for driven piles).

The accuracy of the above equation in evaluating the pullout capacity of helical soil nail was proved by comparing the obtained results with experimental results [15].
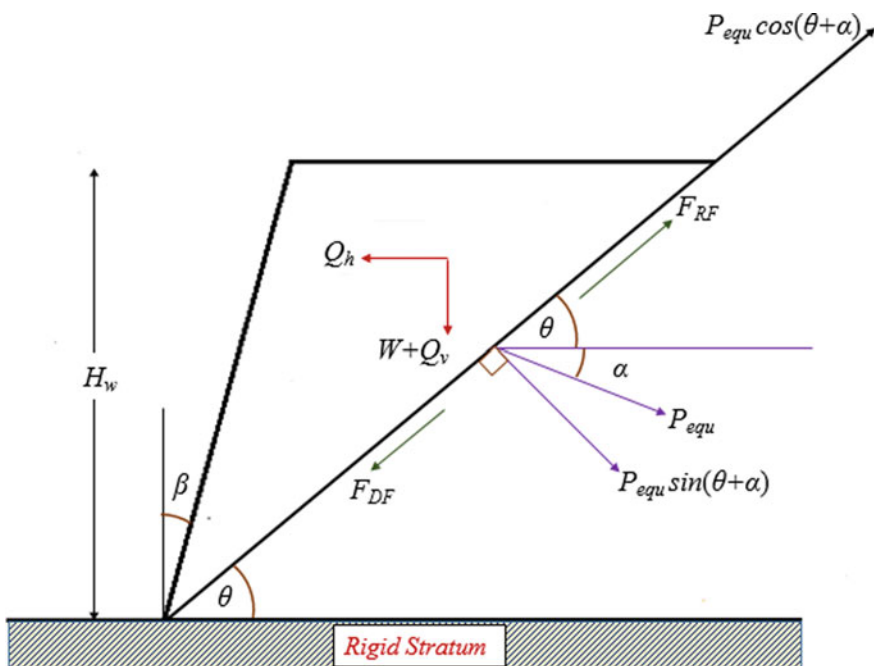
Fig. 1 Free Body Diagram of a soil nailed slope

2.1 Implementation of the Modified Pseudo-Dynamic Method of Analysis

The free body diagram of soil–nail model used in the present study is shown in Fig. 1. The backfill soil is considered to be visco–elastic in nature, which is modeled using the Kelvin–Voigt (K–V) equation. The respective planar S and P waves, traveling vertically upward in a K–V medium, are governed by the differential equations mentioned below:

$$\rho \frac{\partial^2 x_h}{\partial t^2} = G_s \frac{\partial^2 x_h}{\partial z^2} + \eta_s \frac{\partial^3 x_h}{\partial z^2 \partial t} \tag{2a}$$

$$\rho \frac{\partial^2 x_v}{\partial t^2} = (\lambda + G_s) \frac{\partial^2 x_v}{\partial z^2} + (\eta_l + 2\eta_s) \frac{\partial^3 x_v}{\partial z^2 \partial t} \tag{2b}$$

where z = depth from the ground surface, t = time, x_h = horizontal displacement, x_v = vertical displacement, ρ = density; λ = Lame's constant, G = Shear modulus, and η_l, η_s = Viscosities.

These equations are solved using the following boundary conditions:

- Shear stress at the free surface is equal to zero (0).
- The displacement at the backfill base is equal to the horizontal and vertical displacements at the rigid base.

The above two equations are solved to obtain the expressions for horizontal and vertical displacement in the backfill soil.

$$x_h(z,t) = \frac{x_{h0}}{C_s^2 + S_s^2} \left[(C_s C_{sz} + S_s S_{sz}) \cos(\omega t) + (S_s C_{sz} - C_s S_{sz}) \sin(\omega t) \right] \tag{3a}$$

$$x_v(z,t) = \frac{x_{v0}}{C_p^2 + S_p^2} \left[(C_p C_{pz} + S_p S_{pz}) \cos(\omega t) + (S_p C_{pz} - C_p S_{pz}) \sin(\omega t) \right] \tag{3b}$$

Differentiating the expressions of horizontal and vertical displacements, respectively, give the final expressions for the horizontal and vertical seismic accelerations.

$$a_h(z,t) = \frac{k_h g}{C_s^2 + S_s^2} \left[(C_s C_{sz} + S_s S_{sz}) \cos(\omega t) + (S_s C_{sz} - C_s S_{sz}) \sin(\omega t) \right] \tag{4}$$

where

$$C_{sz} = \cos\left(\frac{y_{s1} z}{H}\right) \cosh\left(\frac{y_{s2} z}{H}\right) \tag{4a}$$

$$S_{sz} = -\sin\left(\frac{y_{s1}z}{H}\right)\sinh\left(\frac{y_{s2}z}{H}\right) \tag{4b}$$

$$C_s = \cos(y_{s1})\cosh(y_{s2}) \tag{4c}$$

$$S_s = -\sin(y_{s1})\sinh(y_{s2}) \tag{4d}$$

$$y_{s1} = \frac{\omega H}{V_s}\sqrt{\frac{\sqrt{1+4\xi^2}+1}{2(1+4\xi^2)}} \tag{4e}$$

$$y_{s2} = -\frac{\omega H}{V_s}\sqrt{\frac{\sqrt{1+4\xi^2}-1}{2(1+4\xi^2)}} \tag{4f}$$

where ξ is the damping ratio.

$$a_v(z,t) = \frac{k_v g}{C_p^2 + S_p^2}\left[(C_p C_{pz} + S_p S_{pz})\cos\left(2\pi\frac{t}{T}\right) + (S_p C_{pz} - C_p S_{pz})\sin\left(2\pi\frac{t}{T}\right)\right] \tag{5}$$

where the symbols have their usual meanings and can be calculated in a similar way as given above in Eqs. (4a)–(4f).

For more details, readers are encouraged to refer Pain et al. [11] and Sharma et al. [15].

The mass ($m(y)$) of a thin slice of thickness dy considered at a depth y from the free surface is given by:

$$m(y) = \int_0^{H_w} \frac{\gamma}{g}(H_w - y)\left\{\frac{1}{\tan\theta} - \frac{1}{\tan(90° - \beta)}\right\}dy \tag{6}$$

The total horizontal and vertical inertial forces are given by:

$$Q_h(t) = \int_0^{H_w} a_h(y,t)m(y) \tag{7}$$

$$Q_v(t) = \int_0^{H_w} a_v(y,t)m(y) \tag{8}$$

The spacing between the helices (S_{hx}) and vertical spacing between the soil nails (S_v) is fixed as 5 times the helix diameter (D_h) for carrying out the analysis in the present case.

2.2 Computation of Deterministic Factor of Safety (FOS)

The factor of safety of the helical soil nail is calculated by applying the force equilibrium equation for the whole wedge, and is given by:

$$\text{FOS} = \frac{F_{RF}}{F_{DF}} \tag{9}$$

where F_{RF} is the resisting force and F_{DF} is the driving force, given by:

$$F_{\text{RF}} = [(Q_v + W)\cos\theta + P_{\text{equ}}\sin(\alpha + \theta) - Q_h\sin\theta]\tan\phi + P_{\text{equ}}\cos(\alpha + \theta) \tag{9a}$$

$$F_{\text{DF}} = (Q_v + W)\sin\theta + Q_h\cos\theta \tag{9b}$$

$$P_{\text{equ}} = \sum_{i=1}^{n} P_o^i \tag{9c}$$

P_{equ} is the equivalent tensile force per unit horizontal spacing acting along the nail axis.

3 Probabilistic Analysis

As discussed in the introduction section, probabilistic analysis gives us a comprehensive information regarding the stability of reinforced structures. In this section, probabilistic analysis is performed using the MCS to calculate the P_f and β_{min} of the helical soil nailed wall. The pullout mode of failure is considered, while performing the analysis, it being the most critical one in the calculation of the P_f of soil nailed walls and slopes.

3.1 Performance Function

A performance function is the basis of any probabilistic analysis technique and is primarily employed to differentiate between the acceptable and the unacceptable, where the acceptable value is marked by a positive value of limit state function

$(g_{\text{pullnail}}(X) > 0)$. In this study, limit state function for pullout mode of failure is defined by:

$$g_{\text{pullnail}}(X) = \text{FOS} - 1 \tag{10}$$

where FOS is the factor of safety given by Eq. (9).

3.2 Monte-Carlo Simulation

The Monte-Carlo simulation (MCS) is a tool used to predict the probability of varied outcomes, which is difficult to model owing to the involvement of random variables. It is widely used to estimate the risk and uncertainty associated with an event. Due to its versatile use in almost every field, it is also known as the multiple probability simulation. The MCS assigns multiple values to a random variable to obtain multiple results, followed by taking an average of these results. The results estimated using the MCS are highly accurate and are used as a basis in comparison with other reliability methods.

In the present study, the value of performance function $(g_{\text{pullnail}}(X))$ is evaluated finite number of times (e.g., 50,000 or 10^5 or 10^6) for a given set of random variables. The number of times this value of $g_{\text{pullnail}}(X)$ falls less than zero is counted, and the associated probability of failure is calculated as:

$$P_f = \left(\text{No. of times the value of } g_{\text{pullnail}}(X) < 0\right) / (\text{Number of realizations}) \tag{11}$$

In the following section, the P_f and $\beta_{\min}$ of a soil nailed wall are calculated using the MCS, considering the pullout mode of failure.

4 Results and Discussions

The random variables used in the present study along with their distribution are tabulated below (Table 1). The influence, of CoV (ϕ) on the P_f and $\beta_{\min}$ of soil nailed wall for $\beta = 0°$ (with vertical), is presented and plotted. Moreover, the comparison of helical soil nailed wall with conventional soil nailed wall is presented to showcase the superiority of the former over the latter one.

Table 1 Input random variables used in the present study

Random variable	Properties		
	Mean (μ)	(CoV) %	Distribution
γ	20 kN/m^3	5	Normal
ϕ	30°	5–15	Log-normal
V_s	100 m/s	5	Normal

4.1 Comparison of Helical Soil Nailed Wall with Conventional Soil Nailed Wall

Figure 2, presents a comparison of the values of P_f for two different soil nailed walls viz. helical and conventional, for $\beta = 0°$, $\alpha = 0°$, $H = 10$ m, L = 8 m, c = 0, $d = 0.04$ m, $k_v = 0.5*k_h$, $V_s = 100$ m/s, $V_p = 1.87*V_s$; $D = D_p = 0.1$, $f = 1.5$ Hz, $\delta = 0.75*\phi$, $\gamma = 20$ kN/m^3, $\phi = 30°$, and $k_h = 0$. The value of D_h is taken as 6d and d for helical and conventional soil nails, respectively. Also, the values of S_h and S_v are taken as 5d and 0.6 m for helical and conventional soil nails, respectively. It is directly inferred from the plot that the values of P_f for conventional soil nailed wall are greater than that of the helical soil nailed wall for different values of CoV (ϕ). This is due to the reason that the pullout capacity of the conventional soil nail is dependent mainly on the soil–nail interface shear strength [15], whereas in case of the helical soil nail, it is dependent on the helices affixed to the soil nail shaft in addition to the contribution of soil–nail shaft itself. This clearly proves the competency of helical soil nailed wall in decreasing the cost of construction as less number of helical soil nails are required to stabilize the same wall in contrast to the conventional soil nails.

4.2 Influence of CoV(Φ) on P_f

While performing the reliability analysis of geotechnical structures, CoV (ϕ) substantially influences the stability of the structure, be it helical soil nailed wall or geosynthetic reinforced slope/wall. Figure 3 shows the influence of CoV (ϕ) on the
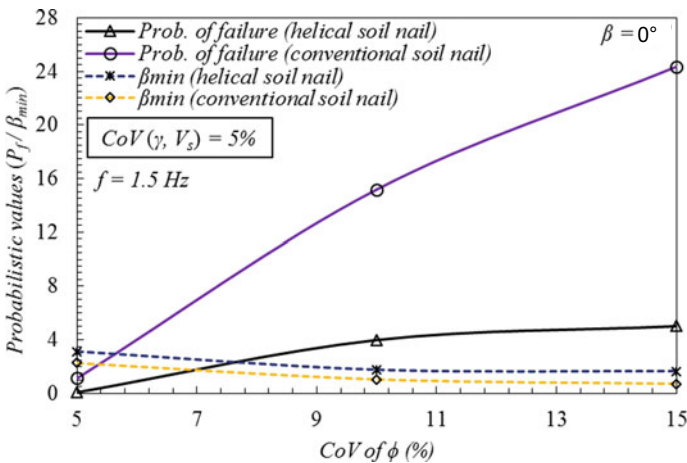
Fig. 2 Comparison of P_f for conventional and helical soil nailed wall
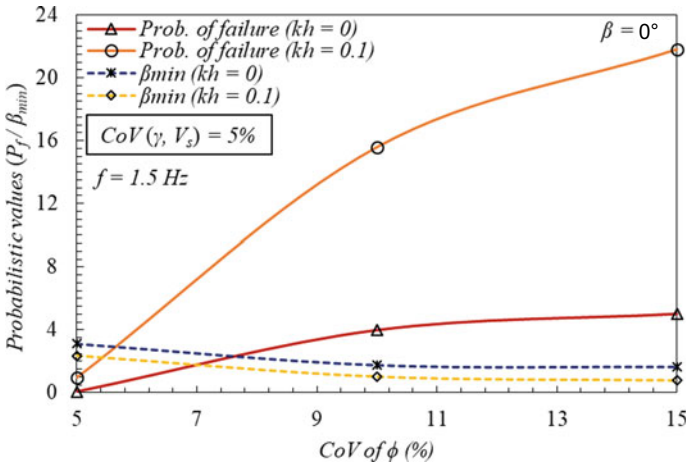
Fig. 3 Influence of CoV (ϕ) on probabilistic values (P_f and β_{min}) of helical soil nailed wall

P_f and β_{min} of soil nailed wall for two different cases of walls viz. $k_h = 0$ and 0.1. The value of $\beta = 0°$. The CoV (γ and V_s) are kept constant at 5%, whereas the CoV (ϕ) is varied from 5 to 15%, keeping in mind the actual field conditions. The results indicate that as the CoV (ϕ) increases, the P_f of helical soil nailed wall also increases and consequently, and the reliability index (β_{min}) decreases. This is due to the increase in value of variance with increasing value of CoV (ϕ). Moreover, as the value of k_h increases, the value of P_f of helical soil nailed wall also increases and consequently, β_{min} decreases.

In Fig. 3, for $\beta = 0°$, $\alpha = 0°$, $H = 10$ m, $L = 8$ m, $c = 0$, $S_v = S_h = S_{hx} = 5*D_h$, $d = 0.04$ m, $D_h = 6d$, $k_v = 0.5*k_h$, $V_s = 100$ m/s, $V_p = 1.87*V_s$; $D = D_p = 0.1$, $f = 1.5$ Hz, $\delta = 0.75*\phi$, $\gamma = 20$ kN/m^3, $\phi = 30°$, and $k_h = 0.1$, the value of P_f for CoV (ϕ) = 5% is less than CoV (ϕ) = 10% and 15% by 93.89% and 95.55%, respectively. The results follow the same trend when the value of $k_h = 0$.

Figure 3, also compares the values of P_f for two different values of k_h. For CoV (ϕ) = 5%, 10%, and 15%, the P_f for $k_h = 0$ is less than $k_h = 0.1$ by 91.75%, 74.41%, and 77%, respectively.

4.3   Influence of Nail Inclination Angle (α) on P_f

Figure 4 shows the influence of α (with the horizontal) on the P_f of soil nailed wall for $\beta = 0°$. The CoV (γ and V_s) are kept constant at 5%, whereas the CoV (ϕ) is varied from 5 to 15%. The results indicate that as the value of α increases, the P_f of helical soil nailed wall also increases and consequently, and the reliability index (β_{min}) decreases.
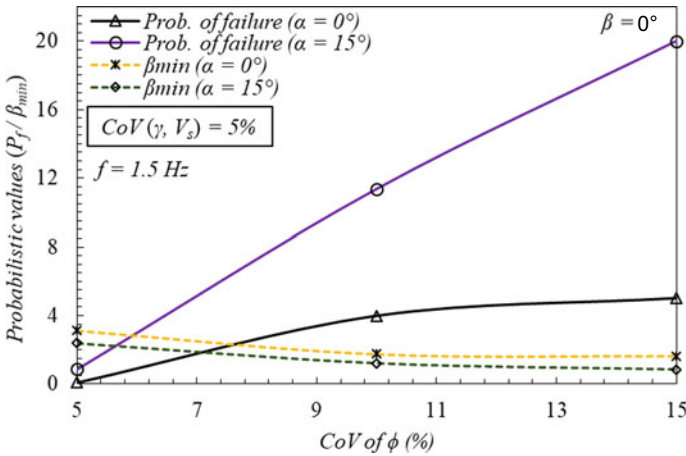
Fig. 4 Influence of α on probabilistic values (P_f and β_{min}) of helical soil nailed wall

In Fig. 4, for $\beta = 0°$, $H = 10$ m, $L = 8$ m, $c = 0$, $S_v = S_h = S_{hx} = 5*D_h$, $d = 0.04$ m, $D_h = 6d$, $k_v = 0.5*k_h$, $V_s = 100$ m/s, $V_p = 1.87*V_s$; $D = D_p = 0.1$, $f = 1.5$ Hz, $\delta = 0.75*\phi$, $\gamma = 20$ kN/m^3, $\phi = 30°$, and $k_h = 0$, the value of P_f for $\alpha = 0°$ is less than $\alpha = 15°$ by 90.69%, 64.90%, and 74.91%, for CoV (ϕ) = 5%, 10%, and 15%, respectively.

Note: The present study is first of its kind and therefore, the comparison of the probabilistic analysis using the MCS in a modified pseudo-dynamic framework is not feasible. However, the results, for the deterministic formulation using the MPD framework, are carefully verified with Sharma et al. [15]. The results for the correctness of the MCS are verified with the results of Babu and Singh [21] for the conventional soil nailed walls.

5   Summary and Conclusions

In the present study, the behavior of helical soil nailed wall is investigated in the probabilistic framework. The value of factor of safety is calculated by running the deterministic algorithm in a modified pseudo-dynamic framework. The soil is modelled as a visco–elastic medium using the K–V model. The present methodology addresses the limitations of its previous counterparts and satisfies the necessary boundary conditions. The probabilistic analysis of the helical soil nailed wall in a modified pseudo-dynamic framework is conducted, which is first of its kind study. The soil is considered to be dry, homogenous, and isotropic. The internal friction angle of soil (ϕ), unit weight (γ) and shear wave velocity (V_s) are chosen as random variables. The probabilistic analysis is conducted using the Monte-Carlo simulation (MCS). The influence of CoV (ϕ) on the P_f of helical soil nailed wall is

illustrated by plotting a graph between the P_f and CoV (ϕ). On the basis of the results, the following conclusions are drawn:

- The modified pseudo-dynamic method is a robust and realistic method to deterministically analyze the helical soil nailed walls.
- The probabilistic analysis is must, while calculating the stability of helical soil nailed walls because it is realistic in nature and considers the uncertainty of the input random variables.
- The MCS is an accurate method to probabilistically analyze the helical soil nailed walls.
- The helical soil nails provide better stability to the soil in comparison with the conventional soil nails as the value of P_f of nailed walls decreases when helical nails are used instead of conventional nails for the same set of input parameters.
- The CoV (ϕ) substantially influences the stability of soil nailed walls. An increase in CoV (ϕ) leads to a noticeable increment in the value of P_f of helical soil nailed wall.
- The value of k_h also influences the stability of soil nailed walls. An increase in the value of k_h leads to a noticeable increment in the value of P_f of helical soil nailed wall.
- The P_f of helical soil nailed wall increases as the angle of soil nail inclination with the horizontal (α) increases.
- The present probabilistic analysis in the modified pseudo-dynamic framework is an accurate and powerful probabilistic tool to analyze the helical soil nailed walls and may lead to an economic design of these structures.

References

1. Sharma, M., Samanta, M., Sarkar, S.: Novel laboratory pullout device for conventional and helical soil nails. Geotech. Test. J. **42**(5), 1314–1335 (2018)
2. Sharma, M., Samanta, M., Punetha, P.: Experimental investigation and modeling of pullout response of soil nails in cohesionless medium. Int. J. Geomech. **19**(3), 04019002 (2019)
3. Sharma, M., Samanta, M., Sarkar, S.: Soil nailing: an effective slope stabilization technique. In: Landslides: Theory, Practice and Modelling. Springer, Cham, pp. 173–199 (2019)
4. Felio, G.Y., Vucetic, M., Hudson, M., Barar, O., Chapman, R.: Performance of soil nailed walls during the October 17, 1989 Loma Prieta earthquake. In: Proceedings of the 43rd Canadian Geotechnical Conference, Quebec, vol. 1, pp. 165–173 (1990)
5. Vucetic, M., Tufenkjian, M., Doroudian, M.: Dynamic centrifuge testing of soil-nailed excavations. Geotech. Test. J. **16**(2), 172–187 (1993)
6. Tufenkjian, M.R., Vucetic, M.: Dynamic failure mechanism of soil-nailed excavation models in centrifuge. ASCE J. Geotech. Geoenviron. Eng. **126**(3), 227–235 (2000)
7. Saran, S., Mittal, S., Meenal, G.: Pseudo static analysis of nailed vertical excavations in sands. Indian Geotech. J. **35**(4), 401–417 (2005)
8. Sarangi, P., Ghosh, P.: Seismic analysis of nailed vertical excavation using pseudo dynamic approach. Earthq. Eng. Eng. Vib. **15**(4), 621–631 (2016)
9. Bellezza, I.: A new pseudo-dynamic approach for seismic active soil thrust. Geotech. Geol. Eng. **32**(2), 561–576 (2014)

10. Pain, A., Choudhury, D., Bhattacharyya, S.K.: Seismic stability of retaining wall–soil sliding interaction using modified pseudo-dynamic method. Géotech. Lett. **5**(1), 56–61 (2015)
11. Pain, A., Choudhury, D., Bhattacharyya, S.K.: Effect of dynamic soil properties and frequency content of harmonic excitation on the internal stability of reinforced soil retaining structure. Geotext. Geomembr. **45**(5), 471–486 (2017)
12. Annapareddy, V.R., Pain, A., Sarkar, S.: Seismic translational failure analysis of MSW landfills using modified pseudo-dynamic approach. Int. J. Geomech. **17**(10), 04017086 (2017)
13. Rajesh, B.G., Choudhury, D.: Seismic passive earth resistance in submerged soils using modified pseudo-dynamic method with curved rupture surface. Mar. Georesour. Geotechnol. **35**(7), 930–938 (2017)
14. Agarwal, E., Pain, A., Mukhopadhyay, T., Metya, S., Sarkar, S.: Efficient computational system reliability analysis of reinforced soil-retaining structures under seismic conditions including the effect of simulated noise. Eng. Comput. 1–23 (2021). https://doi.org/10.1007/s00366-020-01281-8
15. Sharma, M., Choudhury, D., Samanta, M., Sarkar, S., Annapareddy, V.R.: Analysis of helical soil-nailed walls under static and seismic conditions. Can. Geotech. J. **57**(6), 815–827 (2020)
16. Sharma, M., Samanta, M., Sarkar, S.: Laboratory study on pullout capacity of helical soil nail in cohesionless soil. Can. Geotech. J. **54**(10), 1482–1495 (2017)
17. Samanta, M., Sharma, M., Sarkar, S., Punetha, P.: Pullout capacity of driven soil nails in cohesionless soil and its constitutive modelling. In: Proceedings of the Conference on Numerical Modeling in Geomechanics, Indian Institute of Technology, Roorkee, India (2017)
18. Tokhi, H., Ren, G., Li, J.: Laboratory pullout resistance of a new screw soil nail in residual soil. Can. Geotech. J. **55**(5), 609–619 (2018)
19. Yuan, J.X., Yang, Y., Tham, L.G., Lee, P.K.K., Tsui, Y.: New approach to limit equilibrium and reliability analysis of soil nailed walls. Int. J. Geomech. **3**(2), 145–151 (2003)
20. Sivakumar Babu, G.L., Singh, V.P.: Reliability analysis of soil nail walls. In: Georisk: Assessment and Management of Risk for Engineered Systems and Geohazards vol. 3(1), pp. 44–54 (2009)
21. Babu, G.L.S., Singh, V.P.: Reliability based study on seismic stability of soil nail walls (2009)
22. Hu, Y., Lin, P.: Probabilistic prediction of maximum tensile loads in soil nails. Adv. Civil Eng. (2018)
23. Mayerhof, G.G.: Bearing capacity and settlemtn of pile foundations. J. Geotech. Geoenviron. Eng. **102**, 11962 (1976) (.ASCE#)

Effect of Geogrid on Landslide Prevention of Soil Slope Under Static Loading

Shubham Gupta, Vishal Sharma, Raju Sarkar, and Amit Kumar Srivastava

1 Introduction

In the advanced world of engineering, where engineers are making new goals day-by-day, while researchers are contributing to the achievement of those goals. In the geotechnical engineer world, the bearing capacity of the soil is one of the most important parameter and researchers are accord with a lot of ideas and innovations to tackle it.

For a long time, advancement in geogrids manufacturing and its use as reinforcement material in the soil [16] and rock [13] to increase bearing capacity has been seen. A lot of researchers have done humongous work by studying the parametric effect of geogrid placement-namely first reinforcement depth, the width of reinforcement, no. of reinforcement layers, etc. [1, 4, 11, 17, 18, 23]. The study reveals that placement of geogrid as reinforcement in soil leads to an increase in bearing capacity significantly.

In the past, geogrids are successfully used for a different types of soils under different loadings for the shallow isolated foundations of different shapes over different ground types [6, 7, 15, 20].

In recent studies, researchers have studied the effect of placement styling like geogrid with wraparound ends, grid anchors [2, 4, 10] and revealed that placement styling has a great impact on bearing capacity.

Forsyth and Beiber [8], Schneider and Holtz [19] used the geogrid in the construction of slopes to enhance their stability. Over the foundation of these pieces of literature, numerical analysis is carried out using Plaxis 2D, a finite element software working on finite element method (FEM) to study the influence on bearing

S. Gupta · V. Sharma · R. Sarkar · A. K. Srivastava (✉)
Delhi Technological University, New Delhi, India
e-mail: aksrivastava@dce.ac.in

R. Sarkar
e-mail: rajusarkar@dce.ac.in

capacity and stability. An analysis is carried out for a shallow strip foundation with different geogrid placement styling for 30°, 40° and 50° slope. With this, the effect on stability and bearing capacity is also analyzed with the change in edge distance from the crest of the slope.

2 Experimental Data

In this study, researchers are studying the effect of geogrid placement in the sloppy ground having strip footing at ground level. The properties of soil are taken from Zidan [25], who has built the parameters for medium density according to the soil used by Moghaddas-Tafreshi and Dawson [12]. Moghaddas-Tafreshi and Dawson [12] has carried out grain size analysis and reported the soil as poorly graded sand. As sand is cohesion less and formation of 50° slope without cohesion is not possible with those properties so we have added the cohesion property to the soil making it a C-φ soil. The stress in the soil is depicted employing drained triaxial secant stiffness E_{50}^{ref}, oedometer tangent stiffness E_{oed}^{ref} and unloading and reloading stiffness E_{ur}^{ref}. Properties of soil used for analysis is presented in Table 1. In this study, soil is assumed to be dry with no. interference of the groundwater table. A biaxial geogrid is used as a reinforcement material whose properties are provided by Tensar Pvt. Ltd. for both machine direction (MD) and cross-machine direction (CMD) placement of geogrid, presented in Table 2. A parametric study is carried out to learn out the optimum parameter of geogrid placement under different placement styling presented in Figs. 1 and 2 to take out maximum efficiency from reinforcement to have enhanced value of bearing capacity and slope stability.

Table 1 Hardening soil model parameters

Parameter	Y_{bulk} (kPa)	E_{50}^{ref}(kPa)	E_{oed}^{ref}(kPa)	E_{ur}^{ref}(kPa)	C (kPa)	Φ (°)	Ψ (°)	R_{inter}
Values	17	25,000	25,000	75,000	15	30	0	1

Table 2 Bi-axial geogrid properties (Tensar)

Properties	MD	CMD
Material	Polypropylene	
Load at 2% strain (kN/m)	11	12
Load at 5% strain (kN/m)	22	25
Maximum strain (%)	9	9
Load at maximum strain (kN/m)	30	30
Axial stiffness (kN/m)	550	600
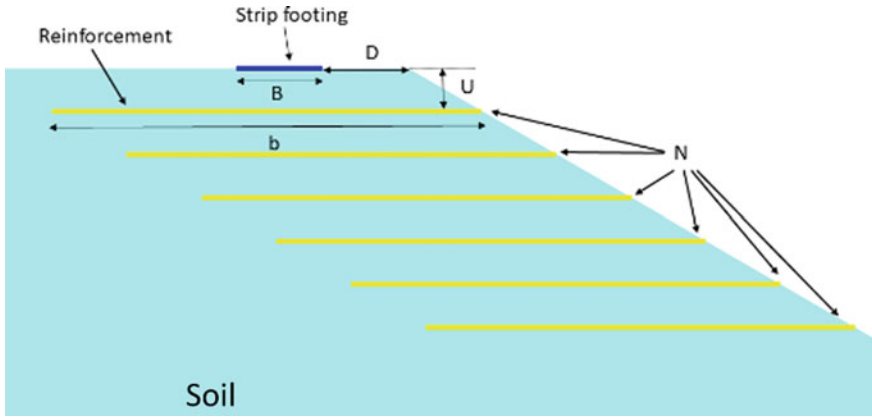
Fig. 1 Flat placement style variables
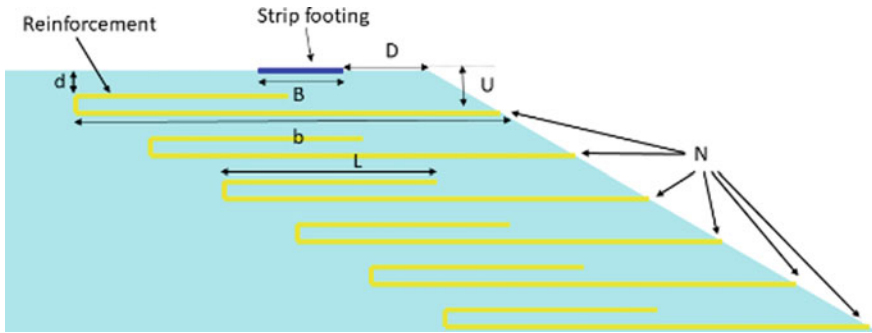
Fig. 2 Wraparound placement style variables

3   Numerical Modeling

Plaxis 2D, a finite element software is used to carry out the analysis. A strip footing of width (B) 1 m was modeled in two dimensions with plane-strain analysis. Normally, fully fixed boundary condition is applied to the bottom of the model, whereas displacement is restrained in the X-axis for side boundaries of the model presented in Fig. 3. There α denotes the slope angle. The footing was modeled as a plate element with properties presented in Table 3. The self-weight of footing is neglected. The footing is placed on the surface having a uniform vertical displacement in Y-direction over it which makes it act like a rigid foundation presented in Fig. 3. Figure 3 also represents the model dimension taken for analysis. Maximum allowable displacement for reinforced concrete structures over the sand and hard clay soil for isolated footing is 50 mm according to IS: 1904-1986 [9]. But
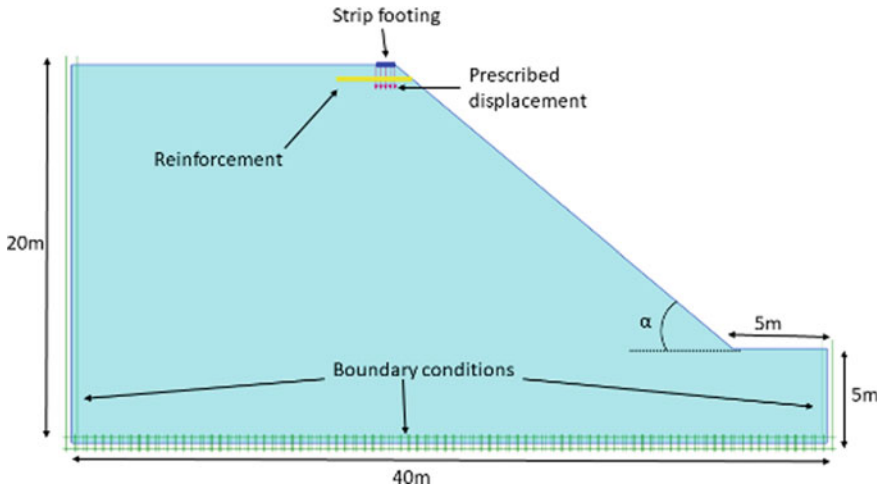
Fig. 3 Model configuration

Table 3 Plate element properties

Properties	Value
Material property	Elastic
Width (m)	1
Thickness (mm)	50
Axial stiffness (kN/m)	1,00,00,000
Flexural stiffness (kN/m)	2083

in the case of a 50° slope, shear failure of soil takes place (before reaching settlement criteria) causing slope failure; therefore, shear failure criteria is used for safe bearing capacity (SBC) calculation. The foundation settlement of 28 mm is observed before slope failure, so for calculation purpose 25 mm of prescribed displacement is applied over the footing and effect of various reinforcement placement styling is observed. The possible reason for failure is less value of cohesion in the soil which helps in initial stage stability. So a prescribed displacement of 25 mm is used for 50° slope, whereas for other slopes displacement remain the same. A 15 nodal triangular mesh element is used to model soil, plate and geogrid element. A very fine finite element mesh is utilized throughout the model so that the effect of mesh size on the model is minimum. Meshing leads to the generation of around 6000 elements and 50,000 nodes in the model. Obtained mesh quality is good because of equilateral triangles connecting each other. Better will be the meshing, more the value of mesh quality.

The soil in plaxis 2D is represented as hardening soil model which is a nonlinear elasto-plastic, hyperbolic stress–strain model. Model is well capable of undertaking the elastoplastic nature of the soil. Table 1 shows all parameters required for the soil model. The geogrids are represented using the N-epsilon curve which is very well

capable of capturing the elastic–plastic nature of geogrid. Table 2 shows the parameters required with elastic axial stiffness taken for analysis.

4 Model Parameters

All parametric analysis done in this study is presented in Table 4. Mainly, three phases are constructed for each run. The first phase is for the generation of initial stresses in soil based on density of soil.

For this phase gravity loading is used as calculation type in which initial stresses are generated based on volumetric weight of soil.

For the second phase, the foundation is placed with geogrid in reinforced soil case and plastic analysis is set as calculation type which is capable of carrying out analysis till either failure occur in soil or prescribed settlement was reached. For the third phase in which stability analysis of slope is carried out, safety is set as calculation type. Plaxis 2D uses SRM (strength reduction method) also known as the C-φ reduction method which is common and popular in finite element software. This method reduces the value of shear strength parameters, i.e., cohesion (C) and angle of internal friction (ϕ) till failure is reached. The factor of safety (FOS) is reported using the relations defined as

$$\text{FOS} = \frac{C_{\text{actual}}}{C_{\text{reduced}}} \tag{1}$$

$$\text{FOS} = \frac{\tan(\phi_{\text{actual}})}{\tan(\phi_{\text{reduced}})} \tag{2}$$

5 Result and Discussion

The motive of this study is to find the best arrangement of reinforcement to get maximum effective change in bearing capacity of soil and safety from the failure of slope. An improvement factor (IF) defined as

$$\text{IF} = \frac{\text{BC}_{\text{R}}}{\text{BC}_{\text{U}}} \tag{3}$$

It is used to analyze the improvement in bearing capacity of soil under each variable. Here, BC_{R} and BC_{U} are the bearing capacity of soil under reinforced and unreinforced conditions. Many researchers have given this improvement factor as a bearing capacity ratio (BCR) [4, 21, 22].

Table 4 Model specifications

Model number	Slope angle	Placement styling	Variable					
			U/B	b/B	L/B	d/B	D/B	N
1–3	30°	Unreinforced					0, 1, 2	
4–18		Flat	0.25, 0.33, 0.5, 0.75, 1	4, 5, 6			0	1
19–36			0.5	5			0, 1, 2	1, 2, 3, 4, 5, 6
37–56		Wraparound	0.5	5	0.1, 0.2, 0.3, 0.4, 0.5	0.1, 0.2, 0.3, 0.4	0	1
57–74			0.5	5	0.5	0.2	0, 1, 2	1, 2, 3, 4, 5, 6
75–77	40°	Unreinforced					0, 1, 2	
78–92		Flat	0.25, 0.33, 0.5, 0.75, 1	4, 5, 6			0	1
93–110			0.5	5			0, 1, 2	1, 2, 3, 4, 5, 6
111–130		Wraparound	0.5	5	0.1, 0.2, 0.3, 0.4, 0.5	0.1, 0.2, 0.3, 0.4	0	1
131–148			0.5	5	0.5	0.2	0, 1, 2	1, 2, 3, 4, 5, 6
149–151	50°	Unreinforced					0, 1, 2	
152–166		Flat	0.25, 0.33, 0.5, 0.75, 1	4, 5, 6			0	1
167–184			0.5	5			0, 1, 2	1, 2, 3, 4, 5, 6
185–204		Wraparound	0.5	5	0.1, 0.2, 0.3, 0.4, 0.5	0.1, 0.2, 0.3, 0.4	0	1
205–222			0.5	5	0.5	0.2	0, 1, 2	1, 2, 3, 4, 5, 6

5.1   Parametric Study

The effect of different variables, including first reinforcement depth ratio (U/B), the width of reinforcement ratio (b/B) is analyzed for flat placement styling whereas lap depth ratio (d/B) & overlap length ratio (L/b) is analyzed for wraparound placement styling. Analysis for edge distance ratio (D/B) vs the number of geogrid layers (N) is done for both placement styling. The effect of the above variables is studied for both bearing capacity and stability analysis.

Effect of first reinforcement depth ratio (U/B) & width of reinforcement ratio (b/B) on bearing capacity

In Fig. 4, it was observed that with increment in the value of first reinforcement depth leads to a rise in the value of bearing capacity up to U/B = 0.5. After that it starts decreasing as the value of U/B further increases. With the increase in the value of the width of reinforcement ratio (b/B), the improvement is observed but improvement is significant up to the ratio of b/B = 5. After this value, an increment occurs but the overall improvement is insignificant. The above effect does not alter with the change in slope angle as seen in Fig. 4. Same observations are also recorded by Yoo [24], El-Sawwaf [6], Mudgal et al. [14] for slope angles of 33°, 34° and 35° respectively. So the most optimum parameter from the above observation is found to be 0.5 for U/B & 5 for b/B for all slope angles.

Effect of edge distance ratio (D/B) & number of geogrid layers (N) on bearing capacity in flat placement styling case

With an increase in edge distance, the improvement in bearing capacity occurs [15]. The same effect was also observed at different D/B ratios for each slope angle presented in Fig. 5. With the increase in the number of geogrid layers (N), the improvement in bearing capacity occurs [6, 14]. But in this study, displacement is
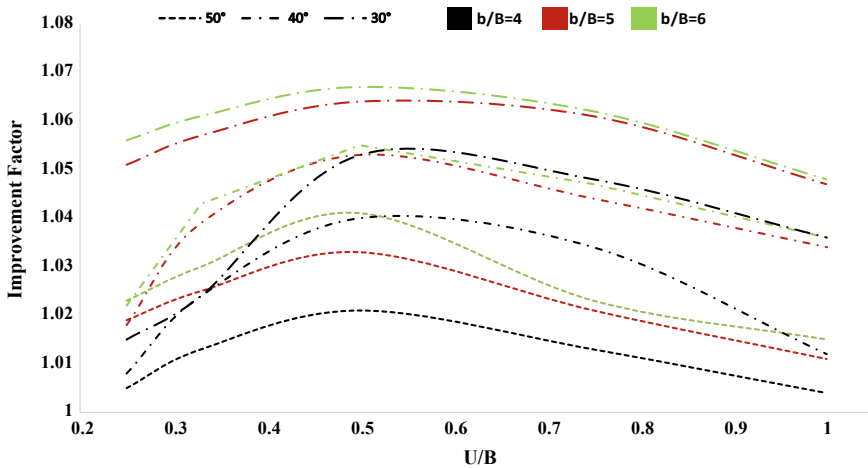
Fig. 4 Variation of IF with first reinforcement depth ratio
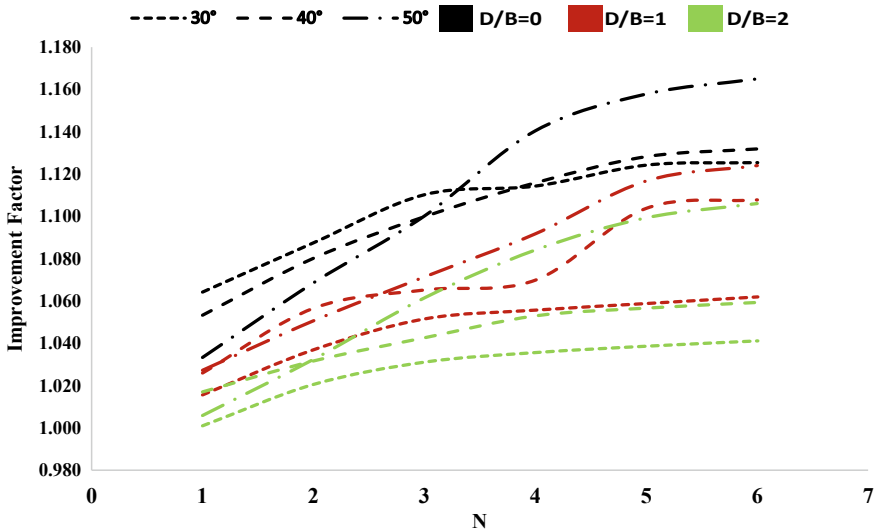
Fig. 5 Variation of IF with number of geogrid layers

fixed and having a small value, because of which the improvement in bearing capacity got declines with an increment of N value as shown in Fig. 5. Also, increment in edge distance ratio leads to the decrease in an effective number of geogrid helping in bearing capacity increment because of no modification in optimum values of parameters with change in D/B value.

Effect of Lap depth ratio (d/B) & overlap length ratio (L/b) on bearing capacity in wraparound placement styling case

From Figs. 6, 7 and 8, it was observed that lap depth ratio has a minuscule effect on bearing capacity improvement of soil as it doesn't help in resistance of any load. This is due to non-generation of axial force in bent geogrid which is a suitable reason for its no helping hand in bearing capacity. It was observed that with an increase in overlap length ratio, the improvement in bearing capacity occurs [4, 10]. It is observed that with an increase in overlap length ratio (L/b), the axial force-carrying capability of geogrid increases. From here, the optimum parameters rises are d/B = 0.2 & L/b = 0.5 for all slope angles. While analysis other parameters like U/B and b/B are taken as optimum observed from the above study of effect.

Effect of edge distance ratio (D/B) & number of geogrid layers (N) on bearing capacity in wraparound placement styling case

The same effect of edge distance ratio (D/B) is observed as observed above for the flat placement style presented in Fig. 9. With an increase in the number of geogrid layers (N), the improvement in bearing capacity is better as compare to the
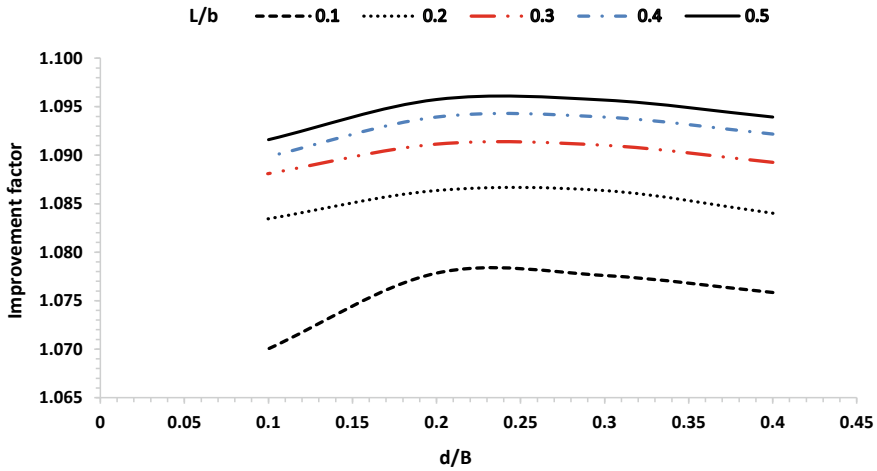
Fig. 6 Variation of IF with lap depth ratio for 30° slope
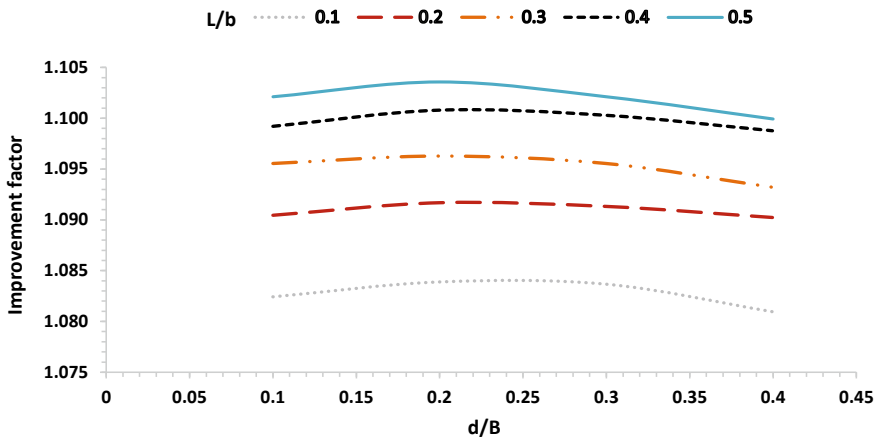
Fig. 7 Variation of IF with lap depth ratio for 40° slope

improvement observed in the flat placement style. This is due to fact that wrap-around placement styling causes the transfer of vertical displacement to a great depth which allows reinforcement layers to provide their helping hand in the improvement of bearing capacity [4].

Effect of flat & wraparound placement styling on the stability of the slope

The stability of slope or the risk of failure of slope reduces if the bearing capacity of that slope increases. The above study shows the respective improvement in bearing capacity with placement of reinforcement at suitable variables. Thus, those
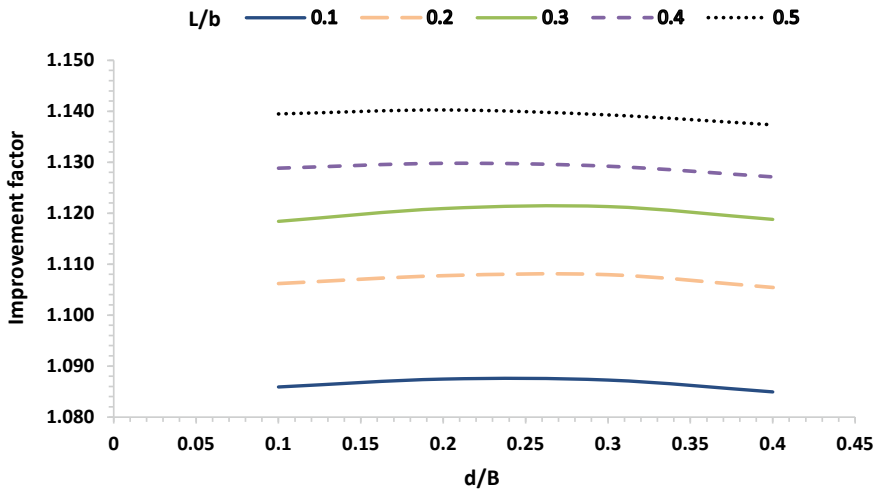
Fig. 8 Variation of IF with lap length ratio for 50° slope
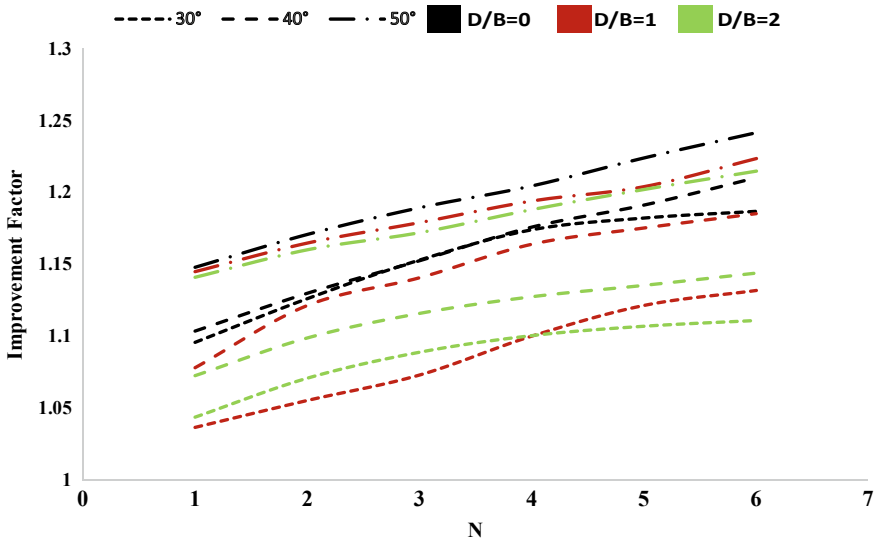
Fig. 9 Variation of IF with number of geogrid layers

optimum variables are used for the stability analysis of different angled slopes using the strength reduction method (SRM) which is an only available method in plaxis 2D. Suitable slip circle is observed for 50° slope angle using this method shown in Fig. 10. Slip circles are imperfect for 30° and 40° angled slopes. An analysis is carried out for two different cases and results are presented in Figs. 11, 12, 13 and
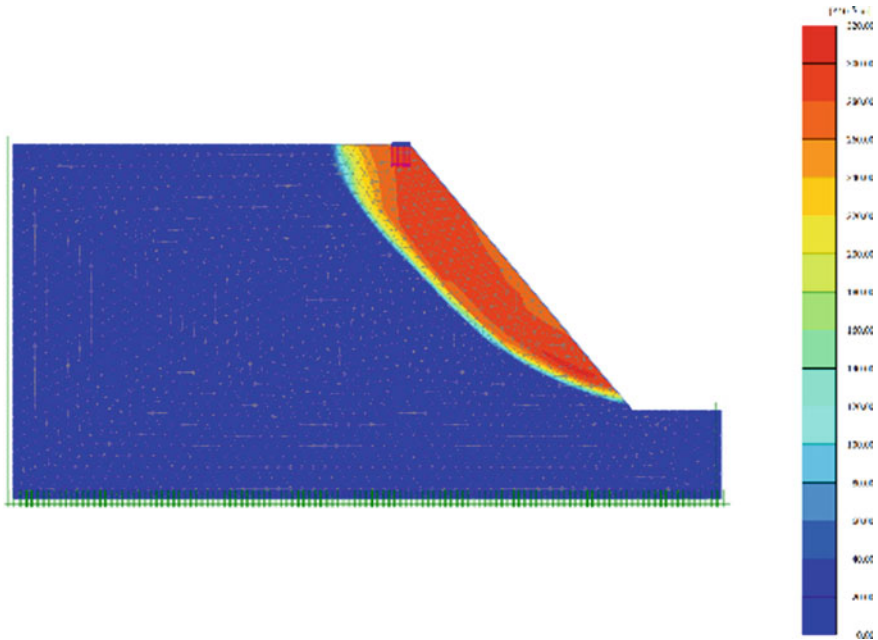
Fig. 10 Displacement of slip circle for 50° slope
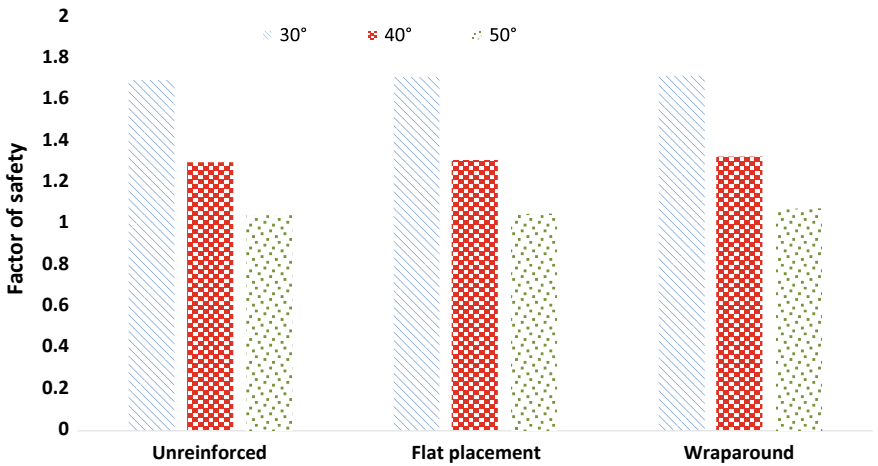
Fig. 11 Variation of FOS for different slope angles with different styling for $N = 1$

14. In the first case, the factor of safety is observed for a single-reinforcement layer. The reinforcement layers are laid at optimum parameters found in the study of bearing capacity. From Fig. 11, it was observed that wraparound reinforcement help in achieving better stability as compare to flat reinforcement placement for all
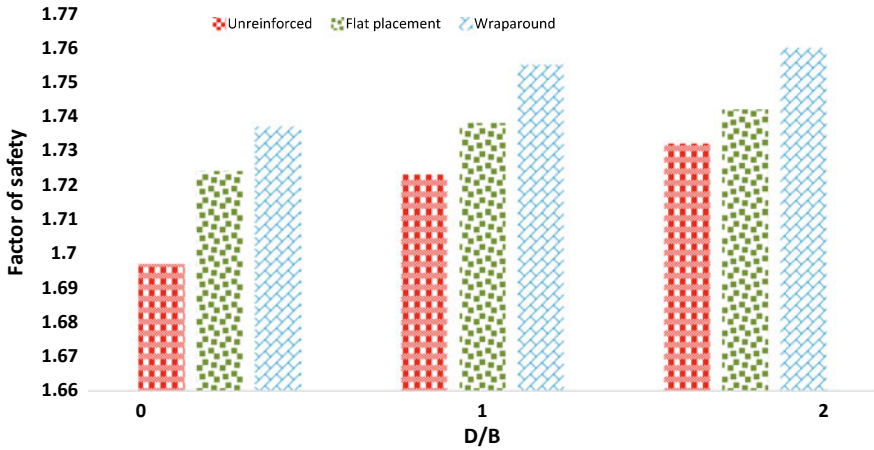
Fig. 12 Variation of FOS with edge distance ratio for 30° slope for $N = 6$
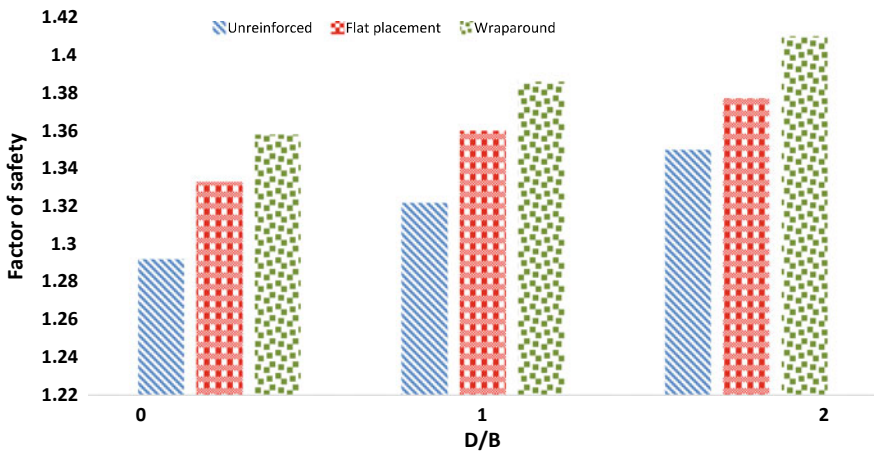
Fig. 13 Variation of FOS with edge distance ratio for 40° slope for $N = 6$

slope angles which ultimately contribute to providing more safety from the land-slide of soil slope. In the second case, the factor of safety is observed for multi-layers of geogrid including the effect of edge distance ratio (D/B). From Figs. 12, 13 and 14, it was observed that maximum safety is observed for wrap-around reinforcement although the safety value increases with a decrease in slope angle and increases with increase in edge distance ratio value [5].
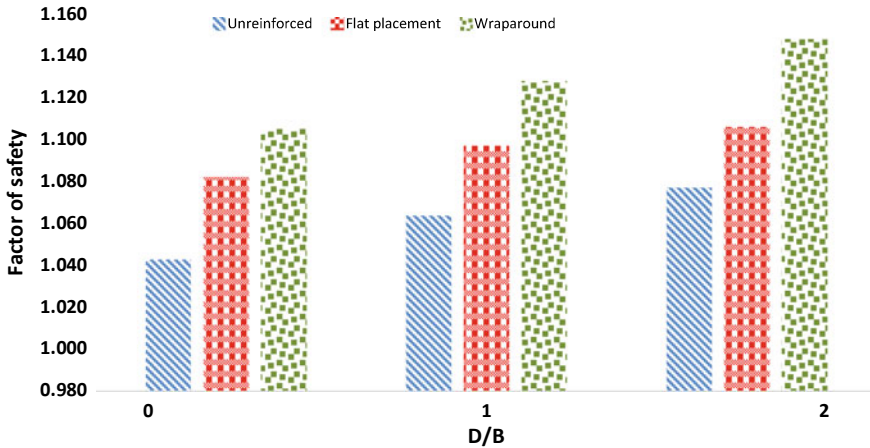
Fig. 14 Variation of FOS with edge distance ratio for 50° slope for $N = 6$

6 Conclusion

The effect on bearing capacity of soil geogrid addition in the soil slope of 30°, 40° and 50° is analyzed, placed in different styling, i.e., flat placement styling and wraparound placement styling. Various variables are analyzed and based on the above results various conclusions are been drawn:

1. Wraparound reinforcement placement styling is found to be more in comparison of unreinforced & flat reinforcement placement styling.
2. As the overlap length ratio (L/b) increases, the axial force in geogrid also increases causing increase in bearing capacity & slope stability.
3. Increment in bearing capacity is not upto the mark due to less allowable settlement over foundation causing low number of geogrid participation.
4. As the slip arc is forming throughout the slope reaching near the toe presented in Fig. 10, all the geogrids placed in slip arc zone provide a helping hand in increasing bearing capacity and stability of the slope.
5. While using SRM (strength reduction method), for 30° & 40° slope the displacement found to be more near the footing, while in 50° slope a good slip arc is formed presented in Fig. 10. The probable reason of this kind of result is failure of soil as general shear failure, causing increase in displacement with reduction in C-φ value of soil.
6. The wraparound reinforcement technique shows less horizontal displacement presented in Fig. 15 as compare to unreinforced case, causing enhanced values of bearing capacity and stability of the slope.
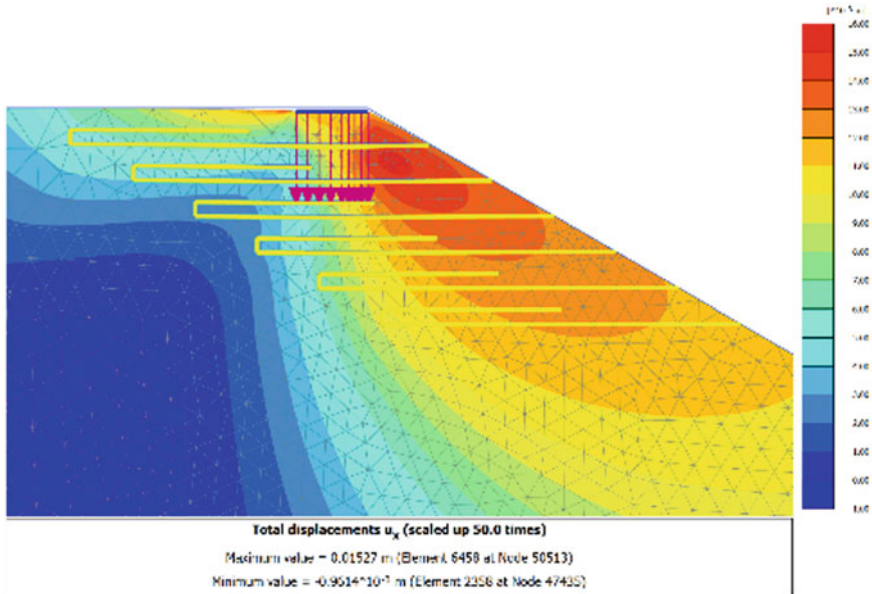
Fig. 15 Horizontal displacement of soil for 30° slope having six reinforcement layers at optimum parameters

Although wraparound placement styling came out with better results but carrying out the process of laying on field with high relative density of soil is challenging task.

References

1. Adams, M.T., Collin, J.G.: Large model spread footing load tests on geosynthetic reinforced soil foundations. J. Geotech. Geoenviron. Eng. **123**(1) (1997)
2. Alamshahi, S., Hataf, N.: Bearing capacity of strip footing on sand slopes reinforced with geogrid & grid-Anchor. Geotext. Geomembr. **27**, 217–226 (2008)
3. Anubhav, Basudhar, P.K.: Finite element simulation of strip footings resting on double faced wrap-around reinforced soil walls. ASCE, 2291–2300 (2010)
4. Aria, S., Shukla, S.K., Mohyeddin, A.: Numerical investigation of wraparound geotextile reinforcement technique for strengthening foundation soil. Int. J. Geomech. ISSN-1532-3641 (2019)
5. Baah-Frempong, E., Shukla, S.K.: Stability analysis & design charts for a sandy soil slope supporting an embedded strip footing. Int. J. Geo-Eng. **9**, 13 (2018)
6. El-Sawwaf, M.A.: Behavior of strip footing on geogrid-reinforced sand over a soft clay slope. Geotext. Geomembr. **25**, 50–60 (2007)
7. El-Sawwaf, M.A., Nazir, A.K.: Cyclic settlement behavior of strip footings resting on reinforced layered sand slope. J. Adv. Res. **3**, 315–324 (2011)

8. Forsyth, A., Bieber, D.A.: La Honda Slope Repair with Geogrid Reinforcement. Department of Transportation, California (2017)
9. IS: 1904.: Code of practice for design and construction of foundations in soils: general requirements (1986)
10. Kazi, M., Kumar Shukla, S., Habibi, D.: An improved method to increase the load-bearing capacity of strip footing resting on geotextile-reinforced sand bed. Indian Geotech. J. **45**(1), 98–109 (2014)
11. Khadra, A.A., Zidan, A.F., Gaber, Y.: Ground improvement technique using reinforcement with additives (experimental study). Life Sci. J. **16**(4) (2019)
12. Moghaddas-Tafreshi, S.N., Dawson, A.R.: Behaviour of footings on reinforced sand subjected to repeated loading—comparing use of 3D and planar geotextile. Geotext. Geomembr. **28**, 434–447 (2010)
13. Moradi, G., Abdolmaleki, A., Soltani, P., Ahmadvand, M.: A laboratory and numerical study on the effect of geogrid-box method on bearing capacity of rock-soil slopes. Geomech. Eng. **14**(4), 345–354 (2018)
14. Mudgal, A., Sarkar, R., Shrivastava, A.K.: Effect of 3D geogrid and glasgrid in the bearing capacity of square footing over soil slope. Int. J. Recent Technol. Eng. **8**(2). ISSN: 2277-3878 (2019)
15. Naeini, S.A., Rabe, B.K., Mahmoodi, E.: Bearing capacity & settlement of strip footing on geosynthetics reinforced clayey slopes. Central South Univ. **19**, 1116–1124 (2012)
16. Palmeira, E.M., Tatsuoka, F., Bathurst, R.J., Stevenson, P.E.: Advances in geosynthetics materials & applications for soil reinforcement & environmental protection works. Electron. J. Geotech. Eng. (2008)
17. Rai, R., Khandelwal, M., Jaiswal, A.: Application of geogrids in waste dump stability: a numerical modelling approach. Environ. Earth Sci. **66**, 1459–1465 (2011)
18. Salahudeen, A.B., Sadeeq, J.A.: Numerical modelling of soil reinforcement using geogrids. In: International Conference on Engineering & Technology Research, vol. 4 (2016). ISBN: 978-2902-58-6
19. Schneider, H.R., Holtz, R.D.: Design of slopes reinforced with geotextiles & geogrids. Geotext. Geomembr. **3**, 29–51 (1986)
20. Shukla, R.P., Jhaka, R.S.: A critical review on bearing capacity of a footing on sloping ground. In: 5th Young Indian Geotechnical Engineering Conference, pp. 58–65 (2015)
21. Shukla, S.K.: Geosynthetics and Their Applications. London. Thomas Telford (2002)
22. Shukla, S.K.: An Introduction to Geosynthetic Engineering. CRC Press/Taylor & Francis Group, Boca Raton, FL (2016)
23. Sri-Wulandari, P., Tjandra, D.: Analysis of geotextile reinforced road embankment using PLAXIS 2D. In: 5th International Conference of Euro Asia Civil Engineering Forum, pp. 358–362 (2015)
24. Yoo, C.: Laboratory investigation of bearing capacity behavior of strip footing on geo-grid-reinforced sand slope. Geotext. Geomembr. **19**, 279–298 (2001)
25. Zidan, A.F.: Numerical study of behavior of circular footing on geogrid-reinforced sand under static and dynamic loading. Geotech. Geol. Eng. **30**, 499–510 (2012)

Recent Advances in Early Warning Systems for Landslide Forecasting

Ram Wanare[ID]**, Kannan K. R. Iyer**[ID]**, and Prathyusha Jayanthi**[ID]

1 Introduction

Slope failure in hilly areas, mines, excavated sites, embankment, and waste dumps causes huge loss to mankind and infrastructure [3]. According to Froude and Petley [9], among the non-seismic landslides occurring between 2004 and 2016 in Asia, the major share was in the Himalayan region. In the Indian subcontinent region, the recent natural disasters due to earthquake (viz., landslides and slope failure) due to heavy rainfall was reported in Uttarakhand state in 2013 [17], Maline village in Maharashtra during 2014 [7] and in Nepal during 2015 [25], have propelled the need to obtain an effective way for preventing huge loss due to landslides and slope failures. Therefore, with respect to the ongoing infrastructure development in hilly terrains, the requirement of robust system that can prevent huge loss has been realized. The common methods to prevent slope failures are the use of ground/slope anchors and reinforced earth wall, which work on the principle of mechanical reinforcement, and generation of passive earth pressure resistance [29]. Additionally, higher values of factor of safety against the failure, have been utilized at most of the failure prone locations [27]. However, the application of these methods/approaches is limited for large slopes and may not be economical. Generally, the chances of failure are maximum for small slopes [27]. However, in continuous rainfall regions, landslides and large slope failures can occur and the conventional measures are not very useful, and the application of slope anchors or slope stabilization might not be effective in preventing such disasters. Before a

R. Wanare · K. K. R. Iyer (✉)
Department of Civil Engineering, Institute of Infrastructure, Technology,
Research and Management, Ahmedabad, India
e-mail: kannaniyer@iitram.ac.in

P. Jayanthi
Department of Civil Engineering, National Institute of Technology Andhra Pradesh,
Tadepalligudem, Andhra Pradesh, India

landslide or slope failure event, the displacement of slope surface can occur [29], and monitoring of the displacement would help in better prediction of slope failure and landslide, and hence would play an important role in preventing fatalities [36].

Earlier studies on slope failure [15, 18] showed pre-deformation of the surface before failure. Hence, researchers have suggested that an approach that can alert about the landslides or slope failure are useful. This approach is known as early warning system (*EWS*) for landslide and slope failure. According to UNISDR [31], the *EWS* can be defined as, the set of instrumentation, which gives an information of soil movement to the people and makes them aware to prepare for the hazardous situation, and can hence minimize losses. This monitoring system consists of various sets of sensors, devices and transmitters to observe, record and transfer the information of slope behavior. The present paper reviews the state of art on *EWS* for monitoring landslides and slope failure, and their approach with advantages and limitations. It is envisaged that the present work would help geotechnical engineers in the direction of adopting suitable *EWS*'s with respect to the requirements of the site.

1.1 Overview of Early Warning Systems

Most of the landslides and slope failures occur due to heavy rainfall or seismic events. Study conducted by Osanai et al. [22] showed that large number of landslides in Japan happened due to heavy rainfall during 1972–2007, and most of the failures occurred at shallow depth (1.2 m depth). To monitor such failures, one of the first geographical early warning system was installed in Hong Kong in 1977 [11]. This system worked on the principle of observation of the soil slope movement and conveying this information to the receiver. Before invention of wireless sensors, the cable connection with transducers and gauges were used to transfer the data of the slope movement. However, this system required huge cable network and number of displacements measuring devices. In recent years, researchers have proposed the wireless sensors and data transmitters that can transfer data without cable connection. Some studies have reported the application of *EWS* based on real time rainfall data [2, 14]. Japan Meteorological Agency (JMA) have also developed the SMI (Soil Moisture Index), which gives an idea about the risk of landslides over a range of 5 km and early warning up to 6 h before failure, [12, 19]. The SMI based approach has been used as the standard guideline for the early warning system since in Japan [27].

Uchimura et al. [27] have developed an economical and simple *EWS*, and presented its applicability by testing the prototype model with artificially induced heavy rainfall condition. In this study, slope inclination and volumetric water content with time are measured by the sensors, which are mounted at near toe of the slope and slope surface, and the data is transferred to the receiving device by means of wireless connections through the optical sensors. To understand the effect of continuous rainfall on unsaturated slope, experimental studies have been carried out

by some researchers [5]. Based on the results, they presented the relationship between rainfall intensity and soil properties and have suggested that, for cohesion less slope, the rainfall intensity strongly affects the failure surface depth. However, the effect of rainfall intensity on failure surface depth can be minimized by improving cohesion of the slope. Some studies explored the micro electro mechanical systems (*MEMS*) based wireless slope monitoring approach for the landslides triggered by heavy rainfall [26, 36]. It has been suggested that the *MEMS* based wireless slope monitoring is efficient, cost effective and simpler in approach and can be used on various mountainous locations that are difficult to access. Towhata et al. [26] suggested a portable and low-cost slope/landslide monitoring system for early warning, which consists of unit of wireless sensors for tilt and moisture measurement, tensiometer for suction measurement and a set of rain gauges for monitoring the rainfall depth. This unit of sensors with required equipment can be easily installed on the slope surfaces. The study validated the performance of the system with a field rainfall test and have noted the threshold tilting rate for the slope failure as 0.1°/h. Yang et al. [36] suggested that the method of slope failure monitoring by using GPS technology and precise extensometer are economically not feasible and difficult for installation. Uchimura et al. [29] pointed out that the *EWS* approach based on rainfall record has not covered the exceptional cases such as cloud burst, and thus, it is not a fully reliable method in the heavy rainfall locations. It has been further suggested to add the displacement monitoring system (extensometer/gauges) on individual slopes for identifying slope failure. Some studies have also presented the application of remote sensing with radar and GPS technology, which can be used to monitor the long-term displacement [4, 37]. Bhardwaj [3] has studied the behavior of hill cuts on the four-lane road at Aravalli Mountain in northwestern part of India by using computer program-based analysis and field monitoring. He carried out the comparison between the analysis results and actual site observations, and suggested that the early warning slope failure monitoring system requires multidisciplinary working and high-technology computer network to collect data from sensors along with behavioral observation by the satellites.

2 Application of Early Warning Systems

Earlier researchers have presented the case histories of slope failures in Japan [30, 32]. They found that most of the slopes consisting of weathered granite failed due to heavy rainfall. Uchimura et al. [29] have prevented loss (due to failure) by using *EWS* during flattening of the slope for highway construction. They reported that the *EWS* started showing abnormal behavior of slope during rainfall, which necessitated evacuation in the respective area before failure,and thereafter, the remedial work has been carried out. Yang et al. [36] proposed an accurate slope failure or landslide prediction approach by using *MEMS* based wireless monitoring at locations of landslide prone areas in Wenchuan, China. They studied different

parameters such as rainfall intensity, water content in soil associated with matric suction, vibration and inclination of the ground. To understand the effects of continuous rainfall on slope stability, Wu et al. [33] have carried out the study on accumulated slope at Beibei district, China. The slope was 237 m long and 23 m high, and composed of silty clay and sandstone gravel, with the unit weight of 19.5 kN/m^3. They have used 2-dimensional particle flow code (PFC2D) numerical simulation software, which is based on discrete element method. They have observed that the accumulated slope was stable for no rain condition, and with increasing rainfall, the horizontal displacement and settlement at the top of the slope was recorded. From this study they suggested that for continuous rainfall condition, failure occurs in layer-by-layer pattern rather than conventional failure pattern. Abraham et al. [1] presented the study on monitoring of unstable slope, based internet of things (*IoT*) at Darjeeling, Himalaya region, India. They also used the *MEMS* approach in which they utilized the tilt and volumetric water content sensors for monitoring unstable slopes during 2017–2019, and presented the relationship between the rate of tilting with volumetric water content and rainfall data. Park et al. [23] have used the upgraded displacement sensors, which was designed and patented by Tamate et al. [24]. They suggested that the length of sensors should be large enough in order to detect the deep soil layer movement during slope failure.

Yang et al. [36] proposed a cost-effective *EWS*, which can be useful in developing countries, and has already been successfully utilized at landslide prone locations of Wenchuan region of China. They presented the correlation between daily rainfall, soil moisture content, matric suction and factor of safety with respect to time, obtained by a set of sensors and rain gauge devices in the failure prone area. The system unit can be embedded into the stabilized slope surface. The sensors unit consisted of 16 cm × 12 cm × 8 cm size and 400 g weight, and works on solar cells and independent batteries. These sensors can record the real time data at an interval of 1 h during dry season and 10 min during rainy season for precise observation, and transfers the data to the host by means of mobile network. Tilt sensors were used in this system instead of long extensometers, to observe the rotation of the slope surface. It has also been suggested that the cost of monitoring was about 25% as compared to the conventional GPS slope monitoring for a single device [36]. However, this system is applicable only for shallow landslide/slope failure monitoring.

2.1 Different EWS Approaches

Based on the literature review, authors have summarized the various approaches of *EWS's* and presented in Fig. 1. These approaches are discussed below.

Wireless data transfer. The working of wireless data transfer method is based on the data transfer from the exact location of soil movement to the server [27]. Server collects data though internet and stores the data, and also gives the alarm in case of possibilities of failure. Sensors (work on battery) are used to measure the
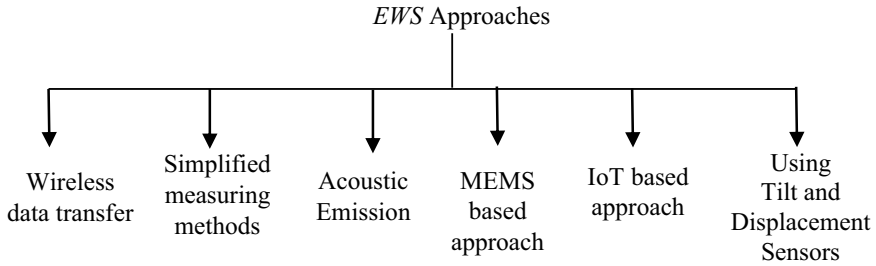
Fig. 1 Different *EWS* approaches used for landslide/slope failure monitoring

physical parameters of the slope and the data can be transferred by means of low-radio signals with the frequency of about 429 MHz [27], which delivers the signal up to 300–600 m distance. However, improved technology is required for long-term battery power supply.

Simplified measuring method. In simplified measuring method, the slope deformation observation is carried out as the gradual movement that can be recorded before failure [20, 21]. Measurement of rotation of the slope surface can be done by inclinometer with length of 515 mm, with high resolution and low consumption of power (3 V and 0.5 mA) [27]. Additionally, the water distribution associated with soil suction (on sloping ground) can be measured by the porous cup. Public Work Research Institute of Sukuba, Japan have conducted similar study to check its effectiveness and found that inclinometer indicated the failure behavior of slope, 30 min before the complete failure [28]. However, extensive care needs to be taken for suction measurement, viz., it needs to be ensured that the porous cup is in saturated condition.

Acoustic emission. Landslide/slope failure early warning system based on acoustic emission principle is an effective approach to prevent the risk of huge loss [6]. This approach is suitable for preventing the collision of vehicles with large soil mass (due to landslide or slope failure) on hilly roads and remote locations, where early responses cannot be provided. The method of warning by acoustic emission is simple and easy to operate. Figure 2 shows the schematic of acoustic emission approach visualized by the authors.

Furthermore, Dixon et al. [6] have presented the details of the acoustic emission measurement sensors, which can be effectively used to communicate the triggering of landslide and slope failure. With solar panels operated chargeable battery, the acoustic emission *EWS* is able to transfer the real time alert with minimal false message to the concerned person using the mobile network. Additionally, the acoustic emission sensors are easy to install by using hand driven wave guide and are noted to be robust and economical *EWS*.

MEMS based approach. *MEMS* (micro electro mechanical systems) technology is based on micro fabrication in which the micro sensors and micro actuators are the basic elements and are used for precise measurement and transfer of the data to the host device. Earlier studies have reported the application of the *MEMS* for
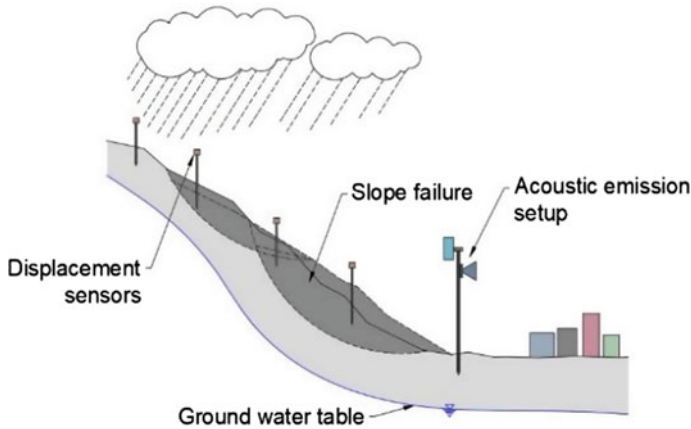
Fig. 2 Schematic of acoustic emission approach

landslide and slope failure monitoring [22, 26, 34, 36]. However, the cost of sensors and actuators is noted to be higher.

EWS based IoT. Park et al. [23] presented the slope failure monitoring study with application of displacement sensors and internet of things (*IoT*). In this approach, pretrained programs were used to measure and analyze the data that was received from the measuring devices. Surface displacement sensors were used to measure the soil movement. Readings were received by the data logger and transferred to the computer. However, for longer period of data collection from a large area, the data logger with higher memory is required, which affect the cost effectiveness of this method.

Using Tilt and Displacement sensor. The tilt sensor was first developed and tested for slope behavior monitoring in Japan [28, 35]. It measured the slope rotation with the precision of 0.017° and the volumetric water content with 3% variation [1]. Figure 3 shows the schematic of tilt sensor prepared by the authors based on understanding from literature.

Tilt sensors have also been installed to monitor the behavior of side slopes of Three Gorge Dam in China [30, 32]. Tilt sensors with the steel rod can be installed on slope at a depth of 1.0–1.5 m from the surface [29]. During rainfall, tilt sensors are found to be capable of monitoring the long-term slope damage with the consistent surface displacement. During failure, the slope starts moving from bottom and the movement propagates in the upward direction; hence, it has been suggested that tilt sensors should be installed at the lower portion of slope to identify early lateral movement [29].

Displacement sensors are also useful for soil deformation measurement. A recent study has reported that with length 80 mm and thickness 1 mm, and it can be easily penetrated into the soil [23]. It has also been noted that to measure the deformation, two active gauges are attached at the central portion with strain gauge. Protective coating is also applied on the surface to make the surface weather resistant [23].
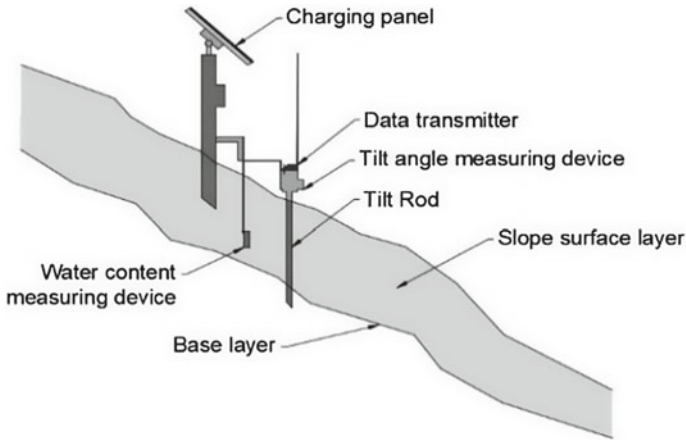
Fig. 3 Schematic diagram of tilt sensors

3 Discussion

Based on the extensive literature review of *EWS* systems presented by many researchers, the details of different methods adopted are summarized in Tables 1 and 2. It has been noted from these earlier studies, that in order to carry out precise observation, tilt sensors can be installed in a grid pattern such as parallel and perpendicular to the slope. In such pattern, the parallel direction tilt angles show the tilting rate of the slope with respect to time before failure. Uchimura et al. [29] observed that the slope failed after about 2 h of attaining peak value of water content, which suggests that reliability of assessment of slope stability on basis of water content may be lower. Towhata et al. [26] suggested that the reliability of slope failure accounted on the basis of rainfall data is less, because the intensity of rainfall is not similar over a larger area, and the geological, topographical and hydrological parameters are variables for assessing the slope failure.

Uchimura et al. [29] observed the tilting rate of slope as 0.01°/h for partial slope failure and 0.1°/h for the complete failure. Therefore, the threshold value at which the failure warning should be issued corresponds to the tilting rate more than 0.1°/h and the estimated time for the slope failure was from 1 to 10 h, after the tilting rate was observed as 0.1°/h [29]. However, the researchers opine that more data should be collected in this direction to establish correlation between tilt angle and time before slope failure. The early indication of slope failure can be observed as muddy water flow or formation of cracks on the ground surface [26]. An earlier study [13] indicated that during the rainfall induced landslide, failure surface forms above the water table, where the pore water pressure is negligible and due to the infiltration of rain water there is a decrease in matric suction.

The research studies also noted that the battery-operated slope alarm is more efficient for acoustic emission in *EWS*, which can transfer the alert message to the

Table 1 Studies on the *EWS* using conventional and numerical approaches

Researchers and year	Method adopted	Details
Uchimura et al. [29]	Tilt sensors	• Slope failed after 2 h of attaining saturation value, less reliability of slope failure prediction based on the water content monitoring • *EWS* based on rainfall record has not covered the exceptional cases such as cloud burst
Lu and Godt [16], Godt et al. [10], Iverson [13]	Simplified measuring method	• Failure surface forms above the water table with decrease in pore water and associated matric suction also decreases
Dixon et al. [6]	Acoustic emission	• Battery-operated slope alarm are used for acoustic emission *EWS*, which can transfer the alert message to the concerned person using mobile network
Bhardwaj [3]	Numerical approach	• *EWS* requires multidisciplinary working and comparison of numerical analysis with data recorded with sensors is suggested. It is also suggested that behavior of slopes shall be observed by satellites which requires a superior computer network
Wu et al. [33]	Numerical approach	• Based on the numerical study, with increase in rainfall, horizontal displacement and settlement at the top of the slope is observed

concerned person using mobile network [6]. Suitable embedment length of displacement sensor is 1000 mm in order to detect the slope failure [23]. Studies on the landslides from 1977 to 2019 show that only few regions have been employing proper early landslide warning systems [11]. However, cost associated with the *EWS* is also one of the governing factors. It has also been reported that there is no accepted standard to verify the quality, forecasting skill and performance of *EWS* for landslides and slope failure. Abraham et al. [1] have reported that *EWS* for landslide/slope failure are not calibrated with real time data. Therefore, these values should be updated by considering site soil parameters and its real time behavior. Failure can precede with crack formation and minor soil movement [34] and monitoring of such observation leads to prevention of loss of life due to landslide. The rate of rainfall induced slope/landslide failure is much higher than the gravity failure [1].

Hence, from these studies, it can be inferred that landslide due to high-rainfall event is more hazardous and awareness programs should be carried out in regions of high rainfall. Many methods are being used to monitor the slope behavior from the satellite, such as light detection and ranging (LiDAR), permanent scatterer synthetic aperture radar interferometry (PSInSAR) and synthetic aperture radars (SAR) [4, 8]. However, these methods require superior computer configuration and network to deal the large size data. Further, continuous observation is not possible with the satellite. According to Dixon et al. [6], the early warning system should be easy to install, are adaptable in different site conditions, record accurate information, and

Table 2 Studies on new approaches for *EWS*

Researchers and year	Method adopted	Details
Uchimura et al. [27]	Wireless data transfer	• Wireless data transfer method is a simplified method of *EWS*
Towhata et al. [26]	*MEMS* based sensors	• Intensity of rainfall is not similar over a larger area, landslide prediction on rainfall basis is less reliable, the cost of sensors is high • Early indication of slope failure observed as muddy water flow formation in cracks on the ground surface
Park et al. [23]	*IoT* based method	• Displacement sensors should be long enough to record the displacement of subsoil layers. It is suggested that suitable length of displacement sensor is 1000 mm in order to arrest the slope failure
Guzzetti et al. [11]	–	• Only few regions have been using proper early warning landslide systems
Abraham et al. [1]	*IoT* based method	• Study highlighted need to consider both short term and long term rainfall. Care is required to identify false alarms due to human/animal interferences
Xie et al. [34]	*MEMS* based sensors	• Failure can precede with crack formation and minor soil movements
Osanai et al. [22]	–	• Most of the failure was recorded as shallow surface failure of average thickness 1.2 m deep
Yang et al. [36], Towhata et al. [26]	*MEMS* based sensors	• Suggested that the *MEMS* based wireless slope monitoring can be applicable on the mountains which are difficult to access. Also proposed that the tilting rate for the slope to be failed as 0.1°/h • Conventional method of slope failure monitoring by using GPS technology and precise extensometer are economically not feasible and difficult to be installed
Casagli et al. [4], Yin et al. [37]	Satellite observation	• Remote sensing with radar technology and GPS technology are also used to monitor the displacement for long term

support continuous data transfer. Installation of large numbers of sensors can give precise observation, which needs to be optimized from economic considerations.

4   Conclusions

Based on the detailed literature review on early warning systems for landslide and slope failure forecasting, following conclusions can be drawn:

- *EWS* is most applicable to the slope failure/landslide prone areas and are capable of preventing loss of life.
- Standard checks or guidelines should be established, and periodical checking should be carried out in order to maintain effective working of *EWS*.
- *EWS* should be capable of measuring the soil displacement during rainfall (at shorter interval of time) and during dry season.
- Slope failure assessment should be carried out on basis of water content, soil suction and soil displacement to predict accurate results.
- Battery-operated self-charging (by means of solar panel) slope alarms are useful and can work for a longer time with periodical maintenance.
- The length of sensor which are used for measuring the displacement should be longer to record the subsurface movement of soil.
- Periodical upgradation of *EWS* should be carried out with the real time rainfall and displacement data for its efficient working.
- It is suggested that combination of early warning systems at large sites prone to landslides, along with finite element based numerical studies, may be quite beneficial for monitoring the local and regional changes, and better forecasting of a landslide event.

References

1. Abraham, M., Satyam, N., Pradhan, B., Alamri, A.: *IoT*-based geotechnical monitoring of unstable slopes for landslide early warning in the Darjeeling Himalayas. Sensors **20**, 2611 (2020)
2. Baum, L., Godt, J.: Early warning of rainfall-induced shallow landslides and debris flows in the USA. Landslides **7**, 259–272 (2010)
3. Bhardwaj, G.: Slope failure early warning system SFEW: safe environ tool. lndian Min. Eng. J. **55**(07), 29–34 (2016)
4. Casagli, N., Catani, F., Ventisette, C., Luzi, G.: Monitoring, prediction and early warning using ground-based radar interferometry. Landslides **7**(3), 291–302 (2010)
5. Chinkulkijniwat, A., Tirametatiparat, T., Supotayan, C., Yubonchit, S., Orpibulsuk, S., Salee, R., Oottipruex, P.: Stability characteristics of shallow landslide triggered by rainfall. J. Mt. Sci. **16**(9), 2171–2183 (2019)
6. Dixon, N., Smith, A., Flint, J., Clark, B., Andjelkovic, M.: An acoustic emission landslide early warning system for communities in low-income and middle-income countries. Landslides (2018)
7. Ering, P., Kulkarni, R., Kolekar, Y., Dasaka, S., babu, S.: Forensic analysis of Malin landslide in India. In: IOP Conf. Series: Earth and Environmental Science, vol. 26 (2015)
8. Ferretti, A., Prati, C., Rocca, F.: Nonlinear subsidence rate estimation using permanent scatterers in deferential SAR interferometry. IEEE Trans. Geosci. Remote Sens. **38**, 2202–2212 (2000)
9. Froude, J., Petley, D.: Global fatal landslide occurrence from 2004 to 2016. Nat. Hazards Earth Syst. Sci. **18** (2018)
10. Godt, J.W., Baum, R., Lu, N.: Landsliding in partially saturated materials. Geophys. Res. Lett. **36** (2009)

11. Guzzetti, F., Gariano, S., Peruccacci, S., Brunetti, M., Marchesini, I., Rossi, M., Melillo, M.: Geographical landslide early warning systems. Earth-Sci. Rev. **200**, 102973 (2020)
12. Ishihara, Y., Kobatake, S.: Runoff Model of Flood Forecasting. Bulletin of the Disaster Prevention Research Institute, Kyoto University, vol. 29 (Part 1), pp. 27–43 (1979)
13. Iverson, R., Reid, M., Iverson, N., LaHusen, R., Logan, M., Mann, J., Brien, D.: Acute sensitivity of landslide rates to initial soil porosity. Science **290**, 513–516 (2000)
14. Keefer, D., Wilson, R., Mark, R., Brabb, E., Brown, W., Ellen, S., Harp, E., Wieczorek, G., Alger, C., Zatkin, R.: Real-time landslide warning during heavy rainfall. Science **238**(4829), 921–925 (1987)
15. Kuroki, K., Ishikawa, K., Nishikawa, J.: Forecast time and analysis of rupture mechanism using video-tape records for a rock failure of out slope. In: Proceedings of the 8th ISRM Congress. Tokyo, pp. 399–402 (1995)
16. Lu, N., Godt, J.: Hillslope Hydrology and Stability. Cambridge University Press, Cambridge, UK (2013)
17. Martha, T., Roy, P., Govindharaj, K., Kumar, V., Diwakar, P., Dhawal, D.: Landslides triggered by the June 2013 extreme rainfall event in parts of Uttarakhand State, India. Landslides **12**, 135–146 (2015)
18. Ochiai, H., Okada, Y., Furuya, G., Okura, Y., Matsui, T., Sammori, T., Terajima, T., Sassa, K.: A fluidized landslide on a natural slope by artificial rainfall. Landslides **1**(3), 211–219 (2004)
19. Okada, K.: Soil water index Sokko-Jiho. Japan Meteorological Agency 69-567-100 (2001)
20. Orense, R., Farooq, K., Towhata, I.: Deformation behavior of sandy slopes during rainwater infiltration. Soils Found. **44**(2), 15–30 (2004)
21. Orense, R., Towhata I., Farooq, K.: Investigation of failure of sandy slopes caused by heavy rainfall. In: Proc. Int. Conf. on Fast Slope Movement-Prediction and Prevention for Risk Mitigation (FSM2003), Sorrento (2003)
22. Osanai, N., Tomita, Y., Akiyama, K., Matsushita, T.: Reality of cliff failure disaster. Technical Note of National Institute for Land and Infrastructure Management, 530 (2009)
23. Park, S., Lim, H., Tamang, B., Jin, J., Lee, S., Chang, S., Kim, Y.: A study on the slope failure monitoring of a model slope by the application of a displacement sensor. Hindawi, J. Sensors 7570517(9) (2019)
24. Tamate, S.: Penetration-type pipe strain gauge. US Patent No. 7,762,143, issued July 27 (2010)
25. Tian, Y., Owen, L., Xu, C., Ma, M., Li, K., Xu, X., Figueiredo, P., Kang, W., Guo, P., Wang, S., Liang, X., Maharjan, S.: Landslide development within 3 years after the 2015 Mw 7.8 Gorkha earthquake, Nepal. Landslides **17**, 1251–1267 (2020)
26. Towhata, I., Uchimura, T., Seko, I., Wang, L.: Monitoring of unstable slopes by *MEMS* tilting sensors and its application to early warning. IOP Conf. Series: Earth and Environmental Science, vol. 26, 012049 (2015)
27. Uchimura, T., Towhata, I., Lin, W., Seko, I.: Simple and low-cost Early Warning System for slope failure due to rainfall and erosion. In: Fourth International Conference on Scour and Erosion (2008)
28. Uchimura, T., Towhata, I., Trinh, T., Jou, F., Carlos, J., Lin, W., Ichiro, S., Taro, U., Akira, M., Yosuke, I., Yuichi, O., Sho, I., Min-Seok, K., Naoki, S.: Simple monitoring method for precaution of landslides watching tilting and water contents on slopes surface. Landslides **7**, 351–357 (2010)
29. Uchimura, T., Towhata, I., Wang, L., Nishie, S., Yamaguchi, H., Seko, I., Qiao, J.: Precaution and early warning of surface failure of slopes using tilt sensors. Soils Found. **55**(5), 1086–1099 (2015)
30. Uchimura, T., Towhata, I., Wang, L., Qiao, J.: Interpretation of monitored behavior of slopes for early warning of failure, geotechnics for sustainable development. Geotech. Hanoi, 807–814 (2011)
31. United Nations Office for Disaster Reduction.: UNISDR Terminology on Disaster Risk Reduction. Retrieved from: Geneva, May 2009

32. Wang, L., Seko, I., Nishie, S., Uchimura, T., Towhata, I., Qiao, J.: Case histories of using a low-cost warning system for preventing slope failure and landslide disasters. In: Proceedings of the International Workshop on ICT in Geo-Engineering, Kyoto, pp. 267–276 (2012)
33. Wu, S., Song, K., Zhang, S.: Research on Early Warning Criterion of Accumulation Slope Instability under Rainfall. IACGE (619–626) (2018)
34. Xie, J., Uchimura, T., Wang, G., Shen, Q., Maqsood, Z., Xie, C., Liu, J., Lei, W., Tao, S., Chen, P., Dong, H., Guo-xiong, M., Shifan, Q.: A new prediction method for the occurrence of landslides based on the time history of tilting of the slope surface. Landslides **17**, 301–312 (2020)
35. Yang, Z., Cai, H., Shao, W., Huang, D., Uchimura, T., Lei, X., Tian, H., Qiao, J.: Clarifying the hydrological mechanisms and thresholds for rainfall-induced landslide: In situ monitoring of big data to unsaturated slope stability analysis. Bull. Eng. Geol. Environ. **78**, 2139–2150 (2018)
36. Yang, Z., Shao, W., Qiao, J., Huang, D., Tian, H., Lei, X., Uchimura, T.: A multi-source early warning system of *MEMS* based wireless monitoring for rainfall-induced landslides. Appl. Sci. **7**(12), 1234 (2017)
37. Yin, Y., Zheng, W., Liu, Y., Zhang, J., Li, X.: Integration of GPS with InSAR to monitoring of the Jiaju landslide in Sichuan, China. Landslides **7**(3), 359–365 (2010)

Numerical Modelling of Mechanically Stabilized Earth Walls for Slope Protection

P. R. Reshma and Sridhar Gangaputhiran

1 Introduction

Slope failures are one of the most common natural/manmade disasters in hilly areas due to the movement of earth, rock or debris down a slope under the direct influence of gravity. Slope failures occur when the shear stress developed due to gravitational or any other force exceeds the shear strength of soil which forms the slope. Major triggers of slope failures are soil erosion, heavy rainfall, heavy construction, deforestation and seismic activities. The consequences of slope failures are far-reaching which includes loss of life, damages to roads, lands, other infrastructures and even block the rivers which results in risk of floods [1]. Landslide destroys everything and anything which comes in their path, and the fatalities due to landslides mainly depends on the place and time of occurrence. Hilly terrains are highly vulnerable to landslides in India mostly the Himalayas and Western Ghats region [2].

In hilly areas, slope failures along roadways are very high which endangers the human lives, even if it is limited to small extent. Even though the technology has developed, the chances of slope failure along hilly areas have increased rather than being decreased. This hike in slope failure can be accredited to the unscientific excavation and inappropriate application of stability methods [3]. So, the construction in hilly area requires great effort and execution. In most of the cases, roads were aligned/constructed through the side of hill for stability purpose. The cutting and filling during construction of road embankment produce an imbalance in the whole stability of slope which substantially reduces the stability of slopes. Hence, suitable stabilization or slope strengthening techniques are mandatory to prevent slope failure.

P. R. Reshma (✉) · S. Gangaputhiran
National Institute of Technology Karnataka, Surathkal 575025, India

Slope stabilization using various polymeric and metallic materials has already been conducted and proved by various researchers. Basic principle behind reinforced earth is that soil and reinforcements together will act as a single block and resistance developed between soil and reinforcement will enhance the shear strength properties of soil. In most of the cases, granular soils are used as backfill material since it won't develop pore pressure which will substantially reduce the shear strength properties of soil [4].

Analytical and numerical modelling tools can be used to evaluate the stability of reinforced soil slopes. At present, the two main streams that are being followed by engineers are (1) limit equilibrium method and (2) finite element method [5]. FEM analysis of slope is very similar to LEM modelling except that numerical modelling requires more parameters than limit equilibrium analysis. Conventional LEM analysis assumes failure surface and only deals with simple geometries, whereas FEM does not assume failure surface and it can be used for complex geometries also [6]. And numerical modelling offers more realistic force distribution along with reinforcement, due to the more sophisticated accommodation of yield behaviour of reinforcement. It also uncovers the stiffness interaction which is not possible in limit equilibrium method [7].

Literature review on effects of various reinforcement materials showed that, all other conditions being same, steel bars performed better than geogrids, especially for slopes with high groundwater level [8]. And among geosynthetic materials, geogrid gives less deformation and higher strength as compared to geotextiles [9].

This paper presents a numerical analysis of a road cut slope with and without reinforcements to identify the effect of MSE wall on global factor of safety of slope. These structures are checked for internal as well as external stability. Internal stability is checked in terms of pull out and rupture failure of reinforcement, and external stability is checked against sliding, overturning and bearing resistance.

The geometry of cut slope used for the modelling is shown in Fig. 1. For calculating critical safety factors for slopes linear Mohr–Coulomb model is used with the help of PLAXIS 2D CONNECT Edition [10].

2   Methodology

Analytical modelling of MSE wall with sloping backfill surcharge is done as per FHWA guidelines [11]. This follows load and resistance factor design (LRFD) method and the assumptions of a coherent gravity mass for external stability, the shape of internal failure planes, and treatment of reinforcements as discrete elements remain unchanged [11].

The reinforcement details obtained from analytical mode are used for numerical modelling in PLAXIS.
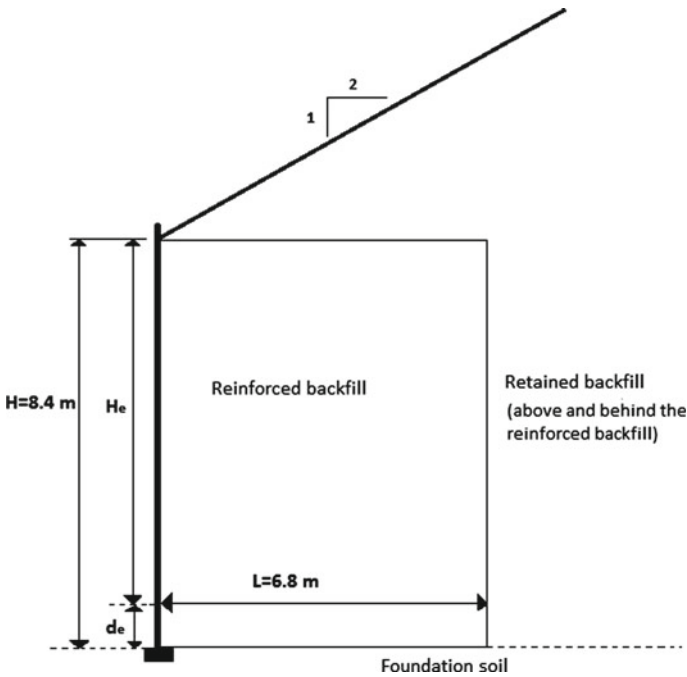
Fig. 1 Geometry of slope used for modelling

3 Slope Stability Analysis

In this study, analytical modelling of a MSE wall for soil slopes is conducted in the first phase and the obtained details are used for numerical modelling to obtain the critical factor of safety. The geometry selected for the numerical modelling is given in Fig. 2. In addition to this, a parametric analysis was also conducted to obtain the most influential factors to be taken care of while designing a MSE wall.

The given slope is composed of two parts, foundation soil and retained soil, and their properties are given in Table 1 [12]. The soil is assumed as linear elastic–plastic material and defined by Mohr–Coulomb model. The single property used for geogrid modelling is axial stiffness, and its value is taken as 1500 kN/m. The facing elements used are MBW blocks, and they are modelled as linear elastic material. Plain strain model with 15 nodded elements was used for the modelling. And medium coarse mesh is used for the analysis.

As mentioned, the effects of variation in cohesion, spacing, length and axial stiffness of geogrid and angle of internal friction on the slope stability are analysed in PLAXIS 2D by using safety analysis, in which the angle of internal friction and cohesion is reduced until the soil body collapses [10]. PLAXIS multiplier Σ_{Msf} is used to define the factor of safety at any stage and is given by
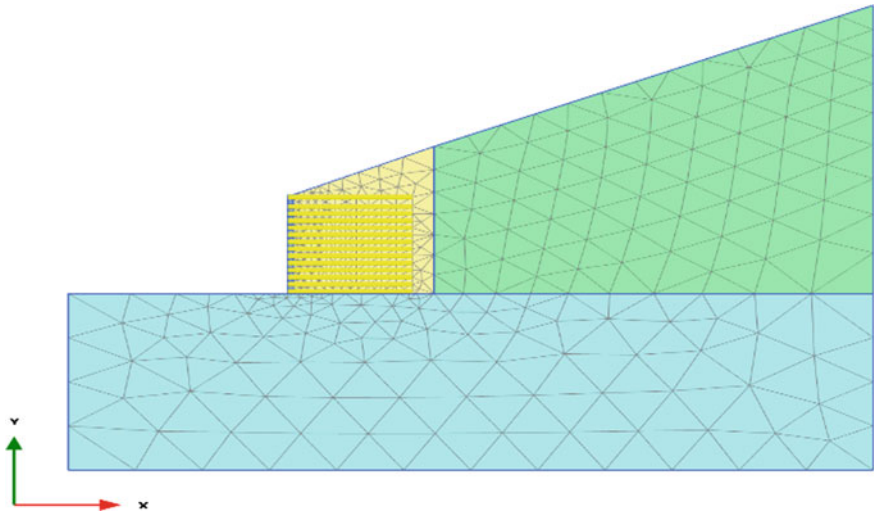
Fig. 2 Finite element mesh generated in PLAXIS 2D

Table 1 Summary of material parameters used FE analysis

Parameter	Value	Unit
Foundation soil		
Unit weight, Υ	18.8	kPa
Young's modulus, E	50	MPa
Poisons ratio, μ	0.3	–
Cohesion, C	5	kPa
Angle of internal friction, ϕ	30	degree
Retained soil		
Unit weight, Υ	18.8	kPa
Young's modulus, E	25	MPa
Poisons ratio, μ	0.3	–
Cohesion, C	30	kPa
Angle of internal friction, ϕ	40	degree
Reinforced soil		
Unit weight, Υ	18.8	kPa
Young's modulus, E	25	MPa
Poisons ratio, μ	0.3	–
Cohesion, C	1	kPa
Angle of internal friction, ϕ	34	degree

$$\Sigma_{\text{Msf}} = \frac{\tan \phi_{\text{input}}}{\tan \phi_{\text{reduced}}} = \frac{C_{\text{input}}}{C_{\text{reduced}}} \tag{1}$$

The variabilities used for the parametric analysis are given in Table 2.

Table 2 Variabilities used for parametric analysis

Parameters	Values
Cohesion of reinforced soil (kPa)	1.0, 10, 15, 20, 25, 30, 35, 40
Angle of internal friction of reinforced soil (degrees)	10, 25, 30, 35, 40
Spacing of reinforcement (m)	0.6, 0.8, 1, 1.2, 1.6
Axial stiffness of geogrid (kN/m)	500, 800, 1000, 1200, 1500
Length of geogrid (m)	5.0, 6.0, 7.0, 8.0, 9.0

4   Results and Discussions

The numerical studies of slopes were carried out with and without reinforcement as two phases. From the results, it is visible that geosynthetics has considerable effect on stability of soil slope. The factor of safety obtained for slopes reinforced with geosynthetics is 1.293 which is around 39% higher than FOS obtained for unreinforced slope (FOS for unreinforced slope = 0.931). The deformations obtained for unreinforced and reinforced slopes are shown in Figs. 3 and 4, respectively. Enhancement in stability of slope with respect to variation in soil cohesion is analysed by keeping all other parameters constant.

Changes in FOS due to changes in cohesion of reinforced fill are analysed, and the relation between them is plotted in Fig. 5. The cohesion value is changed from 1 to 40 kPa with an increment of 5 kPa. Since water table was not considered, as the cohesion of soil increased, the shear strength properties of soil are enhanced and as a result of this FOS of slope increased linearly. This is due to the linear relationship between shear strength and cohesion in Mohr–Coulomb failure formula. 12% change in FOS is observed when the cohesion is increased from 1 to 40 kPa from the parametric analysis.

The factor safety of slopes reinforced with geogrid for various angles of internal friction is calculated. The relation between angle of internal friction of reinforced soil and FOS is plotted in Fig. 6. The internal friction angle is changed from 25 to 45 degrees by an interval of 5 degrees. As like cohesion, internal friction angle has also increased the FOS up to a certain limit, and after that, the changes were observed in FOS which was minimal. An increment of 17% is observed in the FOS when angle of internal friction increased from 25 to 45 degrees.

With increase in cohesion, large horizontal displacements were observed even though it has improved the FOS of slope. For the optimum design of reinforced slope, soil with low cohesion and high angle of internal friction is required as backfill material [13].

With the increase in spacing of reinforcement, the global FOS of slope reduced considerably and their relation is plotted in Fig. 7. As the spacing decreases, the reinforced zone becomes strong and it won't be easy to pass through the reinforced zone [14]. The change in FOS due to spacing is less as compared to the effects of cohesion and angle of internal friction.

With the increase in axial stiffness of geogrid FOS was modified, but still the effects were not remarkable because when the axial stiffness value changed from 500 to 1500 kN/m, the changes in FOS observed were only 9% (Fig. 8).
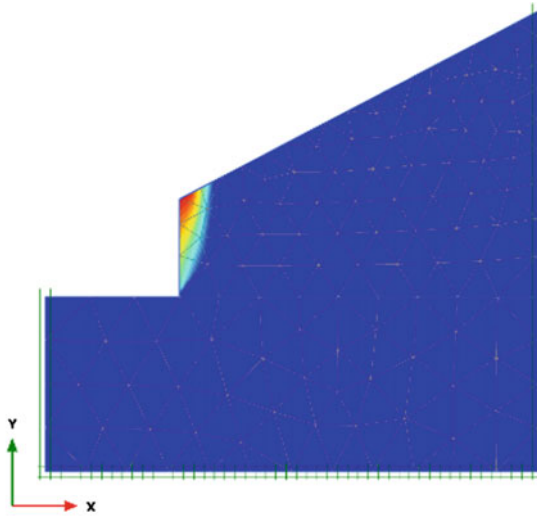
Total displacements |u| (scaled up 0.0500*10^{-3} times)
Maximum value = 39.35*10^3 m (Element 128 at Node 1261)

Fig. 3 Total displacements in unreinforced slope
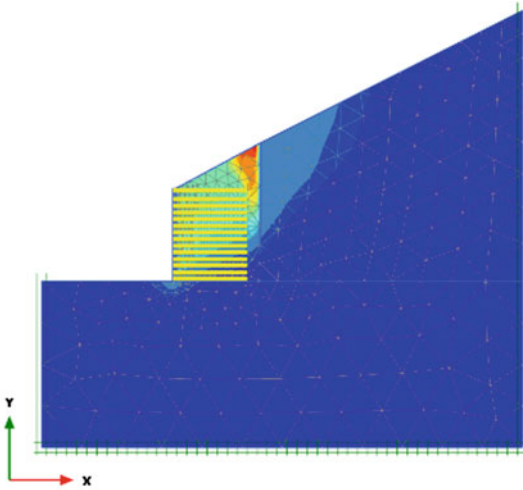
Total displacements |u| (scaled up 5.00 times)
Maximum value = 1.174 m (Element 180 at Node 1247)

Fig. 4 Total displacements in reinforced slope
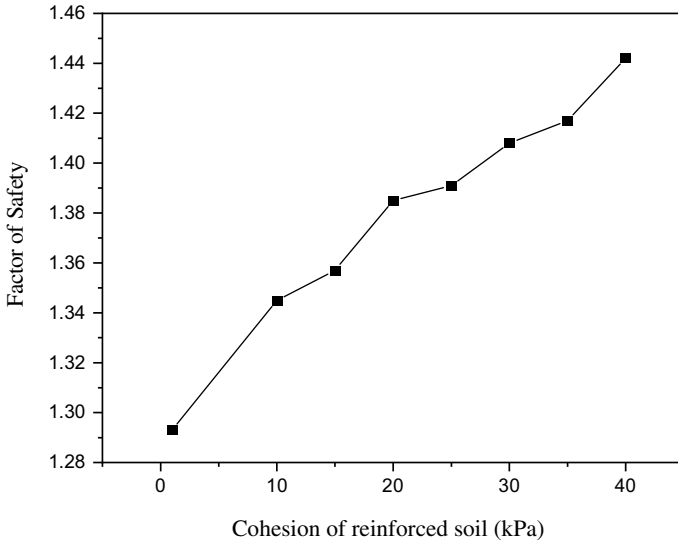
Fig. 5 Variation of factor of safety with cohesion of reinforced soil
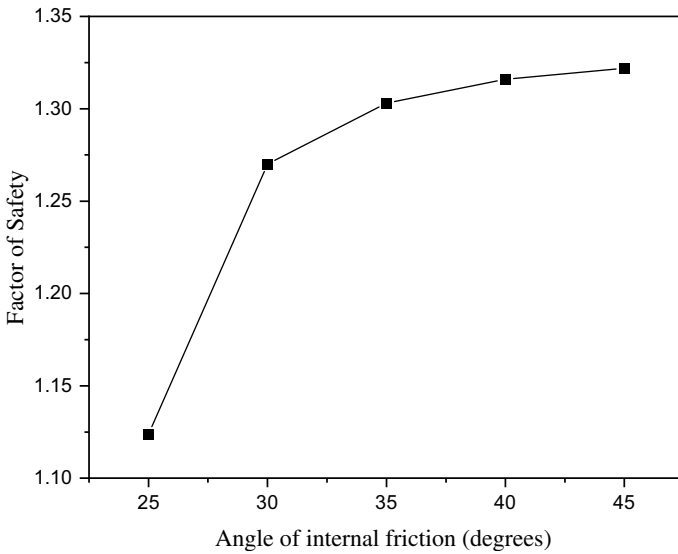
Fig. 6 Variation of factor of safety with angle of internal friction
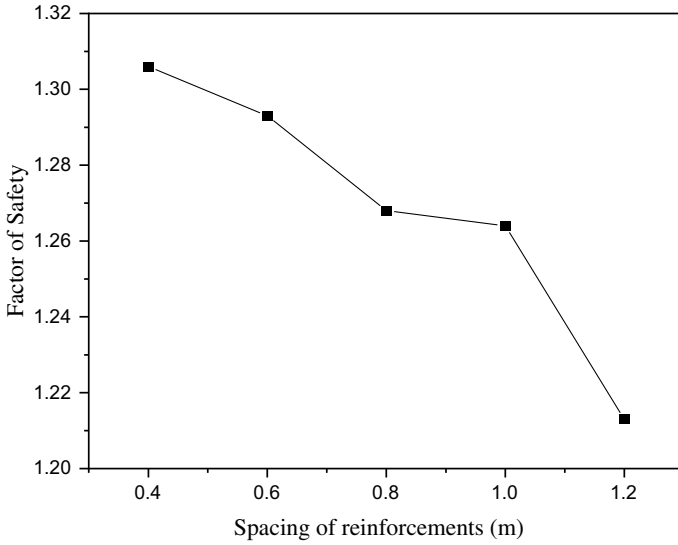
Fig. 7 Variation of factor of safety with spacing of reinforcements
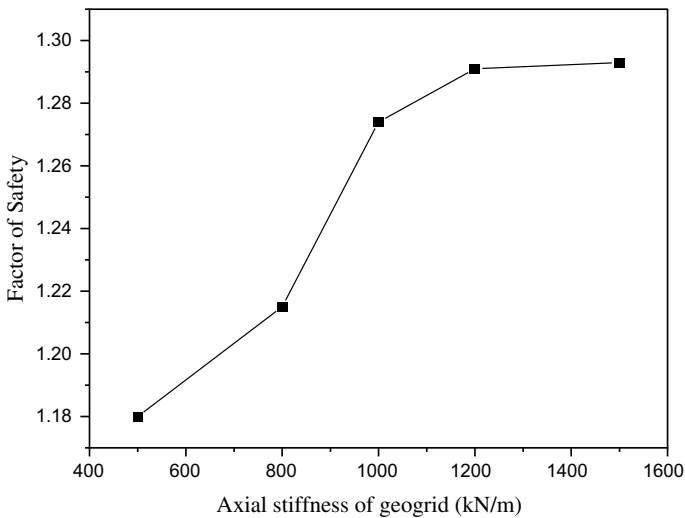
Fig. 8 Variation of factor of safety with axial stiffness of geogrid

With the increase in length of geogrid, the FOS of reinforced slope increased. For reinforcement with small length, the failure plane observed beyond geogrid but for longer reinforcements the failure plane was observed through the reinforced zone. As it is difficult to pass through the reinforced zone, FOS for slope with longer reinforcements has increased (Fig. 9).
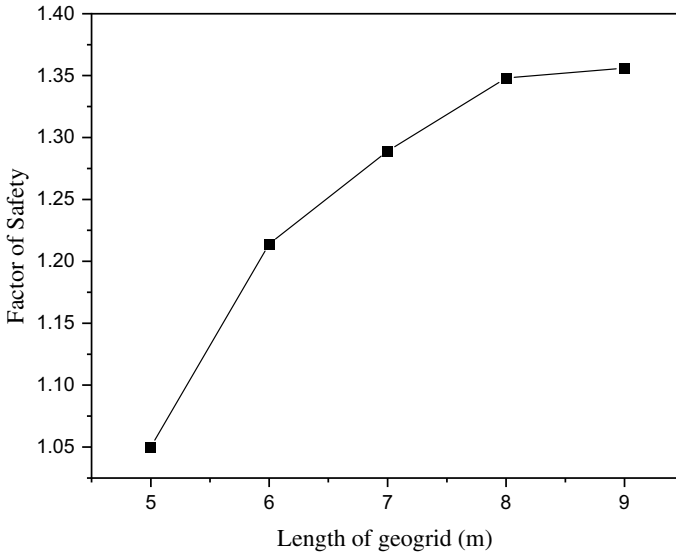
Fig. 9 Variation of factor of safety with the length of geogrid

5 Conclusions

The conclusions arrived at from the study is summarized in the following points.

- Reinforcing with geogrid elements is a suitable method to enhance the stability of a slope. In this study, the insertion of geogrids has made a noticeable effect on slope stability. The FOS value changed from 0.931 to 1.293 after the stabilization, i.e., a 39% change in FOS was observed.
- An increase in soil cohesion and angle of internal friction has made significant improvements in the FOS of the slope. A 12% increase in FOS was observed when the cohesion of backfill soil changed from 1 to 40 kPa. And an increment of 17% is observed when the angle of internal friction increased from 25 to 45 degrees. At the same time increase in cohesion has also increased the horizontal deformation of the facing, which indicates that soil with low cohesion and high angle of internal friction values is best suitable as backfill material.
- An increase in the reinforcement spacing made the soil weaker and reduced the global FOS of the slope. And, a 7% decrease in FOS was observed with the changes in spacing from 0.4 to 1.2 m. Increasing the reinforcement length and improving the axial stiffness of reinforcement value have also increased the FOS of slopes. When the axial stiffness value changed from 500 to 1500 kN/m a 9% increase in FOS was observed. And a 30% increase in FOS was observed when the length of reinforcement increased from 5 to 9 m.

References

1. Landslides: FAO in Emergencies. http://www.fao.org/emergencies/emergency-types/landslides/en
2. Tnau Agritech Portal, Disaster Management: Landslide. https://agritech.tnau.ac.in/agriculture/agri_majorareas_disastermgt_landslide.html
3. Peralta, J.C., Capitani, M., Mousa, R.M.: Road construction: applied concepts in stability analysis and solutions for high cut slope (2016). https://doi.org/10.13140/RG.2.1.2069.8642
4. Jagdish, N.: Reinforced Earth, pp. 1–25. Indian Geotechnical Journal, New Delhi (1985)
5. Lelli, M., Gouw, T.-L., Laneri, R., Cerro, M., Meinata, L.E.: Design of Earth Structures Reinforced with Polymeric and Metallic Reinforcements Using Limit Equilibrium Methods (2016)
6. Sazzad, Md.M., Hie, A., Hossain, Md.: Stability analysis of reinforcement slope using FEM. Int. J. Adv. Struct. Geotech. Eng. **5**, 83–88 (2016)
7. Hammah, R., Yacoub, T., Curran, J.: Investigating the Performance of the Shear Strength Reduction (SSR) Method on the Analysis of Reinforced Slopes (2021)
8. Abolhasan, S.N., Naeem, G., Rahele, R.K.: The effect of reinforcement on stability of slopes. Int. J. Chem. Environ. Biol. Sci. (IJCEBS) **3**(1) (2015). ISSN: 2320–4087
9. Onur, M., Tuncan, M., Evirgen, B., Ozdemir, B., Tuncan, A.: Behavior of soil reinforcements in slopes. Procedia Eng. **143**. 483–489 (2016). https://doi.org/10.1016/j.proeng.2016.06.061
10. PLAXIS 2D Scientific Manual. www.plaxis.com
11. FHWA.: Design and Construction of Mechanically Stabilized Earth Walls and Reinforced Soil Slopes, vols. 1 and 2. Publication FHWA NHI-10-024 and NHI-10-025, Federal Highway Administration and National Highway Institute, Washington, DC, USA (2009)
12. FHWA.: Mechanically Stabilized Earth Walls and Reinforced Soil Slopes: Design and Construction Guidelines. Publication FHWA NHI-00-43, Federal Highway Administration and National Highway Institute, Washington, DC, USA (2001)
13. Sharma, A., Raju, P.T., Sreedhar, V., Mahiyar, H.: Slope stability analysis of steep reinforced soil slopes using finite element method. In: Anirudhan, I.V., Maji, V. (eds.) Geotechnical Applications. Lecture Notes in Civil Engineering, vol. 13. Springer, Singapore (2019). https://doi.org/10.1007/978-981-13-0368-5_18
14. Ozcelik, G., Paşaoğlu, Ö., Huvaj, N.: Analyses of reinforced soil slopes with limit equilibrium and finite element methods. In: 10th International Conference on Geosynthetics, ICG (2014)

Earthquake-Induced Landslides in the Indian Himalayas and Glimpses of Code Provisions for Seismic Design of Slopes: A Review

A. Mugesh and Koushik Pandit

1 Introduction

Earthquakes are one of the major causes of slope instability in the hilly areas which also fall under highly seismic prone zones. Similarly, landslides triggered by earthquakes are widely observed in seismically active zones in India, especially in the Himalayan regions. The landslides are the crucial cause of the destruction and loss of life connected with severe earthquakes in foothill topography [1]. The lateral force caused by the seismic acceleration times weight of the slope mass leads to instability within the slope, ultimately leading to slope failure in some cases. The higher magnitudes of earthquakes may induce a large number of minor and major landslides [2–4]. The earthquake-induced landslides are often found to be highly correlated with peak ground acceleration measurement [5]. The Indian seismicity is categorized by both high and low frequency of moderate earthquakes [6]. Chamoli earthquake (1999) caused major loss of life and infrastructure in the hilly regions of the Uttarakhand State [7]. In 2011, the Sikkim earthquake played a vital role in causing wide destructions in which the majority of the events were caused by the landslides induced by earthquakes [8]. The landslides which were triggered by the Kashmir earthquake (2005) were the deadliest and highly vulnerable in the recent history [7]. Thus, it can be observed that the Indian Himalayas is mostly experiencing this kind of earthquake-induced landslides due to the active fold-thrust belts which are frequently hit by earthquakes. The Himalayan range is the outcome of an impact between the Indian and the Eurasian plates [9]. In general, the slope failures are caused by many factors such as slope inclination, slope height, lithological and structural characteristics, and rainfall patterns. The ground motion of the

A. Mugesh (✉)
Indian Institute of Technology Roorkee, Roorkee 247667, India

K. Pandit
CSIR—Central Building Research Institute, Roorkee 247667, India
e-mail: koushik@cbri.res.in

earthquake-triggered force causes the slope failures during an earthquake event. The earthquake duration, distance of the site from epicenter, depth of the epicenter from the existing ground level, and the magnitude of the earthquake are the major contributors in the earthquake-induced landslide events. The seismic stability analysis of slopes is based on various predictions such as (i) the peak strength of the bedrock, (ii) displacement, (iii) steady-state strength, and (iv) apparent friction angle in motion. In this study, the recent past studies which are related to some of the major landslides in the Indian Himalayas triggered by an earthquake have been discussed. This is followed by a review of seismic slope stability analysis methodology. Also, various code provisions and guidelines have been discussed.

2 Seismicity of the Indian Himalayan Range

The seismic tectonic activities are often produced by several disastrous events in the earlier period. Based on the seismic zonation map, the zones IV and V indicate that the seismic intensity is VIII and IX in the region with the highest peak ground acceleration of $0.25g$ and $0.4g$ for a return period of 500 years, respectively [10]. The tectonic convergence rate between the Indian and the Eurasian plates is in the order of 50 mm/year. The highest elevation of the mountains attributes to the uplift of the rock formation due to the plate movement directed from north to south along the Main Central Thrust (MCT) and the Main Boundary Fault (MBF). Most of the seismic events occurred in the Garhwal and Kumaun region which are located in the area of the surface trace of the Main Central Thrust (MCT). The Garhwal–Kumaun segment of the Himalayas is well known for great levels of seismic activities. The Himalayan longitudinal seismic zone is divided into seismotectonic segments with defined transverse boundaries noticeable by essential faults. These segments are the Kashmir block, Chamba-Keshwar block, Kangra block, Shimla block, Garhwal block, and Kumaun block [9]. Figure 1 shows the seismic instrumentation network existing in India. The landslide hazard zonation is represented in four different categories like severe and very high, high, moderate to low, and unlikely (Fig. 2).

3 Earthquake-Induced Landslides

3.1 Sikkim Earthquake

On September 18th, 2011, a magnitude of M_w 6.9 hits the major part of the Sikkim Himalaya which led to a very high rate of fatalities and severe destruction in buildings and high-rise infrastructures. Also, road communication between Sikkim and the North Bengal was disrupted for several days to follow. Numerous hill slopes got mobilized, and a total of 210 numbers of landslides were recorded out of which 196 were newly originated and 14 were reactivated. In the lower portion of
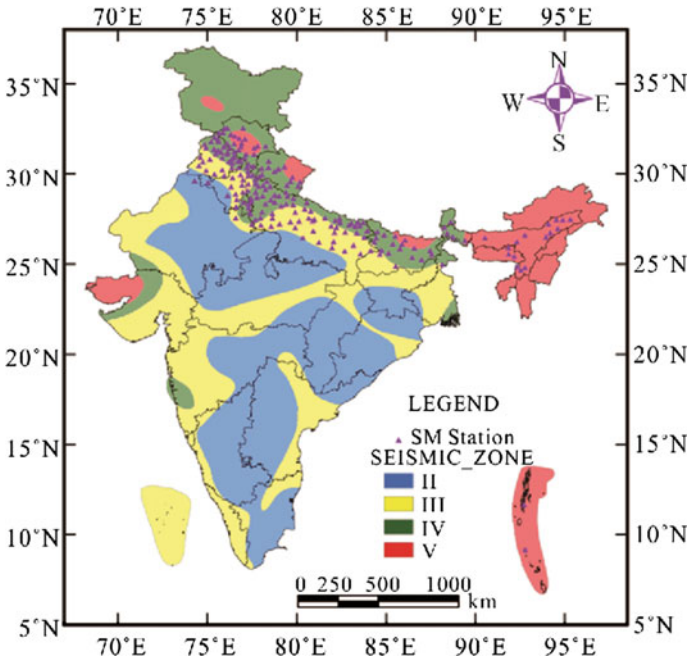
Fig. 1 Strong motion seismic instrumentation network in India (Mittal et al. 2012)

the Himalayas, soil and debris slides were predominant, whereas in the higher level of the Himalayas, rockslides and rockfalls were predominant [7]. The follow-up failures caused by these landslides were (i) failure of retaining walls, (ii) settlement/creep of the soil, (iii) foundation failures, etc. [11]. In terms of fatality, this earthquake, 94 people lost their lives in North Sikkim and also the damage attributed to 70% of loss in the electricity, telecommunication, and the infrastructure sectors [12].

In Fig. 3, the recorded motion time history of the Sikkim earthquake from the Gangtok station was represented in the form of three motion components.

3.2 Kashmir Earthquake

An earthquake of magnitude 7.6 M_w occurred in the epicenter of Hazara on October 8th, 2005, in the Kashmir Himalayan region. The epicenter location is identified at the 10 km north–west part of Muzaffarabad. In the Jhelum Valley, the portion of Baramulla to Uri, landslides were observed which were triggered by the earthquake. These landslides caused failures in the steep slopes along the roadways and some scrap-face failures occurred in the river terraces. The landslides were highly focused in some specific zones and also resulted in a scar of 1 km long, 200 m wide, 60 to
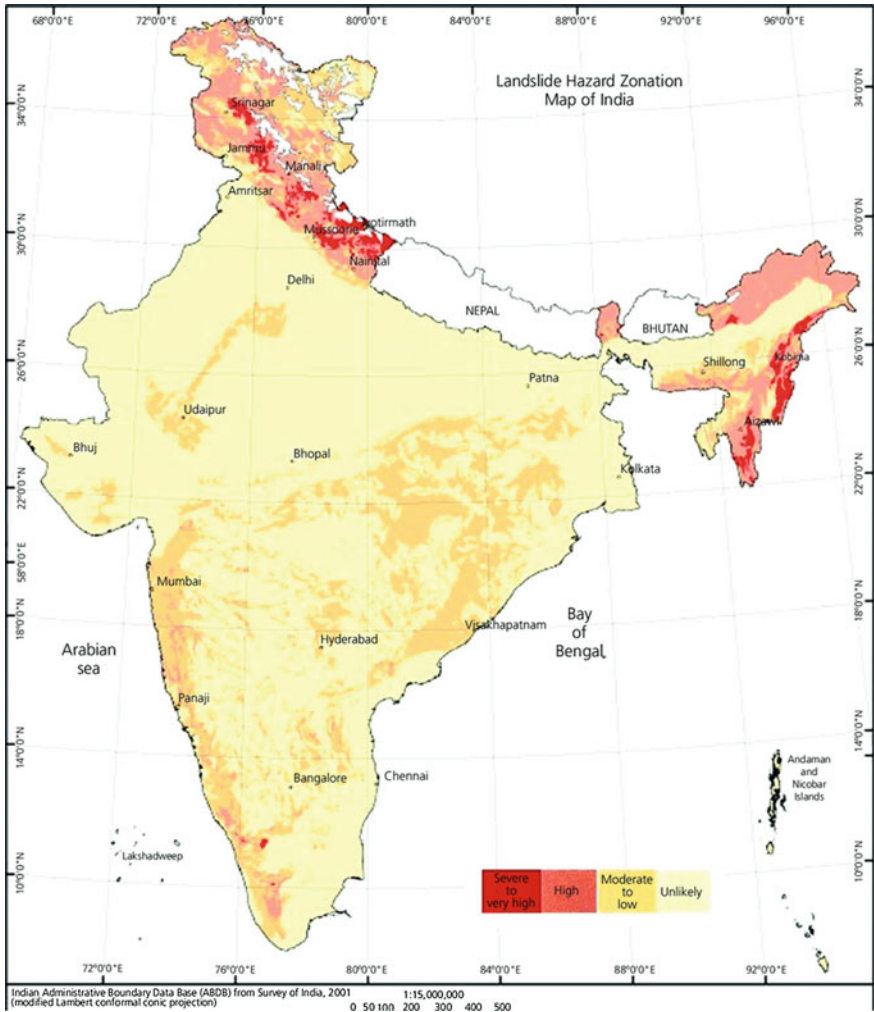
Fig. 2 Landslide hazard zonation map of India (*Source* www.ndma.org)

80 m depth, with an angle of slope between 60° to 70° [7]. The largest landslide, known as the Hattian Bala landslide, caused approximately 1000 human casualties and also in small settlements in the valley areas. The formation of slides included siltstone, sandstone, and the shape of Murree formation, and also, it caused a ground failure like lateral spreading, fissuring, and the creeping on the surrounding area near these landslides [13]. The spectral information and the time history records of the Kashmir earthquake were observed in the report of the earthquake engineering field investigation [14], there NS and EW are the horizontal components, and UD is the vertical component, and also, the highest level of motion amplification is 0.231*g* was shown in the EW component (Fig. 4).
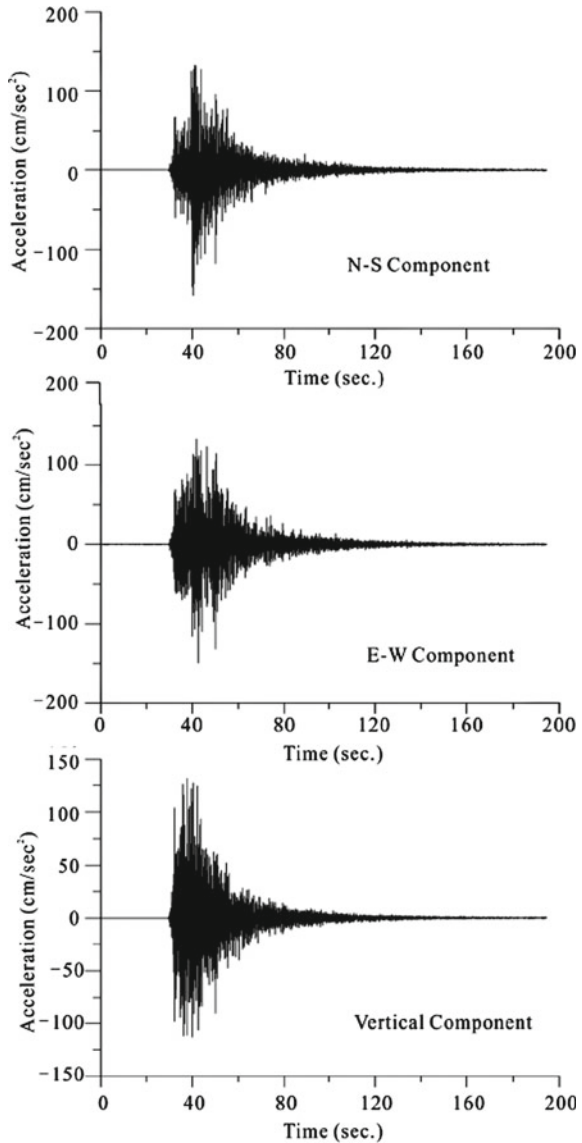
3.3 Chamoli Earthquake

The Chamoli earthquake is a familiar seismic event in the Garhwal part of the Himalayan range with a magnitude of 6.4 which occurred on March 29th, 1999 [7]. This earthquake-triggered more than 100 landslides and the primary slide is observed in the form of the rockslide along the Badrinath Highway with a length of 3 km before Nandprayag. The terraced slope in the region of Nandprayag showed a
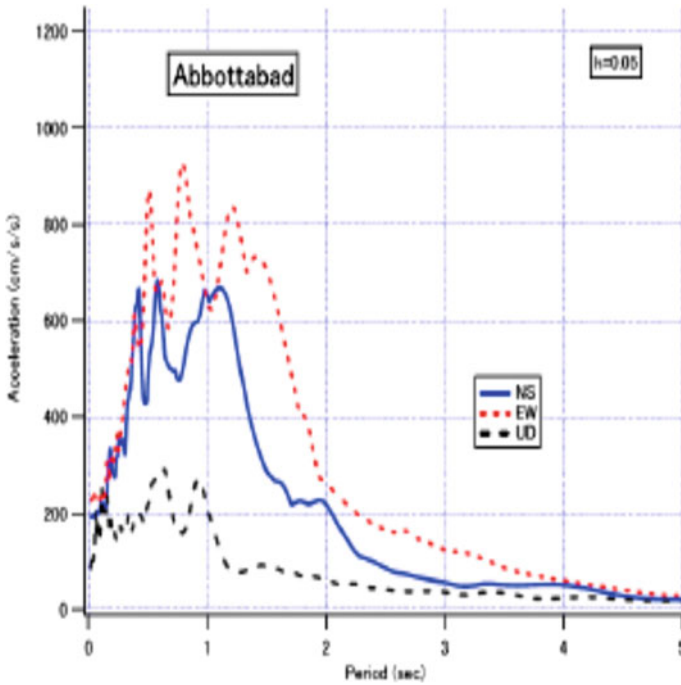
Fig. 4 Elastic response spectra (5% damped) with three components of the Kashmir Earthquake at an Abbottabad station (EEFIT)

slump failure and resulted in a tension crack. The total loss of lives was estimated as 103 and 395 people were injured. A huge number of infrastructures (around 4495 houses) suffered very severe damage. A noticeable ground fissure formed as a result of stress in the steepest slope mass region [9] and also the recorded time history and its frequency spectrum at the Roorkee station is shown in Fig. 5 and the three epicentres of the earthquake are shown in Fig. 6.

4 Codal Provisions for Seismic Design of Slopes

4.1 *IITK-GSDMA Guidelines for Seismic Design of Earth Dams and Embankments*

In general, many factors contribute to slope instability. For evaluating the seismic slope stability, there are various techniques like (i) equivalent static stability analysis, (ii) sliding block method, and (iii) dynamic analysis. These seismic slope stability methods are influenced by the different aspects, such as (i) earthquake vibration-induced cyclic stresses in the slopes and (ii) cyclic stress–strain behavior
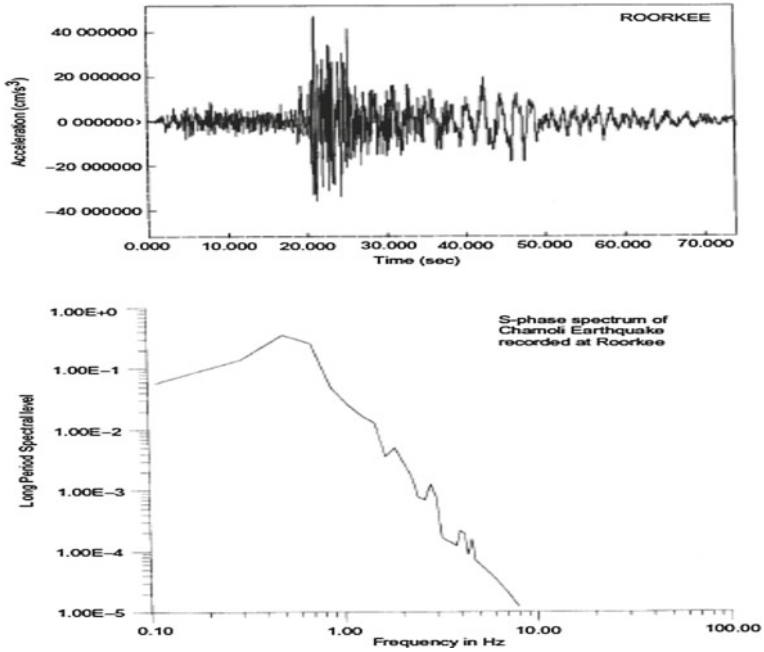
Fig. 5 Chamoli Earthquake fourier spectral motion and its time history at the Roorkee station [15]
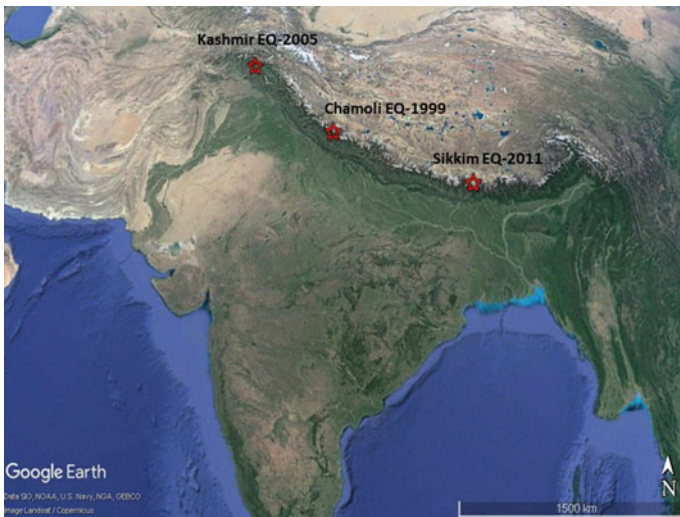
Fig. 6 Epicenters of the Kashmir, Chamoli, and Sikkim Earthquake

of the materials within the slopes. The standard procedure for analysis of seismic stability of slopes requires a comprehensive and suitable characterization of the prior failure, undrained deformation behavior of the soil strata within the slope mass as well as the appropriate earthquake time histories. The dynamic analysis involves the finite element or finite difference method to evaluate the deformation behavior of the slopes. The results are sensitive to the geotechnical and seismological parameters which employ a nonlinear stress–strain relationship that provides a deformation framework of the slopes. This process requires precise characterization of the stress–strain behavior of the materials.

4.2 Eurocode-7 Provisions

The limit equilibrium analysis principles are adopted for the soil and rock engineering designs. Evaluation of seismic slope stability involves the partial safety factors in the limit equilibrium method. The partial safety factor principle involves the partial factors of each element present in soil and rock structure. The partial factor method is in predominant usage in European countries. The following guidelines are present, where the factor of safety (FS > 1.0) does not mean that the slope is stable since based on several input parameters, it may be unstable (Table 1).

4.3 BS-8006 Provisions

This British standard focuses on recommendations and guidance for the application of the strengthened and reinforced soils, in-situ fills, other fills, and also, the partial safety factors of soil materials are estimated by two methods, which are: (i) the ultimate limit state method and (ii) serviceability method. In both these methods, the suitable partial factors are applied to the loads and the materials depending on the load case (Table 2).

Table 1 Factor of safety (FS) values based on Eurocode-7

Parameter	General case	Short-term stability	Long-term stability
FS	FS > 1.0	FS > 1.3	FS > 1.5

Table 2 Partial load factors prescribed by BS-8006

S. No.	Partial factor	Ultimate limit state	Serviceability limit state
1.	Soil unit mass (embankment fill)	1.3	1.0
2.	External dead load cases (line or point loads)	1.2	1.0
3.	External live load cases (traffic loads)	1.3	1.0

4.4   IS 14680:1999 Provisions

This Indian Standard provides the guidelines for the selection of various landslide control methods for effective corrective measures to avoid landslides in hilly regions. The control measures for landslides are classified into two types: (i) direct methods and (ii) indirect methods. Further, the direct methods are divided into four categories, namely (a) restraining structures, (b) easing of pressure by excavation, (c) reconstruction of a slope using reinforced earth, and (d) rock reinforcement. The indirect methods are involved in erosion control measures and improvement in surface and subsurface drainage. Some of the recommended control measures for the landslides as per this standard are:

   (i)   Geotextile nailed on slope/spot bolting
  (ii)   Breast walls/soil nailing
 (iii)   Alteration of slope profile and earth and rockfill buttress
  (iv)   Reinforced earth or rock reinforcement in rock slope
   (v)   Biotechnical measures
  (vi)   Check dams along a gully
 (vii)   Series of check dams
(viii)   Rows of deep piles
  (ix)   Combined system.

5   Conclusion

The present study of the earthquake-induced landslides in the Indian Himalayan region has been covered by investigating a few case studies. The case studies include information about the earthquake size, and the details of the landslides which were triggered by those earthquakes, causes of landslides in surrounding areas, and their vulnerability were discussed. The seismicity of the Indian Himalayan Range was discussed. The geological structure of the landslide materials is also discussed. The code provisions for seismic slope stability analysis were also discussed. Also, the present study provides a list of control measures for mitigating the landslide hazards.

References

1. Swiss Reinsurance Company 2000. Natural catastrophes and man-made disasters in 1999, Economic Research and Consulting. Zurich, Sigma No. 2/2000, 35 p
2. Keefer, D.K.: Landslides caused by earthquakes. Bull. Geol. Soc. Am. **95**, 406–421 (1984)
3. Keefer, D.K.: Statistical analysis of an earthquake-induced landslide distribution—the 1989 Loma Prieta, California Event. Eng. Geol. **58**, 213–249 (2000)

4. Youd, T.L., Perkins, D.M.: Mapping liquefaction-induced ground failure potential. J. Geotech. Eng. Div. ASCE **104**, 433–446 (1978)
5. Meunier, P., Hovius, N., Haines, A.J.: Regional patterns of earthquake-triggered landslides and their relation to ground motion. Geophys. Res. Lett. **34**, L20408 (2007). https://doi.org/10.1029/2007GL031337
6. Lai, C.G., Menon, A., Corigliano, M., Ornthamarrath, T., Sanchez, H.L., Dodagoudar, G.R.: Probabilistic Seismic Hazard Assessment and Stochastic Site Response Analysis At the Archaeological Site of Kancheepuram in Southern India. Research Report EUCENTRE 2009/01, IUSS Press, Pavia, pp. 250 (2009). ISBN: 978-88-6198-037-2
7. Singh, K.K., Singh, A.: Detection of 2011 Sikkim earthquake-induced landslides using neuro-fuzzy classifier and digital elevation model. Nat. Hazards **83**(2), 1027–1044 (2016). https://doi.org/10.1007/s11069-016-2361-6
8. Martha, T.R., Govindharaj, K.B., Kumar, K.V.: Damage and geological assessment of the 18 September 2011 Mw 6.9 earthquake in Sikkim, India using very high resolution satellite data. Geosci. Front. (2014). https://doi.org/10.1016/j.gsf.2013.12.011
9. Nainwal, H.C., Naithani, A.K.: Study of Seismically Induced Landslide Zones, Related to Chamoli Earthquake of 1999, Garhwal Himalaya, India Study of Seismically Induced Landslide Zones (2015)
10. Parkash, S.: Earthquake related landslides in the Indian Himalaya: experiences from the past and implications for the future. Landslide Sci. Pract. Complex Environ. **5**(January), 327–334 (2013). https://doi.org/10.1007/978-3-642-31427-8-42
11. Maheshwari, B.K., Sharma, M.L., Singh, Y., Sinvhal, A.: Geotechnical aspects of Sikkim earthquake of September 18, 2011. Indian Geotech. J. **43**(2), 170–179 (2013). https://doi.org/10.1007/s40098-013-0039-5
12. Mahajan, A.K., Gupta, V., Thakur, V.C.: Macroseismic field observations of 18 September 2011 Sikkim earthquake. Nat. Hazards **63**(2), 589–603 (2012). https://doi.org/10.1007/s11069-012-0170-0
13. Shafique, M., van der Meijde, M., Khan, M.A.: A review of the 2005 Kashmir earthquake-induced landslides; from a remote sensing perspective. J. Asian Earth Sci. **118**, 68–80 (2016). https://doi.org/10.1016/j.jseaes.2016.01.002
14. EEFIT.: The Kashmir, Pakistan Earthquake of 8th October 2005: A Field Report By Eefit (October, 2005)
15. Pandey, Y., Dharmaraju, R., Chauhan, P.K.S.: Estimation of source parameters of Chamoli Earthquake, India. Proc. Indian Acad. Sci. Earth Planet. Sci. **110**(2), 171–177 (2001). https://doi.org/10.1007/BF02702216

Landslide Susceptibility of Madanpura (Fatehpur Sikri, Agra in Vindhyan Hills, India) Using Arc GIS

Jibran Qadri, **M. Masroor Alam**, **and Md. Rehan Sadique**

1 Introduction

Landslides are defined as the movement of slope material such as rock debris and earth whether downward and outward under the influence of gravity [1]. Natural processes of mass wasting and mass movement are ascribed to different kinds of landslides. When landslide events become sudden and fast causing harm to human beings and the infrastructure created by them, then it becomes a disaster. Rocky slopes with degraded rock debris and resultant soil on slope move constantly downward and outward under the influence of gravity aided by the presence of water aids in natural redistribution of sediment and soil. Sudden collapse of rock mass and sluggish to swift surge of mud, rubble, earth has resulted recently in huge losses to life and economy. Landslide events most commonly occur in geodynamic sensitive belts, i.e., area and zones, where earthquake is common and affected by other neotectonic activities, such as Himalayas, Western Ghats, and Deccan Trap regions [2].

1.1 *The Most Important Factors Which Are Responsible to Trigger the Mass Movement Are*

(a) Long and heavy rainfall
(b) Cutting and deep digging of slopes for building, road, canal construction, and mining without convenient disposal of debris
(c) Earthquake shock and tremors.

J. Qadri (✉) · M. M. Alam · Md.R. Sadique
Department of Civil Engineering, Aligarh Muslim University, Aligarh,
Uttar Pradesh 202002, India
e-mail: lncs@springer.com

1.2   Major Forces Working on Slopes as Per Various Studies Are

(a) Shear strength of the materials that act on the slip planes. (b) Weight of the slope material, i.e., rocks, man-made structures, soils, and vegetation acting downwards. All these forces can be resolved into "driving" and "resisting" forces [1–3]. Water is the major cause of mass movement and serves as an agent of weathering that produces self-cohesive and yielding materials and acts as lubricant, hence reduces the friction. It impacts rock shear strength and reduces friction further [3]. The Centre for Research on Epidemiology of Disasters (CRED)—Munich RE scheme of classification (2019) landslides is mainly classified into two types:

1. Geophysical/Geological disaster: In this case, the material involved in mass movement is dry.
2. Hydrological disaster: In this case, the mass movement material is wet.

In India, landslide affects 12.6% of our nation area (as per NDMA [1]) which is prone to landslide which accounts for 0.42 million km^2 area. All 22 states and 5 union territories are affected from hilly states Jammu Kashmir, Himachal Pradesh, Uttrakhand to Kerala, and Tamil Nadu. One of the world's biggest geohazard is landslides which accounts for nearly 9% of the global natural disasters [4, 5]. Any slope failure in habituated areas causes river blockage loss of property, life, injury, traffic disruption, and environmental degradation [6, 7]. In the emergency events database (EMDAT,16), which shows landslide causes 16,500 deaths and affects 4.5 million people worldwide with property damage of USD 3.5 million (OFDA/CRED 2016) [5], the landslide statistics per continent are summarized from 2007 to 2014.

The study area lies on the outskirts of the Indo-Gangetic plain region near Fatehpur Sikri, 40 km away from Agra, covered in Survey of India Topographic Sheet number (54E/12). The region geologically consists of the Vindhyan Supergroup of rocks of Neoproterozoic age. Largely these rocks are covered by thick unconsolidated alluvia. Fatehpur Sikri is famous for Mughal architecture made of as well as cladded with sandstone quarried from nearby hills. The well-known sandstone quarries providing building stones to nearby regions of Uttar Pradesh and Rajasthan from this area till last two decades. The quarrying operations which are now banned by Supreme Court of India used blasting method and have damaged parts of this historical sites like Buland Darwaza due to vibrations.

This work aims to define the stability of slopes in nearby areas of Fatehpur Sikri Fort, in order to assess the impact of past rock excavations. For excavation, steeper paths are often economically desirable rather than flatter tracts involving open cast mines, being non-economic [8, 9]. On vast natural slopes, natural discontinuities that are completely permanent are likely to get grow open and let the rock mass loose creating unstable slopes at local levels.

Seismic vulnerability, progressive tectonics, and ongoing anthropogenic activities are key for predicting the rock mass and their probability to fail. It is evident from various seismic activities in Himalayas which are inalienably delicate [10] and

have ramifications for faraway places, such as UP-Rajasthan border where neo-tectonic activities have been recognized by recurrence of small magnitude tremors.

On basis of weight, assignment relative significance of landslide causative variables can be worked out and can help in "Landslide Hazard Zonation" strategies in a better way [11], by combining remote sensing data and GIS for workout risk assessment and thematic map generation for susceptibility using some "key" parameters responsible for triggering landslide [12]. Each parameter has their significance to probable of landslide activity [13], and various GIS-based case studies [14, 15] have successfully used it for landslide hazard zonation [16]. As already reported in the previous studies [17, 18], all work on susceptibility assessments must be focused on a reliable set of previous records and history of events to serve as the foundation and facilitate the whole operation.

1.3 Study Area

The area identified in this study includes Madanpura, Fatehpur Sikri, Agra in Vindhyan Hills of Neoproterozoic age. The area comes under semiarid region, and the rocks are present in low-lying symmetrical to asymmetrical hills. Some of the hills show natural scarp produced due to faulting or due to mining for the building stones. The thick deposits of Aeolian sand can be seen on the northwest flanks of the hill. The local-level mining still goes on using some crude methods which have made the steep slopes of the hills prone to rockfall and toppling failure (Fig. 1).

Fig. 1 Studied slopes of Madanpura (Fatehpur Sikri)

2 Methodology

2.1 Data Acquisition

The data used in this analysis contains information that is transmitted spatially along with other ancillary data. The following systematic approach involves several steps to acquire the necessary data from the source, processing and analyzing it, generating thematic maps, and conducting field visits to the present research. The available published and unpublished literature, technical reports, special volumes, and research papers published in various national and international journals, relevant to this review, are compiled and extensively reviewed. The SRTM DEM data for the Madanpura (Fatehpur Sikri) region's 90 m spatial resolution was freely downloaded from the usgs.gov website [19] to produce the various components such as height, slope, and aspect.

2.2 Data Used

List of data required and used for analysis is given below:

1. Survey of India (SOI) topographical maps no. **54E/12** on **1:50,000** scale.
2. SRTM DEM 90 m resolution data.
3. Satellite imagery of high resolution freely available on *Google Earth*.

2.3 Software Used

SRTM DEM data processing is performed using ArcGIS10.0

1. The various GIS software used for the study is ArcGIS 10.0.
2. Microsoft Office module from MS-Office 2007 software program
3. ArcGIS 10.0 has also been used for georeferencing maps and making of various thematic maps.

3 Result and Discussion

3.1 Aspect Map

Aspect is the slope's direction and measured as smooth, N, NE, E, SE, S, etc. (Fig. 2). It recognizes the downslope direction of the maximum rate of change in value from each cell to all of its neighbors. One could think of it as slope direction. The raster values for the output will be the compass's aspect direction.
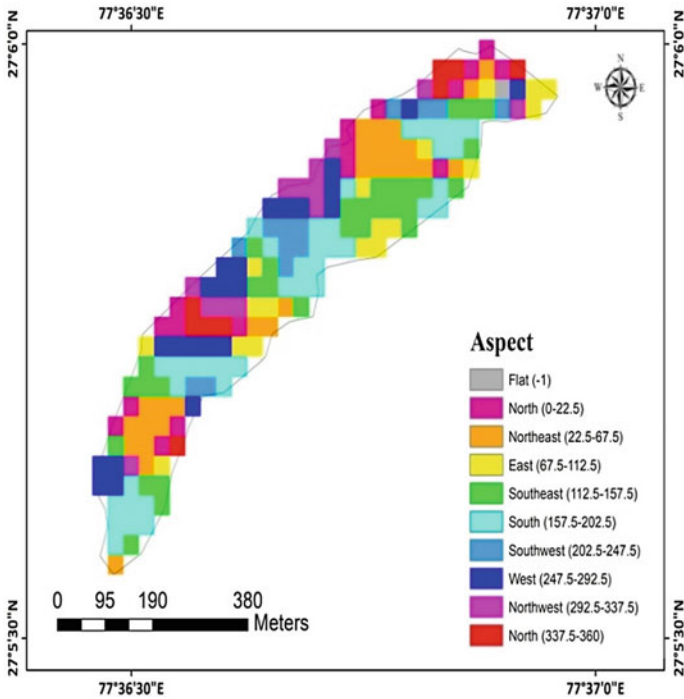
Fig. 2 Aspect map of the slope

3.2 Slope Map

It is measured as an angle in degrees or in percentage. Slope defines a unit of terrain as its steepness or gradient. Slope is a resolution function and is determined by using spatial resolution. In terrain analysis slope, aspect and surface curvature are all obtained from neighborhood operations using elevation values of all neighboring cells. Slope (Fig. 3) is prepared by SRTM DEM data in Arc GIS software. Slope is mostly classified into six classes as plain, gentle, moderate, fairly inclined, inclined, and very inclined. In the study area, maximum area falls under fairly inclined and inclined region, whereas area in northern region falls in very inclined region.

3.3 Contour Map

Contour map generally shows the elevation above sea level and surface feature of land by means of contour lines. Contour map (Fig. 4) was extracted from SRTM DEM data using Arc GIS software with interval of 50 m.
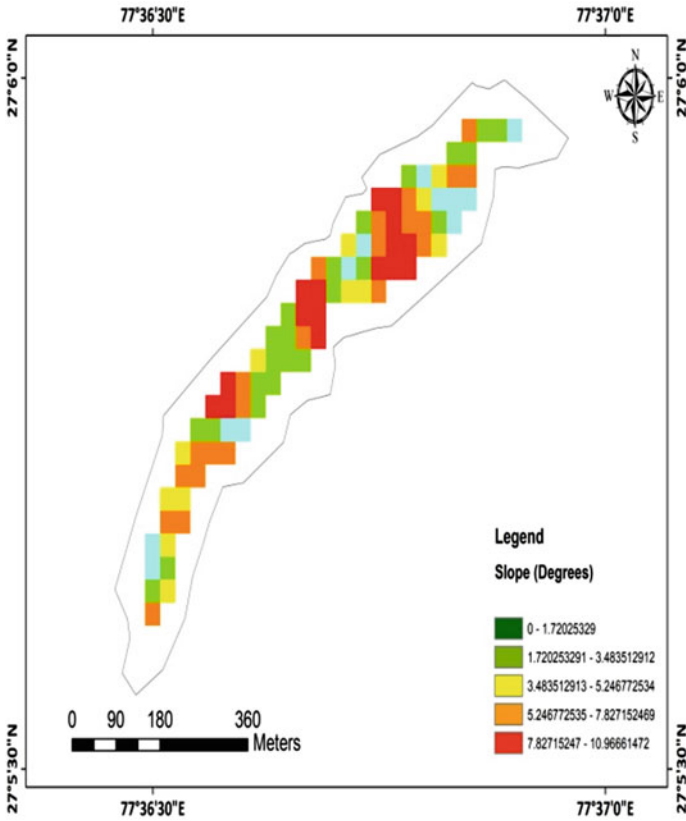
Fig. 3 Slope map of the slope

3.4 Dem

DEM is another important conditioning factor because it is affected by various geomorphic and geologic processes (Fig. 5) [13, 14]. Landslides are generally more prone to occur at high altitude [15]. In the study area, altitude ranges from 171 to 197 m above mean sea level.

3.5 Relief

Relief maps show contours, based on the form and height of landscapes and ground. Detailed variants of topographic maps are relief maps (Fig. 6). To construct two-dimensional models, the topographic maps use contour lines to link areas of the
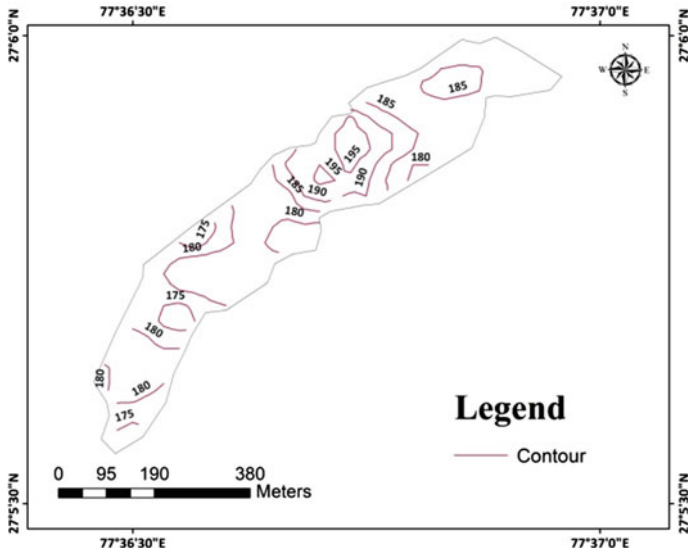
Fig. 4 Contour map of the slope
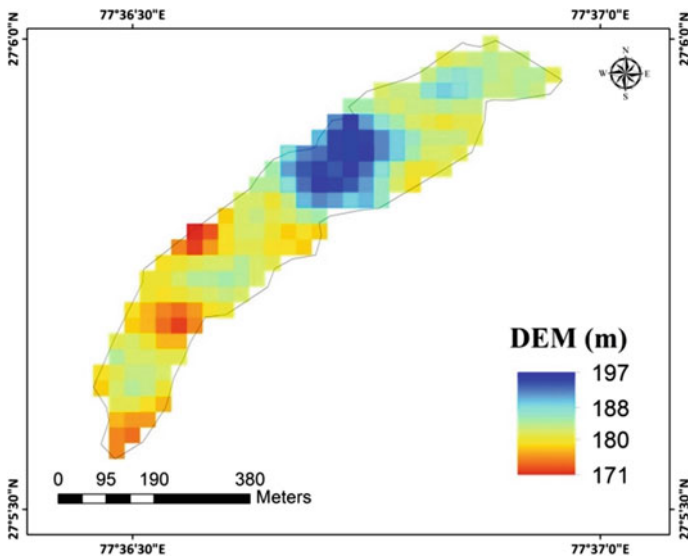
Fig. 5 Digital elevation model of the slope

same elevation. The focus on the three-dimensional elevation of topography is what makes relief maps distinct from other maps; shading is often used between contours for better representation of terrain, known as shaded relief.
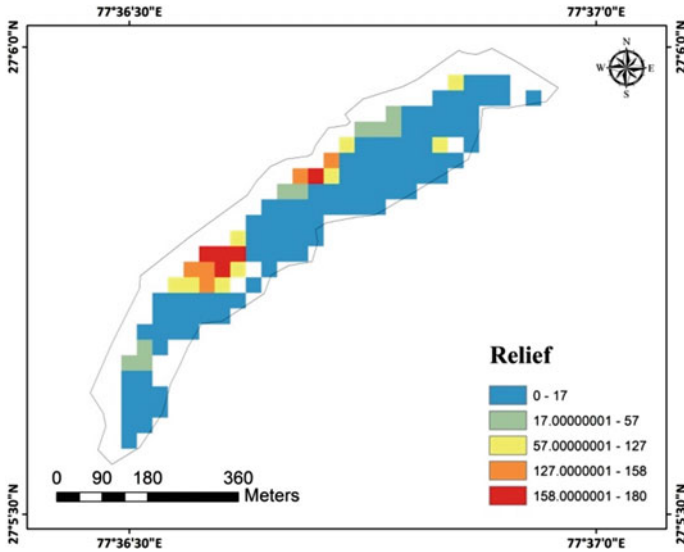
Fig. 6 Relief map of the slope

3.6 Landslide Susceptibility Map

The general estimation for landslide susceptibility zone results in the combination of the vulnerability factors of the individual elements. In particular, the map has been first re-classed then the information layers have been added utilizing Arc GIS (Raster Calculator Tool—Spatial Analyst). In the susceptibility map, the major part of the region is described by a moderate degree of instability. The most susceptible class has moderate potential in LSS map (Fig. 7) which has a high elevation in the study area, i.e., greater than 20 m from local level. DEM analysis has been used to prepare aspect, slope, relief, and contour map of the area. These thematic maps of study area show that the area has near about moderate to low topography but is susceptible to rock failure at local level, due to some natural and/or anthropogenic causes. Some failure, especially a classical rock failure, can be seen as a textbook case of "wedge failure" caused by intersecting joint sets with plunge toward the slope (Fig. 8b).
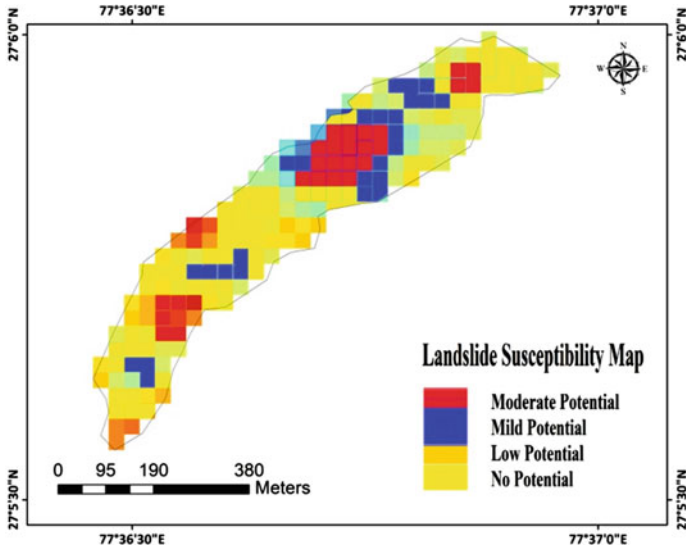
Fig. 7 Landslide susceptibility map

(a). North – West slope, indicate High Hazard, Toppling failure

(b). A classical "Wedge Failure" on the cliff side of the study area.

Fig. 8 **a** Northwest slope, indicate high hazard, toppling failure, **b** a classical "wedge failure" on the cliffside of the study area

4 Conclusion

This study has used various thematic maps prepared from GIS software using inverse distance weight (IDW) method including DEM shows that most of the low-lying areas are lying at the southeast boundary side and high elevation area toward northwest. The slope map of the area shows that maximum part of the hill is under fairly inclined to inclined region. Aspect map shows the direction of slope which is asymmetrical in the study area maximum direction of slope found in northwest and lowest on southeast direction. Relief map of the study area also shows that though the area has low relief but is degraded due to anthropogenic activity making it under moderate risk zone of landslide. These thematic maps suggest that the area susceptible to landslide. Especially the northwestern part of the hill is very inclined with two conjugate sets of joints with their intersection plunging toward the slope have made it highly prone to landslide. The excavation of Aeolian sand deposited in the shadow of the hill along northwestern slope, creating deep pit makes the scarp slope highly vulnerable. Fortunately, there is no habitation around the hill; hence, demarcation of hill site can increase the safety. It is also suggested that barbed fencing may be laid down to prevent any untoward happening.

Conflict of Interest On behalf of all authors, there is no conflict of interest.

References

1. National Disaster Management Guidelines. Management of Landslides and Snow Avalanches, pp. 1–144. A Publication of the National Disaster Management Authority, Government of India (2009)
2. Bolt, B.A.: Landslide Hazard, Geological Hazard, p. 150. Springer, New York (1975)
3. Waltham, T.: Foundations of Engineering Geology, p. 92. Spon Press (2002). ISBN 0-415-25449-3
4. Chae, B.G., Park, H.J., Catani, F., Simoni, A., Berti, M.: Landslide prediction, monitoring, and early warning: a concise review of state-of-the-art. J. Geosci. **21**, 1033–1070 (2017)
5. Christos, C., Maria, F., Polykretis, C.: GIS-based landslide susceptibility mapping on the Peloponnese Peninsula. Greece Geosci. **4**, 176–190 (2014)
6. Gupte, S.S., Singh, R., Vishal, V., Singh, T.N.: Detail investigation of stability of in-pit dump slope and its capacity optimization. Int. J. Earth Sci. Eng. **6**(2), 146–159 (2013)
7. Trivedi, R., Vishal, V., Pradhan, S.P., Singh, T.N., Jhanwar, J.C.: Slope stability analysis in limestone mines. Int. J. Earth Sci. Eng. **5**(4), 759–766 (2012)
8. Pradhan, S.P., Vishal, V., Singh, T.N.: Stability of slope in an open cast mine in Jharia coalfield—a slope mass rating approach. Mining Eng. J. **12**(10), 36–40 (2011)

9. Sarkar, S., Pandit, K., Shamra, M., Pippal, A.: Risk assessment and stability analysis of a recent landslide at Vishnuprayag on the RishikesheBadrinath highway, Uttarakhand, India. Curr. Sci. **114**(7), 1527–1533 (2018)

10. Mithal, R.S.: Lithotectonics landslides and hazards in part of Garhwal-Kumaon Himalayas. In: Proceeding Second International Conference on Case Histories in Geotechnical Engineering, RollaMissouri (1988)

11. Pardeshi, S.D., Autade, S.E., Pardeshi, S.S.: Landslide hazard assessment: recent trends and techniques. SpringerPlus **2**, 523 (2013)

12. Dibs, H., Al-Janabi, A., Chandima, G.: Easy to use remote sensing and GIS analysis for landslide risk assessment. J. Univ. Babylon, Eng. Sci. **26**(1) (2018)

13. Saied, P., Jonathan, L.: Landslides investigations from geoinformatics perspective: quality, challenges, and recommendations. Geomatics Nat. Hazards Risk **8**(2), 448–465 (2017). https://doi.org/10.1080/19475705.2016.1238850

14. Gritzner, M.L., Marcus, W.A., Aspinall, R., Custer, S.G.: Assessing landslide potential using GIS, soil wetness modelling and topographic attributes, Payette River, Idaho. Geomorphology **37**, 149–165 (2001)

15. Dai, F.C., Lee, C.F.: Landslide characteristics and slope instability modeling using GIS, Lantau Island, Hong Kong. Geomorphology **42**, 213–228 (2002)

16. Van Westen, C.J., Ghosh, S., Jaiswal, P., Martha, T.R., Kuriakose, S.L.: From landslide inventories to landslide risk assessment; an attempt to support methodological development in India. In: Proceedings of the Second World Landslide Forum, Rome, Italy (2011)

17. Ahmed, B.: Landslide susceptibility mapping using multi-criteria evaluation techniques in Chittagong Metropolitan Area, Bangladesh. Landslides **12**, 1077–1095 (2015)

18. Van Westen, C.J., Castellanos, E., Kuriakose, S.L.: Spatial data for landslide susceptibility, hazard, and vulnerability assessment: an overview. Eng. Geol. **2008**(102), 112–131 (2008)

19. http:/earthexplorer.usgs.gov

Numerical Investigation of Soil–Structure Interaction Behaviour of Landslide Prevention Piles

G. Sreelakshmi and **M. N. Asha**

1 Introduction

Over the years, India witnessed severe landslides that affected states surrounding western and eastern Konkan ghats hills like Maharashtra, Kerala, Tamil Nadu, Karnataka, Goa as well as north-west Himalaya regions like J&K, Himachal Pradesh, Uttarakhand and north-east Himalaya regions like Sikkim, Arunachal Pradesh, Meghalaya, Assam, Arunachal Pradesh and West Bengal. As per the reports of National Disaster Management Authority, 12.6% of the Indian land terrain is landslide-prone and caused a monetary loss of Rs. 100 crores to Rs. 150 crores per annum. In accordance with the 2019 report of Copernicus Publications on Landslide analysis, human interventions triggered 18% of landslide casualties all over India. Human involvements in urban and regional development activities such as construction, mining, quarrying and hydro-power projects loosen and remove vegetative cover, leading to low groundwater retention capabilities, thereby increasing the risk of flooding. Consequently, when rainfall or earthquakes occur, the surplus water loosens debris creating landslides.

Landslides can be classified according to various parameters such as the presence or absence of a slip plane, materials involved, water content and type and rate of movement. Numerous factors causing a mass of material to slide or flow are nature of slope, water content, composition and compaction of the mass, geological structure as well as external factors like earthquakes and mining activities.

Several techniques are available for regulating the slides such as providing drainage ditches, channels, waterways, trenches, retaining structures, sheet pile walls, joint grouting and slope stabilization treatments. Various researchers investigated

G. Sreelakshmi (✉) · M. N. Asha
CMR Institute of Technology, Bengaluru, India
e-mail: sreelakshmi.g@cmrit.ac.in

M. N. Asha
e-mail: asha.n@cmrit.ac.in

geo-mechanical processes involved in landslide mechanisms, risk analysis and assessments, slope stability analysis and proposed innovative stabilization techniques.

In the year 1978, [1] presented a summary of various slope design procedures, its application and related stability analysis that must be performed for safe and efficient soil–structure force transfer process. Since then researchers like [2, 3] implemented various geophysical and probabilistic approaches to investigate the stability of landslides in terms of shear strength parameters, failure planes, hydrogeological regimes and suggested landslide hazard mitigation measures that have to be adopted in areas of disaster-prone regions.

Over the past years, India has witnessed severe rainfall that prolonged over a long duration that caused excessive overflows coupled with landslides. This has created extreme impacts on live and livelihoods and triggered drastic changes in geographical terrains. Iverson and Major, Glade et al., Dai and Lee [4–6] adopted statistical techniques to examine the rainfall conditions associated with landslide occurrence and adopted regional models to represent the probability of occurrence of land sliding events. Huang et al. and Chen et al. [7, 8] carried out field investigations of various rainfall-induced landslide regions and studied implications of landslide mitigation measures like piles, retaining wall, catching trenches, etc. Recently, [9] evaluated slope stability of rain-induced slope failure and suggested mitigation approaches to minimize the impact of financial loss and damages.

The earthquake-triggered landslide could lead to gradual collapse of huge rock falls through a fatigue process induced by seismic waves. Harp and Jibson [10] concluded that the increased rate of ground shaking in the Pacoima canyon regions caused the high-frequency rock falls and slides. Researcher like [11] performed numerical investigation of landslide due to the pore pressure development in the areas of ground motion through numerical method using FLAC software.

The evaluation of slope stability and selection of suitable slope stabilization have always been a matter of research. Cruden et al. [12] suggested various types of surface drainage for reducing landslide failure mechanisms. Malkawi et al. [13] applied Monte Carlo method for determining critical slip failure surface and factor of safety, which forms the basis for stability analysis for landslide failures. Recently, [14] performed MATLAB-based slope stability analysis to decide critical failure surface through particle swarm optimization and compared results with other slope stability methods.

Since the advent of 1950s, sheet pile wall system was adopted in many civil engineering structures for retention of earth fills for withstanding horizontal earth pressure. They comprise series of piles that are connected and fixed in soils to behave as a confined wall, thus providing stability to overlying ground profile. The construction process consists of sheet pile installation into ground surface and backfilling of soil near pile walls. The type of wall system is selected based on wall function, type of infill conditions and presence of adjoining structures near sheet pile wall system. There are several methods of analysis which has been adopted for investigation of sheet pile wall system. With the advancement in field of various digital processing systems, numerical techniques have accomplished its vast level of prominence in analysing sheet pile systems.

Brits [15] investigated the behaviour of cantilevered and anchored sheet pile wall model using Fast Lagrangian Analysis of Continua (FLAC) and explored variation of infill density and water table near the ground level. In contrast with cantilever sheet pile wall for anchored sheet pile the presence of tie rod reduced the bending moment, wall deflection, soil settlement and imparted greater stability to wall system. The use of analytical and commercially available software's like GEOWALL, PLAXIS, PROSHEET is explored by [16] to study the behaviour of sheet pile wall system with and without anchors by considering and without considering groundwater and surcharge. They have concluded that when foundation depth is enhanced, there is a reduction in the bending moment developed and the presence of anchor bars increased the stability as it reduced the passive earth pressure. Later [17] performed finite element studies on sheet pile walls with anchor bars using GEO5. They then concluded that increase in shear parameters like friction angle and cohesion decreased wall displacement, maximum bending moment and shear force values. Fall et al. [18] examined the response of double-anchored sheet pile system using ABACQUS software and concluded that reduction in positioning of anchor bars caused a significant reduction in the bending moment and vertical displacement along sheet pile walls.

From the various literature works, it can be ascertained that very few researchers have tried to model infill as a layered medium with a sheet pile wall system. The load distribution by sheet pile wall system anchored with tie bars minimizes bending, vertical and horizontal wall displacements. So, the study focuses on investigating the displacement contours and bending moment developed with single and double tie bars along the depth of sheet pile wall. It is also proposed to estimate and then compare the variation in axial forces developed in tie bar groups under a predefined stress condition.

2 Methodology

The methodology adopted for the numerical study involves the following stages:

- Generation of model geometry—Assigning geometrical 'X-' and 'Y-'coordinates
- Selection of suitable finite element mesh-Discretization using 3 Nodes and 6 Node Triangular elements
- Assigning infill properties—Simulation of layered infill medium with sand and clay
- Fixing of external boundary conditions—Constraining rotation and displacement conditions
- Installation of sheet pile wall—Use of beam element between the interfaces
- Application of initial stress conditions—Initialization of element stress conditions

- Execution of excavation sequences and assignment of tieback elements—
  Excavation of top portion of vertical ground to install tieback element and
  assignment of its properties
- Post-processing of data—Generation of displacement plots, structural data, axial
  force

3   Model Setup

The assumptions adopted in ADONIS software for the finite element modelling are
listed as below:

1. Triangular finite elements are adopted for generating two-dimensional models.
2. Sheet piles are simulated as two-dimensional beam element with the translation
   degrees of freedom along X- and Y-directions and rotations at each node.
3. The one-dimensional axial elements are used for modelling tieback elements.
4. Mohr–Coulomb model is being used to replicate shear failure in infill medium.
5. Coulomb shear strength criteria are followed for interface constitutive
   modelling.
6. Element constitutive models are solved through iterative processes till they
   achieve a state of elastic model equilibrium.

3.1   Structural Properties of Sheet Piles Walls and Tieback Elements

For numerical simulation of sheet piles wall system in ADONIS software requires
input parameters like rock mass properties, material properties of pile, tie bar
members and effective stress conditions. The modelled steel sheet pile wall has a
height of 10 m and foundation depth of 2 m. The tie element is subjected to
pretension force of 2.0×10^4 N with grout length ratio of 40%. The characteristics
of sheet pile wall along the properties of tie bars are shown in Tables 1 and 2.

Table 1 Structural properties of sheet pile adopted in numerical study

Material	Cross sectional area (m^2)	Young's modulus (Pa)	Moment of inertia (m^4)	Length (m)
Steel	0.2	2.1×10^5	6.7×10^{-4}	1.5×10^3

Table 2 Structural properties of tie bars adopted in numerical study

Material	Area (m²)	Young's modulus (Pa)	Yield strength (Pa)	Pretension force (N)	Tie bar inclination
Steel	0.002	2.1×10^5	1.0×10^{50}	2.0×10^4	20.5°

3.2 Properties of Infill Medium Adopted in Numerical Study

The ground condition is characterized as in the form of layered infill comprising of sandy soil having an infill density of 1740 kg/m³ till a depth of 4 m, followed by clayey soil with dry density of 1330 kg/m³ for 14 m depth. The values assumed are in conjunction with the literature. Table 3 provides a summary of physical characteristics for sand and clayey soils adopted in experimental study.

Figure 1a, b shows the sheet pile wall system with one and two tie bars used for modelling in ADONIS software.

Figure 2a–d shows the steps involved in geometrical generation of sheet pile retaining wall with tieback element. The details of the following figures can be listed as:

- Figure 2a shows the finite element modelling of infill medium with different soil layers.
- Figure 2b shows the excavation sequences for the installation of sheet pile wall element.
- Figure 2c, d shows the installation of tieback elements at two different locations.

3.3 Initial Stress Conditions Adopted in the Study

The initial vertical and horizontal stress developed in infill medium is calculated based on infill density and geometry of profile chosen for the study. In ADONIS software, a linear variation of stresses is considered over a specified range of section and stresses are updated at every step using Gaussian quadrature method. The ground surface is assumed as flat with horizontal dry-layered infill medium and element stresses along Y are calculated based on effective stress conditions. The earth pressure at rest approach is adopted for calculating element stresses along X- and Z-directions to simulate initial stress conditions.

Table 3 Physical properties of rock mass adopted in experimental study

Material	Infill density (kg/m³)	Young's modulus (Pa)	Poisson's ratio	Cohesion (Pa)	Friction angle
Sand	1740	2.1×10^7	0.26	1.5×10^3	38°
Clay	1330	1.4×10^7	0.20	1.2×10^4	22°
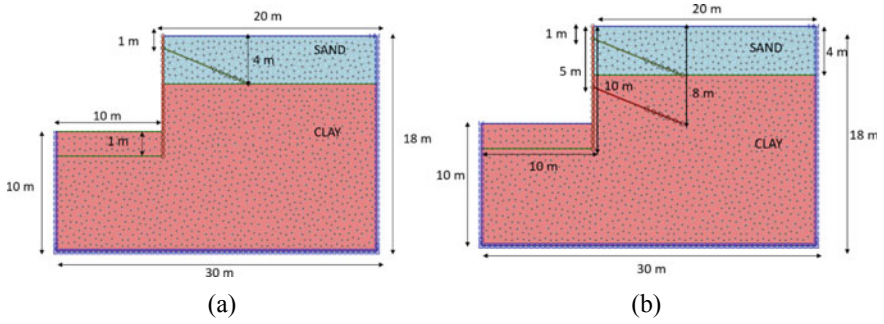
Fig. 1 a, b Sheet pile wall system used for numerical modelling in ADONIS software
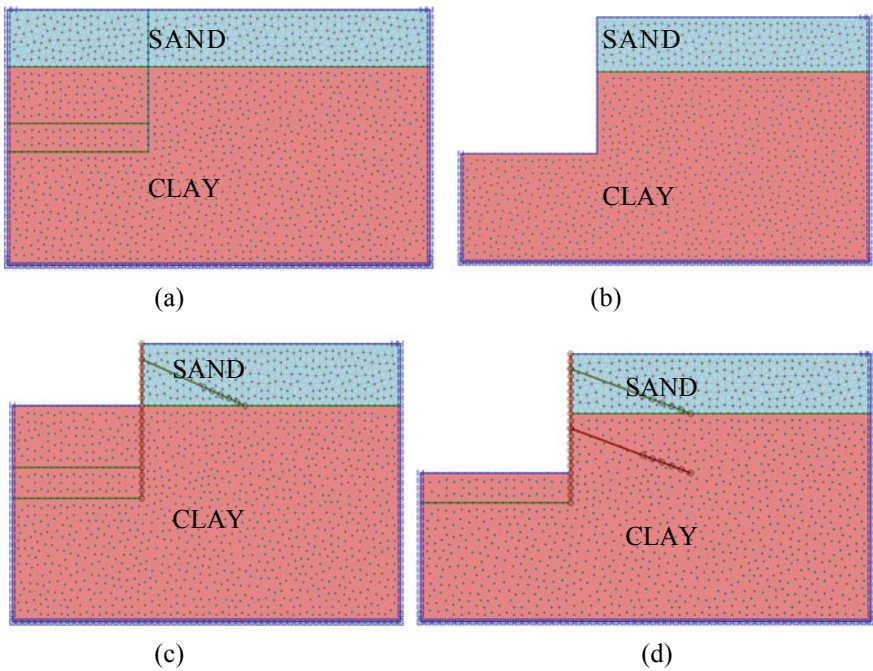
Fig. 2 a–d Sequences of model generation process of sheet pile retaining wall with tieback element

To examine the significance of tie bar elements in layered infill medium a comparison is made between sheet pile wall system with single and double tie bar members. The following section describes the results arrived from the numerical study.

4 Results and Discussion

4.1 Variation of Horizontal Displacement Contours Along the Depth of Section

Figure 3a, b shows the variation of horizontal displacement contours along the depth of the section. For the case of single tie bars, it is seen that there is a maximum horizontal displacement of magnitude 1.96×10^{-2} m near the bottom level of the section followed by minimum displacement of -5.18×10^{-1} m towards the wall near the top level of sheet pile wall. Also, at the position of single tie bar there is reduction in displacement. But in the case of double tie bar members, maximum displacement near top surface of wall as well as bottom level of section reduced by a magnitude of 8.77×10^{-3} m and displacement near the bottom level of the section reduced by -3.06×10^{-3} m. The introduction of pretensioned tie bars groups with concrete grouting prevented ground heave and caused reduction in magnitude of horizontal displacements.

4.2 Variation of Bending Moment Along the Sheet Pile Wall System

Figure 4a, b shows the variation of bending moment contours along with vertical displacement along the depth of the wall section. For the case of single tie bars, it is observed that there is a positive bending moment and total displacement of 1.7×10^5 Nm and -9.38×10^{-2} m at top level of sheet pile wall system followed by a negative bending moment of -4.66×10^4 Nm and total displacement of 7.78×10^{-1} m near the bottom level of the section. With the introduction of double tie bar elements, there is a reduction in positive bending moment value of 4.43×10^3 Nm and total displacement of -1.25×10^{-2} m at mid-level of sheet pile wall system followed by a negative bending moment and total displacement of -1.66×10^1 Nm and -1.15×10^{-1} m near the bottom level of the section. It is observed that when the number of bars is increased, the negative bending moment at bottom level minimized indicating the significance of bar elements. The negative bending moment can initiate the development of tension cracks causing instability issues leading to slope failure.

The angle of inclination of tie bars plays a significant role in withstanding the bending of sheet pile walls. It is observed that inclination of 20.5° as suggested from the literature [19] proved effective in reducing the amount of deflection along the wall surface.
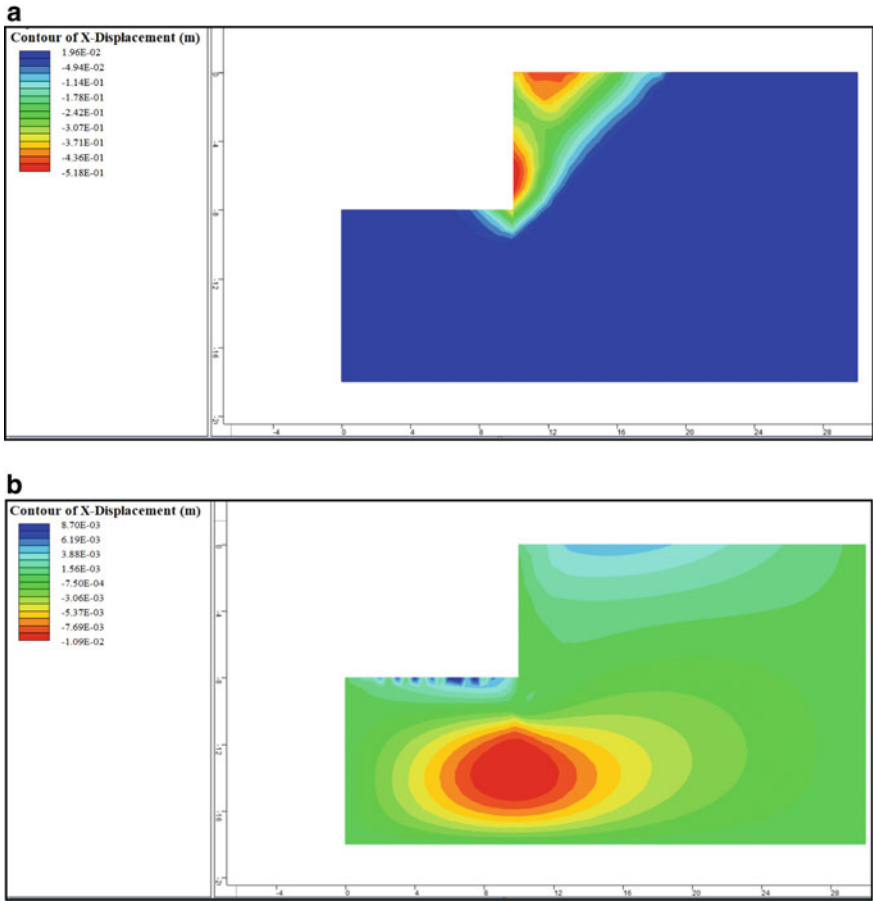
Fig. 3 **a** Variation of horizontal displacement contours along the depth of section with single tie bar, **b** variation of horizontal displacement contours along the depth of section with double tie bars

4.3 Variation of Bond Force in Tie Bar Element Along with Total Displacement

Figure 5a, b shows the variation of bond forces along the tie bar elements. In the case of single tie bar, tensile bond force of 1.00×10^6 N is developed near the wall face, followed by a compressive force of -4.82×10^5 N at inner face. But in the case of double tie bar members, tensile bond force increased for both bars as 6.65×10^3 N and 4.06×10^4 N, followed by a decrease in compressive force by -8.77×10^3 N and -1.54×10^4 N at inner face. The tensile bond prevents the crack development in the infill medium and imparts greater axial load capacity to sheet pile walls.
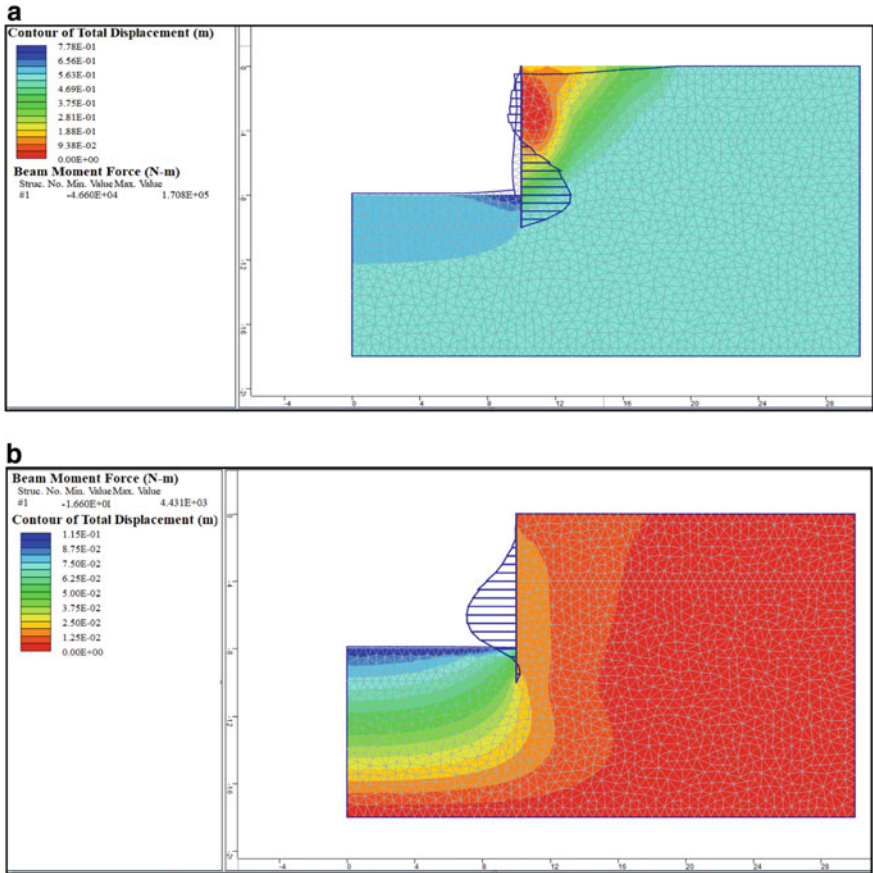
Fig. 4 **a** Variation of bending moment along with total displacement contours along the depth of section with single tie bar, **b** variation of bending moment along with total displacement contours along the depth of section with double tie bars

5   Conclusions Derived from the Study

When the number of tie bar members is increased, the horizontal displacement in the upper part of sheet pile retaining wall is reduced that indicates the suitability under adverse ground conditions. It is also observed that maximum bending moment reduced drastically in the case of two tie bars due to increased lateral resistance offered bars in terms of its axial load-carrying capacity. So, to prevent or to reduce man-made or natural-like landslides, use of these types of anchored sheet pile retaining wall is highly recommended.
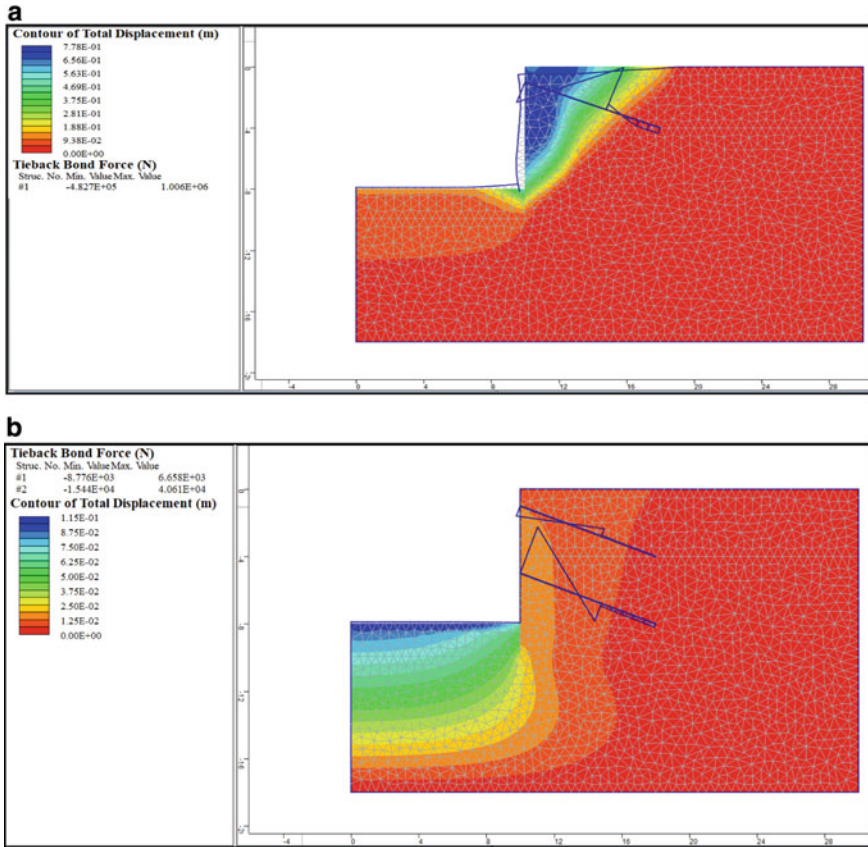
Fig. 5 **a** Variation of bond force with total displacement contours along the depth of section with single tie bar, **b** variation of bond force with total displacement contours along the depth of section with double tie bars

6 Scope of Future Study

For future study, an experimental modelling of anchored sheet pile wall with layered infill can be carried out so that a comparison and validation of numerical work can be assessed. The conclusions drawn from the current research could be implemented in exploring the interfacial soil-sheet wall characteristics. In the present study, clayey infills with sloping ground surface and different water content have not been considered which can be added as a scope for future research. Parametric studies on inclination of tie bar may also be carried out to optimize its optimum orientation.

References

1. Gedney, D., Weber Jr, W.: Design and Construction of soil slopes. Transp. Res. Board Spec. Rep. (1978)
2. Bernknopf, R.L., Campbell, R.H., Brookshire, D.S., Shapiro, C.D.: A Probabilistic Approach to Landslide Hazard Mapping in Cincinnati, Ohio, with Applications for Economic Evaluation (1988). https://doi.org/10.2113/gseegeosci.xxv.1.39
3. McCann, D.M., Forster, A.: Reconnaissance geophysical methods in landslide investigations. Eng. Geol. **29**, 59–78 (1990). https://doi.org/10.1016/0013-7952(90)90082-C
4. Iverson, R.M., Major, J.J.: Rainfall, ground-water flow, and seasonal movement at minor creek landslide, northwestern California: physical interpretation of empirical relations. Geol. Soc. Am. Bull. **99**, 579–594 (1987). https://doi.org/10.1130/0016-7606(1987)99%3c579:RGFASM%3e2.0.CO;2
5. Glade, T., Crozier, M., Smith, P.: Applying probability determination to refine landslide-triggering rainfall thresholds using an empirical "antecedent daily rainfall model." Pure Appl. Geophys. **157**, 1059–1079 (2000). https://doi.org/10.1007/s000240050017
6. Dai, F.C., Lee, C.F.: Frequency-volume relation and prediction of rainfall-induced landslides. Eng. Geol. **59**, 253–266 (2001). https://doi.org/10.1016/S0013-7952(00)00077-6
7. Huang, R., Jiang, L., Shen, X., Dong, Z., Zhou, Q., Yang, B., Wang, H.: An efficient method of monitoring slow-moving landslides with long-range terrestrial laser scanning: a case study of the Dashu landslide in the Three Gorges Reservoir Region, China. Landslides **16**, 839–855 (2019). https://doi.org/10.1007/s10346-018-1118-6
8. Chen, Z., Song, D., Hu, C., Ke, Y.: The September 16, 2017, Linjiabang landslide in Wanyuan County, China: preliminary investigation and emergency mitigation. Landslides **17**, 191–204 (2020). https://doi.org/10.1007/s10346-019-01309-1
9. Kumar, A., Sharma, R.K., Mehta, B.S.: Slope stability analysis and mitigation measures for selected landslide sites along NH-205 in Himachal Pradesh, India. J. Earth Syst. Sci. **129** (2020). https://doi.org/10.1007/s12040-020-01396-y
10. Harp, E.L., Jibson, R.W.: Anomalous concentrations of seismically triggered rock falls in Pacoima Canyon: are they caused by highly susceptible slopes or local amplification of seismic shaking? Bull. Seismol. Soc. Am. **92**, 3180–3189 (2002). https://doi.org/10.1785/0120010171
11. Bourdeau, C., Havenith, H.B.: Site effects modelling applied to the slope affected by the Suusamyr earthquake (Kyrgyzstan, 1992). Eng. Geol. **97**, 126–145 (2008). https://doi.org/10.1016/j.enggeo.2007.12.009
12. Cruden, D.M., Varnes, D.J., Turner, A.K., Schuster, R.L.: Landslides: investigation and mitigation. Special Report 247 (1996)
13. Malkawi, A.I.H., Hassan, W.F., Sarma, S.K.: Global search method for locating general slip surface using Monte Carlo techniques. J. Geotech. Geoenviron. Eng. **127**, 688–698 (2001). https://doi.org/10.1061/(asce)1090-0241(2001)127:8(688)
14. Sharma, R.K., Kaur, A., Kumar, A.: Slope Stability Analysis by Bishop Analysis Using Matlab Program Based on Particle Swarm Optimization Technique. Springer International Publishing (2019). https://doi.org/10.1007/978-3-030-02707-0_34
15. Brits, C.: Developing a Numerical Model for the Design of Sheet Pile Walls Chane Brits (2014)
16. Ingenier, S.E.N.: Título: Comparison of Numerical and Classical Analytical Method for Sheet Pile Wall Analyses (2014)

17. Abd El Raouf, M.: Numerical analysis of anchored sheet pile walls. J. Al-Azhar Univ. Eng. Sect. **15**, 594–603 (2020). https://doi.org/10.21608/auej.2020.87864
18. Fall, M., Gao, Z., Ndiaye, B.C.: Three-dimensional response of double anchored sheet pile walls subjected to excavation and construction sequence. Heliyon **5**, e01348 (2019). https://doi.org/10.1016/j.heliyon.2019.e01348
19. Abdel-fattah, P.E.: Analysis of the behavior of inclined anchor by varying the inclination and elevation of tie (2018)

Antecedent and Cumulative Rainfall as Thresholds in Detecting Possible Landslide Occurrence

N. H. N. Khalid, **Fathoni Usman**, **R. C. Omar**, and **S. Norhisham**

1 Introduction

A landslide or slope failure is an unpredictable natural phenomenon occurred worldwide. The occurrence will affect its surroundings, causing losses to society, and can be classified as life-threatening. New findings from various researches and the implementation of new technology are needed to contribute in minimizing the tremendous effect of landslide. Realizing the need for prevention, monitoring, and identifying the early sign of landslide occurrence, the determination of landslide thresholds has been studied by many researchers. Various methods and theories had been applied to set their local landslide threshold by considering the environmental factors such as rainfall [1–13], historical landslide [14], slope stability conditions [15–18], site monitoring [19–21], and others.

This paper is presenting a method for identifying a threshold for possible landslide occurrence on two slopes that each house an electric transmission tower. The failure on the slopes might affect the stability of the tower and will lead to tower failure. This most unsolicited incident should be avoided as it will affect the company's reputation, as well as losses to be paid to customers during power supply shortage. Preventing a landslide from occurring is almost impossible. However, ways of ensuring the safety and improving the landslide alerting time can be done by identifying the threshold, in order to notify the local authorities on the risk level towards their asset located on the slopes which are susceptible to failure.

N. H. N. Khalid (✉) · S. Norhisham
College of Engineering, Universiti Tenaga Nasional, Jalan IKRAM-UNITEN,
43000 Kajang, Malaysia
e-mail: Hazwani@uniten.edu.my

F. Usman · R. C. Omar
Institute of Energy Infrastructure, Universiti Tenaga Nasional, Jalan IKRAM-UNITEN,
43000 Kajang, Malaysia

2 Past Landslide Event Detected at the Study Areas

Two locations named location A and location B were selected for this study due to their past historical landslide. They were located in the northeast of Peninsular Malaysia, as shown in Fig. 1. Even though they were located 124 km away from each other, the geological and soil properties of both areas are the same. They were located in forestry remote areas with hilly topography and have sandy silt-type soil with a hard layer found at the depth of 15–18 m. Figure 1 shows the location of the study areas on the landslide hazard map (LHM) of Peninsular Malaysia. It is clear that those locations are located in the landslide-prone area.
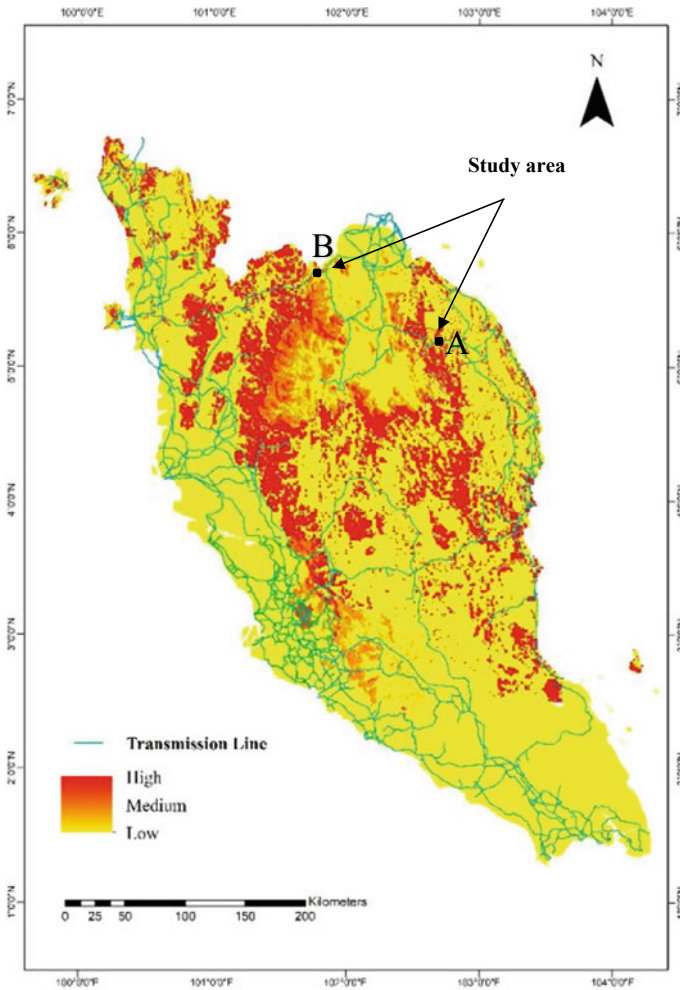
Fig. 1 Location of the study areas on landslide hazard map of Peninsular Malaysia

Landslide incident was identified at location A and location B during transmission tower inspection, and it was believed to have occurred in the past week. For location A, the landslide was identified in June 2011 (Fig. 2), while for location B was in February 2009 (Fig. 3).

In terms of possible failure at the selected transmission towers, Figs. 4 and 5 show the position of the critical leg at each location A and B. It clearly shows that the tower legs were positioned on the slope face occurring landslide. A surface landslide is a sign of a deep landslide. Therefore, monitoring of the slope is crucial in detecting the occurrence of any possible future landslide to monitor the stability of the electric transmission tower.

3 Methodology

Based on the landslide scar that occurred in the study areas, the landslide incident was suspected to have occurred within the past six months before it was detected. It was believed that the possible time for the landslide occurrence can be detected by examining the historical rainfall data for each location, by implementing back analysis.

The condition of slope in locations A and B when the landslide was found is shown previously in Figs. 2 and 3. The landslide events were detected during the site inspection, where location A was found in June 2011, while location B was

Fig. 2 Landslide detected on the slope at Location A (June 2011)

Fig. 3 Landslide detected on the slope at Location B (February 2009)

Fig. 4 Position of critical leg
at Location A
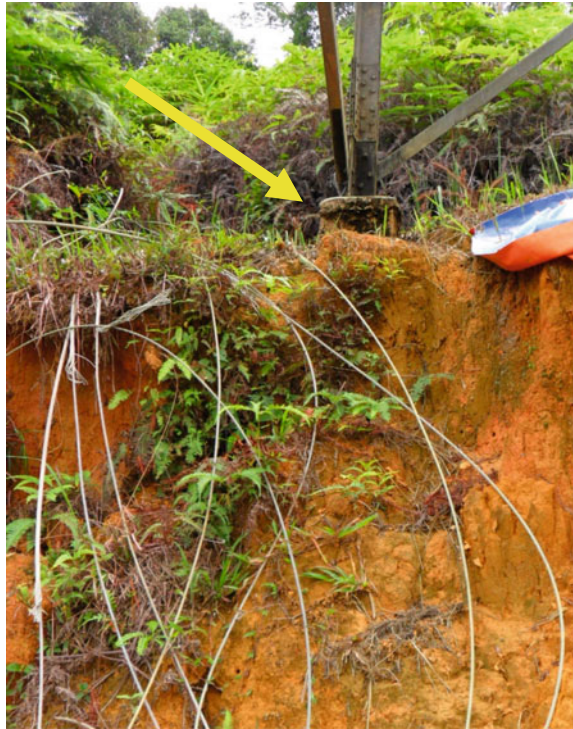
Fig. 5 Position of critical leg at Location B

found in February 2009. Therefore, six (6) months of rainfall data before the inspection for both locations were collected from the nearest rainfall station owned by the Department of Irrigation and Drainage of Malaysia (DID), to be analyzed in order to identify the possible time of the landslide occurrence. This method which is also known as "back analysis" was shown as a linear graph generated for 5-day antecedent versus cumulative rainfall and daily rainfall. Cluster analysis by scatter plot was applied to identify groups of the critical event that might trigger the landslide. The antecedence rainfall was considered since it causes the increment to the pore water pressure in the soil. The 5-day antecedent rainfall was chosen based on the previous research done by Naidu et al. [22], where the study found that 5-day antecedent rainfall contributed 20% of the rainfall threshold value that triggers landslide, compared to 2-day and 3-day antecedent rainfall.

4 Result and Analysis

The occurrence of past landslide events at locations A and B was identified by observing any unusual event from two types of graphs, which are scattered plots and a combination of lines from all parameters. The relationship between daily rainfall and cumulative rainfall to 5-day antecedent rainfall for location A and location B was observed from the graphs in Figs. 6 and 7, respectively. The 5-day antecedent rainfall was considered based on the study conducted by [16, 22, 23], in which research findings indicated the 5-day antecedent rainfall is significant to the landslide occurrence.

Based on the graphs, it was discovered that points marked in red were closed to each other, even with different axis plotted. Those points are classified as irregular conditions (unusual rainfall event) as they are far from the other points (usual rainfall event). For location A, the irregularity of all red points can be seen in Fig. 6a, b, and for location B in Fig. 7a, b. The past landslide incident might occur during this time.
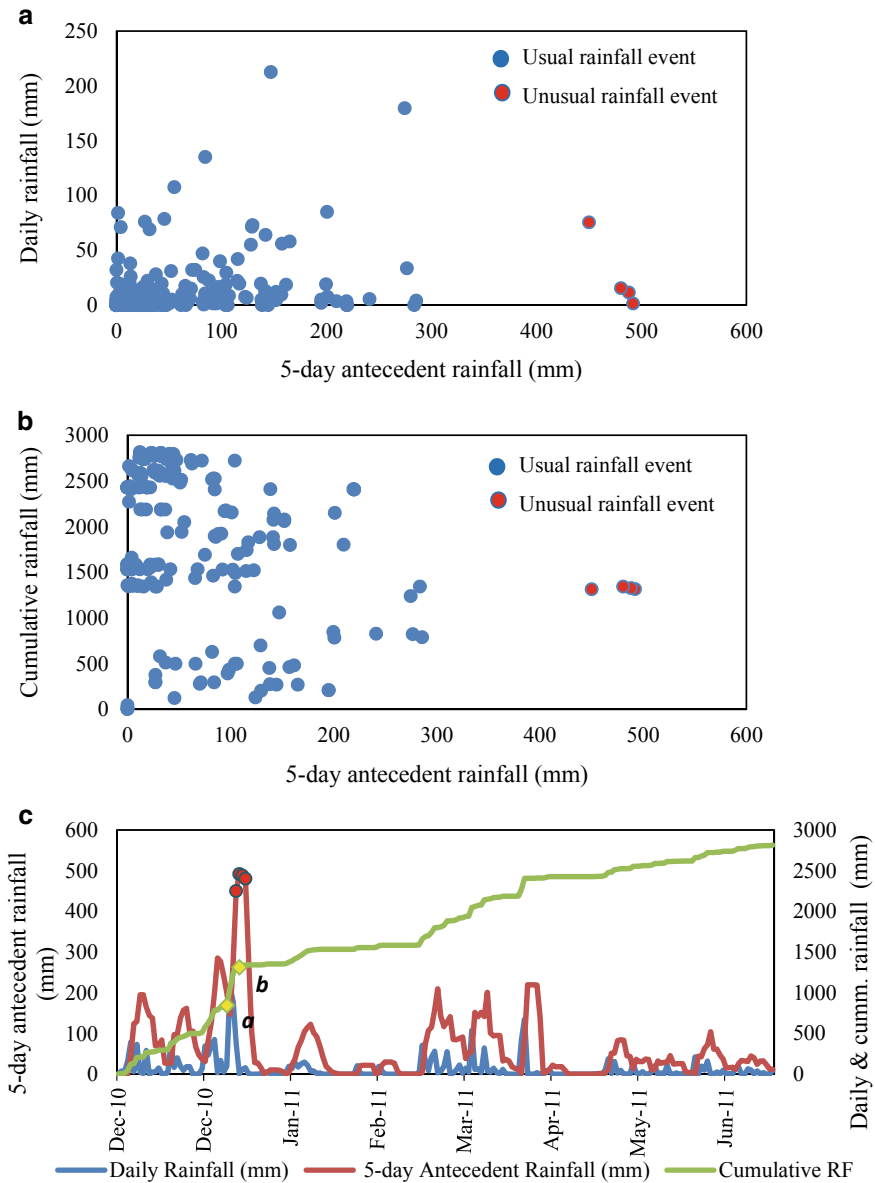
Fig. 6 Detection of landslide occurrence for Location A
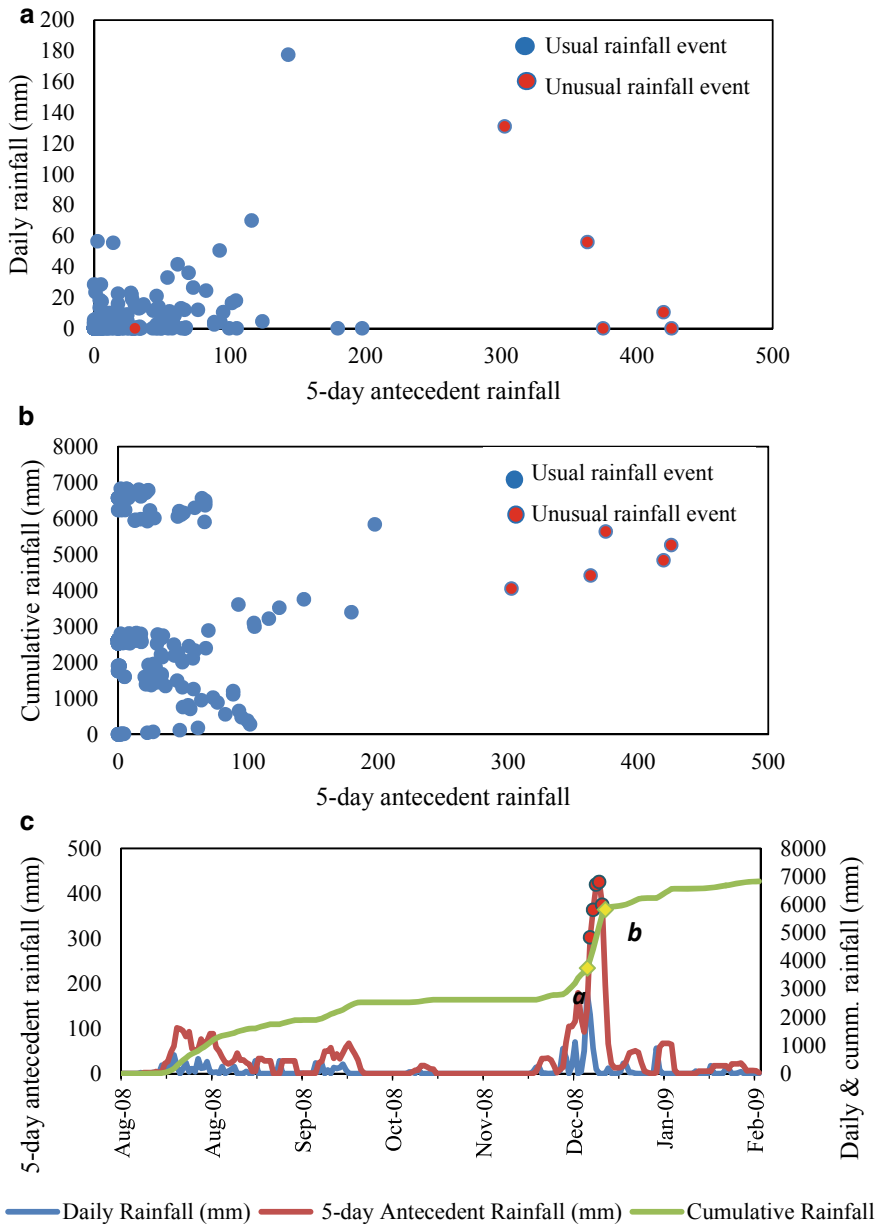
Fig. 7 Detection of landslide occurrence for Location B

When the line graph of 5-day antecedent rainfall, daily rainfall, and cumulative rainfall was plotted in Figs. 6c and 7c, it was discovered that the red points were located at the peak and the line of 5-day antecedent rainfall and go beyond the cumulative rainfall. The sharp increment from point a to point b indicates an increment of volume in daily rainfall and the cumulative rainfall. Furthermore, the peak increment for both locations was found to have occurred in January, even though the rainfall data analyzed were from a different year. This is because January is in the period of the monsoon season. Based on the observation of graphs in Figs. 6c and 7c, it was discovered that the landslide was suspected to have occurred in the study areas when the amount of 5-day antecedent rainfall goes beyond the amount of cumulative rainfall.

5   Conclusion

The analysis of the past landslide occurrence at location A and location B shows that the landslide might have occurred when 5-day antecedent rainfall is higher than the cumulative rainfall. Therefore, these two parameters are suggested to be used as a threshold in detecting possible landslide occurrence. Apart from that, this method can be considered as a low-cost approach that can be applied in determining landslide occurrence, as only one environmental factor should be considered, which is rainfall. For further study on the landslide threshold value, it is suggested to consider factor from the slope itself, such as slope displacement, where it can be monitored by installing strain gauges or inclinometers in the studied slope.

References

1. Lee, C.F.: Rainfall-induced landslide stability analysis. Sci. China Ser. E Technol. Sci. **46**, 52–68 (2003)
2. De Luca, D.L., Versace, P.: A general formulation to describe empirical rainfall thresholds for landslides. Procedia Earth Planet. Sci. **16**, 98–107 (2016)
3. Kim, J., Jeong, S., Park, S., Sharma, J.: Influence of rainfall-induced wetting on the stability of slopes in weathered soils. Eng. Geol. **75**(3–4), 251–262 (2004)
4. Kim, Y., Jeong, S., Lee, K.: Instability analysis of rainfall-induced landslides using hydro-mechanically coupled model. Japanese Geotech. Soc. Spec. Publ. **2**(27), 1002–1007 (2016)
5. Friedel, S., Thielen, A., Springman, S. M.: Investigation of a slope endangered by rainfall-induced landslides using 3D resistivity tomography and geotechnical testing. J. Appl. Geophys. **60**(2), 100–114 (2006)
6. Conte, E., Donato, A., Troncone, A.: A simplified method for predicting rainfall-induced mobility of active landslides. Landslides **14**(1), 35–45 (2017)
7. Zhang, J., Huang, H.W., Zhang, L.M., Zhu, H.H., Shi, B.: Probabilistic prediction of rainfall-induced slope failure using a mechanics-based model. Eng. Geol. **168**, 129–140 (2014)

8. Hossain, M.K.: Effect of rainfall on matric suction and stability of a residual granite soil slope. J. Dhaka Univ. Eng. Technol. **1**(1) (2010)
9. Kristo, C., Rahardjo, H., Satyanaga, A.: Effect of variations in rainfall intensity on slope stability in Singapore. Int. Soil Water Conserv. Res. **5**(4), 258–264 (2017)
10. Zêzere, J.L., Vaz, T., Pereira, S., Oliveira, S.C., Marques, R., Garcia, R.A.C.: Rainfall thresholds for landslide activity in Portugal: a state of the art. Environ. Earth Sci. **73**(6), 2917–2936 (2015)
11. He, S., Wang, J., Liu, S.: Rainfall event-duration thresholds for landslide occurrences in China. Water (Switzerland) **12**(2) (2020)
12. Guzzetti, F., Peruccacci, S., Rossi, M., Stark, C.P.: Rainfall thresholds for the initiation of landslides in central and southern Europe. Meteorol. Atmos. Phys. **98**(3–4), 239–267 (2007)
13. Chikalamo, E.E., Mavrouli, O.C., Ettema, J., van Westen, C.J., Muntohar, A.S., Mustofa, A.: Satellite-derived rainfall thresholds for landslide early warning in Bogowonto Catchment, Central Java, Indonesia. Int. J. Appl. Earth Obs. Geoinf. **89**, 102093 (2020)
14. Peruccacci, S., Brunetti, M.T., Gariano, S.L., Melillo, M., Rossi, M., Guzzetti, F.: Rainfall thresholds for possible landslide occurrence in Italy. Geomorphology **290**(March), 39–57 (2017)
15. Mukhlisin, M., Matlan, S.J., Ahlan, M.J., Taha, M.R.: Analysis of rainfall effect to slope stability in Ulu Klang, Malaysia. J. Teknol. **72**(3), 15–21 (2015)
16. Rahardjo, H., Li, X.W., Toll, D.G., Leong, E.C.: The effect of antecedent rainfall on slope stability. Geotech. Geol. Eng. **19**(3–4), 371–399 (2001)
17. Wieczorek, G., Snyder, J.: Monitoring slope movements. Geololgical Monit. **11**, 245–271 (2009)
18. Wang, Y., Tian, J., Gao, Y.: Stability analysis and case study of rainfall and disturbance on loess slope. In: Proceedings of 2016 International Conference Smart City System Engineering ICSCSE 2016, pp. 64–67 (2017)
19. Gian, Q.A., Tran, D.T., Nguyen, D.C., Nhu, V.H., Tien Bui, D.: Design and implementation of site-specific rainfall-induced landslide early warning and monitoring system: a case study at Nam Dan landslide (Vietnam). Geomatics Nat. Hazards Risk **8**(2), 1978–1996 (2017)
20. Hazwani, N.K., et al.: Integration of multi-sensors data in detecting slope movement based on threshold values. ARPN J. Eng. Appl. Sci. **11**(4), 2592–2596 (2016)
21. Din, N., Omar, R.C., Ismail, A., Hazwani, N., Khalid, N., Sakai, N.: AWAM International Conference on Civil Engineering & Geohazard Information Zonation Early Warning System for Transmission Tower Landslide Hazard Monitoring in Malaysia, vol. 2, no. January (2013)
22. Naidu, S., Sajinkumar, K.S., Oommen, T., Anuja, V.J., Samuel, R.A., Muraleedharan, C.: Early warning system for shallow landslides using rainfall threshold and slope stability analysis. Geosci. Front. (2017)
23. Rahimi, A., Rahardjo, H., Leong, E.C.: Effect of hydraulic properties of soil on rainfall-induced slope failure. Eng. Geol. **114**(3–4), 135–143 (2010)

Geotechnical Engineering

Assessment of Site Amplification Using Borehole and Surface Data: Variability of Site Effect Estimation from Different Phases of the Accelerogram

Parveen Kumar, Sandeep, and Monika

1 Introduction

Earthquakes cause various damaging effects in the regions of its occurrence. It involves damage to buildings along with the loss of human life. The earthquakes usually lead to the shaking of earth, which results destruction of structures such as buildings, bridges and dams. Seismic waves originate from the source of the earthquakes and propagate in all directions. These waves reach the surface after passage through the subsurface medium between source and recording site. The travelling medium of these seismic waves in uppermost crust influences the characteristics of these waves, especially in view of earthquake ground motion at the surface. In general, thicker layer of loose sediments, soft soil or unconsolidated deposits may amplify the amplitude of seismic wave at particular frequencies. This phenomena is known as site effects or site amplification [1–3]. In past and recent earthquakes, it has been observed that the local site effects play an important role in damage distribution [4–6]. Hence, the estimation of site effect is very significant term used for the assessment of the seismic hazard of a region.

In the present work, strong motion data of local earthquake occurred in Central Honshu region, Japan are utilized to estimate site amplification in this region. The Central Honshu region comprises arc juncture of east Japan and the west Japan arc system and, hence, having significance for seismological point of view. The horizontal to vertical spectral ratio method proposed by [7] is employed to estimate site effect of present study region. The strong motion data provided by KiK-net is utilized to compute the result. As site amplification is one of the input used to

P. Kumar (✉) · Monika
Wadia Institute of Himalayan Geology, Dehradun, India

Sandeep
Banaras Hindu University, Varanasi, Uttar Pradesh, India

construct the earthquake resistance structure, and hence, present work has great significance towards the seismic hazard evaluation of the Honshu region, Japan.

2 Study Area and Data Used

The present study region is Honshu region, Japan. Honshu region is originated by tectonic activity of rifting and back-arc spreading of Japan Sea, and it is the largest island of Japan. The arc to arc juncture of the East Japan and the West Japan arc systems includes the Central Honshu region [8, 9].

The main tectonic features of the study area are the Itoigawa-Shizuoka Tectonic Line (ISTL) and the Median Tectonic Line (MTL). The ISTL is a main tectonic feature that splits the Honshu Island into two parts, i.e. NE and SW parts [12, 13]. ISTL is a major geological boundary between the Eurasian Plate and the North American Plate. The MTL is one of the Japan's longest fault system. It joins with ISTL and Fossa Magna region and belongs to major transverse zone of Miocene tectonic depression, which cut the central highland of Honshu Island as a triple juncture of the northeast Japan (NEJ) arc, Izu-Bonin arc, and the southwest Japan (SWJ) arc [14, 15].

The strong motion data of 26 events occurred in Cental Honshu region during the years 2008 to 2017 is utilized in this work. The surface and borehole data of 26 earthquakes recorded at 13 stations are used to estimate site amplification in the present study region. The KiK-net is a strong-motion seismograph network, consisting borehole and surface data of an earthquake so the data of KiK-net is adopted to find out the site effect of the area. Each station has digital strong motion seismograph with a wide frequency band and wide dynamic range. The sampling frequency of the data used in this work is 100 Hz. The KiK-net station used in this work have two accelerographs at each station, one of them is installed at surface and other in borehole at hard rock. The earthquakes are selected on the basis of azimuthal coverage and epicentral distance. The location of earthquakes and recording stations is shown in Fig. 1. The depth of borehole acceleration varies from 100 to 247 m. The earthquake magnitude ranges 2.5–5.6 (M_w), and the focal depth 4–14 km is used for the work. The hypocentral parameters of earthquakes and geographical location of recording stations are reported in Tables 1 and 2, respectively.

3 Methodology

In this work, horizontal to vertical spectral ratio (H/V) method is used to compute the site amplification. The H/V technique was developed by Nagoshi and Igarashi [16], wide spread by Nakamura [3, 15, 17]. The spectral ratio technique is a common useful way to estimate site effects in regions of moderate to high
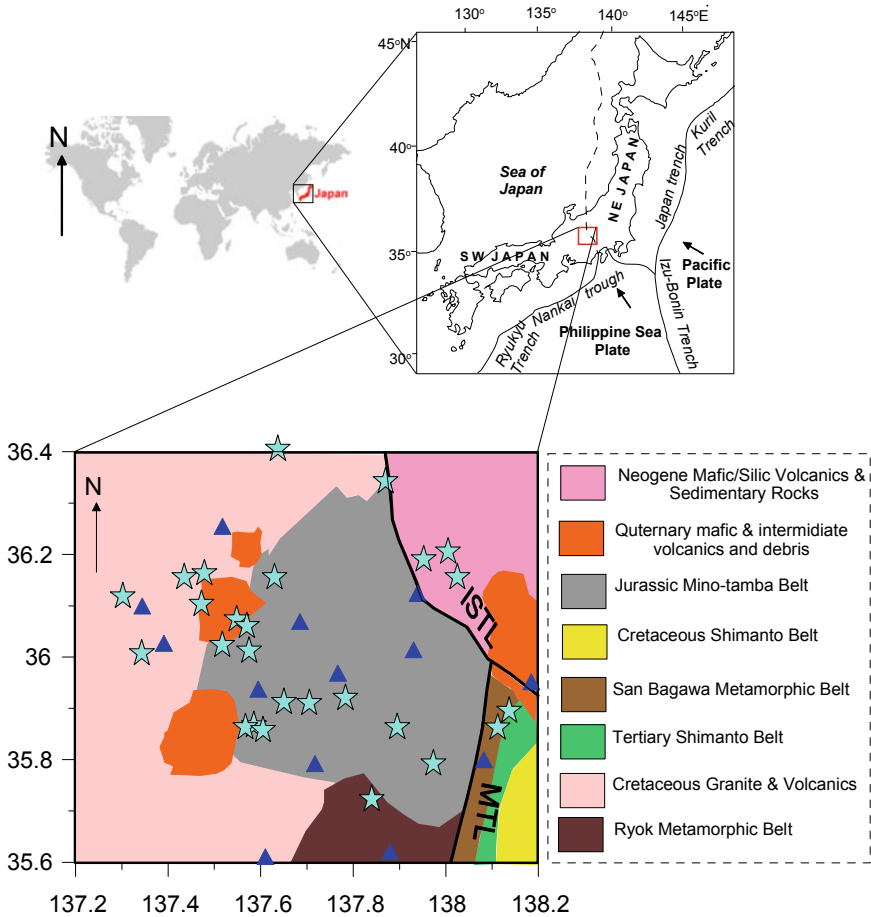
Fig. 1 Study area along with the location of recording stations and earthquakes used in present work. The triangles represent location of recording stations and stars denote the epicentre of the earthquakes. The geology and tectonic is taken after [10, 11]. The ISTL and MTL stand for Itoigawa-Shizuoka Tectonic Line and Median Tectonic Line, respectively

seismicity with respect to the reference station. The [7] modified the H/V technique to estimate the site effects using spectral ratios between horizontal and vertical components without a reference station. The H/V method modified by [7] is used to compute site amplification at each individual station. The spectrum is estimated for North–South (NS), East–West (EW) and vertical (Z) component separately, and Fourier amplitude spectrum of horizontal component is divided by the spectrum of the vertical component. The horizontal spectrum is computed by square root of the sum of square of NS and EW components. Then the H/V spectral ratios are calculated by:

Table 1 Hypocentral parameters of the earthquakes used in present work

Sr. No.	Date dd/mm/yyyy	Origin time HH:MM:SS	Lat (Degree)	Long (Degree)	Depth (km)	Magnitude (M_w)
1	07/02/2015	12:36:00	35.86	137.89	8	3.6
2	04/08/2015	05:13:00	35.86	138.11	7	3.7
3	29/11/2015	03:44:00	36.07	137.54	7	2.8
4	17/01/2016	08:54:00	36.15	137.63	6	3.3
5	03/02/2016	21:28:00	36.40	137.63	5	4.4
6	30/04/2016	01:37:00	36.34	137.87	8	3.3
7	29/10/2016	05:59:00	36.02	137.51	7	2.7
8	03/12/2016	08:29:00	35.91	137.65	6	2.6
9	06/12/2016	09:05:00	36.00	137.34	5	4.5
10	17/03/2017	15:03:00	36.06	137.57	8	3.2
11	08/04/2017	16:50:00	35.89	138.13	5	3.5
12	07/05/2017	12:32:00	36.15	138.02	9	3.8
13	19/06/2017	18:13:00	36.01	137.57	5	2.9
14	25/06/2017	07:02:00	35.86	137.58	7	5.6
15	25/06/2017	09:24:00	35.86	137.56	6	4.5
16	09/07/2017	06:22:00	35.85	137.60	6	2.5
17	10/08/2017	09:39:00	35.91	137.70	6	3.5
18	12/05/2008	11:47:00	35.79	137.97	10	4.0
19	28/02/2011	11:32:00	36.16	137.47	5	3.6
20	06/06/2011	19:24:00	36.10	137.47	8	4.1
21	18/06/2011	04:48:00	36.15	137.43	7	3.8
22	29/06/2011	19:32:00	36.19	137.95	4	3.4
23	08/10/2011	23:29:00	35.72	137.84	14	3.8
24	09/12/2011	15:54:00	36.11	137.30	12	3.0
25	30/07/2013	13:02:00	36.20	138.00	6	3.4
26	06/02/2011	07:25:00	35.92	137.78	11	3.7

$$R = \frac{\sqrt{F_{NS}^2 + F_{EW}^2}}{F_{UD}} \quad (1)$$

where 'R' is the H/V spectral ratio and F_{NS}, F_{EW} and F_{UD} are the Fourier spectrum of North–South, East–West and Vertical components, respectively. The H/V ratio is smoothed to 5% of the number of data point with a Gaussian window [18]. The site amplification is computed by using the different phases of the record, i.e. P-phase, S-phase and full wave form. The earthquakes employed in this work have occurred at different locations, and hence, all these records have different total duration. Therefore, a fixed window length of 1.28 s, 5.12 s and 40.96 s is considered for P-phase, S-phase and full wave form, respectively. It is taken care for selecting the window length of P-phase and S-phase that the maximum peak of the phases must

Table 2 Geographical location of recording stations

Sr. No.	Station name	Station code	Lat (Degree)	Long (Degree)	Depth (m)	Event used*
1	TSUKECHI	GIFH14	36.25	137.56	–	5, 6, 20, 21, 24
2	HICHISO	GIFH16	36.10	137.34	–	7, 9, 10, 19, 20, 21, 24
3	ENA	GIFH19	36.02	137.40	–	7, 9, 10, 13, 19, 20, 21, 24
4	KISO	NGNH10	35.96	137.76	104	1, 14, 17, 18, 19, 20, 22, 23, 25, 26
5	TATSUNO	NGNH15	36.01	137.93	100	11, 12, 15, 17, 18
6	CHINO	NGNH16	35.95	138.18	247	1, 2, 11, 13, 17, 18, 22, 25, 26
7	KAIDA	NGNH18	35.93	137.59	100	3, 4, 6, 7, 8, 17, 19, 20, 21
8	AGEMATSU	NGNH20	35.79	137.72	100	1, 16, 17, 18, 23, 26
9	HASE	NGNH22	35.79	138.08	100	1, 2, 11, 18, 23, 26
10	NAGISO	NGNH23	35.60	137.61	102	1, 14, 17, 23, 26
11	MATSUKAWA	NGNH24	35.62	137.88	107	1, 17, 18, 23, 26
12	NAGAWA	NGNH30	36.06	137.68	101	3, 4, 7, 17, 20, 26
13	SHIOJIRI	NGNH31	36.12	137.94	218	2, 4, 6, 11, 22, 25

*Event number is based on Table 1

be included in the selected window. To maintain the consistency of constant time window for full wave form, those records are excluded, which either too short or too large than 40.96 s window. These constant window are cosine tapered with 10% taper at both ends [19]. Number of events are considered at a single station to get better estimation of final site amplification [4, 20–25]. At particular station, each recording event is utilized to compute the H/V curve, and these individual curve is further used to attain average H/V curve at that specific station. The average H/V ratio provides the final site amplification, and the procedure to attain the site amplification at CHINO station is exemplified in Fig. 2. Figure 2 presents all the H/V curve computed from each and every event recorded at CHINO station, and an average curve is estimated from these individual curves, which yield the site amplification. Similar practice is carried out to estimate site amplification at remaining twelve stations.

4 Results and Discussion

In the present work, P-phase, S-phase and full waveform of acceleration record are used to estimate site amplification by using H/V method. The site amplifications are computed at thirteen different stations installed in the Honshu region. The spectra procured from the fast Fourier transform (FFT) of the earthquake record are applied
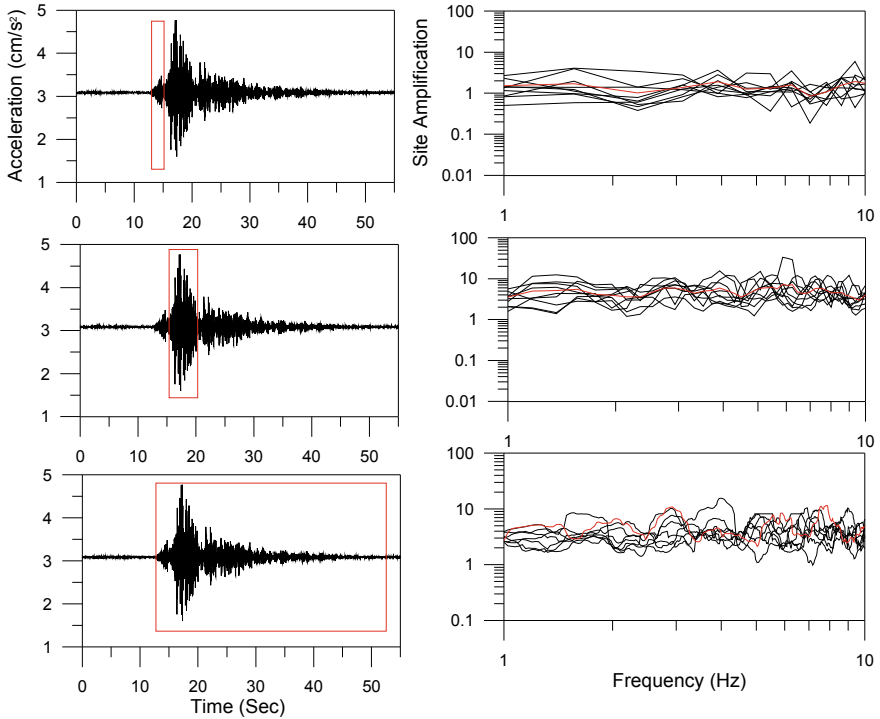
Fig. 2 a P-phase, S-phase and full waveform of the records are used to obtain **b** H/V curves corresponds to different phases. The red colour box in **a** indicates the window used for different phases. The black line in **b** represents the H/V curve for each individual earthquake record and red line represents the average H/V curve

to enumerate the H/V curve by taking the ratio of horizontal and vertical component of the spectra. The borehole and surface data is utilized to estimate the site amplification at each station of P-phase, S-phase and full wave form. Each station consisting different number of events as upon the availability of the data. The final site amplification is estimated by averaging all the H/V curve computed from individual earthquake record. Different recording station provides different site amplification depending upon the local site condition of the recording stations.

Site Amplification Using Surface and Borehole Data

In the present work, both the surface and borehole data is used at each recording site to verify the presence of site amplification at the surface. The comparison is made between the site amplification curve obtained using the surface data and borehole data. The average H/V curve of P-phase, S-phase and full waveform for both the surface and borehole data is plotted in Figs. 3, 4 and 5. The h/v curve of different phases for the borehole data is almost flat, which disclosed that borehole station lies on the hard rock. Figure 3 represents the average h/v curve of P-phase for surface

Fig. 3 Site amplification of P-phase at different recording stations using surface and borehole data. The red line and blue line represent the average H/V curve obtained using the surface data and the borehole data, respectively. The triangle symbol indicates the location of recording stations

and borehole data. It is observed from Fig. 3 that almost similar amplitude is obtained for both surface and borehole data, which depict that P-phase has less site amplification. Figures 4 and 5 represent the average h/v curve of S-phase and full waveform for surface and borehole data, respectively. The large amplitude is observed at the surface for S-phase and full waveform as compared to borehole. It may be due to the reason of accelerometer installed in the borehole is placed at the hard rock as compare to the surface accelerometer.

Site Amplification Using Different Phases of the Seismogram

A numerical experiment is made to check the effect of site amplification on the different phases of the record. In this experiment, site amplification is computed at different station using the different phases of the seismogram, i.e. P-phase, S-phase and full waveform. The average h/v curve of P-phase, S-phase and full waveform
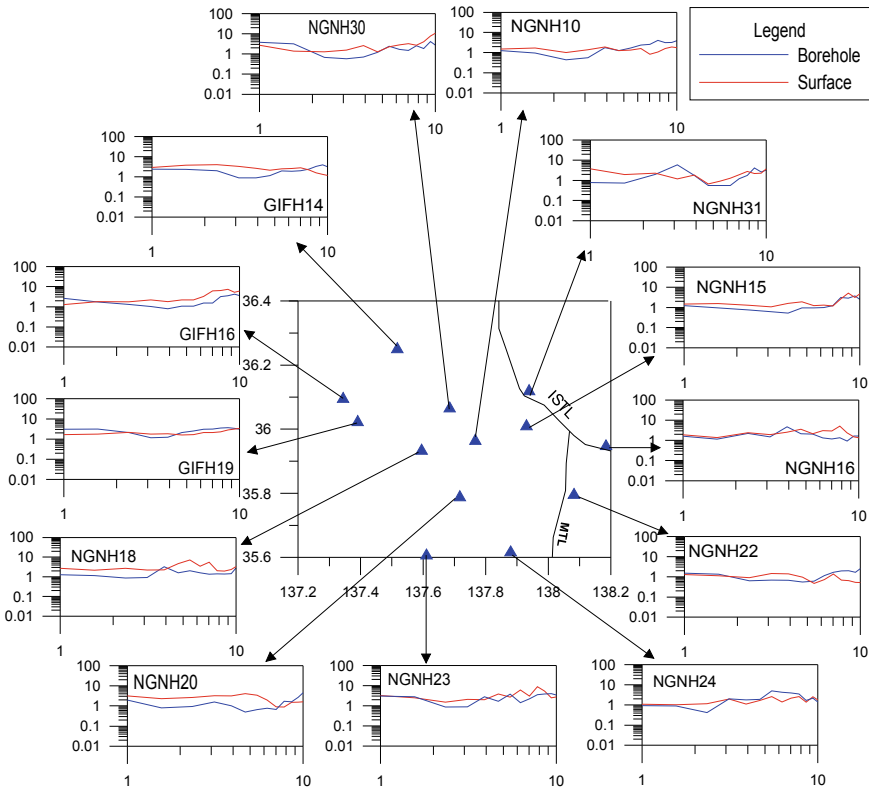
Fig. 4 Site amplification of S-phase at different recording stations using surface and borehole data. The red line and blue line represent the average H/V curve obtained using the surface data and the borehole data, respectively. The triangle symbol indicates the location of recording stations

obtained using the borehole data is plotted in Fig. 6. It is observed that the h/v curve of S-phase has large amplitude as compare to P-phase, which revealed that S-phase is more amplified as compare to P-phase. Similar observation is noted in Fig. 7, where average h/v curve of P-phase and S-phase is plotted by using the surface data. Hence, it is concluded that S-phase is more amplified as compare to P-phase. Now, in next attempt, comparison of full waveform with the P-phase and S-phase is made and shown in Figs. 6 and 7 for borehole and surface data, respectively. Figures 6 and 7 revealed that h/v curve of S-phase and full waveform has large amplitude than h/v curve of P-phase. Hence, it is interpreted that site amplification plays important role for the S-phase, whereas very less site amplification is observed for P-phase. It also noticed that the h/v curve obtained using the S-phase and full waveform have almost similar amplitude, and hence, it is concluded that
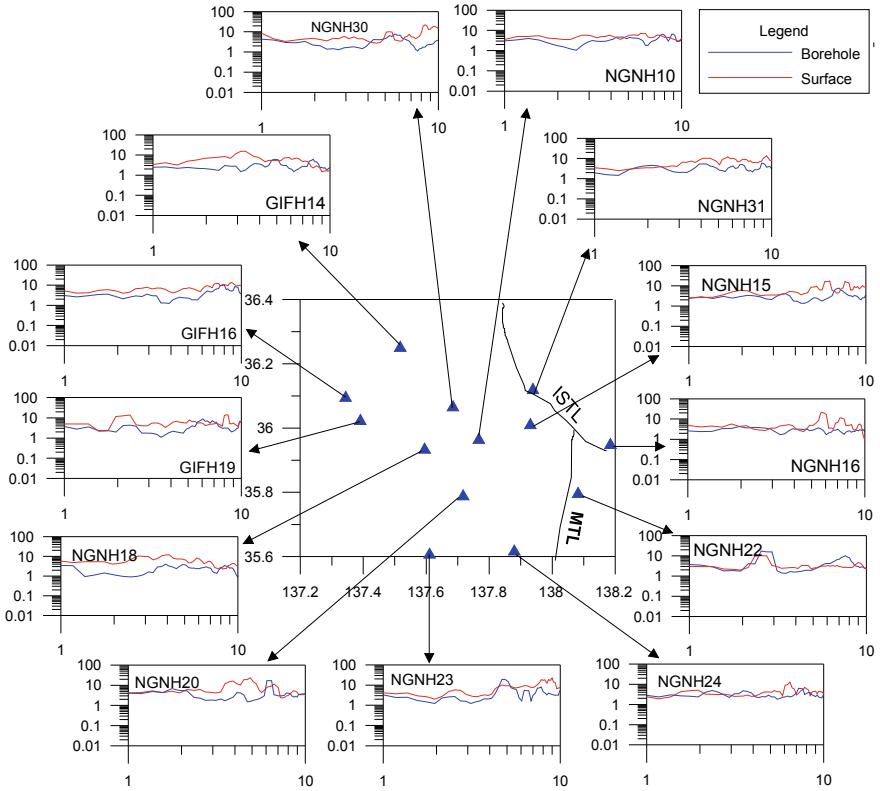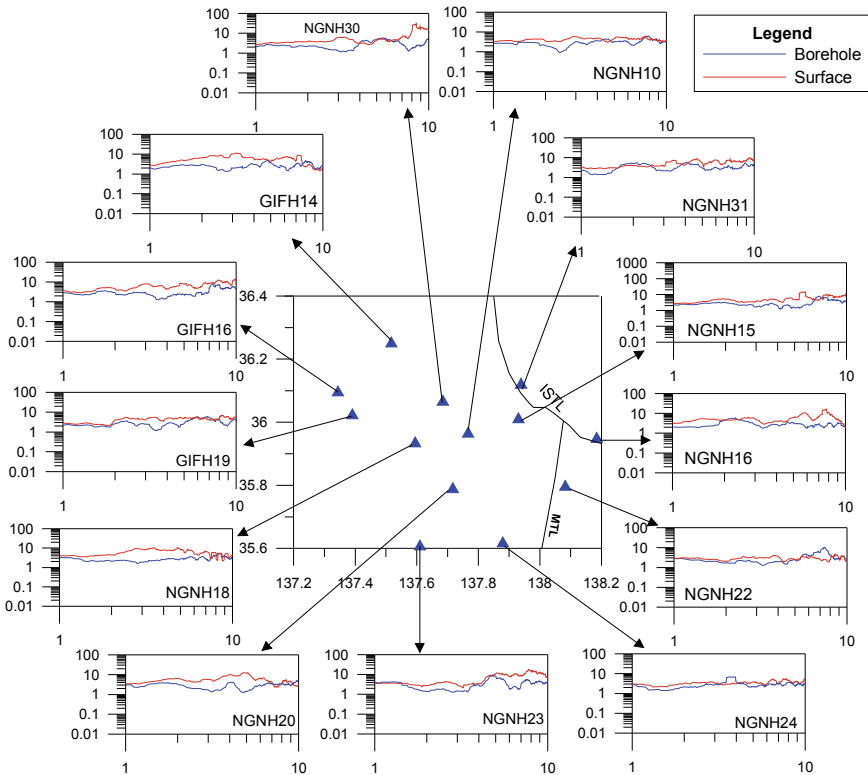
Fig. 5 Site amplification of full waveform at different recording stations using surface and borehole data. The red line and blue line represent the average H/V curve obtained using the surface data and the borehole data, respectively. The triangle denotes the location of recording stations

S-phase has major contribution towards the site amplification of an earthquake record as compare to P-phase.

Correlation of Site Amplification with the Local Site Conditions

The site amplification obtained at different recording stations is compared with the local geology of the region. At each recording site, P-wave and S-wave velocity is provided by the KiK-net. The site amplification obtained by using the P-phase and S-phase with the distribution of P-wave and S-wave velocity of study region is plotted in Figs. 8 and 9, respectively. A close resemblance is observed between the velocity and site amplification. The stations, which lies comparatively in low velocities zone has large h/v amplitude whereas stations consisting high velocity
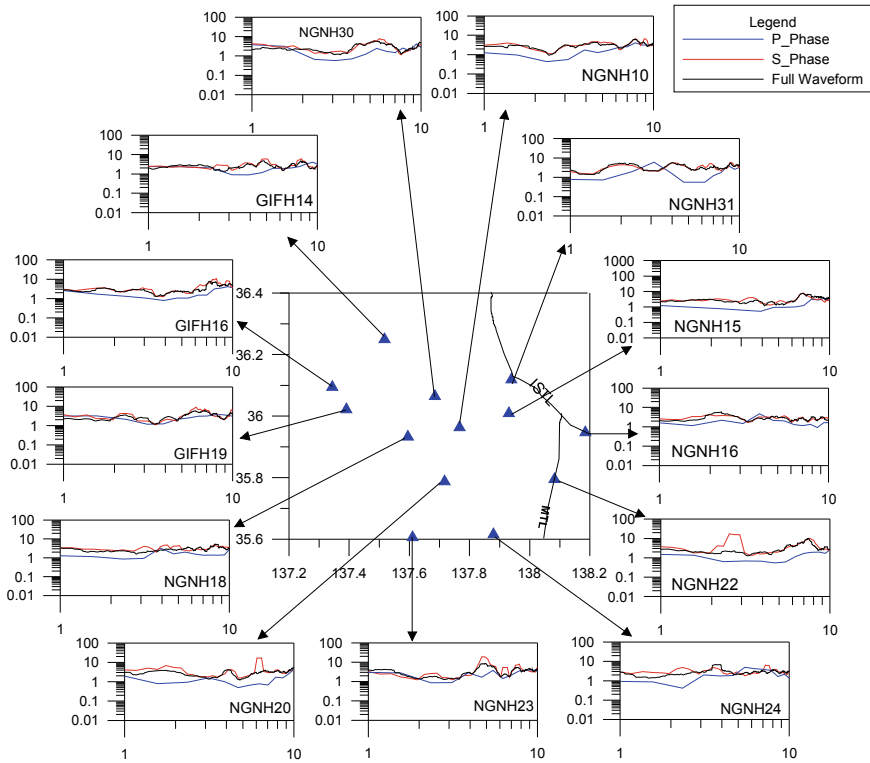
Fig. 6 Site amplification of P-phase, S-phase and full waveform at different stations using borehole data. The red, blue and black line represent the average H/V curve obtained using the S-phase, P-phase and full waveform, respectively. The triangle denotes the location of recording stations

has low h/v amplitude. In general, thicker layers of loss soil, unconsolidated deposits have low velocity, which tend to amplify the record, and it is depicted by Figs. 8 and 9. It is interpreted that stations lie on low velocity zone, i.e. NGNH16, NGNH18 and NGNH20 have more site amplification as compared to other stations named as GIFH14, GIFH16, GIFH19, NGNH10, NGNH15, NGNH22, NGNH23, NGNH24, NGNH30 and NGNH31. Hence, based on the obtained site amplification, it is concluded that the stations, i.e. NGNH16, NGNH18 and NGNH20 have high seismic hazard potential as compared to other stations.
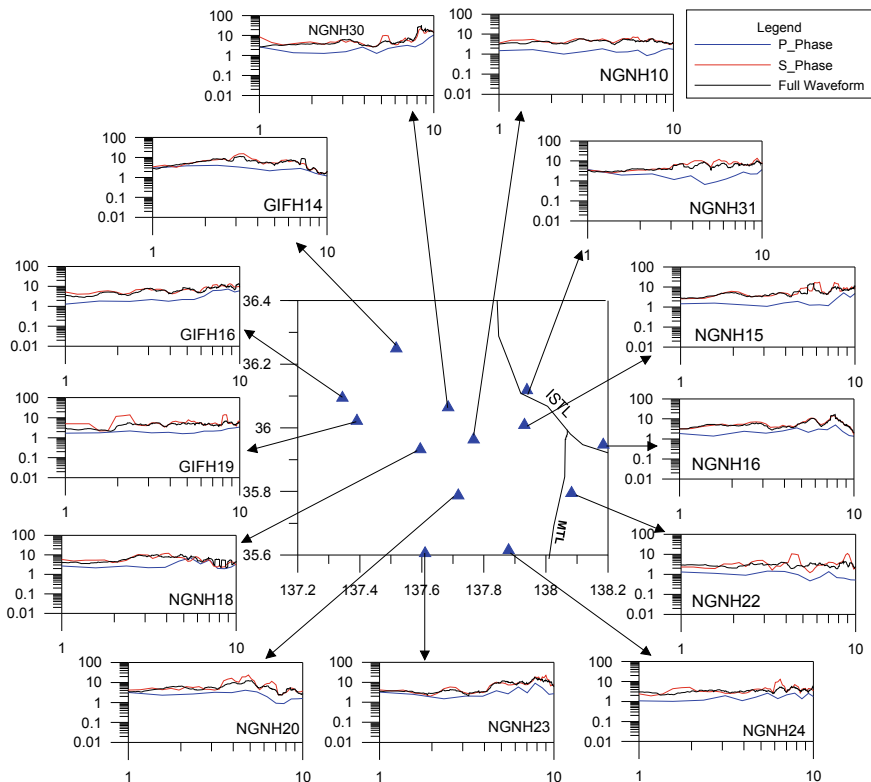
Fig. 7 Site amplification of P-phase, S-phase and full waveform at different stations using surface data. The red, blue and black line represent the average H/V curve obtained using the S-phase, P-phase and full waveform, respectively. The triangle denotes the location of recording stations

5   Conclusion

Site amplification is estimated by using the horizontal to vertical spectral ratio method for the central Honshu region, Japan. The surface and borehole acceleration data of 26 earthquakes recorded at 13 stations are used to estimate site amplification in the present study region in a rectangular grid defined by 35.6° N to 36.4° N and 137.2° E to 138.2° E. The study draws the following conclusions:
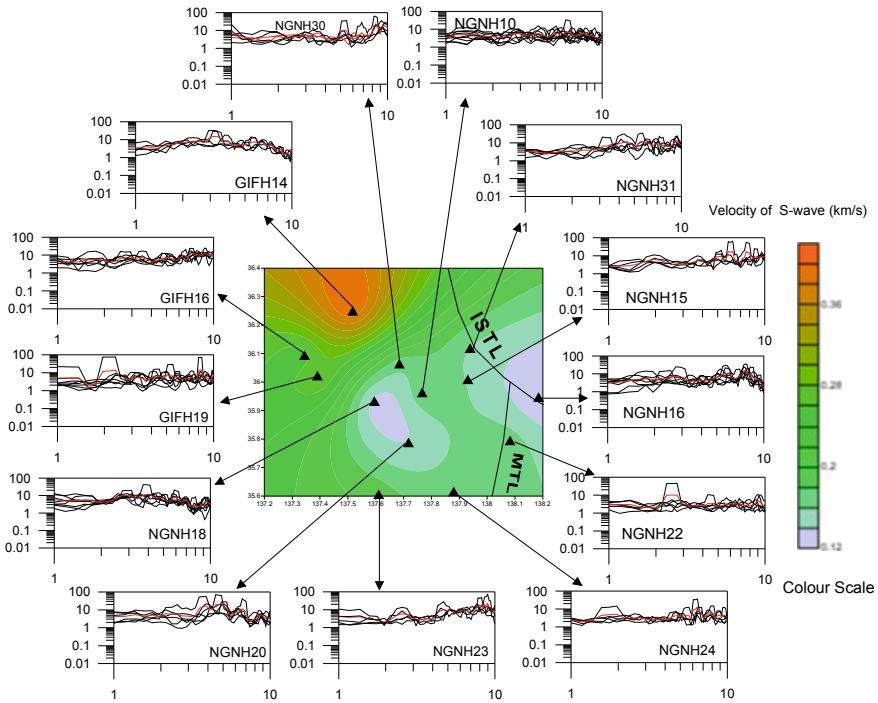
Fig. 8 Distribution of S-wave velocity with site amplification of S-phase obtained using surface data. The black line represents the H/V curve for each individual earthquake record, and red line represents the average H/V curve. The triangle symbol indicates the location of recording stations

- The large amplitude is observed at the surface as compared to borehole, which confirms the soft and unconsolidated deposits on the surface.
- As amplitude of h/v curve obtained using S-phase and full waveform is almost similar, whereas h/v curve of P-phase has low amplitude than h/v curve of S-phase and full waveform. Hence, it is concluded that S-phase has major contribution towards the site amplification as compare to P-phase.
- The stations, which lie on the low velocity zone, provide the large amplitude of site amplification. Hence, the close resemblance of the estimated site amplification with the velocity of the region validates the results of the present work.
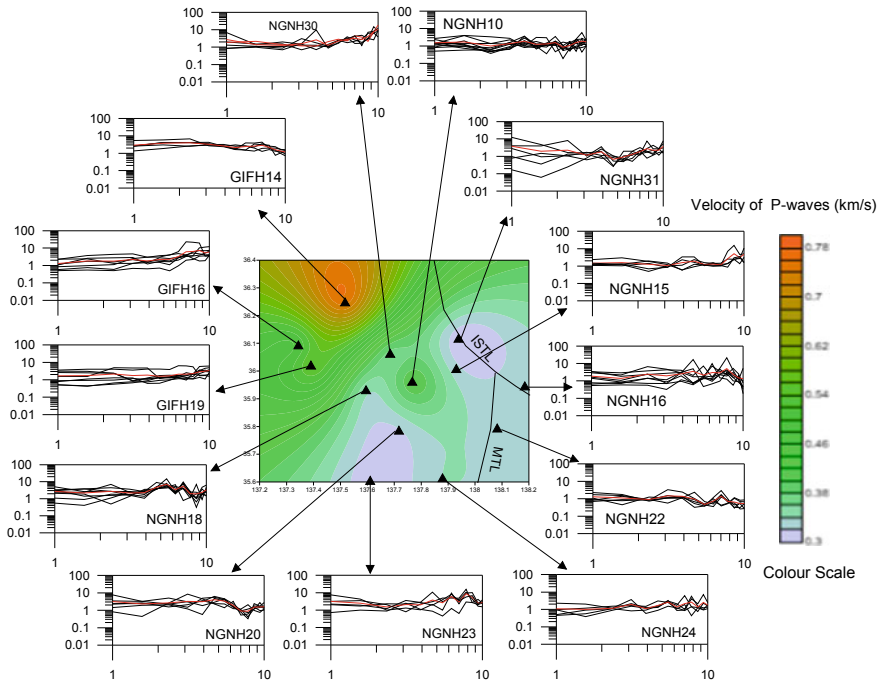
Fig. 9 Distribution of P-wave velocity with site amplification of P-phase obtained using surface data. The black line represents the H/V curve for each individual earthquake record, and red line represents the average H/V curve. The triangle denotes the location of recording stations

- High site amplification corresponds to large sediments thickness or having large basement depth therefore stations having high amplitude of h/v curve (NGNH16, NGNH18 and NGNH20) consist high seismic hazard potential as compare to remaining stations.

References

1. Kumar, P., Joshi, A., Kumar, S., Sandeep, Lal, S.: Determination of site effect and anelastic attenuation at Kathmandu, Nepal Himalaya region and its use in estimation of source parameters of 25 April 2015 Nepal earthquake Mw = 7.8 and its aftershocks including the 12 May 2015 Mw = 7.3 event. Nat. Hazards **91**, 1003–1023 (2018)

2. Kuo, C.H., Wen, K.L., Hsieh, H.H., Lin, C.M., Chang, T.M., Kuo, K.W.: Site classification and Vs30 estimation of free-field TSMIP stations using the logging data of EGDT. Eng. Geol. 129–130, 68–75 (2012)

3. Nakamura, Y.: A method for dynamic characteristics estimation of subsurface using microtremor on the ground surface. Quart. Rep. RTRI **30**(1), 25–33 (1989)

4. Kumari, R., Kumar, P., Kumar, N., Sandeep.: Role of site effect for the evaluation of Attenuation characteristics of P, S and coda waves in Kinnaur region, NW Himalaya. J. Earth Sys. Sci. **129**, 191, 1–18 (2020)

5. Luzon, F., Gil-Zepeda, S.A., Sanchez-Sesma, F.J., Ortiz-Aleman, C.: Three-dimensional simulation of ground motion in the Zafarraya Basin (Southern Spain) up to 1.335 Hz under incident plane waves. Geophys. J. Int. **156**(3), 584–594 (2004)

6. Narayan, J.P., Sharma, M.L., Kumar, A.: A seismological report on the 26 January 2001 Bhuj, India earthquake. Seismol. Res. Lett. **73**(3), 343–355 (2002)

7. Lermo, J., Chavez-Garcia, F.J.: Site effects evaluation using spectral ratios with only one station. Bull. Seism. Soc. Am. **83**, 1574–1594 (1993)

8. Kumar, P., Joshi, A., Verma, O.P.: Attenuation tomography based on strong motion data: case study of central Honshu region, Japan. Pure Appl. Geophys. **170**, 2087–2106 (2013)

9. Takeuchi, A.: Duplex stress regime in the North Fossa Magna, Central Japan. Bull. Earthq. Res. Inst. Univ. Tokyo. **83**, 155–162 (2008)

10. Fergusson, C.: Provenance of Miocene–Pleistocene Turbidite Sands and Sandstones, Nankai Trough, Ocean Drilling Program Leg 190. In: Mikada, H., Moore, G.F., Taira, A., Becker, K., Moore, J.C., Klaus, A. (eds.) Proceedings of the Ocean Drilling Program, Scientific Results Volume 190/196 (2003)

11. Ishibashi, K.: Status of historical seismology in Japan. Ann. Geophys. **47**, 2–3 (2004)

12. Kato, H.: Fossa Magna-A masked border region separating southwest and northeast Japan. Bull. Geol. Sur. Jpn. **43**, 1–30 (1992)

13. Yabe, H.: Itoigawa-Shizuoka Tectonic Line. Gendai-no-Kagaku **6**, 147–150 (1918)

14. Kobayashi, Y.: Incipient subduction of a lithospheric plate under the eastern margin of the Japan Sea. Earth Mon. **5**, 510–514 (1983)

15. Nakamura, K.: Possible nascent trench along the eastern Japan Sea as the convergent boundary between Eurasian and North American plates. Bull. Earthq. Res. Inst. Univ. Tokyo **58**, 711–722 (1983)

16. Nogoshi, M., Igarashi, T.: On the amplitude characteristics of microtremor-part 2. J. Seism. Soc. Japan **24**, 26–40 (1971)

17. Nakamura, Y.: Clear identification of fundamental idea of Nakamura's technique and its applications. In: 12th World Conference on Earthquake Engineering, p. 2656 (2000)

18. Seekins, L.C., Wennerberg, L., Margheriti, L., Liu, H.P.: Site amplification at five locations in San Francisco, California: a comparison of S waves, codas, and microtremors. Bull. Seismol. Soc. Am. **86**(3), 627–635 (1996)

19. Sharma, M.L., Wason, H.R.: Occurrence of low stress drop earthquakes in the Garhwal Himalaya region. Phys. Earth Planet Interior **34**, 159–172 (1994)

20. Joshi, A., Kumar, P., Arora, S.: Use of site amplification, anelastic attenuation for determination of source parameters of the Sikkim earthquake of 18 September, 2011 using far field strong motion data. Nat. Hazards **70**, 217–235 (2014)

21. Joshi, A., Kumar, P., Mohanty, M., Bansal, A.R., Dimri, V.P., Chadha, R.K.: Determination of $Q_\beta(f)$ in different parts of Kumaon Himalaya from the inversion of spectral acceleration data. Pure Appl. Geophys. **169**, 1821–1845 (2012)

22. Kumar, N., Kumar, P., Chauhan, V., Hazarika, D.: Variable anelastic attenuation and site effect in estimating source parameters of various major earthquakes including Mw 7.8 Nepal and Mw 7.5 Hindu kush earthquake by using far field strong motion data. Int. J. Earth Sci. **106**, 2371–2386 (2017)

23. Kumar, P., Devi, S., Monika, Srivastava, A., Sandeep, Joshi, A., Kumari, R.: Site response study based on H/V method using S-wave: a case study in the Kumaon Himalaya, India. Himalayan Geol. **40**(2), 213–219 (2019)

24. Kumar, P., Joshi, A., Sandeep, Kumar, A., Chadha, R.K.: Detailed attenuation characteristics of shear waves in Kumaon Himalaya, India using the inversion of strong motion data. Bull. Seism. Soc. Am. **105**(4), 1836–1851 (2015a)
25. Kumar, P., Joshi, A., Sandeep, Kumar, A.: Three-dimensional attenuation structure in the region of Kumaon Himalaya, India based on inversion of strong motion data. Pure Appl. Geophys. **172**(2), 333–358 (2015b)

Effects of Complex Valley Topography on De-amplification Scenerio for SH-Waves

Neeraj Kumar, Vinay Kumar, J. P. Narayan, Vishvendra Tiwari, and Sanjay Kumar

1 Introduction

A valley refers to the low-lying area between mountains. There are numerous valleys and ridges in the Himalayas. The irregular topography results in alteration of amplitude, frequency, and total duration of ground motion during an earthquake in comparison with the flat, free surface ground motion. The spatial amplification and de-amplification of ground motion depend upon various phenomena like focusing, de-focusing, scattering, reflection, and diffraction of seismic waves by irregular surface geometry. The recorded ground motion at the Pacoima Dam during the San Fernando earthquake in 1971 [1] and at the Tarzana hill during the Northridge earthquake in 1994 [2] has revealed the scenario of topographic amplification. The role of topography in devastation of structures was also reported during the Chile earthquake in 1985 [3], Superstition hill earthquake in 1987 [4], Whitter Narrows earthquake in 1987 [5], and Chamoli-India earthquake in 1999 [6]. Recently, thousands of the houses and old historical buildings were destroyed in Kathmandu valley during the Gorkha Nepal earthquake of 2015. The long period ground motion posed serious risk to even old monuments and residential buildings in the Nepal valley [7]. The recent studies have revealed that hills and valleys not only affect the characteristics of body waves, but they also affect the characteristics of surface waves and a string of ridges and valleys can act as an insulator for the Rayleigh waves [8].

N. Kumar (✉)
Central University of Haryana, Mahendergarh, India
e-mail: neerajlohchab@cuh.ac.in

V. Kumar
CCS Haryana Agriculture University, Hisar, India

J. P. Narayan · V. Tiwari · S. Kumar
Indian Institute of Technology Roorkee, Roorkee, India

The extensive literature review on the topography effects on the ground motion characteristics reveals that most of the researchers have numerically computed the (SH-, SV-, and P-waves) response of a single hill and valley for different shapes (triangular, U-shape, elliptical) and shape-ratios and reported that the amplification factor rarely exceed 2.5 in the frequency band of earthquake engineering interest [9–14]. Moreover, the topographic amplification factor exceeding 10 is also reported based on the spectral ratio of earthquake records on crest and base of the same hill [9, 15, 16]. Recently, Kumar et al. [17] studied the effects of complex ridge topography on the ground motion characteristics. But, very limited literature is available for complex valley topography effects, although most of the population of the hilly region resides in the valleys and call for a holistic study. In order to fulfill the research gap and infer the possible reasons for the failure in valleys, complex valley topography models have been considered. The SH-wave responses of the considered complex triangular valley models have been computed and analyzed in this paper. The rapid growth, increase in employment opportunities, and tourist influx from last few decades have resulted in the tremendous development and construction of structures in the environmentally fragile hill towns, which calls for the accurate prediction of effects of ridge and valley topography on the ground motion characteristics. A forth-order accurate SH-wave viscoelastic FD program has been used for the simulation of responses of the considered various models [18]. To avoid the numerical noise and reflections, improved vacuum formulation is applied as free surface boundary condition and the sponge-absorbing boundary condition is applied at model edges [19, 20].

2 Discretization of Complex Topography Models

In order to fulfill the aim of the paper, three triangular valley models namely TV1, TV3, and TV7 with one, three, and seven valleys are considered, as given in Table 1. The overall dimension of all the triangular valley models is same (depth = 1000 m and width as 2000 m). Although, the dimensions of the considered sub-valleys and ridges are hypothetical, there are various such valleys and ridges having similar dimension and slopes in the Himalayan region. Further, 51 receivers are placed, with R1 from left side to R51 toward right side along the valley profile at equal spacing of 40 m, as shown in Fig. 1. The considered rheological parameters for the homogeneous rock and air are given in Table 2. The size of models in the north–south direction is 6000 m and 5750 m in the vertical direction. The model is discretized into uniform grid size of 4 m in horizontal direction and 4 m up to depth of 300 m in vertical direction, and 10 m thereafter. A plane horizontal SH-wave front is generated in the FD numerical grid at 550 m depth from free surface, using various point sources along a line. A particular point source was generated using shear stress σ_{zy} in the form of Gabor wavelet having frequency bandwidth 0–15 Hz. The used Gabor wavelet as source time function has dominant frequency $fp = 5$ Hz, oscillatory parameter $\gamma = 1.5$, and phase $\phi = 0$.

Table 1 List of considered triangular valley topography models

Model name	Number of valleys	Number of ridges
TV1	1	0
TV3	3	2
TV7	7	6

Fig. 1 a–c Consider TV1, TV3 and TV7 triangular valley models
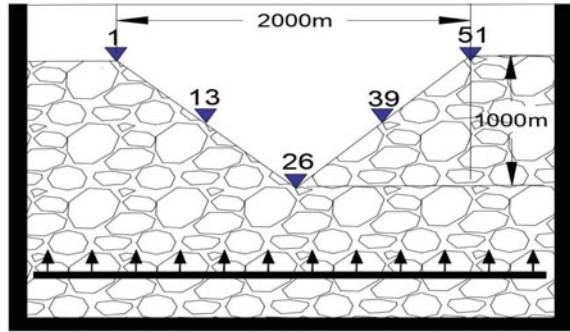
(a)
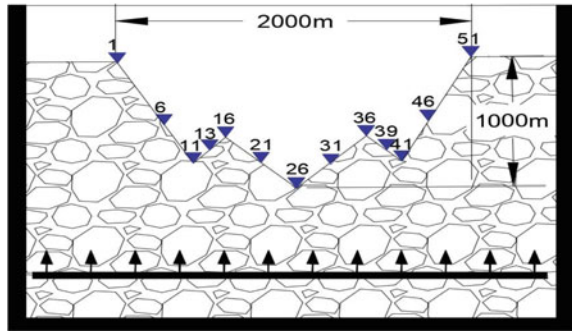
(b)
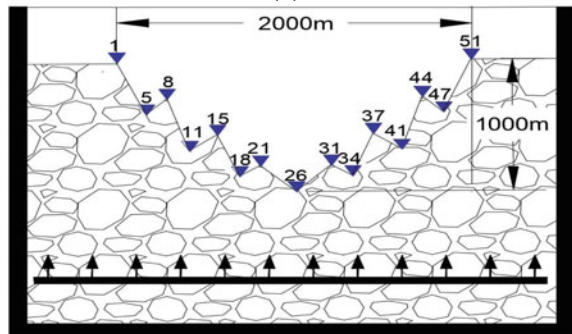
(c)

Table 2 Parameters for the homogeneous viscoelastic material

Material	Density (kg/m^3)	V_s (m/s)	Q_s
Air	200	0	∞
Rock	2000	1500	150

3 SH-Wave Response of TV1 Model

3.1 Time Domain Response

The SH-wave response of the TV1 valley model is shown in Fig. 2. The investigation shows the de-amplification of SH-wave at the trough of the valley compared to homogenous half-space model. Figure 2 shows that the amplitude of the SH-wave decreases toward the trough of the valley due to de-focusing of the SH-waves. The incident SH-wave and the diffracted SH-waves from the base-corners and trough of the valley are very clearly visible.

3.2 Snapshots of SH-Wave Field

To infer the behavior of SH-wave after interacting with the triangular valley, snapshots have been computed at different moments from 0.5 s to 2.25 s and shown in Fig. 3. The snapshot at time 0.5 s shows only the incident SH-wave in the considered area. The snapshot at time 0.75 s shows the incident SH-wave as well as the reflected SH-waves from the flanks of the triangular valley. The incident, diffracted wave from the trough of the valley and reflected waves from the flank of triangular valley are annotated in the snapshot at time 1.0 s. The snapshot at time 1.25 s clearly illustrates that the incident SH-waves are reaching at the base-corner of the valley. The phenomenon like de-focusing, diffraction, and mode conversion
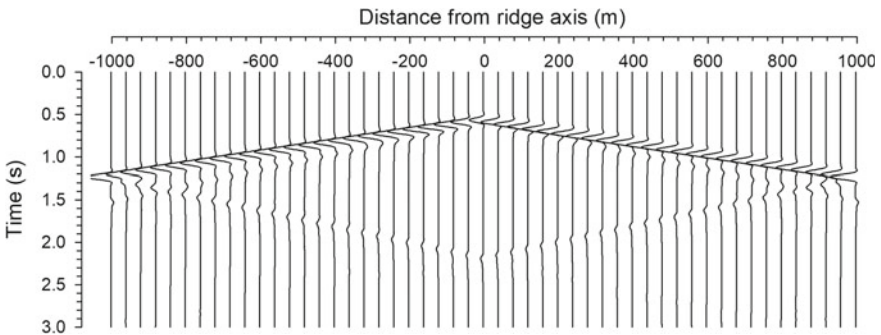
Fig. 2 SH-wave response of the TV1 valley model
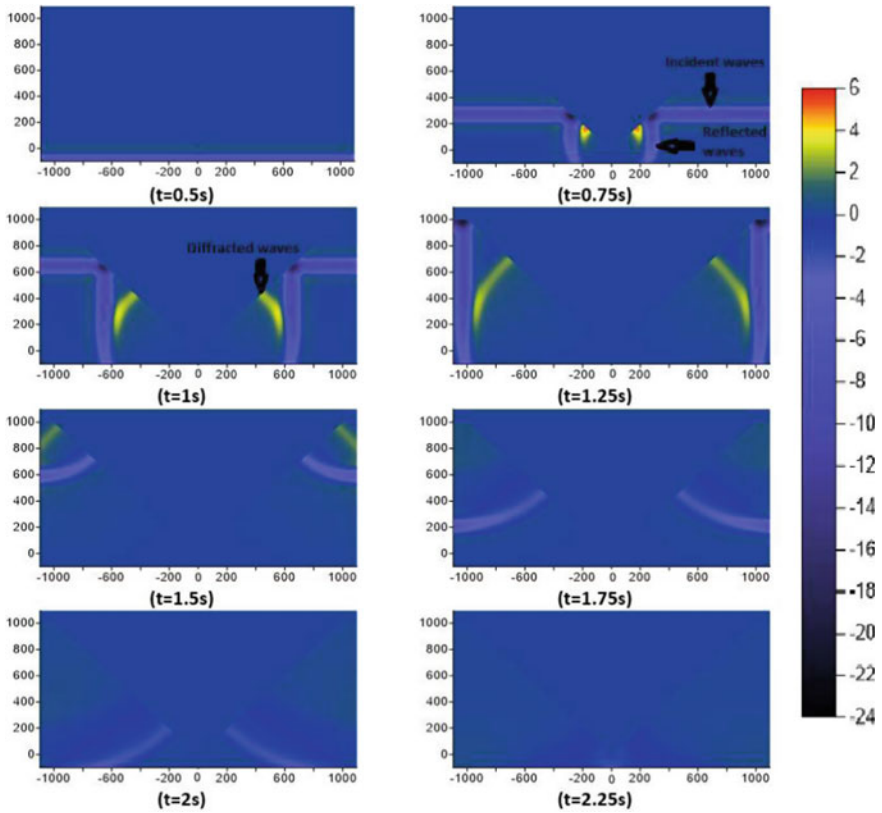
Fig. 3 Snapshots of SH-wave at different moments for TV1 valley model

Table 3 Triangular valley topography models with wedge angles and corresponding receiver positions (R26-R1)

TR models	Valley (T)	Ridge (C)	Valley (T)	Ridge (C)	Valley (T)	Ridge (C)	Valley (T)
TV1	3π/2 (at 26)	–	–	–	–	–	–
TV3	3π/2 (at 26)	22π/45 (at 16)	289π/180 (at 11)	–	–	–	–
TV7	3π/2 (at 26)	101π/180 (at 21)	283π/180 (at 18)	37π/90 (at 15)	29π/18 (at 11)	31π/90 (at 8)	293π/180 (at 5)

are the reason for de-amplification at the valley trough in the case of a symmetrical triangular valley. The reflected waves are the only phases present in the snapshot at time 2.0 s and 2.25 s (Fig. 3).

3.3 Spectral Amplifications

Figure 4 shows the spectral amplification factors (SAF) at R13 and R26 receiver points, which is obtained by dividing the spectral amplitude of the response of the TV1 model to that of half-space model at the corresponding location. The analytically obtained SAF for a wavelength corresponding to frequency 0.75 Hz is 0.67. An analysis of Table 4 reveals that the numerically obtained SAF at receiver R26 is 0.74 at frequency 0.75 Hz which is larger than that obtained analytically. Analytical value of amplification factor is found lesser than numerical value. This may be because of non-consideration of diffracted waves in the analytical solution. Further, the obtained average spectral amplifications (ASA) at the valley trough is also lesser than that at the flank of the ridge as clearly visible in Table 4. The spectral amplifications at the trough of valley with respect to the record at the top-corner of valley, as shown in Fig. 5, depicts that the SAF is 0.41 at frequency 2.4 Hz. This is much lesser than the same obtained using numerical/analytical one. This may be due to the diffracted waves which have amplified the ground motion at the top-corner of the valley. So, it may be the reason behind which makes the scientist to ignore the valley effects in earthquake engineering and only focused on the hill topography amplification.

Fig. 4 SAF at two locations for TV1 valley model

Table 4 Comparisons of SAF and ASA at different receiver points with the analytical one

Receivers	R13	R26
Largest SAF: numerical	1.05	0.74 at 0.75 Hz
ASA: numerical	0.76	0.70
SAF: analytical	–	0.67 at 0.75 Hz
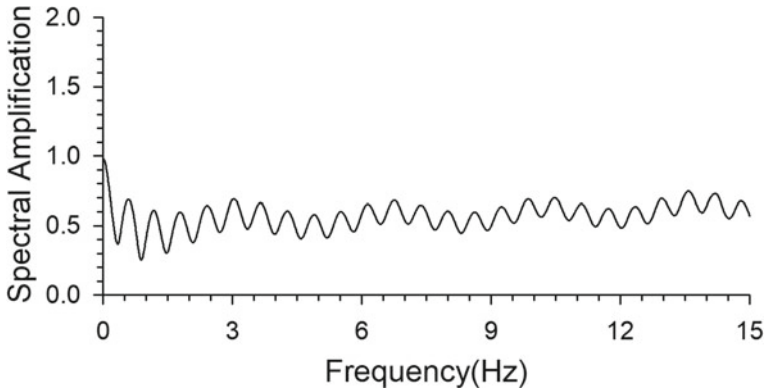
Fig. 5 Spectral amplification at the trough of TV1 valley wrt to the **record at the top-corner of the** valley

4 SH-Wave Response of TR3 Model

4.1 Time Domain Response

A topography model with three triangular valleys (TV3) is shown in Fig. 1b. The SH-wave response of the TV3 model is shown in Fig. 6. The investigation of this figure shows the amplification of SH-wave at the crest of sub-ridges due to focusing and de-amplification of the SH-wave at base of the valleys due to de-focusing of the SH-waves, respectively. The incident SH-wave and the diffracted waves from the top-corners of the valleys/base-corners of the ridges are very clearly visible. An increase of duration of ground motion in the case of complex valley topography as compared to the solo-topography can be inferred.

Fig. 6 SH-wave response of the TV3 complex valley model

4.2 Spectral Amplifications

Figure 7 shows the SAF at different recording points along the base of the TV3 valley model. An analysis of Table 5 reveals that the difference in the numerically obtained SAF and that obtained analytically increases with the increase of number of sub-valleys in the model. For example, the obtained least SAF at the base of central valley is 0.79 as to that obtained analytically (Table 5). Analytical value of amplification factor is found lesser than numerical value at the base of the first valley also. Further, at the crest of the sub-ridge, there is larger amplification (2.04) of ground motion as compared to the amplification obtained analytically (1.45). However, ASA at the crest of the ridge depicts even larger amplification of ground motion.

The obtained ASA is larger at the trough of the first valley then than of the central valley. Amplification factor for mid sub-valley is larger than that of adjacent sub-valleys even though it has more depth. It reveals that apex angle or shape ratio is major factor for governing the amplification factor. Amplification factor can be found small at lesser depth valley with large apex angle than more depth valley with less apex angle. Amplification factor for a valley is affected by its own shape features as well as features of surrounding neighboring valleys. The spectral
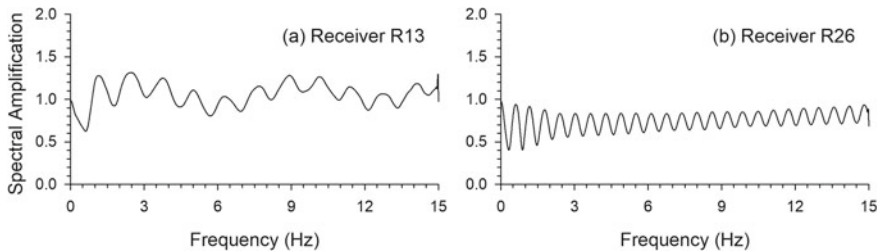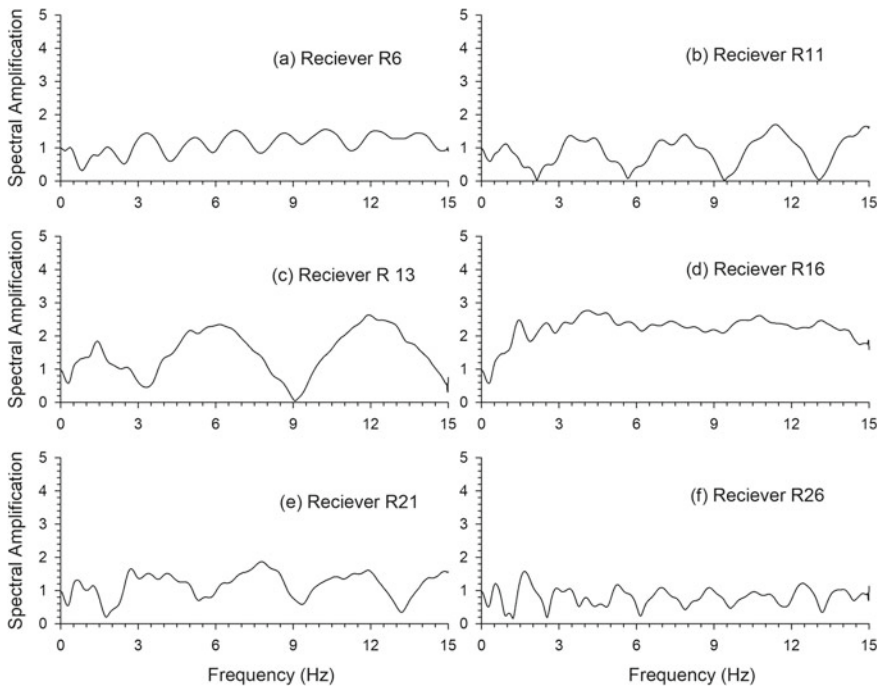

Fig. 7 SAF at six locations for TV3 complex valley model

Table 5 Comparison of SAF and ASA at different receiver points with the analytical one

Receivers	R6 (F)	R11 (T)	R13 (F)	R16 (C)	R21 (F)	R26 (T)
Largest SAF: numerical	0.35	1.00	1.30	1.45	1.25	0.79
ASA: numerical	1.12	0.88	1.48	2.21	1.17	0.80
SAF: analytical	–	0.62	–	2.04	–	0.67

Note The alphabets "F," "C," and "T" are used for "Flank," "Crest," and "Trough," respectively
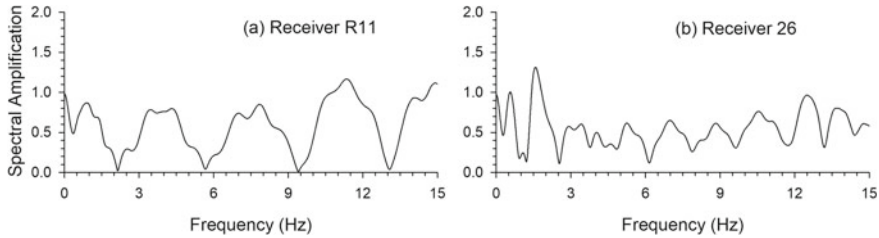
Fig. 8 Spectral amplification at trough of the TV3 complex valley wrt to the record at top-corner of the valley

amplifications at the trough of valley wrt the record at top-corner of the valley, as shown in Fig. 8, depict that the obtained negligible SAF at frequency 2.1 Hz at the trough of the first sub-valley. Similarly, the obtained lesser SAF is 0.1 at frequency 2.54 Hz at the trough of the central valley. Again, this is much lesser than the same obtained using numerical/analytical one.

5 SH-Wave Response of TV7 Model

5.1 Time Domain Response

A topography model with seven triangular valleys (TV7 model) is shown in Fig. 1c. The SH-wave response of the TV7 model is shown in Fig. 9. The investigation of this figure shows the amplification of SH-wave at the crest of sub-ridges and de-amplification of the SH-wave at trough of the sub-valleys as compared to the amplitude in the case of homogenous half-space model. The incident SH-wave and the diffracted waves from the base-corners of the ridges/top-corners of the valley are very clearly visible. Further, increase of duration of ground motion in the case of TV7 valley topography model as compared to the solo-topography model can be inferred.
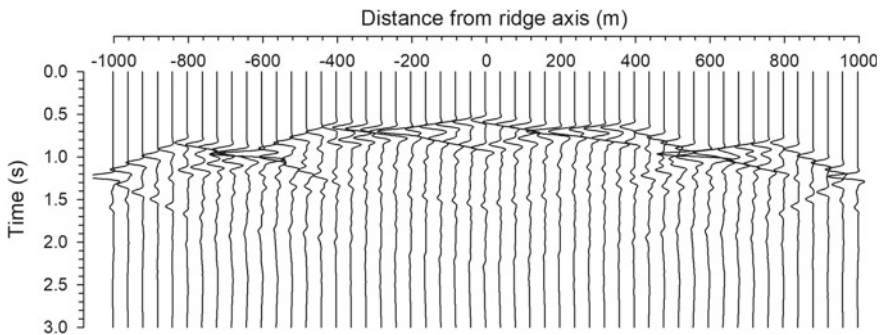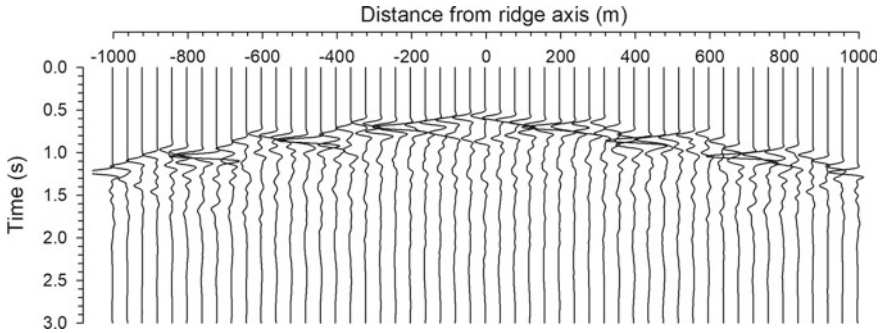
Fig. 9 SH-wave response of the TV7 complex valley model

5.2 *Spectral Amplifications*

Figure 10 shows the SAF at different recording points along the trough of the TV7 valley model. An analysis of Tables 4, 5 and 6 reveals that the difference between numerically and analytically obtained SAF increases with the increase of number of sub-valleys in the model. For example, the obtained largest SAF at the trough of central valley of TV7 model is 0.95 as to that obtained analytically (0.67). Analytical value of amplification factor is found lesser than numerical value at the trough of the first, second, and third valleys also. Further, at the crest of the sub-ridges, there is more amplification of ground motion as compared to the amplification obtained analytically (1.78, 2.43, and 2.90, at the crest of first, second, and third ridge). However, ASA at the crest of the sub-ridges depicts a de-amplification of ground motion at first and third ridge. The obtained ASA is largest at the crest of the second ridge and least for the third sub-trough. It reveals that amplification factor for a valley is affected by its own shape as well as features of surrounding neighboring sub-ridges. Diffraction and reflection of waves occur and may be the reason of some unusual behavior in the case of multi-valley.

6 Conclusions

The analysis of the SH-wave responses of the TV1, TV3, and TV7 triangular complex valley models revealed a decrease of de-amplification and increase of duration at the trough of the sub-valleys with the increase of complexity in the model as compared to the same obtained analytically. On an average, an increase in spectral amplification as compared to the analytical one at the trough of sub-valleys and crest of the sub-ridges with the increase of complexity in the models is also observed. Peak spectral amplification values at the flanks of the topography are also increasing with the increase of complexity in the model, which means neighboring
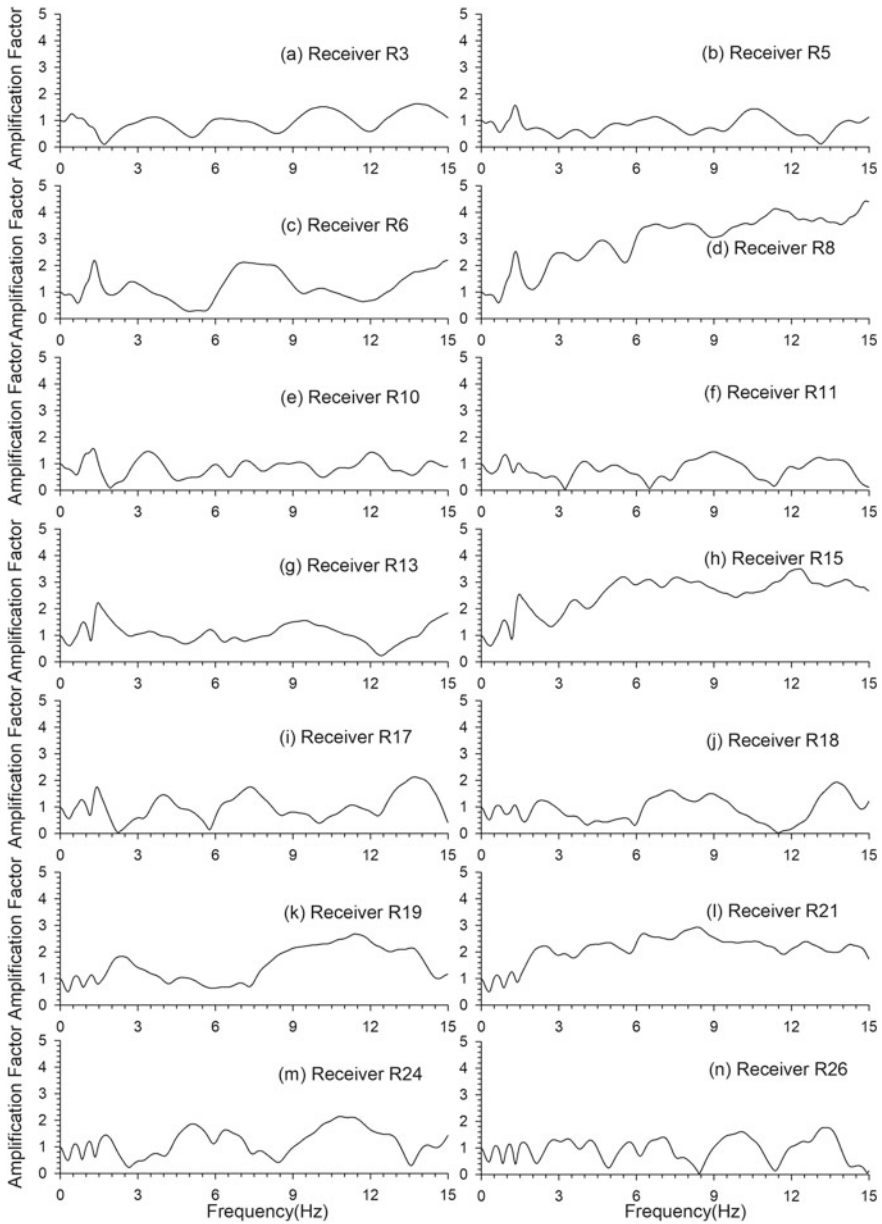
Fig. 10 SAF at various locations for TV7 complex valley model

topographic features affect the response of the sub-valley/ridge due to the occur-
rence of interference of the reflected and diffracted waves from the adjacent
topographic features with the wave field within the considered valley/ridge due to

Table 6 Comparison of SAF and ASA at different receiver points with the analytical one

Receivers	R5 (T)	R8 (C)	R11 (T)	R15 (C)	R18 (T)	R21 (C)	R26 (T)
Largest SAF: numerical	0.78	2.96	0.78	2.54	0.90	2.11	0.95
ASA: numerical	0.57	0.73	1.09	1.36	0.98	0.90	0.63
SAF: analytical	0.61	2.90	0.62	2.43	0.63	1.78	0.67

Note The alphabets "F," "C," and "T" are used for "Flank," "Crest," and "Trough," respectively

the incident waves. The apex angle or shape ratio is the major factor for governing the amplification scenario across the multi-ridge-valley model. It is also inferred that the amplification at the crest of the sub-ridges of a larger valley at certain frequency may be one of the reasons behind reported very large amplification and damages in the valleys based on the earthquake records. Recently, Kumar et al. [17] have stated that the amplification reported based on the records at the crest and base of the ridge generally over predicts the amplification. Further, Narayan and Arafat [14] documented that the weathering plays a major role in the topography amplifications. Finally, it is recommended to consider the shape and size of the realistic 3D topography along-with weathering in the simulation to predict the amplification/de-amplification scenario across the topography.

References

1. Trifunac, M.D., Hudson, D.E.: Analysis of the Pacoima dam accelerogram—San Fernando, California, earthquake of 1971. Bull. Seismol. Soc. Am. **61**(5), 1393–1411 (1971)
2. Spudich, P., Hellweg, M., Lee, W.H.K.: Directional topographic site response at Tarzana observed in aftershocks of the 1994 Northridge, California, earthquake: implications for mainshock motions. Bull. Seismol. Soc. Am. **86**(1B), 193–208 (1996)
3. Celebi, M.: Topographical and geological amplifications determined from strong-motion and aftershock records of the 3 March 1985 Chile earthquake. Bull. Seismol. Soc. Am. **77**(4), 1147–1167 (1987)
4. Celebi, M.: Topographical and geological amplification: case studies and engineering implications. Struct. Saf. **10**(1–3), 199–217 (1991)
5. Kawase, H., Aki, K.: Topography effect at the critical SV-wave incidence: possible explanation of damage pattern by the Whittier Narrows, California, earthquake of 1 October 1987. Bull. Seismol. Soc. Am. **80**(1), 1–22 (1990)
6. Narayan, J.P., Rai, D.C.: An observational study of local site effects in Chamoli earthquake. In: Proc. Workshop on Recent Earthquakes of Chamoli and Bhuj, pp. 273–280 ISET, Roorkee, India (2001)
7. Goda, K., Kiyota, T., Pokhrel, R.M., Chiaro, G., Katagiri, T., Sharma, K., Wilkinson, S.: The 2015 Gorkha Nepal earthquake: insights from earthquake damage survey. Front. Built Environ. **1**, 1–8 (2015)
8. Narayan, J.P., Kumar, N., Chauhan, R.: Role of shape and numbers of ridges and valleys in the insulating effects of topography on the Rayleigh wave characteristics. Pure Appl. Geophys. **175**(8), 2623–2642 (2018)

9. Geli, L., Bard, P.Y., Jullien, B.: The effect of topography on earthquake ground motion: a review and new results. Bull. Seismol. Soc. Am. **78**(1), 42–63 (1988)
10. Sánchez-Sesma, F.J., Campillo, M.: Diffraction of P, SV, and Rayleigh waves by topographic features: a boundary integral formulation. Bull. Seismol. Soc. Am. **81**(6), 2234–2253 (1991)
11. Assimaki, D., Gazetas, G., Kausel, E.: Effects of local soil conditions on the topographic aggravation of seismic motion: parametric investigation and recorded field evidence from the 1999 Athens earthquake. Bull. Seismol. Soc. Am. **95**(3), 1059–1089 (2005)
12. Kamalian, M., Jafari, M.K., Sohrabi-Bidar, A., Razmkhah, A., Gatmiri, B.: Time-domain two-dimensional site response analysis of non-homogeneous topographic structures by a hybrid BE/FE method. Soil Dyn. Earthq. Eng. **26**(8), 753–765 (2006)
13. Chaljub, E., Moczo, P., Tsuno, S., Bard, P.Y., Kristek, J., Käser, M., Stupazzini, M., Kristekova, M.: Quantitative comparison of four numerical predictions of 3D ground motion in the Grenoble Valley, France. Bull. Seismol. Soc. Am. **100**(4), 1427–1455 (2010)
14. Narayan, J.P., Arafat, M.Y.: A numerical study of effects of valley-weathering and valley-shape-ratio on the ground motion characteristics. Acta Geophys. **63**(1), 154–175 (2015)
15. Pedersen, H., Le Brun, B., Hatzfeld, D., Campillo, M., Bard, P.Y.: Ground-motion amplitude across ridges. Bull. Seismol. Soc. Am. **84**(6), 1786–1800 (1994)
16. Lee, S.J., Komatitsch, D., Huang, B.S., Tromp, J.: Effects of topography on seismic-wave propagation: an example from northern Taiwan. Bull. Seismol. Soc. Am. **99**(1), 314–325 (2009)
17. Kumar, N., Narayan, J.P., Kumar, V., Tiwari, V.: Effects of shape and complexity of ridge topography on the comparative amplification scenario for the SH- and SV-waves. J. Earth Syst. Sci. **136**(36), 1–20 (2021)
18. Narayan, J.P., Kumar, V.: A fourth-order accurate finite-difference program for the simulation of SH-wave propagation in heterogeneous viscoelastic medium. Geofizika **30**(2), 173–189 (2013)
19. Israeli, M., Orszag, S.A.: Approximation of radiation boundary conditions. J. Comput. Phys. **41**(1), 115–135 (1981)
20. Zeng, C., Xia, J., Miller, R.D., Tsoflias, G.P.: An improved vacuum formulation for 2D finite-difference modeling of Rayleigh waves including surface topography and internal discontinuities. Geophysics **77**(1), T1–T9 (2012)

Assessment of Soil Gas Radon (Rn222) Emission in Kachchh, Gujarat, India: Influence of Meteorological Parameters and Identification of Precursors to Impending Earthquakes

Sushanta Kumar Sahoo and Katlamudi Madhusudan Rao

1 Introduction

Radon is generated as a decay product in the radioactive disintegration of uranium. There are 39 isotopes formed from uranium during decay, and radon (Rn222) is considered to be the most stable isotope with a half-life of 3.82 days among these isotopes. Thoron (Rn220) is found to be the second most stable isotope having a half-life period of 54.5 s. Such a low half-life allows detection of thoron lower than that of radon. Radon is completely diluted in water, but in porous media and fragmented rocks, some of the radon is emitted and migrates through the pore fluid. In the process of diffusion, radon migrates through the pores of the soil (gas/liquid) under the influence of a concentration gradient [1], while in the process of convection, the porous liquid moves through the pores of the soil under the influence of an external force such as a pressure gradient [2]. The diffusion process is dominated when there is low permeability, while the existence of a high permeability soil promotes convective transport.

During migration, soil radon is influenced by various meteorological parameters such as pressure, temperature, humidity, wind speed, and rainfall. [3]. The influence of meteorological parameters on radon emissions from soil gases is studied and reported in various places around the world [4–6]. The soil radon emanation is mainly influenced by moisture content and to a lesser extent by temperature [2]. With a moisture content of 15–20%, the emanation power of the soil increases and decreases with increasing moisture content. With higher moisture content, radon is trapped in the pore fluid by a thicker layer on the soil grains. Here too, soil radon emissions are affected by the capping effect. Such a cover in the top layer prevents the exhalation of radon gas from the soil [24]. In addition to air humidity, air pressure and temperature also influence the release and transport of soil radon. Due to this influence of meteorological parameters, periodic vibrations dominate the

S. K. Sahoo · K. M. Rao (✉)
Institute of Seismological Research, Gandhinagar, Gujarat 382009, India

radon concentration in the soil [7, 8]. Therefore, it is essential to suppress these periodic oscillations in order to successfully correlate the variation of soil radon with the short-term occurrence of earthquakes [9, 10]. Because the Earth is dynamic, soil radon emissions are intrinsically nonlinear and non-stationary. Such dynamic behavior of soil radon allows the use of a possible nonlinear approach for the elimination of periodic oscillations and a successful correlation of soil radon with earthquakes [7, 11–13]. In this study, the Hilbert–Huang transform (HHT) [13] based on empirical mode decomposition (EMD) is applied to the time series of soil radon data recorded at Badargadh, Kachchh, Gujarat, to remove the periodic oscillations and identification of earthquake precursors.

2   Geology of Study Area

Kachchh region is a pericratonic basin made up of Phanerozoic sediments of different ages in the western part of the Indian subcontinent. The formation of the Kachchh Rift basin began in the Mesozoic era with the disintegration of the lands of Gondwana and the drift of the Indian subcontinent to the north. The main tectonic feature of the region is revealed by the E-W orientation of the main faults [14]. The rift zone is bounded by two major E-W faults, i.e., Nagar-Parkar fault to the north and the North Kathiawar fault to the south. Apart from these faults, the Radhanpur–Barmer arc is present on the east side while the Arabian Sea covers the west side of the rift zone. Apart from this, the region also includes other major faults like Kachchh Mainland Fault (KMF), Katrol Hill Fault (KHF), Gedi Fault (GF), South Wagad Fault (SWF), Island Belt Fault (IBF), Banni Fault (BF), etc. The sequence of these faults can be explained by a reactivated Precambrian signature, provided that the Delhi-Aravalli orogenic trend, which is heading NE-SW, has changed direction to the west after touching the Gujarat plain. Such an active tectonic feature allows the region to experience a range of seismic activities ranging from low to high magnitude in the past, such as the Indus Delta of 1668 (MM X), 1819 Kachchh (Mw 7.9), 1845 Lakhpat (MM VIII), 1956 Anjar (Mw 6.0), and the 2001 earthquake in Bhuj (Mw 7.6). Therefore, the Kachchh region is in zone V of the seismic zoning map of India (Fig. 1).

3   Experimental Set Up

The radon concentration in soil gas has been continuously monitored by Institute of Seismological Research at Badargarh in the Kachchh region, Gujarat. The soil radon meter, i.e., RTM 1688-2, manufactured by SARAD Instruments, Germany, is used for data acquisition. In addition to soil radon, the instrument also measures other parameters such as temperature (−20 to 40 °C), pressure (800–1200 mBar), and humidity (0–100%). Detailed schematic diagram of instrumentation and
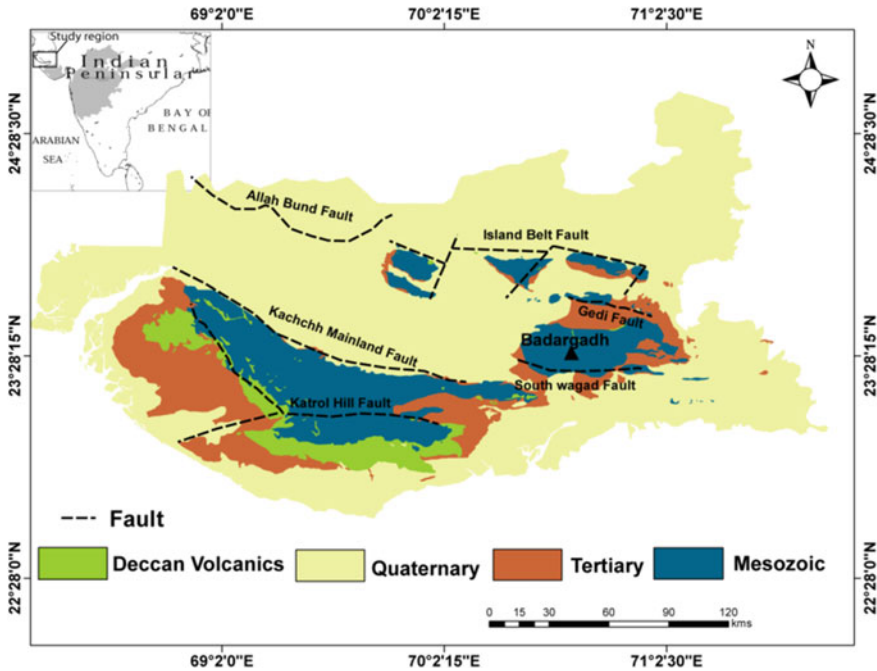
Fig. 1 Location of monitoring station along with faults in the study area

installation process are shown in Fig. 2. As illustrated, the radon sensor is held in a suspended position by a cable of 3 feet underground in a hole. The cable is connected to a data logger. The bottom of the hole is covered with gravel to avoid contaminating the water. The cable and the radon sensor are surrounded by a PVC pipe below the surface of the earth. For real-time viewing and downloading of raw data, the data logger is connected to a PC or laptop using a DC battery for power.

4 Methodology

4.1 Empirical Mode Decomposition (EMD)

The empirical mode decomposition (EMD)-based Hilbert–Huang Transform (HHT) developed by Huang et al. [13] is used for analysis in this study. This is a two-step process where the first step involves the empirical decomposition of the observed soil radon time series into a number of oscillation modes called intrinsic mode functions (IMF). In the second step, the Hilbert–Huang transformation (HHT) is applied to significant or non-periodic IMFs. Huang et al. [13] suggested two necessary conditions for IMF formation when applying EMD, namely (i) in the
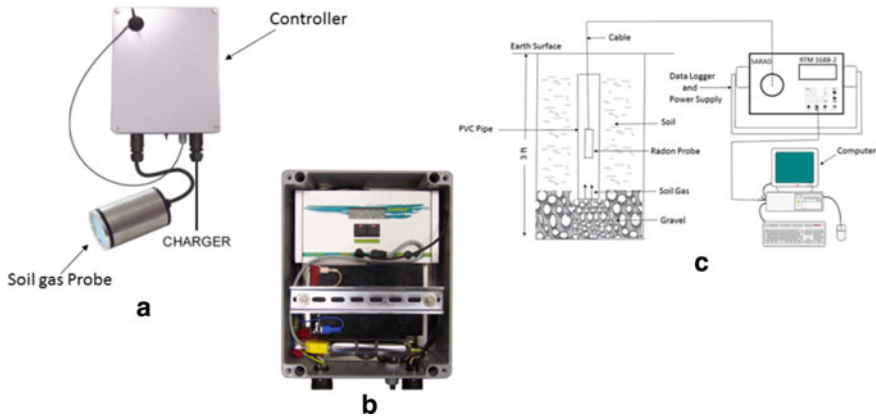
Fig. 2 Soil radon meter showing **a** complete set, **b** the schematic diagram of its installation, and **c** the inside view of its controller

dataset, the number of extrema and the number of zero crossings should be the same or differ by one and (ii) at each point, the mean of the envelopes, which are defined by the local minima and the local maxima, must be zero. Depending on the character of the IMF, the decomposition method can use envelopes which are determined by local maxima and local minima. Once all the extrema are identified, all the local maxima are connected by a cubic spline as an upper shell, and similarly, connecting the lower extrema forms a lower shell. The entire data set is bounded between the lower and upper envelope curve, and its average value is selected as $m1$. The difference between data and $m1$ is the first component, $h1$, that is

$$X(t) - m1 = h1 \qquad (1)$$

Again, the procedure is repeated by taking $h1$ as the data and $m11$ as the mean of $h1$ and the second component is obtained from the difference between $h1$ and $m11$, i.e.,

$$h1 - m11 = h11 \qquad (2)$$

This process is continued for k times to eliminate the riding waves and making the wave more symmetric and thereby, getting the IMF $h1k$ as,

$$h1_{(k-1)} - m1k = h1k \qquad (3)$$

And it is designated as, $c1 = h1k$, where $c1$ is the first IMF. It contains the lowest period and finest scale of the data and the frequency gets decreased with increase in the rank of IMFs. The first IMF ($c1$) can be extracted from the rest of the data by,

$$X(t) - c1 = r1 \tag{4}$$

Being the residue, $r1$ still carries the information of longer period components, which is again considered as the raw data and subjected to the same sifting process as given above. The sifting procedure is reiterated on all the subsequent rjs, i.e.,

$$r1 - c2 = r \tag{5}$$

$$f(x) = r2 - c3 = r3 \qquad r_{(n-1)} - c_n = r_n \tag{6}$$

The sifting procedure continues until a moment, when either the residue becomes small, i.e., similar with pre-detected value of substantial consequences or become so monotonic that no IMF can be extracted further. This final monotonic residue is treated as the trend of the data.

4.2 Hilbert–Huang Transform (HHT)

As per the methodology developed by Huang et al. [13], the Hilbert transform is applied to the significant IMFs obtained by the EMD process to get the instantaneous amplitude $(A(t))$ and phase $(\phi(t))$. The instantaneous frequency of the significant IMFs are defined as the differentiation of phase $(\phi(t))$ as,

$$\omega = \frac{d\phi(t)}{dt} \tag{7}$$

The time–frequency distribution of amplitude is called as the Hilbert–Huang spectrum (HH spectrum) and is defined as,

$$H(t, w) = \text{Re} \sum_i A_i(t) \exp\left(j \int w_i(t) dt\right) \tag{8}$$

There are other statistical parameters like mean marginal spectrum, degree of non-stationarity, instantaneous energy, etc., are also obtained from the HH-spectrum. The mean marginal spectrum is defined as the entire energy of each frequency cell, i.e.,

$$h(w) = \frac{1}{T} \int_0^T H(t, w) dt \tag{9}$$

The degree of non-stationarity defines the range of nonlinearity present in the input time series of radon and is defined as,

$$DNS(w) = \int\limits_0^T \left[1 - \frac{H(t,w)}{h(w)} \right] dt \qquad (10)$$

The instantaneous energy depicts the real time change of energy of the input time series and is defined as,

$$IE = \sum_w H^2(t,w) \qquad (11)$$

5 Result and Discussion

5.1 Descriptive Statistics of Soil Radon and Other Parameters

Soil radon (Rn222) is continuously monitored from January 1, 2017 to December 31, 2017 along with other parameters such as pressure, temperature, and humidity in the Kachchh region (Fig. 3). Data on rainfall and wind speed are collected from meteorological stations located near the observatory by the Government of Gujarat's Directorate of Agriculture during the monitoring period. Full statistics for all parameters are given in Table 1. As the study covers the entire duration of one year, the seasonal statistics for soil radon is examined (Table 2). Seasonal statistics show that a maximum radon concentration is measured during the rainy season compared to the other two seasons. The increase of soil gas radon along with rainfall is observed at various places in past [6, 15]. During rain, when rainwater seeps into the soil, it increases the permeability of soil pores and thus stimulates the transport of soil gases.

The normality test of the observed soil gas radon data during monitoring period has been conducted by plotting the quantile plot (q-q plot) (Fig. 4). In the quantile plot, there is a close relation obtained between the quantile of observed and expected values. Such a good correlation enables us to reach at a conclusion that, during monitoring period, soil gas radon followed a normal distribution.

5.2 Correlation of Soil Radon with Meteorological Parameters

Meteorological parameters such as pressure, temperature, humidity, and rainfall have a significant influence on soil radon emissions [6, 16, 17]. In the present work, a linear regression technique was applied to quantify the influence of meteorological parameters on soil radon emission during the monitoring period. The correlation coefficient for each parameter is obtained and given in Table 3. It is
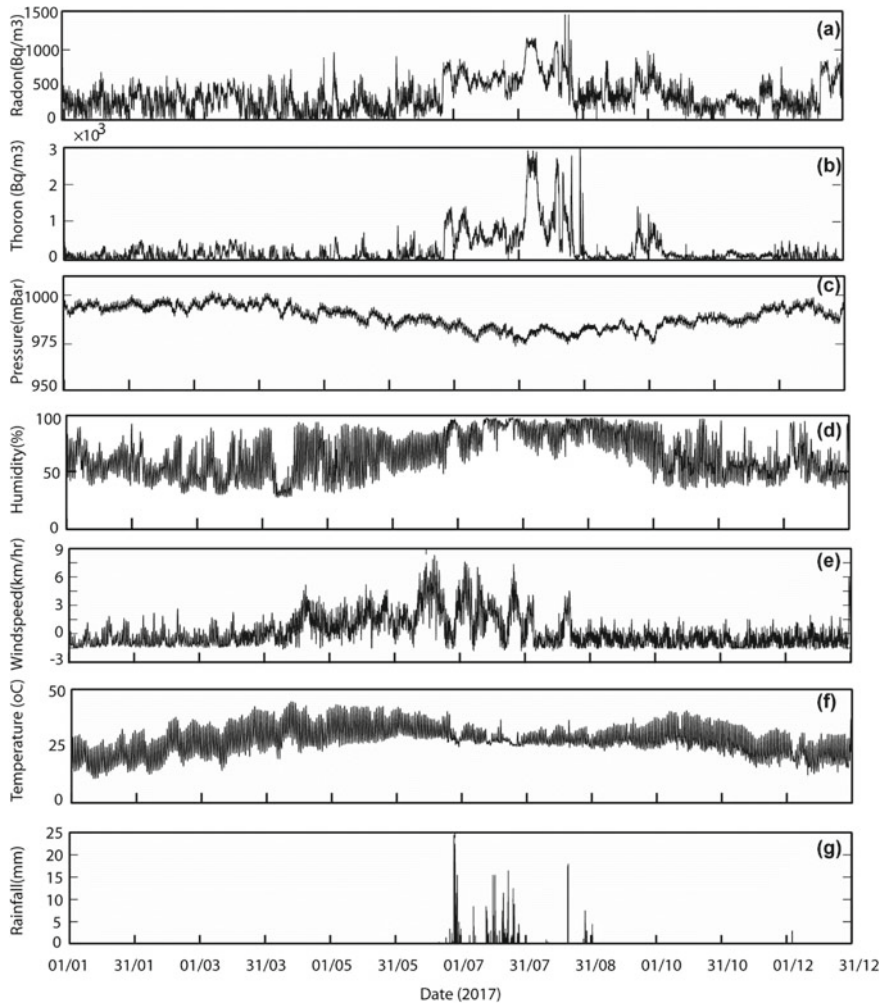
Fig. 3 Soil radon, thoron, pressure, humidity, wind speed, temperature, and rainfall data recorded during January–December, 2017

Table 1 Descriptive statistics of soil radon and other parameters during the monitoring period

Parameters	Minimum	Maximum	Average	Standard deviation
Radon (Bq/m^3)	6	1134	344	89
Thoron (Bq/m^3)	14	2993	1172	59
Pressure (mBar)	973	1002	989	6
Temperature (°C)	11	45	28	6
Humidity (%)	33	97	56	15
Wind speed (km/hr)	0.69	7.6	2.11	0.89

Table 2 Descriptive statistics of soil radon during all the three seasons

Radon (Bq/m^3)	Minimum	Maximum	Average	Std. dev
Summer	6	964	247	70
Rainy	353	1500	550	136
Winter	116	1051	319	90

Fig. 4 Quantile (*q-q*) plot of radon time series at Badargadh

Normal Q-Q Plot of radon
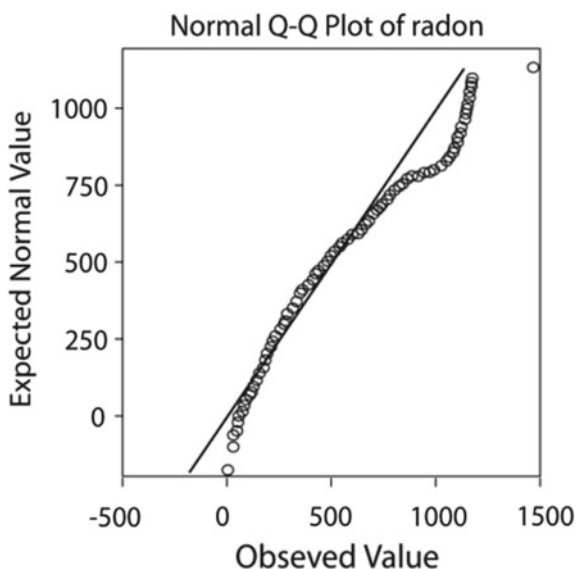
Table 3 Correlation coefficient of soil radon and other meteorological parameters

Parameters	Correlation coefficient
Radon and pressure	−0.51
Radon and temperature	−0.37
Radon and humidity	0.42
Radon and wind speed	0.22
Radon and rainfall	0.19

observed that a moderate to high correlation range is observed during the monitoring period. Temperature and pressure are found to be having a negative correlation with radon, while all other parameters are positively correlated with radon (Fig. 5).
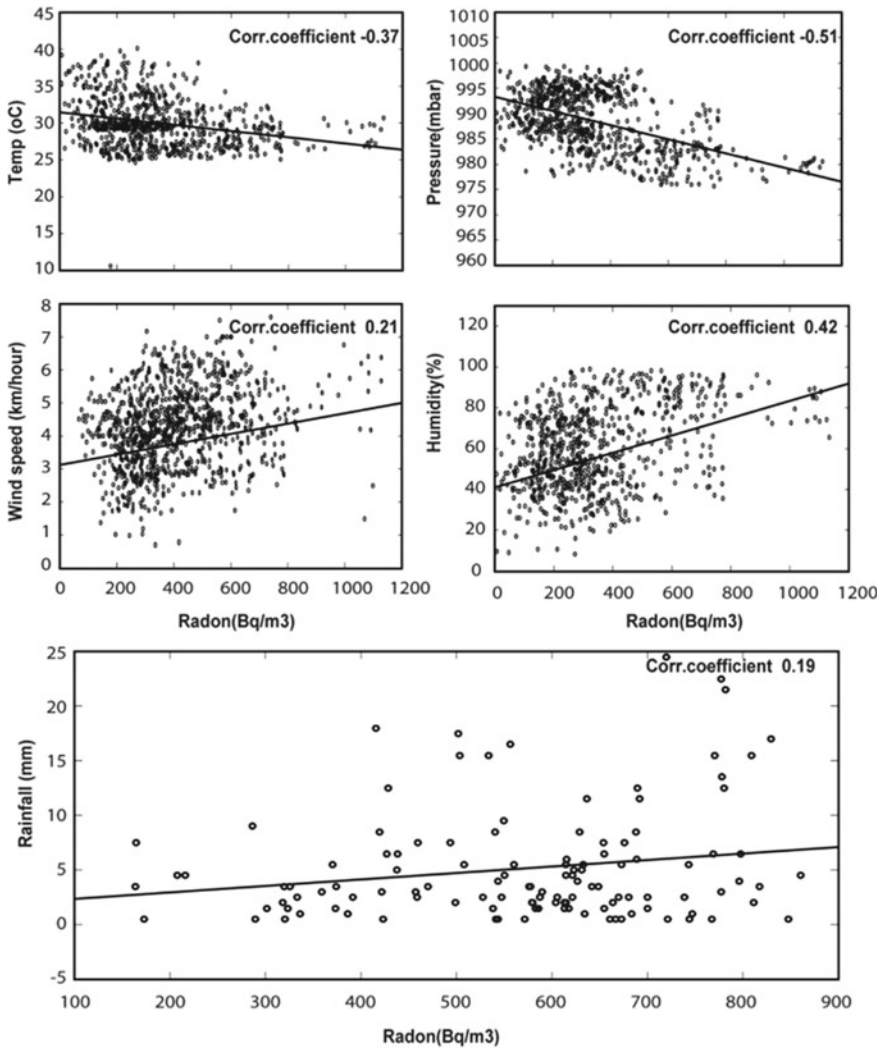
Fig. 5 Linear regression of meteorological parameters with soil gas radon

5.3 Application of Empirical Mode Decomposition (EMD) on Soil Gas Radon

The above analysis confirms that there is a possible influence of various meteorological parameters on the radon emission of soil gas during the monitoring period. Therefore, it has become an essential approach for the authors to eliminate this influence in order to establish a successful correlation of the soil radon concentration with the occurrence of earthquakes near the monitoring station during the

investigation period. Due to the influence of these meteorological parameters, there are periodic oscillations which correspond to the diurnal and semi-diurnal period and dominate the soil radon time series. These periodic oscillations are identified by applying an FFT power spectrum analysis to each parameter. There is a clear harmonic of the diurnal period which is observed in all parameters (Fig. 6).

Apart from that, there is also an additional harmonic of semi-diurnal periods obtained from time series of pressure and humidity. Such presence of diurnal oscillation in radon and other meteorological parameters clearly shows that meteorological parameters have an influence on radon emissions in soil during the investigation period. To eliminate these periodicities, empirical mode decomposition (EMD) is applied to the time series of soil radon. It is possible to divide the
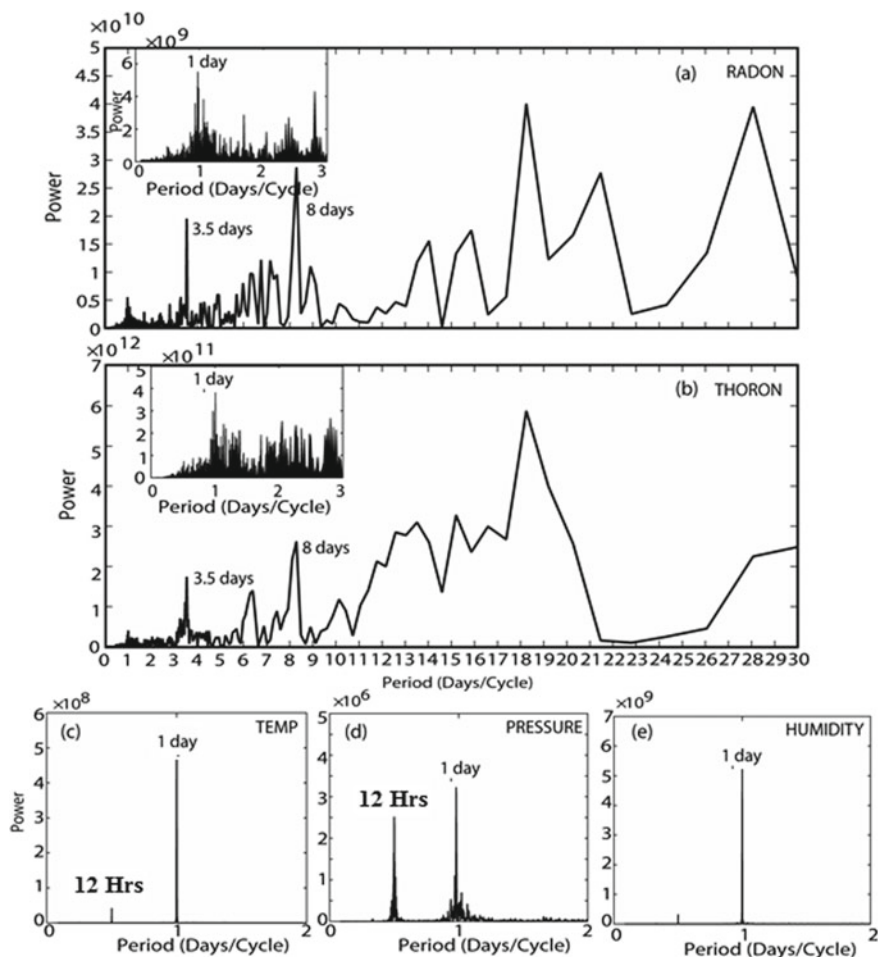
Fig. 6 FFT power spectrum analysis of all parameters

original signal into different frequency bands using the EMD process [13]. There are signals of different oscillatory characters obtained, and these are known as intrinsic mode functions (IMF). In this study, the complete time series of soil radon is broken down into 13 IMFs using EMD (Figs. 7 and 8). IMFs obtained by EMD show variation in both positive and negative directions and are due to the non-negative value of the input soil radon time series.

The unwrapped phase of each IMF is determined and plotted during the monitoring period (Fig. 9). It is observed that each IMF is linear with a certain phase and that such a different phase of each IMF clearly shows that the IMFs obtained are mono-frequent in nature. The next step is to look at each IMF's period and select the significant IMFs that are free from periodic oscillations for further analysis.

FFT power spectrum analysis was applied to detect the period of each IMF (Table 4). It is observed that the first two IMFs (IMF1 and IMF2) have periods of 2.15 and 7.87 h, respectively, and these low periods are due to the noise of the instrument and are therefore discarded. Here, again the 3rd and 4th IMF display a
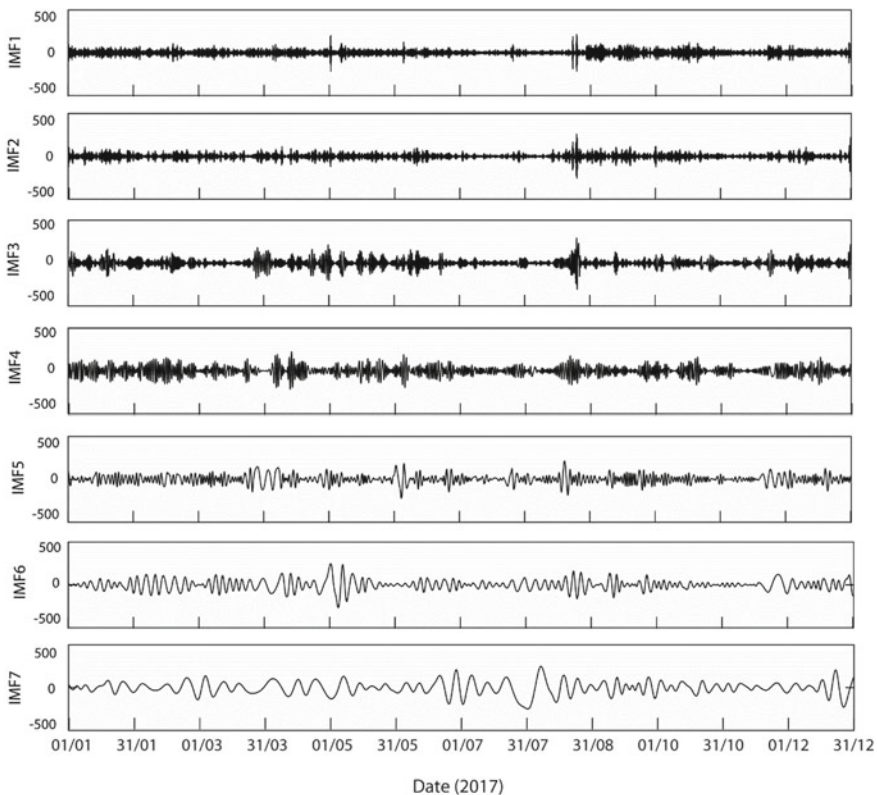
Fig. 7 Empirical mode decomposition (EMD)-intrinsic mode functions (IMFs 1-7) of radon time series at Badargadh
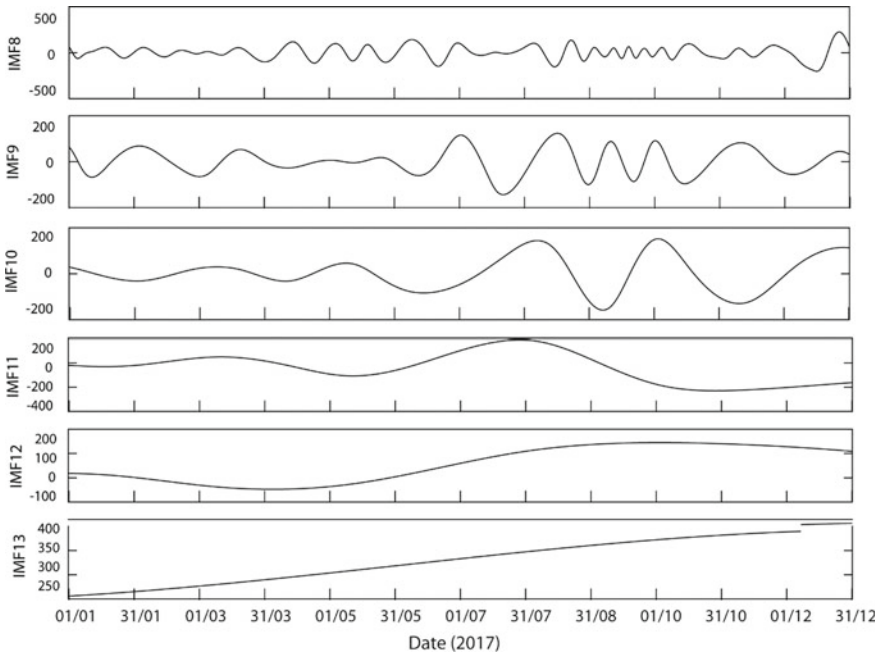
Fig. 8 Empirical mode decomposition (EMD)-intrinsic mode functions (IMFs 8-13) of radon time series at Badargadh
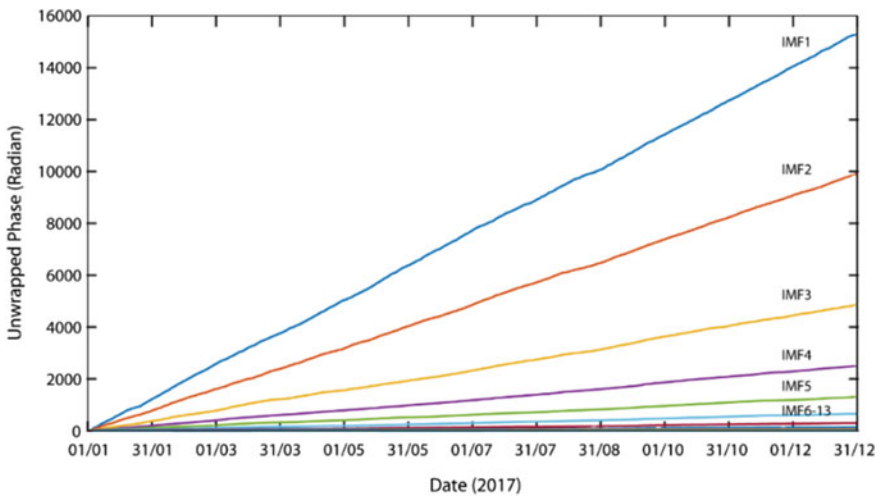
Fig. 9 Unwrapped phase of IMFs obtained by EMD

Table 4 Period of each IMF determined by FFT power spectrum analysis

	IMF 1	IMF 2	IMF 3	IMF 4	IMF 5	IMF 6	IMF 7	IMF 8	IMF 9	IMF 10	IMF 11	IMF 12
Harmonic period	2.15 h	7.87 h	1 day	1 day	2.76 Days	3.54 Days	8.87 Days	15.6 Days	45 Days	72 Days	182 Days	364 Days
Correlation coefficients	0.15	0.15	0.25	0.25	0.2	0.25	0.24	0.32	0.22	0.35	0.37	0.33
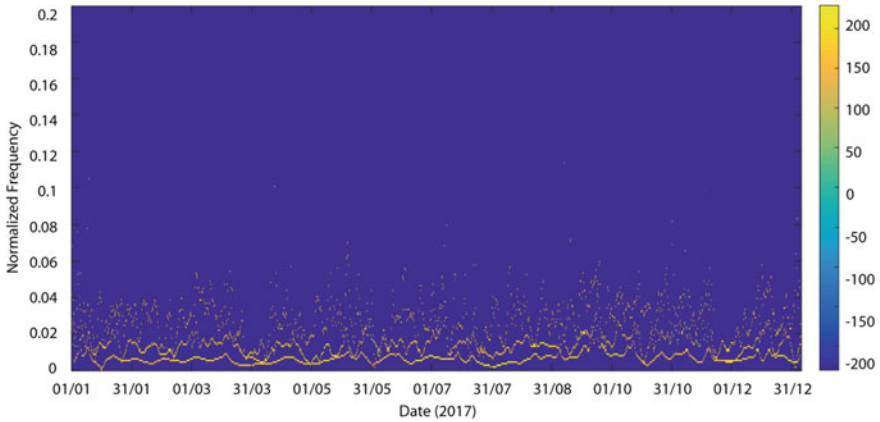
Fig. 10 HH spectrum of significant IMFs
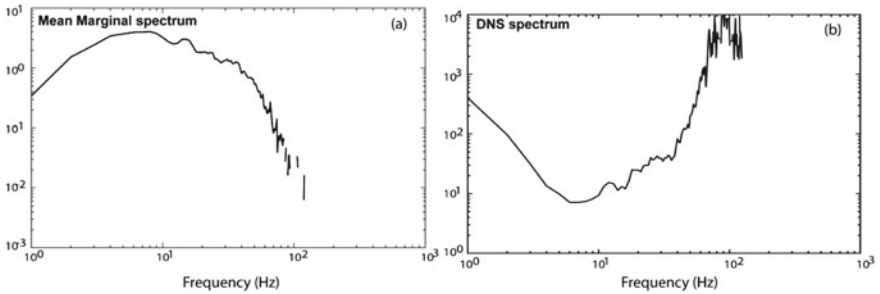
Fig. 11 **a** Mean marginal spectrum and **b** DNS spectrum of soil radon time series

period of 1 day and are therefore considered as daily IMFs. The 8th IMF shows a period of 15.6 days, which is due to the influence of tidal oscillations and is discarded. Higher-order IMFs (9th, 10th, 11th, and 12th IMF) have a period of more than 30 days, which corresponds to long-period oscillations. Now, the 5th, 6th, and 7th IMFs remain and are therefore considered important IMFs and are selected in the next step as the input for the Hilbert–Huang transform (HHT). HHT is an advantageous technique over Fourier transform for capturing an immediate change in frequency over time.

The Hilbert–Huang spectrum (HH spectrum) is defined as an assimilation of both the amplitude and the frequency of significant IMFs in the form of a time–frequency spectrum. It should be noted here that the HH spectrum is not the spectral density function, but a sparse matrix which contains the amplitudes of the significant modes in the time–frequency domain. The HH spectrum of significant IMFs is plotted, and the normalized frequency is between 0 and 0.2 Hz (Fig. 10). Again, other parameters such as the mean marginal spectrum, degree of non-stationarity (DNS), and instantaneous energy are also determined from the HH spectrum.
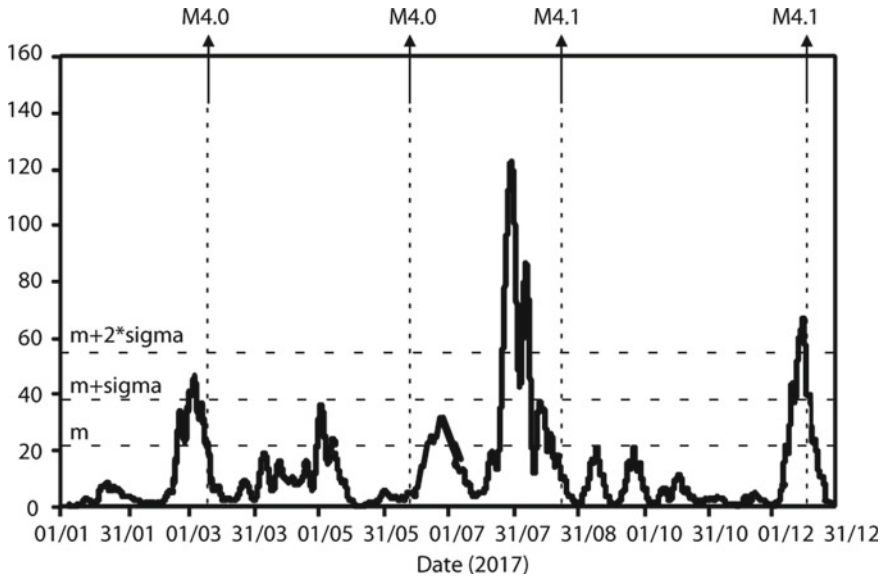
Fig. 12 Instantaneous energy (IE) of radon time series at Badargadh along with earthquakes

Figure 11a shows the mean marginal spectrum of the soil radon time series during the monitoring period. It is observed that the high frequency part exhibits higher fluctuations, while the lower part is stable. Figure 11b shows the degree of non-stationarity of the radon time series. It is observed that the high frequency range has a higher order of non-stationarity than that of the low frequency range.

The instantaneous energy (IE) is defined as the summation of squared amplitude of HH spectrum, and it assists in detecting the intermittent character of input time series [13]. In this study, it is detected that the instantaneous energy of soil radon during the whole monitoring period and correlated it with the seismic activities of magnitude more than 4 that occurred within 100 km radius of the monitoring station (Fig. 12). There were four such moderate earthquakes with magnitude greater than 4 occurred near the monitoring station during study period, and these are considered for correlation with instantaneous energy. It is observed that the instantaneous energy was enhanced and crossed its Mean +2*sigma level before the two earthquakes of M (4.1) occurred on August 23 and December 11, 2017. There was an increase of the energy which is crossed mean + sigma level 5 days before the March 5th earthquake (M 4.0). There is a little enhancement before occurrence of June 13th earthquake as well. Such radon anomalies can be explained with the help of diffusion–dilatancy model, where one can expect the development of cracks/micro-cracks prior to the occurrence of earthquakes, which enhances the soil radon emission.

6   Conclusions

The soil radon which continuously measured at the Badargarh monitoring station in the Kachchh region is analyzed to study the influence of various meteorological parameters on the soil radon emission as well as the correlation between the radon emission and the occurrence of earthquakes. First, the linear regression technique allowed us to quantify the influence of meteorological parameters on soil radon emissions by extracting the correlation coefficient. A moderate to good correlation was obtained between meteorological parameters and soil radon emission. In the later phase, a two-step process, i.e., EMD-HHT, applied to remove periodic oscillations in the soil radon time series and to establish a successful correlation with seismic activity. The EMD technique has helped us identify and remove periodic oscillations in soil radon time series by breaking down observed radon time series into number of modes (IMF). In the next step, significant IMFs are considered as inputs for the HHT. The HH spectrum of these significant IMFs allows us to extract the time evolution of both the instantaneous frequency and the energy of soil radon during the monitoring period. The temporal evolution of the momentary energy of soil radon is well correlated with earthquakes of medium magnitude that occurred near the monitoring station during the investigation period.

References

1. Nazaroff, W.W., Nero, A.V., (Eds.): Soil as a Source of In-Door Radon: Generation, Migration and Entry: Radon and its Decay Products in Indoor Air. Wiley-Inter-Science Publication, pp. 57–112 (1988)
2. Schumann, R., Owen, D., Asher-Bolinder, S.: Factors affecting soil-gas radon concentrations at a single site in the semiarid western U.S. In: EPA Symposium on Radon and Radon Reduction Technology 2. Publication (1988)
3. Chaudhuri, H., Das, N.K., Bhandari, R.K., Sen, P., Sinha, B.: Radon activity measurements around Bakreswar thermal springs. Radiat. Meas. **45**(1), 143–146 (2010)
4. Arora, B., Kumar, A., Walia, V., Yang, T., Fu, C.-C., Liu, T.-K., Wen, K.-L., Chen, C.-H.: Assessment of the response of the meteorological/hydrological parameters on the soil gas radon emission at Hsinchu, northern Taiwan: a prerequisite to identify earthquake precursors. J. Asian Earth Sci. **149**, 49–63 (2017). https://doi.org/10.1016/j.jseaes.2017.06.033
5. Chambers, S.D., Hong, S.-B., Williams, A.G., Crawford, J., Griffiths, A.D., Park, S.-J.: Characterizing terrestrial influences on Antarctic air masses using Radon-222 measurements at King George Island. Atmos. Chem. Phys. **14**, 9903–9916 (2014)
6. Hamada, H.: Estimation of groundwater flow rate using the decay of 222Rn in a well. J. Environ. Radioact. **47**, 1–13 (2000)
7. Baykut, S., Akgul, T., Inan, S., Seyis, C.: Observation and removal of daily quasi-periodic components in soil radon data. Radiat. Meas. **45**(7), 872–879. https://doi.org/10.1016/j.radmeas.2010.04.002 (2010)
8. Fujiyoshi, R., Sakamoto, K., Imanishi, T., Sumiyoshi, T., Sawamura, S., Vaupotic, J., Kobal, I.: Meteorological parameters contributing to variability in 222Rn activity concentration in soil gas at a site in Sapporo. Japan. Sci. Total Environ. **370**, 224–234 (2006)

9. Barman, C., Ghose, D., Sinha, B., Deb, A.: Detection of earthquake induced radon precursors by Hilbert Huang. Transform. J. Appl. Geophys. **133**, 123–131. Baskaran, M.: Radon: A Tracer for Geological, Geophysical and Geochemical Studies. Springer Geochemistry, Switzerland. https://doi.org/10.1007/978-3-319-21329-3 (2016)

10. Chowdhury, S., Deb, A., Nurujjaman, Md, Barman, C.: Identification of pre-seismic anomalies of soil radon-222 signal using Hilbert–Huang transform. Nat. Hazards March **87**(3), 1587–1606 (2017)

11. Crockett, R.G.M., Perrier, F., Richon, P.: Spectral decomposition techniques for the identification of periodic and anomalous phenomena in radon time-series. Nat. Hazards Earth Syst. Sci. **10**, 559–564 (2010)

12. Echeverria, J., Crowe, J., Woolfson, M., Hayes-Gill, B.: Application of empirical mode decomposition to heart rate variability analysis. Med. Biol. Eng. Comput. **39**(4), 471–479 (2001)

13. Huang, N.E., Shen, Z., Long, S.R., Wu, C.M., Shih, H.H., Zheng, Q., Yen, N.-C., Tung, C.C., Liu, H.H.: The empirical mode decomposition and the spectrum for nonlinear and non-stationary time series analysis. Proc. Roy. Soc. Lond. A **454**, 903–995 (1998)

14. Biswas, S.K.: Regional framework, structure and evolution of the western marginal basins of India. Tectonophysics **135**, 302–327 (1987)

15. Fukui, M.: 222Rn concentrations and variations in unconfined groundwater. J. Hydrol. **79**, 83–94 (1985)

16. Chowdhury, S., Barman, C., Deb, A., Raha, Sibaji, Ghose, Debasis. Study of variation of soil radon exhalation rate with meteorological parameters in Bakreswar–Tantloi geothermal region of West Bengal and Jharkhand, India. J. Radio Anal. Nucl. Chem. 1–10 (2018)

17. Cigolini, C., Poggib, P., Ripepec, M., Laioloa, M., Ciamberlinib, C., DelleDonnec, D., Ulivieric, D., Coppolaa, G., Lacannac, E., Marchettic, D., Piscopoa, R.: Gencocet. Radon surveys and real time monitoring at Stromboli volcano: influence oftemperature, atmospheric pressure and tidal forces on 222Rn degassing. J. Volcanol.Geoth. Res. **184**, 381–388 (2009)

Ground Responses Due to the Effect of Tunnelling in Sandy Soil

Vishalatchi Ramasamy and S. Karthigeyan

1 Introduction

The problem of urban transport to suffice the growing population is supported by faster transit systems such as metro rails that utilize spaces below the crowded and densely populated surfaces. Although, it is considered to be a greener solution it has tremendous effects on to an adjacent ground and the existing buildings built on it. Such constructions pose uncertain and unforeseen disasters that have been already witnessed in many places. Ground settlement (surface vertical movement) is a critical concern to the surface [1, 2] and subsurface facilities [3], particularly in urban settings. Longitudinal movement and transverse movements are studied to understand the effects of ground movement on adjacent surfaces.

The ground movement behavior has been studied using various methods including field observations, geotechnical centrifuge modelling, analytical, and numerical modelling. Chung-Jung et al. [4] proposed failure mechanism that enables accurate prediction of two of the key quantities in the design of linings for tunnels embedded in sandy soils, namely the minimum supporting pressure needed to retain tunnel stability and the vertical soil pressure acting on the tunnel crown around tunnels embedded in sandy soils below the ground water table was investigated in a series of model tunnel tests in a centrifuge.

Studies showed that the prediction of the shape of the tunnelling-induced ground movements in sands is very complex, and that estimates made using traditional empirical methods may not be adequate [5]. The surface and subsurface settlements along with lateral deformations are induced by tunnelling, which is examined based on closed-form analytic solutions [6]. Various conclusions expressed the inaccurate assumptions regarding the constant volumes owing to dilation/contraction of sands [7]. It is difficult to estimate the volumetric deformation in sand and thus, the constant volume assumption is still used in practice. It is of interest to the

V. Ramasamy (✉) · S. Karthigeyan
College of Engineering Guindy, Anna University, Chennai, India

365

examination of the volumetric strain caused by tunnelling. Studies have concluded that earth pressure balance (EPB) and slurry machines can achieve a high degree of settlement control, particularly in sands with volume losses as low as 0.5% [8]. The capability of Adaptive Neuro-Fuzzy Inference System (ANFIS) and Gene Expression Programming (GEP) methods were studied for settlement prediction as these methods have no limitations in the number of input parameters to predict the geotechnical parameters [9]. Tunnel construction induces soil movement and imposes lateral load on existing buildings closer to tunnelling, and it may cause displacement, rotation, overturning, and settlement of the pile. The interaction between the ground and a tunnel under construction is three-dimensional problems, and modelling the influence of tunnel is only possible if the tunnelling-induced ground movements are assessed accurately.

It can be noted from the review of literature that in most of the studies [10–14], the ground movement was analyzed only to study the surface settlement. Also, the analysis and discussion of stress [15, 16] and study of its variation was very scarce. In this paper, it is intended to study the ground deformation during the tunnelling process along with the stress and strain analysis. The extent to which the soil could be strained due to tunnelling is also to be discussed in the paper.

2 Soil Model and Material Properties

A finite element-based PLAXIS3D software is used to investigate the effect of tunnel volume loss on adjacent ground. In order to consider a realistic simulation of the soil–tunnel interaction, a three-dimensional finite element model was employed. Sand layers were assumed to behave as elastic-perfectly plastic material, as described by Mohr–Coloumb model. The soil in this study is the medium dense sand, and parameters are presented in Table 1. The lining segments and EPBS were also modelled as linear elastic, and the parameters of which are given in Table 2.

Table 1 Soil parameters obeying Mohr–Coulomb failure criterion (PC Varghese 2005)

Angle of internal friction ($\phi°$)	Relative density 'Dr' (%)		E_s (10^3 kN/m^2)	Poisson's ratio (υ)	Unit weight of soil (γ_d) (kN/m^3)
	Description	Values (%)			
33	Medium dense	55	50	0.35	18

Table 2 Concrete parameters used in the numerical analysis

Parameters	Tunnel lining	TBM shield	Unit	Model
Diameter (d)	–	–	m	Linear elastic model
Thickness (t)	0.25	0.35	m	
Elastic modulus (E)	27×10^6	210×10^6	kN/m^2	
Unit weight (γ)	24	210	kN/m^3	
Poisson's ratio	0.2	0.3	–	

2.1 Discretization and Boundary Conditions

The mesh dimensions used in the analyses are based on literature [17]. Mesh dimensions in x-direction are 10 D_t that is 5 D_t in each side from the center line of the tunnel, in y-direction 13.5 D_t, and in z-direction 6 D_t, where D_t is the diameter of the tunnel. The model boundary is fixed in all directions, and the ground surface is free in all directions to predict the deformations. The accuracy of the finite element analysis depends on the meshing density of the model. In the present study, a finer mesh was adopted in the tunnelling area, and coarser mesh was used for the remaining model due to concentration of larger shear strains. Figure 1 shows a typical finite element mesh used in the study.

2.2 Procedures of Numerical Analysis

A series of numerical analyses were performed with respect to varying parameters, and separate numerical analyses were performed for each parameter. Each numerical analysis is modelled according to the following procedure:
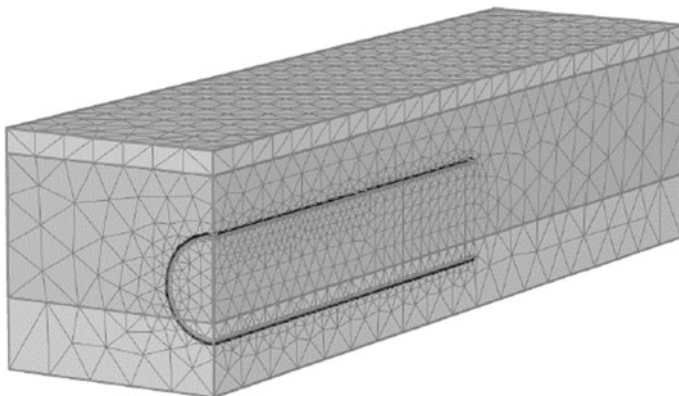
Fig. 1 Three-dimensional model of the tunnel with mesh

1. Establish the initial boundary and the initial stress conditions of the mesh.
2. The ground loss for a TBM excavated tunnel occurs in three stages namely the face loss, shield loss, and tail loss. Thus, the advancement of tunnel considers the above by specifying zero horizontal displacement at the tunnel face of the first tunnel segment to be excavated. Deactivating the soil segments denote the "excavated soil". Shell elements representing the lining are activated simultaneously. Before tunneling, the volume loss is predetermined for the parametric study by specifying the area of annulus gap between the tunnel lining and the soil excavated [18].

   Figure 2 shows the oval-shaped ground deformation pattern around the tunnel. The tunnel lining settles on the bottom of the annulus gap (due to self-weight), and the distance between the crown of the excavated surface becomes twice the thickness of the annulus gap. The stress around the tunnel are released in a non-uniform manner due to oval-shaped gap geometry. Figure 3 shows the schematic diagram of the tail void and shield.
3. In the present study, a modified grout pressure method was employed having considered tunnel face pressure, excavation sequence, shield elements, pre-fabricated concrete liner, and grouting in the annular gap. Only the gap method allows all three components involved in the ground loss owing to shield tunnelling (i.e., face loss, shield loss, and tail loss) to be taken, individually, into consideration.
4. In the first phase of tunnelling, the soil cluster inside the tunnel boring machine (TBM) was deactivated. Simultaneously, the face pressure was applied to an entire area of the TBM cross section. This pressure represents the slurry pressure inside the TBM chamber, which increases linearly with depth at a gradient equal to the unit weight of the slurry. Tunnel lining, as modelled by the plate element, was activated in the second calculation phase. The area surrounding the tunnel

Fig. 2 Gap parameter
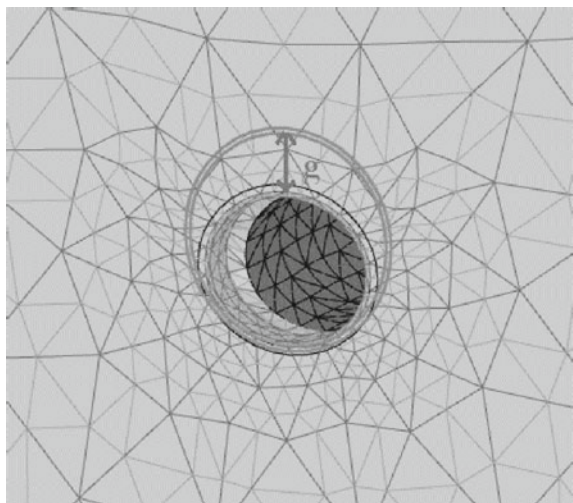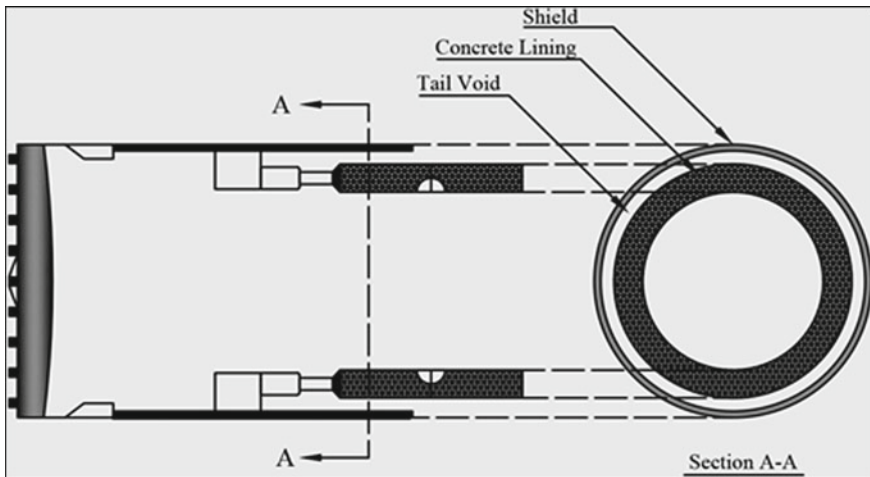
Fig. 3 Schematic diagram showing a tail void between tunnel lining and the shield [19]

lining representing the physical gap was then filled with fresh grout, and the grout pressure was applied to the physical gap area. The grout pressure was selected in accordance with the applied grout pressure at the tail of the TBM. The unit weight of the grout can be used as an increment of the grout pressure. Importantly, the continuum element was used to model the grout material. Further, cluster inside the tunnel lining was set as a dry cluster. In the last phase, the grout pressure was removed, with the physical gap area being replaced by the harden grout material.

3 Parametric Study

A series of three-dimensional finite element analyses were carried out to study the behavior of ground due to the effect of tunnel by incorporating various design parameters. The various parameters were considered which include varying the volume loss (for constant tunnel depth and diameter of tunnel), dimensions of tunnel, and location of the tunnel with respect to the ground surface. Details of the parameters used in the finite element analyses to study the effect of induced ground movement due to tunnelling are shown in Fig. 4. The tunnel diameters are varied as 6, 8, and 10 m, with contraction losses studied for six variations ranging 0.5–3%. All the above parameters are considered in the analysis and the tunnel to be placed in medium dense sand. A separate numerical analysis was carried out with respect to each of the parameters. In Fig. 4, 'D' represents the tunnel diameter, and 'C' represents the distance of the top of the tunnel from the ground surface. 'S'
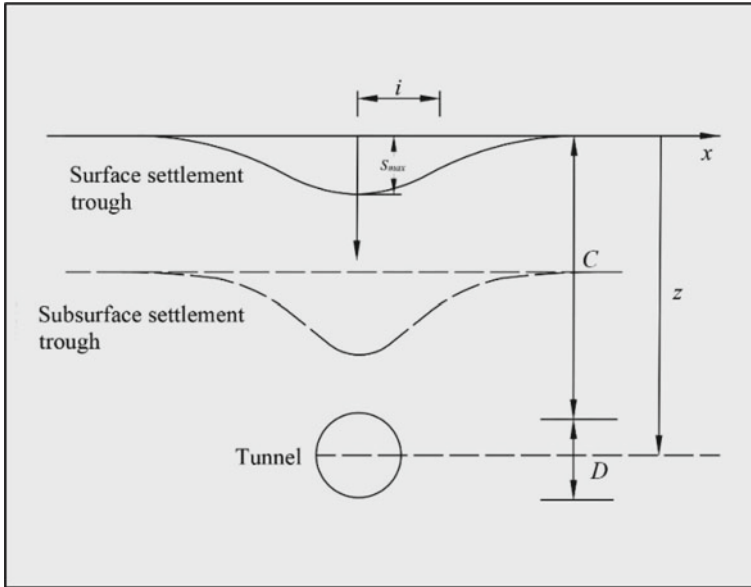
Fig. 4 Parameters used in the study [4]

represents the settlement of the ground surface. To study the effect of ground movement with respect to depth of the tunnel, the *C/D* ratio values of 1, 2, and 2.5 are considered in the study.

4 Results and Discussion

The numerical results with respect to varying parameters are discussed in the following headings.

4.1 Effect of Volume Loss

The grout injection in the annular void is controlled in by the volume and the pressure. The grout is simulated by adopting a uniform pressure corresponding to the position of the injection pipes, which are distributed over the entire perimeter of the shield tail. The grout elements are reactivated in an initial compression state equal to the pressure with which they were injected. The injection pressure is applied to both the cylindrical surface of the excavated soil and external surface of the tunnel lining. It is set on measurement of the vertical displacement the closest to the tunnel crown. The annular void between the outside surface of the shield and the

excavated soil makes the migration of some grout toward the shield possible. This migration is simulated by a correction of the shield volume loss. Thus, first critical volume loss was determined to study the other parameters for the worst-case scenario.

Figures 5 and 6 show the settlement trough and horizontal ground movement with respect to varying percentage of volume loss varied from 0.5 to 3% and diameter of the tunnel is 6 m. It could be observed from Fig. 5 that the ground settlement is increasing with increase in volume loss and maximum settlement occurs at slightly above the tunnel axis. It is seen that the maximum ground movement observed in the case of 3% volume loss. It is also observed that the maximum settlement occurs at center of the tunnel with decreasing trend while moving away from center of the tunnel axis and become constant at 10 m. This trend is observed to be the same almost in all the case of volume loss. Figure 6 shows the horizontal ground movement with respect to varying volume loss. It could be seen that the horizontal movement is increasing with increase in volume loss of the tunnel. It is also observed that maximum horizontal movement occurs at center of the horizontal tunnel axis.

In order to understand the depth at which maximum settlement occurs, the vertical ground deformations were plotted with respect to different surface levels such as at the ground surface, just above the tunnel, and just below the tunnel surface. Figure 7 shows the vertical ground movements with respect to different surface level. It could be seen that the maximum vertical deformation of the ground occurs at just above the tunnel axis and starts decreasing away from the tunnel axis. Figure 8 shows the horizontal stress from center of the horizontal axis with respect to varying volume loss at the ground surface. The horizontal stress is high at closer to the tunnel and keeps decreasing away from the tunnel axis. The maximum horizontal stress is found to 90 kN/m^2 in pertaining to the volume loss of 3%.
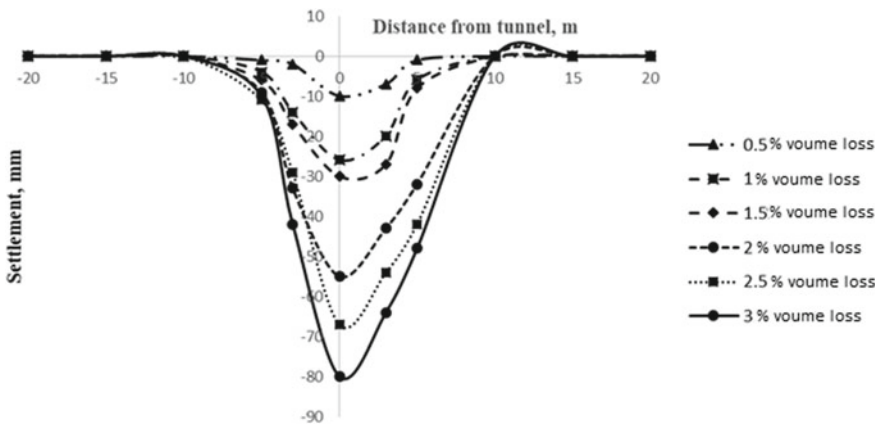
Fig. 5 Vertical ground deformation for various volume losses
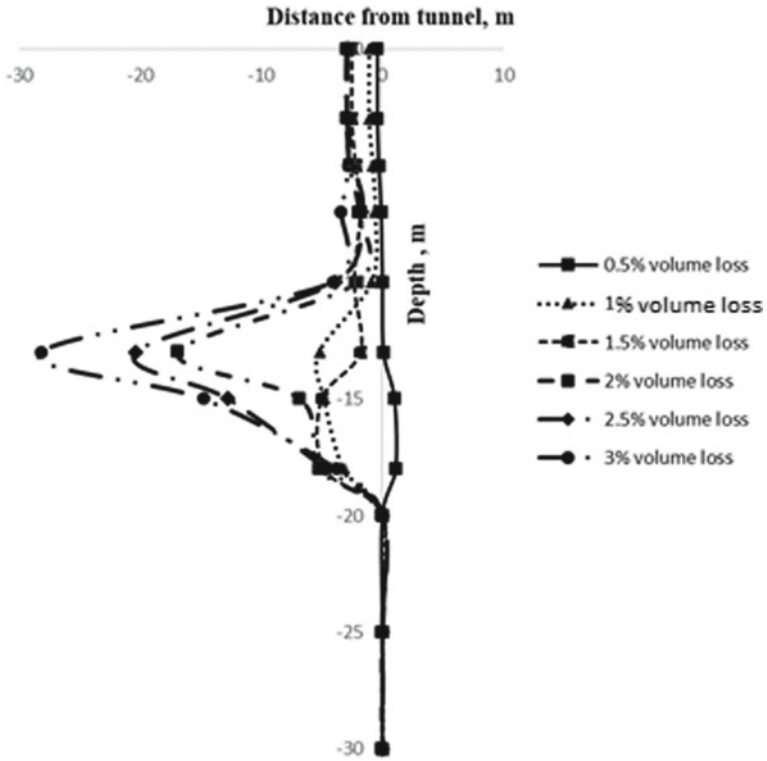
Fig. 6 Horizontal ground deformation for various volume losses
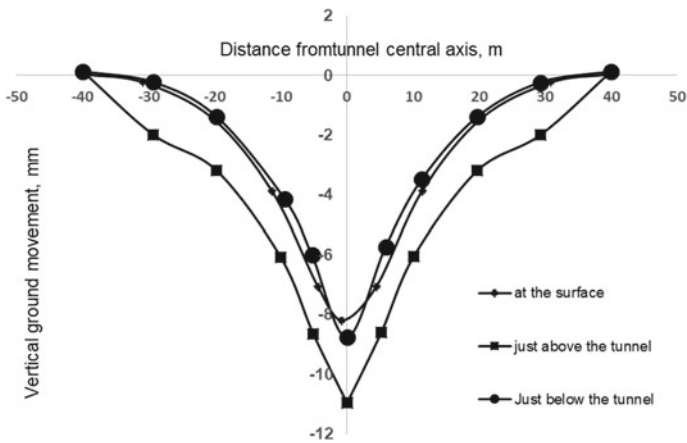
Fig. 7 Vertical ground deformation at various depths

Fig. 8 Variation of horizontal stress at ground level during the excavation in loose sand
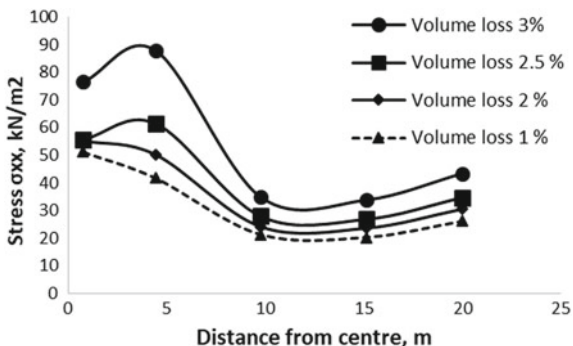
4.2 Effect of Tunnel Diameter

In order to study the effect of tunnel diameter on the ground movement, the C/D ratio of 2 and volume loss of 3 are being kept as constant and varied the diameter of the tunnel. Figures 9 and 10 show the vertical and horizontal ground deformations with respect to varying diameter of the tunnel. It could be seen from the figures that both vertical and horizontal ground movements are increasing with increase in diameter of the tunnel. It is also seen that the maximum vertical ground movement of 70 mm occurs for the tunnel diameter of 10 m. Figure 10 shows the horizontal ground deformations with respect to varying diameter of the tunnel. The inversion of the curve to attain a maximum value is just above the tunnel center, and it is evident that the horizontal deformations are positive values above the tunnel center axis and negative below it due to the volume lost due to excavation.
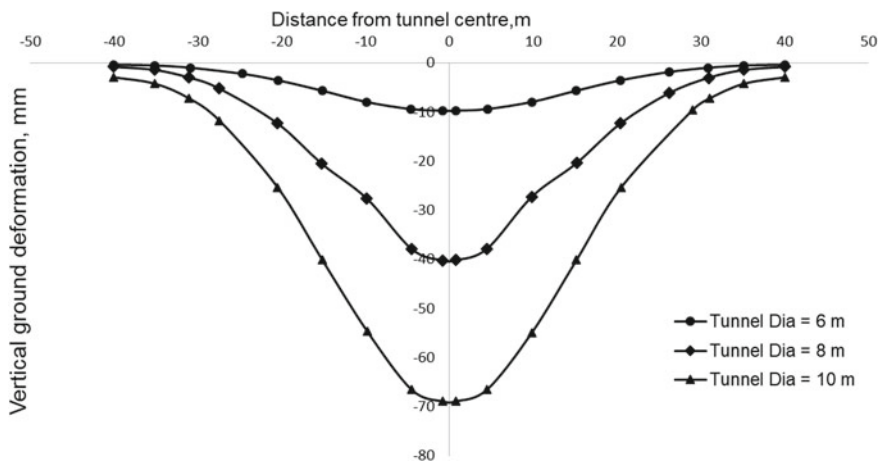
Fig. 9 Vertical ground movement for various tunnel diameters
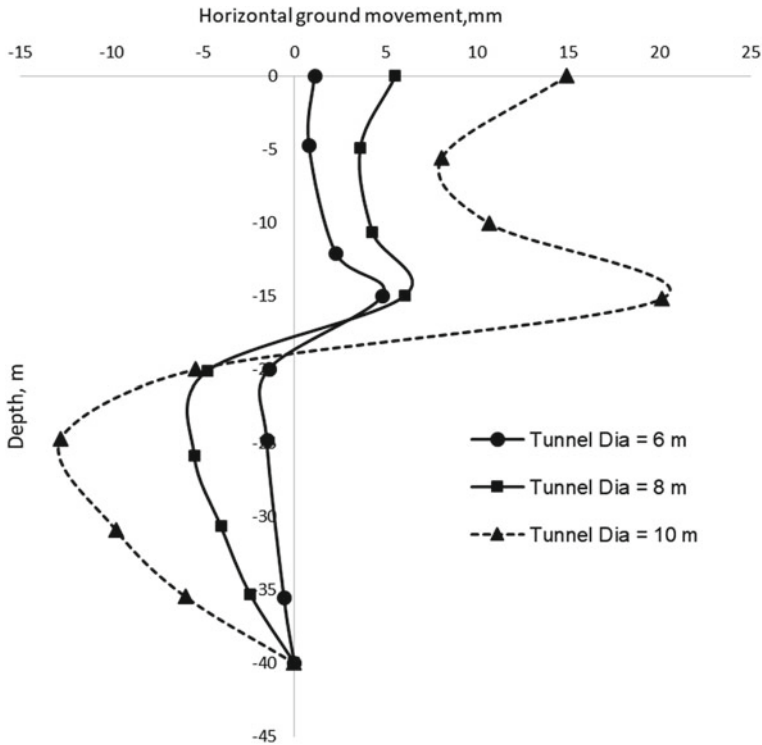
Fig. 10 Horizontal ground movement for various tunnel diameters

4.3 Stress and Strain Analysis

The horizontal stresses just above the tunnel with the distance from the center for various diameter of the tunnel were plotted. Figure 11 presents the variation of horizontal stress with the distance from tunnel center line with respect to varying diameter of the tunnel. Varying the tunnel diameter shows a significant change in the stress condition, with increase in distance up to at closer to the tunnel surface with decreasing of an increase in distance up to 10 m from the tunnel and beyond this almost becomes constant. Tunnel diameter of 6 m initially shows a higher value and beyond 10 m from tunnel center the value becomes almost constant. Horizontal stress, σ_{xx} slightly increases in the whole region above the bottom of the tunnel for tunnel diameter of 10 m. Deformation of soil shows the stress transfer function of the tunnel zone and the stability might tend to increase.

In order to further understand the effect of tunnelling on ground disturbance, the horizontal strain of distance from the tunnel surface was studied. Figure 12 shows the horizontal strain relative to the distance from the tunnel with respect to the varying diameter of the tunnel. The strain value observed from the figure indicates
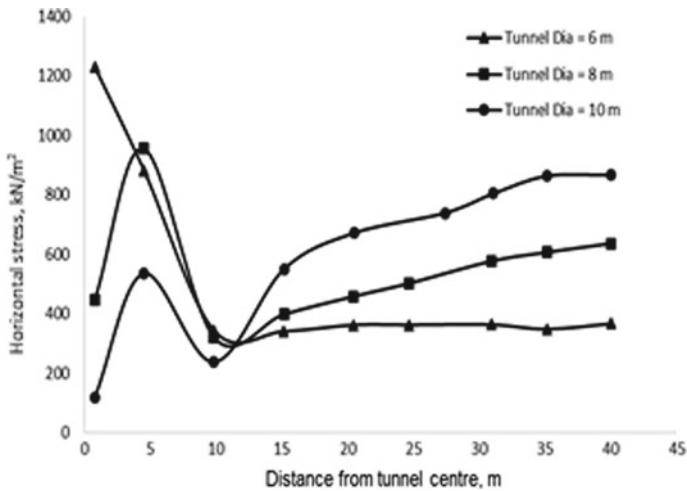
Fig. 11 Variation of horizontal stress for various tunnel diameter
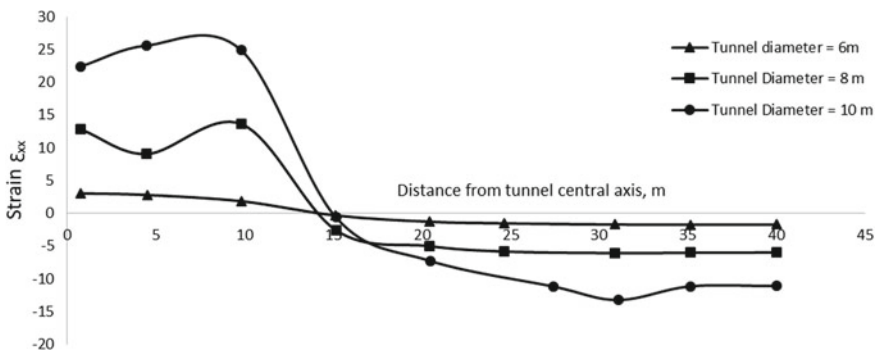
Fig. 12 Variation of horizontal strain for various tunnel diameters

that the soil adjacent to the tunnel is more strained up to the distance of 10 m with starts decreasing away from the distance up to 15 m and almost become constant beyond this distance. This allows us to understand that the problematic situations may arise when any structure is built within these zones. This trend is observed to be the same for all diameter of the tunnel. It is also observed that the soil is strained more for the tunnel diameter of 10 m. The effect of tunnelling on the soil strain for the tunnel diameter of 6 m and 8 m is minimal as compared to the tunnel diameter of 10 m.

Figures 13, 14, and 15 shows the major principal stress contour with respect to the varying tunnel diameters of 6 m, 8 m, and 10 m, respectively. The major principal stress contours showed that the concentration of stress closer to the tunnel
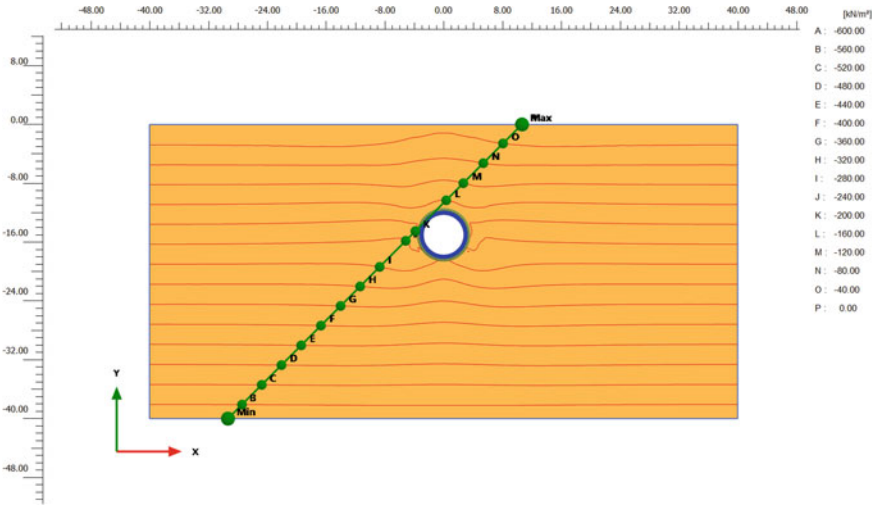
Fig. 13 Stress contour for tunnel diameter = 6 m
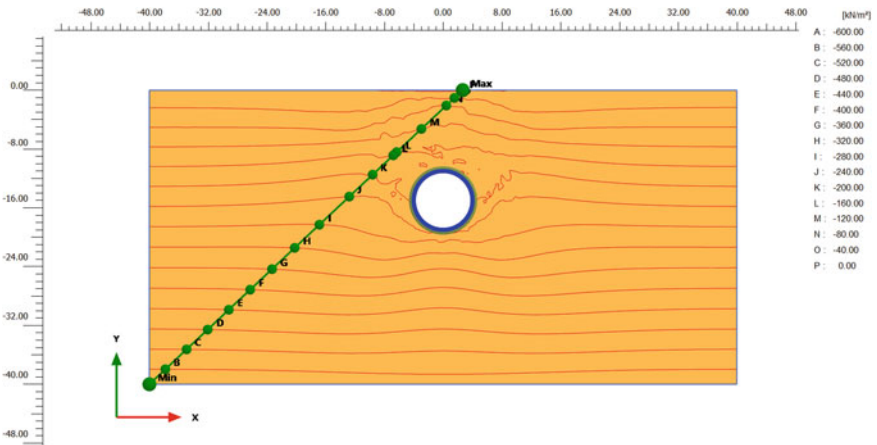
Fig. 14 Stress contour for tunnel diameter = 8 m

is more and decreasing with increase in distance from the tunnel. It could be seen from the figures that the stress concentration is less and the concentration of stress is almost closer to the tunnel in case of the tunnel diameter of 6 m. However, the stress concentration is more and expanding up to the larger distance in case of the tunnel diameter of 8 m and 10 m. This indicates that the stress concentration around the tunnel is increasing with increase in diameter of the tunnel. This trend is also conforming from the strain value as shown in Fig. 12.
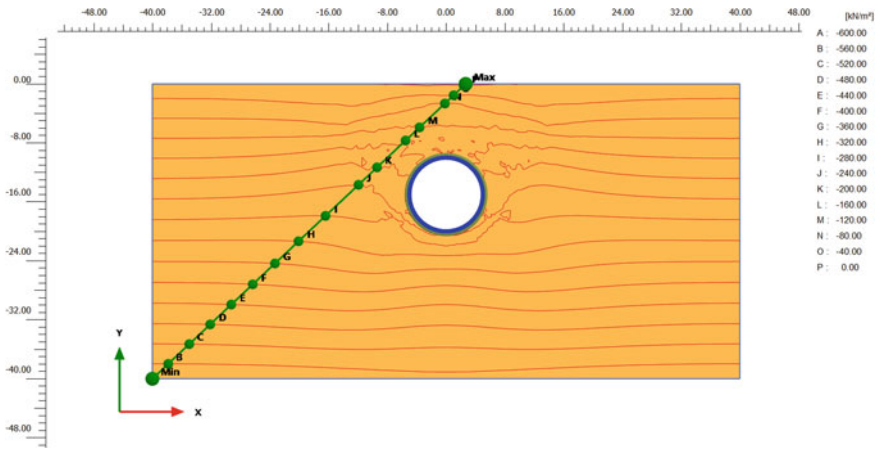
Fig. 15 Stress contour for tunnel diameter = 10 m
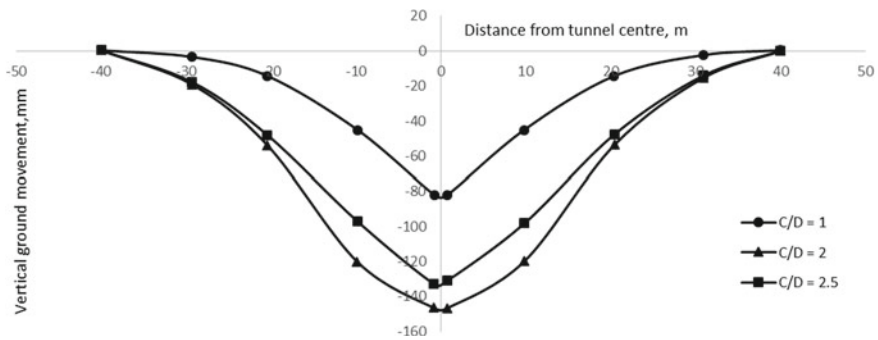
Fig. 16 Vertical ground movement for varying tunnel depth

4.4 Effect of Cover to Diameter Ratio

The cover 'C' with respect to tunnel diameter 'D' was varied for medium dense sand condition keeping all other parameters constant. C/D ratio was varied as 1, 2, and 2.5. Figure 16 shows the vertical ground movement variation with respect to the various C/D ratios. When the C/D ratio goes beyond 2, the settlement values obtained at the surface tend to attain a constant value and beyond which the depth is insignificant on the surface settlement.

5 Conclusion

This paper has presented the numerical results based on three-dimensional analysis performed on to study the response of the ground due to tunnelling in sands. Based on the results of 3D finite element idealization concerning the ground–tunnelling interaction, the following conclusions can be drawn:

1. The numerical modelling of ground–tunnel interaction analysis is very complex and needs to consider the details of tunnelling consequences, ground, lining, and grout behavior and the nature of interaction through different phases.
2. The ground condition is significantly altered due to tunnelling in medium dense sand condition. However, it depends on various factors such as the percentage of volume loss, diameter of the tunnel, and C/D ratios.
3. The vertical and horizontal ground movements in around the tunnel are increasing with increase in volume loss. This trend is significant up to the distance of 10 m from the tunnel and almost constant beyond this value.
4. The vertical ground movement for the volume loss of 3% is deeper but narrower as compared to that for other cases and the horizontal ground movement shows similar pattern for all the values of volume loss, with maximum just above the horizontal center axis of the tunnel.
5. The vertical and horizontal ground movements in around the tunnel are increasing with increase in diameter of the tunnel. However, ground movements are decreasing with increase in distance from the tunnel for the entire diameter considered in the analysis.
6. The concentration of stress and strain on the soil due to tunnelling is significant closer to the tunnel. It starts decreasing with increase in distance from the tunnel.
7. It is observed from the ground movement, stress, and strain that the ground condition may altered significantly up to the distance of almost 15 m from the tunnel in medium dense sand condition. This indicates that the existing and new structures found within this zone are to be designed carefully by considering the effect of tunnelling.

References

1. Melis, M.J., Rodriguez Otiz, J.M.: Consideration of the stiffness of buildings in the estimation of subsidence damage by EPB tunnelling in the Madrid subway. International Conference on the Response of Buildings to Excavation Induced Ground Movements, pp. 387–394 (CIRIA SP201)
2. Papastamos, G., Stiros, S., Saltogianni, V., Kontogianni, V.: 3-D strong tilting observed in tall, isolated brick chimneys during the excavation of the Athens Metro. Appl. Geomat. https://doi.org/10.1007/s12518-014-0138-8
3. Vorster, T.E., Klar, A., Soga, K., Mair, R.J.: Estimating the effects of tunneling on existing pipelines. J. Geotech. Geoenviron. Eng. 1399–1410 (2005)

4. Lee, C-J., Chiang, K-H., Kuo, C-M.: Ground movement and tunnel stability when tunnelling in sandy ground. J. Chin. Inst. Eng. **27**(7), 1021–1032 (2004). https://doi.org/10.1080/02533839.2004.9670957

5. Marshall, A.M., Klar, A.: Tunnels in sands: the effect of size, depth and volume loss on greenfield. Displacements. Géotechnique **62**(5), 385–399 (2012)

6. Chang, C.S., Yin, Z.Y., Hicher, P.Y.: Micromechanical analysis for interparticle and assembly instability of sand. J. Eng. Mech. **137**(3), 155–168 (2010)

7. Marshall, A.M., Farrell, R., Klar, A., Mair, R.: Tunnels in sands: the effect of size, depth and volume loss on greenfield displacements. Géotechnique, **62**(5), 385–399 (2012)

8. Mair, R.J., Taylor, R.N.: Theme lecture: bored tunnelling in the urban environment. In: 14th International Conference on soil Mechanics and Foundation Engineering, pp. 2353–2385. Balkema, Hamburg (1997)

9. Ahangari, K., Moeinossadat, S.R., Behnia, D.: Estimation of tunnelling-induced settlement by modern intelligent methods. 2015 The Japanese Geotechnical Society, Soils and Foundations, vol. 55, pp. 737–748 (2015)

10. Chen, R.P., Li, J., Kong, L.G., Tang, L.J.: Experimental study on face instability of shield tunnel in sand. Tunn. Undergr. Space Technol. **33**(1), 12–21 (2013)

11. Chen, R.P., Tang, L.J., Ling, D.S., Chen, Y.M.: Face stability analysis of shallow shield tunnels in dry sandy ground using the discrete element method. Comput. Geotech. **38**(2), 187–195 (2011)

12. Chen, R.P., Tang, L.J., Yin, X.S., Chen, Y.M., Bian, X.C.: An improved 3D wedge-prism model for the face stability analysis of the shield tunnel in cohesionless soils. Acta Geotech. **10**(5), 683–692 (2015)

13. Chen, R.P., Yin, X.S., Tang, L.J., Chen, Y.M.: Centrifugal model tests on face failure of earth pressure balance shield induced by steady state seepage in saturated sandy silt ground. Tunn. Undergr. Space Technol. **81**, 315–325 (2018)

14. Chiang, K.-H., Kuo, C.-M.: Ground movement and tunnel stability when tunneling in sandy ground. J. Chin. Inst. Eng. **27**(7), 1021–1032 (2011)

15. Chen, C.N., Huang, W.Y., Tseng, C.T.: Stress redistribution and ground arch development during tunnelling, Tunn. Undergr. Space Technol. **26**(1), 228–235 (2011)

16. Chen, R.P., Lin, X.T., Kang, X., Zhong, Z.Q., Liu, Y., Zhang, P., Wu, H.N.: Deformation and stress characteristics of existing twin tunnels induced by close-distance EPBS under-crossing. Tunn. Undergr. Space Technol. **82**, 468–481 (2018)

17. Al-Omari, R.R., Al-Soud, M.S., Al-Zuhairi, O.I.: Effect of Tunnel Progress on the Settlement of Existing Pile Foundation. Published by sciendo (2019)

18. Hong, Y., Soomro, M.A., Ng, C.W.W., Wang, L.Z., Yan, J.J., Li, B.: Tunnelling under pile groups and rafts: Numerical parametric study on tension effects. Comput. Geotech. **68**, 54–65 (2015)

19. Kohestani, V.R., Bazargan-Lari, M.R., Asgari-marnani, J.: Prediction of maximum surface settlement caused by earth pressure balance shield tunneling using random forest. J. AI Data Mining **5**(1), 127–135 (2017). https://doi.org/10.22044/jadm.2016.748

Dynamic Analysis of Soil Reinforced with Polypropylene Geotextile Using PLAXIS

Bhagya Baburajan, Surya Muthukumar, and Dhanya Sathyan

1 Introduction

The machine base provides a robust mechanical platform for efficient and reliable operation. Vendors continue to improve the efficiency and effectiveness of their machine by increasing machine size and speed. On the contrary, to minimize or control vibration in advanced equipment, the requirements for vibration control can be very strong due to the strict specification of the advanced equipment. As a result, modern mechanical foundations are required to withstand high power forces with high operating speed while vibrating control. Unexpected vibrations can have detrimental influence on equipment parts, structural integrity, other equipment or personnel working near it, and foundation repairs. Uncontrollable excessive vibration may force the machine to shut down, leading to catastrophic event resulting in fatigue failure in parts of the machine. Therefore, an important step taken to ensure safety of the machine and operation is a strong analysis of the machine base.

Machine foundations are special types of foundations required for machinery, equipment and heavy equipment with high speed, loads, and working conditions. The foundations of the machine are under the dynamic force of the machine. This dynamic force is transmitted to the base that supports the machine. Although the moving parts of a machine are generally balanced, there are always inequalities in the working sector that cause variations in rotating parts. The machine base must meet the requirements for more powerful loading and unloading. At the base of the machine, the heavy load is used repeatedly for a very long duration. But if its size is small, then the soil structure would become stretchy. Else, the deformity will go higher with each loading cycle. The machine has some operating frequency. Therefore, knowing magnitude of the vibration of its operating frequency is the

B. Baburajan · S. Muthukumar (✉) · D. Sathyan
Department of Civil Engineering, Amrita School of Engineering, Coimbatore,
Amrita Vishwa Vidyapeetham, India
e-mail: m_surya@cb.amrita.edu

crucial parameter that has to be determined in the construction of the machine base, in addition to the natural frequency of the ground.

The use of geosynthetics as reinforcing elements can improve the engineering properties of soil to a large extent [1]. Soil by itself can carry only shear and compressive forces. Geosynthetic reinforcing elements makes it possible for the soil to carry tensile forces as well. There are three methods of reinforcement namely shear or sliding, anchorage, and membrane. These methods relate to different actions of reinforcing element to support different types of load supported by geosynthetics. The optimized design of structures along with the use of geosynthetic reinforcement elements can bring down the cost of construction to a notable level. Apart from this, many researches have been carries out to understand the benefits of using geosynthetics in soil for reinforcement [2–4]. The safety factor of geotextiles also has to be considered while selecting the geotextile for a particular work, since this influences the strength of a geotextile strongly [5]. For the present study, a polypropylene geotextile is been used to improve the dynamic behavior of soil underlain by a machine foundation.

In literature, various studies on the improvement on dynamic behavior of soil were encountered. The effects of the incorporation of polypropylene fiber into the dynamic behavior of sandy loam soils and the subsequent result in the difference in shear modulus values and the deviation values by shear deformation were calculated to take into account the effects of fiber length and input rate [6]. In another study, a feedback of reinforced geocell beds given by mechanical vibrations was studied using four different geomaterials. The results obtained from the study enabled to understand the influence of optimum depth and width of placement of the geomaterial [7].

Also, in literature, a number of researchers focused on the improvement in the engineering properties of soil by using natural and semi-natural geomaterials such as coir cell networks, jute, and sisal geocells as alternative to a synthetic geocell [8–10]. Also, studies were conducted to understand the behavior soil reinforced with geocells, in taking the vibrations induced by industrial machines [11]. In another study, few researchers looked into the ability of geosynthetics in changing the soil profile to handle the amplitude of machine vibration [12–14].

From the various literature, it is found that geocell reinforcement with jute geocells is effective solution for improving the bearing capacity and the settlement behavior of soil [8, 15]. Also, use of geocell developed from sisal mat can improve the tensile strength of soil [10]. Apart from choices offered by these geosynthetic reinforcing materials, various other alternatives could also be used.

2 Method

Geotechnical structures under severe stress generated by earthquakes, mechanical movements or vehicle loads require intensive analysis to evaluate their responses and reduce hazards. The base of the machine must withstand fixed and strong loads.

The base will be designed heavier compared to the weight of the machine to withstand the heavy load. A strong load with a small size that works repeatedly over a large period of time results in a continuous transformation of the supporting soil. To counteract this, the soil must be made strong enough to stand against the continuous repeated heavy load.

In this study, numerical analysis to simulate the cyclic plate load test performed in laboratory was done using a finite element software, PLAXIS, with which it is easy to simulate soil connections. Interface elements in PLAXIS helps to simulate interaction between soil and the structure by creating node pairs at the interface of soil and the structure. Thus, each node in a node pair takes care of gap displacement and slip displacement.

2.1 Materials

This section explains the properties of various materials selected for the study.

Soil classification
The soil compounds used in this study were river sand and were classified as sparse sand (SP) from the graph shown in Fig. 1. The various characteristics of sand were identified by laboratory tests and listed in Table 1.

Polypropylene geotextile
The polypropylene geotextile material required for this work have Young's modulus of 1325 kN/m^2. Other advantages of using this material were that it shows good durability and moderate impact even at low temperatures, ESCR (environmental resistance), and optimized application for a wide range of applications.
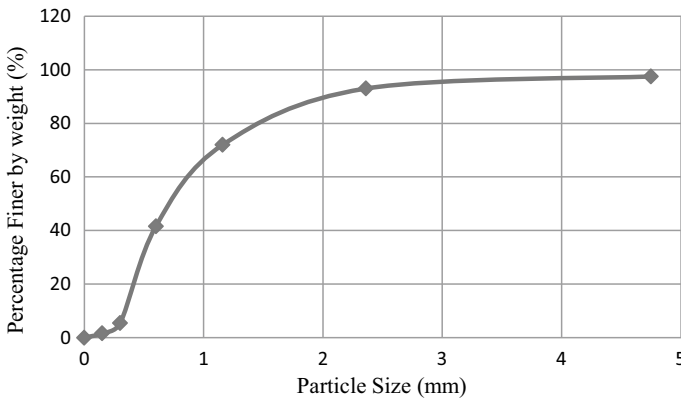
Fig. 1 Grain size distribution of soil

Table 1 Sand properties

Parameters	Value
Soil classification	Poorly graded sand
Unsaturated unit weight	17.13 kN/m^3
Saturated unit weight	20.405 kN/m^3
Permeability horizontal and vertical	2.55×10^{-5} m/s
Poisson's ratio	0.3
Young's modulus	25 MPa
Cohesion	0.04 kg/cm^2
Friction angle	38°

2.2 Numerical Analysis

The cyclic plate load test was simulated using PLAXIS. Numerical analysis used 15 nodded triangular elements for interpolation. The laboratory test modeling using the software package, PLAXIS, is only a little time consuming with a user-friendly environment, and it evaluates the model considering the soil–geotextile interaction as well as the boundary conditions [16, 17].

Scale effect
The physical model of plate load test is to be carried out in a large (near full-scale) system of tank dimensions (inside dimensions) of 500 mm × 500 mm. Boundary conditions, particle size, and side friction do not have a noteworthy effect reflected on the results obtained from laboratory model, since the dimensions of the container and its side walls are smooth [18]. Therefore, in numerical analysis, modeling at full scale was performed to consider the real laboratory experimental instrument's dimensions, the real layout, and geometry. Also, the boundary conditions can be easily simulated along with materials sets and loading conditions.

Materials modeling and mesh data
Soil characteristics used in the model were γ_{unsat} and γ_{sat} weights of soil units, Young modulus, E; internal friction angle, ϕ; cohesion, c; and poisson's ratio, v. Model data obtained in ground-based computation and visual interface is based on a mid-range machine, 15 node wedge elements resulting in 690 items, 3355 nodes, and 4140 stress points. Simulation of geotextile reinforcement was done using the geogrid material option combined with PLAXIS [19]. A polypropylene geosynthetic reinforcement is provided at an optimum depth and width, studied from literature.

Considering the specific problem, explicit weights and axisymmetric conditions were used, because it is a vibration problem of one source. The waves emanating from the source by the axisymmetric model are dispersed in a manner similar to the 3D case. The geometric model is shown in Fig. 2a. Therefore, a Rayleigh damping coefficient that takes care of the visible effects, plastic, or collision should not be used here.

Arrangements to avoid deceptive vibrations, which actually do not occur in a real case scenario, should be given special border conditions. The suction limits were given an order to absorb the waves that reach the limits. This system of boundaries is given taking into account the fact that the soil is actually a medium to infinite scale. The shared load system B was used to mimic heavy loads, and another load system A was used to simulate a dead load on the footing. The dynamic loads system was set to load system B in loads menu. To ensure proper contact exists between soil grain, footing, and geotextile, a roughness interaction factor had to be modeled. A strength reduction factor of 0.85 was given at the interface of soil and geotextile and 1 at the interface of soil and steel footing plate [19, 20].

Due to the high pressure under the footing, the meshing below the footing line is repeated twice. Mesh is generated by distributing coarse elements in the global coarseness option from the mesh menu. Figure 2b shows a mesh made of both models (excluding and geotextile). Since, the sand is in dry state, the generation of water pressure can be skipped. Initial stresses (Fig. 2c) are set using default K_0 procedure where K_0 equals to (1-sinϕ).

3 Results and Discussions

PLAXIS 2D 8.6 displays the deformed shape of the mesh and deformed value to a particular scale after running the analysis. The deformed shapes of the mesh along with few other relevant displacements and deformations for both models (with and without using geotextile) are depicted in the following figures in this section. This gives a picture on the improvement on dynamic behavior of soil on incorporation of geotextile in the sand below machine foundation.

3.1 Deformed Mesh

Deformed mesh depicts the plot of finite element mesh in deformed shape. Figure 3 shows the deformed shape in true scale. Maximum value of the deformation came out to be 16.32×10^{-3} m and 6.94×10^{-3} m for the model without and with geotextile, respectively.

3.2 Total, Horizontal, and Vertical Displacement

Finite element analysis in PLAXIS enables to visualize the displacements in horizontal (x) and (y) direction, as well as the total displacements at every node in the end of each step of calculation. In this section, the output taken at the final step of
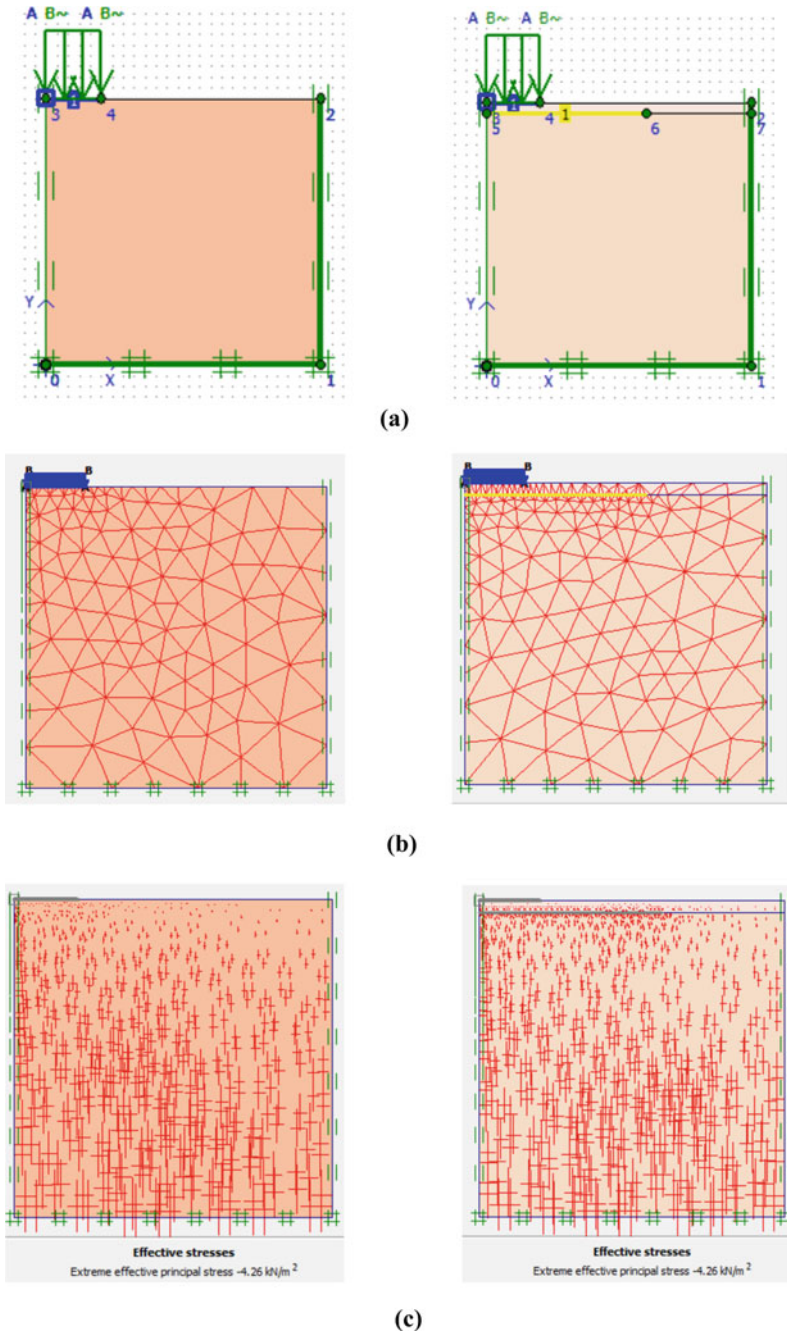
Fig. 2 **a** Simulation of load setup, **b** generated mesh, and **c** effective stress developed on the models with and without usage of geotextile
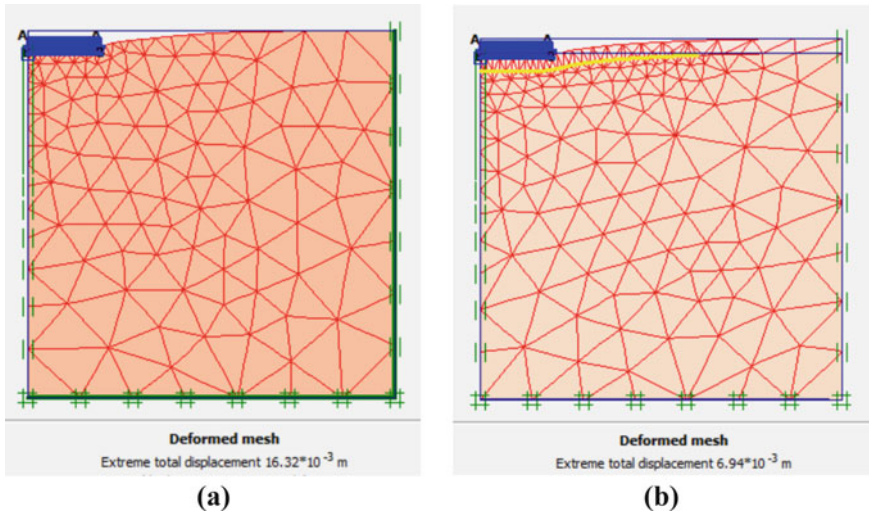
Fig. 3 Deformed shape of the model **a** without and **b** with geotextile

calculation is shown. Figure 4a, b depicts the accumulated deformation components in horizontal (U_x) and vertical (U_y) directions, and the extreme displacement values came out to be 1.83×10^{-3} m and 16.32×10^{-3} m for the model without geotextile and 769.51×10^{-6} m and 6.94×10^{-3} m for the model with geotextile. The value of absolute accumulated displacements or extreme total displacement (Fig. 4c) is the value combined from horizontal and vertical displacement (Table 2).

3.3 Total and Incremental Strains

Total and incremental strains represented in principle strain directions are shown in Fig. 5. Since the modeling was done using 15 node elements, three stress points were displayed for each element. The magnitude of total principal strain in the model with geotextile is higher than that without using geotextile, and it came out to be tensile and compressive for the model without and with geotextile, respectively. On the other hand, when incremental strain is considered, the magnitudes of principle strains are almost similar for both the models (Table 3).

(a)

(b)

(c)
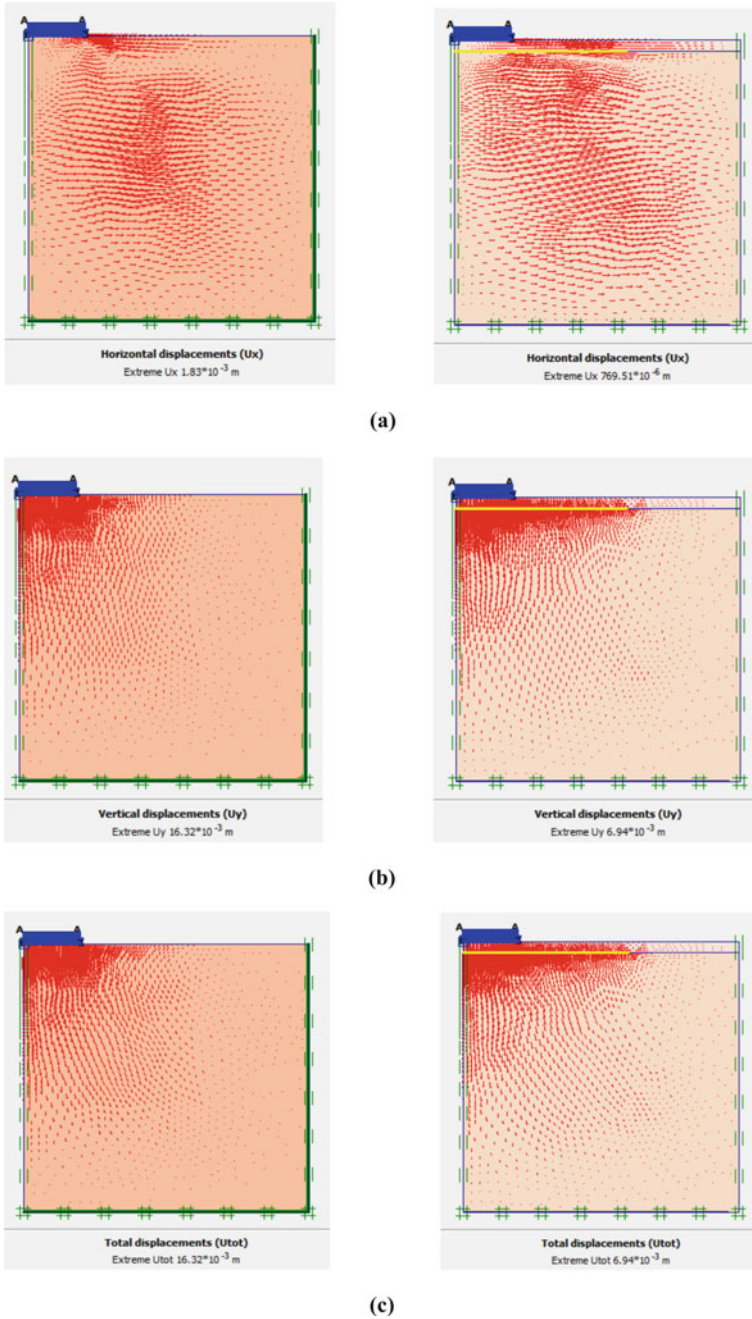
Fig. 4 **a** Horizontal, **b** vertical, and **c** total displacements for the models without and with usage of geotextile

Table 2 Extreme values of displacements obtained from PLAXIS

Parameter	Value for unreinforced sand	Value for reinforced sand
Total displacement	16.32×10^{-3} m	6.94×10^{-3} m
Horizontal displacement	1.83×10^{-3} m	769.51×10^{-6} m
Vertical displacement	16.32×10^{-3} m	6.94×10^{-3} m
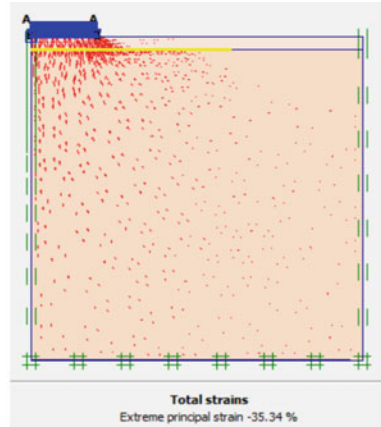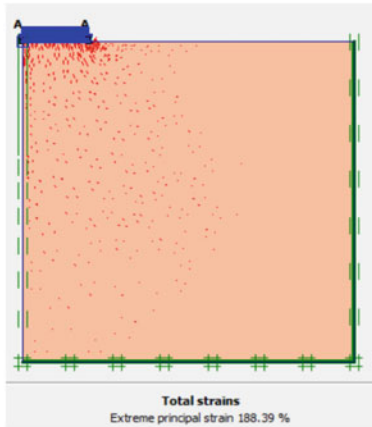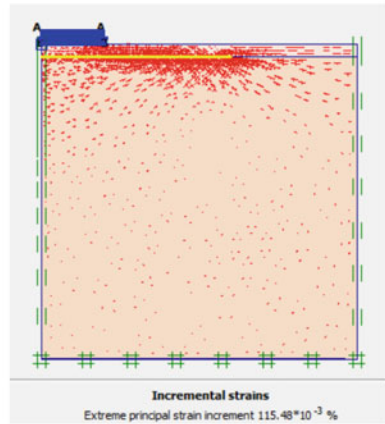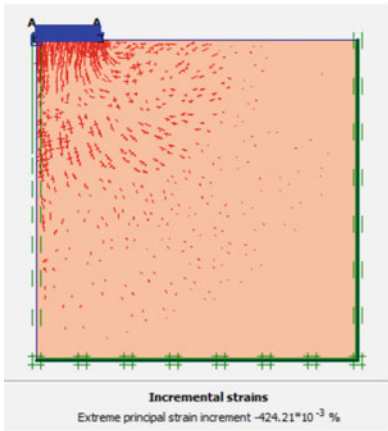
Fig. 5 a Total and **b** incremental strains represented as principal strains for the models without and with usage of geotextile

Table 3 Extreme values of principal strains obtained from PLAXIS

Parameter	Value for unreinforced sand	Value for reinforced sand
Total strain	188.39%	−35.34%
Incremental strain	$-424.21 \times 10^{-3}\%$	$10^{-3}\%$

4   Conclusions

Soil structures are weak in tension and can carry only compressive and shear forces by its own. From this numerical study, it is found that the soil structures that are intended to carry dynamic forces from systems like machine foundation can be made strong with the incorporation of a polypropylene geotextile. This study presents a significant solution concerning the cost-effectiveness in relation to the area required to build a machine foundation.

From the above results, the following conclusions can be made.

1. The percentage improvement in total, horizontal, and vertical displacements were found to be 57.47%, 57.95%, and 57.47%, respectively.
2. The total strain in terms of extreme principal strain showed a considerable improvement in the behavior of soil in handling the tensile forces.
3. The accumulated incremental strain near the area of geotextile placement reveals that this area is very crucial in handling the dynamic loads. The soil in this area can be further improved with the help of other soil improvement techniques that use geosynthetic materials. The incremental strains could be handled by the newly incorporated geosynthetic reinforcement like geocell.

References

1. Heerten, G., Klompmaker, J.: Improving the bearing capacity of soils with geosynthetics. In: 8th International Geotechnical Conference. Bratislava, Slovakia (2007)
2. Shukla, S.K., Sivakugan, N., Singh, A.K.: Analytical model for fiber-reinforced granular soils under high confining stresses. J. Mater. Civ. Eng. **22**(9), 935–942 (2010)
3. Hegde, A., Venkateswarlu, H.: Mitigation of traffic induced vibration using Geocell inclusions. Front. Built Environ. **5**, 136 (2019)
4. Mehdipour, I., Ghazavi, M., Moayed, R.Z.: Numerical study on stability analysis of geocell reinforced slopes by considering the bending effect. Geotext. Geomembr. **37**, 23–34 (2013)
5. Wulandari, P.S., Tjandra, D.: Analysis of geotextile reinforced road embankment using PLAXIS 2D. Doctoral dissertation, Petra Christian University
6. Bozyigit, I., Tanrınıan, N., Karakan, E., Sezer, A., Erdoğan, D., Altun, S.: Dynamic behavior of a clayey sand reinforced with polypropylene fiber. Acta Phys. Pol., A **132**(3), 674–678 (2017)
7. Venkateswarlu, H., Hegde, A.: Factors influencing dynamic response of geocell reinforced soil beds. In: Geo-Congress 2020: Engineering, Monitoring, and Management of Geotechnical Infrastructure, pp. 569–578. American Society of Civil Engineers, Reston, VA (2020)

8. Muthukumar, S., Sakthivelu, A., Shanmugasundaram, K., Mahendran, N.: Performance assessment of square footing on Jute Geocell—reinforced sand. Int. J. Geosynth. Gr. Eng. **8** (2019)
9. Kolathayar, S., Narasimhan, S., Kamaludeen, R., Sitharam, T.G.: Performance of footing on clay bed reinforced with coir cell networks. Int. J. Geomech. **20**(8), 04020106 (2020)
10. Kolathayar, S., Sowmya, S., Priyanka, E.: Comparative study for performance of soil bed reinforced with Jute and Sisal Geocells as alternatives to HDPE geocells. Int. J. Geosynthetics Ground Eng. **6**(4), 1–8 (2020)
11. Haldar, S., Sivakumar Babu, G.L.: Improvement of machine foundations using reinforcement. Proc. Instit. Civil Eng. Ground Improve. **162**, 199–204 (2009). https://doi.org/10.1680/grim.2009.162.4.199
12. Baidya, D.K., Rathi, A.: Dynamic response of footings resting on a sand layer of finite thickness. J. Geotech. Geoenviron. Eng. **130**(6), 651–655 (2004)
13. Baidya, D.K., Muralikrishna, G., Pradhan, P.K.: Investigation of foundation vibrations resting on a layered soil system. J. Geotech. Geoenviron. Eng. **132**(1), 116–123 (2006)
14. Mandal, A., Baidya, D.K., Roy, D.: Dynamic response of the foundations resting on a two-layered soil underlain by a rigid layer. Geotech. Geol. Eng. **30**(4), 775–786 (2012)
15. Kolathayar, S., Suja, P., Nair, V., Krishna, S., Tamilarasi, G.: Performance evaluation of seashell and sand as infill materials in HDPE and coir geocells. Innovative Infrastruct. Solutions **4**(1), 17 (2019)
16. Sieira, A.C.F.: Pullout behavior of geotextiles: numerical prediction. Int. J. Eng. Res. Appl **6** (11–4), 15–18 (2016)
17. PLAXIS: Plaxis materials model manual. Delft, The Netherlands. Plaxis bv (2011)
18. Bransby, P.L., Smith, I.A.: Side friction in model retaining-wall experiments. J. Geotechn. Geoenviron. Eng. **101**(ASCE# 11447 Proceeding) (1975)
19. Touahmia, M., Rouili, A., Boukendakdji, M., Achour, B.: Experimental and numerical analysis of geogrid-reinforced soil systems. Arab. J. Sci. Eng. **43**(10), 5295–5303 (2018)
20. Gamal, A.M., Belal, A.M., Elsoud, S.A.: Numerical Modeling of Geogrid Reinforced Soil Bed under Strip Footings using Finite Element Analysis

Numerical Analysis of Soil Nailed Vertical Wall Using PLAXIS

P. S. Sreedevi, Surya Muthukumar, and Dhanya Sathyan

1 Introduction

One of the most fundamental problem occurring during design and construction of various geotechnical structures like retaining walls, existing fill slopes, and embankment is slope stability [1]. The failure of these types of slopes can occur due to many reasons. The main reason behind slope instability is due to static loading, dynamic loading, and improper design consideration [2–4]. This leads to introduction of new technologies to minimize the failure mechanism. For this, it is necessary to know and study the characteristics and stability of soil slopes before design and construction [5]. Soil nailing is one of the most important ground improvement technique, which is focused on Improving and achieving stability on soil slopes. Soil nailing found to be an economical and most stable method when compared to other earth retaining walls [6]. The methodology of soil nailing, which includes different types of steel bars or metal bars that are reinforced with the ground surface, i.e., generally termed as nails that are placed in the drilled holes for establishing stability [7]. The main idea behind soil nailing is that the soil nails provide resistance to wall deformation and reduce the risk of global slope stability failure mainly through mobilization of shear stresses along the soil interface. The application of soil nail wall is to limit distortion of the slope and make sure adequate safety factor against sliding, bearing, and global instability [8]. The main components to be considered for determining soil nail wall is first, and the condition of the ground and stability of the soil surface layers are to be analyzed. Further the cost and benefits for a soil nail wall system shall be evaluated based on the design

P. S. Sreedevi · S. Muthukumar (✉) · D. Sathyan
Department of Civil Engineering, Amrita School of Engineering, Coimbatore,
Amrita Vishwa Vidyapeetham, India
e-mail: m_surya@cb.amrita.edu

conditions [9]. While designing soil nail, wall the nail elements have greater importance, because if any displacements occur in the soil surface due to various types of static, dynamic loads, the nail elements resist the displacement and movement and provide better stability [10].

The soil nails show good stability and efficiency on static and dynamic conditions [11]. The slope stability analysis of soil nail walls is conventionally studied and analyzed using finite element method, and this analysis has been highly recommended suitable for performing stability calculations [12, 13]. By using finite element method, the analysis can provide the possible interaction between the soil and nails and other various parameters which has greater impact on soil stability. In FEM, the main system is to analyze and stimulate an elastic behavior of the material [14]. In order to carry out the FEM, a numerical simulation software named as PLAXIS 2D is followed in this study. PLAXIS 2D provides various advanced material models by involving specific features and parametric optimization. The efficiency and reliability of the analysis is significantly high when compared to other conventional software. Moreover, PLAXIS is less complex and time efficient for the purpose of analysis [15, 16]. In this paper, static analysis approach is implemented to analyze the characteristic behavior and to determine the soil nail wall stability in a vertical excavation. In this approach, various procedures have been applied and developed, by considering the entire soil nailed mass as a composite failure surface. Compared to other types, composite soil nailing wall is a widely accepted technology which is stronger and more stable [17]. A numerical analysis is executed using FEM to study the behavior of soil nail wall under static load conditions [18, 19]. The main advantages of finite element approach are to study and analyze the stress deformation, the failure zone in the actual site condition. Numerical modeling of nailed slopes under finite element method has substantiate high accuracy in achieving slope stability [20]. The approach of analysis and the numerical stimulations of modeling were studied and analyzed using PLAXIS. It is a numerical stimulation software, which is used to design and manipulate soil nail walls. The analysis is carried out for 0.5 m height vertical excavation. By including other parameters, the soil nail wall modeled and analyzed.

2 Materials

2.1 Sand

In this study, sand excavation was considered. The properties of sand used in this study are given in Table 1.

Table 1 Properties adopted for numerical simulations using PLAXIS 2D simulation

Properties	Values
Material model	Mohr–Coulomb
Drainage type	Drained
Cohesion (c)	0.04 kg/cm^2
Internal friction angle (ϕ)	38°
Unit weight (Υ)	17 kN/m^3
Poisson's ratio (V_s)	0.3
Stiffness (E_{ref})	35,000 kN/m^2
Elastic modulus E_s (MPa)	20 MPa

2.2 Nails

In order to achieve high-quality soil nails, the selection of appropriate soil nails has great role in it. By selecting suitable nail components, durability and efficiency of the soil nail wall system increase. Soil nail and soil surface layers act together like a rigid compound which improves the strength of the soil surface.

3 Modeling and Analysis

The simulation and modeling of soil nail wall under static condition is studied and analyzed using PLAXIS 2D (version 8.2). Numerical modeling is carried out using plane strain mode. The fifteen node triangular element is used for finite element discretization [15]. The Mohr–Coulomb model is used to model soil, and for nails along with facing element, an elastic model is used. Plate elements were used to model nails and facing elements [16]. Horizontal fixity is provided, since soil continuous on both sides. The deformed soil models with soil nails is shown in Fig. 1. The design parameters used for the soil nail modeling is given in Tables 2 and 3.

4 Results and Discussion

As a result of analysis, the deformed shape of the mesh and the deformed value of the particular mesh have been generated using PLAXIS 8.2. In this section, the deformed shape of the mesh, displacements, and stresses for both the models (with nails and without nails) are shown in the following figures. This shows the soil stability improvement under static load condition by using the grouted nails.
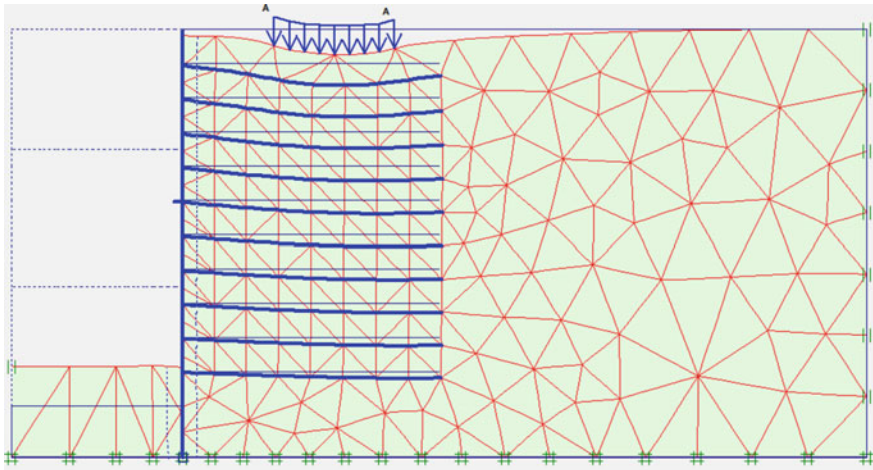
Fig. 1 Numerical stimulated soil nail wall

Table 2 Design parameters used for modeling

Parameters	Values
Height of the soil nail wall	0.5 m
Length of the soil nail wall	1 m
Vertical nail spacing (S_v)	0.04 m
Horizontal nail spacing (S_h)	0.04 m
Diameter of soil nail	10 mm
Length/Height (L/H)	0.8
S_v/H	0.08
Range of horizontal acceleration (g)	0.5 g
Number of nails	10

Table 3 Material properties for soil nail wall

Parameters	Grouted nail	Facing element	Unit
Axial stiffness (EA)	2.229×10^3	2.280×10^6	kN/m
Bending stiffness (EI)	1.239×10^2	1.420×10^5	kNm^2/m

4.1 Deformed Mesh

A composition of finite elements generates a mesh. In this study, basic type of element used in a mesh is 15 noded triangular element. Figure 2 shows deformed mesh in true scale. The value for deformation came to be 9.43×10^{-6} m and 10.77×10^{-6} m for the model with nails and without nails, respectively.

Deformed mesh	Deformed mesh
Extreme total displacement 9.43×10⁻⁶ m	Extreme total displacement 10.77×10⁻⁶ m
(a)	(b)
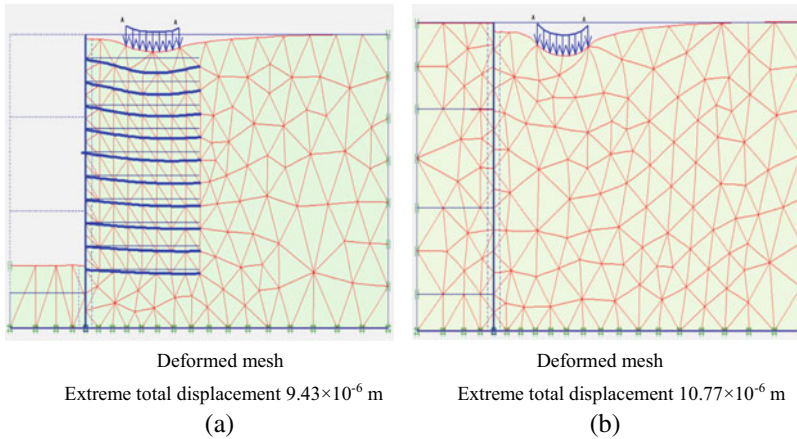
Fig. 2 Deformed shape of model **a** with nails and **b** without nails

4.2 Model Displacement

The variation of horizontal, vertical, and total displacement in a nailed slope under static load is represented below. In PLAXIS, the axisymmetric model coordination system represents the horizontal displacement in x-direction and vertical displacement in y-direction. Horizontal displacement and vertical displacement are denoted by U_x and U_y. The extreme deformation value came to be 1.51×10^{-6} m and 9.43×10^{-6} m for the model with the nails and 2.74×10^{-6} m and 10.72×10^{-6} m without nails [a, b]. The value of extreme total displacement is obtained from both horizontal and vertical displacements [c] (Fig. 3).

4.3 Effective and Mean Stresses

The effective stress and mean stress represented in principal stress direction are shown in Figs. 4 and 5. The magnitude of effective principal stress in model with nails is higher than that of without nails. The extreme effective principal stress with nails is -9.06 kN/m^2 and for without nails -8.85 kN/m^2. The effective stress of soil nail wall in vertical excavation increases from top to bottom. On the other hand, when the magnitude of the extreme mean stresses is almost similar in both cases. According to the stress zone value, the extreme mean stress value which is shown in red color is occurred at the bottom portion of the vertical cut.

Horizontal displacement (U_x)

Extreme U_x 1.5×10^{-6}

(a)

Horizontal displacement (U_x)

Extreme U_x 2.74×10^{-6} m

Vertical displacement (U_y)

Extreme U_y 9.43×10^{-6} m

(b)

Vertical displacement (U_y)

Extreme U_y 10.72×10^{-6} m

Total displacement (u_{tot})

Extreme u_{tot} 9.43×10^{-6} m

(c)

Total displacement (u_{tot})

Extreme u_{tot} 10.77×10^{-6} m
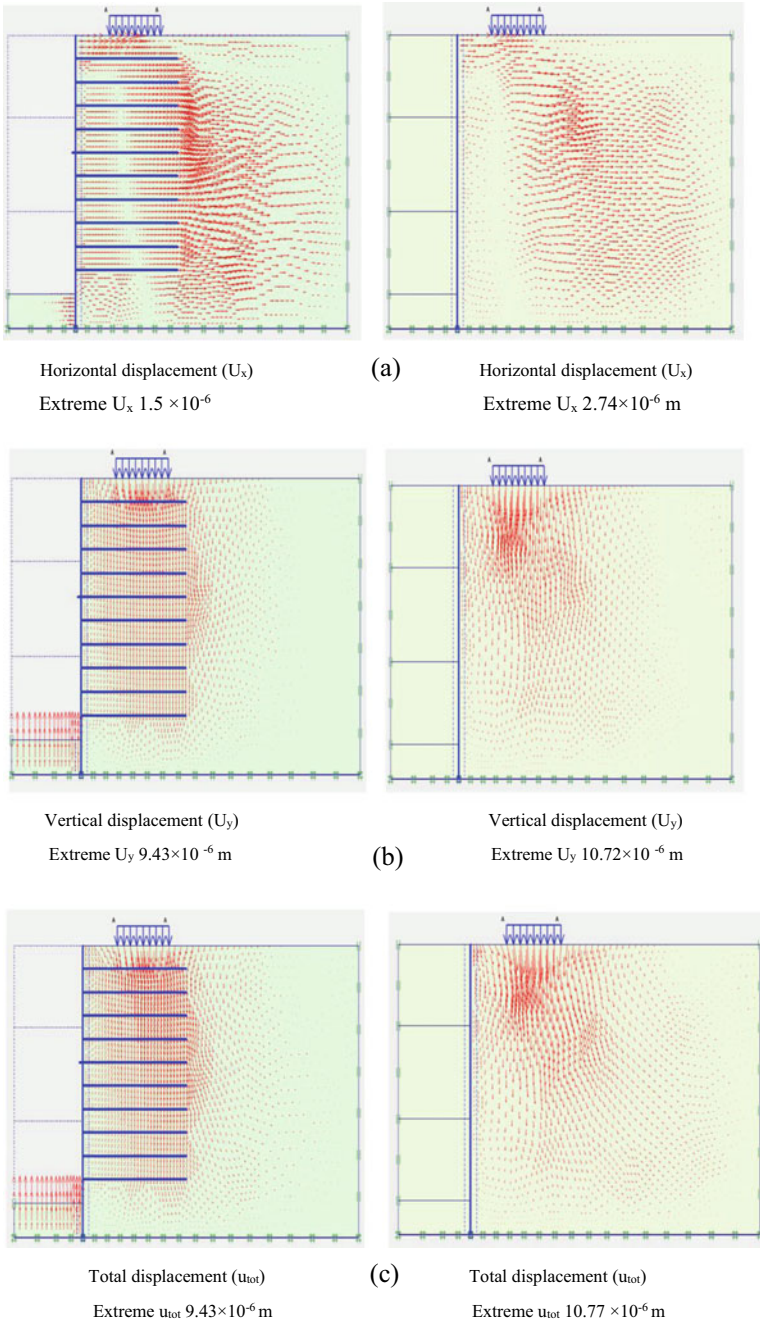
Fig. 3 **a** Horizontal, **b** vertical, and **c** total displacements for the models with and without the usage of nails

Effective stresses

Effective stresses

Extreme effective principal stresses -9.06 kN/m²

Extreme effective principal stresses -8.85 kN/m²
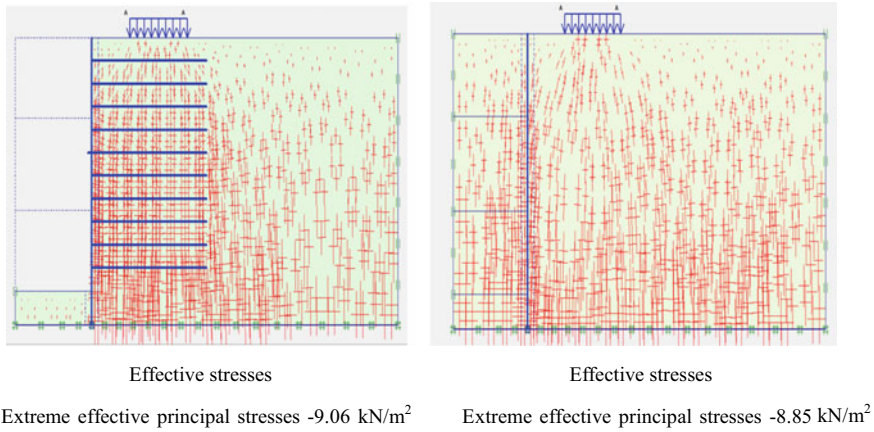
Fig. 4 Effective stresses with nails and without nails

Mean stress

Mean stress

Extreme mean stress -5.38 kN/m²

Extreme mean stress -5.26 kN/m²
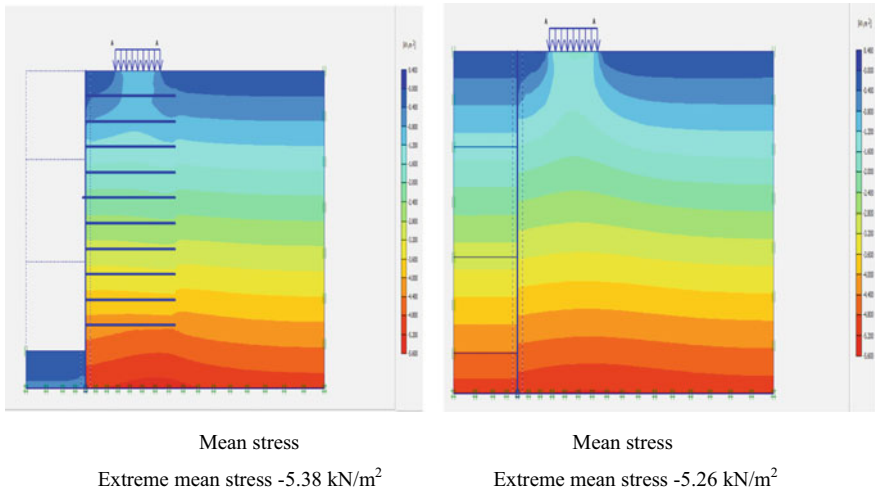
Fig. 5 Mean stress with nails and without nails

5 Conclusions

As a result of studies implemented in this paper, the conclusions made are written as follows.

1. In this paper, static analysis methodology is carried out to analyze and determine the stability of soil nails in a vertical excavation, assuming the failure surface to be composite. After analyzing obtained outputs, it is found that static analysis

approach using finite element method is more reasonable and effective compared to other conventional methods.

2. From static analysis, the vertical and horizontal displacement of soil nail wall in a vertical excavation is 9.43×10^{-6} m and 1.5×10^{-6} m in case of with nails, similarly 10.72×10^{-6} m and 2.74×10^{-6} m for without nails. Analyzing the result obtained from static approach, it can be found that the horizontal displacement and vertical displacement without nails is significantly higher than with nails. So it is clearly evident that the inclusion of nails provides better stability.

3. The magnitude of total displacement with nails is 1.34×10^{-6} m lesser than when compared to without nails. The net value of effective stress and mean stress with nails significantly increases when compared to without nails.

4. Therefore, it can be concluded that using static analysis approach, the entire stability of the soil nail wall increases when nails are grouted rather than without using nails.

References

1. Panah, M.Y.K., Sadeghzadegan, R.: Evaluation of pseudo static coefficient for soil nailed walls on the basis of seismic behavior levels. Res. J. Recent Sci. **3**(11), 6–16 (2014)
2. Ann, T.S., Cheang, W., Hai, O.P., Tan, D.: Finite element analysis of a soil nailed slope-some recent experience. In: 3rd Asian Regional Conference on Geosynthetics: Now and Future of Geosynthetics in Civil Engineering (2004)
3. Ramesh, M.V.: Slope stability investigation of Chandmari in Sikkim, northeastern India. In: Workshop on World Landslide Forum, pp. 363–369. Springer, Cham (2017)
4. Muthukumar, S., Kolathayar, S., Valli, A., Sathyan, D.: Pseudostatic analysis of soil nailed vertical wall for composite failure. Geomech. Geoeng. 1–13 (2020)
5. Padmavathi, Srinivas, C.H.: Static and dynamic analysis of Nailed slope. Int. J. Sci. Res. 2319–7064 (2018)
6. Babu, G.S., Singh, V.P.: Numerical analysis of performance of soil nail walls in seismic conditions. ISET J. Earthq. Technol. **45**(1–2), 31–40 (2008)
7. Jaya, V., Annie, J., Student, M.T.: A numerical investigation of nailed vertical soil wall using pseudo-static approach. In: Proceedings of Indian Geotechnical Conference, pp. 899–902 (2011)
8. Melo, C., Sharma, S.: Seismic coefficients for pseudostatic slope analysis. In: 13th World Conference on Earthquake Engineering, Vancouver, Canada (2004)
9. Sharma, P.: Theoretical analysis of soil nailing: design, performance and future aspects. Int. J. Eng. Res. General Sci. **3**(6) (2015)
10. Chen, L., Zeng, L.: Numerical analysis for the effect of soil nailing to the stress and deformation behavior of foundation pit. Electron. J. Geotech. Eng. 17 (2012)
11. Zhu, Y., Xie, Q., Dong, J.: FEM Analysis of Composite Soil Nailed Wall on the Dynamic Response of Earthquake
12. Manjularani, P., Manasa, C.K.: Static and dynamic analysis of soil nail wall and retaining wall for vertical cut. In: Proceedings of International Conference on Current Trends in Engineering, Science and Technology, pp. 750–754 (2017)
13. Zolqadr, E., Yasrobi, S.S., Norouz Olyaei, M.: Analysis of soil nail walls performance-Case study. Geomech. Geoeng. **11**(1), 1–12 (2016)

14. Rawat, S., Gupta, A.K.: Analysis of a nailed soil slope using limit equilibrium and finite element methods. Int. J. Geosynth. Ground Eng. **2**(4), 1–23 (2016)
15. Babu, G.S., Singh, V.P.: Simulation of soil nail structures using PLAXIS 2D. Plaxis Bull. **25**, 16–21 (2009)
16. Lazarte, C.A., Robinson, H., Gomez, J.E., Baxter, A., Cadden, A., Berg, R.R., Berg, R.R.: Geotechnical engineering circular No. 7 soil nail walls-reference manual (No. FHWA-NHI-14–007). National Highway Institute (US) (2015)
17. Swathi, B., Kumar, M.N., Pullarkatt, D., Ramesh, M.V.: Wireless movement sensor network for real-time monitoring of slope instability. In: 2017 International Conference on Wireless Communications, Signal Processing and Networking (WiSPNET), pp. 1518–1523. IEEE (2017)
18. Hossain, M.A., Islam, A.: Numerical analysis of the effects of soil nail on slope stability. Int. J. Comput. Appl. **141**(8), 12–15 (2016)
19. guang Fu, W.: The application of composite soil nailing wall in China. Japan. Geotech. Soc. Spec. Publ.**2**(64), 2192–2195 (2016)
20. Rashidi, F., Torabipour, A.: 2D Numerical Simulation of Stabilized Soil Wall by Nailing and Anchorage Methods

Dynamic Soil–Structure Interaction Effects in Integrated Retaining Wall-Building System

N. Sri Vinay, Amrita, B. R. Jayalekshmi, and R. Shivashankar

1 Introduction

Land mass accounts for only one third of the entire surface area of Earth. Further, land suitable for construction is being depleted. This puts forward a challenge to civil engineers to utilise all the space available, even in hilly and harsh terrains. One of the major aspects involved in the construction of buildings in hilly terrain is soil stabilisation. This is achieved by the construction of retaining walls, soil nailing, soldier piles, sheet piling, etc. And if any construction is to be made near this stabilised soil mass, the space has to be efficiently utilised.

Many studies have been carried out to understand the dynamic response of building and the dynamic response of retaining wall in association with the soil–structure interaction, separately. Studies are done on failure mechanisms of retaining wall by Huang et al. [1], Cakir [2, 3], etc. However, characteristics of an integrated system consisting of building and retaining wall is not seen in the literature. The present study is an effort to effectively utilise the space between a building frame and retaining wall. The work has been further carried out to evaluate the changes in response of building and retaining wall due to the integration and also to determine any advantages or disadvantages provided by the integrated system. This study has been more focused on response variation caused in the building due to the integration of retaining wall.

N. S. Vinay · Amrita (✉) · B. R. Jayalekshmi · R. Shivashankar
Department of Civil Engineering, NITK Surathkal, Mangalore, Karnataka 575025, India

2   Methodology

In this study, transient analysis of a building frame consisting of G+5 configuration having 4 × 4 bays considering the supporting ground as well as the adjoining elevated ground was carried out. The building was placed on 18 m wide raft and the thickness of the raft was taken to be 1 m. The other properties of the building used for the analysis are given in Table 1. The retaining wall for the adjoining elevated ground is to be integrated with the building was 6 m high having a thickness of 0.5 m.

The analysis was carried out with three different building-retaining wall systems and in three different soil conditions corresponding to stiff and very dense soil. The classification of soil provided by National Earthquake Hazards Reduction Program (NEHRP) was utilised, which is based on the shear wave velocity (V_s) through them [4]. The shear wave velocities of 180 m/s, 360 m/s and 760 m/s were considered which represents the upper limit of Soil Class C, D and E as per NEHRP classification. The other properties of the soil considered for the analysis were calculated based on these values of shear wave velocity. The soil properties used in the analysis are given in Table 2.

Three different types of models were considered for the analysis. They are denoted as 'Frame only setup', 'Wall attached setup' and 'Wall at 4 m setup'. Frame only setup consisted of only the building frame placed on the raft. In Wall attached setup, the retaining wall was attached to the building as shear wall leaving no space between them. And in Wall at 4 m setup, the retaining wall placed at a distance of 4 m from the building frame was connected to the building using beams at the first and second floor level, i.e. at a height of 3 m and 6 m from the ground surface. In all these models, the supporting ground as well as the retaining soil of the elevated ground was also considered.

Table 1 Building parameters

Properties	Value
Floor height (m)	3
Bay width (m)	4
Beam section (m × m)	0.3 × 0.45
Column section (m × m)	0.5 × 0.5
Grade of concrete	M40
Density of concrete (kg/m^3)	2500
Poisson's ratio	0.2

Table 2 Soil parameters

Shear wave velocity, V_s (m/s)	Soil density (kg/m^3)	Poisson's ratio
180	1631	0.3
360	1835	0.25
760	2039	0.2

3   Numerical Analysis

The simulation of the above models and the numerical analysis was carried out using finite element software, ANSYS. The accuracy of modelling was first determined through a validation study. Transient analysis of G+2 and G+3 RC buildings were conducted and obtained results were compared with the numerical results of Nanda et al. [5]. The acceleration and modal frequencies obtained from software were found to be in good agreement with the results of Nanda et al. [5]. Thus, ANSYS software was further used for modelling and analysis of the present work.

The three-dimensional finite element models were generated, and the dynamic analysis was carried out by applying earthquake time history data at the base of the model. The soil domain was taken as 4.5 times the base width of the raft on either side, thus making a total of 180 m × 180 m square dimension of the foundation soil. The depth of the foundation soil was 20 m. The backfill was extended from the back face of retaining wall up to the edge of boundary of foundation soil.

In all the models, raft was 18 m wide and 1 m thick. The top surface of raft was in line with the top surface of foundation soil. The effect of embedment is not considered. The retaining wall with a thickness of 0.5 m was extended up to 6 m height to retain the soil in the elevated ground. The Wall at 4 m setup had a retaining wall with toe of length 1.5 m at a depth of 0.5 m below ground surface and a shear key of depth 0.5 m. In the Wall attached setup, a filter material was placed behind the wall flushing with edge of raft having elastic properties identical to backfill soil and having a density of 25 kg/m^3. Isometric views and elevation of different setups are shown in Figs. 1, 2 and 3 presenting the meshing qualitatively.

Soil was modelled as eight-nodded solid element (SOLID 185) and as a linearly elastic and isotropic material. For this study, a simple material model was adopted. The foundation soil and backfill were assumed to be of same soil type as seen in the case of normal ground. Retaining wall and raft on which the building frame was
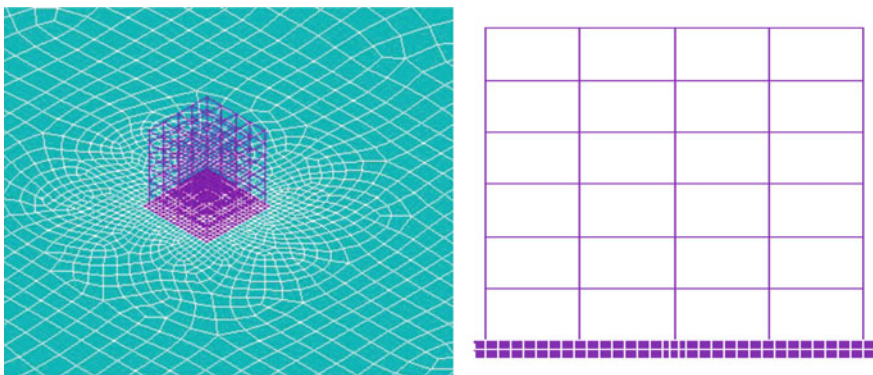
Fig. 1   Frame only setup
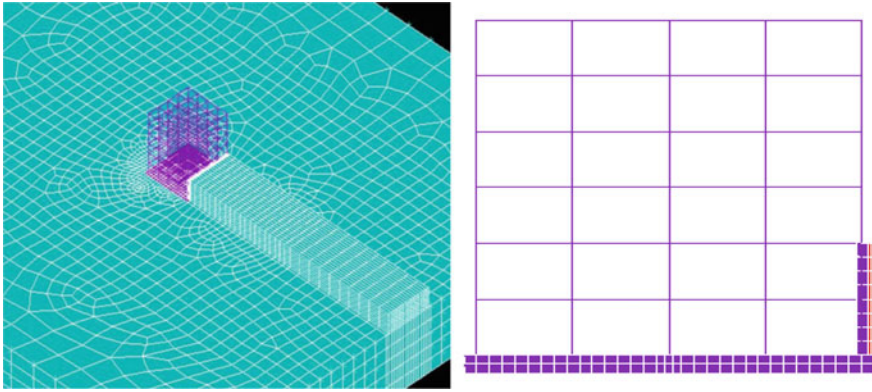
Fig. 2 Wall attached setup
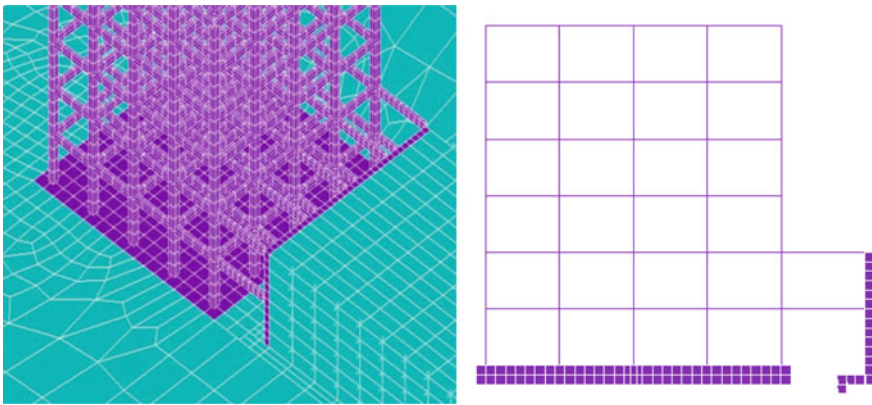
Fig. 3 Wall at 4 m setup

placed were both modelled using SOLID 185 element. Beams and columns were modelled as beam elements using BEAM 188 element. The type of contact between all types of surfaces were set to bonded type of contact during the analysis.

On all the vertical boundary surfaces depending on dimensions of area into which each element is divided, spring dampers were placed at each node for the purpose of simulating a viscous boundary to avoid reflection of seismic waves back into the soil mass [6]. All nodes at the bottom surface of foundation soil were fixed. For the dynamic loading, actual time history earthquake data of El-Centro earthquake, 1940, scaled to 0.3 g was chosen. The data corresponding to first 10 s was used and applied at the base of the model along the direction of backfill (*X*-axis in model). The El-Centro earthquake data used for analysis is shown in Fig. 4.
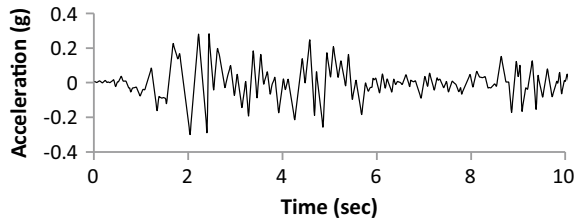
Fig. 4 Time history data of El-Centro earthquake

4 Results and Discussion

The dynamic analysis of the integrated retaining wall-building systems were performed using the finite element method. The results of the analysis are compared in terms of maximum deflection and acceleration of building frame, bending moments and shear forces on building components and maximum deflection at the top of the retaining wall obtained from the time history of these response parameters. The equivalent stresses were recorded along the height of retaining wall.

The results obtained through analysis are presented below. Table 3 represents the maximum deflection and acceleration of building which occurred at top of the building. Table 4 shows the percentage reduction in maximum deflection and acceleration at top of the building when the retaining wall is integrated with the building.

The time history of deflection of the top of the building is represented in Figs. 5, 6 and 7 for different soil types.

It can be observed that the deflection at top of building is maximum for the frame only setup. And this deflection is reduced when the frame is integrated with the retaining wall. The deflection is the least in case of Wall at 4 m setup for soil in the stiff soil range. The deflection of the building founded on soil with $V_s = 760$ m/s is least in the Wall attached setup. Thus, it can be concluded that the Wall attached setup is more advantageous over Wall at 4 m setup in very dense soil when the deflection of the building is considered.

Table 3 Maximum deflection and acceleration at top of building

Shear wave velocity (V_s)	$V_s = 180$m/s		$V_s = 360$m/s		$V_s = 760$m/s	
	Deflection (mm)	Acceleration (m/s^2)	Deflection (mm)	Acceleration (m/s^2)	Deflection (mm)	Acceleration (m/s^2)
Frame only	167.09	29.66	66.49	13.46	51.65	10.68
Wall attached	31.94	10.26	21.22	11.15	14.84	9.11
Wall at 4m	28.82	5.42	21.13	5.87	16.94	9.5

Table 4 Percentage reduction in maximum deflection and acceleration at top of building

Shear wave velocity (V_s)	V_s = 180 m/s		V_s = 360 m/s		V_s = 760 m/s	
	Deflection reduction (%)	Acceleration reduction (%)	Deflection reduction (%)	Acceleration reduction (%)	Deflection reduction (%)	Acceleration reduction (%)
Wall attached	80.88	65.41	68.09	17.16	71.27	14.7
Wall at 4 m	82.75	81.73	68.22	56.39	67.20	11.05
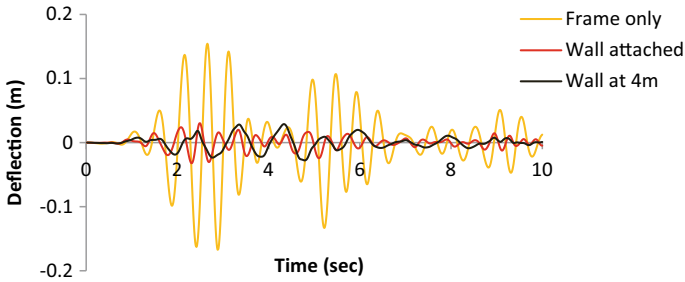
Fig. 5 Deflection at top of building for V_s = 180 m/s
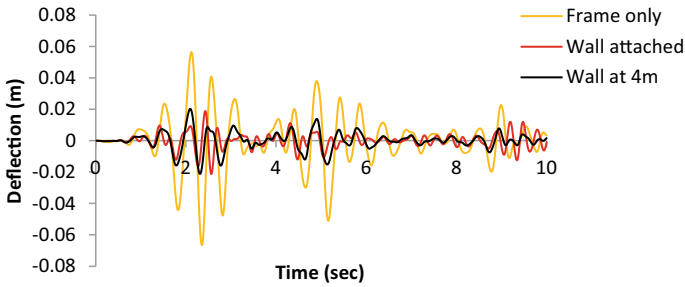
Fig. 6 Deflection at top of building for V_s = 360 m/s
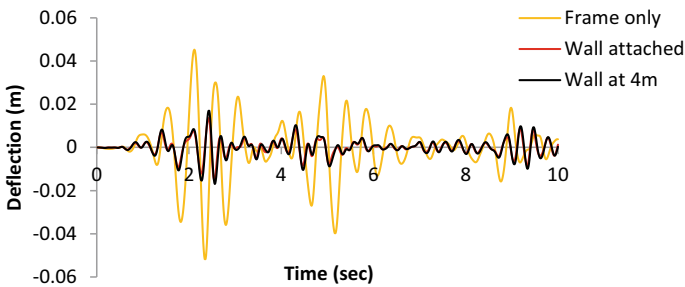
Fig. 7 Deflection at top of building for V_s = 760 m/s

Tables 5 and 6 show the maximum bending moments and shear forces observed on farthest corner column in ground floor from the position of retaining wall and on the adjoining beam parallel to direction of input earthquake motion. In case of moments, negative values indicate clockwise moments and positive values indicate anti-clockwise moments.

From the results, it is found that the maximum percentage reduction in bending moments and shear forces have occurred in case of soil with $V_s = 760$ m/s, and this reduction is maximum in the case of Wall attached setup. The reduction in bending moment and shear force in case of Wall attached setup for soil with $V_s = 760$ m/s is obtained as 94.3% and 93.9% in column and 96.1% and 96.1% in beam, respectively.

The deflection along the centre line of building frame in every storey level at the instant of time when the top deflection of the frame was maximum is given in Table 7 for different types of soil. The percentage reduction in deflection while integrating the wall is also tabulated.

Figures 8, 9 and 10 show the graphical representation of the deflection profile of the building frame. The stiffening of the frame is observed at levels where wall is attached to the frame.

It can be concluded that integrating the retaining wall to the building in both the setups, i.e. Wall attached setup and Wall at 4 m setup, has provided advantage. However, the Wall attached setup has resulted in more reduction of deflection along the centre line. In soil with $V_s = 180$ m/s, it is observed that the Wall at 4 m setup shows slightly more reduction of deflection at upper storeys. The deflection is maximum when the supporting soil is stiff ($V_s = 180$ m/s).

Table 5 Maximum bending moments and shear forces in column

Shear wave velocity, V_s (m/s)	Frame only		Wall attached		Wall at 4 m	
	Bending moment (kN m)	Shear force (kN)	Bending moment (kN m)	Shear force (kN)	Bending moment (kN m)	Shear force (kN)
180	297.91	397.41	−63.12	−85.39	255.59	341.34
360	118.57	158.12	−20.85	−28.96	−192.98	−258.6
760	90.97	121.38	5.21	7.4	−43.22	−58.71

Table 6 Maximum bending moments and shear forces in beam

Shear wave velocity, V_s (m/s)	Frame only		Wall attached		Wall at 4 m	
	Bending moment (kN m)	Shear force (kN)	Bending moment (kN m)	Shear force (kN)	Bending moment (kN m)	Shear force (kN)
180	674.93	628.98	−95.47	−88.27	−386.86	−358.19
360	267.78	249.46	−35.14	−32.68	−283.01	−261.77
760	−205.92	191.88	−8.08	−7.49	−54.31	−49.94

Table 7 Variation of deflection along centre line of building at every storey level

Storey level	5	4	3	2	1	G
Shear wave velocity, V_s	Deflection (m)/Reduction (%)					
$V_s = 180$ m/s						
Frame only (m)	−0.169	−0.157	−0.14	−0.117	−0.088	−0.05
Wall attached (%)	81.12	81.15	81.5	81.79	79.2	59
Wall at 4 m (%)	83.43	83.44	82.14	79.49	71.59	30
$V_s = 360$ m/s						
Frame only (m)	−0.067	−0.063	−0.057	−0.048	−0.037	−0.023
Wall attached (%)	68.66	71.43	75.44	83.33	93.51	94.35
Wall at 4 m (%)	68.66	69.84	70.18	70.8	64.86	26.09
$V_s = 760$ m/s						
Frame only (m)	−0.052	−0.049	−0.045	−0.038	−0.029	−0.019
Wall attached (%)	71.15	73.47	80	88.42	97.76	98.63
Wall at 4 m (%)	67.31	69.39	75.56	82.89	91.03	85.26

Fig. 8 Deflection along centre line of building at different storey for $V_s = 180$ m/s
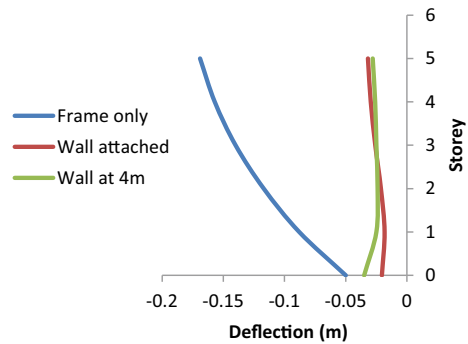
Fig. 9 Deflection along centre line of building at different storey for $V_s = 360$ m/s
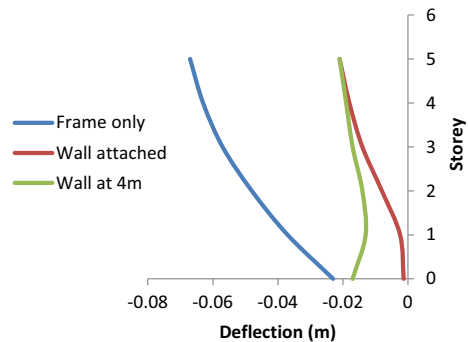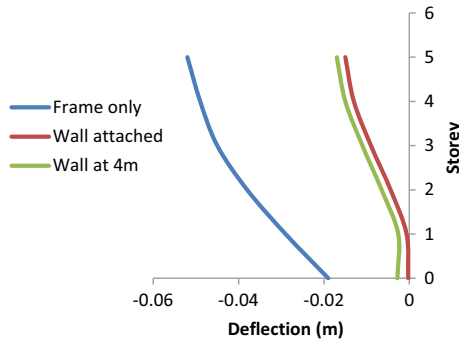
Fig. 10 Deflection along centre line of building at different storey for V_s = 760 m/s

Table 8 Maximum deflection at the top of retaining wall

Shear wave velocity (V_s)	V_s = 180 m/s	V_s = 360 m/s	V_s = 760 m/s
	Deflection (mm)		
Wall attached	16.95	3	0.5
Wall at 4 m	25.39	12.13	2.05

The time history of seismic response in retaining wall is analysed. The maximum deflection at top of the retaining wall at the midpoint is tabulated in Table 8.

From Table 8, it can be observed that the deflection is more in case of Wall at 4 m setup when compared to Wall attached setup. This is true for all the three soil types. The deflection decreases with the increase of shear wave velocity of soil.

Stresses along the height of retaining wall along the mid-line was also computed and are given in Tables 9 and 10 for Wall attached and Wall at 4 m setup, respectively. The stresses tabulated are the equivalent von-Mises stresses. It is observed that in Wall attached setup, the maximum stress in the retaining wall occurs at top most point which is against the general case where maximum stress occurs near to the bottom of the stem in retaining wall alone condition. This may be due to the fact that top of the wall is attached to beams in building and hence resulted in a higher value of stress while sharing the lateral load.

In case of Wall at 4 m setup, the maximum stress occurs at bottom of wall for soil with V_s = 360 m/s and 760 m/s, but the behaviour is slightly different for soil with V_s = 180 m/s. Slightly higher value of stress is observed at mid-height, which may be due to the presence of connecting beam at mid-height of wall.

The maximum bending moments and shear forces in beams connecting the frame to retaining wall are given in Table 11. There were a total of ten connecting beams in the four bay structure, i.e. five beams at 3 m and other five beams at 6 m from ground surface. First set of beams are denoted as outer most beams, second set as intermediate beams and third set as middle beams with reference to plan of the structure. Each set contains two beams, top beam at 6 m level and bottom beam at 3 m level.

Table 9 Stresses along the height of retaining wall in Wall attached setup

Shear wave velocity (V_s)	V_s = 180 m/s		V_s = 360 m/s		V_s = 760 m/s	
Height from bottom of wall (m)	Maximum stresses in edge panel (MPa)	Maximum stresses in mid-panel (MPa)	Maximum stresses in edge panel (MPa)	Maximum stresses in mid-panel (MPa)	Maximum stresses in edge panel (MPa)	Maximum stresses in mid-panel (MPa)
6	8.96	1.83	4.54	2.45	2.07	1.36
5.25	5.07	1.65	2.46	0.99	1.02	0.59
4.5	3.22	3.11	1.01	1.02	0.27	0.49
3.75	4.03	3.64	1.18	1.08	0.26	0.43
3	4.69	3.86	1.46	1.13	0.21	0.36
2.25	4.92	3.86	1.74	1.25	0.29	0.36
1.5	4.47	3.37	1.77	1.23	0.43	0.35
0.75	3.77	2.68	1.76	1.21	0.67	0.55
0	3.07	1.97	1.55	0.96	1.1	0.54

Table 10 Stresses along the height of retaining wall in Wall at 4 m setup

Shear wave velocity (V_s)	V_s = 180 m/s	V_s = 360 m/s	V_s = 760 m/s
Height from bottom of the wall (m)	Maximum stresses in middle line (MPa)		
6	5.67	4.5	7.44
5	3.27	2.93	2.22
4	5.14	2.46	1.91
3	8.42	4.63	1.16
2	7.17	7.5	1.88
1	5.81	8.8	3.67
0	4.06	9.25	5.24

Table 11 Bending moments and shear forces in connecting beams

Shear wave velocity (V_s)	V_s = 180 m/s		V_s = 360 m/s		V_s = 760 m/s	
Beam location	Bending moment (kN m)	Shear force (kN)	Bending moment (kN m)	Shear force (kN)	Bending moment (kN m)	Shear force (kN)
Outer most beams						
Top beam	−102.1	22.86	−46.48	−10.82	30.67	−7.75
Bottom beam	−320.2	71.29	−216.9	48.2	−38.46	−8.55
Intermediate beams						
Top beam	−100.2	22.42	−45.36	−10.74	30.37	−7.85
Bottom beam	−296.8	55.07	−193.0	42.81	−35.29	−8.03
Middle beams						
Top beam	−105.4	23.56	−47.46	−11.25	30.98	−7.94
Bottom beam	−276.5	64.54	−178.7	−36.69	−33.17	−7.62

The response of beams on the other half side is similar to intermediate and outer most beams, respectively, owing to the symmetry of the model. The maximum bending moment and shear force occur in bottom beams which are attached to frame at 3 m level. This is due to the increased storey forces towards the lower levels. The outermost bottom beams are subjected to more bending moments and shear forces.

5 Conclusions

The three-dimensional finite element analysis of integrated retaining wall-building system for optimum space utilisation was carried out under dynamic loading. From the results of the numerical analysis, it can be concluded that:

- There are advantages in integrating the building frame and retaining wall by utilising the available space effectively and reducing the seismic response in the building.
- The displacement of the building is considerably reduced by connecting or attaching the retaining wall.
- Wall attached setup is more useful in reducing demand on structural members in all types of soil.
- The deflection of the retaining wall is minimum in case of wall attached setup.

In the case of buildings to be constructed in grounds with different levels in high demand localities, the integrated retaining wall-building system could be a better alternative.

References

1. Huang, C.C., Wu, S.H., Wu, H.J.: Seismic displacement criterion for soil retaining walls based on soil strength mobilization. J. Geotech. Geoenviron. Eng. **135**(1), 74–83 (2009)
2. Cakir, T.: Evaluation of the effect of earthquake frequency content on seismic behavior of cantilever retaining wall including soil–structure interaction. Soil Dyn. Earthq. Eng. **45**, 96–111 (2013)
3. Cakir, T.: Finite element based investigation of Backfill effects on Seismic behavior of a Cantilever Wall. Proc. Earth Planet. Sci. **15**, 231–236 (2015)
4. Council, B.S.S.: NEHRP Recommended Provisions for Seismic Regulations for New Buildings and Other Structures, FEMA 450, Washington, DC (2003)
5. Nanda, R.P., Dutta, S., Das, A., Khan, H.A.: Geosynthetic liner as foundation isolation for seismic protection. Int. J. Geosynthetics Ground Eng. **3**(3), 1–7 (2017)
6. Lysmer, J., Kuhlemeyer, R.L.: Finite dynamic model for infinite media. J. Eng. Mech. Div. **95**(4), 859–878 (1969)

Laboratory Model Study on Erosion Control Using Coir Geotextile

Surya Muthukumar, Sruthi Priyanka, and Shanmuga Priya

1 Introduction

Soil erosion is one of the most important soil degradation processes, and it influences more than one billion hectares [1]. Erosion mainly takes place when excessive surface runoff flows with high velocity. This excessive runoff causes detachment of the soil particles and carries them down slope. It causes detriment to the infrastructure of the hilly regions. Hence, soil erosion is an economic and environmental issue that needs to be suitably managed [2]. Soil erosion depends on soil erodibility, rainfall erosivity, and spatial variability. Soil erodibility is the inherent resistance of soil to erosive force [3, 4]. The resistant forces depend on cohesion, friction, and weight of the soil particles [5].

It is important to evaluate the sensitivity of soil to cause erosion [6]. It is crucial to study soil erodibility in order to understand the mechanism of soil erosion [4]. Soils with higher permeability and good soil structural arrangement offer more resistance to erosion, whereas soils with a higher content of intermediate particle size fractions such as very fine sand and silt are highly erosive. Apart from the hill slope erosion, estimation of erodibility of soils is important for dealing with problems such as riverbank erosion, shoreline erosion, and on the banks of water storage structures. The storage structures in Nilgiris include the dams in and around the Moyar basin, Bhavani basin, Kabini basin, and Chaliyar basin.

An extensive database of soil erodibility values to a specific area obtained from the past data may lead to uncertainty. It is necessary to include large data from a specific location, improve the methods for mapping the soil loss, and to revise published values of soil erodibility over time.

S. Muthukumar (✉) · S. Priyanka · S. Priya
Department of Civil Engineering, Amrita School of Engineering, Coimbatore,
Amrita Vishwa Vidyapeetham, India
e-mail: m_surya@cb.amrita.edu

To protect and reclaim susceptible areas, it is necessary to evaluate the land degradation by soil erodibility, by using geostatistical modeling [7]. Conventional methods like USLE, RUSLE, MUSLE, etc., are used to calculate the intensity of soil erosion; they are expensive and time-consuming. Mapping soil erosion using GIS can easily identify the areas that are at potential risk of extensive soil erosion and provide information on expected soil loss on that particular region [8]. The complexity of the interacting processes involved in calculating soil erosion may be avoided using stochastic modeling to predict the hill slope response to erodibility dynamics. The erosion model effectively predicts the spatial and temporal distribution of soil detachment.

Rainfall-induced soil erosion can lead to landslides, and there are several forecasting techniques to identifying the triggering landslide [9, 10]. Forecasting the possibility of land sliding is accomplished by monitoring the variation in the pore water pressure at different soil layers [10]. In this study, the Nilgiris is selected as the study area, which had experienced several landslides recorded since 1824 till 2015 [11]. From the land-use study of the region, it indicates that the total sediment yield has markedly increased due to the change in the land cover. It resulted in a significant rise in the soil erosion in the deforested region which has changed from forest to orchard, infrastructure, and to barren land [12].

Soil loss during erosion can be reduced by adopting suitable surface treatment. It is mostly done by the application of natural or synthetic geotextile over the soil followed by growing vegetation over it. The use of natural geotextiles like coir, jute, bamboo, etc., is more suitable than synthetic fibers as it may result in soil pollution [1, 13]. Now, synthetic geotextiles are replaced by natural geotextiles to reduce the carbon footprints during their life cycle. Various natural geotextiles are having great potential to solve various geotechnical-related problems [14]. Natural geotextiles result in economical, environment friendly, and ecologically compatible than the synthetic geotextiles. These natural geotextiles are affected by seasonal variation and biodegradation. It is evaluated that structural and mechanical properties can be retained by suitable treatment of these fibers [15]. Coir geotextile is a natural material made of coccus nucifera fiber which can retain its strength and resist degradation when compared to other natural fibers [14, 16]. They have good drapability characteristics, and the ability to withstand impact and pull makes them suitable for erosion control and various slope protection application [16, 17].

The detrimental impacts of soil erosion and sediment deposition resulted in vulnerable soil slopes. Several policies were made to prevent soil loss to protect land, water, and soil resources [3]. Natural geotextiles which are installed over the bare soil slopes help to protect the soil from erosive forces due to rainfall and surface runoff [3]. The limited laboratory tests on assessing the performance of natural geotextiles result in the complexity to identify the suitable material by the end user [3]. The effectiveness of the geotextile in controlling soil erosion can be evaluated by rain splash test on different surface treatments and by studying the process of minimum soil detachment and transport [3]. Natural geotextiles are mostly made up of locally available materials like bamboo, rice straw, coir, jute, etc. These geotextiles are used on the bare plot with different surface spraying to

protect it. These geotextiles are very effective to control soil loss and decrease the rate of soil loss to a range of 67–99%. It also reduces the runoff volume to a range of 26–81% [18].

Erosion control can prevent problems from ever beginning. There are several conventional methods such as rock gabion, crib wall, live fascines, and brush mattress [19]. The erosion rate can be reduced by adopting suitable surface treatment which reduces runoff, sediment control, and soil loss. The surface protection of the slopes dissipates the energy of raindrop impact, increases infiltration, and reduces the velocity of overland flow. In the uncovered soil surface, raindrops loosen the soil particles, which cause an incremental movement toward the downslope.

2 Study Area

The area selected for the study is Nilgiris district, Tamil Nadu state in India. It extends to an area of 36 sq. km. Soil poses a hazard in this region as it is subjected to erosion predominantly. These erosional surfaces are capped by residual laterite. In the study area, landforms such as peaks, structural hills, and rocky escarpments are in existence [11]. The Nilgiris district is one of the severe to high landslide hazard-prone areas in India. Many landslide hazard mapping studies were carried out in that area on different scales.

In Nilgiris, Western Ghats, the soil erosion led to the deposition of soil in the water storage locations and has reduced the capacity of those structures. The desilting processes head to spend several crores every year (The Hindu 2018). Sediments and sedimentation cause the problems commonly associated with erosion [20].

2.1 Sample Collection

Georeferenced undisturbed top soil (0–10 cm) samples are collected from fifteen locations spatially covered all over as shown in Fig. 1. The undisturbed soil samples are collected in soil samplers and sealed completely to avoid changes in moisture content. The coordinates of the sample location are determined using a geographical position system.

The location details are given in Table 1. The information required is the soil type, elevation, rainfall, and land cover, and its conservation practices are collected.
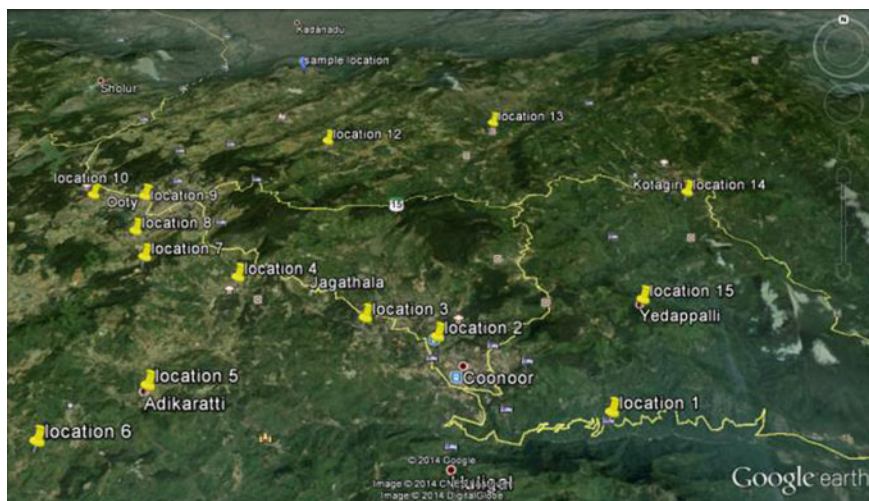
Fig. 1 Sample location for the study

Table 1 Latitude, longitude, and elevation of the sample locations

Sample number	Latitude	Longitude	Elevation
1	11.3376	76.8308	+939
2	11.3717	76.7807	+1821
3	11.3535	76.7919	+1758
4	11.3761	76.7293	+1988
5	11.3394	76.7139	+1964
6	11.3096	76.6914	+1904
7	11.3818	76.7019	+2243
8	11.3926	76.6961	+2242
9	11.4078	76.6946	+2249
10	11.4094	76.6779	+2199
11	11.5059	76.4961	+924
12	11.4394	76.7480	+2061
13	11.4543	76.8051	+1811
14	11.4203	76.8601	+1891
15	11.3791	76.8108	+2056

3   Materials and Methodology

3.1   Soil

The undisturbed soil samples from the various locations are tested for their natural moisture content, organic content, specific gravity, and grain size distribution.

Table 2 Physical properties of sample collected at different locations

Sample number	Field density (g/cc)	Natural moisture content (%)	Organic content (%)	Gravel (%)	Sand (%)	Silt (%)	Clay (%)
1	1.588	4	8	3.1	29.85	57	10
2	**1.481**	6	11	17.1	41.2	23.7	18
3	1.622	12	9.5	3.65	63.95	20	12.4
4	1.594	4	6	4.9	46.1	22.6	26.4
5	1.508	10	10.5	1.6	58.3	20.4	19.7
6	1.460	6	10	1.9	45.1	29	24
7	1.570	8	9	2.8	47.6	34.9	14.7
8	1.527	6	8.5	0	58.3	22.2	19.5
9	1.547	8	10	9	42.7	35.8	12.5
10	1.577	6	10	0	37.2	52	10.8
11	1.491	10	24	3.8	64	16.5	15.7
12	1.521	6	8	1.6	28.6	55.7	14.1
13	1.464	4	22	3.2	43.8	29.6	23.4
14	1.563	6	8	4.6	29.2	51.9	14.3
15	1.508	8	7	0	53.8	34.5	11.7

The in situ densities of the soil are determined by using a core cutter. These properties of the samples helped in identifying the erodibility and critical shear stress of the different soil samples. The properties of the soil sample collected from the different locations are tested, identified, and listed in Table 2.

3.2 Materials

In this study, the surface protection is done by adopting three different methodologies. They are surface treatment with

- Coir geotextile;
- Asphalt emulsion;
- Coir geotextile and asphalt emulsion.

Coir geotextiles and asphalt emulsion have a great variety of engineering properties and physical characteristics. Coir geotextiles are more extensively used in erosion control on natural slopes, canal linings, stream banks, and embankments [21]. The properties of coir geotextile are listed in Table 3. Geotextiles help to mitigate immediate erosion problems and provide long-term stabilization. It absorbs the kinetic energy during the impact of raindrops and reduces the surface runoff. Coir geotextile can be used to give tractive resistance and resist water velocity on slopes. Coir has the greatest tearing strength and retains this property even in wet

Table 3 Physical properties of coir geotextile

Properties	Value
Mass of the geotextile (g/m^2)	768
Ultimate load (kN/m)	16
Failure strain (%)	17.5
Aperture size (mm × mm)	6 × 10
Thickness mm	6.47

conditions. They are stronger than the other natural fibers with high water absorption, maximum swelling of 15%, and high extensibility of 30% [16]. The coir nets can be easily rolled on the sloping surface. Asphalt emulsion is a combination of asphalt, water, and a small amount of an emulsifying agent. It provides great flexibility in its application and an eco-friendly material. The water holding capacity of the soil is increased by treating it with asphalt emulsion. The surface application of asphalt by the process of spraying controls the erosion rate [22].

3.3 Experimental Methodology

3.3.1 Soil Erodibility

Soil erodibility is the inherent resistance of soil to erosive force, and it is an important parameter to evaluate the sensitivity of soil to get eroded. Erodibility helps to understand the mechanism of soil erosion [6]. It can be measured under natural or simulated rainfall conditions and estimated by empirical regression [7]. It is complicated to assess the erodibility of soil as it is influenced by various properties of the soil. It also depends on the soil profile characteristics and its influence on vegetative growth. A single property cannot predict the integrated response that constitutes soil erodibility. Usually, properties like soil texture, aggregation, consistency, and shear strength influence erosive response, and other properties are ineffective. It is difficult to find the suitable erodibility index for soils at a particular location using existing nomograms [23]. Many attempts are made to devise a simple index of erodibility based on the properties of the soil [8]. The most widely used and frequently cited relationship is the soil erodibility factor using the physical properties of the soil which forms the soil erodibility nomograph. This nomograph is a set of empirically determined soil erodibility values based on various soil properties [24].

The erodibility equation is given as

$$K_n = \left(k_t k_o + k_s + k_p\right)/100 \tag{1}$$

where

K_n = soil erodibility value
k_t = soil texture subfactor
k_o = soil organic matter subfactor
k_s = soil structure subfactor
k_p = soil permeability subfactor

The soil texture subfactor is determined using the following condition

$$\text{If } (P_{sl} + P_{vfs}) \leq 68\%, \text{ then } k_t = k_{tb} = 2.1 \times 10^{-4}[(P_{sl} + P_{vfs})(100 - P_{cl})]^{1.14}$$
(2)

$$\text{If } (P_{sl} + P_{vfs}) > 68\%, \text{ then } k_t = k_{tb} - [0.67(k_{tb} - k_{t68})] \tag{3}$$

where

$k_{tb} = k_t$ at $(P_{sl} + P_{vfs}) \leq 68\%$
P_{sl} = percentage of silt
P_{vfs} = percentage of very fine sand
P_{cl} = percentage of clay
$k_{t68} = k_t$ at $(P_{sl} + P_{vfs}) = 68\%$.

Values for sand, silt, and clay content are for the top soil layer that is highly susceptible to erosion. The erosion thickness is usually assumed to be 100 mm.

$$k_o = (12 - O_m)$$

where

O_m = percentage of soil organic matter

$$ks = 3.25(2 - s)$$

where

s = soil structure class.
Very fine granular = 1;
Fine granular = 2;
Medium or coarse granular = 3;
Blocky, platy, or massive = 4.

The soil structure class is derived from the soil structure code based on textural classification [25]

$$k_p = 2.5(P_r - 3)$$

where

P_r = Permeability class.

The permeability class is determined from the soil permeability code based on soil texture class in National Soil Handbook (USDA) [26].

3.3.2   Critical Shear Stress

The erosive level of a soil is quantified by its critical shear stress (τ_c). It is the stress at which soil detachment begins or the condition that initiates soil detachment. Critical shear stress can be estimated based on soil parameters such as particle size and soil specific gravity. The tests conducted for the determination of critical shear stress are difficult. Therefore, it is always given by the empirical relation based on the percentage of clay content in the sample [27].

$$a_{\mathrm{ct}} = 0.0103 \times 100.0182 \, P_c \tag{4}$$

where Pc is the percentage of clay.

3.3.3   Erosion Control

Research done in the field of erosion control has suggested different surface treatments. Among them geotextiles are used to mitigate immediate erosion problems and provide long-term stabilization. The natural coir geotextile is easily available, economical and provides better erosion control. Normally it is found that coir geotextiles lose their 50% strength in 6 months when it is in contact with the soil. Therefore, it is required to increase the durability of coir geotextiles. The life of the coir geotextiles is improved by spraying asphalt emulsion. It is noted from various studies that uniform application of asphalt emulsion over the slope improves the water holding capacity of the soil. Therefore, in order to find the suitable surface protector to control soil erosion, a model slope is tested with coir geotextile, asphalt emulsion, and combination of both. The rate of erosion is recorded for the slope model with and without surface treatment. The maximum rainfall intensity is observed to be 60 mm/hr. Hence, the model is tested for 60, 70, and 80 mm/hr rainfall intensities. The model test is conducted by varying slope angle, surface application, and intensity of rainfall. The angle of the model slope can be changed by adjusting the bolted connection. The rainfall simulation is done using a constant head rainfall simulator [28, 29].

3.3.4 Design and Fabrication of Hydraulic Flume

The hydraulic flume is fabricated to study the erosion rate. Soil erosion is a surface phenomenon, and hence, the depth of the model soil profile is taken as 150 mm. The size of the model is 1 m × 0.5 m × 0.15 m. It has been established that erosion rates increase as slope angles increase. The slope angle influences the flow velocity and particle carrying capacity. The slope angle can be varied as 10°, 20°, and 30°. The model is fabricated such that the angle of the slope can be changed by using bolted connection to simulate different slope angles. The soil sample with maximum erodibility was used in the model test.

3.3.5 Design of the Rainfall Simulator

The rainfall simulation is attained using a tank of size 1 m × 0.5 m × 0.2 m that can be placed over the hydraulic flume. The discharge required for different intensities is calculated. The base plate of the tank is drilled with holes with equal spacing. The hole will be passed by water to form beads of rain; this is intended to obtain the desired rainfall intensity I = 60 mm/hr, I = 70 mm/hr, and 80 mm/hr. The rainfall intensity is simulated by maintaining a particular head of water in the tank for an hour. The intensity is obtained by filling water tank up to a certain height, where height is intended to provide different pressures resulting intensity variation. The rainfall simulator designed by this method is called as rainfall simulator with the constant head [30]. The schematic diagram of hydraulic flume with rainfall simulator is shown in Fig. 2.

4 Results and Discussions

4.1 Erodibility and Critical Shear Stress

Based on the data available, the soil erodibility factor for 15 soil series in the Nilgiris district has been calculated using soil erodibility nomograph equation. If the erodibility factor is less, then the soil possesses high resistance to erosion. Higher the factor, then the soil is more prone to erosion. From the results, the sample location 3 has a minimum erodibility factor. The critical shear stresses of the samples are listed in Table 4.

The experimental study is carried out under different hydraulic conditions such as slope angle and intensity of rainfall on the soil sample with maximum erodibility from the collected samples.

Erosion rate is the rate of removal of soil and rock materials from the surface and is measured as mass removed per unit time. The soil sample with natural moisture content is compacted to field density. In order to attain the rainfall simulation,
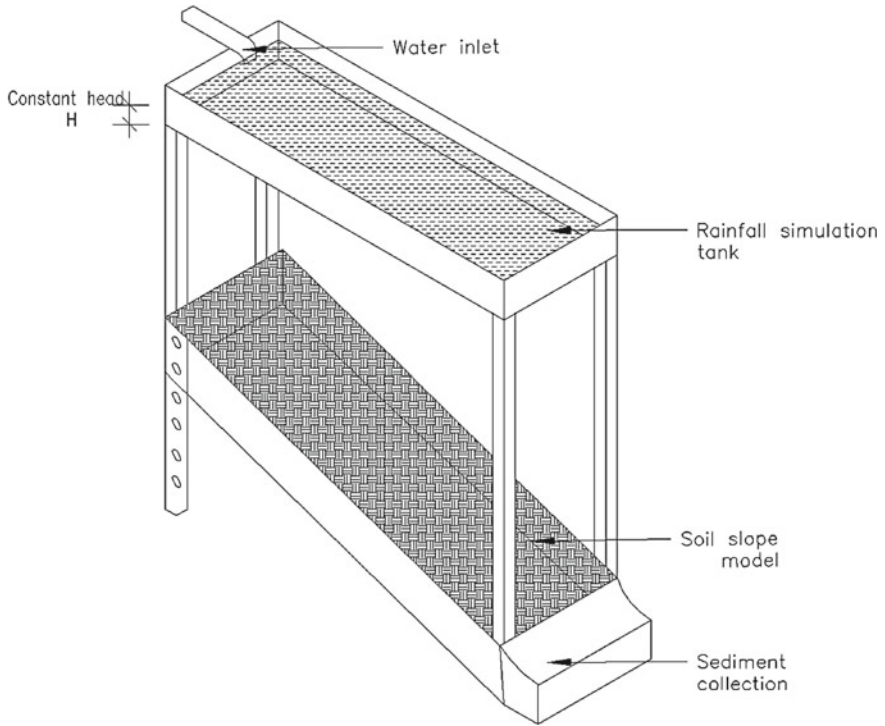
Fig. 2 Schematic diagram of hydraulic flume with rainfall simulator

Table 4 Erodibility and critical shear stress of the samples

Sample number	Erodibility factor	Critical shear stress (N/m^2)
1	0.2803	0.7496
2	0.155875	1.048207
3	0.034012	0.828947
4	0.052237	1.490483
5	0.127845	1.125607
6	0.033318	1.347867
7	0.068366	0.912824
8	0.068431	1.116213
9	0.165533	0.832428
10	0.14577	0.775188
11	0.045928	0.95189
12	0.427404	0.890158
13	0.101193	1.314398
14	0.32218	0.89765
15	0.164514	0.804983

the tank is filled up to a specific depth which is required to maintain the constant head. The water inflow is adjusted to maintain the constant water level in the rainfall simulation tank. The rainfall simulation is done for a period of one hour in order to attain the hourly rainfall effect.

The simulated raindrops loosen the soil particles, which cause an incremental movement toward the down slope. Soil particles get detached by the impact force of the droplets and get detached. The detached particles transported to the down slope along with the runoff water. The eroded soil is collected at the lower portion of the hydraulic flume. Runoff along with the eroded soil is collected for an hour for the intensity of rainfall. The water along with the eroded soil is kept still to settle down the soil particles. Then, the erosion sediment is filtered on straining paper. The sediment filtered is dried for 24 h in an oven and then weighted. From the weighed sediment, the erosion rate is calculated for the specific rainfall intensity.

4.2 Erosion Studies for Different Rainfall Intensities

The erosion test was carried out for different rainfall intensities. The soil slope was tested with 60, 70, and 80 mm/hr rainfall intensities for an inclination of 10°, 20°, and 30°. The different intensities were obtained by maintaining various constant head. The rainfall simulation tank was meant to maintain these heads for an hour to achieve the particular intensity [28]. The uncovered soil slope was subjected to erosion, the eroded soil was collected for sedimentation, and the erosion rate was shown in Table 5.

Table 5 Erosion rate without surface protection

S. no	Slope (Degrees)	Intensity of rainfall (mm/hr)	Erosion rate $(g/m^2/hr)$
1	10	60	859
2	10	70	981
3	10	80	1074
4	20	60	1175
5	20	70	1263
6	20	80	1368
7	30	60	1290
8	30	70	1388
9	30	80	1452

Table 6 Erosion rate for slope with coir geotextile

S. no	Slope (Degrees)	Intensity of rainfall (mm/hr)	Erosion rate (g/m²/hr)	Reduction rate (%)
1	10	60	273	68.22
2	10	70	352	64.12
3	10	80	386	64.06
4	20	60	336	71.40
5	20	70	429	66.03
6	20	80	502	63.30
7	30	60	489	62.09
8	30	70	520	62.54
9	30	80	561	61.36

4.3 Surface Treatment with Coir Geotextile

The slope with coir geotextile on its surface is subjected to the rainfall intensities 60, 70, and 80 mm/hr. The tests are conducted for an inclination of 10°, 20°, and 30°. The eroded soil sample is collected. From the eroded sample, the erosion rate is calculated. Table 6 shows the erosion test for the slope with coir geotextile.

The coir geotextile is rolled over the sloping soil surface [1]. The coir geotextile absorbs the impact of the raindrops and reduces the surface runoff. It improves the infiltration of rainwater into the soil. The coir geotextile can be used to provide tractive resistance and resist the heavy rainfall velocity on the soil slopes.

4.4 Surface Treatment with Asphalt Emulsion

Soil sample is sprayed with liquefied emulsified asphalt. There is a decrease in erosion rate by 86.14% for 100 cc/sq.m asphalt application on the sloping surface [22]. That was used as the optimum percentage of asphalt over the surface of the soil. The rapid setting emulsion was used over the surface, and the slope was tested for the rainfall intensities 60, 70, and 80 mm/hr by varying the soil angle as 10°, 20°, and 30°. Table 7 shows the erosion rate with asphalt emulsion as surface treatment.

4.5 Surface Treatment with Coir Geotextile and Asphalt Emulsion

Coir geotextiles lose its strength over a period of time [14]. In order to enhance the longevity of the coir geotextile, it should be coated with suitable material. From the

Table 7 Erosion rate for slope with asphalt emulsion

S. no	Slope (Degrees)	Intensity of rainfall (mm/hr)	Erosion rate (g/m^2/hr)	Reduction rate (%)
1	10	60	327	61.93
2	10	70	369	62.39
3	10	80	407	62.10
4	20	60	460	60.85
5	20	70	529	58.12
6	20	80	570	58.33
7	30	60	593	54.03
8	30	70	607	56.27
9	30	80	624	57.02

Table 8 Erosion rate for slope with coir geotextile and asphalt emulsion

S. no	Slope (Degrees)	Intensity of rainfall (mm/hr)	Erosion rate (g/m^2/hr)	Reduction rate (%)
1	10	60	217	74.74
2	10	70	260	73.50
3	10	80	294	72.63
4	20	60	329	72.00
5	20	70	373	70.47
6	20	80	390	71.49
7	30	60	342	73.49
8	30	70	393	71.69
9	30	80	429	70.45

various materials tested with coir geotextile, asphalt emulsion provides a better performance [22]. The asphalt-coated coir geotextiles which are eco-friendly have superior mechanical properties and better durability compared to the conventional uncoated coir geotextiles.

The coir netting geotextile is placed over the soil slope, and asphalt emulsion is sprayed over it. Then, the soil model is simulated to artificial rainfall effect for the three different rainfall intensities 60, 70, and 80 mm/hr, and the erosion rate is shown in Table 8.

Based on the laboratory results, the soil erodibility factor for 15 soil samples in Nilgiris, Western Ghats has been calculated using soil erodibility nomograph equation. By knowing the basic soil properties at a particular location, the erodibility can be determined. This erodibility factor helps in estimating the soil loss at any location. Out of the 15 sample locations, it is found that three locations are with very low erodible factor and two locations are with high erodible factor. The erodibility factors of the soil location vary from 0.012 to 0.427.

5   Conclusions

- From the erodibility values, Ottupattarai, Conoor, Nilgiris is found to have high erodibility value. The vulnerable soil slopes in that region should be provided suitable surface treatment to prevent soil loss.
- The surface treatments adopted in the model study are compared for their erosion rate with the soil slope without any treatment. The erosion rate of the slope is reduced with the application of these surface measures.
- From the various model tests, it is seen that the combination of coir and asphalt shows an improved reduction rate irrespective of the slope angle and intensity of rainfall. The erosion rates get reduced from 70–74% for the increase in the rainfall intensity from 60 to 80 mm/hr and the change in slope angle from 10° to 30°.
- The coir geotextile on the slopes varies, and the erosion rate gets reduced from 61–68% for the intensities 60, 70, and 80 mm/hr and changes in slope angle.
- The maximum erosion rate 561 $g/m^2/hr$ is observed for the slope of 30° tested with an intensity of 80 mm/hr.
- The erosion rate exists in the range of 327–624 $g/m^2/hr$ for the three different intensities and slope angle. The performance of asphalt emulsion is lower when compared to the coir geotextile.
- Different surface treatments, namely asphalt emulsion, coir geotextile, and the combination of both, are tested against soil erosion in slopes. All the surface treatments serve the function of erosion control. Among them, coir geotextile with asphalt emulsion proved to be a good and reliable material in erosion control. The places of high soil loss, identified using its erodibility mapping, can be treated with coir geotextile and asphalt emulsion to control soil erosion.

References

1. Lekha, K.R.: Field instrumentation and monitoring of soil erosion in coir geotextile stabilised slopes—a case study. Geotext. Geomembr. **22**(5), 399–413 (2004)
2. McNeill, J., MacEwan, R., Crawford, D.: Using GIS and a land use impact model to assess risk of soil erosion in West Gippsland (2006)
3. Rickson, R.J.: Controlling sediment at source: an evaluation of erosion control geotextiles. Earth Surf. Process. Land. J. British Geomorphol. Res. Group **31**(5), 550–560 (2006)
4. Song, Y., Liu, L., Yan, P., Cao, T.: A review of soil erodibility in water and wind erosion research. J. Geog. Sci. **15**(2), 167–176 (2005)
5. Bryan, R.B.: Soil erodibility and processes of water erosion on hillslope. Geomorphology **32**(3–4), 385–415 (2000)
6. Song, Y., Liu, L., Ping, Y.A.N., Tong, CA.: A review of soil erodibility in water and wind erosion research. J. Geog. Sci. **15**, 2, 167–176, ISSN: 1009-637X (2005)

7. Saygın, S.D., Mustafa, M., Ozcan, A.U., Melda, D., Timur, O.B.: Land degradation assessment by geo-spatially modeling different soil erodibility equations in a semi-arid catchment. J. Environ. Monit. Assess. **180**, 201–215 (2011)
8. Fazly, Y.M., Azamathulla, H.M., Rozi, A.: Prediction of soil erodibility factor for Peninsular Malaysia soil series using ANN. Neural Comput. Appl. **24**, 383–389 (2014)
9. Harilal, G.T., Madhu, D., Ramesh, M.V., Pullarkatt, D.: Towards establishing rainfall thresholds for a real-time landslide early warning system in Sikkim India. Landslides **16**(12), 2395–2408 (2019)
10. Hemalatha, T., Ramesh, M.V., Rangan, V.P.: Adaptive learning techniques for landslide forecasting and the validation in a real world deployment. In: Workshop on World Landslide Forum, pp. 439–447. Springer, Cham (2017)
11. Thennavan, E., Ganapathy, G.P.: Evaluation of landslide hazard and its impacts on hilly environment of the Nilgiris District—a geospatial approach. Geoenvironmental Disasters **7**(1), 1–14 (2020)
12. Saravanan, S., Jacinth, J.J., Singh, L., Saranya, T., Sivaranjani, S.: Impact of land-use change on soil erosion in the Coonoor watershed, Nilgiris mountain range, Tamil Nadu, India. In: Conference of the Arabian Journal of Geosciences, pp. 109–111. Springer, Cham (2018)
13. Christopher, B.R., Holtz, R.D.: Geotextile engineering manual (No. FHWA-TS-86/203) (1985)
14. Sumi, S., Unnikrishnan, N., Mathew, L.: Durability studies of surface-modified coir geotextiles. Geotext. Geomembr. **46**(6), 699–706 (2018)
15. Marques, A.R., de Oliveira Patrício, P.S., dos Santos, F.S., Monteiro, M.L., de Carvalho Urashima, D., de Souza Rodrigues, C.: Effects of the climatic conditions of the southeastern Brazil on degradation the fibers of coir-geotextile: evaluation of mechanical and structural properties. Geotext. Geomembr. **42**(1), 76–82 (2014)
16. Sumi, S., Unnikrishnan, N., Mathew, L.: Experimental investigations on biological resistance of surface modified coir geotextiles. Int. J. Geosynthetics Ground Eng. **2**(4), 31 (2016)
17. Muthukumar, S., Sakthivelu, A., Shanmugasundaram, K., Mahendran, N., Ravichandran, V.: Performance assessment of square footing on jute geocell-reinforced sand. Int. J. Geosynthetics Ground Eng. **5**(3), 25 (2019)
18. Bhattacharyya, R., Fullen, M.A., Booth, C.A., Kertesz, A., Toth, A., Szalai, Z., ... Bühmann, C.: Effectiveness of biological geotextiles for soil and water conservation in different agro-environments. Land Degrad. Dev. **22**(5), 495–504 (2011)
19. Iyer Annapoorni, KorullaMinimol: Control soil erosion with nature's own products. In: Indian Geotechnical Conference, Guntur (2009)
20. Muthukumar, S., Ghanesh, G., Balasubramaniam, P.: Estimation of the soil loss in micro watersheds using morphometric analysis and GIS techniques. In: IOP Conf. Series: Mater. Sci. Eng. **872**(1), 012102 (2020)
21. Vishnudas, S., Savenije, H.H.G., Van der Zaag, P., Anil, K.R., Balan, K.: The protective and attractive covering of a vegetated embankment using coir geotextiles (2006)
22. Bunga, E.: Stabilization effect of emulsified asphalt on erosion rate of sandy clay loam. Int. J. Civil Environ. Eng. IJCEE-IJENS **12**(02) (2012)
23. Vanelslande, A., Rousseau, P., Lal, R., Gabriels, D., Ghuman, B.S.: Testing the applicability of soil erodibility nomogram for some tropical soils (1984)
24. Wischmeier, W.H., Meyer, L.D.: Soil erodibility on construction areas. Soil Erosion: Causes, Mechanisms, Prevention and Control. US Highway Research Board Special Report **135**, 20–29 (1973)
25. Guelph Agriculture Centre, Schut, L.W., Irvine, D.E., Ontario Centre for Soil Resource Evaluation.: Field manual for describing soils in Ontario. [Guelph]: Ontario Centre for Soil Resource Evaluation (1993)
26. Schoeneberger, P.J., Wysocki, D.A., Benham, E.C. (eds.): Field Book for Describing and Sampling Soils. Government Printing Office (2012)

27. Smerdon, E.T., Beasley, R.P.: The Tractive Force Theory Applied to Stability of Open Channels in Cohesive Soils. University of Missouri, College of Agriculture, Agricultural Experiment Station (1959)
28. Ogbobe, O., Essien, K.S., Adebayo, A.: A study of biodegradable geotextiles used for erosion control. Geosynth. Int. **5**(5), 545–553 (1998)
29. Akbarzadeh, A., Mehrjardi, R.T., Rouhipour, H., Gorji, M., Rahimi, H.G.: Estimating of soil erosion covered with rolled erosion control systems using rainfall simulator (neuro-fuzzy and artificial neural network approaches). J. Appl. Sci. Res. **5**(5), 505–514 (2009)
30. Aksoy, H., Unal, N.E., Cokgor, S., Gedikli, A., Yoon, J., Koca, K., ... Eris, E.: A rainfall simulator for laboratory-scale assessment of rainfall-runoff-sediment transport processes over a two-dimensional flume. Catena **98**, 63–72 (2012)

Recent Innovations and Practices in Geotechnical Engineering for Sustainable Infrastructure Development

Parishi H. Dalal[ID]**, Mahi Patil**[ID]**, Ram Wanare**[ID]**,
Trudeep N. Dave**[ID]**, and Kannan K. R. Iyer**[ID]

1   Introduction

Rapid urbanization and industrialization have resulted in exhaustive consumption of natural resources over the years. This has already resulted in scarcity of natural materials like aggregates, river sand, and other soils, which are being widely utilized directly and/or indirectly in civil engineering applications [52]. Transporting these materials from other places of availability to the project sites is not always feasible due to the involved cost and efforts for labor and transportation. Natural/ native soil may not always possess the desired characteristics as required for some civil engineering projects. Materials such as cement, lime, and other admixtures have been utilized for soil stabilization for improving their properties. Stabilizers such as cement and chemical admixtures may not be environmentally sustainable, as they cause either depletion of natural resources (viz. coal, limestone) and/or cause environmental pollution [74]. Thus, soil stabilization using low-cost sustainable materials, for making the construction environmental friendly and relatively economical, is one of the suitable solutions [59].

On another front, large variety and quantity of waste/by-products are being generated from different industries. Industrial waste/by-products like industrial ash, microsilica, ground granulated blast furnace slag (GGBS), red mud, sludge ash, biosolids, and lignin-based stabilizer create issues related to storage, processing, and their final disposal along with their possible environmental impacts [75]. However, over the last few years, researchers have been working on reutilization of these industrial by-products for civil engineering applications as a sustainable material, i.e., as replacement of filler and/or binder material or as admixtures [20, 45].

P. H. Dalal · M. Patil · R. Wanare · T. N. Dave · K. K. R. Iyer (✉)
Department of Civil Engineering, Institute of Infrastructure, Technology,
Research And Management, Ahmedabad, Gujarat, India
e-mail: kannaniyer@iitram.ac.in

Scarcity of natural sand and other conventionally used filling materials has made it necessary to explore alternative and sustainable fill materials. One such potential material is the soil-like fraction from old mined municipal solid waste, and it constitutes a significant portion of the municipal solid mined waste. While this material possesses characteristics similar to that of soil, the residual organic matter is still a concern which needs attention. The application of pond ash as a sustainable filler material in flowable fill has also been explored. To overcome the limitation of backfilling at inaccessible locations (especially where compaction equipment cannot reach), flowable fill can be utilized as an alternative fill material [1]. The application of geosynthetics in geotechnical engineering has also been one of the important contributions toward sustainable infrastructure development.

The present review tries to capture some of these recent sustainable innovations and practices in civil/geotechnical engineering that would play a vital role in the development of resilient rural and urban infrastructure. The application of some of the industrial by-products as a sustainable material for treatment/stabilization of civil engineering materials, especially for geotechnical applications, is also discussed briefly in this paper.

2   Application of Industrial By-Products as Stabilizers (Admixture/Additives)

2.1   *Ground Granulated Blast Furnace Slag (GGBS)*

Ground granulated blast furnace slag (GGBS) is a by-product of steel/iron manufacturing industries and is obtained by the rapid cooling of molten iron slag. The reaction of limestone flux with ash from coke, and the aluminous and siliceous residues that remain after reduction and separation of iron from its ore, are responsible in production of GGBS. It mainly consists of silicates and aluminosilicates of lime and other bases [45, 59, 69]. GGBS has received considerable attention as an admixture/stabilizer for improving soil properties, and details of some of the studies along with the properties improved are presented in Table 1.

It was observed from the studies that the stabilized soils with up to 30% of GGBS content achieved effective improvement in unconfined compressive strength (UCS), and beyond 30% GGBS, the UCS values for stabilized soils reduced. On the other hand, California bearing ratio (CBR) values for stabilized soil significantly improved up to 15% GGBS content, and it further reduced at higher GGBS content. Few studies also reported improvement in shear strength properties of soil stabilized with 4–10% of GGBS content.

Table 1 Studies on soil stabilization using GGBS

References	Material/application	Optimum content (%)	UCS KN/m^2	CBR (%)	Shear strength (kN/m^2)
Yadu and Tripathi [69]	Stabilization of norganic fine grained expansive soil	9	150	10 (Soaked) 19 (Unsoaked)	–
Neeladharan et al. [45]	Stabilization of sandy and clayey soils	10	–	16.97 (Unsoaked)	33.16
Saravanan [59]	Stabilization of sandy and clayey soils for l ocal village roads	4	275	11.82 (Unsoaked)	–
		4	–	24.82 (Unsoaked)	221.78
		4	365	14.11 (Unsoaked)	–
		4	300	17.52 (Unsoaked)	–
Sharma and Sivapullaiah [60]	Black cotton soil	40	600	–	–
Neeraja and Narasimha [46]	Stabilization of expansive clayey soil for pavement construction	15	166.42	9.57 (Unsoaked)	–
Mujtaba et al. [42]	Stabilization of: Expansive soil (a)	50	–	11.5 (Unsoaked)	–
	Expansive soil (b)	50		10.7 (Unsoaked)	–
	Expansive soil (a)	30	1100	–	–
	Expansive soil (b)	30	1300	–	–

2.2   Red Mud

Red mud is an insoluble material that is generated from aluminum industries, after caustic leaching of bauxite process with sodium hydroxide at higher pressure and temperature [12]. It is disposed in slurry form with about 10–30% of solid concentration. Red mud has high ionic strength with pH of 10–13 [12] and is also called as bauxite residue [55]. Red mud consists of iron oxide, sodium oxide, calcium oxide, silicon dioxide, aluminum oxide with trace quantities of earth elements [56]. Due to high iron oxide content, it is red in color [66], and the properties of red mud are affected by process of alumina production and bauxite ore source [68]. Processed bauxite contains 35–40% of red mud which is considered as waste material [29]. Disposal of such waste is a serious challenge [5]. According to Lima et al. [34], the total amount of red mud production around the world in 2015 was around 160 million tons, out of which China holds the largest share [24]. Based on the literature review, the summary of studies on application of red mud for soil stabilization is presented in Table 2.

Table 2 Studies on red mud for soil stabilization

References	Findings and applications
Kalkan [29]	Red mud can be useful for clay liners and clayey soil stabilization Permeability for 75% clay, 20% red mud and 5% cement composition value is reported as 3.78×10^{-8} cm/sec. It is also observed that red mud increases the dry density of soil
Sridevi et al. [64]	Red mud can be used for stabilization of expansive soil. Optimum percentage of red mud and lime is observed as 30% in expansive soil stabilization
Deelwal et al. [12]	Red mud can be used for cement clinker production. Permeability of red mud is about 5×10^{-8} cm/sec, which satisfies the requirement of the material for road construction. The application can also be extended for production of bricks, tiles production, and in bituminous and cement mixtures
Wang et al. [67]	Red mud is noted to be useful for removing ions from soils and aqueous solution such as phenolic compounds and dyes, metal and non-metal ions
Mukiza et al. [43]	Red mud has been used for improvement of subgrade soil properties

Figure 1a shows the UCS values for different percentage of red mud, fly ash, lime, clay, and cement, as reported by various researchers, and Fig. 1b shows the variation of CBR value for different percentage of red mud, fly ash, and cement reported by different researchers. Other researchers have observed maximum CBR and split tensile shear strength at 28 days of curing for 25% of GGBS with red mud, and the higher tensile strength is due to the pozzolanic action of GGBS and red mud particles [56]. Addition of red mud in clayey soil has been noted to yield considerably high shear strength than the soil shear strength [12]. Jha et al. [28] investigated the effect of addition of fly ash (Class F) on the properties of red mud, and
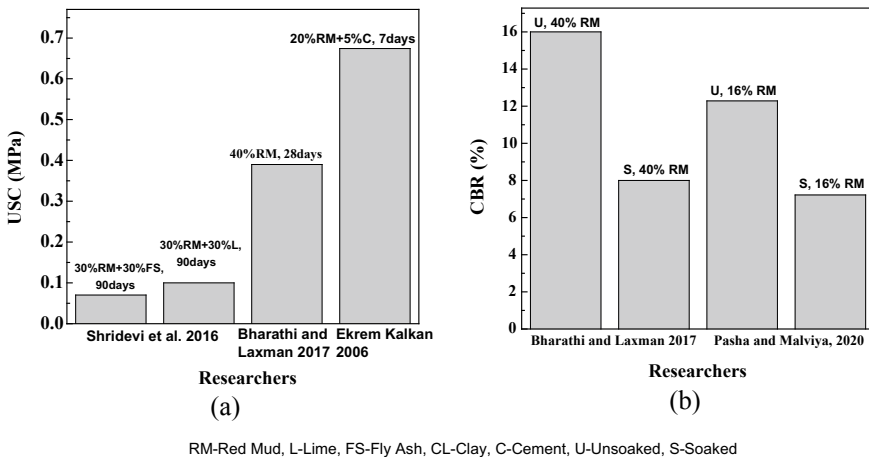

RM-Red Mud, L-Lime, FS-Fly Ash, CL-Clay, C-Cement, U-Unsoaked, S-Soaked

Fig. 1 Variation of (**a**) UCS and (**b**) CBR values presented by researchers

noted significant reduction in liquid limit, plastic limit and optimum moisture content with increase in the fly ash content. The maximum value of unconfirmed compression strength was observed for 15% fly ash content.

2.3 Biosolids

Biosolids are by-product from the domestic and industrial sewage treatment processes in liquid and/or semi-solid state, and constitutes about 0.2 to 25% solid content by weight in the wastewater [65]. It may be also defined as the solid residue of wastewater after treatment, or biological sewage sludge separated during municipal wastewater treatment process [11]. An earlier study reported that the production of biosolids increased by almost two times the estimated value in USA during 1972 to 1990 [7]. Therefore, due to large quantity of biosolids generation, there is a need to explore methods for its safe disposal as well as reutilization. Heavy metals especially chromium, nickel, iron, and aluminum in variable proportion have been found in biosolids from the industrial areas [39]. Hence, disposal of biosolids can have hazardous effects on the environment (viz., air, water, land pollution, and negative health effects on living biodiversity). Disposal of biosolids is generally carried out by landfilling and incineration. One of the potential ways of its reutilization is by its stabilization for improving its properties and immobilization of the contaminants present in the biosolids. Table 3 shows the summary of different studies on biosolids and their applications.

Table 3 Studies on biosolids and its applications by various authors

References	Findings and applications
Maghoolpilehrood et al. [38] and Arulrajah et al. [6]	Hydraulic conductivity and compressibility characteristics of biosolids can be improved by stabilization with fly ash and lime
Maghoolpilehrood et al. [37]	With 3% of cement and 5% of lime, the stabilized biosolids can satisfy the requirements of road fill material, coefficient of permeability decreases with 3% of lime and 5% of cement. It can be utilized as embankment fill material
Ona et al. [49]	Application of sludge to promote plants growth and species for increasing slope stability by revegetation and reducing erosion. Maximum erosion control between 63 and 90% occurs when mixture of compost and sludge was applied on the embankment slopes
Mohajerani et al. [41]	Presented application of biosolids as an embankment fill material
Ingunza et al. [27]	The study explored the application of biosolids for brick and aggregate manufacturing
Collivignarelli et al. [11]	Presented the utilization of biosolids in construction industry

2.4 Lignin-Based Stabilizer

Lignin is a naturally occurring substance, which refers to a group of phenolic polymers that provide strength and rigidity to the woody cell wall of plants. This is one of the reasons, why lignin-based conditioners are known to have significant adhesive properties. Lignin and lignin derivatives are non-toxic natural by-products produced during the manufacturing of pulp and paper [74]. Commercial lignin is produced as a by-product of the paper industry, separated from trees by a chemical pulping process. Lignosulfonates are the soluble derivatives of lignin, and when used as a binder, the lignosulfonate increases the strength and durability of the material [20]. Geotechnical applications of lignin-based stabilizers are summarized in Table 4.

Highway subgrade construction has been identified as one of the viable applications, to consume significant quantity of lignin, as an environmentally friendly, low-cost, and less energy intensive additive for soil stabilization. Researchers have also improved the swelling behavior and erosion resistance of soils using lignin-based stabilizer. The formation of a stabilized product is due to the precipitation of lignin-based matter, that bonds with the soil particles and fills the pores to produce a more stable soil structure [74].

2.5 Silica Fume

Silica fume is a by-product obtained during the manufacturing of ferrosilicon and silicon metal and generally contains more than 90% of amorphous silicon dioxide and other constituents such as carbon, sulfur, and the oxides of aluminum, iron,

Table 4 Application of lignin-based stabilizer in geotechnical engineering

References	Material	Optimum content	Properties improved (MPa)	Applications
Cai et al. [8]	Silty soil	12%	UCS—0.65	Improvement in engineering properties of silty soil
Chen et al. [9]	Sandy silt soil	2%	UCS—0.28	Stabilization of sandy silt as an embankment fill
Zhang et al. [72]	Silt	12%	UCS—increased from 0.06 to 0.65	Stabilization of silt for its application as foundation soil
Zhang et al. [71]	Silt	12%	UCS—0.65 Resilient modulus—65	Enhancement of mechanical properties of lignin stabilized silt with a short curing time
Zhang et al. [73]	Silty soil	8%	UCS—0.55	Stabilizing mechanical properties silty soil for application as a base fill material

calcium, magnesium, sodium, and potassium. However, the composition of silica fume varies depending on the type of alloy or metal being manufactured [30, 61]. Silica fume is pozzolanic in nature, as it is reactive and consists of the fine particles with specific surface area about six times that of cement [51]. Even though silica fume is an industrial waste, it has become one of the beneficial and valuable material among the pozzolanic materials [30]. Silica fume has been mainly used as an admixture in cementitious materials to produce high strength concrete.

Researchers have widely used silica fume for improving the UCS and swelling behavior (reduction in swelling potential of soil) of various soils and has been effectively employed for up to 25% replacement in soil stabilization. Other properties like cation exchange capacity (CEC), specific surface area (SSA), CBR, optimum moisture content (OMC), maximum dry density (MDD), hydraulic conductivity, and cracking behavior have also been improved. Fineness and pozzolanicity of silica fume are responsible for the significant improvement in the soil properties. The different geotechnical applications of silica fume are summarized in Table 5.

Table 5 Improvement in soil properties using silica fume

References	Material and applications	OC (%)	UCS (kPa)	Swelling behavior	Other properties
Silitonga [61]	Reuse in sub-base and foundations on marine dredged sediments	4	800 (UT) 1500 (T)	–	–
		6	800 (UT) 1700 (T)	–	–
Negi et al. [47]	Stabilization of black cotton soil	20	125.1 (UT) 165 (T)	–	CBR—2.8 (Soaked) DFS—6%
AL-Soudany [2]	Stabilization of expansive soil (a)	7	–	S_{pre}–85 kPa (UT) 50 kPa (T) Free swell— 6.8% (UT) 4% (T)	–
	Soil (b)	7	–	S_{pre}– 105 kPa (UT) 70 kPa (T) Free swell-8% (UT) 6% (T)	–

Table 5 (continued)

References	Material and applications	OC (%)	UCS (kPa)	Swelling behavior	Other properties
Phanikumar et al. [54]	Stabilization of expansive soil	9–12	–	FSI-110% (UT) FSI—80% (T)	OMC-110%(UT) 24.21%(T) MDD—13.48 KN/m^3 (UT) 14.26 KN/m^3 (T) CBR—0.76% (UT) 2.63% (T)
	Stabilization of laterite soil, used as a cushion over the expansive clay subgrade	9–12	213 (UT) 734 (T)	–	OMC—17.69% (UT) 12.75% (T) MDD—17.80 KN/m^3 (UT) 18.85 KN/m^3 (T) CBR—2.41% (UT) 7.74% (T)
Ghavami et al. [18]	Stabilization of soft kaolinite clay	15	129 (UT) 220 (T)	–	CBR—3% (Soaked UT) 6.6% (Soaked, T)
Al-Azzawi et al. [3]	Reduction of desiccation cracks in compacted clayey liner and cover systems, enhance permeability of silty clayey soils	10–15	420 kPa (UT) 450 kPa (T)	S_{pre}–89 kPa (UT) 11 kPa (T) Swelling— 12% (UT) 2% (T)	Crack width 0.4 mm (UT) 0.1 mm (T)

OC—Optimum content, S—Swelling, S_{po}—Swelling Potential, S_{pre}—Swelling pressure, DFS—Differential free swell, T—Treated, UT—Untreated, CBR—California bearing ratio

2.6 Sustainable Fill Materials

2.6.1 Old Mined Municipal Solid Waste

Landfill reclamation is the process of excavation/mining and processing of the formerly landfilled waste to reclaim/recover the available recyclable and combustible matter, while reducing the expenses of post-closure and/or site remediation [25, 63]. The reutilization of such mined material would reduce the consumption of natural resources for future infrastructure development, contribute toward conservation of landfill space, reduce the landfill footprint, and result in rehabilitation of dumpsite; while minimizing the potential contamination sources. The various applications of old mined municipal solid waste have been presented in Table 6.

Table 6 Applications of old mined municipal solid waste

References	Applications
Parrodi et al. [53], Masi et al. [40], Hull et al. [25]	As a cover material on site (daily cover) and/or final cover
Hull et al. [25], Parrodi et al. [53]	As an offsite fill material for road sides
Parrodi et al. [53], Somani et al. [63]	As a geotechnical material in earth fill for road subgrade and embankment
Parrodi et al. [53]; Rubinos and Spagnoli [57]	As a landfill bottom and side slope liners
Masi et al. [40]; Parrodi et al. [53]	For cultivating of non-edible plants
Masi et al. [40]; Rubinos and Spagnoli [57]	Construction of barrier layers of landfill, as a substitution to natural soil layer
Hull et al. [25]	Fines from old mined waste can be used to predict the moisture content of old waste samples containing different waste fractions

The excavated waste from old open landfills usually consists of fine fraction with some organic content, and other fractions like wood, cardboard, textile, glass, metal, paper, plastics, rubber, and debris. Components such as paper, textile, cardboard, and wood are decayed and are converted into fines over a period of time in the landfill [16, 25]. This fine fraction along with other inorganic fraction may constitute about 40–70% of the total mined waste [25, 53, 63]. The process of formation of fine fraction is quite similar to the natural humification process [53]. Indian Standard (IS) code defines the fine fraction as the component of old landfill finer than 4.75 mm in size and may constitute of sand, silt, and clay-sized particles [27].

2.6.2 Sustainable Flowable Fill

Flowable fill is also known as controlled low strength material (CLSM). It is a mixture of fine aggregates, water, portland cement, and other recycling materials that can flow like liquid, and sets up to form a low strength fill [35, 48]. The purpose of cement in flowable fill mixtures is to facilitate the binding of particles. There is no need of external load or compaction for setting of the flowable fill [1]. According to American Concrete Institute (ACI) 229, flowable fill has a compressive strength of 8.3 MPa or less at the age of 28 days [1]. Researchers have developed sustainable flowable fill by using different types of recycling material such as fly ash, pond ash, wood fly ash, quarry dust foundry sand, and recycled fine aggregate [10, 14, 15, 21, 32, 44, 62]. This material has wide range of non-structural and light-structural applications in pavement subgrade and bases, structural fill, underground pipe trench filling and bedding, voids filling, and

Table 7 Studies on development of sustainable flowable fill with different recycled materials

References	Recycled material	Flowability (mm)	Compressive strength (MPa)	Hardening time (Hours)	Application
Chompoorat et al. [10]	Fly ash	–	10.13	11.05	Pavement bases
Alizadeh et al. [4]	Fly ash	210	1.4	–	Structural fill in bridge abutment
Kim et al. [32]	Quartz-based mine tailing	210	0.5	–	Thermal grout for ground source heat pump system
Kim et al. [31]	Steel making raw slag	235	2.7	11.5	
	Ground steel making slag	215	3.5	10.5	
Okuyucu et al. [48]	Steel fiber with lime stone sand	290	1.6	–	Pavement base layer
Yao and Sun [70]	Coal refuse + fly ash	270	1.4	–	Backfill
Lachemi et al. [33]	Cement kiln dust	215	2.99	–	–

backfill for retaining walls [10, 15, 36]. The details from literature on sustainable flowable fill are presented in Table 7.

Pond ash-based flowable fill has been reported to exhibit no segregation with desired flowability (200–300 mm), even with less amount of cement (2–4%) and water content ranging from 41.5 to 47%. For flowable fill with 4% cement and with pond ash, the compressive strength has been noted to increase to a value of 0.7 MPa at the end of 28 days [13]. Permeability for CLSM from pond ash is reported in range of 10^{-5} cm/s for 2–3% of cement in the mix [13]. With increase in cement content and decrease in flowability, the CBR value has been observed to increase [13]. Pond ash-based flowable fill can also be supplemented using different industrial waste such as sewage sludge [22]. The compressive strength in the range of 0.7–9 MPa has been achieved at the end of 28 days for flowable fill. The researchers have concluded that the increase in the amount other waste material utilized with pond ash, will decrease the strength of the flowable fill.

3 Utilization of Geosynthetics for Soil Improvement

Researchers [17, 19] have presented the application of geosynthetics in road embankment, ground improvement, and pavement construction. They suggested many functions of geosynthetics such as filtration, drainage, separation,

Table 8 Application of geosynthetics in geotechnical engineering

References	Findings and applications
Gohil et al. [19]	Applications include soil reinforcement, ground improvement, and pavement construction. It is noted that geosynthetics can be useful for better performance of geotechnical structures against earthquake
Palmeira [50]	Application of waste tyre, recyclable residue along with geosynthetics and an alternative sub-ballast material in railway and alternative constructional material in retaining and road structures has been reported. It has been suggested as very useful for reinforcement and other functions in retaining and road structures
Frischknecht et al. [17]	Application of geosynthetics in place of traditional construction material has been reported. Geosynthetics filters can result in 85% less impact on environment than conventional granular fill material, and geosynthetics reinforced walls can produce 52–87% less impact than concrete retaining wall construction
Santos et al. [58]	The combination of geosynthetics with waste material with low grade can impart benefits to environment, by reducing the utilization of conventional construction materials
Harish et al. [23]	Rut depths are reduced by 28% and 56% by using biaxial geogrid and geocell, respectively. Application for sustainable pavement construction has also been reported

reinforcement, barrier to fluid flow, and protection. Based on the literature review, Table 8 presents the study on geosynthetics and their application in geotechnical engineering.

4 Concluding Remarks

Considering the need for utilization of different waste material for different applications, a detailed review has been done. It has been observed that utilization of GGBS, red mud, biosolids, lignin-based stabilizer, and silica fume, as admixtures, has a great potential in stabilizing/improving basic and geotechnical properties of variety of soils for mitigating slope erosion, subgrade and foundation soil stabilization, crack reduction, and for pavement applications. For significant improvement, the optimum content has been suggested as about 10–15% (GGBS), 30% (red mud), 12% (lignin-based stabilizer), and 15% (silica fume). Also, old landfill mined material and sustainable flowable fill, as a fill material, have good potential applications in geotechnical engineering as backfill, embankment fill, daily/final cover, and as a bottom/slope liner material. The application of recyclable residue along with geosynthetics can satisfy the requirement of strengthening the soil and reduce the requirement of concrete for various infrastructure facilities. The review highlights the recent innovations and practices in geotechnical engineering that would play a vital role in the development of sustainable infrastructure.

References

1. ACI 229R–99.: Controlled Low Strength Materials, American Concrete Institute (2005)
2. AL-Soudany, K.Y.: Improvement of expansive soil by using silica fume. Kufa J. Eng. **9**(1), 222–239 (2017)
3. Al-Azzawi, A., Daud, K., Sattar, M.: Effect of silica fume addition on the behavior of silty-clayey soils. J. Eng. Dev. **16**(1) (2012)
4. Alizadeh, V., Helwany, S., Ghorbanpoor, A., Soboldev, K.: Design and application of controlled low strength materials as a structural fill. Constr. Build. Mater. **53**, 425–431 (2014)
5. Altundogan, H., Altundogan, S., Tumen, F., Bildik, M.: Arsenic adsorption from aqueous slutions by activated red mud. Waste Manage. **22**, 357–363 (2002)
6. Arulrajah, A., Disfani, M., Suthagaran, V., Inteaz.: Select chemical and engineering properties of wastewater biosolids. Elsevier J. Waste Manage. **31**, 2522–2526 (2011)
7. Bastian. R.: The biosolids (sludge) treatment, beneficial use, and disposal situation in the USA. European Water Pollut. Control J. **7**(2), 62–79 (1997)
8. Cai, G., Zhang, T., Liu, S., Li, J., Jie, D.: Stabilization mechanism and effect evaluation of stabilized silt with lignin based on laboratory data. Marine Georesour. Geotechn. (2014)
9. Chen, Q., Indraratna, B., Carter, J., Rujikiatkamjorn, C.: A theoretical and experimental study on the behavior of lignosulfonate-treated sandy silt. Comput. Geotech. **61**, 316–327 (2014)
10. Chompoorat, T., Likitlersuang, S., Jongvivatsakul, P.: The performance of controlled low-strength material base supporting a high-volume asphalt pavement. KSCE J. Civ. Eng. **22**(6), 2055–2063 (2018)
11. Collivignarelli, M., Canato, M., Abba, A., Miino, M.: Biosolids: what are the different types of reuse? Elsevier J. Cleaner Prod. 238 (2019)
12. Deelwal, K., Dharavath, K., Kulshreshtha, M.: Evaluation of characteristic properties of red mud for possible use as a geotechnical material in civil construction. Int. J. Adv. Eng. Technol. **7**, 1053–1059 (2014)
13. Dev, K., Robinson, R.: Pond ash based controlled low strength flowable fills for geotechnical pond ash based controlled low strength flowable fills for geotechnical engineering applications. Int. J. Geosynthetics Ground Eng. **1**(32), 1–13 (2015)
14. Do, T.M., Kim, Y.S.: Engineering properties of controlled low strength material (CLSM) incorporating red mud. Int. J. Geo-Eng. **7**(7), 1–17 (2016)
15. Fang, X., Wang, L., Poon, C.S., Baek, K., Tsang, D.C.W., Kwok, S.K.: Transforming waterworks sludge into controlled low-strength material: bench-scale optimization and field test validation. J. Environ. Manage. **232**, 254–263 (2019)
16. Feng, S., Gao, K., Chen, Y., Li, Y., Zhang, L.M., Chen, H.X.: Geotechnical properties of municipal solid waste at Laogang Landfill, China. Waste Manage. (2016)
17. Frischknecht, R., Stucki, M., Büsser, S., Itten, R.: Comparative life cycle assessment of geosynthetics vs conventional construction materials. Ground Eng. **45**(10), 24–28 (2012)
18. Ghavami, S., Farahani, B., Jahanbakhsh, H., Nejad, F.M.: Effects of silica fume and nano-silica on the engineering properties of kaolinite clay. AUT J. Civil Eng. **2**(2), 135–142 (2018)
19. Gohil, D., Solanki, C., Desai, A.: Application of Geosynthetics for Ground Improvement: an overview. IGC 2009, Guntur, India (2009)
20. Goren, S., Alagha, O.: Soil treatment with lignin sulphide chemical stabilizer: environmental and structural assessment. J. Residuals Sci. Technol. **5**(4) (2008)
21. Griffin, J.R., Brown, E.R.: Flowable fill for rapid pavement repair. J. Transp. Res. Board **2235**, 88–94 (2011)
22. Guangyin, Z., Haiyan, Z., Tiantao, Z., Youchi, Z.: Performance appraisal of controlled low-strength material using sewage sludge and refuse incineration bottom ash. Chin. J. Chem. Eng. **20**(1), 80–88 (2012)
23. Harish, G., Madesh, N., Swati G., Reddy, V., Deepak, H.: Use of Geosynthetics for Sustainable Pavements. Sustainable Engineering, Lecture Notes in Civil Engineering (2019)

24. Hua, Y., Heal, K.V., Friesl-hanl, W.: The use of red mud as an immobilizer for metal/metalloid-contaminated soil: a review. J. Hazard. Mater **325**, 17–30 (2017)

25. Hull, R.M., Krogmann, U., Strom, P.F.: Composition and characteristics of excavated materials from a new jersey landfill. J. Environ. Eng. **131**(3), 478–490 (2005)

26. IS 2720-4.: Methods of test for soils, Part 4: grain size analysis, Bureau of Indian Standards, New Delhi, India (1985)

27. Ingunza, M., Duarte, A., Nascimento, R.: Use of sewage sludge as raw material in the manufacture of soft-mud bricks. J. Mater. Civil Eng. **23**(6) (2011)

28. Jha, G., Kumar, D., Sivapullaiah, P.: Influence of fly ash on geotechnical behaviour of red mud: a micro-mechanistic Study. Geotech. Geol. Eng. **38**, 6157–6176 (2020)

29. Kalkan, E.: Utilization of red mud as a stabilization material for the preparation of clay liners. Eng. Geol. **87**, 220–229 (2006)

30. Kalkan, E.: Impact of wetting-drying cycles on swelling behavior of clayey soils modified by silica fume. Appl. Clay Sci. **52**(4), 345–352 (2011)

31. Kim, Y., Dinh, B.H., Do, T.M., Kang, G.: Development of thermally enhanced controlled low-strength material incorporating different types of steel-making slag for ground-source heat pump system. Renewable Energy **150**, 116–127 (2020)

32. Kim, Y.S., Do, T.M., Kim, M.J., Kim, B.J., Kim, H.K.: Utilization of by-product in controlled low-strength material for geothermal systems: engineering performances, environmental impact, and cost analysis. J. Cleaner Prod. **172**, 909–920 (2018)

33. Lachemi, M., Sahmaran, M., Hossain, K.M.A., Lotfy, A., Shehata, M.: Properties of controlled low-strength materials incorporating cement kiln dust and slag. Cement Concr. Compos. **32**, 623–629 (2010)

34. Lima, M., Thives, L., Haritonovs, V., Bajars, K.: Red mud application in construction industry: review of benefits and possibilities. IOP Conf. Series: Mater. Sci. Eng. **251** (2017)

35. Lin, W., Weng, T., Cheng, A., Chao, S., Hsu, H.: Properties of controlled low strength material with circulating fluidized bed combustion ash and recycled aggregates. Materials **5**, 1–11 (2018)

36. Ling, T.C., Kaliyavaradhan, S.K., Poon, C.S.: Global perspective on application of controlled low-strength material (CLSM) for trench backfilling—an overview. Constr. Build. Mater. **158**, 535–548 (2018)

37. Maghoolpilehrood, F., Disfani, M., Arulrajah, A.: Geotechnical characteristics of aged biosolids stabilized with cement and lime. Aust. Geomech. J. **48**(3), 113–120 (2013)

38. Maghoolpilehrood, F., Disfani, M., Arulrajah, A.: Geotechnical investigation of stabilized municipal biosolids. Int. Conf. Adv. Civil Eng. Sustain. Dev. 27–29 (2014)

39. Manara, P., Zabaniotou, Z.: Towards sewage sludge-based biofuels via thermochemical conversion—a review. Elsevier J. Renew. Sustain. Energy Rev. **16**, 2566–2582 (2012)

40. Masi, S., Caniani, D., Grieco, E., Lioi, D.S., Mancini, I.M.: Assessment of the possible reuse of MSW coming from landfill mining of old open dumpsites. Waste Manage. **34**(3), 702–710 (2014)

41. Mohajerani, A., Lound, S., Liassos, G., Kurmus, H., Ukwatta, A., Nazari, M.: Physical mechanical and chemical properties of biosolids and raw brown coal fly ash, their combination for road structure fill applications. J. Cleaner Prod. (2017)

42. Mujtaba, H., Aziz, T., Farooq, K., Sivakugan, N., Das, B.: Improvement in engineering properties of expansive soils using ground granulated blast furnace slag. J. Geol. Soc. India **92**, 357–362 (2018)

43. Mukiza, E., Zhang, L., Liu, X., Zhang, N.: Utilization of red mud in road base and subgrade materials: a review. Resour. Conserv. Recycl. **141**, 187–199 (2019)

44. Naganathan, S., Razak, H.A., Hamid, S.N.A.: Properties of controlled low-strength material made using industrial waste incineration bottom ash and quarry dust. Mater. Design **33**, 56–63 (2012)

45. Neeladharan, C., Muralidharan, A., Mohan, K., Sayeed, M., Azeez, A., Faizan, M., Arafath, Y.: Stabilization of soil using fly ash with ground granulated blast furnace slag (GGBS) as binder. Suraj Punj J. Multi. Res. **9**(4), 23–29 (2019)

46. Neeraja, D., Narsimha, R.: Use of certain admixtures in the construction of pavement on expansive clayey subgrade. Int. J. Eng. Sci. Technol. **2**(11), 6108–6114 (2010)
47. Negi, C., Yadav, R.K., Singhai, A.K.: Effect of silica fume on engineering properties of black cotton soil. Int. J. Comput. Eng. Res. **3**(7) (2013)
48. Okuyucu, O., Jayawickrama, P., Senadheera, S.: Mechanical properties of steel fiber–reinforced self-consolidating controlled low-strength material for pavement base layers. J. Mater. Civil Eng. **31**(9) (2020)
49. Ona, J., Ferrer, A., Osorio, F.: Erosion and vegetation cover in road slopes hydro seeded with sewage sludge. Elsevier J. Trans. Res. Part D **16**, 465–468 (2011)
50. Palmeira, E.: Sustainability and innovation in geotechnics: contributions from geosynthetics. Soils and Rocks, São Paulo **39**(2), 113–135 (2016)
51. Panjehpour, M., Abdullah, A., Demirboga, R.: A review for characterization of silica fume and its effects on concrete properties. Int. J. Sustain. Constr. Eng. Technol. **2**(2) (2011)
52. Parashar, P., Choudhary, M., Nagar, B.: Utilization of reclaimed asphalt pavement materials in rigid pavement. Int. J. Eng. Res. Technol. **9**(6), 99–102 (2020)
53. Parrodi, J., Höllen, D., Pomberger, R.: Characterization of fine fractions from landfill mining: a review of previous investigations. Detritus **2**(1), 46 (2018)
54. Phanikumar, B.R., Jagapathi, R., Ramanjaneya, R.: Silica fume stabilization of an expansive clay subgrade and the effect of silica fume-stabilised soil cushion on its CBR. Geomech. Geoeng. (2019)
55. Pontikes, Y., Angelopoulos, G.: Resources, conservation and recycling bauxite residue in ccement and cementitious applications: current status and a possible way forward. Resour. Conserv. Recycl. **73**, 53–63 (2013)
56. Rao, C., Naidu, P., Adiseshu, P.: Application of GGBS stabilized red mud in road construction. IOSR J. Eng. (IOSRJEN) **2**(8), 14–20 (2012)
57. Rubinos, D., Spagnoli, G.: Utilization of waste products as alternative landfill liner and cover materials–a critical review. Crit. Rev. Environ. Sci. Technol. **48**(4), 376–438 (2018)
58. Santos, E., Vilar, O., Palmeira, E.: The use of recycled construction and demolition waste in geosynthetic reinforced structures: influence of the recycling process. In: Proceedings 6th International Conference on Environmental Geotechnics, vol. 1, pp. 1105–1108 (2010)
59. Saravanan, R., Udhayakumar, T., Dinesh, S., Venkatasubramanian, C., Muthu, D.: Effect of addition of GGBS and lime in soil stabilisation for stabilising local village roads in Thanjavur region. Earth Environ. Sci. **80** (2017)
60. Sharma, A., Sivapullaiah, P.: Improvement of Strength of Expansive soil with waste Granulated Blast Furnace Slag. GeoCongress, ASCE (2012)
61. Silitonga, E.: Experimental research of stabilization of polluted marine dredged sediments by using silica fume. In: MATEC Web of Conferences 138, EACEF (2017)
62. Singh, V.K., Das, S.K.: Performance of controlled low strength material made using industrial by-products. IOP Conf. Series: Earth Environ. Sci. **491**, 1–9 (2020)
63. Somani, M., Datta, M., Ramana, G.V., Sreekrishnan, T.R.: Investigations on fine fraction of aged municipal solid waste recovered through landfill mining: case study of three dumpsites from India. Waste Manage. Res. **36**(8), 744–755 (2018)
64. Sridevi, G., Sahoo, S., Sen, S.: Stabilization of Expansive Soil with Red Mud and Lime. Ground Improvement Techniques and Geosynthetics. Lecture Notes in Civil Engineering, (14). Springer, Singapore (2019)
65. Tchobanoglous, G., Burton F., Stensel, H.: Wastewater Engineering Treatment and Reuse, fourth ed. McGraw-Hill Higher Education, Boston, US (2003)
66. Tsakiridis, P., Agatzini, S., Oustadakis, P.: Red mud addition in the raw meal for the production of portland cement clinker. J. Hazard. Mater. **116**, 103–110 (2004)
67. Wang, L., Hu, G., Lyu, F., Yue, T., Tang, H., Han, H., Yang, Y., Liu, R., Sun, W.: Application of red mud in wastewater treatment. Minerals **9**(5), 281 (2019)
68. Wu, C., Liu, D.: Mineral phase and physical properties of red mud calcined at different temperatures. J. Nanomater (2012)

69. Yadu, L., Tripathi, R.K.: Effect of granulated blast furnace slag in the engineering behaviour of stabilized soft soil. Procedia Eng. **51**, 125–131 (2013)
70. Yao, Y., Sun, H.: A novel silica alumina-based backfill material composed of coal refuse and fly ash. J. Hazard. Mater. **213–214**, 71–82 (2012)
71. Zhang, T., Cai, G., Liu, G., Puppala, A.: Experimental investigation of thermal and mechanical properties of lignin treated silt. Eng. Geol. **196**, 1–11 (2015)
72. Zhang, T., Cai, G., Liu, G., Puppala, A.: Engineering properties and microstructural characteristics of foundation silt stabilized by lignin-based industrial by-product. KSCE J. Civil Eng. 1–12 (2016)
73. Zhang, T., Cai, G., Liu, S.: Assessment of mechanical properties in recycled lignin-stabilized silty soil as base fill material. J. Cleaner Prod. 1–12 (2017)
74. Zhang, T., Cai, G., Liu, S.: Application of lignin-stabilized silty soil in highway subgrade: a macroscale laboratory study. J. Mater. Civil Eng. **30**(4) (2018)
75. Zhang, T., Yang, Y., Liu, S.: Application of biomass by-product lignin stabilized soils as sustainable geomaterials: a review. Sci. Total Environ. 728 (2020)

Analysis of Cushion Effects in Unconnected Piled Raft Foundation

P. A. Amalu and B. R. Jayalekshmi

1 Introduction

Piled raft foundation system has been one of the most efficient system practiced as a foundation construction method in the recent few decades to transfer the load from superstructure to the underlying soil through the combined action of raft and pile. The piled raft foundations are a combination of shallow and deep type foundations where the limitations of one type is overcome by the advantages of other. Generally, raft foundations are provided to reduce differential settlement of a structure to desirable limit. The size and depth of raft foundation play a vital role in determining the amount of settlement. Since raft foundations are costlier to construct, reducing the settlement of structure without increasing the size of a raft is an economical solution. In this point of view, piles are provided beneath the raft. Pile footings are designed to function as an effective settlement reducer. Thus, the combination of pile and raft points towards a much economical foundation solution especially for high-rise buildings.

Pile–raft foundations were practiced from early days date back to 1957 as reported by Zeevaert [1] in his article about the high-rise building constructed over piled raft foundations at Mexico City. After the studies of [2, 3], the design and analysis of piled raft foundations had emerged into a promising research area where a lot of innovative alterations have been experimented. The contact stress distribution of raft foundations when compared with piled raft systems proved that the piles considerably reduce the differential settlement [4]. These foundation systems can be designed in two types. The first type of system connects the raft foundation and pile footings. Here the raft acts as a pile cap, but with considerable load bearing capacity, whereas in the second type of foundation systems, the raft foundation and pile foundation are constructed without any connection. In these types of foundations, a gap will be provided between the bottom of raft foundation and top of pile

P. A. Amalu (✉) · B. R. Jayalekshmi
National Institute of Technology, Karnataka, Surathkal, India

footings. The conventional design of piled raft footings has considered either the load bearing by raft and settlement reduction by pile foundation or the other way around. These methods resulted in uneconomical designs [5]. Therefore, developing a method that incorporates the combined load bearing effect of pile foundation and raft footing was targeted in many research works.

Different methods of analysis were proposed by researchers on the design of piled raft foundation systems. The pioneer research work includes the book on pile foundation analysis and design [3]. With the development in computational techniques, rigorous analysis was carried on the piled raft foundations under various loading conditions. The behaviours of piled raft foundations under static and dynamic loadings are not similar [6]. There was a marginal variation in the results of deformation and load proportions in these foundations under dynamic loading conditions, when compared to static loading conditions. This was due to the incapability of incorporating all the parameters involved in the soil–structure interfaces and the load distribution pattern between raft and pile. It was pointed out in many literature that the proportion of load shared between pile and raft foundation is not a constant value under the influence of lateral loads [6–10]. On the contrary, the load proportions shared by both these foundations were not varying considerably under static vertical loads.

The provision of a cushion layer between the raft and pile head has been introduced later [11, 12]. It was reported that the cushion between the raft and pile reduced the differential settlement of raft foundation and acted as an additional damping layer when subjected to dynamic lateral loads. The provision of cushion layer also forces the subsoil to utilize its maximum bearing capacity [13]. However, the behaviour of cushion layer under an event of earthquake loading was least addressed and hence is the focus of the present study.

2 Methodology

The numerical analysis of connected and unconnected piled raft foundation beneath a multistorey building was performed using ANSYS software. The study aims to investigate the effects of different parameters of the cushion layer provided in an unconnected piled raft foundation when subjected to seismic load. A typical layout of the unconnected piled raft foundation is shown in Fig. 1. The piled raft foundation was placed in a very soft clayey soil. The parameters varied in this study are the thickness of the cushion layer which was varied from 0.25 to 0.75 m and modulus of elasticity of the cushion material which was varied from 20 to 100 MPa which represents material ranging from soft clay to sandy clay. Since the study focuses on the seismic behaviour of cushion layer in a piled raft foundation, the shape and size parameters of raft and pile foundations were kept constant.
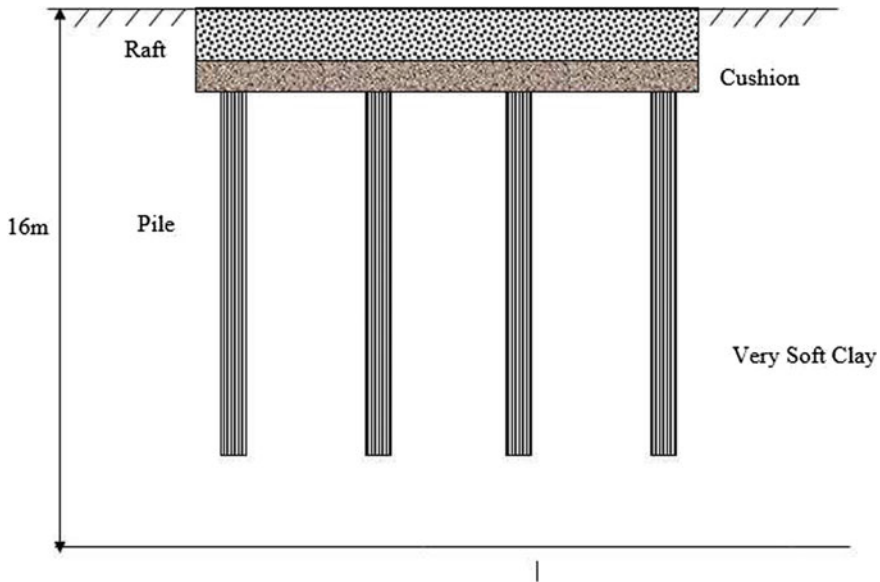
Fig. 1 Schematic representation of unconnected piled raft

Square-shaped raft and pile foundations were considered to simplify the numerical evaluation. The vertical and lateral displacements at the top of the raft were analysed in the study. The vertical and lateral deformations of the piled raft system under the influence of a cushion layer were numerically evaluated based on stiffness parameters as detailed in Eqs. 1 and 2 [13]. The overall stiffness of the piled raft system with cushion was estimated using Eq. 1, and the stiffness of cushion layer was determined using Eq. 2.

$$k_{\text{pr}} = \frac{\mathbf{P}}{\mathbf{wE_s d}} \tag{1}$$

$$k_c = \frac{\mathbf{E_c}}{\mathbf{E_S}} \tag{2}$$

where k_{pr} is the dimensionless parameter representing the stiffness of unconnected piled raft system, P is the normal load, w is the settlement of foundation system, E_s is the Young's modulus of soil, E_c is the Young's modulus of cushion, d is the least lateral dimension of pile, and k_c represents the dimensionless parameter for stiffness of cushion with respect to subsoil.

3   Modelling and Analysis of Unconnected Piled Raft Foundation

The square raft foundation of dimensions 8 m × 8 m with a thickness of 1 m was modelled as a linear elastic concrete member. A total of sixteen numbers of square pile footings was provided beneath the raft foundation of dimension 0.4 m × 0.4 m with a depth of 12 m. The pile foundations were also modelled as linear elastic concrete member. The modelled piled raft foundation was placed in a very soft clay of dimension 16 m × 16 m × 16 m. The bottom boundary of the soil domain was kept as fixed support, and the lateral boundaries were assigned as viscous boundaries by providing springs on every node with a spring coefficient of 1875 kN/m based on the shear wave velocity of the soil (150 m/s). The damping coefficients of the spring were determined to be Cv = 5400 kN/s, Cp = 62,626.56 kN/s. The hex-dominant meshing was applied on the modelled structures, and then transient structural analysis was carried out. The time history of acceleration of earthquake was applied on the soil domain in the direction of X-axis of the global coordinate system. The selected earthquake data was from the north–south component of El-Centro earthquake occurred on May 19,1940 as shown in Fig. 2. The peak ground acceleration (PGA) of the earthquake was 0.318 g with a duration of 31.18 s. A uniform loading of 0.2 Mpa was applied over the raft foundation which represented the load from the superstructure. The material parameters used are listed in Table 1.
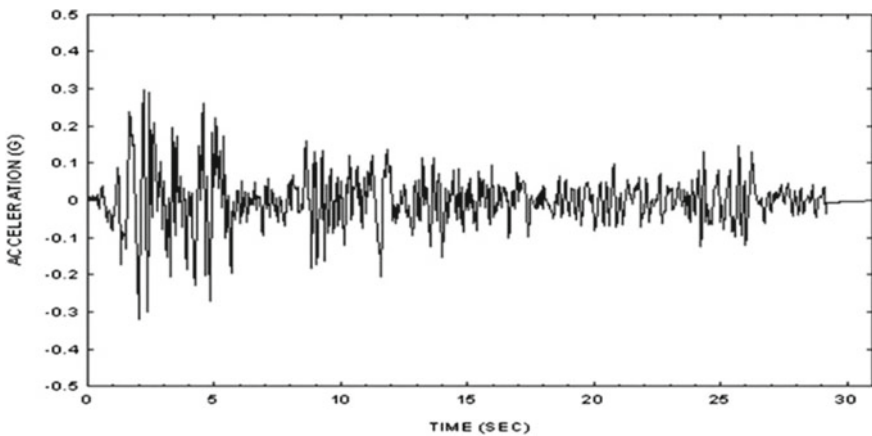
Fig. 2   Accelerogram data of El-Centro earthquake 1940

Table 1 Material properties used in analysis [14]

Material	Density γ (kN/m^3)	Modulus of elasticity E (kN/m^2)	Poisson's ratio (υ)	Undrained cohesion C_u (kPa)
Very soft clay	16.0	1250	0.45	12.5
Raft	25	3.4×10^7	0.20	
Cushion	20	40,000	0.25	
Pile	25	2.1×10^7	0.20	

4 Parametric Study

The numerical analysis was performed on ANSYS software for unconnected piled raft foundation with varying thickness and elastic modulus of cushion layer. The parameters considered in the study include thickness of cushion which was varied from 0.25 to 0.75 m and elastic modulus of the cushion material which was varied from 20 to 100 MPa. Two cases corresponding to the effect of elastic modulus and thickness of the cushion material considered in the study are summarized in Table 2.

5 Results and Discussion

The physical parameters of cushion were varied to analyse the effect of these parameters as mentioned in the subsequent sections. Table 3 shows the comparison of the settlements of the raft, connected piled raft and unconnected piled raft systems. The settlement of raft foundation was found to be uniform across the width of the foundation as highlighted in Fig. 3. The provision of cushion layer has evidently reduced the settlement of piled raft system by 69% when compared with the case of provision of raft foundation alone as shown in Fig. 4. However, the reduced settlement of unconnected piled raft foundation could also be justified by the provision of cushion layer with higher stiffness of 40 MPa, whereas the lateral deformation measured at the top of raft foundation in all the three types of

Table 2 Summary of parametric study

Parametric study	Raft	Cushion		Pile group	
	Length $\times$ width $\times$ thickness (m)	Thickness (m)	Elastic modulus (MPa)	Cross section (m)	Length (m)
Case 1	8 $\times$ 8 $\times$ 1	0.5	Varies from 20 to 100	0.4 $\times$ 0.4	12
Case 2	8 $\times$ 8 $\times$ 1	0.25,0.5,0.75	40	0.4 $\times$ 0.4	12

Table 3 Maximum settlement at the top of raft for various type of foundations

Foundation type	Vertical settlement (mm)	Lateral deformation (mm)
Raft	609.14	24.7
Connected piled raft foundation	197.39	9.75
Unconnected piled raft foundation	191.72	20.07
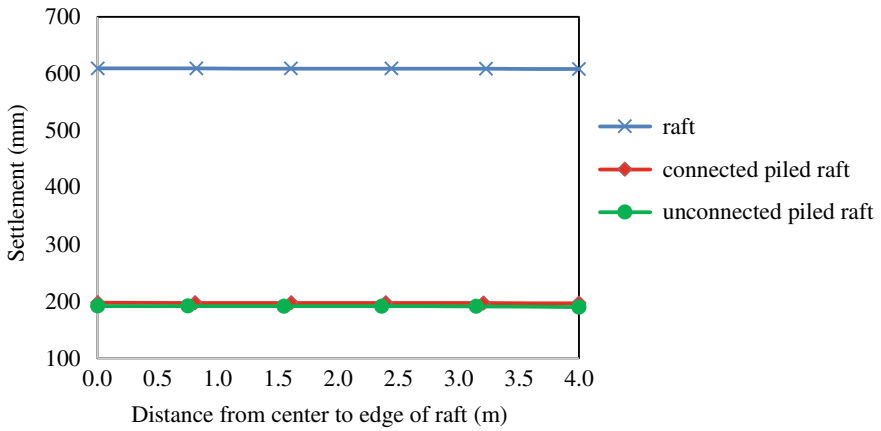
Fig. 3 Settlement at the top of the raft for different types of footings
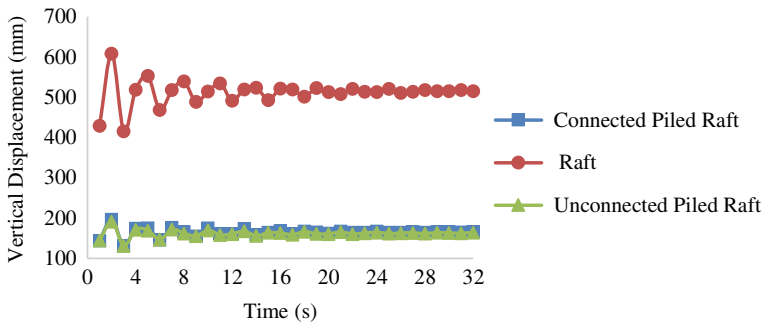
Fig. 4 Vertical displacement time history plot at the top of raft

foundations showed that the unconnected piled raft foundation has reduced the deformation by 19% when compared with that of raft foundation as shown in Fig. 5. However, the connected piled raft foundation shown a lower lateral deformation since connection between the pile heads and raft foundation was rigid.
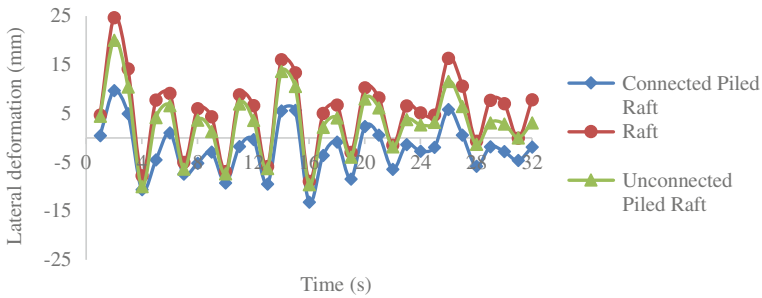
Fig. 5 Lateral deformation time history plot at the top of the raft

5.1 Influence of Elastic Modulus of Cushion

The increase in stiffness of cushion material has reduced the vertical deformation of the piled raft system considerably. The trend plotted in Fig. 6 highlights that the elastic modulus of cushion has a negative correlation with the settlement of foundation. The settlement of the foundation was reduced by 8.6% when the modulus of elasticity was increased from 20 to 100 MPa. When compared with the connected piled raft foundation, a reduction of 6.5% in settlement was observed for the unconnected piled raft with cushion of elastic modulus 100 MPa. The variation in stiffness was representing the soils as soft clay, medium clay, stiff clay and sandy clay. The vertical settlement time history detailed in Fig. 7 shows that the settlement was reduced by increasing the elastic modulus of the cushion material. As the elastic modulus of the cushion increases, the shear strength of the layer improves which reduces the deformations under dynamic loading conditions, whereas the lateral deformation was observed to be least affected by the change in elastic modulus as detailed in Fig. 8. The settlement of the top of raft was observed to be uniform across the width of the raft foundation as shown in Fig. 9.
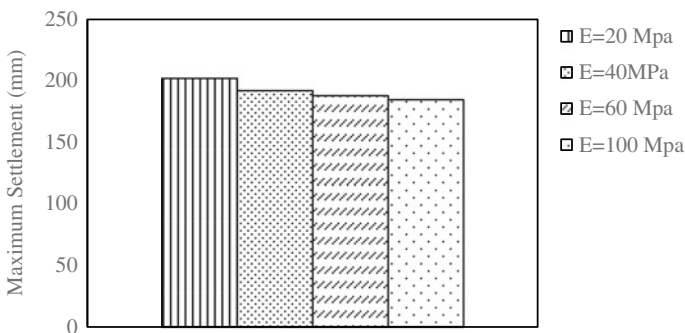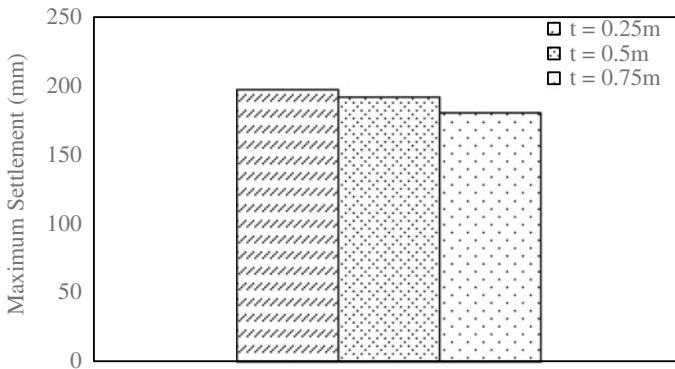

Fig. 6 Settlement of unconnected piled raft foundation with cushion layer of different elastic modulus
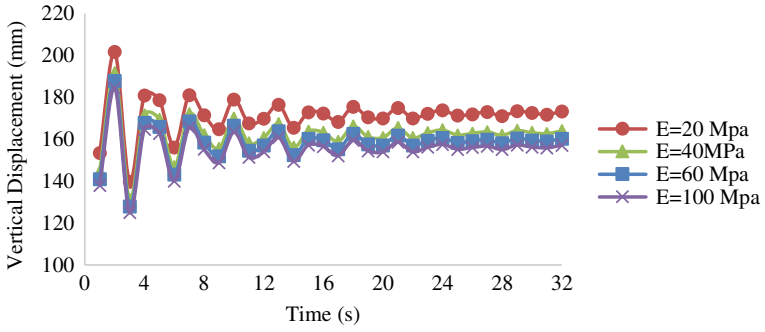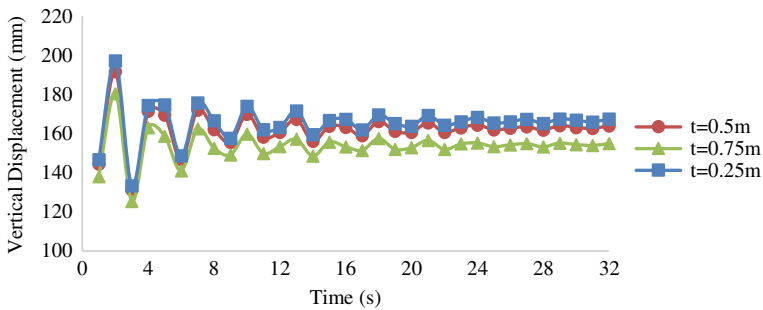
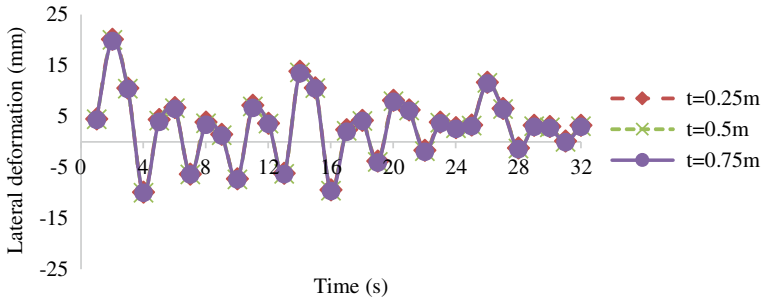**Fig. 7** Vertical displacement time history plot at the top of raft for various elastic modulus of cushion
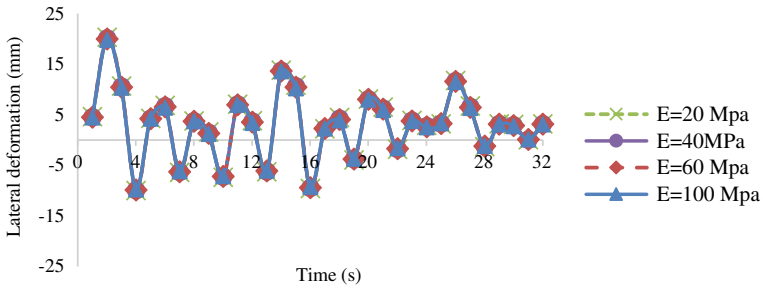
Fig. 8 Lateral deformation time history plot at the top of raft for various elastic modulus of cushion
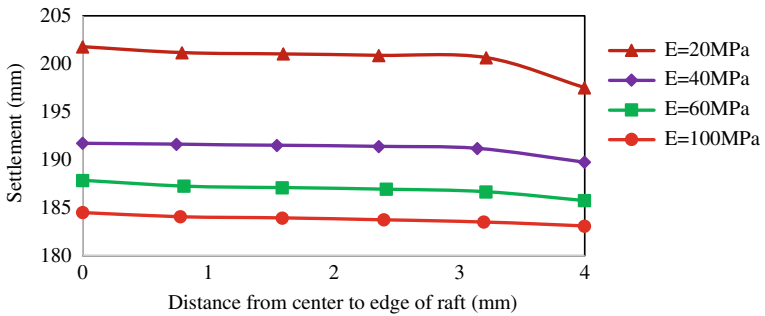

Fig. 9 Settlement behaviour of different types of cushion

5.2 Influence of Cushion Thickness

The thickness of the cushion layer was increased from 0.25 m to 0.75 m. The increase in thickness of cushion had correspondingly decreased the vertical deformation of the foundation system. The modulus of elasticity of the cushion layer was chosen as 40 MPa which was thirty times more than the Young's modulus of surrounding soil. This could possibly result in the reduction of settlement by 8.5% with increase in depth of cushion layer from 0.25 to 0.75 m as shown in Fig. 10. A reduction in vertical settlement was observed in Fig. 11 while increasing the thickness of cushion layer, whereas the effect of cushion thickness in lateral deformation was negligible as observed in Fig. 12. The trend in vertical settlement of the top of raft was found to be evenly distributed across the width as shown in Fig. 13.

Fig. 10 Settlement of unconnected piled raft foundation with cushion layer of different thickness

Fig. 11 Vertical displacement time history plot at the top of raft for various thickness of cushion

Fig. 12 Lateral deformation time history plot at the top of raft for various thickness of cushion
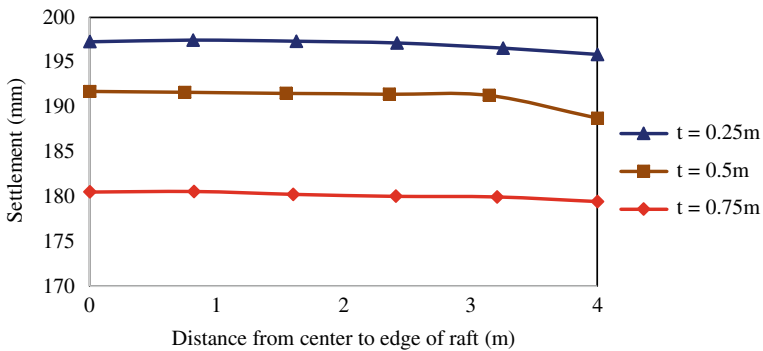
Fig. 13 Settlement behaviour of cushions of varying thickness

5.3 Influence of Foundation Stiffness on Settlement

The plot shown in Fig. 14 based on the non-dimensional parameters as in Eqs. 1 and 2 proves that the increase in stiffness of cushion material has correspondingly improved the overall stiffness of the unconnected piled raft foundation. This can be inferred from the positive slope of the curve in the plot. The settlement of the foundation is reduced with the increase in overall stiffness of the foundation, since the stiffness of the unconnected piled raft foundation (k_{pr}) is inversely proportional to the maximum settlement occurred under a loading condition.

6 Conclusion

The following inferences were made after the numerical evaluation of the unconnected piled raft system when subjected to seismic loading.
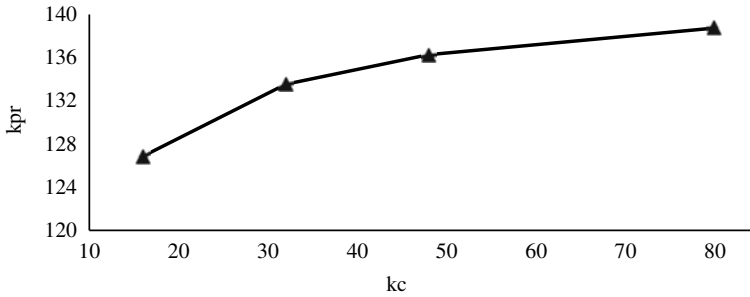
Fig. 14 Variation of stiffness of the unconnected piled raft system (k_{pr}) with that of cushion stiffness (k_c)

- The type of material used in cushion was varied from soft clay to sandy clay. The higher modulus of elasticity of the cushion layer tends to reduce the settlement by 8.6%, which is obvious since increase in stiffness would reduce the deformation.
- The thickness of cushion layer in piled raft foundation has a considerable effect in controlling the settlement under dynamic load. The increase in the thickness of the cushion layer has a positive impact in reducing the settlement by 8.5% with increase in depth of cushion layer from 0.25 m to 0.75 m. This trend depends on the stiffness of the cushion layer with respect to the surrounding soil.
- The stiffness of the unconnected piled raft foundation was improved when the stiffness of cushion layer was increased. The improved stiffness of the foundation system offered better resistance to deformations under dynamic loading.

The study concludes that the stiffness and thickness parameters are the primary properties of a cushion layer that affect the performance of an unconnected piled raft foundation system. Even though the numerical investigation incorporated considerable range of these variables in cushion layer, a detailed analysis by varying the effect of geometry of the raft and pile footings can be studied further.

References

1. Zeevaert, L.: Foundation design and behaviour of Tower Latino Americana in Mexico City. Géotechnique **7**, 115–133 (1957)
2. Burland, J.B., Broms, B.B., De Mello, V.F.B.: Behaviour of foundations and structures. In: 7th International Conference on Soil Mechanics and Foundtion Engineering, pp. 495–548. Tokyo (1977)
3. Poulos, H.G., Davis, E.H.: Pile Foundation Analysis and Design. Rainbow Bridge Book Co. (1990)
4. Randolph, M.F.: Design methods for pile groups and piled rafts. In: 13th International Conference on Soil Mechanics and Foundation Engineering, pp. 61–82 (1994)
5. Jayarajan, P., Kouzer, K.: Analysis of piled raft foundations. Indian J. Sci. **23**, 75–88 (2016)

6. Kumar, A., Choudhury, D., Katzenbach, R.: Effect of earthquake on combined pile-raft foundation. Int. J. Geomech. **16**, 1–16 (2016)
7. Han, X., Li, Y., Ji, J., Ying, J., Li, W., Dai, B.: Numerical simulation on the seismic absorption effect of the cushion in rigid-pile composite foundation. Earthq. Eng. Eng. Vib. **15**, 369–378 (2016)
8. Horikoshi, K., Matsumoto, T., Hashizume, Y., Watanabe, T., Fukuyama, H.: Performance of piled raft foundations subjected to static horizontal loads. Int. J. Phys. Model. Geotech. **3**, 37–50 (2003)
9. Horikoshi, K., Matsumoto, T., Hashizume, Y., Watanabe, T.: Performance of piled raft foundations subjected to dynamic loading. Int. J. Phys. Model. Geotech. **3**, 51–62 (2003)
10. Saadatinezhad, M., Lakirouhani, A., Jabini Asli, S.: Seismic response of non-connected piled raft foundations. Int. J. Geotech. Eng. 1–15 (2019)
11. Dong, C.X., Hieng, W.I., Ming-Fang, C.: Behavior of model rafts resting on pile-reinforced sand. J. Geotech. Geoenviron. Eng. **130**, 129–138 (2004)
12. Wong, I.H., Chang, M.F., Cao, X.D.: Raft foundations with disconnected settlement-reducing piles. In: Design Applications of Raft Foundations, pp. 469–486 (2000)
13. Liang, F.Y., Chen, L.Z., Shi, X.G.: Numerical analysis of composite piled raft with cushion subjected to vertical load. Comput. Geotech. **30**, 443–453 (2003)
14. Ata, A., Badrawi, E., Nabil, M.: Numerical analysis of unconnected piled raft with cushion. Ain Shams En. J. **6**, 421–428 (2015)

Development of Innovative Soil Nails Using Recycled Plastic and C&D Waste in Nilgiris District for Slope Upgradation Works Using Slide Program

Sooriya Narayanan Perumal and Meghna Raghoothaman Sreedevi

1 Introduction

Landslides are translational slides occurring in the form of mass wasting as a result of the ground movement resulting in rock falls, slope failures, mud, and debris flow. Moderate-to-steep slopes and embankments by expansive clay soils are vulnerable to shallow landslides during intense and prolonged rainfall events. Progressive wetting of the near-surface soil causes failure due to pore water pressure and reduction in soil strength. This condition is further exacerbated by moisture variations due to seasonal climatic changes, which cause cyclic shrinkage and swelling of the upper soils. Cyclic shrinkage and swelling lead to the change in the void ratio of soil and lower the shear strength. Reduction of shear strength leads to sloughing and shallow slope failures. The depth of the shallow slope failure ranges between 0.9 m (3 ft.) and 1.8 m (6 ft.). Shallow failures often cause significant hazards to guard rails, shoulders, and roadways, which, if not properly maintained, may require extensive and expensive repairs.

Reinforcement is an efficient remediation technique for relatively shallow slope failure conditions. The various in situ reinforcement techniques for stabilizing slopes and embankments include soil nails, drilled piers, micro-piles, and RPPs. The usage of recycled plastic in places of steel rods as reinforcement material reduces both environmental impacts and proves to be highly economical. Recycling old and waste products into new products reduces the amount that goes to the landfills and recycling one ton of plastic can save 7.4 cubic yards of landfill space by reducing the necessity for conventional waste disposal, and it reduces the greenhouse gases emissions.

S. N. Perumal (✉) · M. R. Sreedevi
Department of Civil Engineering, Sri Ramakrishna Engineering College,
Coimbatore, Tamil Nadu, India
e-mail: lncs@springer.com

The adoption of these recycled plastics for soil nailing techniques serves as a major protector against landslides. Using recycled plastics has the advantage of providing reinforcing members with low susceptibility to degradation and provides a marketplace for which may rather be landfilled.

The application of such technique focuses on slope stability with the implementation of soil nailing technique or micro-piles; therefore, with modifications brought into the conventional design and construction satisfactory, remedial measures can be obtained against such natural hazards.

2   Materials

The material used for the stabilization of soil is the waste high-density polyethylene (HDPE) plastics as well as the construction and demolition waste. High-density polyethylene (HDPE plastic) may be a polyolefin thermoplastic that features endless use temperature range of −50 °F (−46 °C) to 180 °F (82 °C). HDPE features amazing corrosion resistance and generally outlasts other plastics. HDPE has the tremendous quality of resisting wear and tear as it offers low friction surfaces and high resistance to chemicals. HDPE retains its rigid structure until its freezing point is reached. It is immune to mold and rotting, making it a perfect choice for creating underground water pipes. While the C&D wastes are in close proximity to normal concrete in terms of split tensile and compressive strength. The nails used in model testing are the diameter of 19 mm (outer dia.) and 3.5 m in length. The sample nail dimensions and their corresponding dimensions were utilized for model generation using the software.

3   Methods

Literature is a basic reference for known and unknown idea generation of any project work. Many works of literatures have been collected and studied to adopt a right procedure to achieve the objectives of this investigation. Based on the reviews, the aim of the project work and experimental investigation has been carried out (Fig. 1).

4   SLIDE2 Software

4.1   Insight into the Software

SLIDE2 formerly known as Slide is a slope stability software in two-dimensional form evaluating the factor of safety or the occurrence of failure of circular and
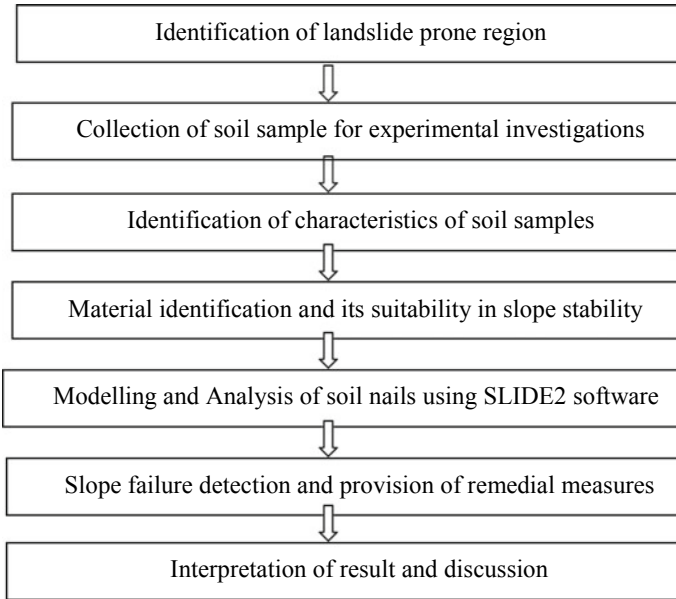
Fig. 1 Methodology chart constituting the working of the project

non-circular in soil surface as well as rock slopes. SLIDE2 is very user-friendly which helps in quick modeling and analyzing. SLIDE2 analyzes the stability of slip surfaces and individual surfaces using limit equilibrium methods like Bishop, Janbu, Spencer, and Sarma among others.

Different methods are applicable for the location of critical slip surface for given slopes along with deterministic (Factor of safety) or probabilistic analyses. This software enables the analysis program for all types of soil and rock slopes, embankments, earth dams, and retaining walls. In-built features like finite elements groundwater seepage analysis, probabilistic analysis as mentioned above with multi-scenario modeling, and support design can also be performed with the assistance provided through this software.

4.2 Application of Software into the Project

Results obtained from experiments performed under laboratory conditions were incorporated into the software. Soil samples collected were subjected to various laboratory tests such as moisture content, specific gravity, organic content, standard proctor compaction, unconfined compressive strength, Vane shear test, California bearing ratio. Assigning the required parameters, the probability of failure was

calculated and objective measures were provided. Input data such as soil type, unit weight, strength type, cohesion, and angle of friction were fed in along with the support system details which included the force application, support type, tensile capacity, bond strength, length, diameter, and spacing.

4.3 Experimental Investigation

Investigations were performed on soil samples collected from the Wellington area located in the Nilgiris District of Tamil Nadu, approximately 80 km from Coimbatore and 14 km from the hill resort region of Udhagamandalam (also called Ooty or Ootacamund). The average elevation is estimated to be 1855 m (6085 feet). The soil samples have been collected from the Nilgiris region at the depth of 1.5 m. The site for investigation has been selected based on the organic soil location. The site was also selected based on the organic content of the region (Tables 1 and 2).

The results obtained from the test are required for the execution of the model. The data obtained from the laboratory tests were entered as input data in the required fields while working with SLIDE2 software and the final interruption of the results led to the conclusion for slope stability.

5   Analysis Through SLIDE2 Software

The Slide is comprehensive software that can be used for slope stability analysis, required data are fed in and the final output is obtained. The initial step is the creation of the model. But before the creation of the model, the main analysis parameters must be well defined which includes the failure direction, units of

Table 1 Latitude and longitude of the selected site in Ooty

Location	Latitude	Longitude
Wellington, Ooty	11.4064° N	76.6932° E

Table 2 Table showing test result from various laboratory test

Laboratory experiments	Results obtained
Initial moisture content	37.5%
Specific gravity	2
Organic content	90.47%
Standard proctor compaction test	1.935 g/cc
Unconfined compressive strength	77.08 kPa
Shear strength	38.54 kPa
Vane Shear strength	21.47 kPa

measurement, analysis methods, etc. which is done with the help of project setting dialog. The next step of modeling involves the creation of boundaries in the form of a closed polyline representing the solid region for analyzes. SLIDE2 analysis for stability is mainly done either for circular or non-circular slip surfaces. In an attempt to find the slip surface with the lowest safety factor, individual surface can be analyzed or a critical surface search can be performed. Auto-refine search and grid search are the most commonly used method for circular slip surfaces. Property defining is the next process of modeling which involves the following: Name, unit weight, strength, cohesion, angle of internal friction (phi), and water surface following which auto-girds are created for the project. The slope limit gets automatically calculated along with external boundary creation in SLIDE2. Finally, toward the approach of analysis, various methods of the same can be observed from Janbu simplified to Spencer and Sarma. Compute engine will proceed in running the analysis and SLIDE2 will start interpreting the program. After the execution of the model, provision of supports to overcome slope failure is carried out. Various types of supports are available in SLIDE2 including geotextiles, drilled or launched soil nails, tiebacks, rock bolts, piles, and micro-piles. Through add support pattern option in the support menu, multiple supports can be added. Proceedings are carried out for defining the properties of the support system viz. the type of support, method of force application, bond length, tensile force orientation, pullout strength, capacity, and spacing. The final output is a slope failure rectified image with color code of slip surface according to safety factors which will vary concerning the analysis method chosen (Table 3).

The following figures show the entire procedure for the execution of the model (Figs. 2, 3, 4, 5, 6, 7, 8, 9, 10, 11, 12, 13, 14 and 15).

| Table 3 Input data for analysis using SLIDE2	Input characteristics	Required data
	(A) For Soil	
	Soil type	Peat soil
	Unit weight (KN/m^3)	18 KN/m^3
	Strength type	Mohr-Columb
	Cohesion (kPa)	1 kPa
	Phi (deg.)	35°
	(B) For Support	
	Support type	Soil Nail
	Force application	Active method
	Tensile capacity	250 KN
	Bond strength	50 KN/m
	Force orientation	Parallel to reinforcement
	Diameter of rod	19 mm
	Length of rod	3.5 m
	Spacing between the rods	3 m
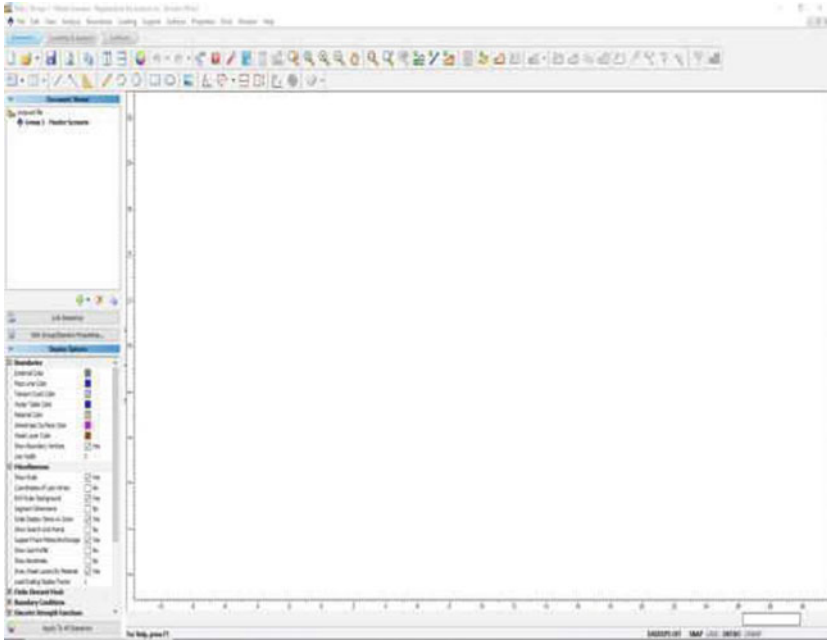
Fig. 2 New blank document
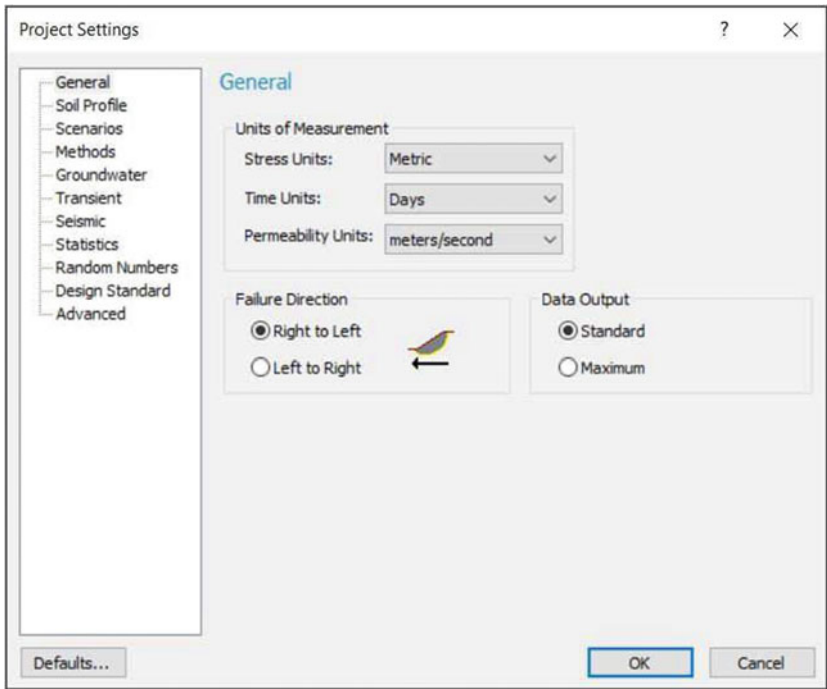
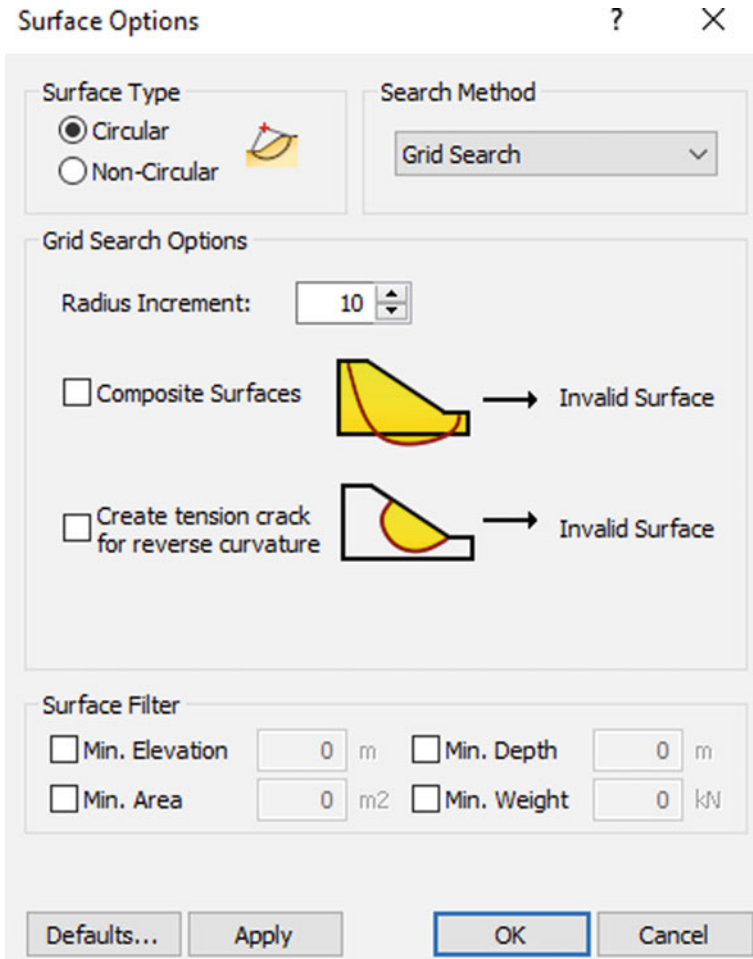**Fig. 3** Project setting dialogue x

Fig. 4 Setting up of boundary areas

6 Result and Discussion

Following observations can be inferred from the detailed analytical results of the collected soil sample. The sieve analysis result shows that the soil samples are medium to very fine sand consisting of medium (37%) to fine grain (57%) with a small amount of silt and clay. The unit weight of soil samples is found to be 18 KN/m³. The internal angle of friction (ϕ) and the cohesive strength (c) were measured from the direct shear test which shows that the soil of the wellington area has ϕ values 35°. Cohesive strength seems to be low due to loosen soil samples.
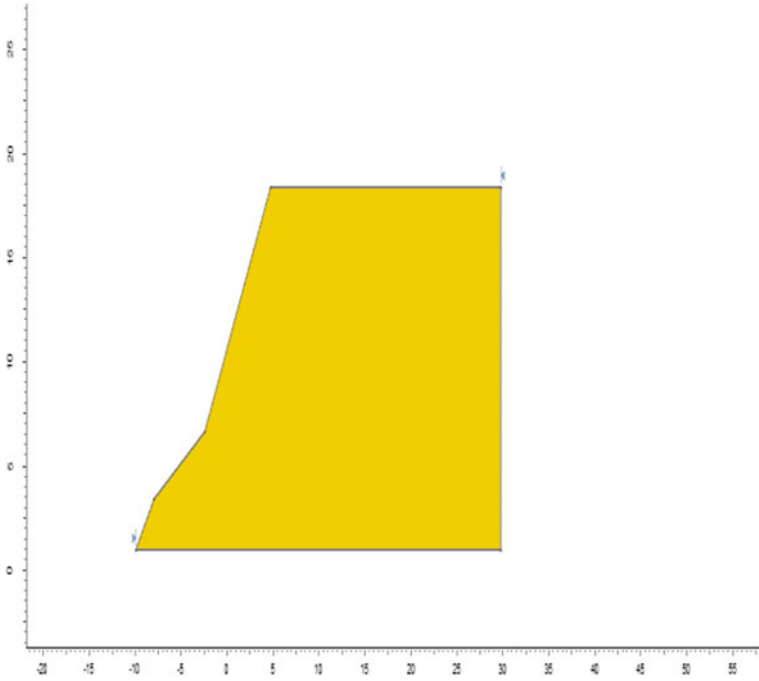
Fig. 5 To determine the slip circle
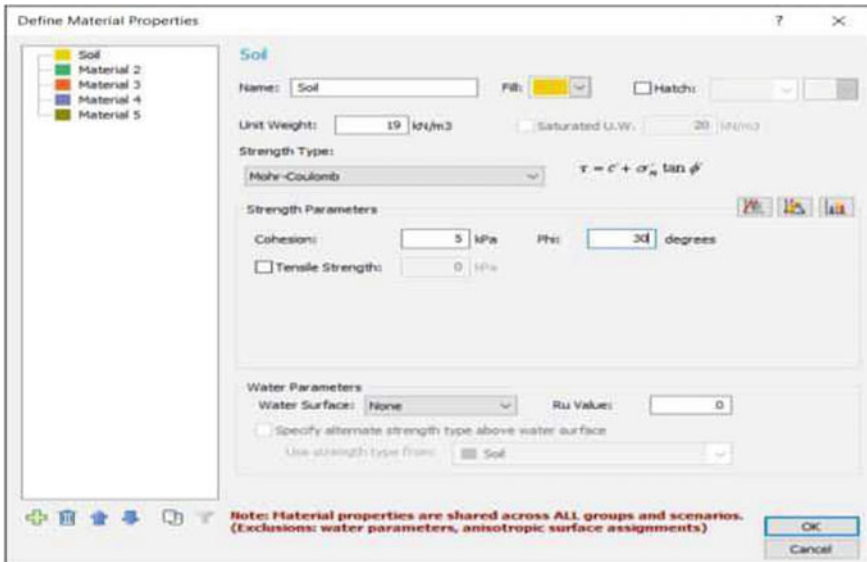
Fig. 6 Input data for defining the material type
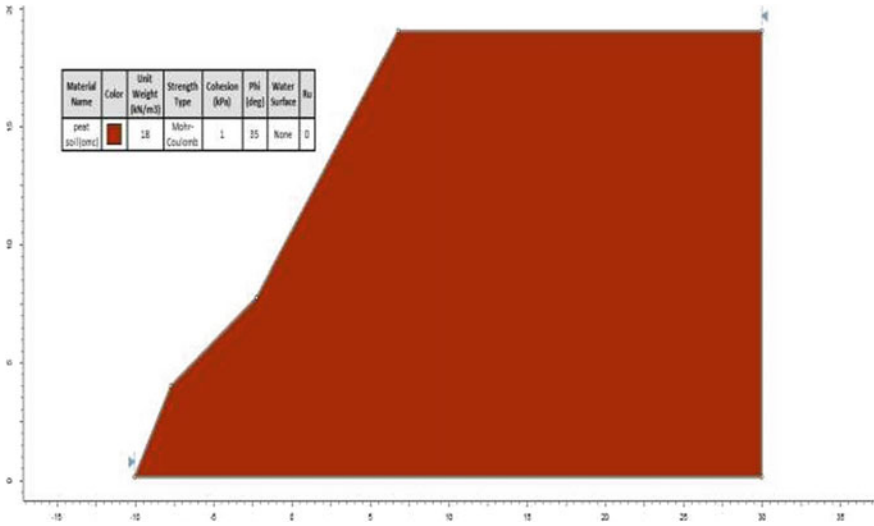
Fig. 7 Defining of soil type and its properties
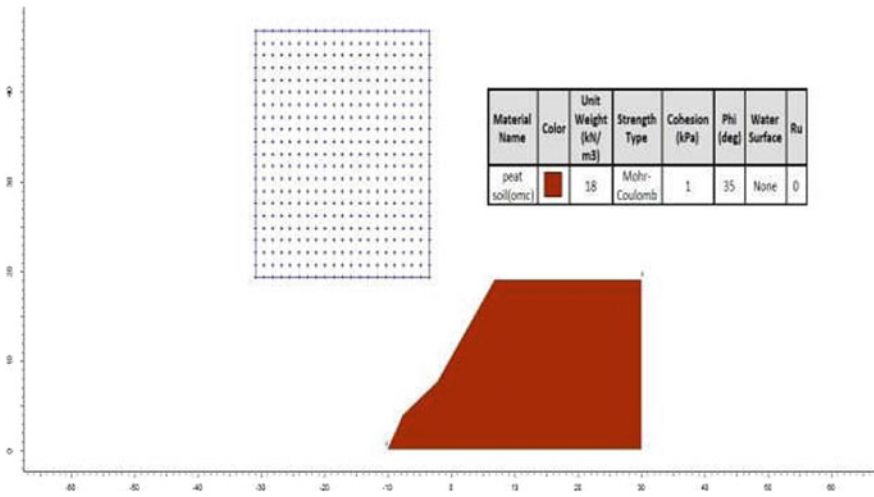
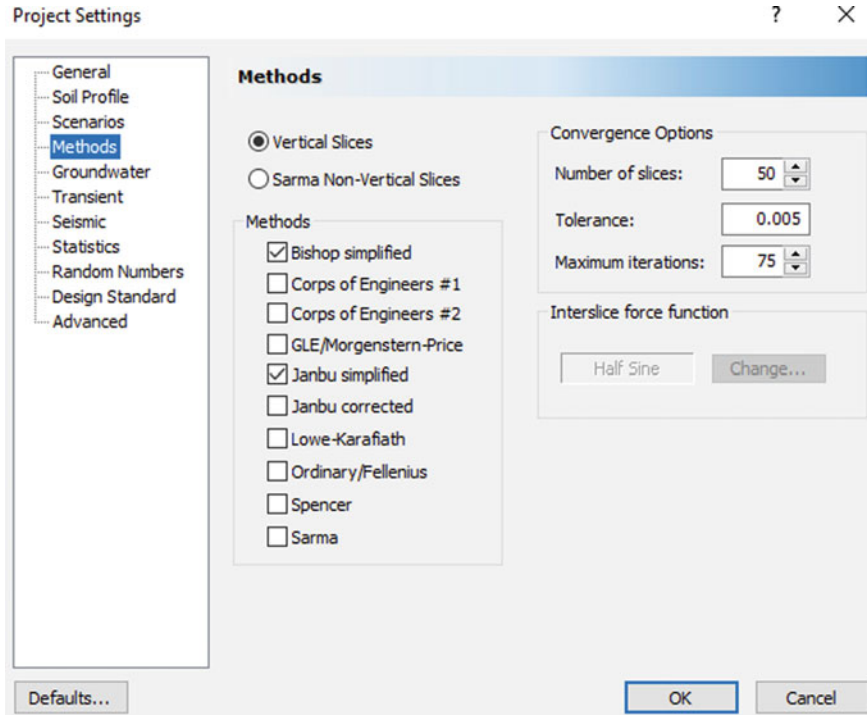**Fig. 8** Auto-grid defining to detect the critical slip circle and its radius

Fig. 9 Different methods for analyzing the result

The 2D stability calculations in rocks or soils using the rigorous and non-rigorous analysis methods for circular surfaces are performed using the limit state of equilibrium of SLIDE software. Slopes based on the most vulnerable area were analyzed with an existing minimum slope angle of 30° for its stability. The factor of safety (FS) was determined. The results show that slopes will be stable with a lesser slope angle (at 30°) at dry conditions (loosen soil). However, during wet conditions, all slopes seem to be unstable. Landslides occurred mostly due to extreme rainfall intensity and also may happen after cutting of hill slopes and after earthquakes when the slope stability is disturbed and the modeling result shows that steeper slope with lesser cohesive strength and lesser angle of friction is also key parameters along with excess water pressure due to heavy rainfall. Results from modeling make it evident that most of the areas investigated for this project (Wellington) are vulnerable under wet conditions due to the building up of water pressure for heavy rainfall. But for the protection of slope failure and to save lives, 100% coverage with different support patterns for existing slopes is suggested.
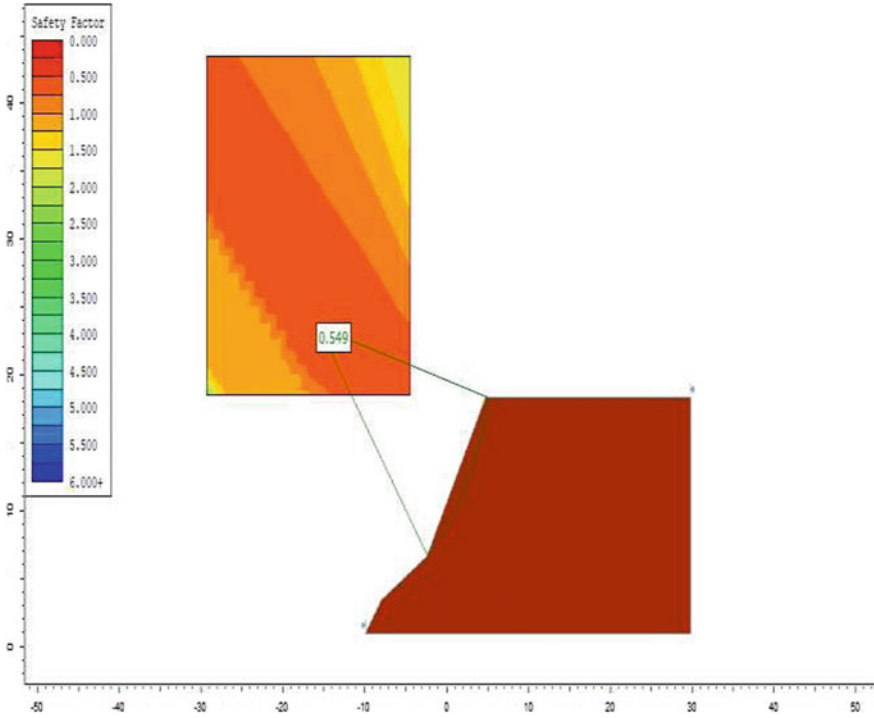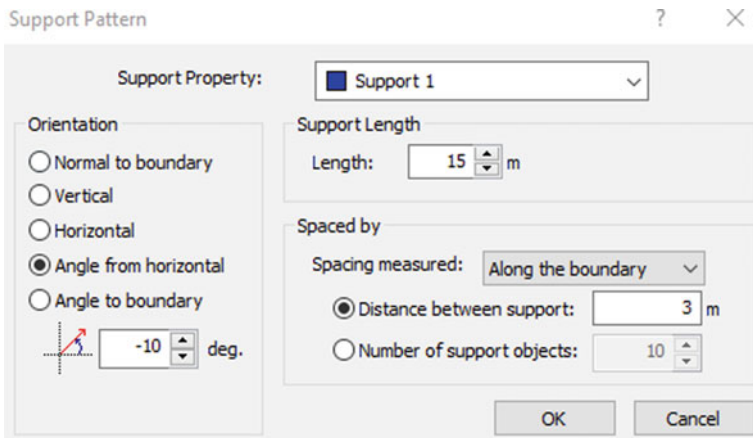
Fig. 10 Interpreting the slope failure (FOS < 1)

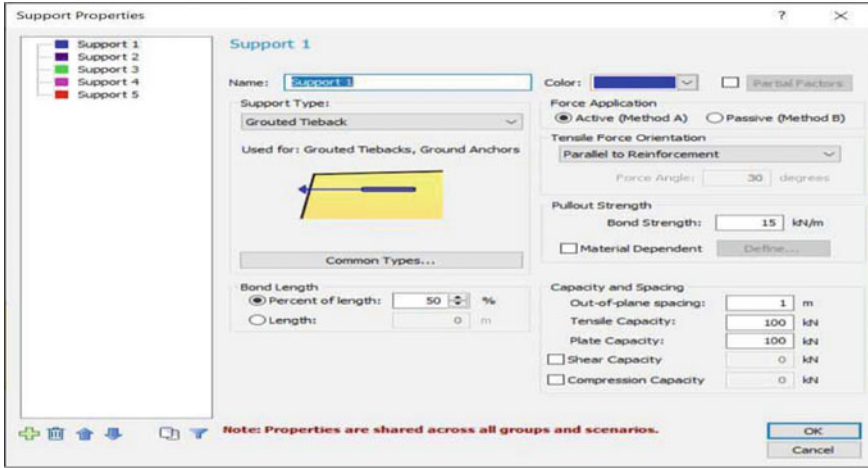**Fig. 11** Input data for the support pattern

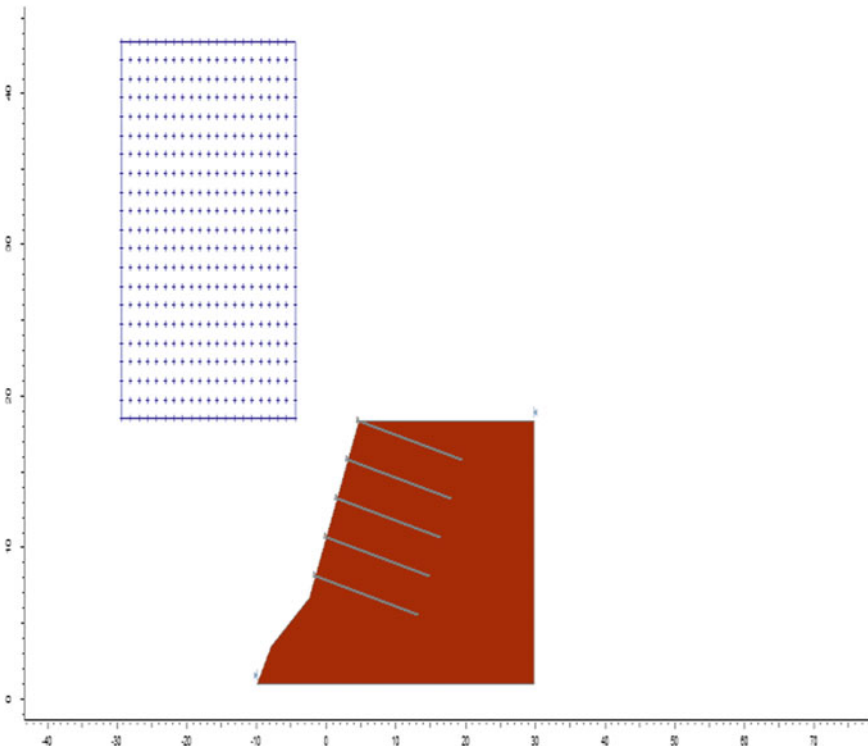**Fig. 12** Defining the type and properties of the type of support

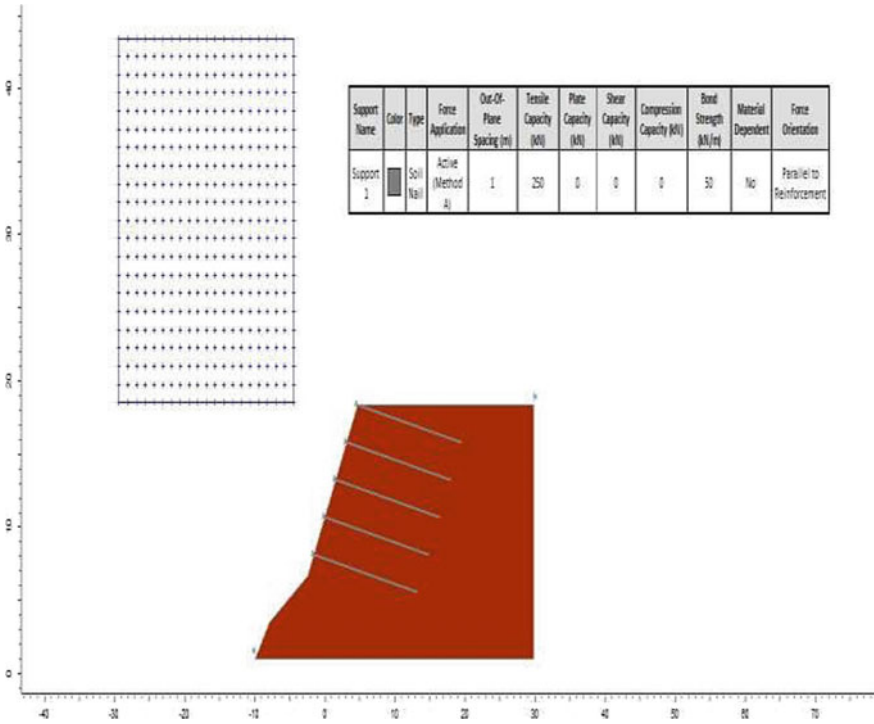**Fig. 13** Output of the entered values for the support

Support Name	Color	Type	Force Application	Out-Of-Plane Spacing (m)	Tensile Capacity (kN)	Plate Capacity (kN)	Shear Capacity (kN)	Compression Capacity (kN)	Bond Strength (kN/m)	Material Dependent	Force Orientation
Support 1		Soil Nail	Active (Method A)	1	250	0	0	0	50	No	Parallel to Reinforcement

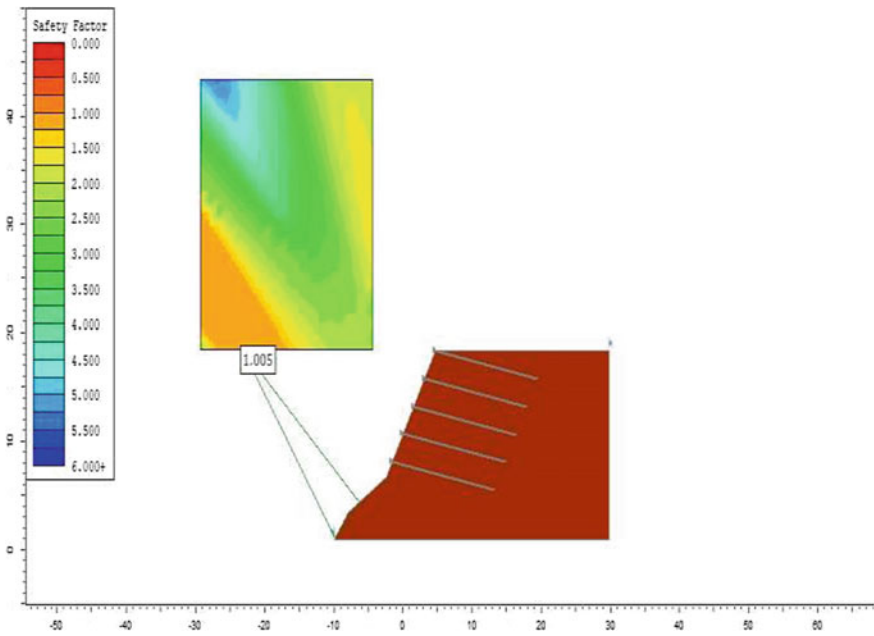**Fig. 14** Specification and detailing of the support

Fig. 15 Rectification of failure (FOS > 1)

7 Conclusion

For relatively shallow slope failure conditions, reinforcement is an effective remediation technique. High waste reduction can be obtained by recycling old waste products into new products this, in turn, reduces the amount of waste that goes to landfills and recent statistical data proves that recycling one ton of plastic can save approximately 7.4 cubic yards of landfill space. By making significant modifications to the conventional design and construction, stabilization of slopes with soil nails or micro-piles accounts for the reduced strength and increases ductility and creep exhibited by plastic materials when compared to concrete and steel materials. The project focuses on the modeling of innovative soil nails using recycled plastic waste (HDPE strips) and construction and demolition wastes. Identification of characteristics of soil was performed through laboratory experiments collected from peat soils found in Nilgiris areas (11.4064o N, 76.6932o E) which had a moisture content of 37.5%, specific gravity 2, organic content 90.47%, Vane shear value of 21.47 kPa, and the CBR value 1.5. These data helped in modeling and analysis of the nails is through software called SLIDE. The Slide is a slope stability software in two-dimensional form evaluating the factor of safety or the occurrence of failure of circular and non-circular in soil surface as well as rock slopes. Slope instability analyses were done with SLIDE2 based on a factor of safety of the slope. The analyses were performed under the Mohr–Coulomb strength type to measure the factor of safety. The major parameters of soil are apparent cohesion of soil (c = 1 kPa), angle of internal friction (ϕ = 35o), unit weight of soil (=18 KN/m^3) directly taken from the laboratory test result for calculating FS. To save the lives and properties of the vulnerable area of the city protection of slope from failure is mandatory, for which adequate supports have to be suggested. Results obtained from the software indicated that the soil without any support system had a slope failure due to factor of safety less than 1(0.549) and when support systems in the form of soil nails were provided (19 mm dia. and 3.5 m length), there was a sudden increase in the factor of safety value (1.005). For the remedial measure, support such as geotextile and masonry wall is put forth which can improve the soil stability and save lives and properties.

Efficacy of Pervious Concrete Columns Vis-A-Vis Stone Columns in Sandy Strata in Mitigating Liquefaction

R. S. V. Rashma[iD]**, B. R. Jayalekshmi**[iD]**, and R. Shivashankar**[iD]

1 Background

Stone columns are widely used for mitigating liquefaction in saturated sand strata. The effectiveness of stone columns in mitigating liquefaction is reported by conducting full scale physical tests, centrifuge studies, and shake table tests [1–3]. Numerical modeling of stone column improved ground and the various parameters influencing seismic performance is also reported [4–9]. It is also stated that the performance of stone column is highly dependent on surrounding soil properties [10–12].

Though many modifications to stone columns are available in literature, very few modified methods are used in practice such as deep cement mixing columns, geo-synthetic encased stone columns. Recently, pervious concrete columns are suggested as an alternative to stone columns with 4 times vertical load carrying capacity than conventional stone columns and with similar hydraulic properties as that of stone columns [13, 14]. Pervious concrete column can also be considered as rigid inclusion whose performance is independent of surrounding soil properties. The seismic modeling and performance of geo-synthetic encased stone column improved ground are recently reported by Tang et al. [6] and Geng et al. [15]. The liquefaction mitigation potential of pervious concrete column improved ground is not investigated. Therefore, in this study, the seismic performance of pervious concrete column improved ground in mitigating liquefaction is carried out and compared with conventional stone column improved ground. Also, the stone column permeability can be varied in field [10, 16, 17]. Similarly, the influence of varying pervious concrete column permeability on seismic performance of

R. S. V. Rashma (✉) · B. R. Jayalekshmi · R. Shivashankar
National Institute of Technology Karnataka, Surathkal, India

improved ground is addressed in the study. In addition to this, the influence of permeability of surrounding soil strata on the performance of pervious concrete column improved ground is studied.

2   Present Study

In this study, the performance of pervious concrete column improved ground is compared with stone column improved ground based on lateral displacement criteria, excess pore pressure generation, and shear stress-strain behavior. Further, the study is extended to understand the influence of permeability of column inclusion as well as surrounding soil on lateral displacement ratio. Lateral displacement ratio is defined as the ratio of lateral displacement of improved ground to the lateral displacement of unimproved sand strata.

3   Numerical Modeling

Three-dimensional finite element software OpenSeesPL is used to model sand strata and improved ground with stone column and pervious concrete column inclusion. Firstly, the model generated using OpenSeesPL software is validated with well documented experimental results of VELACS model 2. The results are compared in terms of excess pore pressure generation and lateral displacement reported by Ghasemi and Pak [18] in prototype scale and is found to be in good agreement with experimental results. The experiment VELACS model 2 was performed to study the phenomenon of lateral spreading on mildly sloping ground using inclined experimental model [19]. Therefore, in this study, an inclined fully saturated soil model of 4° is considered, representing mildly inclined strata of infinite extend.

Unit cell modeling approach is used to model improved ground with column inclusions [3–9, 15]. The center to center spacing between columns of diameter 0.6 m is considered as 2.5 D as per IS codal provisions [20]. The spacing of 2.5 D corresponds to an area ratio of 13%, and the overall depth of soil model is taken as 10 m as shown in Fig. 1a. The column inclusion is assumed to be extended up to hard rock located at the lower boundary of soil model. Periodic boundary conditions at the left and right sides of the soil model are employed [21]. The sand strata correspond to cohesionless soil with 40% relative density. The properties of stone column are taken as that of dense cohesionless soil properties with gravel permeability [4–6, 8, 9, 15]. The pervious concrete properties are assumed as similar to normal concrete. The soil model is fully saturated up to ground level. The properties used for modeling soil and column inclusions with PDMY 02 material model are given in Table 1. Eight noded BRICKUP element is used to model soil models, and

Fig. 1 **a** Numerical model;
b scaled input excitation
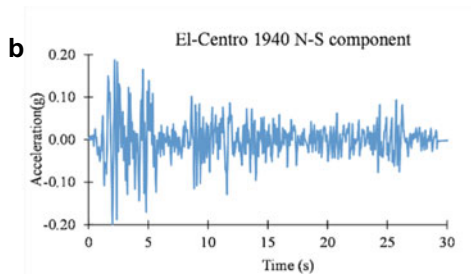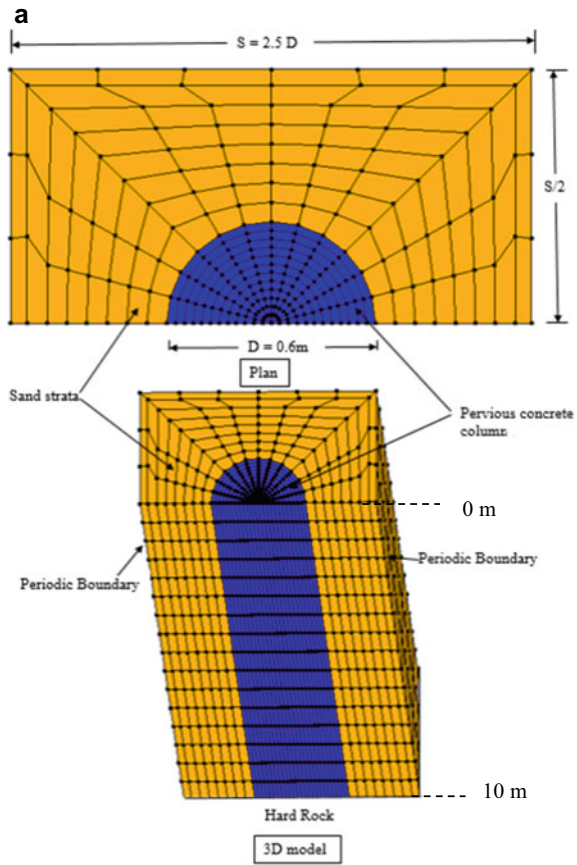
the interaction between column inclusions and surrounding sand strata is assumed to be fully bonded for simplicity. The soil models are subjected to seismic excitation at the base of the model conforming to El-Centro N-S component scaled to 0.2 g (Fig. 1b).

Table 1 Material properties

| Soil model parameters	Sand	Stone column	Pervious concrete
Saturated soil density, ρ (t/m^3)	1.8	2.1	2.15
Low strain shear modulus at reference pressure G_{max} (MPa)	90	130	10,580
Bulk Modulus at reference pressure B_r (MPa)	220	260	14,460
Shear strength at zero effective confining pressure (cohesion) (kPa)	0.1	0.1	3000
Model friction angle, same as triaxial friction angle ϕ_{TC}	36°	42°	38°
Phase transformation angle ϕ_{PT}	26°	26°	26°
Permeability (m/s)	6.6×10^{-5}	0.01	0.01
Relative density (%)	40	75	75

4   Results

Firstly, the typical seismic responses of sand strata, improved ground with stone column and pervious concrete column are explained. Thereafter, the influence of column and soil permeability on lateral displacement is discussed. For the improved ground, the diameter of the column considered is 0.6 m. Also, the center to center spacing between columns is 2.5 D, where D is the diameter of column. The 2.5 D spacing represents an area ratio of 13% calculated as the ratio of area of column to total area of improved ground.

4.1   Typical Seismic Response of Improved Ground

The performance of PCC is assessed in terms of lateral displacement, excess pore pressure generation and shear stress-strain behavior. The lateral displacement plot for sand strata, SC improved ground and PCC improved ground is shown in Fig. 2. The maximum lateral displacement at the center of finite element mesh is 1.36 m, 0.3 m, and 0.1 m, respectively, for sand, SC case, and PCC case (Fig. 2). Therefore, the percentage reduction in lateral displacement response of PCC improved case is 67% higher than SC improved case. The reduction in lateral displacement response of PCC improved ground is attributed to its higher rigidity similar to normal concrete piles.

Figure 3 represents the excess pore pressure generation plot of three cases at varying depths of 2 m, 4 m, 6 m, and 8 m. The location is selected at the center of mesh representing column location in improvement cases. It is seen that the excess pore pressure generated is lesser in case of SC and PCC when compared to sand

Fig. 2 Lateral displacement response of improved ground
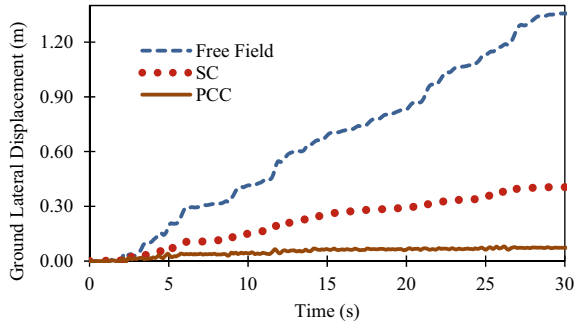
strata. The limited excess pore pressure generation for PCC case shows the dissipation of pore water quickly through the pores of PCC than SC inclusion, thereby performing better than SC.

The shear stress-strain behavior of three cases at a distance of 0.7 m representing surrounding soil at varying depths of 1.4 m, 3.4 m. 5.4 m, and 7.4 m is presented in Fig. 4. It is observed that the shear strain amplitude reduced drastically for all depths. However, the shear strain amplitude of SC case and sand case shows almost similar shear strain amplitude for 1.4 m and 3.4 m. It is also noted that at depths 1.4 m and 3.4 m, the shear stress values reached zero suddenly indicating that the SC improved ground and unimproved sand strata liquefied at these depths.

4.2 Effect of Column Permeability

The influence of column permeability on lateral displacement ratio is studied by varying the column permeability ranges as 0.01 m/s, 0.1 m/s, and 1.0 m/s. The column permeability is also kept as that of surrounding soil to simulate the clogged nature of PCC and SC in terms of hydraulic conductivity. The variation of lateral displacement ratio with column permeability is as shown in Fig. 5. It is noted that the lateral displacement depends on the column permeability of stone column inclusions and is seen that the lateral displacement ratio decreases with increase in stone column permeability. However, for PCC improved ground, the lateral displacement ratio is found to be independent of column permeability. This independent column permeability variation on lateral displacement ratio of PCC shows its significance in providing less deformation even in its clogged condition.

4.3 Effect of Surrounding Soil Permeability

To study the effect of soil permeability on lateral displacement ratio, the soil permeability is varied from 6.6×10^{-07} m/s to 6.6×10^{-02} m/s. Figure 6 shows the
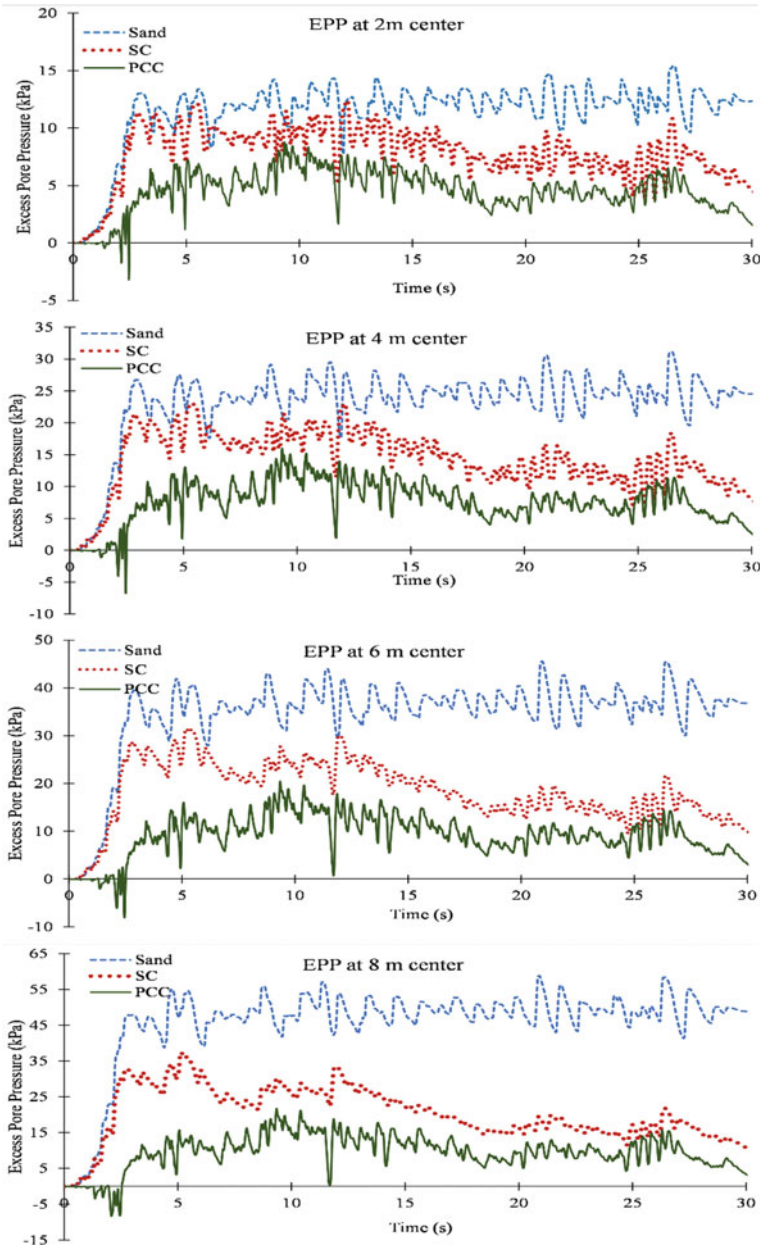
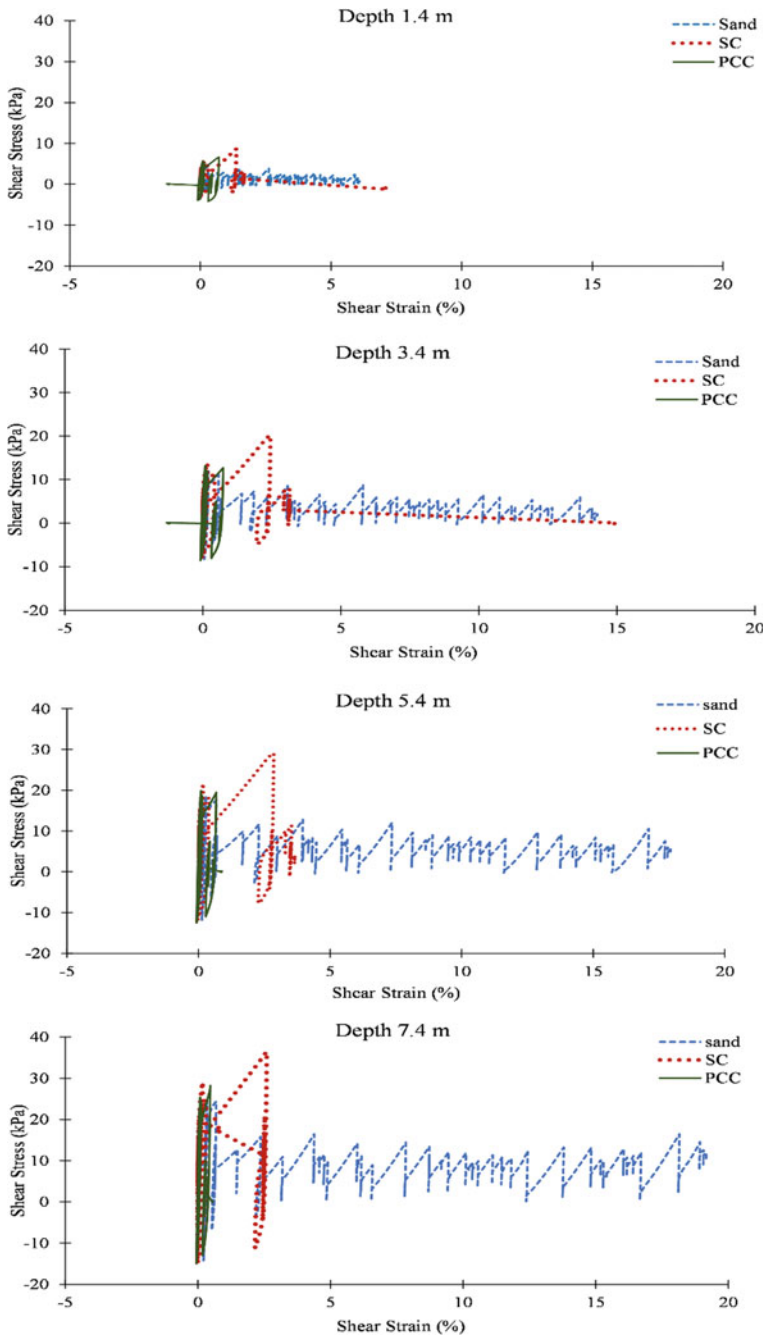**Fig. 3** Excess pore pressure response at various depths

Fig. 4 Shear stress-strain behavior at various depths
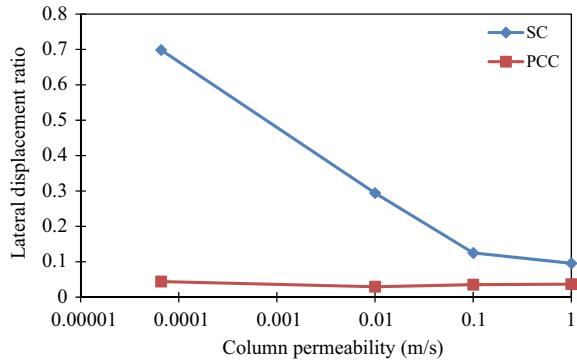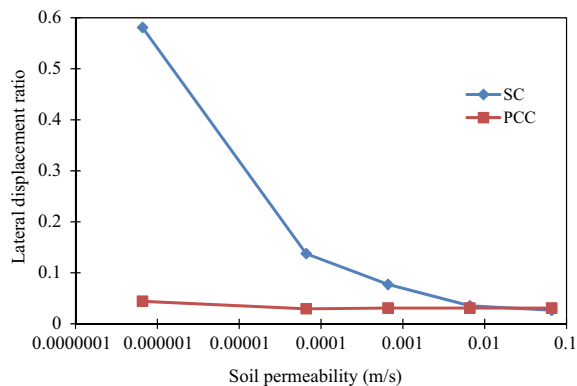
Fig. 5 Effect of column permeability

Fig. 6 Effect of surrounding soil permeability

variation of lateral displacement ratio with soil permeability. It is found that the lateral displacement ratio is highly dependent on soil permeability up to 6.6×10^{-02} m/s, and thereafter, the lateral displacement ratio is constant. However, for PCC improved ground, the lateral displacement ratio is found to be independent of soil permeability. This also indicates the wider range of applicability of PCC on soil strata with varying permeability.

5 Conclusions

The seismic performance of pervious concrete column in place of conventional stone column on sand strata is evaluated in terms of lateral displacement, excess pore pressure generation, and shear strain amplitude. It is concluded that the pervious concrete column improved ground has better liquefaction resistance than stone column improved ground. The lateral displacement ratio of stone column improved ground is observed to be highly dependent on the hydraulic conductivity of stone column permeability and surrounding sand strata. However, the lateral

displacement ratio of pervious concrete column improved ground is found to be independent of hydraulic conductivity of pervious concrete column as well as surrounding sand strata. The reduction in lateral displacement, independent of sand permeability makes pervious concrete column a better liquefaction mitigation measure in place of stone columns, for a wider range of liquefiable soil profiles with varying permeability ranges.

References

1. Ashford, S.A., Rollins, K.M., Case Bradford, V.S., Weaver, T.J., Baez, J.I.: Liquefaction mitigation using stone columns around deep foundations: full-scale test results. Transp. Res. Rec. 110–118 (2000). https://doi.org/10.3141/1736-14
2. Adalier, K., Elgamal, A., Meneses, J., Baez, J.I.: Stone columns as liquefaction countermeasure in non-plastic silty soils. Soil Dyn. Earthq. Eng. **23**, 571–584 (2003). https://doi.org/10.1016/S0267-7261(03)00070-8
3. Rayamajhi, D.: Shear reinforcement effects of discrete columns in liquefiable soils (2014)
4. Elgamal, A., Lu, J., Forcellini, D.: Mitigation of liquefaction-induced lateral deformation in a sloping stratum: three-dimensional numerical simulation. J. Geotech. Geoenvironmental Eng. **135**, 1672–1682 (2009). https://doi.org/10.1061/(ASCE)GT.1943-5606.0000137
5. Asgari, A., Oliaei, M., Bagheri, M.: Numerical simulation of improvement of a liquefiable soil layer using stone column and pile-pinning techniques. Soil Dyn. Earthq. Eng. **51**, 77–96 (2013). https://doi.org/10.1016/j.soildyn.2013.04.006
6. Tang, L., Cong, S., Ling, X., Lu, J., Elgamal, A.: Numerical study on ground improvement for liquefaction mitigation using stone columns encased with geosynthetics. Geotext. Geomembranes. **43**, 190–195 (2015). https://doi.org/10.1016/j.geotexmem.2014.11.011
7. Tang, L., Zhang, X., Ling, X.: Numerical simulation of centrifuge experiments on liquefaction mitigation of silty soils using stone columns. KSCE J. Civ. Eng. **20**, 631–638 (2016). https://doi.org/10.1007/s12205-015-0363-7
8. Rayamajhi, D., Ashford, S.A., Boulanger, R.W., Elgamal, A.: Dense granular columns in liquefiable ground. I: shear reinforcement and cyclic stress ratio reduction. J. Geotech. Geoenvironmental Eng. **142**, 1–11 (2016). https://doi.org/10.1061/(ASCE)GT.1943-5606.0001474
9. Rayamajhi, D., Boulanger, R.W., Ashford, S.A., Elgamal, A.: Dense granular columns in liquefiable ground. II: effects on deformations. J. Geotech. Geoenvironmental Eng. **142**, 1–10 (2016). https://doi.org/10.1061/(ASCE)GT.1943-5606.0001475
10. Barksdale, R.D., Bachus, R.C.: Design and constrcution of stone columns volume **1** (1983)
11. Ni, L.: Pervious Concrete Piles : Development and Investigation of an Innovative Ground Improvement System (2014)
12. Kempfert, H.G.: Ground improvement methods with special emphasis on column-type techniques. In: International Workshop on Geotechnics of Soft Soils-Theory and Practice. pp. 101–112 (2003)
13. Suleiman, M.T., Ni, L., Raich, A.: Development of pervious concrete pile ground-improvement alternative and behavior under vertical loading. J. Geotech. Geoenvironmental Eng. **140**, 4014035 (2014). https://doi.org/10.1061/(asce)gt.1943-5606.0001135
14. Ni, L., Suleiman, M.T., Raich, A.: Behavior and soil-structure interaction of pervious concrete ground-improvement piles under lateral loading. J. Geotech. Geoenvironmental Eng. **142**, 4015071 (2016). https://doi.org/10.1061/(asce)gt.1943-5606.0001393

15. Geng, L., Tang, L., Cong, S.Y., Ling, X.Z., Lu, J.: Three-dimensional analysis of geosynthetic-encased granular columns for liquefaction mitigation. Geosynth. Int. **24**, 45–59 (2017). https://doi.org/10.1680/jgein.16.00014

16. Mitchell, J.: Soil improvement—state of the art report. In: International Society for Soil Mechanics and Geotechnical Engineering (ISSMGE), pp. 536–537 (1981)

17. Baez, J.I.: A Design Model for the Reduction of Soil Liquefaction by Vibro-Stone Columns. http://digitallibrary.usc.edu/cdm/ref/collection/p15799coll17/id/496383, http://www.ncbi.nlm.nih.gov/pubmed/18605031 (1995)

18. Ghasemi-Fare, O., Pak, A.: Numerical investigation of the effects of geometric and seismic parameters on liquefaction-induced lateral spreading. Soil Dyn. Earthq. Eng. **89**, 233–247 (2016). https://doi.org/10.1016/j.soildyn.2016.08.014

19. Victor, M., Taboada-Urtuzuastegui, R.D.: Centrifuge modeling of earthquake-induced lateral spreading in sand. J. Geotech. Geoenvironmental Eng. 1195–1206 (1998)

20. IS 15284 (part 1): Design and construction for ground improvement-Guidelines (2003)

21. Law, H.K., Lam, I.P.: Lam periodic boundary 2001.pdf. J. Geotech. Geoenvironmental Eng. **127** 889–891 (2001)

Direct Shear Strength of Natural Rock Joints

Sandeep Bhardwaj and K. Seshagiri Rao

Abbreviations

τ	Shear strength of the split kota sandstone
σ_n	Normal stress in direct shear
φ_r	Residual angle of split kota sandstone
φ	Angle of internal friction in direct shear for split kota sandstone a, b, d are constants in power law
JCS	Joint compressive strength of split kota sandstone
C	Compresive strength of the joints
JRC	Joint roughness coefficient of split kota sandstone

1 Introduction

The basic concept of joint roughness was given by Barton [2] and Barton and Choubey [3] through joint roughness coefficient (JRC) in jointed rock mass. As suggested by Muralha et al. [7], a profilometer was employed to determine the joint roughness, and this is a simple devices that produce a series of linear roughness profiles of the specimen surface along the shear and transversal directions.

Tse and Cruden [13] and Maerz et al. [6] suggested the first derivative root mean square of Z coordinates in 3D space (Z_2) and roughness profile index (Rp) is used for calculation of estimation of joint roughness of the natural rock joint, and this joint roughness was strongly correlated with the shear strength of the joints.

Niktabar et al. [8] assumes that the natural rock joint is irregular and they described the JRC of the jointed Jodhpur sandstone as half of the triangular asperity angle, and joint compressive strength (JCS) of the jointed Jodhpur sandstone is similar to the unconfined compressive strength (UCS) value of the natural rock mass. They also suggest that asperity degradation in natural rock joints has larger

S. Bhardwaj (✉) · K. S. Rao
Indian Institute of Technology Delhi, New Delhi, India

impact in constant normal stiffness (CNS) condition as compared to constant normal load (CNL) boundary condition, and rate of asperity degradation was nonlinear for Jodhpur sandstone.

Thirukumaran [11] and Indrarantana et al. [5] considered shear strength of natural joint rock is dependent upon constant normal stiffness boundary condition. However, they assume Fourier series for calculation of dilation in shear strength of the natural joint. They also suggest that surface properties of the joint and boundary condition are critical for shear strength of the natural rock joints. Thirukumaran and Indraratna [12] suggest that rough joints were severely affected by constant normal stiffness boundary condition; however, low rough joints were less affected by constant normal stiffness boundary condition.

However, [1] suggest that as the joint length increases in the natural rock joints, the peak shear strength, peak dilation rate and shear stiffness decreases as the peak shear displacement increases.

The main objective of this paper is to co-relate the joint surface roughness of the split Kota sandstone with different joint shear strength criteria and to arrive at an impact assessment of joint roughness values on shear strength of the natural rock joints.

1.1 Material

Kota sandstone block of size $300 \times 300 \times 125$ mm of Rewa series of the Vindhyan formation (600 million years) was chosen for the study. Kota sandstone mainly consists of moderately sorted, well cemented and fine to medium sand grains. The SEM and XRD of this sandstone suggest that quartz is the predominant mineral bonded with ferruginous cementing material as shown in Figs. 1 and 2.

The index property of the Kota sandstone is shown below in Table 1.

2 Methodology

This Kota sandstone specimen of size 300 mm $\times$ 300 mm $\times$ 125 mm was split under the action of tensile force with the help of chisels and hammer, and a groove is cut of 2 cm on all four edges of the Kota sandstone specimen. And chisels were inserted in the groove by hammering; this induces tensile force in the rock and rock split into two halves of natural joints after two to three days. The split surface of the sandstone forms due to natural tensile force similar to in situ condition prevailing in the formation of joint. The methodology of splitting was taken from [8].
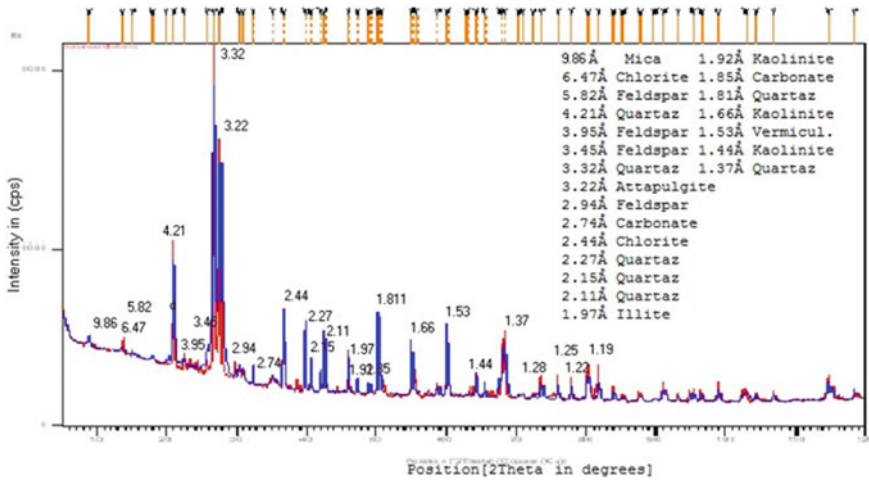
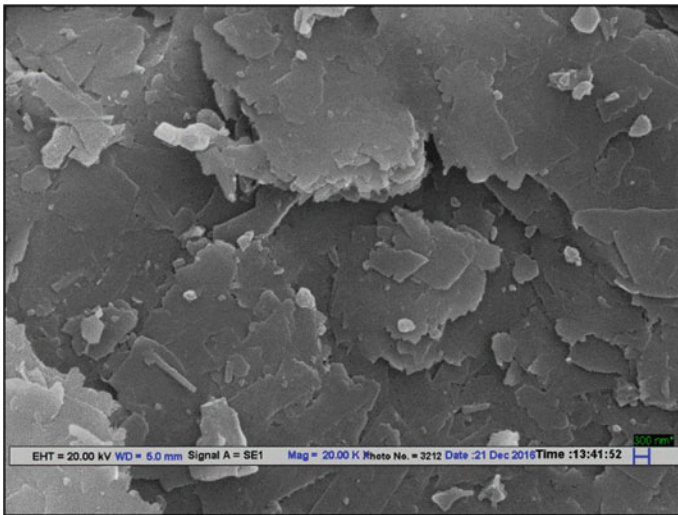Fig. 1 X-Ray diffraction (XRD) analysis of Kota sandstone

Fig. 2 Scanning electron microscopic (SEM) analysis of Kota sandstone

2.1 Roughness Measurement Through Profilometer

The surface roughness of the split sandstone specimen was obtained using the profilometer developed by Niktabar [9]. The specimen is placed on the profilometer table, which can be moved horizontally in both direction that is forward and backward. The X- distance is measured with a sampling interval of 10 mm. and

Table 1 Index properties of the Kota sandstone

S. No.	Property name	Value	Standard deviation	Ref. ISRM (2007)
1	Density, gm per cc	2.22		ISRM(1977)
2	Specific gravity	2.76		ISRM(1977)
3	Saturated density, gm per cc	2.31		ISRM(1977)
4	Brazilian tensile strength, MPa	2.45	0.04	ISRM(1978)
5	Point load index, MPa	3.21	0.44	ISRM(1985)
6	Uniaxial compressive strength, MPa	65.86	0.425	ISRM(1979)
7	Poisson's ratio	0.25	0.425	ISRM(1979)
8	Modulus of elasticity, GPa	11.76	0.425	ISRM(1979)

Y-distance is measured with a sampling interval of 5 mm. Z-distance is measured with the help of data acquisition system consisting of LVDT of length 20 cm. Analysis of profilometer data was detailed in [4].

Total four ranges of JRC values were identified for split Kota sandstone through profilometer. They are in Tables 2, 3, 4 and 5.

Table 2 First range of joint roughness coefficient varies from 7 to 10 on Barton scale

S. No.	Sample No	Joint roughness calculated through Z_2	Joint roughness calculated through Rp
1	ST2	5.90	7.76
2	ST5	6.91	9.91
3	ST14	5.46	8.37

Table 3 Second range of joint roughness coefficient varies from 11 to 14 on Barton scale

S. No.	Sample No	Joint roughness calculated through Z_2	Joint roughness calculated through Rp
1	ST6	6.66	13.33
2	ST9	9.65	13.94
3	ST10	7.59	11.93
4	ST13	6.58	10.66
5	ST17	7.44	11.91
6	AB1	5.88	14.45

Table 4 Third range of joint roughness coefficient varies from 15 to 18 on Barton scale

S. No.	Sample No	Joint roughness calculated through Z_2	Joint roughness calculated through Rp
1	ST11	8.14	16.37
2	ST12	7.36	15.12
3	ST16	7.57	15.76
4	ST37	10.02	18.10
7	B9	8.22	16.92
8	B4	8.64	17.49

Table 5 Fourth range of joint roughness coefficient varies from 19 to 20 on Barton scale

S. No.	Sample No	Joint roughness calculated through Z_2	Joint roughness calculated through Rp
1	ST8	7.03	21.44
2	ST15	8.08	22.85
3	AB16	11.43	17.95
4	B3	6.75	19.93
5	ST4	6.56	19.36
6	AB6	7.19	21.67

2.2 Direct Shear Facility

Direct shear test machine was developed by Shrivastava and Rao [10] at IIT Delhi, and testing was done in constant normal load (CNL) and constant normal stiffness (CNS) boundary condition at Rock Lab, IIT Delhi. The shear box size of the machine is 300 mm × 300 mm × 448 mm, with a gap of 5 mm between the boxes. Direct shear testing of Kota sandstone was done for three normal loads viz. 0.1 MPa, 0.5 MPa, and 1 MPa for four ranges of joint roughness of Kota sandstone. Peak shear-strength curve was plotted in Rocscience software for comparison with respect to joint roughness under CNL and CNS boundary condition.

3 Results and Discussion

3.1 Direct Shear Test Results of First Range

In Fig. 3, plotting was done for CNL boundary condition; in this range, specimen ST5 has maximum JRC, but highest peak shear strength was observed for specimen ST14. This clearly indicates that normal stress has larger influence as compared to joint roughness.
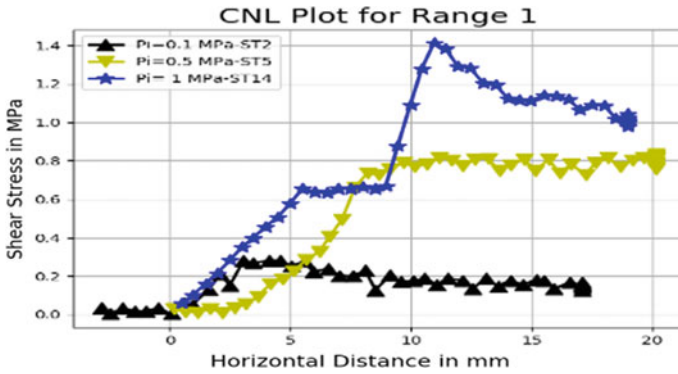
Fig. 3 Constant normal load plot for first range of JRC of Kota sandstone

3.2 Direct Shear Test Results of Second Range

In Fig. 4, plotting was done for CNL boundary condition; in this range, specimen ST6 and ST9 have similar JRC, but shear strength was influenced by normal stress.

In the above Fig. 5, plotting was done for CNS boundary condition; specimen AB1 has maximum JRC and normal stress in this range, and hence, it attained maximum peak shear strength.
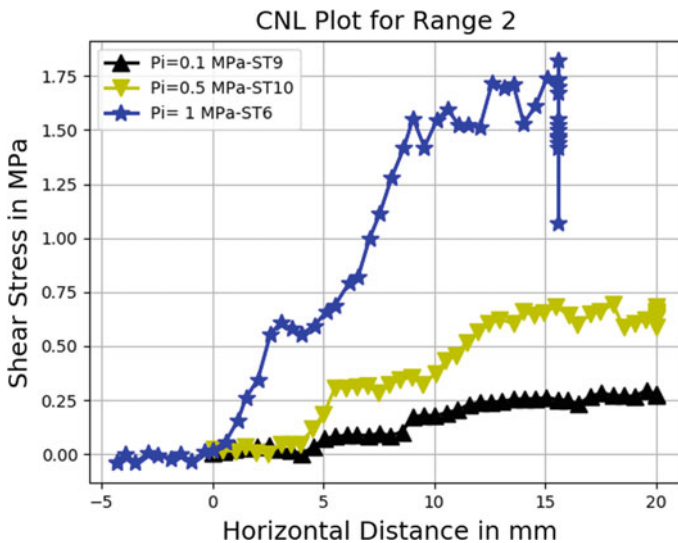

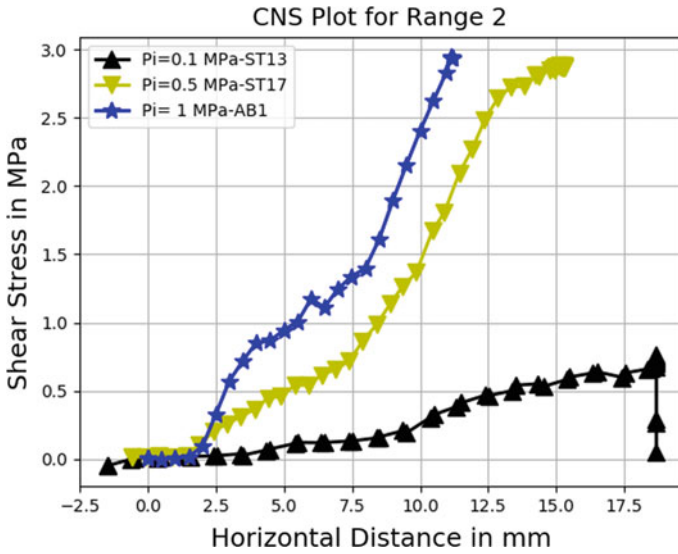Fig. 4 Constant normal load plot for second range of JRC of Kota sandstone

Fig. 5 Constant normal stiffness plot for second range of JRC of Kota sandstone

3.3 Direct Shear Test Results of Third Range

In the above Fig. 6, plotting was done for CNL boundary condition; specimen B9 and B4 have similar JRC, but ST37 have slightly higher JRC, the impact come in the form of sharp peak in shear-strength envelope despite lower normal stress for ST37.
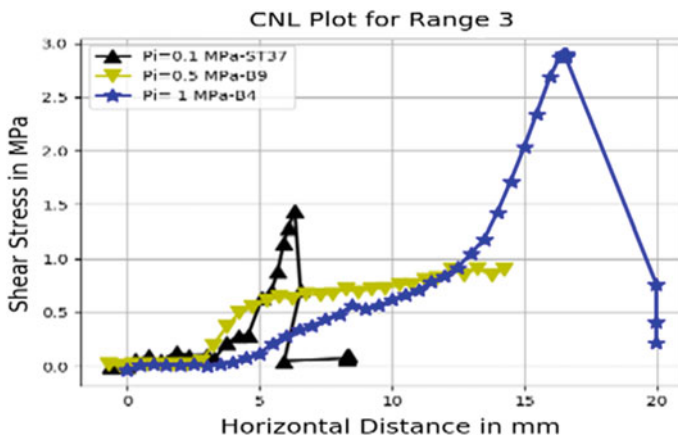

Fig. 6 Constant normal load plot for third range of JRC of Kota sandstone

In Fig. 7, plotting was done for CNS boundary condition, and specimen ST16 and ST12 have similar JRC, but ST11 have slightly higher JRC, the impact come in the form of sharp peak in shear-strength envelope despite lower normal stress for ST11.

3.4 Direct Shear Test Results of Fourth Range

In Fig. 8, plotting was done for CNL boundary condition; specimen ST8, AB16 and B3 have 20 plus order of JRC; here peak shear strength was influenced by normal stress only.

In Fig. 9, plotting was done for CNS boundary condition; sample ST15, ST4 and AB6 have 20 plus order of JRC, and here maximum peak shear strength was observed for ST4 and AB6, despite highest JRC was observed for ST15.

3.5 Shear-Strength Envelope for Direct Shear Test Results of First Range

In the analysis, shear-strength envelope was best fit with all suggested curve fitting method for first range of JRC. Plotting was done with the help of Rocscience. The summary of results is given below in Table 6.
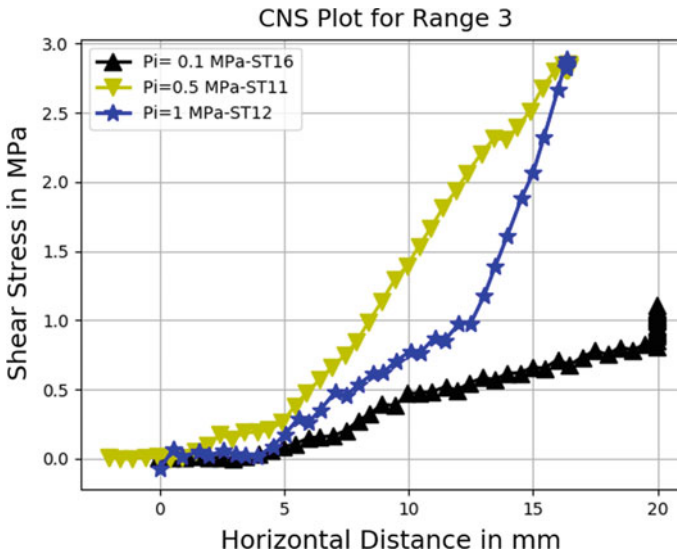

Fig. 7 Constant normal stiffness plot for third range of JRC of Kota sandstone
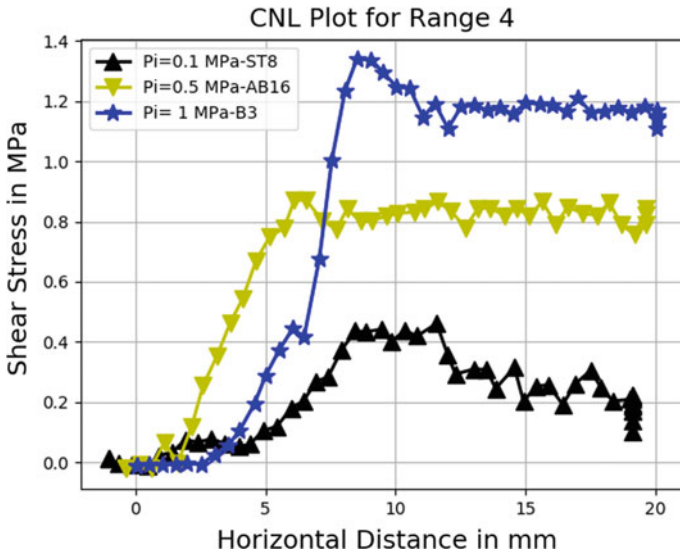
Fig. 8 Constant normal load plot for fourth range of JRC of Kota sandstone
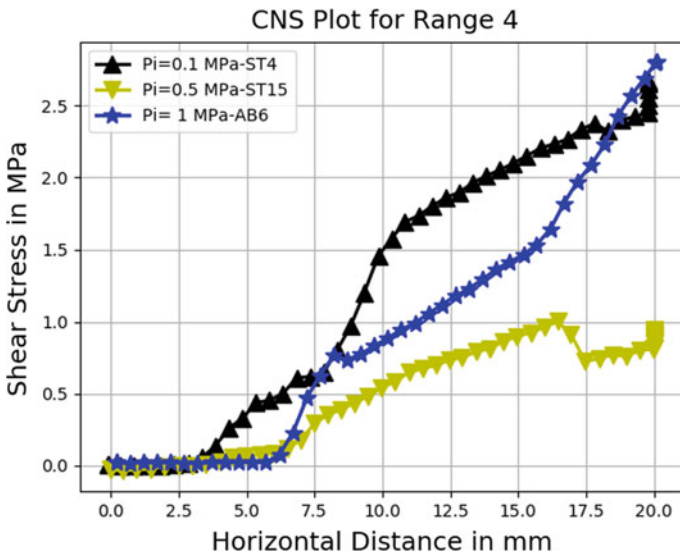

Fig. 9 Constant normal stiffness plot for fourth range of JRC of Kota sandstone

In the analysis, traditional shear-strength curve fitting method not giving satisfactorily result for second range of JRC under CNL boundary condition. However, power law fit gave satisfactory results for low normal stress. The summary of results is given in Table 6. Similar results were obtained for second range, and no

Table 6 Shear-strength envelope fitting for jointed Kota sandstone

S. No.	Barton Bandis Fit	Mohr coulomb fit	Power law fit	
1	$\tau = \sigma_n \tan\left[\varphi_r + \text{JRC } \log_{10}\left(\frac{\text{JCS}}{\sigma_n}\right)\right]$ $\varphi_r = 40°$ JRC = 12.588 JCS = 14.539 MPa	$\tau = C + \sigma_n \tan\varphi$ $\varphi = 51.213°$ $C = 0.179$ MPa	$\tau = a(\sigma_n + d)^b$ $a = 1.317$ $d = 0.084$ $b = 0.887$	Range 1 (CNL)
2	$\tau = \sigma_n \tan\left[\varphi_r + \text{JRC } \log_{10}\left(\frac{\text{JCS}}{\sigma_n}\right)\right]$ $\varphi_r = 35°$ JRC = 4.652	$\tau = C + \sigma_n \tan\varphi$ $\varphi = 58.296°$ $C = 0.052$ MPa	$\tau = a(\sigma_n + d)^b$ $a = 1.198$ $d = 0.271$ $b = 1$	Range 2 (CNL)
3	$\tau = \sigma_n \tan\left[\varphi_r + \text{JRC } \log_{10}\left(\frac{\text{JCS}}{\sigma_n}\right)\right]$ $\varphi_r = 60°$ JRC = 4.216 JCS = 11.305 MPa	$\tau = C + \sigma_n \tan\varphi$ $\varphi = 67.455°$ $C = 0.893$ MPa	$\tau = a(\sigma_n + d)^b$ $a = 3.262$ $d = 2.92e - 035$ $b = 0.5$	Range 2 (CNS)
4	$\tau = \sigma_n \tan\left[\varphi_r + \text{JRC } \log_{10}\left(\frac{\text{JCS}}{\sigma_n}\right)\right]$ $\varphi_r = 71°$ JRC = 5.278 JCS = 0.297 MPa	$\tau = C + \sigma_n \tan\varphi$ $\varphi = 59.731°$ $C = 0.843$ MPa	$a = 1.576$ $d = 0.568$ $b = 1$	Range 3 (CNL)
5	$\tau = \sigma_n \tan\left[\varphi_r + \text{JRC } \log_{10}\left(\frac{\text{JCS}}{\sigma_n}\right)\right]$ $\varphi_r = 10°$ JRC = 20 JCS = 69.163 MPa	$\varphi = 65.702°$ $C = 1.007$ MPa	$\tau = a(\sigma_n + d)^b$ $a = 3.231$ $d = 5.139e - 047$ $b = 0.5$	Range 3 (CNS)
6	$\tau = \sigma_n \tan\left[\varphi_r + \text{JRC } \log_{10}\left(\frac{\text{JCS}}{\sigma_n}\right)\right]$ $\varphi_r = 45°$ JRC = 20 JCS = 2.835 MPa	$\tau = C + \sigma_n \tan\varphi$ $\varphi = 44.307°$ $C = 0.375$ MPa	$\tau = a(\sigma_n + d)^b$ $a = 1.114$ $d = 0.253$ $b = 0.838$	Range 4 (CNL)
7	$\tau = \sigma_n \tan\left[\varphi_r + \text{JRC } \log_{10}\left(\frac{\text{JCS}}{\sigma_n}\right)\right]$ $\varphi_r = 10°$ JRC = 20 JCS = 91.624 MPa	$\tau = C + \sigma_n \tan\varphi$ $C = 1.054$ MPa	$\tau = a(\sigma_n + d)^b$ $a = 2.944$ $d = 0.039$ $b = 0.5$	Range 4 (CNS)

traditional curve fitting method works satisfactorily. However, power law fit gives satisfactory results for low normal stress under CNS boundary condition for second range of JRC. The summary of results is given in Table 6. No traditional shear-strength curve fitting method works satisfactorily for third range of JRC under CNL boundary condition. However, power law fit was suggested for shear-strength envelope for this range under low normal stress. The summary of results is given below in Table 6. Similar trend was obtained for third range of JRC under CNS boundary condition. However, power law fit will be suggested for this range of JRC of Kota sandstone for low normal stress. The summary of results is given in Table 6. For fourth range of JRC under CNL boundary condition results were similar to first range of JRC under CNL boundary condition. All traditional curve

fitting method works fine for this range. However, for sake of uniformity, power law fit was suggested for this range of JRC. The summary of results is given in Table 6. As previous fourth range of JRC under CNS boundary condition, no traditional curve fitting method works fine. However, for sake of uniformity, power law fit was suggested for this range of JRC. The summary of results is given in Table 6.

4 Conclusions

Following conclusions were drawn from the above analysis.

1. For constant normal s(CNS), no uniform traditional shear-strength curve fit gave satisfactory results. However, power law fit giving satisfactory results for all ranges of JRC under CNS boundary condition under low normal stress.
2. For first and fourth range of JRC giving best fit for all traditional shear-strength curve fit under constant normal load.
3. For CNS boundary condition, JRC has more influence as compared to CNL boundary condition.

References

1. Bahaaddini, M., Hagan, P.C., Mitra, R., Hebblewhite, B.K.: Scale effect on the shear behaviour of rock joints based on a numerical study. Eng. Geol. **181**, 212–223 (2014)
2. Barton, N.: Review of a new shear-strength criterion for rock joints. Eng. Geol. **7**(4), 287–332 (1973)
3. Barton, N.R., Choubey, V.: The shear strength of rock joints in theory and practice. Rock Mech. Rock Eng. **10**(1–2), 1–54 (1977)
4. Bhardwaj, S., Rao, K.S.: Quantification of joint roughness for Kota sandstone. In: Proceeding Indorock-2017, 7th Indian Rock Conf. New Delhi, India, pp. 161–170 (2017)
5. Indraratna, B., Thirukumaran, S., Brown, E.T., Zhu, S.P.: Modelling the shear behaviour of rock joints with asperity damage under constant normal stiffness. Rock Mech. Rock Eng. **48**(1), 179–195 (2014)
6. Maerz, N.H., Franklin, J.A., Bennett, C.P.: Joint roughness measurement using shadow profilometry. Int. J. Rock Mech. Min. Sci. Geomech. Abstr. **27**(5), 329–343 (1990)
7. Muralha, J., Grasselli, G., Tatone, B., Blümel, M., Chryssanthakis, P., Yujing, J.: ISRM suggested method for laboratory determination of the shear strength of rock joints: revised version. Rock Mech. Rock Eng. **47**(1), 291–302 (2014)
8. Niktabar, S.M.M., Shrivastava, A.K., Rao, K.S.: Shear behaviour of natural rock joint under CNS condition. In: Proceeding of Indian Geotechnology Conference Kakinada, India, pp. 1816–1825 (2014)

9. Niktabar, S.M.M.: Cyclic shear behaviour of jointed rocks under cnl and cns boundary conditions. Doctor of Philosophy thesis, Department of Civil Engineering, Indian Institute of Technology-Delhi (2016)

10. Shrivastava, A.K., Rao, K.S.: Development of a large-scale direct shear testing machine for unfilled and infilled rock joints under constant normal stiffness conditions. Geotech. Test. J. **36**(5), 1–10 (2013)

11. Thirukumaran, S.: Shear strength of degradable rock joints. Doctor of Philosophy thesis, School of Civil, Mining, and Environmental Engineering, University of Wollongong (2014)

12. Thirukumaran, S., Indraratna, B.: A review of shear strength models for rock joints subjected to constant normal stiffness. J. Rock Mech. Geotech. Eng. **8**(3), 405–414 (2016)

13. Tse, R., Cruden, D.M.: Estimating joint roughness coefficients. Int. J. Rock Mech. Mining Sci. **16**(5), 303–307 (1979)